CRITICAL CURRENT DEGRADATION IN Nb_3Sn SUPERCONDUCTORS IN ACCELERATOR MAGNETS

CIP-GEGEVENS KONINKLIJKE BIBLIOTHEEK, DEN HAAG

Oort, J.M. van

Critical current degradation in Nb_3Sn superconductors in accelerator magnets/ J.M. van Oort.
Proefschrift Universiteit Twente Enschede. - Met lit. opg.
- Met samenvatting in het Nederlands.
ISBN 90-36514029
Trefw.: supergeleiding / I_c degradatie / deeltjesversneller / magneet

Eerste Uitgave 2000
Druk: Universiteit Twente

CRITICAL CURRENT DEGRADATION IN Nb_3Sn SUPERCONDUCTORS IN ACCELERATOR MAGNETS

PROEFSCHRIFT

ter verkrijging van
de graad van doctor aan de Universiteit Twente,
op gezag de rector magnificus,
prof.dr. F.A. van Vught,
volgens besluit van het College voor Promoties
in het openbaar te verdedigen
op donderdag 3 februari 2000 te 16.45 uur.

door

Johannes Martinus van Oort
geboren op 7 mei 1967
te Roosendaal

Dit proefschrift is goedgekeurd door:

prof.dr. C. Daum (promotor),
prof.dr.ir. H.H.J. ten Kate (promotor).

Opgedragen aan Sjoerd en Tjeard

Contents

Preface and acknowledgment

The work described in this thesis has been carried out mainly in the Superconducting Magnet Group, Accelerator and Fusion Research Division, at the E.O. Lawrence Berkeley National Laboratory (LBNL), Berkeley, CA, USA. Most of the critical current degradation experiments were performed in the Low Temperature group at the University of Twente (UT), Enschede, The Netherlands. The majority of the writing phase has been completed during the evening hours and late at night, while at the GE Corporate Research and Development Center (GE-CRD), Niskayuna, NY, USA.

The text follows the American English spelling standard.

Certain figures that originate from color graphs are reproduced in full color in Appendix A for additional clarity.

I would like to thank all my friends and colleagues at LBNL for their input, support and many fun hours at Café Strada. I also thank my friends and fellow students at the UT for their help with the experiments and interpretation of the data. Next, I want to thank Kees Daum and Herman ten Kate for their patience, support and many red markings in the drafts leading to this thesis. Finally, many thanks to Gerda van Petersen for countless hours of reading, correcting, and rightfully criticizing and Trifon Laskaris and Bijan Dorri for their support during the part-time writing phase at GE-CRD.

This thesis has been printed with financial support of the GE Corporate Research & Development Center.

My apologies go to Gerda, Sjoerd and Tjeard for robbing them of many hours of family fun.

Niskayuna, September 1999 Johannes van Oort

Chapter 1

Introduction

As particle physicists strive to build colliders with higher and higher collision energies, the need for magnets with high field, exceeding 10 T, becomes more and more important. In order to achieve magnetic fields exceeding 10 T, the use of Nb_3Sn over NbTi becomes a necessity. Nb_3Sn, like other superconductors of the A15[1] class of materials, is inherently brittle.

This thesis deals with various aspects in the construction of a 13 T Nb_3Sn model accelerator dipole magnet. The basis for the successful construction of such a magnet is a thorough understanding of the sensitivity of the Nb_3Sn conductor to stress and strain, and a detailed measurement of the stress and strain in the magnet windings.

In this chapter the structure of the thesis is described. The objective of the research - the characterization of the critical current degradation as a function of stress and strain in a Nb_3Sn accelerator dipole magnet - is described.

[1] The A15 materials denote a certain class of materials with similar microstructure. They include, but are not limited to V_3Si, Nb_3Sn, Nb_3Al and Nb_3Ge.

1.1 Next generation colliders: towards very high field dipole magnets

The extension of the collision energy range in future hadron colliders towards 100 TeV requires a strong push for research into the properties of superconducting materials at fields exceeding 10 T. Currently, the work-horse of the superconducting magnet industry is the ductile material NbTi. This material has an upper critical field of approximately 10.8 T at 4.2 K. The practical use of NbTi in high field magnets is limited to a field range up to about 8.5 T. The majority of accelerator dipole magnet designs use NbTi at fields up to 8.4 T.

Unless very large collider rings are designed, such as the Eloisatron with a length of 355 km [1.1], dipole magnets with fields in the range of 10-12 T (VLHC) are required. Magnets of this field strength are also potential candidates for energy doublers in the LHC (currently under construction, with a dipole strength of 8.4 T and a length of 27 km), and other proposed colliders such as muon colliders and 100 TeV colliders.

With the emphasis on required maximum fields well below 10 T in the large scale projects currently under construction (LHC, Tevatron upgrade), Nb_3Sn research was placed in the background, since this material is more interesting for fields exceeding the 10 T range, where the applicability of NbTi is definitely exhausted.

However, much progress has been made in the research of both NbTi and Nb_3Sn, increasing the critical current density of NbTi in technical conductors two-fold in the years 1985-1990 [1.2]. Most of the research on Nb_3Sn has been focused on the increase of the critical current by improved manufacturing processes, and the inclusion of artificial pinning centers. The critical current behavior as a function of applied stress and strain has been studied for 20 years now in bulk material and wires.

The major difficulty in reaching 11-15 T with Nb_3Sn lies in the fact that Nb_3Sn is a brittle intermetallic compound. The combination of very high stress (120-180 MPa), low temperature (1.8-4.2 K) and high field (11-15 T) significantly complicates the design of the dipole magnets.

A few research groups around the world are working on technical solutions towards Nb_3Sn accelerator magnets that are economically viable for use in high energy colliders. Among these groups are several with significant research programs, such as CERN (Switzerland), Fermi National Laboratory (USA), E.O. Lawrence Berkeley National Laboratory (USA) and the University of Twente (The Netherlands).

The work described in this thesis was performed at the E.O. Lawrence Berkeley National Laboratory and the University of Twente under a joint research program.

1.2 Objective of the research

The research program closely follows the design, construction and finally testing, of the 13 T Nb_3Sn 1meter model accelerator dipole magnet "D20"[2], at the E.O. Lawrence Berkeley National Laboratory (LBNL). The objective of the research is the successful design, construction and test of this magnet.

During construction and operation of superconducting dipole magnets, high stresses and large strains can develop in the conductor windings. Critical to the success of the magnet is a good understanding of the sensitivity of the Nb_3Sn material to stress and strain.

The critical current carrying capability of Nb_3Sn decreases with increasing stress and strain. Large differences in the sensitivity of the material and conductors to stress and strain are documented in literature [1.3]. The differences are attributed to the composition of the material, geometry of the wire, heat treatment, and so on.

This study is an attempt to understand what improvements can be made of the critical current characteristics of Nb_3Sn Rutherford[3] cables in accelerator dipole magnets, and use this knowledge to optimize the magnet performance by minimizing the critical current degradation.

---

[2] All dipole magnets constructed at the E.O. Lawrence Berkeley National Laboratory (LBNL) are numbered sequentially as D1, D2, etc; D20 is the second all Nb_3Sn dipole magnet.

[3] A Rutherford cable is a multi-strand twisted cable in which the strands (wires) are wound around a mandrel and then flattened into a rectangular or trapezoidal cross-section.

1.3 What is needed

To develop an understanding of the critical current characteristics of the cables in the magnet, the research is divided in three different areas.

1) *The critical current degradation as a function of applied transverse stress in the cables*
   Significant differences are found in sensitivity, even for samples of the same material and wire geometry. In order to investigate this behavior, a systematic study of the critical current degradation as a function of applied stress in cabled Nb_3Sn is needed.
2) *The micro-structure of the wires in the cable*
   To determine the cause of the different behavior of geometrically identical samples, a detailed analysis of the microstructure before and after loading is required.
3) *The stress and strain distributions in the magnet coil windings*
   The next step is the determination of the actual stress and strain to which the cables will be subjected inside the magnet coil windings. Accurate measurement of the local stress and strain in the cables is a necessity, as well as a measurement of the pressure gradients on the magnet pole faces and median plane[4].

The next paragraph describes the strategy for investigating the cause of the variation in critical current degradation.

1.4 Experimental approach

In order to investigate the three separate areas described in the previous paragraph, several experiments are performed.

1) *Critical current degradation measurements*
   The critical current in a wire or cable can be defined in several ways. A definition of the critical current to be used in the critical current degradation experiments is given, based on a measurement of the voltage-current characteristics.
   To determine the critical current degradation in a cabled superconductor, several experimental methods can be used. They range from measurements on wires, wires extracted from cables, short cable samples to long cable samples and up to full magnet tests.
   The methods used for this thesis are tests on wires, extracted wires and short cable samples. The wire and extracted wire experiments are performed at LNBL, the cable measurements at the University of Twente (UT), The Netherlands.
2) *Analysis of the micro-structure*
   This analysis is performed with Scanning Electron Microscope (SEM) photos, in combination with Finite Element Analysis (FEA) modeling of the microstructure. The SEM photos are made before and after the cable experiments, and sections are taken out of unloaded and loaded parts of the cable for comparison.
   FEA models are made in ANSYS®[5]of the magnet, the cable geometry in the experiment, the cable structure itself, the wire structure, and finally the micro-structure of the filament areas.
3) *Stress and strain measurements in the coil windings*
   To accurately predict the performance of a magnet in which the coil winding stresses are of such magnitude that they contribute to critical current degradation, a detailed analysis of the stress and strain distribution is needed.
   Until the present, these stress and strain distributions are only computed using FEA, and in some cases, measured with large strain gauges averaging over a significant surface area in dedicated mechanical model coils called “cookies”.

---

[4] The median plane of a dipole magnet is defined as the x-z symmetry plane when the magnet is positioned with the bore along the z-axis. The pole face is defined as the face of the outermost conductor going from the x-axis (phi=0 degrees) towards the y-axis (phi=90 degrees)

[5] ANSYS is a Finite Element Analysis package by Swanson Analysis Systems.

A novel stress and strain measurement technique is designed, tested and used in the magnet, with greatly enhanced accuracy and spacial resolution. The method uses fiber-optic interferometers as sensing devices, directly embedded in the coil windings. The fiber-optic strain gauges are used in the tests of the mechanical model of the magnet alongside the resistive strain gauges to verify their operation.

1.5 Magnet performance prediction and experimental verification

Based on the cable measurements and the tests of the mechanical model, a prediction of the performance of the magnet can be made. This prediction is compared with the experimental data obtained in the final test of the magnet.

1.6 Structure of the thesis

Figure 1.1 shows a schematic overview of the thesis structure and the chapter relations and numbering. The following paragraph contains a brief summary of each chapter.

1.7 Chapter descriptions

The main line of this thesis follows the design and construction of a 13 T model accelerator dipole magnet, dealt with in chapters 2 and 8. Two side-lines look closer at FEA modeling of the magnet structure, cables, wires and wire internal structure in chapters 3 and 4, and the materials aspect of the design in chapters 5 and 6. The use of fiber-optics to measure stress and strain in an accelerator dipole magnet is presented in chapter 7.

Chapter 2 starts with a brief description of generic accelerator dipole magnet design. It is followed by an analysis of the origin of stress and strain.

With the inherent cause of the high stresses in the windings established in chapter 2, an analysis of the Rutherford cable geometry is presented in chapter 3. Using a novel FEA model of the deformation of a generic cable under transverse pressure, a model for the expected critical current degradation under transverse pressure is proposed.

Using FEA models, the influence of the internal structure of the different wire types is examined in chapter 4, and a correlation is found between the amount of voids present in the wire cross section and the observed critical current reduction under pressure. Based on the analysis presented, an ideal wire geometry for low stress sensitivity is defined.

In chapter 5 the results from the critical current measurements under transverse pressure are correlated with the cabling parameters and material properties of the wire. The results from the experiments, combined with data from the models in chapters 3 and 4, lead to a definition of an optimal cable design for low stress sensitivity.

The critical current measurements are directly followed by a microscopic analysis of the internal wire geometry, presented in chapter 6. Following the microscopic studies, a brief look at the void formation process, and the tin diffusion in the wire is presented. With the voids in the filament regions identified as one of the primary causes of the critical current degradation, methods are suggested to reduce the void formation during the reaction process by using a HIP[6]-step.

A novel fiber-optic stress and strain measurement technique, using intrinsic Fabry-Perot fiber-optic interferometers at cryogenic temperatures (4 K) is presented in chapter 7. This measurement technique is designed to measure the stress and strain, and particularly the high gradients, with a higher spatial resolution than possible with conventional resistive strain gauges. The design and construction of several conventional strain and stress sensors for use in the magnet is presented. Also described here is the design of the pressure transducers used to convert pressure in the coil windings to strain to be measured with the

[6] Hot Isostatic Pressure treatment.

interferometers. Calibration procedures and results, and an error analysis of the results of the measurements, are presented.

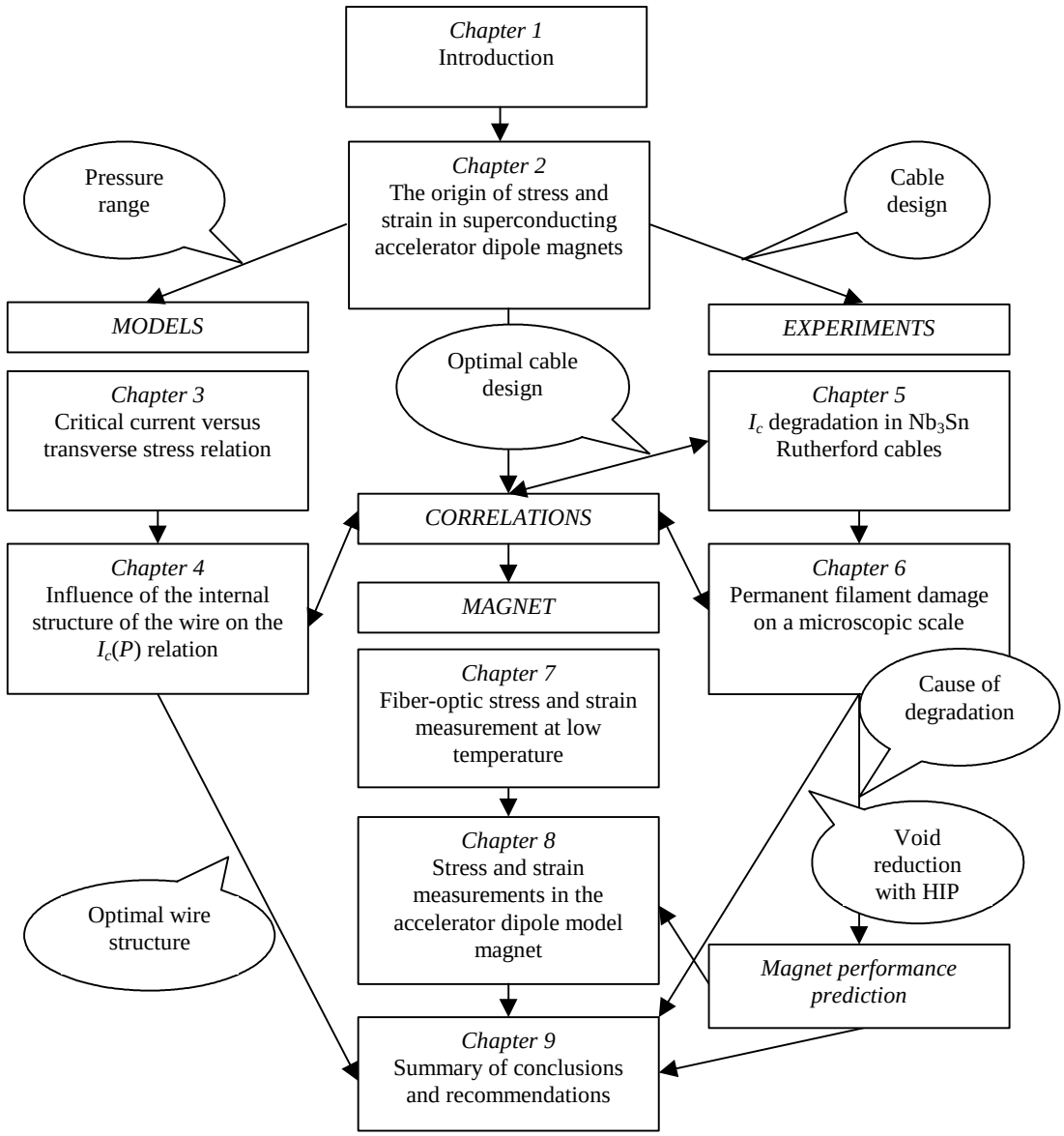

Figure 1.1 Thesis structure, chapter relations and numbering.

Chapter 8 picks up the main line with a detailed description of the mechanical design of the accelerator dipole magnet. The design choices are analyzed, and an overview of the construction process is presented. Also included in this chapter is a prediction of the maximum current the cables for the magnet are expected to carry under the computed stress, using the measurements presented in chapter 5. Based on this computation a prediction is made for the ultimate field of the magnet. The chapter is concluded with the

final test results of the magnet. It contains the test data and an analysis of the data for the first series of *training* quenches[7]. The test data is compared with the prediction of the performance. The training behavior is analyzed with both conventional strain gauges as well as with the novel fiber-optic sensors. A correlation between the results of the two systems is discussed. Based on the strain measurements, recommendations for the cool-down and warm-up phase of the magnet are made.

Chapter 9 contains a summary of the conclusions for each chapter.

1.8 Summary

This thesis attempts to push the material, conductor and magnet designers into the right direction to alleviate problems experienced with critical current degradation in Nb_3Sn accelerator dipole magnets.

Not only the design of the cross section of the wire plays an important role, but also the method in which the material is used afterwards, i.e. the cabling process, the winding design, and stress applied in the final magnet configuration. Wherever possible, optimal process parameters and suggestions for the minimization of the critical current degradation are given.

[7] A quench is the event in which the superconductor switches suddenly from the superconducting state to the normal state. Usually this causes the entire magnet to switch to the normal state. When the magnet is then ramped again, it generally reaches a higher field than before. This phenomenon is called *training* of the magnet. A magnet is usually trained until it no longer gains in field with each consecutive quench; it is then said to have reached the *plateau*. Training is an undesirable phenomenon, since it is more desirable to never have to quench a magnet to reach the operating field.

Chapter 2

The origin of stress and strain in superconducting accelerator dipole magnets

In this chapter the principles of generic superconducting accelerator dipole magnet design are described. A brief history is given of previous high field accelerator dipole magnets.

Several coil geometries that can be used to generate a dipole field are presented.

Next, the origin of stress and strain in accelerator dipole magnets during construction, cooling-down, operation and warming-up is discussed.

The chapter concludes with a description of the implications of the overall stress and strain patterns on the cable stress and strain.

This chapter is the general introduction to the main topic of the thesis with respect to stress and strain analysis and measurements.

2.1 Introduction

Most modern high energy accelerators utilize a so-called storage ring collider, in which the particles circulate in *bunches* around the ring. Over a given period of time, the ring is filled with particle bunches traveling clockwise and counter-clockwise. When enough bunches are stored in the ring, bending and focusing magnets redirect the beams to collide at intersection points. The resulting collisions are investigated using detectors around the intersection points.

A particle with mass m, charge q and relativistic momentum $\vec{p}$, traveling at a relativistic velocity $\vec{u} = \vec{p}/m$ in a magnetic field $\vec{B}$, experiences a bending force $\vec{F}$ as in

$$\vec{F} = q\vec{u} \times \vec{B} = q\frac{\vec{p}}{m} \times \vec{B}. \tag{2.1}$$

Equation (2.1) shows that a particle can be bent around a horizontal arc by applying a magnetic field in the vertical direction. In a collider, dipole magnets are used to bend the particle beam. The radius R of the ring is determined by

$$R = \frac{p}{qB}, \tag{2.2}$$

with p the magnitude of the particle's momentum, and B the magnitude of the bending field of the dipole magnets. The collider radius is inversely proportional to the *magnetic length* of the dipole. The magnetic length is the integral of the dipole field over the length of the magnet. Since only part of the ring length is available to place dipole magnets, the actual ring length L required is greater than the minimum derived from equation (2.2) ($L = 2pR$ for a circular collider).

In order to keep the collider length at a minimum, the magnetic field has to be as high as possible. Also, increasing the particle momentum while maintaining the same radius requires a higher magnetic field.

With an upper critical field[1] B_{c2} of approximately 10.8 T (at 4.2 K) for NbTi, in practice this material is limited to use in magnets with central fields of up to about 9 T. For higher central fields, a material with a higher B_{c2} such as Nb_3Sn, Nb_3Al or BSCCO has to be used. Due to the higher cost of these materials as compared to NbTi, the design field is usually limited to 10 T. NbTi still remains the "work-horse" of the large scale magnet industry. Table 2.1 lists the relevant parameters of several large colliders [2.1], all using NbTi for the magnets.

Accelerator	Ring circumference [km]	Particle energy [TeV]	B [T]	Magnet length [m]	Number of dipole magnets
RHIC	3.8	0.1 per amu (Au)	3.5	9.5	288
Tevatron	4.7	1	4.4	6.0	774
HERA	6.3	0.8	4.7	9.0	422
UNK	20	3	5.0	6.0	2160
SSC	86	20	6.6	17	8000
LHC	27	7	8.4	12	1792

Table 2.1 Relevant parameters of several large colliders. Listed are circumference, particle energy, dipole magnetic field B, magnet length and number of dipole magnets in the ring.

The particle beam traveling in the bore of the magnet is not restricted to the center of the beam pipe. Since each particle trajectory has to curve an equal amount, the magnetic field has to be uniform in the entire area traversed by the particles. The maximum tolerated inhomogeneity is generally set at 100 ppm (10^{-4}) on a radius of 1 cm around the center of the beam pipe.

[1] The upper critical field B_{c2} is the maximum field at which the bulk of the material can be in the superconductive state. B_{c2} is an intrinsic material property, and is a function of temperature and mechanical stress (lattice size).

2.2 History

Up until 1996 several attempts have been made to build an accelerator dipole magnet with a central field in excess of 10 T using NbTi or Nb_3Sn, however none of the designs were successful in exceeding 10 T. The first magnet to surpass the "10 T barrier" was a 1 m NbTi model dipole (D19) at LBNL [2.2].

Figure 2.1 shows a history of selected accelerator dipole magnets.

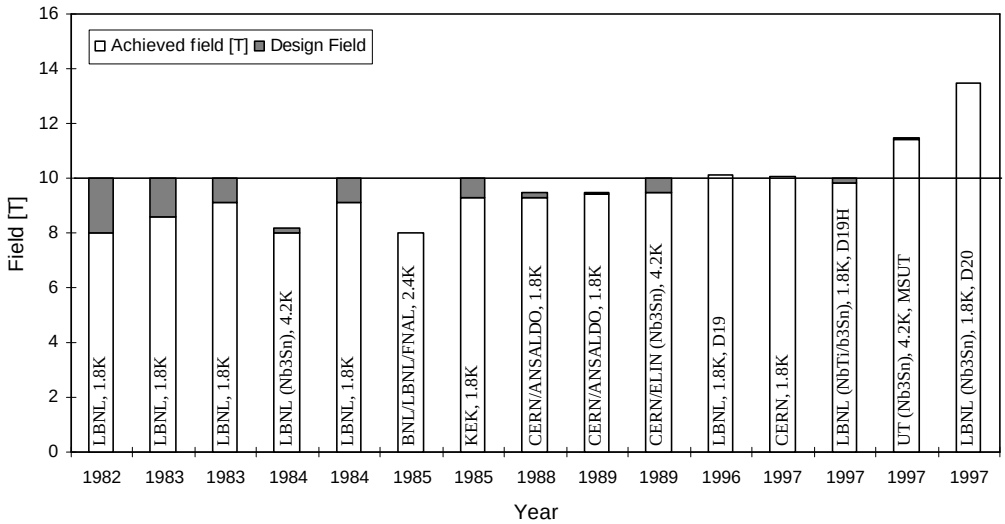

Figure 2.1 History of accelerator dipole model magnets from 1982 to 1997. The gray bar indicates the design field, whereas the white bar shows the achieved field. The horizontal line denotes the "10 T barrier". The designing laboratory and/or company is printed in the bar together with the operating temperature at which the field is stated. The superconductor used is NbTi unless noted.

This success was quickly followed by a model magnet for the future LHC collider at CERN [2.3] in 1997. Both magnets used superfluid helium at 1.8 to 1.9 K to achieve this field.

The next magnet to reach a field close to 10 T was a hybrid NbTi/Nb_3Sn model dipole (D19H) at LBNL [2.4]. This magnet was a modification of the earlier successful NbTi magnet, in which the inner NbTi layer was replaced with Nb_3Sn.

A big breakthrough came with the completion of a model dipole (MSUT) at the University of Twente. This magnet was initially designed as a dual-bore 10 T, all Nb_3Sn magnet. It was later modified to a 12.5 T design field (at 1.8 K) single-bore dipole magnet. During testing, the magnet ramped up to 11.1 T (at 4.2 K) without a single training quench [2.5].

The last magnet in the timeline is the Nb_3Sn 13 T magnet (D20) described in this thesis [2.6]. The magnet was tested successfully in 1997, and reached a maximum field of 13.5 T (at 1.8 K) after many training steps.

2.3 Coil winding geometries

For accelerator magnets, the coil windings are usually placed outside of the vacuum space containing the particle beam. The type of magnet desired, i.e. a dipole field for bending, quadrupole field for focusing, or higher order fields for error correction, determines the geometry of the windings.

The magnetic field $\vec{B}$ can be written as a complex variable $\vec{B} = B_y + iB_x$. With $\vec{z} = x + iy$, m_0 the permeability of free space, $\vec{J}$ the current density, and $\vec{B}$ satisfying Maxwell's equation $\nabla \times \vec{B} = m_0 \vec{J} = 0$ in a current free region, this yields

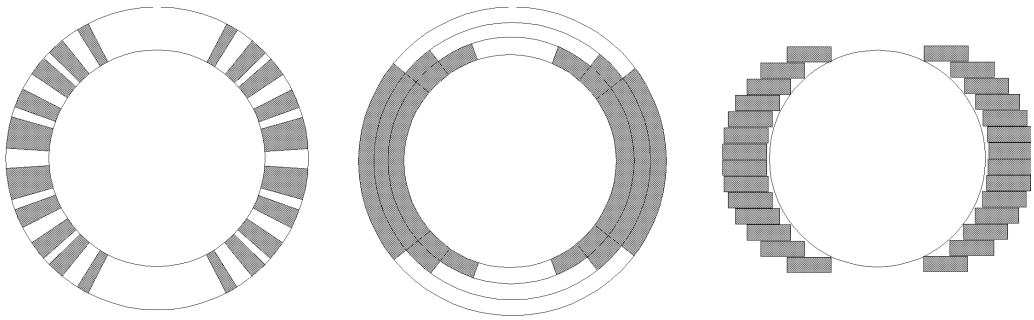

Figure 2.3 Several coil cross-sections that approximate an ideal cosine-q geometry.

Several other geometries can be used to produce a satisfactory dipole field, such as block (or window-frame) designs [2.7], [2.8], split pair magnets [2.9], the Vobly designs [2.10] or even more exotic ones like the pipe dipoles [2.11]. However, all of these require more ampere-turns to produce the same central bore dipole field. These geometries will not be treated in this thesis.

2.4 Stress and strain in accelerator dipole magnets

The combination of current, field and radius causes large forces in the coils. These forces are balanced by a containment structure, preventing large deformations in the coils. Large stresses are generated by these forces, resulting in strain in the superconductor. These forces will also elongate the coils in the longitudinal direction due to the Poisson effect[2], usually requiring a containment structure.

The following sections describe the different components of the force, stress and strain. First, the Lorentz force is described, followed by a definition of pre-stress. Next, the transverse and longitudinal components of pre-stress are discussed, and several methods of applying it are illustrated.

2.4.1 Lorentz force and transverse pre-stress

The Lorentz force $\vec{F}$ exerted by a conductor carrying a current $\vec{I}$ in a magnetic field $\vec{B}$ is equal to

$$\vec{F} = \vec{I} \times \vec{B} \,. \tag{2.6}$$

Since both the current and the magnetic field are large, the force on the conductor can become very large. For example, in the D20 magnet this amounts to approximately 13 MN. The force on the coils is proportional to the square of the magnetic field, as the field is proportional to the current. Outside of the coil winding region, the resultant force from the coil windings is directed radially outwards. This results in a large force exerted against the containment structure.

This force has to be balanced by an equal and opposite force from the containment structure to prevent the conductors from deforming, defining the first part of the so-called *pre-stress*. This pre-stress can either be applied indirectly by a force F_x in the horizontal direction [2.7], [2.11], or directly by a uniform radial force [2.5],[2.6].

In magnet mechanical design, the following four distinct stages are considered :

1) *assembly at room temperature :* at this time the pre-stress is applied to the coil windings. In most cases, this is the stage where the stress is the highest on the coils;
2) *cooling-down from room temperature to operating temperature* : the stress changes due to coils shrinking with a different amount compared to collar and yoke;

[2] When a material with length l is stretched in the longitudinal direction by Δl, it will contract in the unconstrained directions perpendicular to the stretch (width w and height h) as $\Delta w/w = \Delta h/h = -\nu \cdot \Delta l/l$. The constant ν is a material property called the Poisson's ratio. Conversely, compressing the material in width and height (or radially) results in a longitudinal elongation.

3) *operation at full current* : the stress changes due to the Lorentz forces acting on the coils. Stress will increase at the median plane and decrease at the poles;
4) *warming-up from operating temperature to room temperature*: the stress changes due to coils expanding by a different amount compared to collar and yoke.

The following paragraphs describe the four stages in detail, using a generic dipole magnet as an example.

In chapter 8 the details of the D20 assembly are discussed.

2.5 Assembly at room temperature

The first stage in the design is the application of pre-stress at room temperature. Two components are discussed, the transverse (radial), and the longitudinal pre-stress.

To prevent the coils from deforming too much (excessive strain could damage the superconductor, and distortion of the coil shape causes field errors), radial pre-stress is applied to the coils through the collar or yoke. Depending on the magnitude of the required pre-stress, the collar can be designed to provide the full load, part of it, or be used as an alignment structure only.

The load itself can be applied by using a hydraulic press [2.3], by bolt structures [2.7], shrink cylinders [2.5] or a tensioned wire wrap method [2.6]. The method chosen for the D20 magnet is a wire wrap technique, as described in detail in chapter 8. Several methods of transverse (radial) pre-stress application are shown in paragraph 2.5.1.

The stress originating from radial pre-stress application, compression due to cooling-down, and Lorentz force results in the need for longitudinal pre-stress of the magnet. This is caused by the radial stress that generates a longitudinal elongation due to the Poisson effect.

In order to control and limit this elongation, a longitudinal pre-stress is applied to the ends of the magnet in most cases (the pre-stress is not needed if elongation is not exceeding limits imposed by the materials used, and might even be beneficial due to a slight increase in critical current in the superconductor). The application of longitudinal pre-stress is discussed in paragraph 2.5.2.

2.5.1 Application of transverse (radial) pre-stress

There are several methods to constrain forces in the coil system, as illustrated in figure 2.4:

A) freestanding collar method: the Lorentz force is entirely constrained by a strong collar around the coils. The collar is generally made of high strength aluminum or stainless steel. Indexing slots in the iron yokes for returning the field are matched to pins or ribs on the collar to align the coils. A thin outer shell is used for alignment only. The advantage is a stiff coil system with good tolerance; the disadvantage is the need for a large structural collar (several cm radially), thus reducing the effectiveness of the contribution of the iron to the field;
B) all forces through the yoke: this method uses the entire magnet structure to constrain the forces. The Lorentz force is transmitted through a thin collar (used for alignment only, which can be a few mm in thickness), through the iron yoke to an outside containment structure, such as a stainless steel cylinder. The thinner collar allows the iron yoke to be closer, thus enhancing the field strength. The disadvantages are the need for higher mechanical tolerances on the large yoke parts, since they are now part of the constraining structure, and lower field quality (non-linear load-line) due to saturation in the iron yoke;
C) partial collar support: this is a mix of both methods. Part of the force is constrained by a medium size collar (of the order of a cm radially), the remainder is constrained by the yoke. The advantages are a higher field strength due to the smaller collar, and the tolerances on the yoke parts are not as stringent as with the previous method. The disadvantage is the need for good strain or stress instrumentation during the assembly to assure the application of the correct amount of pre-stress in each step.

$$\frac{\partial B_x}{\partial x} + \frac{\partial B_y}{\partial y} = 0,$$
$$\frac{\partial B_y}{\partial x} - \frac{\partial B_x}{\partial y} = 0. \tag{2.3}$$

A possible solution of (2.3) is a current sheet with a current density distribution $j_q = j_0\cos(nq)$ on a cylinder $\vec{z} = re^{iq}$. This current distribution is generally called a *cosine-q* distribution. For $n = 1$ this produces a perfect dipole field, $n = 2$ produces a perfect quadrupole field, and so on. The cosine-q current distribution on a sheet is very difficult to realize in a practical manner.

A more practical method to produce a perfect dipole or quadrupole field is to use overlapping cylinders. The field in a plane perpendicular to the axis of a cylinder carrying a uniform current density j with radius r_c at a distance $r < r_c$ from the cylinder axis is

$$B_t = m_0 j \frac{r}{2}. \tag{2.4}$$

Then, the field produced in the central area of two overlapping cylinders with opposite current is equal to

$$B_y = \frac{m_0 j}{2}\{-r_1\cos q_1 + r_2\cos q_2\} = \frac{-m_0 j s}{2},$$
$$B_x = \frac{m_0 j}{2}\{r_1\sin q_1 - r_2\sin q_2\} = 0. \tag{2.5}$$

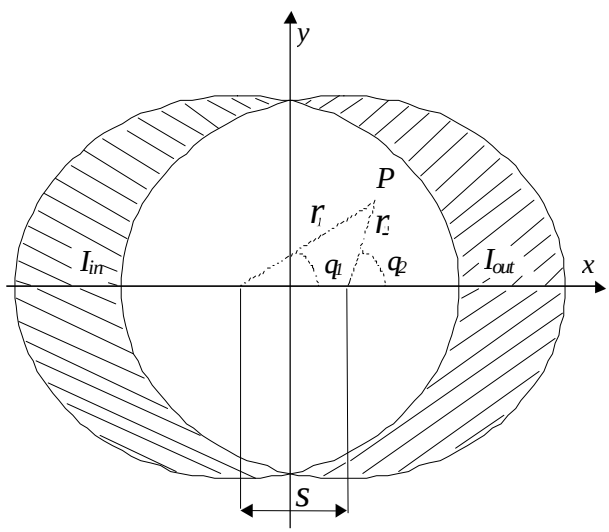

Figure 2.2 Two overlapping cylinders with a center distance s carrying equal currents in opposite direction produce a perfect dipole field at any point P in the overlap region.

These equations describe a perfect dipole field B_y over the entire overlapping area. Since this area would carry equal opposing currents, it is a current free region. Thus, it can be eliminated, forming the aperture for the particle beam. Figure 2.2 illustrates the concept of the overlapping cylinders, and defines the symbols used in (2.5).

Since it is impractical to wind a current sheet with a continuously variable current density, the cosine-q form is approximated by stacking discrete conductors to simulate the continuous current distribution as close as possible. The required high field quality is achieved by shaping the conductor area to generate an as perfect as possible dipole field in a large region of the beam-pipe. Figure 2.3 shows several coil configurations based on these layouts that produce high quality dipole fields.

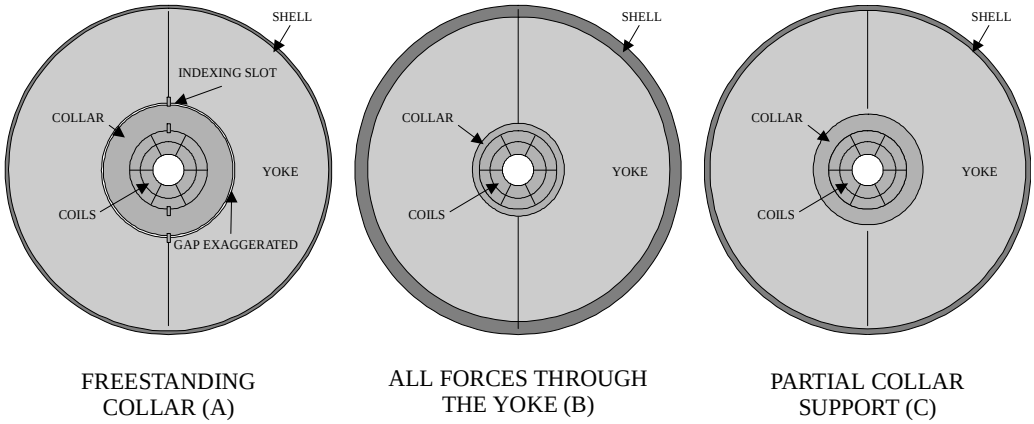

Figure 2.4 Illustration of three different methods for pre-stress application. In the freestanding collar, all forces are contained within a thick collar, that only touches the yoke at indexing slots for alignment. A thin outer shell is used for alignment only (A). If all forces are supported by the yoke, a thin collar and thick shell are used. The collar is in full contact with the yokes, but does not support the load (B). With partial collar support, the collar touches the yokes, and part of the load is transmitted to the yokes. A medium thickness shell is used to support the transmitted load (C).

2.5.2 Application of longitudinal pre-stress

Longitudinal pre-stress can be applied by constraining the coils with end-plates connected to a shell around the magnet, as illustrated in figure 2.5. The magnet winding, collar and yoke are inserted in a free-standing shell. The shell is then connected to the flanges at both ends.

The load is either applied by welding the shell to the flanges while the magnet is under longitudinal compression, or by torque-bolts pushing on the coil through the flanges. The reaction load is supported by the shell, which is in tension.

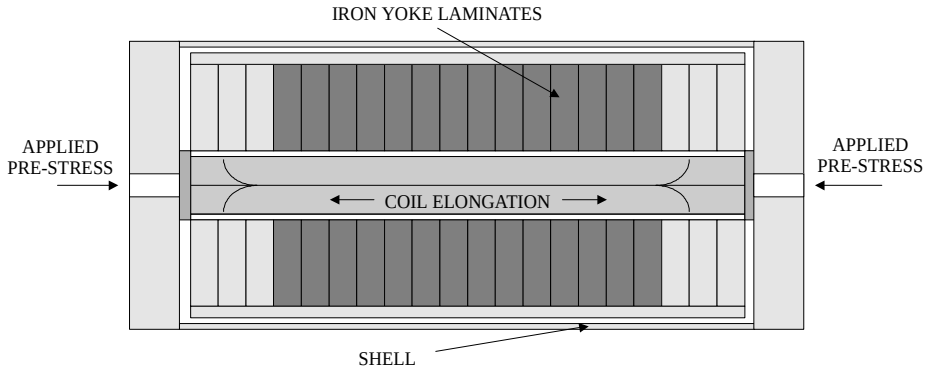

Figure 2.5 Schematic of longitudinal pre-stress application. A longitudinal cross-section of a generic dipole magnet is shown, illustrating the coil, yoke, end-plates and shell.

Another method to apply the end load is to combine the function of the radial shell and the longitudinal shell into one. In this case, the shell is in direct contact with the yoke, and the end plates are welded to the shell. Longitudinal pre-stress is applied by loading the ends while the welds are made, or by

bolts through the end plates. The reaction load is distributed to the yokes, collar and coil by friction. In this case, the yokes are generally held together by tie-bolts (in tension) through the structure.

Generally, the end plates are designed to limit the elongation of the coils to a safe value, determined by the maximum superconductor strain divided by a safety factor. The details of the magnet end load are analyzed in chapter 8. The following three paragraphs describe pre-stress in the three stages related to magnet operation.

2.6 Cooling-down

The second stage in the design is the cooling-down to 4.2 K or 1.8 K. The different components of the magnet cross section have different thermal expansion coefficients, which will cause a change in the stress distribution of the coil package. When the temperature of the coil system is lowered from 293 K to 4.2 K or 1.8 K, the pre-stress on the coil will decrease. The directions of the dimensional changes are illustrated in figure 2.6.

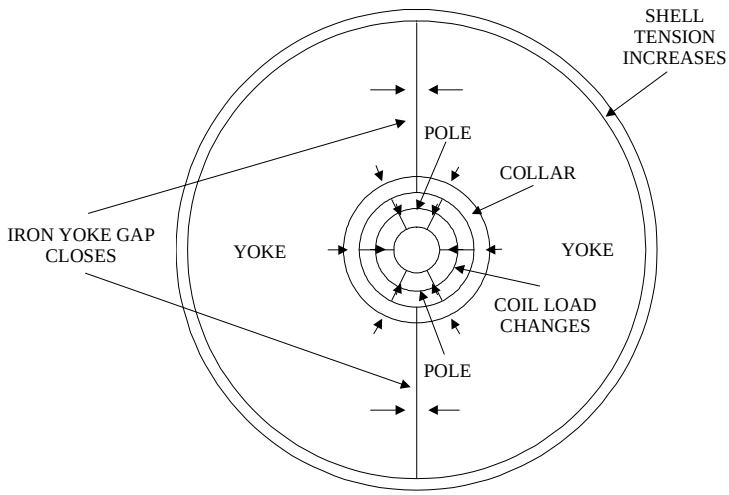

Figure 2.6 Cross-section of a generic dipole magnet structure during cooling-down. Differences in thermal expansion will cause a stress reduction on the coil windings.

The total shrinkage of each component is determined by the integral of the thermal expansion coefficient $\alpha(T)$ from room temperature to liquid helium temperature times the length l (or radius), given by

$$\Delta l = -l \cdot \int_{T=293}^{T=4.2} \alpha(T)\, dT. \tag{2.17}$$

Table 2.2 lists the integrated thermal expansion of the materials used in the magnet. The cooling-down is assumed to be slow enough to allow all magnet components to be at the same temperature.

As is evident from table 2.2, the coil and stainless steel wire wrap will shrink more than the iron yoke. While the structure is shrinking, the iron will initially follow the shrinking coil (it is pressed against the coil by the tensioned wire wrap) until the gap in the iron yoke is closed. Further lowering of the temperature results in reduction of pre-stress on the coils.

In the longitudinal direction, the same difference in shrinkage changes the stress on the ends of the coil, as is illustrated in figure 2.7.

Material	Integrated thermal expansion coefficient α	Reference
Coil structure/Nb_3Sn cables (impregnated)	-2.8×10^{-3} to -3.5×10^{-3}	[2.13]
Aluminum (5%) bronze (collar)	-3.8×10^{-3}	[2.14]
Iron yoke	-2.0×10^{-3}	[2.14]
Stainless steel (yoke)	-2.97×10^{-3}	[2.14]
Stainless steel (wire wrap)	-2.97×10^{-3}	[2.14]
CTD-101 epoxy	-12×10^{-3}	[2.12]

Table 2.2 Integrated thermal expansion coefficients for the materials used in the magnet.

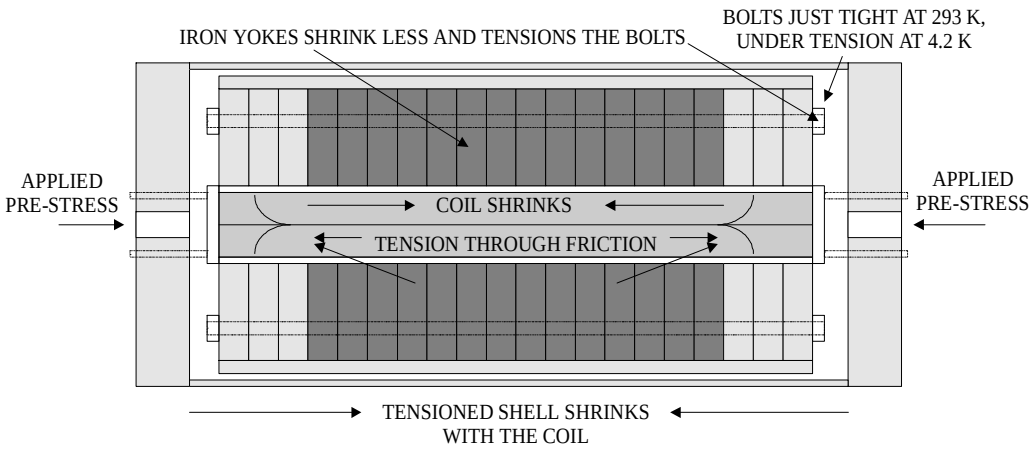

Figure 2.7 Longitudinal cross-section of the D20 coil structure.

The yoke plates are held together by tension bolts. These bolts shrink by about the same amount as the coils and the stainless steel outer shell. The iron yoke plates shrink less, thus straining the coil and the bolts. Because the smaller shrinkage of the iron yokes counteracts the larger shrinkage of the coils and stainless steel shell, the final pre-stress on the coil ends is difficult to determine. Assuming that the friction coefficient is high enough to prevent the coil from slipping inside the iron yokes, the pre-stress will increase on the end plates during the cooling-down of the magnet.

2.7 Lorentz force at the operating current

The third stage is operation at low temperature and full current. At this point, the stress on the pole faces is low, but still compressive. When the magnet is energized, the coils will try to move towards each other in the median plane, and outward radially, thereby increasing the pressure on the horizontal symmetry plane. This will be the area of highest stress in the magnet during all stages.

A balance has to be found in the design to assure contact at all times in the pole areas to avoid the epoxy bond with the pole from breaking, while minimizing the stress on the horizontal median plane to avoid damaging the conductor.

Figure 2.8 illustrates the direction of the forces. The Lorentz force on the coils tries to bend the yoke plates outward, decreasing the compression on the yoke gap. Since this gap has to remain closed during operation to ensure structural integrity of the support structure, the applied pre-stress has to be large enough to counteract the bending moment on the yoke plates.

Figure 2.9 illustrates the forces on the coils in the longitudinal direction. The Lorentz force elongates the coils due to the radial constraint and the Poisson effect. This longitudinal force is partially reacted directly against the end plates through bolts pushing against the coil ends.

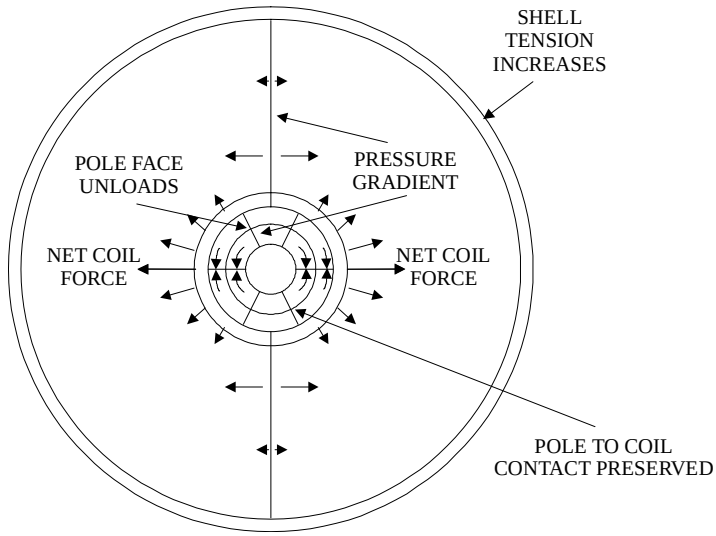

Figure 2.8 Simplified illustration of the direction of the radial forces during operation of the magnet.

The rest of the force is transmitted through the yoke plates onto the tension bolts holding the yoke plates together. The actual ratio of the two forces is determined by the friction coefficient between the coil, collar and yoke.

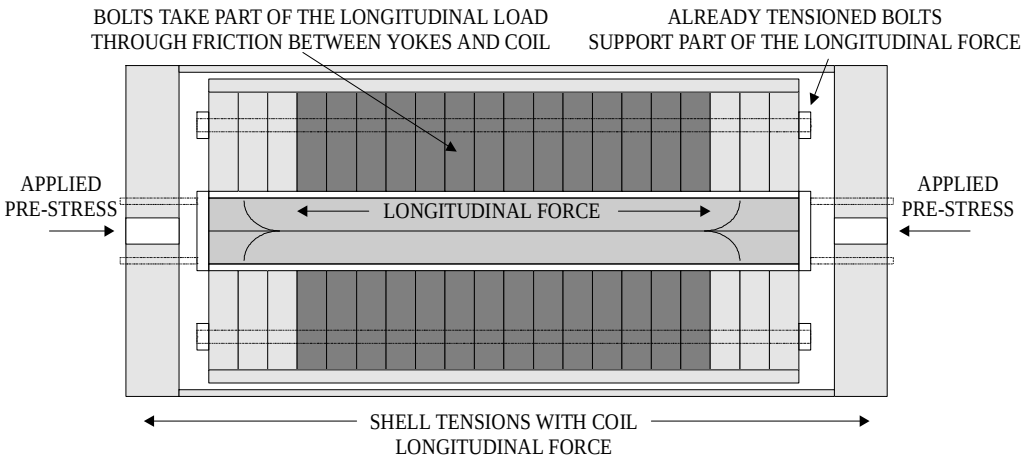

Figure 2.9 Simplified illustration of the direction of the longitudinal forces during operation of the magnet.

2.8 Warming-up

The fourth and last stage in the design is the warming-up from operating temperature to room temperature. If the warming-up is performed slow enough to ensure that all magnet components are at the same temperature throughout the process, there is no difference between cooling-down and warming-up.

However, in the experiments performed on the magnet, both the cooling-down and warming-up rates were high enough to cause significant temperature gradients in the magnet structure. For the cooling-down, this is not an issue, since the coil windings cool down faster than the iron yoke, causing a temporary reduction in both transverse and longitudinal pre-stress.

In the warming-up, the coil windings warm up faster than the iron yoke, causing the stress on the windings to increase to values far above the design pre-stress. Depending on the magnitude of the temperature gradient, this increased stress has the potential to cause damage to the superconductor.

2.9 Stress concentrations in the coil cross-section

The local stresses can be higher than the overall stress due to the difference in material properties and shape of the coil, amounting in stress concentrations of up to 120 MPa in the magnet under full operating current. FEA models of the coil cross-section [2.15] show stress concentrations around the aluminum-bronze wedges in the poles (see figure 2.6) and between coil blocks (see figure 2.3 left cross-section). These effects have to be taken into account in the design of the magnet by adding a safety margin to the maximum pre-stress on the coils.

2.10 Stress and strain on the individual cables

The stress and strain distributions described in this chapter can now be applied directly to the cables for a correlation with actual cable measurements. From the FEA models of the coil structure in chapter 3, the actual pressure and pressure gradient across the cable surface can be determined. Given this information, an estimate can be made of the internal stress on the individual wires within the cable, and of the stresses on the Nb_3Sn filaments within the wires.

2.11 Summary

In this chapter the origin of stress and strain in accelerator dipole magnets is described. Both the radial (or transverse) and longitudinal components are discussed. The design of the magnet mechanical structure is described in four stages, the pre-stress at room temperature, the cooling-down, the operation at low temperature, and finally the warming-up.

The stress patterns described in this chapter can now be applied to the next smaller level, the cable in the coil windings. In chapter 3, the FEA models of a dipole magnet, and the cables in the magnet, are described. Stress concentrations in the coil windings, as briefly mentioned in paragraph 2.9, will be discussed in detail. Chapter 4 describes the FEA models of the internal wire structure.

Chapter 3

Critical current versus transverse stress relation

In chapter 2, the cause of the high stresses in the magnet windings is discussed. Here an analysis of the transverse stress in the Rutherford cable geometry is presented. First, a short introduction to the theory of superconductivity, where directly related to this thesis, is given. The criteria for critical current are given, followed by the definition of the terminology used in the cable degradation models. To illustrate the critical current degradation in a superconductor the effect of axial strain on I_c in a wire is described first. Next, the influence of transverse stress on the critical current in cables is discussed.

To correctly predict the critical current degradation in the cables in a magnet winding, both the stress distribution and the critical current degradation as a function of that local stress need to be understood. To enhance the understanding of the stress distribution, several FEA models are constructed. The strands in a cable, and the cable in the experimental setup for critical current degradation measurements are modeled. The FEA models are built and analyzed using the ANSYS FEA package.

A new combined model for the expected critical current degradation under transverse pressure is proposed. It is based on the cabling parameters and a novel FEA model of the plastic deformation of a generic cable under transverse pressure, for a well impregnated cable and a dry cable. The FEA model features a stepped non-linear analysis, and takes material yield and filament breakage into account. The computed plastic deformation from the FEA model is used as a correction factor to eliminate the effect of the cable impregnation from the critical current degradation model.

3.1 Introduction

In order to increase the understanding of the observed critical current degradation under transverse load in composite Nb_3Sn wires and cables, the influence of the internal structure of the material is investigated. Over the past years, several authors have extensively researched the topic of critical current degradation in bulk material [3.1], tapes [3.2], [3.3] and wires [3.4]-[3.6].

A few empirical models have been proposed [3.7]-[3.9]; all giving a reasonably accurate prediction of the reversible degradation as measured in tapes and composite wires. However, no model exists at present that predicts the permanent critical current degradation with increasing load.

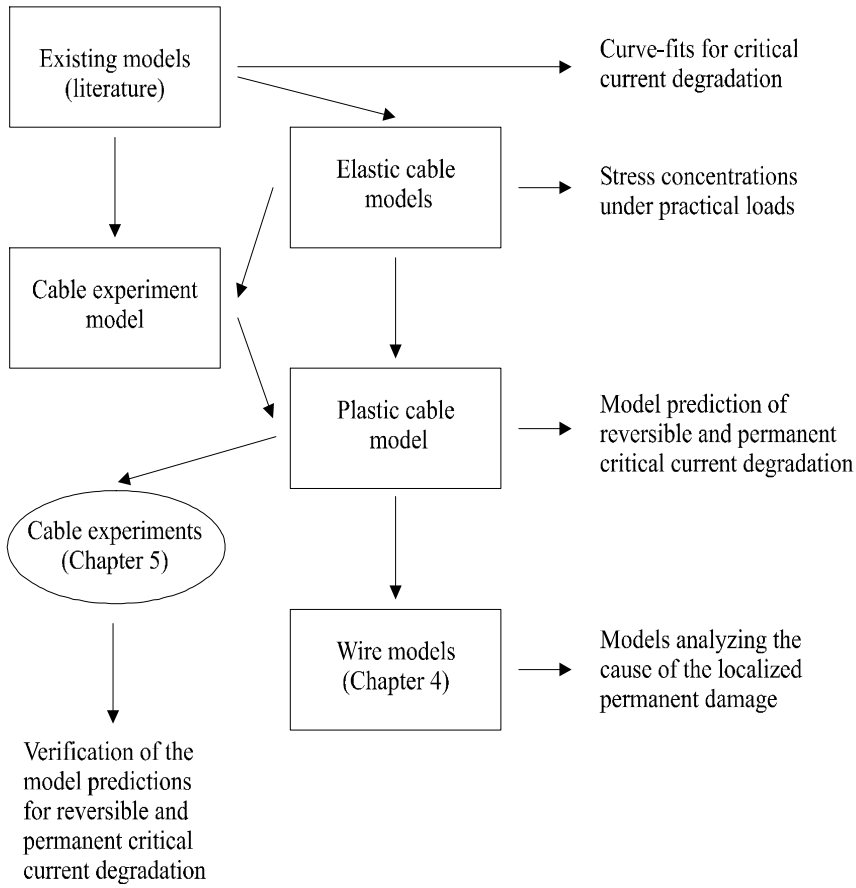

Figure 3.1 Overview of the FEA models presented in this chapter.

When the stress in the conductor is released after having been subjected to a high transverse load, the material usually shows an irreversible degradation of the current carrying capability. This permanent degradation is thought to be primarily due to plastic deformation of the filament matrix resulting in fractures in the brittle Nb_3Sn filaments. Results from FEA models of cable cross-sections and a cable in the critical current test configuration are analyzed. Detailed descriptions of the models can be found in section 3.7.

The ANSYS FEA package is used for the modeling. ANSYS was chosen because of the availability at LBNL, and because it is well suited to model complex geometries using non-linear material properties in combination with contact/gap elements. Emphasis is placed on correctly meshing the geometry to minimize

the numerical error resulting from the model representation. For each model, the final mesh error contributions are listed in the detailed description in section 3.7.

In experiments with cables comprising strands made by different methods of production, wide spreads in the onset and severity of the permanent damage are found. This indicates that both the cabling parameters and the internal structure of the composite conductor play a role in the degradation process.

This chapter describes models that take into account the plastic deformation process to predict the critical current degradation. Figure 3.1 shows the inter-relations of the FEA models created to generate the plastic deformation model of section 3.9.

The following sections discuss the definitions of stress and strain, superconductivity where related to the critical current degradation, the voltage-current relation, and the influence of stress and strain on the critical current.

3.2 Stress and strain definitions

This section introduces the stress and strain definitions used in the FEA models. The stress and strain definitions are based on elastic strain theory, the plastic deformation calculations are purely numerical.

The coordinate systems used in the cable models are shown in figure 3.2. For coil geometries radial (r) refers to the direction outward from the center, and transverse (y) is tangential to the coil surface. For cables, horizontal (x) refers to the direction along the width of the cable, and transverse (y) perpendicular to the wide surface of the cable. For coils the longitudinal (z) direction is defined along the axis of the magnet; for cables the z-direction follows the cable.

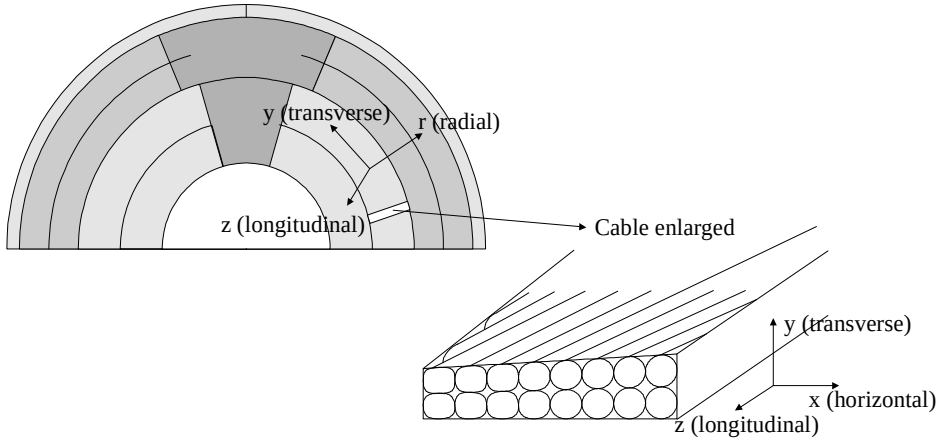

Figure 3.2 Coordinate systems used in the cable and coil models.

In a Cartesian coordinate system, the deformation of a solid body is described by the position dependent displacement vector $\vec{u}(\vec{r})$. The strain e at position $\vec{r}$ is defined [3.10] as

$$[e] \equiv \begin{bmatrix} \frac{\partial u_x}{\partial x} & \frac{1}{2}\left(\frac{\partial u_x}{\partial y} + \frac{\partial u_y}{\partial x}\right) & \frac{1}{2}\left(\frac{\partial u_x}{\partial z} + \frac{\partial u_z}{\partial x}\right) \\ \frac{1}{2}\left(\frac{\partial u_y}{\partial x} + \frac{\partial u_x}{\partial y}\right) & \frac{\partial u_y}{\partial y} & \frac{1}{2}\left(\frac{\partial u_y}{\partial z} + \frac{\partial u_z}{\partial y}\right) \\ \frac{1}{2}\left(\frac{\partial u_z}{\partial x} + \frac{\partial u_x}{\partial z}\right) & \frac{1}{2}\left(\frac{\partial u_z}{\partial y} + \frac{\partial u_y}{\partial z}\right) & \frac{\partial u_z}{\partial z} \end{bmatrix} \tag{3.1}$$

for small strains with the primary strain component on the main diagonal and the shear strains off-axis. The local coordinate system can be rotated to eliminate all three shear components, defining three remaining strain components on the main diagonal as e_1, e_2 and e_3. These components are called the principal strain components.

Three invariants of the principal strains can be defined:

1) the hydrostatic strain e_{hyd}, defined as

$$e_{hyd} \equiv \frac{e_1 + e_2 + e_3}{3} \tag{3.2}$$

is a measure for the change of volume;

2) the Von Mises or equivalent strain e_{eqv} is defined as

$$e_{eqv} \equiv \sqrt{\tfrac{1}{2}\left((e_1 - e_2)^2 + (e_2 - e_3)^2 + (e_3 - e_1)^2\right)}\,. \tag{3.3}$$

Sometimes, the deviatoric strain e_{dev} is used instead, as in the models of Ten Haken [3.11], defined by

$$e_{dev} \equiv \frac{2\sqrt{2}}{3} e_{eqv} \approx 0.943 e_{eqv}\,. \tag{3.4}$$

The equivalent strain is a measure for the change of shape of the material;

3) the product of all three principal strains

$$e_{diag} \equiv e_1 e_2 e_3\,. \tag{3.5}$$

The stress and strain in isotropic materials are related as in :

$$\begin{pmatrix} e_1 \\ e_2 \\ e_3 \end{pmatrix} = \frac{1}{E} \begin{pmatrix} 1 & -n & -n \\ -n & 1 & -n \\ -n & -n & 1 \end{pmatrix} \cdot \begin{pmatrix} s_1 \\ s_2 \\ s_3 \end{pmatrix}, \tag{3.6}$$

with E the elasticity or Young's modulus of the material and n the Poisson's ratio. Isotropy is assumed for the 2D models ($E_x = E_y = E_z = E$). The cables are anisotropic in nature, with the effective E_x and E_y approximately equal to 42 GPa (epoxy impregnated), and E_z larger in compression (the actual value depends on the packing factor and is approximated with a rule of mixtures model, typical values range from 80 to 100 GPa).

In the plastic cable models the anisotropy is taken into account by adjusting the value of n in the z-direction. This is the simplest possible way.

The hydrostatic strain e_{hyd} is related to the hydrostatic pressure P_{hyd} as in

$$e_{hyd} = -\frac{1-2n}{E} P_{hyd}\,. \tag{3.7}$$

The Von Mises stress s_{eqv} is defined similarly to the Von Mises strain.

In contrast to the models applied by Ten Haken [3.11], the FEA models used to predict the permanent critical current degradation are based on elastic-plastic deformation of the materials. For some materials, such as the Nb_3Sn in the filaments, the plastic behavior is not well known, and a bi-linear[1] approach is chosen for the unknown material properties.

The annealed copper and the epoxies are modeled with non-linear material properties [3.12]. For the Nb_3Sn, fracture of the filaments is assumed when the equivalent strain exceeds 0.2 % from the intrinsic strain e_0 (see figure 3.6), a value generally used as an upper limit for the longitudinal strain on a Nb_3Sn wire. The fractured elements are eliminated from the structure in each successive load-step to simulate propagation of the structural damage.

[1] In order to achieve rapid convergence in the FEM analysis, the stress-strain relation of the material is modelled as linearly increasing strain with increasing stress, up to the yield stress. Above the yield stress usually a slope of 0.1 times the Young's modulus of the material is used.

3.3 Introduction to superconductivity

This section gives an introduction to superconductivity based on measurable quantities like sample current and voltage. The theory is valid for both alloyed superconductors like NbTi as well as the A15 materials like Nb_3Al and Nb_3Sn.

When a current I passes through a superconducting material with an overall cross sectional area A, a voltage U can be measured across its length l. When the temperature T is steadily lowered from room temperature, the resulting $U(I)$ behavior is Ohmic, following the relation

$$U(I,T) = \rho(T)\frac{l}{A}I, \tag{3.8}$$

with $\rho(T)$ the resistivity of the sample. The resistivity gradually drops with the lowering temperature, until at the *critical temperature* T_c it suddenly drops to almost zero. Below T_c the material is in the superconducting state, as shown in figure 3.3. T_c is an intrinsic material property, for pure Nb_3Sn it is 18.5 K, in practical conductors about 17 K.

If a magnetic field B is applied at constant current, the material will transfer to a normal resistive state when the *upper critical field* B_{c2} is exceeded. B_{c2} is also an intrinsic material property and a function of temperature T [3.13], described by

$$B_{c2}(T) = B_{c2,T=0}\left(1-(T/T_c)^2\right) \equiv B_{c2,T=0}(1-t)^2, \tag{3.9}$$

with $t = T/T_c$. Similarly, if the current I is increased at a given temperature below T_c, the material will transfer to a normal resistive state when the *critical current* I_c is exceeded. Dividing this current I_c by the area A defines the overall *critical current density* j_c of the material.

The critical current I_c can be written as a function of the magnetic field B and temperature T using the Fietz-Webb law [3.14]:

$$I_c(B,T) = C\,k(T)^{-g} B_{c2}(T)^n\, B^{-1} b^p (1-b)^q, \tag{3.10}$$

with C a scaling constant for the maximum critical current, $k(T)$ the temperature dependent Ginzburg-Landau parameter [3.9] , with $1 < g < 3$, $2 \le n \le 3$, and $p \approx 0.5$, $q \approx 2$ for Nb_3Sn. The ratio b is defined as $b = B/B_{c2}$. Typically, the value used for n in the Fietz-Webb law is 2.5. In section 3.6, the introduction of the strain dependency will add a multiplier that will influence the value of n.

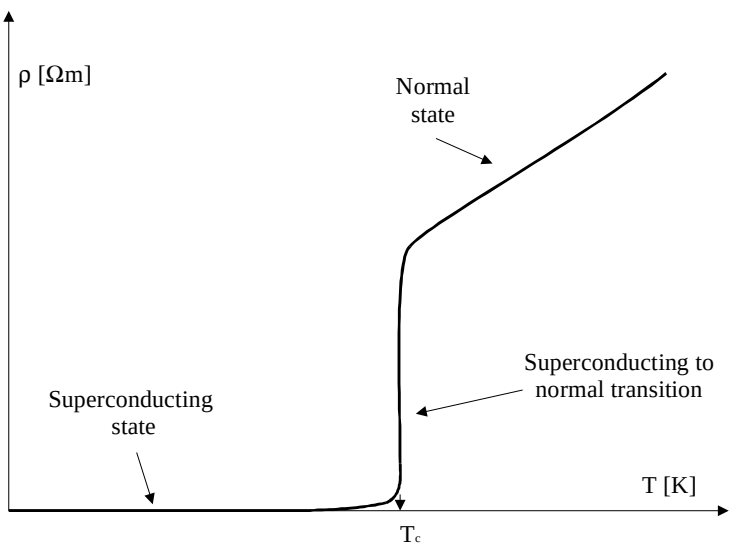

Figure 3.3 Resistivity in a superconductor as a function of temperature. The resistivity ρ drops to almost zero below the critical temperature T_c. The sharpness of the transition depends on the sample purity; the purer the sample, the sharper the transition.

Figure 3.4 shows the critical current I_c as a function of magnetic field B and temperature T. The surface defined by (3.10) is called the critical surface. The material is in the superconducting state below the surface, and in the normal state above the surface.

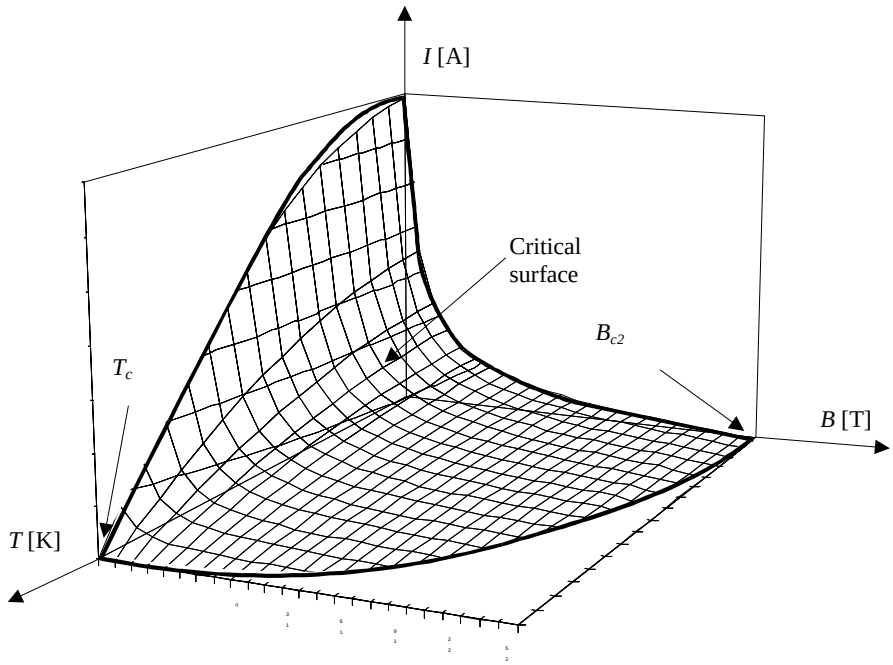

Figure 3.4 The critical current I_c as a function of magnetic field B and temperature T.

For the experiments described in chapter 5, the temperature is fixed at 4.2 K. The critical current is measured as a function of the magnetic field. In order to measure the critical current, a criterion has to be defined for the location of the transition from the superconducting to the normal state.

3.4 Voltage versus current relation of superconducting wires

The critical current I_c of a superconductor is usually determined by measuring the voltage U across the sample as a function of the current I. An empirical and generally accurate relation to describe the *U(I)* curve is

$$U = C \cdot I^n , \tag{3.11}$$

with C a constant determined by $C = U_c / I_c^n$, and n a fitting parameter referred to as the *n-value* of the superconductor. U_c is the voltage measured at I_c. The higher the n-value, the sharper the transition from the superconducting to the normal state. The n-value is determined by multiple factors, of which the uniformity of the conductor and the external field are the major ones. Figure 3.5 shows typical *U(I)* curves for a sample with low n-value and high n-value.

For large n-values, the determination of the exact critical current is difficult, since increasingly smaller steps in the current have to be taken to measure the voltage at the steep slope of the *U(I)* curve below the quench current I_q. For this reason, a criterion is used to determine where the sample is considered to have reached I_c.

Two criteria are generally used for superconducting wires and cables. The first is a constant voltage criterion, defining I_c at the point on the curve where the voltage reaches 0.1 or 1 μV/cm of sample length. The second is a constant resistivity criterion, defining the critical current at the point where the line for

$r = 1 \cdot 10^{-14}$ or $1 \cdot 10^{-13}$ Ω·m intersects with the *U(I)* curve. The constant resistivity criterion is used mostly in the measurements in this thesis. If the constant voltage criterion is used, it will be specifically noted. The two criteria are illustrated in figure 3.5.

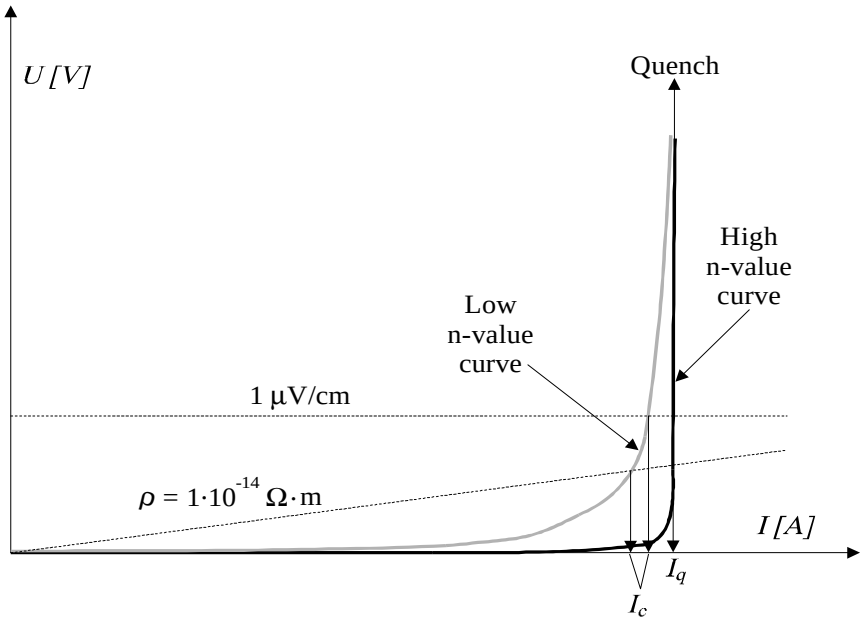

Figure 3.5 Usual voltage-current relations of a sample. Shown is the effect of the n-value on the shape of the transition. The higher the n-value, the steeper the transition from the superconducting to the normal state. Two critical current criteria are shown for critical current determination, the top one a constant voltage, the bottom one a constant resistivity criterion. In addition, a quench is shown (indicated by the arrow), by which a sample rapidly transfers to the normal state due to thermal run-away.

3.5 Influence of strain on the critical current

This thesis focuses on strain as an additional parameter that determines the critical current. For alloyed materials like NbTi this is not an important issue, since the degradation with increasing strain is usually negligible [3.15].

In the case of the brittle A15 compounds, the strain sensitivity plays an important role in the overall magnet design and behavior. The current carrying capability of wires is sensitive to axial strain. The structure of the wire, and the cable, determine the sensitivity to an applied transverse pressure.

The formulas given in section 3.6 include strain in the expression of the critical current. The formulation of a model describing the reversible and permanent critical current degradation in a cable as a function of transverse pressure is described. This is an extension of the critical current degradation study by Ten Haken [3.16], and includes the cabling manufacturing process and related critical current degradation.

3.5.1 A15 superconductors

A15 superconducting materials are characterized by their crystal structure and inherent brittleness. They are formed by a high temperature reaction step. Of the A15 materials, Nb_3Al exhibits the lowest strain sensitivity [3.17], but it is difficult to manufacture and to use in large scale applications due to the high reaction temperature generally used to form the material (850 °C for 50 hours). Nb_3Sn is the most widely used A15 in large scale applications.

At the time this thesis is written, commercial Nb_3Sn wires are produced by several manufacturers, with Oxford, TWCA [3.18] and IGC [3.19] supplying the largest volume in the USA. Other suppliers include SMI, Supercon, Sumitomo, Vacuumschmelze (VAC) and Europa Metalli.

The two conductors mainly investigated here are made by the Modified Jelly Roll (MJR) process from TWCA and the Internal Tin process from IGC. A more detailed description of the various manufacturing processes is given in chapter 6.

3.5.2 I_c versus axial strain

The $I_c(e)$ dependency of Nb_3Sn wires has been well characterized [3.20], [3.21]. The critical current reduction due to axial strain observed in a generic wire follows the behavior as depicted in figure 3.6. Due to the differential shrinkage of the Nb_3Sn and the matrix material, the superconductor is under compressive stress after the heat treatment (a detailed analysis is given in chapter 6).

In order to find the maximum in the critical current I_c in a wire, the wire has to be elongated to the point where the axial strain cancels the strain due to the thermal contraction. This offset is labeled e_0. When the wire is either compressed or elongated in the axial direction from this point, the I_c will decrease. The shape of the curve has been described by several models that predict a decrease in tension and compression [3.22], [3.23].

If a wire is subjected to transverse stress, the critical current degradation curve has a similar shape. Further analysis of the critical current versus applied stress and strain in cables focuses on the transverse components.

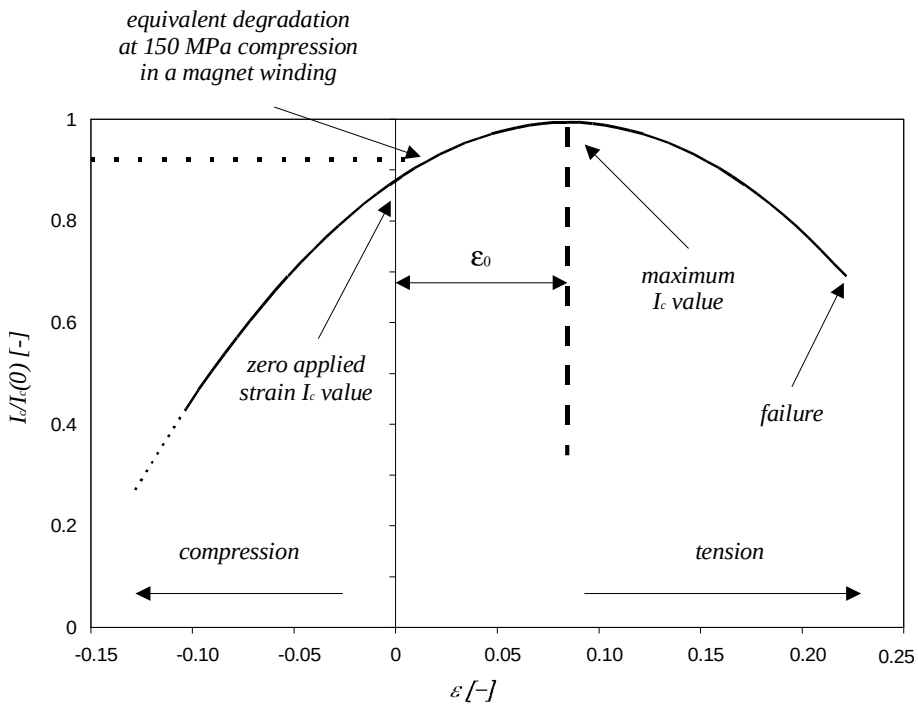

Figure 3.6 The critical current versus axial strain of Nb_3Sn wires.

3.5.3 Rutherford cables

A Rutherford cable[2] is manufactured by flattening a twisted ring of strands into a rectangular (or slightly keystoned) cross-section. Figure 3.7 shows the layout of a typical Rutherford cable with the characteristic parameters. The most important parameters used are the *keystone angle* j and the *compaction factor* C_p (3.12) of the cable.

The keystone angle is defined as the inverse tangent of the difference in edge thickness of the wide and the narrow side divided by the cable width. The keystone angle generally varies between 0 and 1.5 degrees for practical cables.

The compaction factor is defined as the volume occupied by the strands over a certain length multiplied by $\pi/4$, divided by the volume needed by strands if they were loosely packed on top of each other over the same length. This definition takes the twist pitch of the cable into account. The correction for the twist pitch is generally small, in the order of 1-2 % of the total compaction factor as compared to a two-dimensional approach with the area occupied divided by the area needed without twist pitch. The compaction factor C_p is

$$C_p = \frac{2w(t_1 + t_2)\cos j}{npd^2} \times \frac{p}{4} \times 100\%, \tag{3.12}$$

with n the number of strands in the cable, d the strand diameter, w the cable width, t_1 the minor edge thickness, t_2 the major edge thickness and j the cabling pitch angle, defined as

$$j = \arctan\frac{2w}{L_p}, \tag{3.13}$$

with L_p the pitch length. A characteristic and practical range for j is 13 to 18 degrees, with a pitch length ranging from 73 to 160 mm for the tested samples, and the width between 11.6 and 18.2 mm. The inner cable for the MSUT dipole is 21.7 mm wide, but it is not tested under transverse load due to the maximum acceptable width of 20 mm for cable samples in the test set-up.

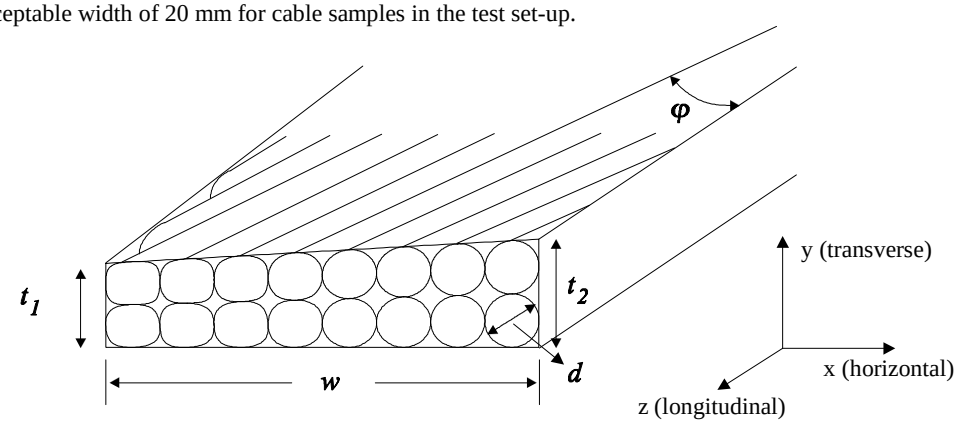

Figure 3.7 Cabling parameters of a Rutherford cable.

A loose cable (no compaction at all) has a compaction factor equivalent to 100 %, while the compaction in the cables discussed below ranges from 83 to 92 %.

Most cables used in the thesis were manufactured at LBNL using a dedicated research cabling machine.

[2] The Rutherford cable is named after the Rutherford Appleton Laboratory where the cable design was invented.

3.5.4 Definitions used in describing $I_c(s)$ relations for transverse stress in cables

When a comparison is made between the critical current degradation due to axial tension in wires, and critical current degradation versus transverse pressure in cables, several complications arise:

1) the complex internal geometry of the Rutherford cable makes it hard to define the direction of the individual strain components;
2) the cable has a different mechanical behavior under compression as compared to tension, i.e. when put under tension the strands can come out of position and distort the cable;
3) a wire can be easily restrained in all directions; for a cable this is more difficult, since there is free space between the strands composing the cable.

A typical critical current degradation plot as a function of the transverse pressure is shown in figure 3.8.

When the critical current of an *n*-strand cable in a fixed background field (corrected for self-field) is compared to that of *n* times the critical current of the individual strand before cabling, one usually observes a reduced value due to damage caused by the cabling process.

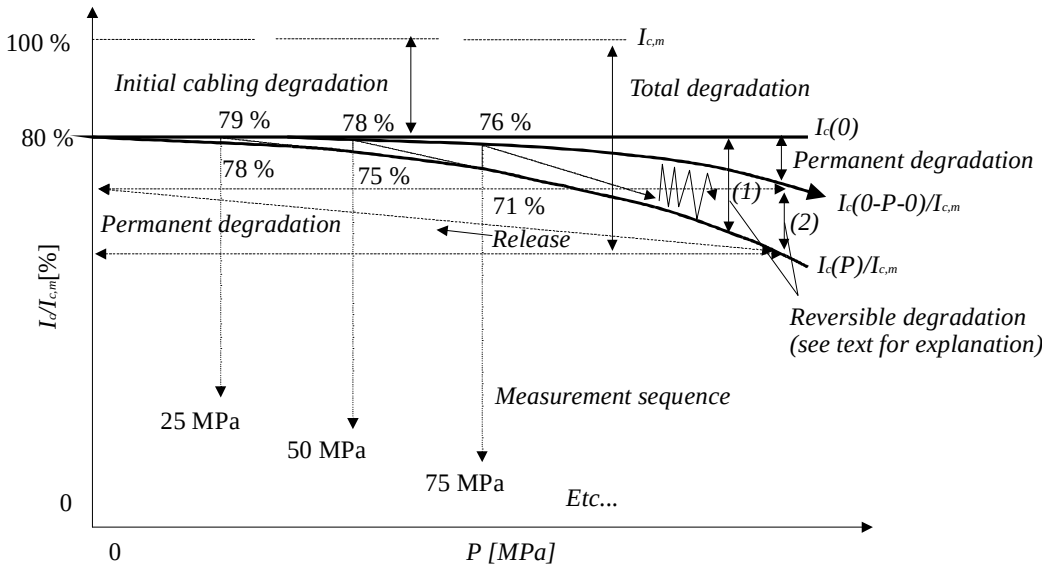

Figure 3.8 Definitions of the terms used to describe the critical current degradation in Rutherford cables as a function of applied transverse pressure P.

When the I_c of a cable is measured for the first time at no load, the initial cabling degradation is determined. This initial drop in the critical current is defined as the *initial cabling degradation*, and is determined by the cabling parameters and the sensitivity to deformation of the internal structure of the strands. As an example, the definition of degradation is the 20 % reduction in critical current from the manufacturers value $I_{c,m}$ at 100 % to the first measured value I_c (0) at for instance 80 %. In graphical format it is typically indicated by I_c (0)/$I_{c,m}$, which is the reciprocal of the 20 % degradation.

Increasing the load further reduces the critical current. The curve marked $I_c(P)/I_{c,m}$ shows the ratio of the maximum critical current $I_c(P)$ as a function of applied pressure P, measured at the same pressure P, and the.

Upon release of the load, the critical current returns to a reduced value I_c(0-P-0). This value is determined by the permanent degradation caused by the maximum applied load to the cable. The curve marked I_c(0-P-0)/$I_{c,m}$ shows the ratio of the maximum critical current at zero load I_c(0-P-0) that the cable can carry after having been subjected to a certain applied pressure P, and the critical current as specified by the manufacturer.

Next, the applied transverse pressure is increased in steps; for every step the critical current is measured with the pressure applied, and after releasing the pressure. This procedure is repeated until a predetermined maximum pressure is reached. This method produces two curves, the upper one indicates the

critical current to which the cable recovers, loaded to the pressure indicated on the horizontal axis. The difference between the starting point at $I_c(0)$ and the upper curve is defined as the *permanent degradation*, and is typically represented by the reciprocal $I_c(0\text{-}P\text{-}0)/I_c(0)$. The degradation is caused by excessive strain within the filaments, that causes permanent damage to the Nb_3Sn.

The lower line indicates the measured critical current $I_c(P)$ at the applied pressure P. This is the maximum current the cable will carry under this load; the drop in current is caused by additional reversible strain in the Nb_3Sn. The difference between the lower curve and $I_c(0)$, or the upper and lower curve, is defined as the *reversible degradation* at applied pressure P, and can be represented in these two ways:

1) the first method, which is typically used in literature is to represent the reversible degradation by $I_c(P)/I_c(0)$, which is the ratio of the critical current $I_c(P)$ measured at applied pressure P and the critical current measured at the first measurement point at zero load $I_c(0)$. In this case, the reversible degradation is always computed using the current after the initial critical current degradation as a reference of 100 %. This method is used throughout this thesis;
2) the second method, which is a more accurate representation of the physical process, refers to the reversible degradation as the difference between the line of $I_c(0\text{-}P\text{-}0)/I_c(0)$ and the line of $I_c(P)/I_c(0)$. In this case, the reversible degradation truly represents the amount of change in I_c if the pressure is cycled between zero and P. Although this method provides a more accurate definition of the term reversible degradation, the latter method is used to conform to the definitions used in literature.

Finally, the sum of the initial degradation and the reversible degradation (for the first method) or the sum of all three degradation components (for the second method) is defined as the *total degradation*, typically represented by $I_c(P)/I_{c,m}$. This last value is of importance to the magnet designer, since it determines the actual current that the cable can carry when operated in the magnetic field and under load.

3.6 Definition of a model describing the effect of transverse stress on the critical current in Nb_3Sn cables

When trying to understand the behavior of a complex composite Nb_3Sn wire, it is convenient to start as a reference with the properties of pure Nb_3Sn material. This behavior is then compared with models that simulate raw material, tapes and wires. The models show a successive increase in complexity. Extensive research on the strain behavior of bulk Nb_3Sn, tapes and wires [3.24]-[3.30], has resulted in a fair understanding of the basic degradation mechanisms.

The results from these studies are used here as a basis for modeling more complex internal structures of the wire. The critical current degradation in a cable is even more complicated, as plastic deformation of the cable structure and insulation has to be taken into account. In section 3.7.4 a model of the critical current degradation in a Rutherford cable is described. Since the model is dependent on the material properties of the components of the composite Nb_3Sn strand, empirical relations are used to account for the contribution of each individual component. A correlation with experimental data will be discussed in chapter 5.

For comparison with earlier published results, the next sections describe relations for the critical current degradation in crystals, tapes and wires. The relations are described briefly, and a curve is fitted to each relation to allow for a quick prediction of the critical current degradation as compared to the experimental data and the FEA models presented in this chapter.

3.6.1 Pressure sensitivity in crystals

The critical temperature T_c and the upper critical field B_{c2} are suppressed by an increase in hydrostatic pressure P_{hyd}. The two effects can be combined into a single function describing the sensitivity $j_c(B,T,P_{hyd})$ of a crystal as a function of the magnetic field B, temperature T and hydrostatic pressure P_{hyd}. Using $T_c(P_{hyd})$ as described in [3.31] and $B_{c2}(P_{hyd})$ from [3.32] one can write $j_c(B,T,P_{hyd})$ by combining (3.9) and (3.10) to form:

$$j_c(B,T,P_{hyd}) = C\frac{(1-t^2)^{2.5}}{B}K(T,P_{hyd})b^{0.5}(1-b)^2, \tag{3.14}$$

Now substitute $B_{c2}(P_{hyd}) = B_{c20}(1+(dB_{c2}/dP_{hyd})P_{hyd})$ and $T_c(P_{hyd}) = T_{c0}(1+(dT_c/dP_{hyd})P_{hyd})$. Next, fill in dT_c/dP_{hyd} = -0.14 K/GPa [3.31], dB_{c2}/dP_{hyd} = -1.7 T/GPa [3.32], B_{c20} = 28 T and T_{c0} = 18.5 K (Nb_3Sn

crystal), and C = 59.6 (by setting degradation to 0 % at 0 MPa). The multiplier $K(T,P_{hyd})$ is introduced as a refinement on the temperature dependency of the Ginzburg-Landau parameter $k(T)$, given by the empirical relation [3.9]

$$K(T) = 1 - 0.31\, t^2 (1 - 1.77 \ln t)\,. \tag{3.15}$$

For easy comparison, the resulting relation is simplified to a 2nd order curve and taken at B = 10 T and T = 4.2 K. This yields (P_{hyd} in GPa):

$$j_c(P_{hyd}) = j_c(0)(1 - 0.0563 P_{hyd} - 0.0041 P_{hyd}^2)\,;\ (\mathrm{B} = 10\ \mathrm{T},\ \mathrm{T} = 4.2\ \mathrm{K}). \tag{3.16}$$

The curves for applied magnetic fields of 8 T, 10 T and 12 T are shown in figure 3.9. The crystal strain relation predicts a reduction in critical current density of less than 1 % at 10 T, 4.2 K and 150 MPa hydrostatic pressure.

A model such as (3.14) does not predict the enhanced strain sensitivity in tapes and wires correctly; it underestimates the observed critical current degradation by an order of magnitude in most cases. To describe the enhanced critical current degradation more accurately, two derivative models are discussed next. The first is based on a model describing the I_c degradation in a tape geometry using a linear scaling constant for the dependency of B_{c2} on applied pressure, and is discussed in section 3.6.2. This model is followed by one for a wire by Ekin in section 3.6.3, using an empirical scaling law for $B_{c2}(e)$ [3.22].

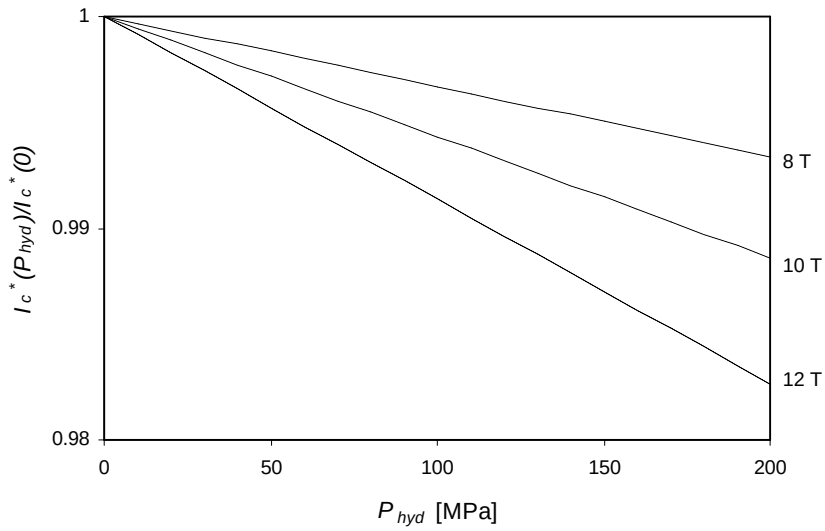

Figure 3.9 *Plots of the reduced critical current $I_c^*(P_{hyd}) / I_c^*(0)$ (I_c^* derived from j_c of the crystal) as a function of applied hydrostatic pressure P_{hyd} in a Nb_3Sn crystal for three magnitudes of the magnetic field B (T = 4.2 K).*

3.6.2 Strain sensitivity in tapes

One level up in complexity, in a tape geometry, the stresses in all three directions have to be taken into account. In a tape, the thickness is usually several orders of magnitude smaller than the width or length. A proposed relation [3.33] for the B_{c2} as a function of axial strain and transverse stress is

$$B_{c2} = B_0 - C\left(e_z^2 + (s_x / E)^2 + (s_y / E)^2\right)^{0.5}, \tag{3.17}$$

with C and $B_0 = B_{c20}$ constants that can be fitted for a particular conductor. The x-direction is along the width, the y-direction is along the thickness, and the z-direction is along the length of the tape. In the case

of applying a transverse pressure, the tape is free to expand or contract in the y-direction, but constrained in the x-direction. This means the formula can be modified in the following way

$$B_{c2} = B_{c20} - C(1+n)P / E \,, \tag{3.18}$$

resulting in a linear decrease of B_{c2} with applied transverse pressure P. The tape is treated as a solid mass, quite different from individual strands packed into the Rutherford cable. Ignoring this, and using a value of $n = 0.35$ and E = 50 GPa for an insulated and impregnated cable, equation (3.18) can be combined with (3.10). The result is combined with

$$I_c(T) = I_c(0)\left(1 - T / T_c(P)\right) \tag{3.19}$$

[3.34]. This yields

$$I_c(B,T,P) / I_c(0) = D\left(1 - T / T_c(P)\right)\left(B / B_{c2}(P)\right)^{0.5} B^{-1}\left(1 - B / B_{c2}(P)\right)^2 . \tag{3.20}$$

Equation (3.20) differs from the model in (3.14) in the exponents of the temperature sensitivity and field dependence, which are compensated for with a different scaling constant C, and can be approximated by

$$I_c(P) = I_c(0)(1 - 0.699P - 1.993P^2) \text{; (B = 10 T, T = 4.2 K)}, \tag{3.21}$$

for a scaling constant C = 1244 T as reported by Ten Haken [3.11], and D = 52.4 T at 10 T, 4.2 K. The predicted critical current degradation at 150 MPa applied pressure is 15 % in a cable based on a tape geometry at 4.2 K. The curves for applied magnetic fields of 8 T, 10 T and 12 T are shown in figure 3.10.

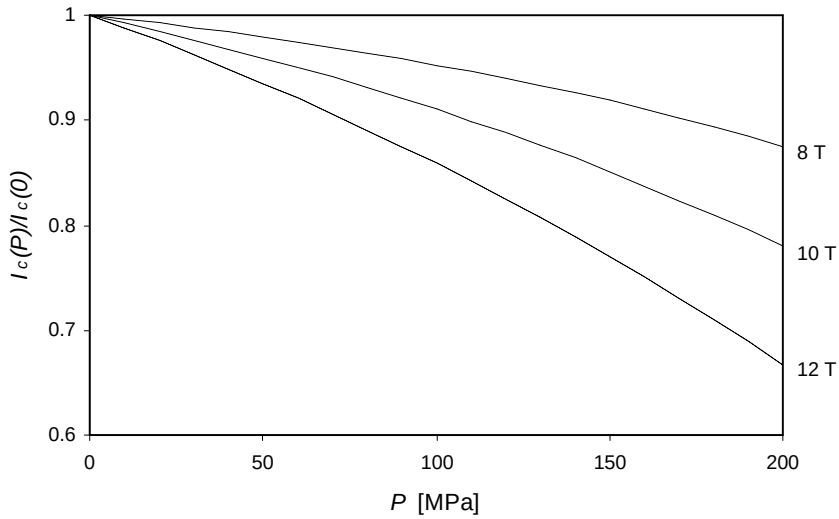

Figure 3.10 Plots of the reduced critical current $I_c(P)/I_c(0)$ as a function of applied transverse pressure in a Nb_3Sn tape for three magnitudes of the magnetic field B (T = 4.2 K).

3.6.3 Strain sensitivity in wires

In a wire, the complex internal geometry of the twisted filaments prevents the use of a simple orthogonal model. The twist length of the filaments is of the same order of magnitude as the wire diameter, thus the rotation of the filaments has to be considered in the stress and strain analysis. At present, no mechanical analysis of the internal structure exists that predicts the observed critical current degradation under longitudinal strain or transverse pressure.

The model used here for comparison is an empirical one, based on a scaling law for the applied transverse pressure P on a wire. The approximation by Ekin [3.22], with strain scaling laws for B_{c2} and T_c is given by

$$B_{c2}(P) = B_{c20}(1-900\,|\,P/E\,|^{1.7}),$$
$$T_c(P) = T_{c0}(1-900\,|\,P/E\,|^{1.7})^{1/3}. \qquad (3.22)$$

Combining equations (3.22), (3.10) and using E = 50 GPa, this yields

$$j_c(P) = j_c(0)(1-0.048P-1.432P^2)\ ;\ (\mathrm{B}\ = 10\ \mathrm{T},\ \mathrm{T} = 4.2\ \mathrm{K}). \qquad (3.23)$$

The curves for applied magnetic fields of 8 T, 10 T and 12 T are shown in figure 3.11. This fit predicts a critical current degradation of 4 % at 10 T, 150 MPa applied transverse pressure for a cable based on a wire geometry at 4.2 K.

The critical current degradation as a function of the applied pressure is lower for a wire as compared to tapes. The primary reason is that the wire geometry has a copper matrix around the superconducting filaments, essentially forming a protective jacket. When the wire is subjected to transverse pressure, the copper matrix will carry part of the resulting stress in the wire, effectively reducing the strain on the filaments.

In the tape geometry, applying a transverse pressure immediately results in strain on the superconductor, hence the larger critical current degradation. The initial critical current degradation in the wire geometry is not included in the model.

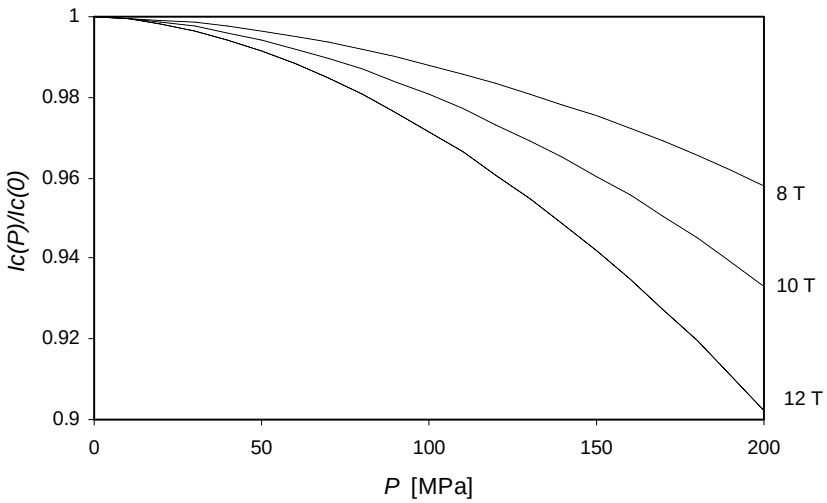

Figure 3.11 Plots of the reduced critical current $I_c(P)/I_c(0)$ as a function of applied transverse pressure in a Nb_3Sn wire for three magnitudes of the magnetic field B (T = 4.2 K).

3.6.4 A comparison of the crystal, tape and wire models to cable critical current degradation

Let us compare the results from the crystal, tape and wire model obtained so far with the measured result of a cable critical current degradation experiment. Figure 3.12 shows the measured critical current degradation as a function of the applied load compared to the model predictions. The critical current degradation is measured at a field of 10 T and a temperature of 4.2 K. As is evident from the calculated curves, only the models based on the wire and tape geometry approximate the shape of the measured curve for a low compaction cable fairly well.

The shape of the degradation curves in the high compaction cable is not predicted well with any of the three models. The difference between the models and the experimental data can be explained by the difference in internal geometry of the low compaction cable versus the high compaction cable, and the resulting variation in the local stress and strain on the superconductor.

In the case of a typical cable where the Nb_3Sn is not subjected to large deformations, only the hydrostatic pressure will affect the critical current. This can be the case for cables made of strands that are

not highly deformed during cabling, and are contained in a well epoxy-impregnated cable. Also, the filament structure is uniformly loaded, thus avoiding any internal stress concentrations on the Nb_3Sn.

In a low compaction cable, the strands will first deform when a transverse load is applied, causing the strands to yield and imprint on each other. When the load increases further, the strands will tend to deform and close the void space in the cable.

The initially loose cable geometry is gradually changed to a more compacted cable, with a behavior more similar to a tape. This essentially results in an increase of the effective Young's modulus[3] of the cable, reducing the strain in the y-direction, but also increasing the hydrostatic pressure in the entire cable. Above a certain value for the compressive stress, the filaments start to break, rendering the model prediction invalid.

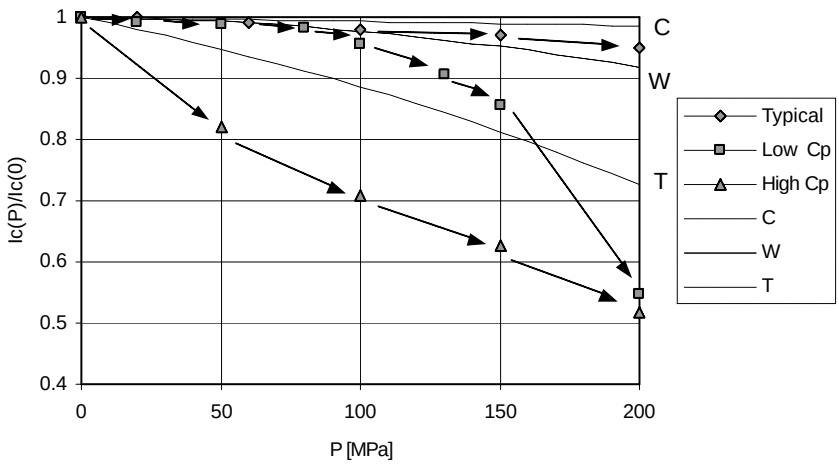

Figure 3.12 Comparison of the three normalized $I_c(P)/I_c(0)$ models (C for crystal, W for wire and T for tape) at B = 10 T (T = 4.2 K) with a high compaction cable sample (High C_p), low compaction cable sample (Low C_p) and a typical result measured for the same material (Typical) (see chapter 5 for data tables).

In a high compaction cable, the behavior more closely resembles that of a tape geometry. The onset of the critical current degradation is immediate, since the internal structure is loaded right from the start of the application of the transverse pressure.

Recently, two new models were derived by Cheggour and Hampshire [3.35] and Ten Haken, Godeke and Ten Kate [3.36] in an attempt to more precisely describe recent more extensive experimental results. Both models follow a similar approach, in which the original scaling formula from Fietz and Webb is augmented by a multiplier function that is dependent on strain. This addition of a separate strain dependent multiplier allows for a more precise scaling with strain, and also allows for the introduction of a scaling function that is dependent on the material parameters of the superconductor under investigation.

The model described in section 3.9 partly follows a similar approach, in which the I_c dependency on deviatoric stress is included directly in $B_{c2}(P)$, and plastic stress is added as a separate multiplier f_{pl}.

3.7 FEA cable models

In order to investigate the pressure distribution in the cross-section of a cabled conductor as accurate as possible, three ANSYS FEA models of the cable are made.

The first two FEA models are designed to determine the intensity of the stress concentrations at the contact points between the strands. Also computed are the plastic deformation within the strand, and the

[3] The effective Young's modulus is computed as the quotient of the applied transverse pressure and the overall strain in the transverse direction of the cable.

magnitude of the individual components of stress as a function of the applied transverse pressure. The first simulates a cable with epoxy between the strands, the second a cable without epoxy, to demonstrate the effect of epoxy impregnation on the plastic deformation of the cable.

The results of these two FEA models are used to generate a model of the critical current degradation that includes the permanent degradation. The permanent degradation is based on the magnitude of the plastic deformation in the strands. The shape of the critical current degradation curve is related to the hydrostatic, deviatoric and plastic components of the total stress through the use of weight factors for each component.

The selection of model A versus B is made by looking at the quality of the impregnation; for a well impregnated cable model A is used, for a dry cable model B is used. The computed stress on the Nb_3Sn from the FEA model is then used as input for the empirical model of (3.21) to compute the critical current degradation.

The third FEA model is used to analyze the stress concentrations in the cable specific to the test setup used for the cable critical current degradation experiments. The results from the FEA model are used in chapter 5 to correct the applied transverse pressure for the added stress concentration in the test geometry.

The FEA models are summarized in tables 3.1 and 3.2 and discussed in more detail in the following sections.

Model geometry	Material properties	Purpose
A : Cable cross-section impregnated	Non-linear	Computation of the magnitude of the initial stress concentration at the strand contact point in a well impregnated cable
B : Cable cross-section dry	Non-linear	Computation of the deformation in the strand due to plastic deformation in the corner section of a dry cable
Cable test sample	Linear	Computation of the overall stress and strain in the cable test sample as a function of the applied transverse pressure

Table 3.1 FEA model summary.

3.7.1 Element type selection and motivation

The following elements are used in the FEA models :

PLANE82 : a second order element with 8 nodes (6 for triangular shape) specifically suited for automatic mixed (quadrilateral and triangular) meshing of irregular shapes without loss of accuracy. The 8 node element is well suited to model curved boundaries.

VISCO106 : a first order element with 4 nodes (3 for triangular shape) designed to solve rate-independent and rate-dependent large strain plasticity problems. The element is used to model highly nonlinear behavior.

CONTAC48: a 3 node point to surface contact element used to represent contact and sliding between two surfaces (or between a node and a surface) in two dimensions. Contact occurs when the contact node penetrates the target line defined by the other two nodes. The element is capable of modeling friction between the contact node and the sliding surface defined by the nodes on the target line.

Table 3.2 contains information on the finite element type used in each model, whether contact elements were incorporated, and the range over which the material properties are varied. Details about the elements and motivation of the choice are given below.

The second order PLANE82 element is chosen over the first order PLANE42 element because the former produces a more accurate result with large curvatures and difficult to model shapes. Although it is possible to achieve the same accuracy with the latter element, this is obtained at the expense of more than

just doubling the mesh density. This increases the running time of the model at a disproportionate ratio to the achievable accuracy.

The first order VISCO106 element is chosen in the model of the cable without epoxy impregnation solely due to memory limitations. Use of the second order element VISCO107 together with the contact elements at the interfaces causes the model to exceed the maximum memory limit for the machine on which the program solving the model is to be executed. Use of the VISCO106 element reduces the memory requirements. For this reason, the accuracy of the model of the cable without epoxy impregnation is lower than that of the impregnated cable.

Model	ANSYS Elements used	Element types	Contact elements	Relevant material properties		
				E [GPa]	n_{xy}	Yield Stress [MPa]
A : Impregnated cable cross-section non-linear (fig. 3.13)	PLANE82[4]	2nd order plastic	No	Strand : 117 Epoxy : 40 Sleeve : 56	0.36 0.30 0.30	Strand : 40-60 Epoxy : 20 Sleeve : 30
B : Dry cable cross-section non-linear (fig. 3.14)	VISCO106[5], CONTAC48[6]	1st order plastic with large deformation effects and contacts	Yes	Strand : 117	0.36	Strand : 40
Cable test sample linear (fig. 3.17)	PLANE82, CONTAC48	2nd order elastic with contacts	Yes	Cable: 26-50 Glass-epoxy : 56 Steel : 193	0.30 0.30 0.30	NA NA NA

Table 3.2 ANSYS FEA model elements, type of analysis and relevant material properties.

3.7.2 Error estimation in the FEA models

The accuracy of the models is determined by the following three factors :

1) choice of the element (first versus second order);
2) mesh discretization error (mesh does not accurately describe the real physical shape);
3) successive errors in the non-linear solution phase.

The choice of the element is made based on the availability of the element for the analysis, model size and running time limitations. For instance, second order structural elements exist, but ANSYS does not have a second order contact element.

The mesh discretization error is caused by the mesh being either to coarse to represent a complex shape, or by the use of elements that exceed the recommended aspect ratio (quadrilaterals) or corner angles (triangles).

This type of error can be estimated in ANSYS through the use of the PRERR command, which lists the percent error in structural energy norm (SEPC). SEPC represents the error associated with the discrepancy between the calculated stress field and the globally continuous stress field.

[4] PLANE82 is a 2D second order structural element. See the ANSYS 5.4 Elements Manual, Ch.4.82.

[5] VISCO106 is a 2D first order structural element with large deformation capability. See the ANSYS 5.4 Elements Manual, Ch.4.106.

[6] CONTAC48 is a 2D point to surface interface element. See the ANSYS 5.4 Elements Manual, Ch. 4.48.

The continuity assumption used in the FEA formulation results in a continuous displacement field, but a discontinuous stress field [3.37]. Therefore, the stresses are averaged over the elements at each node. The stress error vector at node *n* of element *i* is now determined by

$$\Delta \vec{s}_n^{\,i} = \vec{s}_n^{\,a} - \vec{s}_n^{\,i}, \tag{3.24}$$

with $\vec{s}_n^{\,a}$ the averaged stress vector at node *n*, and $\vec{s}_n^{\,i}$ the stress vector at node *n* of element *i*. For each element *i*, the energy error is

$$e_i = \frac{1}{2}\int_V \Delta \vec{s}^{\,T} [D]^{-1} \Delta s \; dV, \tag{3.25}$$

with [*D*] the stress-strain matrix, and *V* the volume of the element. The energy error can be normalized against the strain energy U_{en} over *N* elements, as in

$$e_{en} = 100\sqrt{\sum_{i=1}^{N} e_i \,/(U_{en} + \sum_{i=1}^{N} e_i)}\,. \tag{3.26}$$

The most efficient mesh is found if e_i is equal for all elements. A plot of the normalized error energy is used to determine areas of the mesh that still produce high error levels. Local refinement of the mesh is used to reduce the normalized error energy until a satisfactory maximum error level is obtained. The final error level for each FEA model is listed in table 3.3.

Material	Impregnated cable model	Dry cable model	Cable sample model
strands	0.3	0.6	NA
epoxy	0.8	1.2	NA
insulation	6.6	0.1	NA
cable	NA	NA	14
steel	NA	NA	9.8
G10 sheet	NA	NA	11

Table 3.3 Error levels (in percent) in the ANSYS FEA models. The cable sample model mesh did not reach a high resolution due to limitations on the model size. Local refinements in the corner points are used to increase the resolution in the important areas.

In non-linear elements, the final accuracy of the solution depends on the amount of steps and the convergence tolerance criteria for each step. ANSYS computes each successive step with a Newton-Raphson algorithm, and terminates the solution when the square root of the sum of the squares (SRSS) of the force imbalance is less than the tolerance times SRSS of the applied loads.

For each successive step, the error set by the tolerance then accumulates to yield the final error. Therefore, when increasing the amount of steps in the solution one should also decrease the solution tolerance. The tolerance value used for the cable models is the default value of 0.001. With the largest number of steps used of 15, the maximum convergence error is 1.5 %.

3.7.3 The use of contact elements

In the FEA models of the dry cable (without epoxy) and the model of the cable test sample, areas exist that could overlap with each other when the transverse load is applied. This is caused by the mesh representation of the physical shape of the strands or cable. When two sections of the FEA model are separated by air, ANSYS has no method of knowing whether the two sections touch when displaced under load. To prevent the overlap, contact elements are used.

A contact element has no stiffness when the nodes (or surface) on the first part is not touching the node (or surface) of the second part. When the applied load causes the nodes (or surfaces) to touch each other, the contact element has a large stiffness (usually set to 10-100 times the contacting material stiffness). This prevents the two sections from overlapping, and loads can now be transmitted from one section to the other. The elements can also transfer friction loads along their surfaces.

Contact elements are used in the FEA model of the dry cable between the surfaces of the strands, and between the strands and the pressure plates, to prevent the strands from penetrating each other and the plates. In the model of the cable test sample contact elements are used between the cable and the sample holder, and between the cable and the pressure block. The elements are used to allow the cable to slide between the holder and the pressure block under load.

3.7.4 Model A: non-linear model of an impregnated cable cross-section

The first model is of a two-dimensional cross-section of the cable in the transverse direction, to analyze the pressure distribution in the individual strands as a function of the applied transverse load. The model is shown in figure 3.13, and is set up to calculate the stress profile in the strands of an impregnated and insulated cable due to the stress concentration on the contact points between the strands.

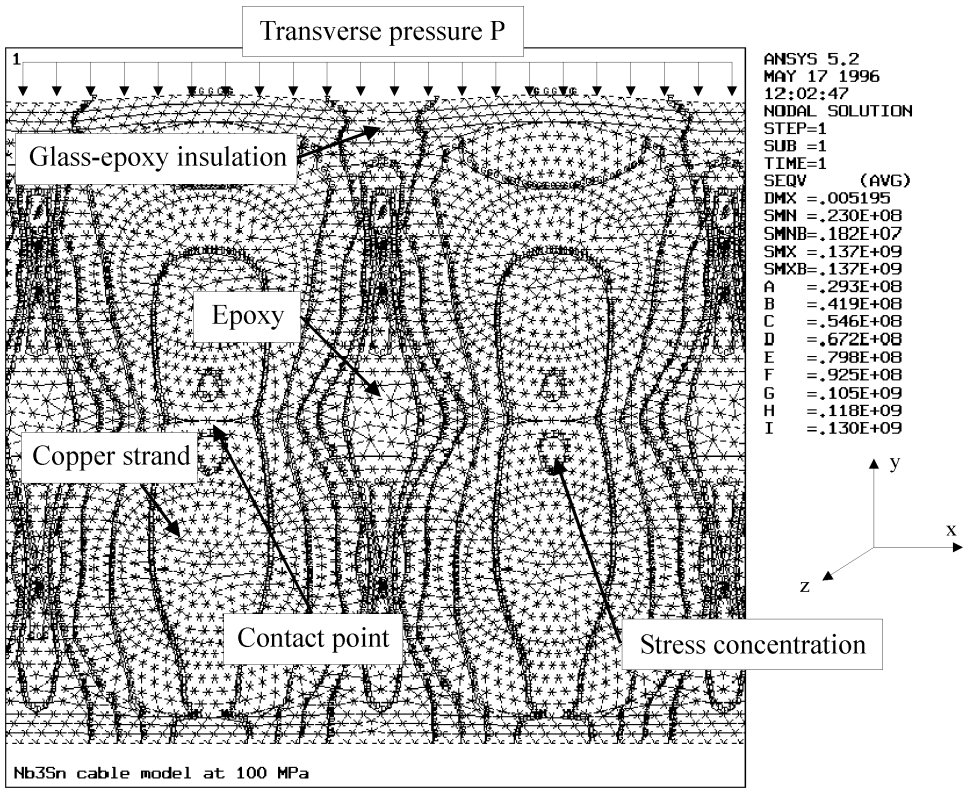

Figure 3.13 Part of the cable cross-section model to calculate the stress distribution in the individual strands at 100 MPa transverse pressure in the y-direction on the top surface. The y-axis is along the transverse direction, the x-axis along the radial direction, the z-axis is along the length of the cable. Shown is the initial coarse mesh before refinement to reduce the model error level. A full-color version of this plot is reproduced in Appendix A.

This is achieved by modeling the strands as round wires with isotropic material properties, and filling the voids between the strands with elements simulating the epoxy filler. The cable is surrounded by a glass-epoxy sleeve, modeled as glass-fiber filled epoxy with a Young's modulus of 56 GPa.

Special care is taken to ensure a good match between the elements at the copper-epoxy-copper interface near the contact point. This is needed to achieve the necessary numerical resolution at the location where the stress gradient will be the highest. The model is run with both linear and non-linear material parameters.

An important conclusion is that the local stress near the contact points can be up to 30-40 % higher in the strands compared to the overall pressure exerted on the cable surface. If the strands in the cable were already flattened during the cabling operation, and reacted in this shape, the resultant local stress increase is reduced. More detailed results are discussed in section 3.8.1.

3.7.5 Model B: non-linear model of a dry cable cross-section

A non-linear two-dimensional model is used to determine the stress at the contact points between the strands as compared to the transverse load applied to the cable surface. This information is needed to accurately predict the load on the individual strands for the wire models. The model is shown in figure 3.14. It consists of two strands in contact with each other, compressed between two stainless steel plates. This configuration actually will occur in the cabling machine at the pinch point between the rollers. In addition, it serves as a good illustration of the strand deformation that occurs when a loosely compacted cable is compressed under transverse load.

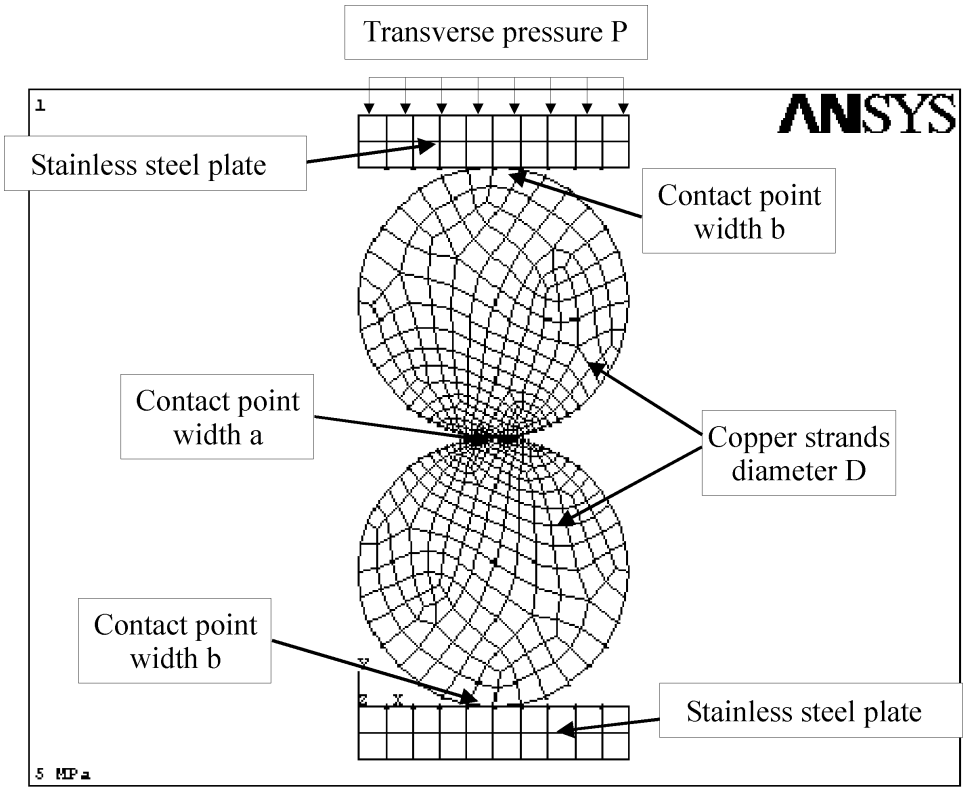

Figure 3.14 The two-dimensional dry cable cross-section model to calculate the stress distribution in the individual strands for increasing transverse pressure on the top plate. The y-axis is along the transverse direction, the x-axis along the radial direction in a magnet. Shown is the initial coarse mesh before refinement to reduce the model error level.

A solution for the linear problem is found in [3.38]. The maximum stress for two strands with diameter *D* loaded on top of each other between two plates is

$$s_c = 0.798\sqrt{\frac{pE}{D(1-\nu^2)}}, \tag{3.27}$$

with a load per unit length p, E the Young's-modulus and v the Poisson's ratio of the strand. The displacement y between the two plates (equal to the compression of the strand or cable) is given by

$$y = \frac{4p(1-v^2)}{pE}\left(\tfrac{1}{3} + \ln\frac{2D}{b}\right) + \frac{2p(1-v^2)}{pE}\left(\tfrac{2}{3} + 2\ln\frac{2D}{a}\right), \tag{3.28}$$

with $a = 2.263\sqrt{pD(1-v^2)/2E}$ and $b = 2.263\sqrt{pD(1-v^2)/E}$.

From (3.28), the effective Young's modulus of a cable can be computed from the quotient of $y/2Dp$. Figure 3.15 shows the effective Young's modulus as a function of the applied load per unit length p for a cable made from a typical strand with E = 117 GPa, v = 0.36 (copper matrix) and for E ≈100 GPa, v = 0.3 (bronze matrix). The curves clearly illustrate that a dry cable has a non-linear stress-strain relation, and behaves as a much softer material than the matrix material under transverse compression, even when material yield is not taken into account. The FEA model is run without epoxy filler between the strands to illustrate the large effect an insufficient epoxy impregnation can have on the critical current degradation when the yield in the copper of the strand is taken into account. In section 3.8.2, the results from the model are discussed in detail.

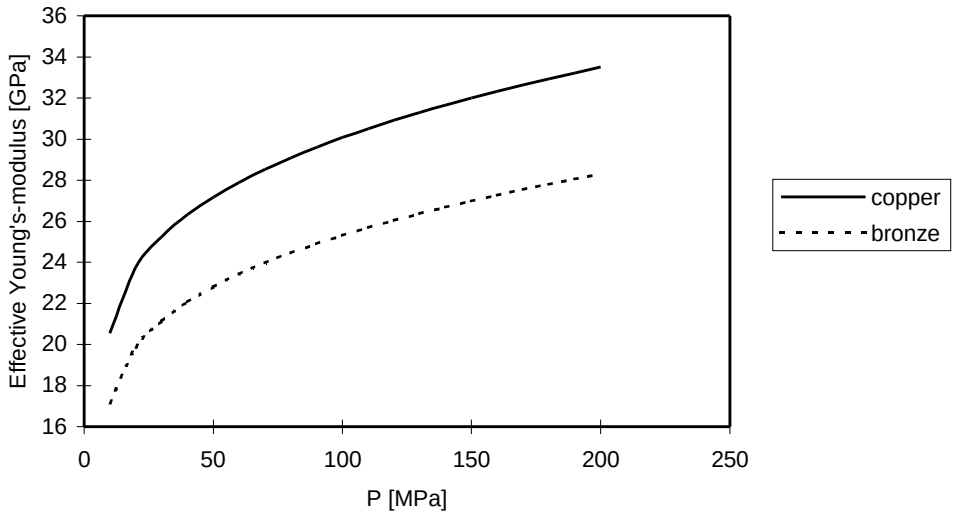

Figure 3.15 Effective Young's modulus as a function of the applied load per unit length p for a cable made from a copper matrix strand and a bronze matrix strand.

3.7.6 Linear model of a cable test sample

Finally, a model of the cable as it is in the experimental setup is presented. A schematic of the test fixture is shown in figure 3.16.

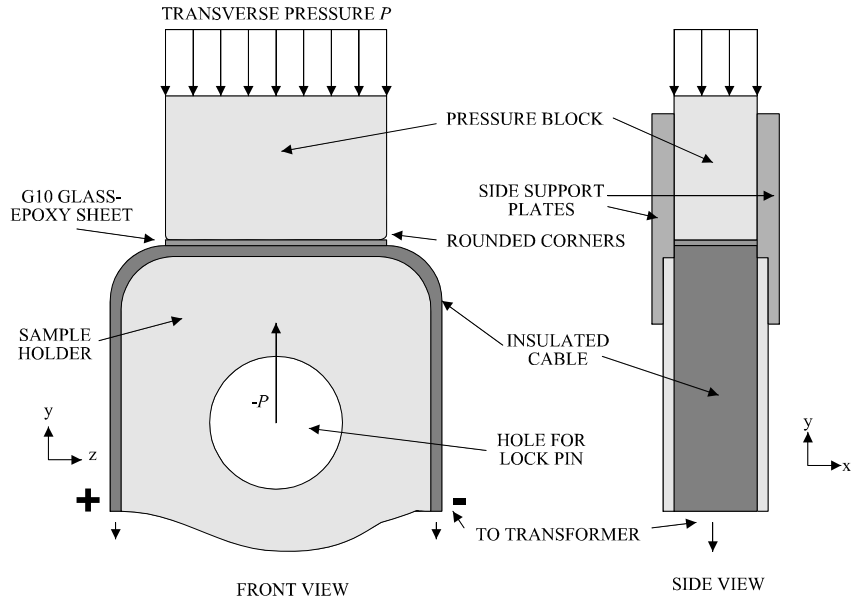

Figure 3.16 Schematic of the test fixture for the cable critical current measurements under transverse load P. The load is applied in the y-direction by a stainless steel pressure block, and reacted against the sample holder which in turn is pinned in place. The cable sample surface can be covered with a thin glass-epoxy sheet on the top and bottom. The sides of the cable are constrained by stainless steel plates restricting movement in the x-direction.

Cables are wrapped in a U-shape and impregnated onto a stainless steel sample holder. The sample is then compressed in the y-direction by a stainless steel pressure block, while being constrained in the x-direction. The cable is free to expand in the longitudinal direction at the area under the pressure block. The pressure is applied either directly to the cable surface, or through a thin sheet of glass-epoxy to lessen the stress concentrations at the interfaces between the strands and the pressure block and the sample holder. Details of the experimental setup are discussed in chapter 5. Results from the finite element model are shown in figure 3.17. It is used to estimate the average compressive stress in the cable samples tested in the U-shaped configuration [3.39], and to determine the magnitude of the local stress concentrations at the edges of the pressure block. The effect of an extra glass-epoxy sheet below and above the cable sample to apply a more uniformly distributed load is analyzed.

The model uses the PLANE82 2D second order element, and the CONTAC48 point to surface contact element. The cable Young's modulus is varied from 26 to 50 GPa, the glass-epoxy sheet Young's modulus is 56 GPa in the transverse (y) direction and 10 GPa in the x and z direction. The stainless steel holder and pressure block have a Young's modulus of 193 GPa. The glass-epoxy sheet is modeled as a sheet glued to the pressure block and the stainless steel holder. The cable bottom surface is glued to the glass-epoxy sheet. The interface between the cable top surface and the pressure block or glass-epoxy sheet is allowed to slide in the z-direction. Contact elements are used on the entire top cable surface, and on the bottom cable surface where it is not in contact with the glass-epoxy. The cable is held onto the sides of the sample holder by a small positive pressure of 5 MPa along the entire side length.

When the transverse pressure is applied, the cable will compress in the y-direction, while expanding in the z-direction. The highest stress will occur at the edges of the pressure block, since the pressure in the y-direction is uniform along the pressure surface, but the strain in the z-direction causes a stress concentration at the edges.

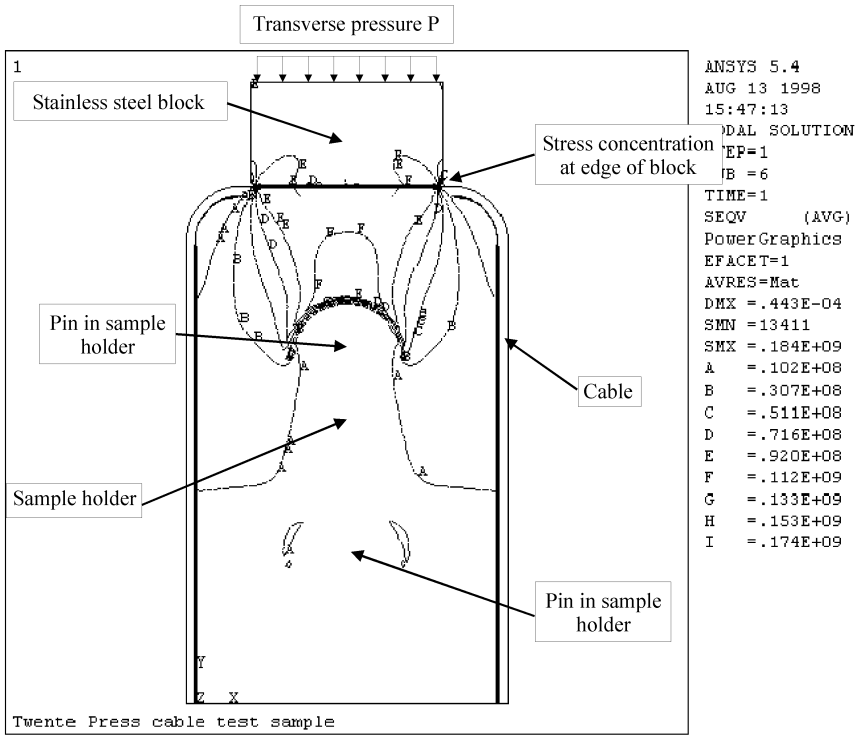

Figure 3.17 The linear test sample model for the U-shape configuration in the critical current versus applied transverse pressure experiments. Shown is the Von Mises stress in the cable and sample holder for an applied stress of 100 MPa on the top surface of the pressure block. A full-color version of this plot is reproduced in Appendix A.

3.8 FEA model results

This section discusses the results of the FEA models in more detail. First, the non-linear models of the cable cross-sections are analyzed. The purpose is to formulate a relation between the critical current and the hydrostatic, deviatoric and plastic stress components as a function of applied transverse pressure, that can predict the shape rather well.

For the FEA cable models, the transverse load is increased in steps of 5, 10 and 25 MPa. The results for each run are stored, after which the separate components of the stress are analyzed.

3.8.1 Model A: non-linear model of an impregnated cable cross-section

Figures 3.18 and 3.22 show the calculated increase in the stress and strain components as a function of the applied pressure *P* on the cable surface. The graphs are used to illustrate the effect of the plastic deformation on the effective Young's modulus of the cable, the resulting changes in the stress components for applied stress that causes the strands to yield, and to estimate the amount of yield of the copper matrix in the strands.

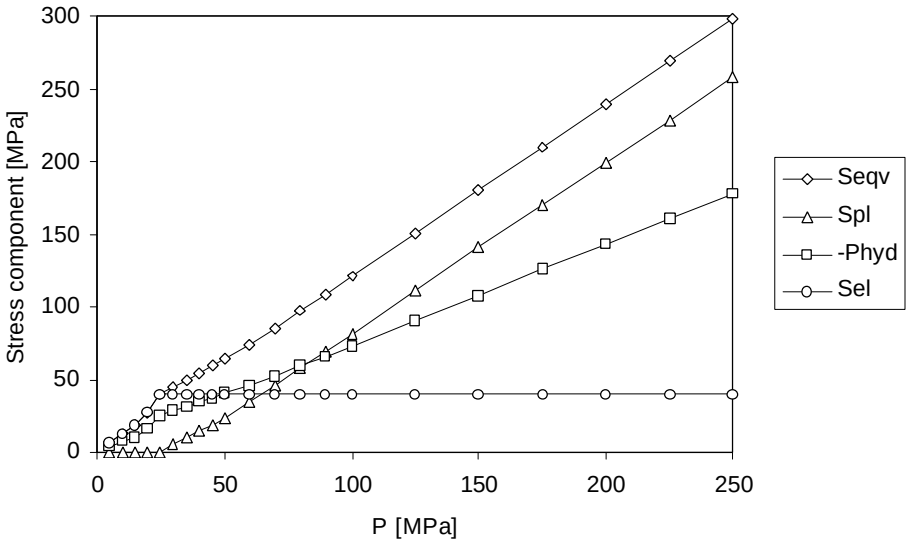

Figure 3.18 The (maximum) Von Mises stress (Seqv), plastic equivalent stress (Spl), hydrostatic pressure (Phyd, inverted) and elastic stress (Sel) in the strands in a cable as a function of the applied pressure on the cable surface. The maximum values of the components are found near the stress concentration marked in figure 3.13 Increasing pressure does not tend to shift the location significantly. The markers on the curves indicate the results from each consecutive FEA run.

Figure 3.18 shows the Von Mises stress, plastic equivalent stress, hydrostatic pressure and elastic stress as computed from the FEA model. Above the yield stress, the hydrostatic pressure increases linearly with applied transverse pressure on the cable surface. This means that the hydrostatic pressure component is not useful to predict the onset of the permanent degradation in the critical current.

The Von Mises stress shows a decrease in slope for higher values of the transverse pressure *P*. This is due to the fact that above the yield strength of the material the plastic component becomes the dominant factor. The larger the fraction of strand that is stressed past the yield point, the larger the contribution of the plastic stress component. The stress-strain curves of the materials used in the model are shown in figure 3.19.

The maximum elastic component of the stress increases until the yield stress is reached. After that, further increase of the applied transverse pressure does not change the maximum elastic component, but only contributes to an increase in the plastic component. The maximum Von Mises stress then follows the plastic component for increasing applied transverse pressure.

The computed maximum values of the stress components are used to predict the onset of the permanent degradation, and the shape of the curve, but can not be used to determine the magnitude of the critical current degradation. The reason is that the maximum value is not representative of the stress in the entire strand. In order to compute the magnitude of the critical current degradation, the integral of the stress components over the strand cross-sectional area is computed. The area (or volume) of the strand affected by the particular stress or strain component can now be used to predict the shape of the critical current degradation curve as a function of applied transverse pressure. The relative volume of the strand where the stress exceeds yield, and the strain exceeds 0.2 %, is shown in figure 3.20.

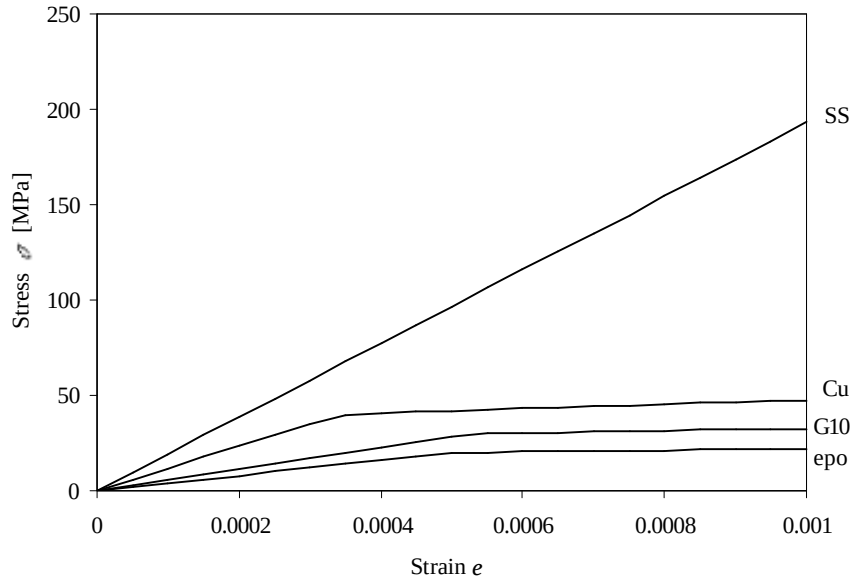

Figure 3.19 Non-linear material properties for the components of the FEA cable model. The labels are Cu (copper or strand matrix), G10 (glass-epoxy), SS (stainless steel) and epo (epoxy).

In regions where the stress exceeds the yield stress of the material, the strands are locally subjected to large strains, causing permanent deformation of the cross-section. Since the copper matrix is soft, and the thin brittle Nb_3Sn filaments can not support large stresses to resist the movement, they will deform with the softer matrix material and crack under high loads. Cracks will naturally occur in the most severely deformed areas, which lie near the contact points of the strands in the cable, as marked in figure 3.13.

Figure 3.21 shows the elastic and plastic components of the Von Mises or equivalent stress for an applied transverse pressure of 40 MPa. The lower figure illustrates the onset of the plastic deformation near the contact point of the strands. Only a small percentage of the cross-section of the strand is above the yield stress. When the applied pressure is increased, more and more of the cross-section exceeds the yield stress. Consequently, an increasing percentage of the area exceeds a strain of 0.2 %.

In figure 3.22 the maximum equivalent elastic strain component $e_{el,eqv}$ (Elastic) and $e_{pl,eqv}$ (Plastic) are shown. This figure illustrates that for compressive stress higher than the yield stress of the strands the equivalent plastic strain is the dominant component. The model calculations yield local values up to 1.3 % at 150 MPa for the plastic component. With a fracture strain of the Nb_3Sn filaments around 0.2 %, the filaments will probably sustain permanent damage. Extrapolation of $e_{pl,eqv}$ to the breaking strain of 0.2 % yields a transverse pressure of approximately 50 MPa on the cable surface, marking the onset of permanent damage.

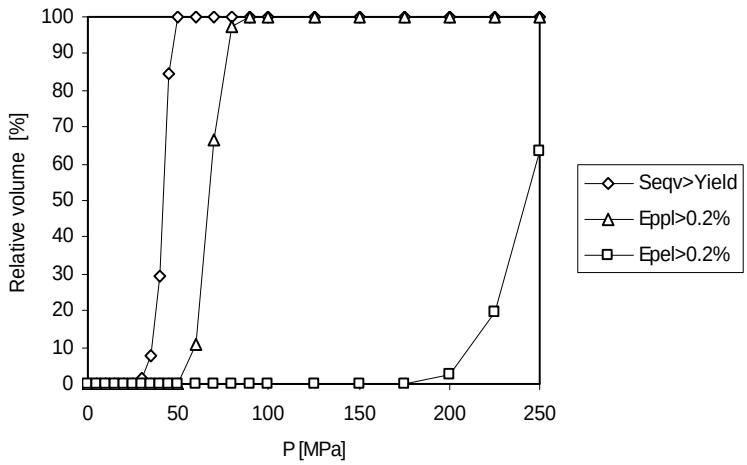

Figure 3.20 A plot of the relative volume of the strand where the plastic component of the Von Mises or equivalent stress (S_{eqv}) exceeds the yield stress. Also plotted is the relative volume of the strand where the plastic (EP_{pl}) and elastic (EP_{el}) component of the strain exceed 0.2%.

Extrapolation of $e_{el,eqv}$ to the breaking strain of 0.2 % yields a transverse pressure of approximately 200 MPa, marking a point where most of the strand will probably sustain permanent damage. The few TWCA cable samples that were actually tested to such high pressure indeed show a very large I_c degradation at 250 MPa. S. Ochiai et.al. [3.40] report no observed critical current in bronze processed Nb_3Sn wires above applied transverse pressures (the pressure was applied at room temperature) of 280 MPa, indicating that all filaments were broken. More recent experiments with LMI cable up to 200 MPa showed a reduction of only 8 % in I_c, contradicting the results reported by S. Ochiai et.al.

Figure 3.23 illustrates the differences in shape of the curves due to differences in compaction factor. The curves labeled hydrostatic, deviatoric and plastic show the I_c degradation for each component of the total stress in the strand computed with the FEA model. The curves shown are based solely on the maximum stress and strain values, in contrast to the model discussed in section 3.9, where the area exceeding a set strain limit is taken into account.

The curve labeled combined is the sum of the stress components. The model data is compared to three measurements on a cable made of similar strands, one with a high, one with a low, and one with moderate compaction (best data obtained with this material).

A high compaction factor causes a large I_c degradation. The shape of the degradation curve indicates that deviatoric and hydrostatic stresses are the dominating effects.

A moderate compaction factor causes minimal I_c degradation. The shape of the curve is dominated by plastic deformation stress.

For a very low compaction factor, plastic deformation causes severe I_c degradation for high loads.

The combined curve in figure 3.23 is computed with equal weight factors (unity) for the three components.

In chapter 5, weight factors are obtained for the measured cable samples as a function of the conductor type and cabling parameters. The weight factors range from 0.1 (hydrostatic and deviatoric component) to about 10 (for the plastic component in a low compaction cable), and are a function of the conductor type and the cabling parameters.

Table 3.4 shows the effect of the material properties on the shape of the I_c degradation curve computed from the FEA model.

The effects of small changes in the material properties listed in the table are computed with the FEA model. The changes are based on a cable with a 10 % reversible degradation at 100 MPa (typical), and 0.5 % permanent degradation (strand Young's-modulus 117 GPa, coefficients –0.3 for hydrostatic, 0.3 for deviatoric and 0.3 for plastic). The table lists the qualitative change in the shape of the I_c degradation curve for various changes in the material properties of the FEA model.

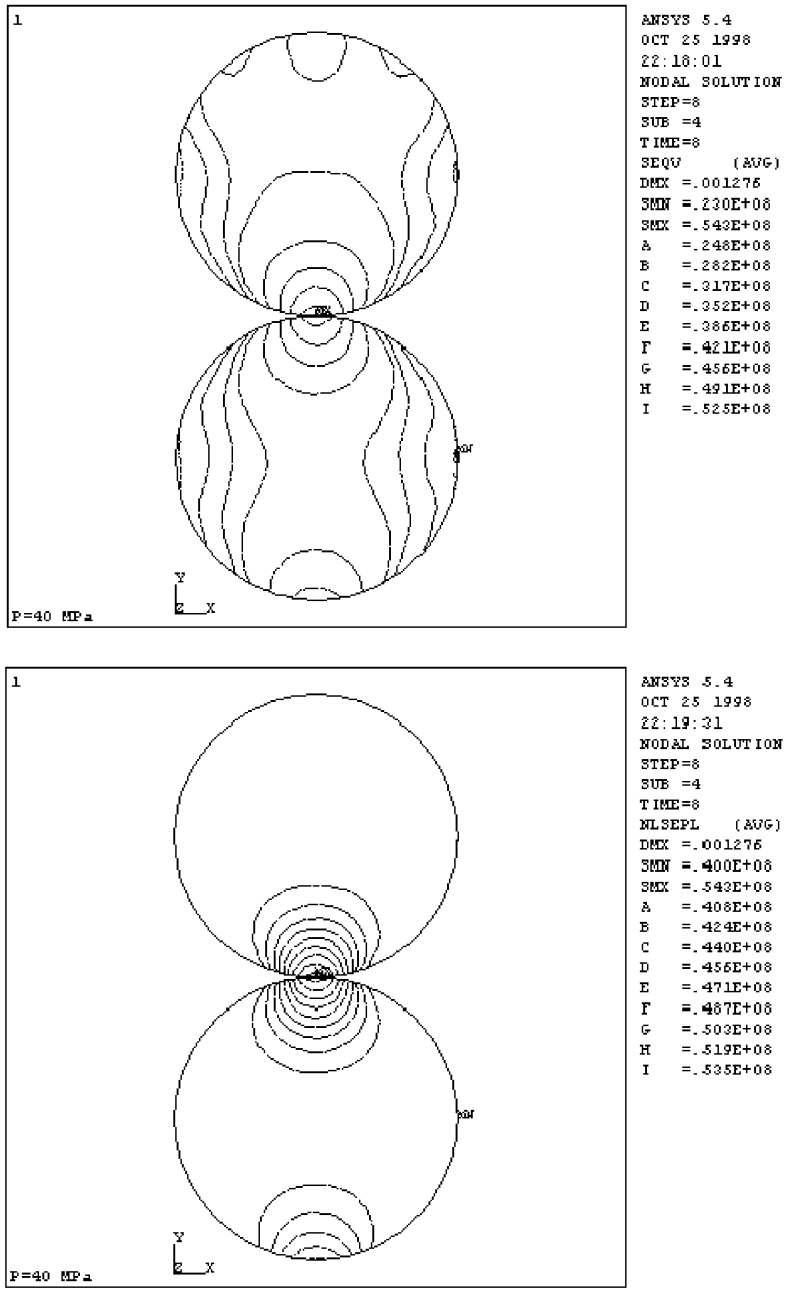

Figure 3.21 A plot of the elastic (top) and plastic (bottom) component of the Von Mises or equivalent stress in the strands for an applied transverse pressure of 40 MPa. The stress is the highest near the contact point of the strands. Note the onset of plastic deformation near the contact point for an applied transverse pressure equal to the yield stress of the strand material. Full-color versions of these plots are reproduced in Appendix A.

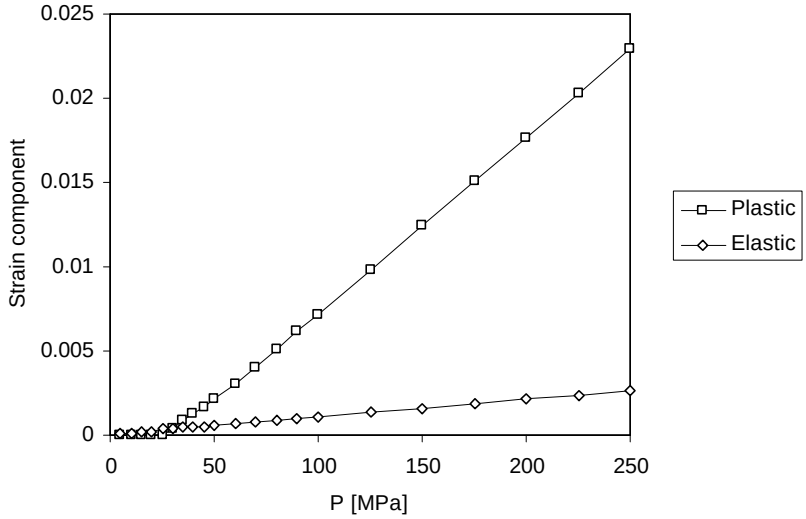

Figure 3.22 The maximum equivalent elastic (EPELEQV) and plastic strain (EPPLEQV) components of a strand in a cable as a function of the applied pressure on the cable surface.

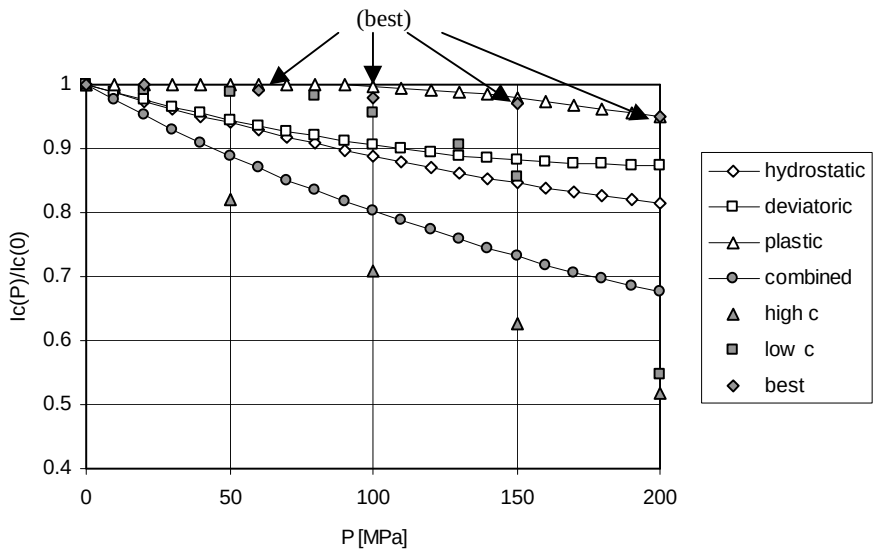

Figure 3.23 Results from the impregnated cable model with non-linear material parameters. Critical current degradation as a function of the applied pressure is computed with the model based on equation (3.20).

A decrease in the Young's modulus of the strand causes an increase in I_c degradation. This is due to an increase in the strain within the strand for a given applied transverse pressure. For small variations in the Young's modulus, the shape of the curve remains the same. A reduction of 10 GPa in the Young's modulus raises the I_c degradation by 0.05 % (a relative change of 0.5 %).

For a cable that is inherently more sensitive to applied transverse pressure (-0.5/0.5/5 for the hydrostatic, deviatoric and plastic coefficients), the I_c degradation changes about 0.7 % from a reversible degradation of 21.7 % (a relative change of 3 %). Thus, increasing the Young's modulus of the matrix

material of a strand reduces the I_c degradation, but is most effective for cables that are already sensitive to applied pressure.

A change in the yield stress of the strand matrix material moves the point on the I_c degradation curve where permanent damage starts to occur. A decrease of the strand yield stress from 40 MPa to 30 MPa increases the I_c degradation by 3 % for a typical cable, and 13 % for the more sensitive cable.

Increasing the Young's modulus of the epoxy results in less strain in the overall cable cross-section, hence a reduction in I_c degradation. An increase in the Young's modulus from 40 GPa to 50 GPa (unfilled epoxy to filled epoxy) reduces the I_c degradation by 1 % for a typical cable, and 8 % for the more sensitive cable. Similarly, increasing the epoxy yield stress is beneficial, since the cable will yield at a higher applied pressure, thus reducing the strain in the strands.

Material property	Change	I_c degradation	Dominating effect
Strand Young's modulus	decrease	increase, similar shape	increase in strain on Nb_3Sn
Strand yield stress	decrease	increase, onset lower	more plastic deformation
Epoxy Young's modulus	increase	decrease, more linear	epoxy carrier more of the load
Epoxy yield stress	increase	decrease, onset higher	less plastic deformation
Sleeve Young's modulus	increase	increase, onset lower	more plastic deformation in strand
Sleeve yield stress	decrease	decrease, similar shape	more cushioning by the sleeve

Table 3.4 Effect of the material properties on the shape of the I_c degradation curve.

Changes in the material properties of the insulation sleeve are included for completeness, but the influence on the I_c degradation is very small (less that 0.1 % change). This is due to the small thickness of the sleeve compared to the cable thickness. Increasing the Young's modulus of the sleeve causes the contact point of the strand with the sleeve to deform earlier than with a less stiff sleeve. Using a sleeve with a low yield stress causes the sleeve material to redistribute and fill the unevenness in the cable surface, hence a reduction in the I_c degradation due to a more uniform stress distribution.

3.8.2 Model B: non-linear model of a dry cable cross-section

This section describes the results of the FEA model of two strands on top of each other without the support of epoxy. This is equivalent to loading of a cable in absence of epoxy filling.

Figures 3.24 through 3.26 show the average Von Mises stress (SEQV) in the strands with transverse pressure increasing from 20 to 40 MPa. The graphs illustrate the permanent deformation of the strand. Displacement scaling in the plots is 1:1.

At 20 MPa compressive load, the contact surface is already increased to about 25 % of the strand diameter, compared to 2.8 % for the linear case from (3.28). The maximum stress in the strand is equal to the yield stress of annealed copper (40 MPa). About 19 % of the strand volume is plastically deformed.

At 30 MPa compressive load, the contact surface is about 75 % of the strand diameter. Almost 60 % of the strand volume is stressed past the yield point. The cable is now compacted to 105.9 % (no compaction equals $4/\pi \approx 127.3$ %), and 76 % of the strand volume is strained past 0.2 % plastic strain.

At 40 MPa compressive load, the strands are almost flattened to rectangles, with a compaction factor of 91.4 %. About 81 % of the strand volume is strained past 0.2 % plastic strain, and 69 % of the volume is stressed past the yield point.

All results for the FEA runs are tabulated in table 3.5. The percentages of strand volume with strain exceeding 0.2 %, and strand volume with stress exceeding the yield stress are shown in figure 3.27. The effective Young's modulus of the cable is shown in figure 3.28.

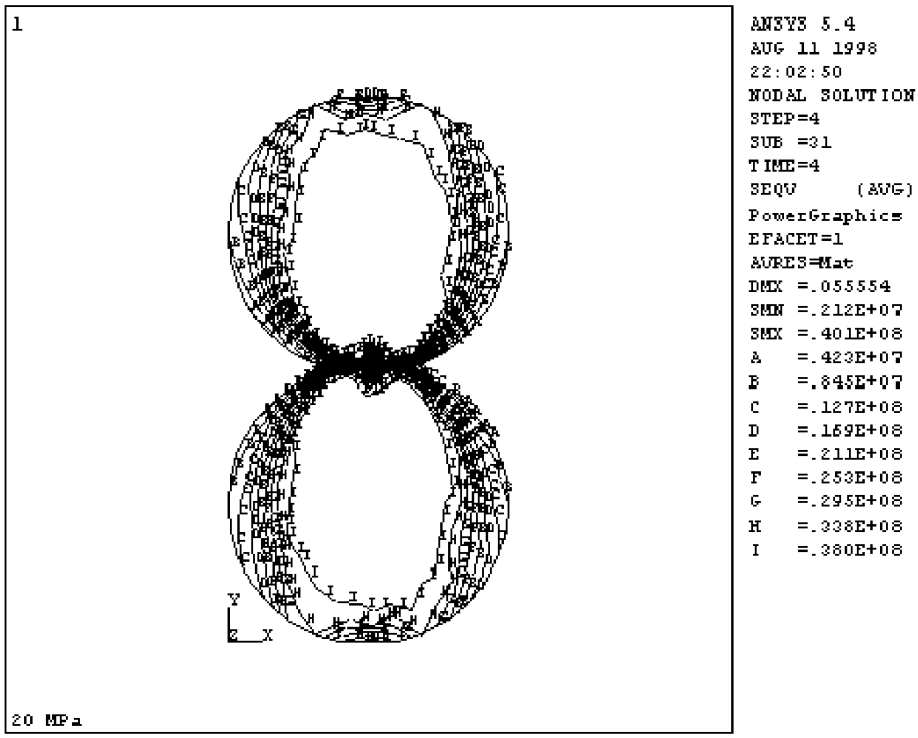

Figure 3.24 *The non-linear dry cable cross-section model to calculate the stress distribution in the individual strands for increasing transverse pressure on the top plate. The y-axis is along the transverse direction, the x-axis along the wide side of a cable. The applied pressure is 20 MPa. A full-color version of this figure is reproduced in Appendix A.*

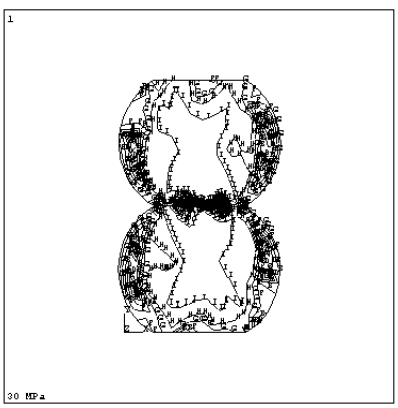

Figure 3.25 *The non-linear dry cable cross-section model at an applied pressure of 30 MPa. A full-color version of this figure is reproduced in Appendix A.*

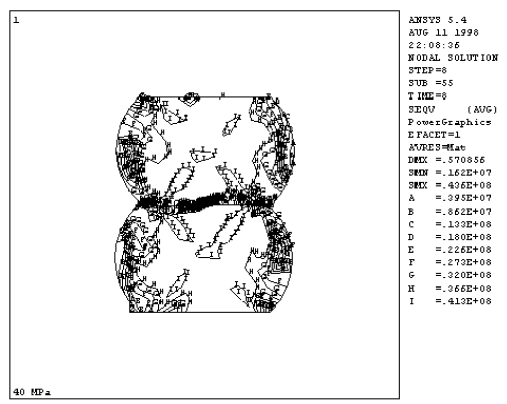

Figure 3.26 *The non-linear dry cable cross-section model at an applied pressure of 40 MPa. A full-color version of this figure is reproduced in Appendix A.*

Pressure [MPa]	Thickness (in y-dir.) [mm]	Compaction factor [%]	$e_{pl,eqv}$ > 0.2% [%]	s_{eqv}>Yield [%]	EffectiveYoung's modulus [GPa]
0	2.0	127.3	0.0	0.0	
5	2.0	127.2	0.5	0.0	4.05
10	2.0	126.4	9.3	0.2	2.60
15	2.0	125.9	17.8	1.5	1.43
20	2.0	124.2	54.0	19.2	0.36
25	1.8	117.3	69.6	44.9	0.09
30	1.7	105.9	76.4	59.0	0.06
35	1.5	98.2	78.9	67.8	0.08
40	1.4	91.4	81.2	69.0	0.09

Table 3.5 Computational results from the non-linear dry cable cross-section model.

Similar to the results from the FEA model with the epoxy impregnation, a reduction in Young's modulus of the strand increases the compaction. In addition the percentage of the area with stress exceeding the yield stress at a given applied pressure is increased. Increasing the strand material yield stress reduces the compaction. The percentage of the area with stress exceeding the yield stress is decreased.

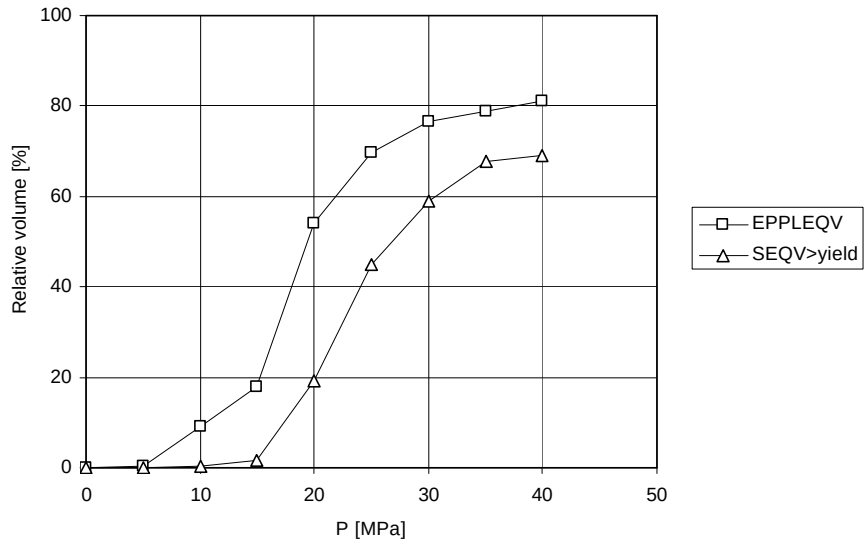

Figure 3.27 The percentage of the strand volume with strain exceeding a plastic strain $e_{pl,eqv}$ of 0.2 % (EPPLEQV) and the Von Mises stress exceeding the yield stress (SEQV > yield).

The effective Young's modulus is almost an order of magnitude lower when compared to the effective Young's modulus of the epoxy-impregnated cable. This is due to the large plastic deformation in the strands when they are deformed to occupy the rectangular space available for each strand in a cable. Calculations are terminated at an applied pressure of 40 MPa due to model instability.

Further increase of the applied pressure will result in an asymptotic increase in the effective Young's modulus. The value reached is equal to the strand material property at the load required to fully squeeze the strand into a rectangle (all void space is then filled, thus the cable behaves as a solid material).

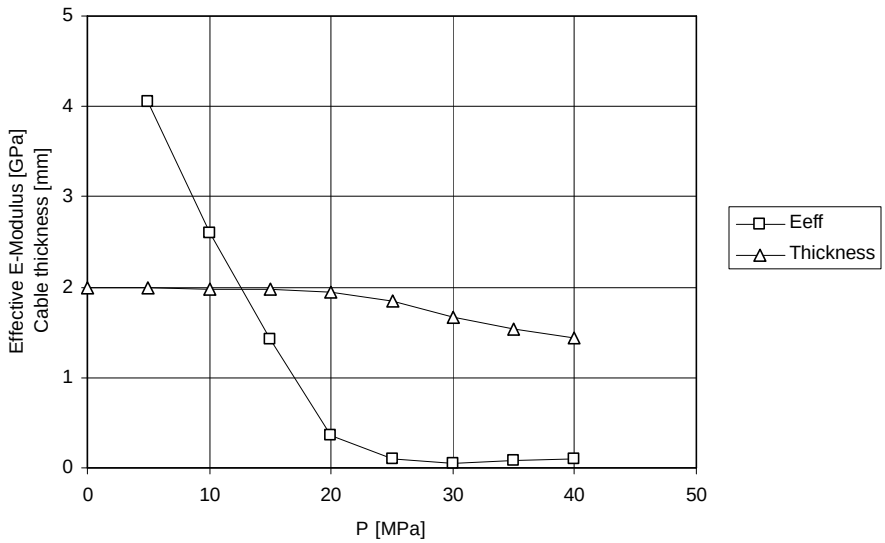

Figure 3.28 The effective Young's modulus computed from the FEA model (E_{eff}), and the thickness of the cable as a function of the applied transverse pressure (the thickness without load is 2 mm).

3.8.3 Linear model of a cable test sample

The FEA model of the cable test sample shows stress concentrations at the edge of the pressure block. Although the corners of the pressure block have a 1 mm radius to reduce the stress concentration, the local stress can be up to about 34 % higher in the top layer of the cable. Figure 3.29 shows an enlargement of the affected area. Table 3.6 lists the magnitude of the stress concentration as a function of the material property of the cable and the surface (glass-epoxy sheet/no sheet) in contact with the cable.

Contact material	Cable Young's modulus [GPa]	Contact surface Young's modulus [GPa]	Maximum stress in cable [MPa]
glass-epoxy	26	56/10/10 (E_x/E_y/E_z)	134
glass-epoxy	50	56/10/10 (E_x/E_y/E_z)	130
stainless steel	26	193	131
stainless steel	50	193	127

Table 3.6 Magnitude of the stress concentration as a function of the material property of the cable and the surface in contact with the cable.

The presence of a stress concentration at the corners of the pressure block raises the question whether the experimental setup is representative of a cable in a magnet. The ideal situation for an experimental setup is a long cable sample, with several times the twist pitch of the cable loaded by the pressure block. Due to the limited bore size of the magnet used to generate the background field, only 40 mm of the cable is loaded. A more detailed discussion of the validity of the experimental setup is presented in chapter 5.

3.8.4 General results

Figure 3.30 shows the effective stress-strain relation of the insulated and impregnated cable (A) (from the model shown in figure 3.13) compared to the dry cable (B).

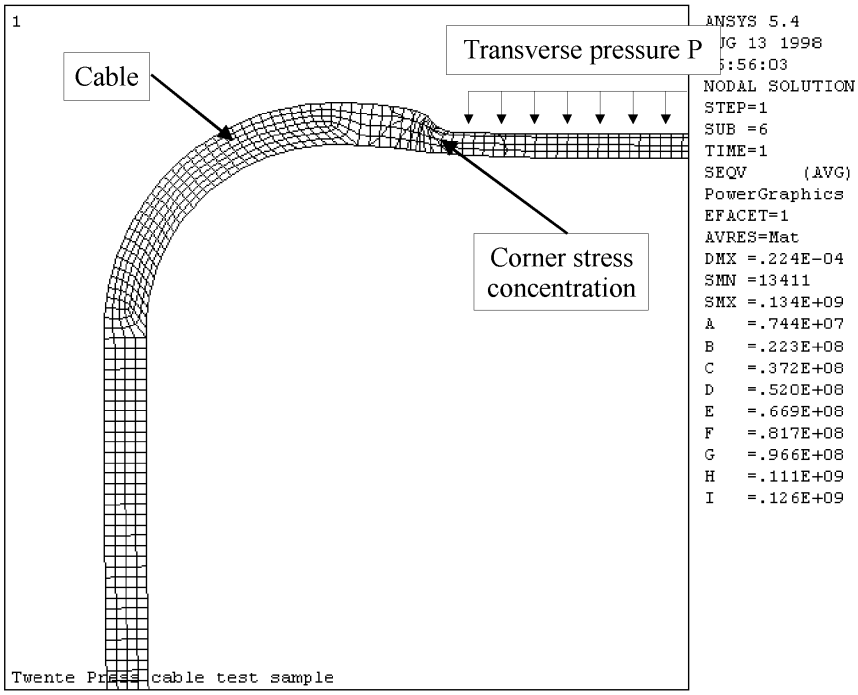

Figure 3.29 The corner area where the pressure block imprints on the cable enlarged. Shown is the Von Mises stress in the cable elements. The cable deformation is enlarged tenfold. A full-color version of this figure is reproduced in Appendix A.

The total displacement of the top surface of the insulated cable is calculated as a function of the applied transverse pressure in the plastic model. The cable is constrained in the x and z-direction, simulating the actual setup of the cable test experiments. The curve is compared to that of a dry cable with the same material properties for the strand.

The curve shows a decrease of the Young's modulus with increasing pressure, with an effective Young's modulus of about 44 GPa for pressures around 150 MPa. The value corresponds to a Young's modulus of 42 GPa measured in tests done at LBNL on stacks of 10 cables impregnated with CTD-101 epoxy [3.41], but is higher than the value of about 20 GPa measured by Den Ouden et al. [3.42].

3.9 Inclusion of the plastic deformation in the I_c(s) model: permanent degradation

As is evident from figure 3.18, the local Von Mises stress and the hydrostatic stress increase almost linearly with applied transverse pressure. There is only a slight yielding effect visible in the hydrostatic stress when the yield strength of the annealed copper [3.43] is exceeded.

Using the plastic component of the equivalent stress from the FEA models (A and B), a realistic dependency of I_c on the applied transverse pressure is obtained. The computed equivalent plastic stress is directly based on the deviatoric stress. The hydrostatic component is separated from the plastic stress component in the analysis. Thus, as Ten Haken [3.44] suggested, the deformation of the material plays a more important role in the I_c degradation than the hydrostatic pressure in the strands.

It is thought that the plastic component of the equivalent stress is mostly responsible for the observed permanent degradation due to structural damage, whereas the elastic components (equivalent stress and hydrostatic stress) are responsible for the gradual decrease in I_c due to a decrease in the B_{c2} and T_c as described by the model in equation (3.20).

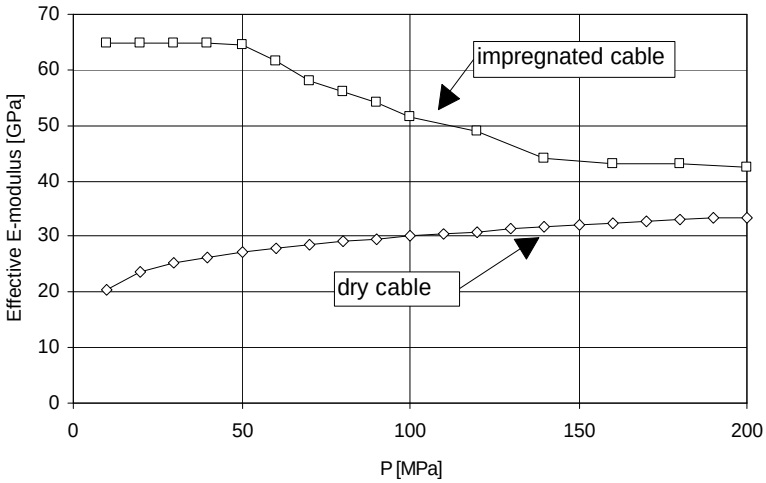

Figure 3.30 The calculated effective Young's modulus of an insulated and epoxy-impregnated cable (A) compared to a dry cable (B). The pressure is applied on the cable surface.

By the separation of the hydrostatic component and the deviatoric component (that determines the amount of plastic deformation in the FEA analysis) a new $I_c(s)$ model is formulated that predicts both the reversible I_c degradation as well as the permanent damage to the filaments. The critical current is written as a function of both the hydrostatic stress s_{hyd}, deviatoric stress s_{dev} and the plastic component of the equivalent stress, which are all a function of the applied transverse pressure P.

The two elastic components of the stress are combined into one stress factor s_{elast} for the $I_c(P)$ model to form

$$s_{elast}(P) = C_1 s_{hyd}(P) + C_2 s_{dev}(P), \tag{3.29}$$

with C_1 and C_2 constants determined by the material properties of the composite strand and the buildup of the cross section.

The plastic equivalent stress component is included in the model by computing the area of all elements where the yield strain of the Nb_3Sn filaments is exceeded, then reducing the overall critical current of the strand by a proportional amount based on the total area affected. The maximum yield strain e_{max} of the filaments is set at 0.2 %.

The multiplication factor is given by

$$f_{pl}(P \le P_{\max}) = 1 - \frac{C_3}{A_{total}} \sum_{i=1}^{n} \begin{cases} 0 (e_n(P) < e_{\max}) \\ A_n (e_n(P) < e_{\max}) \end{cases}, \tag{3.30}$$

with A_{total} the total area of all elements, $e_n(P)$ the strain in the element as a function of the applied transverse pressure P, and C_3 a scaling factor based on the internal structure of the strand. P_{max} is the maximum value of P reached in a given time; the corresponding maximum strain is e_{max}. If P is increased to P_{max}, f_{pl} increases. If P is subsequently reduced, f_{pl} remains constant.

In the following derivation, B_{c2} and I_c refer to the average (extrinsic) values of the strand. Combining (3.18) and (3.29) gives

$$B_{c2}(P) = B_{c20} - C_0 \frac{(1+n) s_{elast}(P)}{E(P)}, \tag{3.31}$$

with the Young's modulus a function of P to account for the change in effective Young's modulus of the composite cable under load, and C_0 (in Tesla) a fit factor based on the conductor. Combining equation (3.18) with equation (3.27), the critical current I_c as a function of the applied pressure P for given values of the field B and the temperature T can be expressed as

$$I_c(B,T,P) = I_c(0) \times f_{pl}(P \le P_{\max}) \times \left(1 - \frac{T}{T_c(P)}\right) \frac{\sqrt{B / B_{c2}(P)}}{B} \times \left(1 - \frac{B}{B_{c2}(P)}\right)^2 . \qquad (3.32)$$

The model takes into account the plastic effects of the strands in the cable by a combination of *E(P)* for the non-linear Young's modulus and scale factor C_3 for the permanent damage to the filaments.
The elastic effects are included through C_0 times a combination of C_1 for the hydrostatic stress and C_2 for the deviatoric stress. $B_{c2}(P)$ is derived directly from the FEA models A and B, hence the influence of the impregnation quality is compensated for by the selection of the appropriate FEA model.

Figure 3.31 shows the predicted reversible and permanent I_c reduction (after having been subjected to a given load and released) in the critical current for a cable with the scaling coefficients set to C_1 = -0.8, C_2 = 2.8, C_3 = 49 with a fairly high permanent critical current degradation (see sample TW1 in table 5.25) and for a less degraded cable with C_1 = -0.4, C_2 = 0.0, C_3 = 10 (see sample EC4 in table 5.27). Constant C_0 is set to 693 T). In chapter 5 the scaling constants related to the different production methods of the strands in the cables are determined.

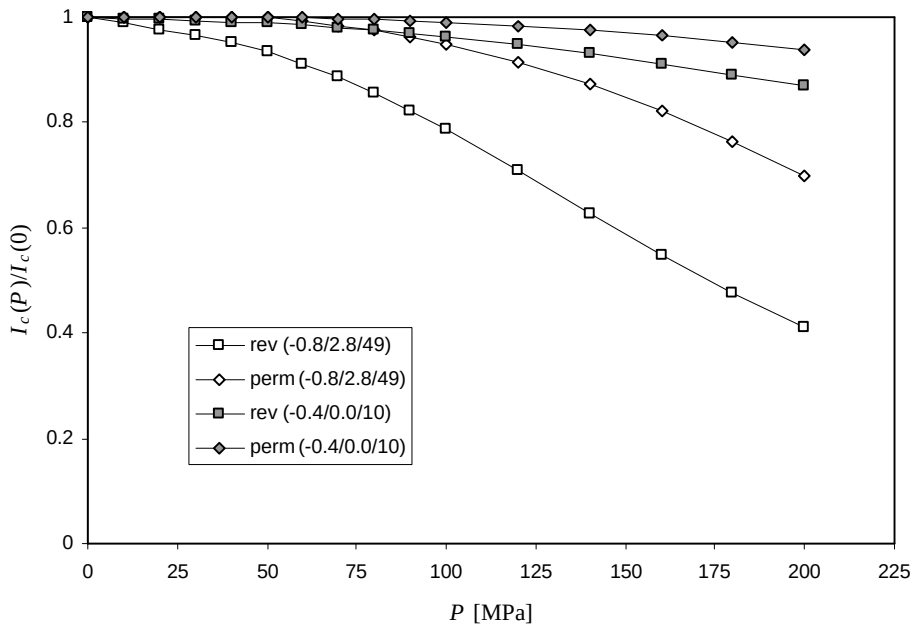

Figure 3.31 The predicted reversible (rev) and permanent (perm) reduction in the critical current as a function of the applied transverse pressure for a cable without initial cabling degradation. Two pairs of curves are computed, one for a cable with coefficients C_1=-0.8, C_2=2.8, C_3=49, the second pair with C_1=-0.4, C_2=0.0, C_3=10. For both pairs C_0 is equal to 693 T and model A is used.

The two pairs of curves presented in figure 3.31 represent the calculated reduction in critical current as a function of the applied transverse pressure in a well impregnated and insulated Nb_3Sn cable (model A). The upper curve of a pair shows the estimated reduction in I_c due to the permanent damage done to the filaments. It initially shows no reduction in I_c.

When the yield strength of the strand matrix is exceeded, the strands begin to deform at the contact points. Loading the cable to a given pressure (on the x-axis of the figure), and then releasing the pressure, results in permanent I_c degradation (labeled perm). When the plastic deformation becomes larger with increasing transverse pressure, the yield strength of the Nb_3Sn filaments will be exceeded. Above that pressure, the strands will be permanently damaged. The lower curve of a pair shows the effects of the reversible degradation. The lower curve is based on the influence of the hydrostatic and deviatoric strain components in the strands affecting the T_c and B_{c2} of the Nb_3Sn. The actual strain components are derived directly from the FEA calculation of the stress in the strands of the cable.

3.10 Summary and conclusions

The critical current as a function of elastic strain and transverse stress has been discussed. The criteria for critical current are given, followed by the definition of the terminology used in the cable degradation experiments. The influence of stress on the critical current in cables is discussed, based on a set of FEA models designed to determine the plastic deformation of the strands in a cable. The scaling constants in the model are determined in the critical current degradation experiments discussed in chapter 5.

Following the elastic models described in section 3.8.1, a high compaction cable is best described with a model emphasizing the deviatoric stress. A cable exhibiting a medium to low compaction is better described with a model based on a wire geometry.

The effective Young's modulus of a cable with a high strength epoxy impregnation is initially higher, then decreases when the yield strength of the strand material is exceeded. A further increase of the applied pressure leads to an asymptotic value for the Young's modulus, determined by the initial compaction of the cable (epoxy content of the cable). The model predicts the measured Young's modulus of 42 GPa at 150 MPa applied pressure rather well.

A linear elastic displacement model can estimate the effective Young's modulus of a cable dominated by the strand material (dry or impregnated with a low strength epoxy). For a typical strand with E = 117 GPa, the initial Young's modulus can be as low as 20 GPa, then increases to about 26-30 GPa at 150 MPa applied transverse pressure.

A matrix material with a higher Young's modulus (stiffer) is preferred over a softer material (copper) with a lower yield point to reduce the total strain on the filaments. The effective Young's modulus of the cable is also increased.

In a cable impregnated with high strength epoxy, the behavior of the critical current versus applied pressure relation is initially dominated by the hydrostatic and deviatoric stresses. When the strands in the cable start yielding, the plastic component of the stress becomes dominant, and permanent critical current degradation is evident. A cable with an epoxy with higher Young's modulus will degrade less under applied pressure.

The local stress on the top layer of strands in the critical current degradation experiments described in chapter 5 can be as much as 34 % higher than the average applied pressure.

The reversible and permanent critical current degradation can be predicted with a model based on independent relations for the plastic deformation and elastic stress. The permanent degradation is determined by the amount of plastic deformation of the strands in the cable. The amount of plastic deformation is computed with two separate FEA models, model A simulating a well impregnated cable, and model B simulating a dry cable.

The selection of the appropriate model to use to predict the critical current degradation in a cable is thus made based on the quality of the impregnation. Essentially, the selection of model A versus model B eliminates the influence of the quality of the experimental sample from the critical current degradation model. This method is used in chapter 5 to compare the critical current degradation of samples with different impregnation quality to each other in an objective way.

Chapter 4

Influence of the internal structure of the wire on the $I_c(P)$ relation

This chapter describes the influence of the internal structure of a Nb_3Sn wire on the $I_c(P)$ relation. It is a further extension of the macroscopic FEA models of chapter 3 to the microscopic level of the filament structure of the wire.

Several manufacturing methods are discussed. For those methods that have associated cable experiments in chapter 5, the influence of the internal structure on the $I_c(P)$ relation is investigated.

Next, Finite Element Models are created for a generic composite superconducting wire, and for wires made following the various manufacturing methods. Stress concentration factors are determined for each of these wires in relation to the applied load direction, and for various values of the material properties of the Nb_3Sn and diffusion barriers.

Finally, the influence of the presence of Kirkendall voids in the cross-section is investigated for the different manufacturing methods. Stress concentration factors are determined for the methods, and recommendations are made to reduce the critical current degradation through modification of the wire sub-structure.

4.1 Introduction

A more detailed FEA study is performed to gain a further understanding of the behavior of the complex internal structure of Nb_3Sn composite wires under transverse load. First, a generic model of a composite superconducting wire is created to investigate whether a single sub-element in the wire can be used to represent the overall stress pattern in the other sub-elements.

Next, FEA models are created of the sub-elements of several internal structures, such as the TWCA[1] Modified Jelly Roll (MJR) wire, the IGC[2] Internal Tin (IT) wire, and the ECN[3]/SMI[4] Powder-In-Tube (PIT) wire. The geometrical models are built using Scanning Electron Microscope (SEM) photos of the microstructure. Also discussed briefly is the internal structure of the EM[5] Internal Tin conductor.

After a comparison of the various geometries, the models are perturbed by the introduction of Kirkendall voids[6] [4.1] in realistic locations throughout the cross-section. The most likely locations of the voids are determined by investigation of SEM photos of the wire cross-section.

The results from the calculations are used to predict the susceptibility of the internal structure to permanent, irreversible damage under transverse load. If the formation of the Kirkendall voids can not be prevented, the preferred location to minimize stress concentrations caused by the voids can be found from these studies.

4.2 The internal structure of the wire

Nb_3Sn wires can be manufactured using several processes, briefly introduced here. The descriptions are by no means complete, but are merely given to illustrate the differences between the internal structures that are a result of the manufacturing process. Four processes are described:

1) the Bronze Process;
2) the Modified Jelly Roll;
3) Internal Tin;
4) Powder-In-Tube.

In the following sections the manufacturing process of each type of wire is described in more detail.

4.2.1 Bronze process

An array of holes is bored in a CuSn bronze rod, which is then filled with rods of pure niobium. The rod is then surrounded by a diffusion barrier, generally tantalum or niobium, and placed in a high purity copper tube. Alternatively, CuSn hexagons are placed around a niobium hexagon, and then the stack is surrounded by a diffusion barrier. The assembly is then sealed at the ends and drawn down to the final wire size in many steps.

During the reaction process, the tin in the bronze reacts with the niobium to form Nb_3Sn filaments. The critical current I_c is limited by the amount of tin available in the bronze, and the number of filaments in the rod. The process is included here for completeness, but not discussed any further. Figure 4.1 shows a cross-section of a bronze process wire.

---

[1] Teledyne Wah Chang Albany, USA
[2] Intermagnetics General Corporation, USA
[3] Energieonderzoek Centrum Nederland, Netherlands Energy Research Foundation, The Netherlands
[4] Shape Metal Innovations, The Netherlands
[5] Europa Metalli, Italy; locally referred to as La Mettali, Italy (LMI)
[6] Kirkendall voids can form when two solids form different phases during a diffusion process. When the phase formed occupies less volume than the two phases before the diffusion, voids tend to form at the phase boundary.

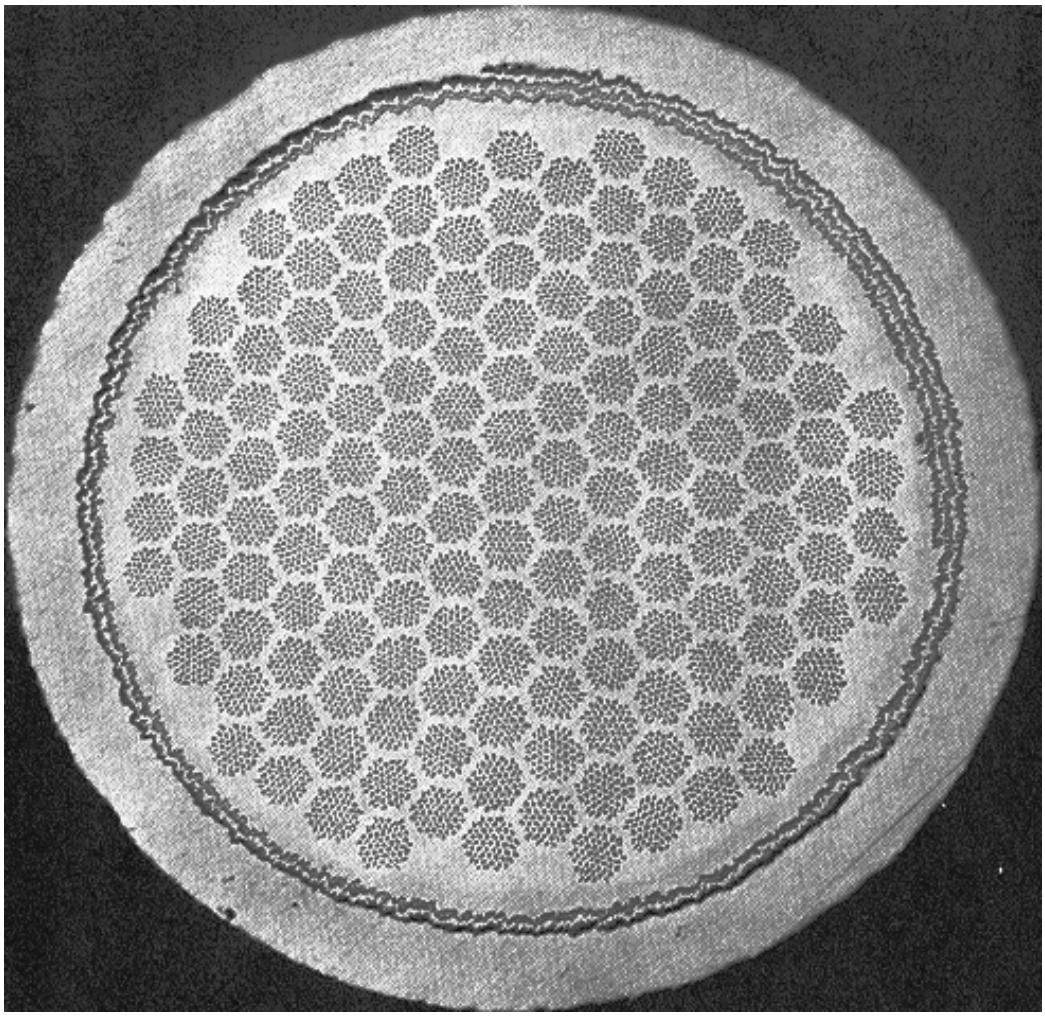

Figure 4.1 Cross-section of a bronze-process wire [4.2].

4.2.2 Modified Jelly Roll (MJR)

Alternating layers of copper sheet and expanded niobium mesh are wrapped around a tin rod. The resulting roll is surrounded by a Nb and/or Ta diffusion barrier, inserted in a copper tube, drawn down to mm size, and then drawn into a hexagonal shape. Thereafter resulting hexagonal rods are cut and re-stacked in a second copper tube.

This assembly is drawn down to the desired final wire size. The expanded mesh, in which the eventual filaments are initially interconnected, elongates in length to form long diamond-like shapes. The dimensions of the diamond shapes are drawn from 6 mm by 25 mm to 1 μm by 1.5 km. This process forms essentially separate filaments in the wire.

Most of the TWCA wires tested consist of five layers with a total of 120 filament bundles, each with a titanium diffusion barrier around it. The core of the wire and the outer shell are copper. The inside of each bundle holds the tin for the Nb_3Sn formation during the reaction and a number of thin niobium filaments formed by drawing the niobium mesh [4.3].

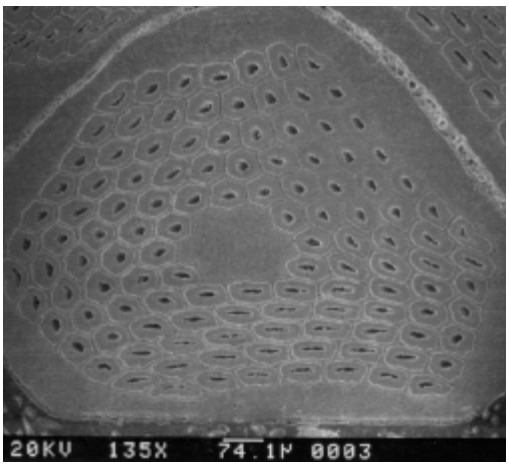

Figure 4.2 Cross-section of a TWCA Modified Jelly Roll (MJR) wire showing the individual filament bundles.

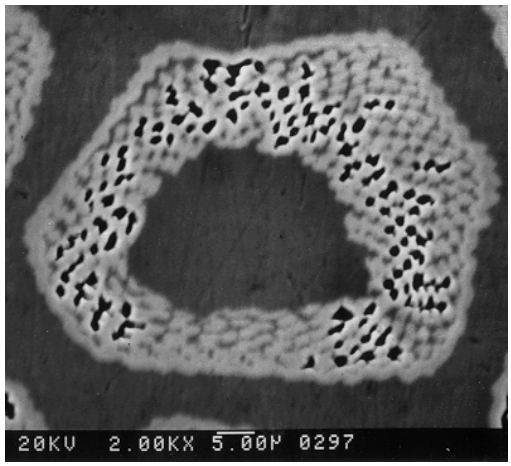

Figure 4.3 Close-up of a filament bundle in a TWCA MJR conductor.

During the initial reaction process, the tin in the core diffuses through the copper in each element (formerly a single roll), forming CuSn bronze. In the final heat treatment the niobium filaments react with the tin in the CuSn bronze to form Nb_3Sn. The critical current I_c is limited by the amount of tin inserted in the core of the element and the number of niobium mesh layers. Since the percentage of tin can be raised as compared to the bronze process, the I_c can be increased. Figure 4.2 shows the cross-section of a typical MJR wire. Figure 4.3 shows an enlargement of a filament bundle in an MJR conductor.

The TWCA method for fabrication of a relatively inexpensive Nb_3Sn superconductor using the Modified Jelly Roll process has been very successful. When in 1985 the switch was made from a niobium-bronze sandwich roll to the niobium-copper sandwich around a tin rod, a problem with filament degradation during drawing and annealing steps was replaced by a problem of the enhanced formation of Kirkendall voids during the tin diffusion and reaction heat treatment steps [4.4]. These voids are clearly visible in figures 4.2 and 4.3.

4.2.3 Internal Tin (IT)

The Internal Tin process has been designed to increase the critical current I_c of a bronze process wire by adding more tin to the elements. Instead of stacking only niobium rods in the assembly, one or several rods are replaced by tin stacked in a copper matrix material. The rest of the wire processing is similar to that of the bronze process.

The result is a wire in which more tin is available for reaction with the niobium rods, effectively increasing the I_c. The benefit of this process is the ease with which the process can be adjusted for a specified I_c.

In the IGC Internal Tin wires, the outer diffusion barrier is made of two layers, one Nb and one Ta. The purpose of this double layer is to prevent tin leakage to the outer copper jacket. Figure 4.4 shows the cross-section of an IGC Internal Tin wire; figure 4.5 shows the cross-section of an EM Internal Tin wire.

The IGC Internal Tin wire was chosen over the TWCA MJR wire for use in the inner cable of the D20 magnet since the filament bundles have a thick diffusion barrier around them. This limits possible tin leakage into the Cu matrix due to deformation during the cabling operation. The major difference with the TWCA wire layout is the thick diffusion barrier of Nb and Ta in the wire [4.5].

Details of the EM Internal Tin wire can be found in [4.6]. The mechanical structure of the EM conductor is similar to the IGC Internal Tin conductor, with the exception of the three additional copper spacers within the filament bundle. These spacers are added to decrease the coupling of the filaments, thereby reducing AC losses. The location of the spacers opposite the copper matrix straight edges is probably structurally superior to the IGC wire, since this geometry transfers the load through the copper instead of the filament bundles.

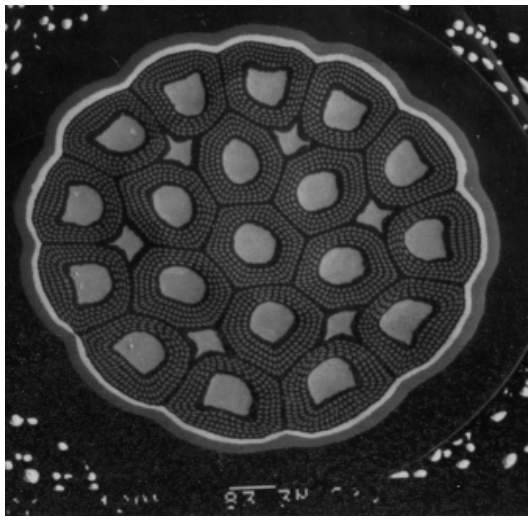

Figure 4.4 Cross-section of the IGC Internal Tin wire structure.

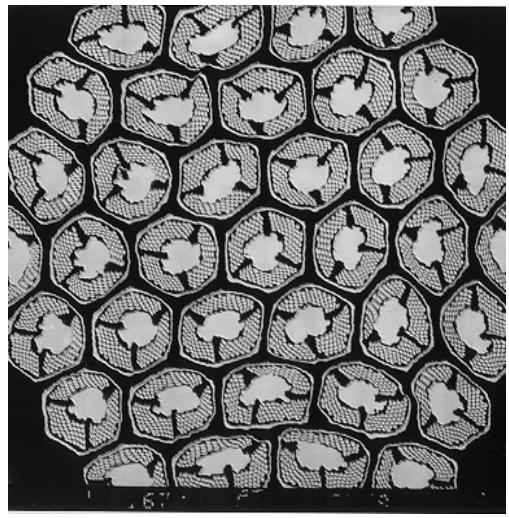

Figure 4.5 Cross-section of the EM Internal Tin wire structure.

The increased thickness of the copper matrix between the individual bundles may lessen the effect of stress concentrations at the corners of the hexagons. For this reason, the critical current degradation under pressure is expected to be less as compared to the IGC conductor.

4.2.4 Powder-In-Tube (PIT)

In the Powder-In-Tube process, a niobium tube is filled with Nb_2Sn powder. The tubes are placed inside copper hexagons, stacked together, and the assembly is drawn down to size.

The resulting rod is then drawn to a hexagonal shape, re-stacked and drawn down several times to form the final wire. During the reaction process, the Nb_2Sn powder reacts with the niobium wall, forming Nb_3Sn, and leaving a porous area or a void in the center.

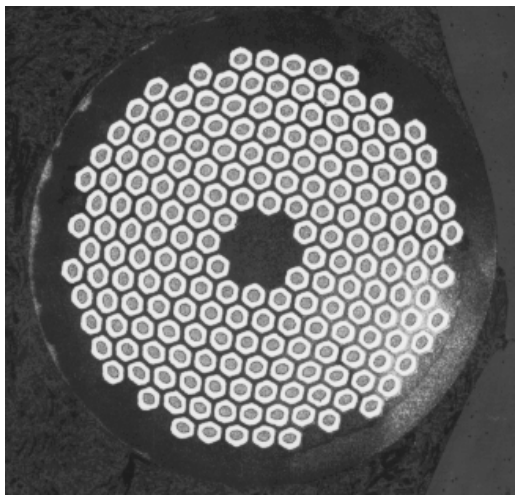

Figure 4.6a Cross section of a PIT conductor with 192 filaments.

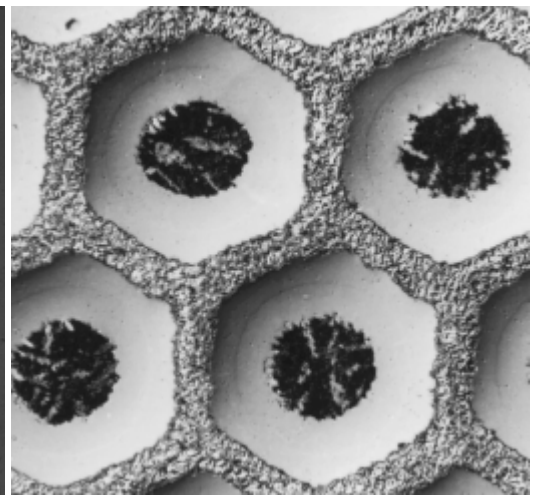

Figure 4.6b Close-up of the filament structure of a PIT conductor.

The PIT Nb_3Sn wire used in the cable tests contains 192 filaments, with a typical 1:1.27 (45%/55%) SC/Cu ratio. Figure 4.6a shows a cross-section of the wire, illustrating the internal structure. Figure 4.6b shows a close-up of the filament structure, illustrating the void in the center, the Nb_3Sn region, the niobium wall and the copper matrix. The 192 filament wire data is found in more detail in [4.7].

4.3 Wire parameters

The following section describes the wires that are modeled in the FEA study. Detailed information about the mesh generation and material properties can be found in section 4.4. The wires tested here are primarily used in cables for experimental model dipoles.

The MJR and IT conductors are used for the dipole magnets D19H ($NbTi/Nb_3Sn$ hybrid) [2.4] and D20 (Nb_3Sn, four layer) [2.6]. The PIT conductors are used for the 11.5 T dipole model MSUT [2.5]. The wire specifications are given in tables 4.1 for the wires used in the D20 dipole, and in table 4.2 for the other wires tested within the scope of this thesis.

All critical current (density) values listed are given by the manufacturer. The conductor types are labeled *inner* and *outer* to refer to the location of the cable in the inner layer or outer layer of the winding package. The D19H and MSUT magnets both have two layer windings, the D20 magnet has two double layers of each type.

	TWCA inner cable	**TWCA outer cable**	**IGC inner cable**	**IGC outer cable**
Type	Modified Jelly Roll	Modified Jelly Roll	Internal Tin	Internal Tin
Diameter [mm]	0.750±0.003 mm	0.480±0.003 mm	0.750±0.003 mm	0.480±0.003 mm
Composition	Nb_3Sn/Ti/Ta	Nb_3Sn/Ti/Ta	Nb_3Sn/Ti/Ta	Nb_3Sn/Ti/Ta
Twist [mm]	12±3 mm	12±3 mm	12±5 mm	12.0±2.5 mm
I_c [A] (min) at 4.2 K	110 at 14.6 T	110 at 10.4 T	170 at 14.6 T	130 at 10.4 T
non-Cu j_c [A/mm^2] at 4.2 K	510 at 14.6 T	1300 at 10.4 T	540 at 14.6 T	1600 at 10.4 T
Cu/SC ratio	1.0±0.1/1	1.15±0.10/1	0.4±0.1/1	1.15±0.10/1

Table 4.1 Conductor specifications of the wires used in the cables for the $I_c(s)$ tests. The table lists the parameters for the wires used for the D20 dipole.

	D19H outer cable	**MSUT[7] inner cable**	**MSUT[8] outer cable**	**EM[9] cable**
Type	Internal Tin	Powder-In-Tube	Powder-In-Tube	Internal Tin
Diameter [mm]	0.800±0.003 mm	1.260±0.003 mm	1.000±0.003 mm	0.825±0.003 mm
Composition	Nb_3Sn/Ti/Ta	Nb_3Sn/Ti	Nb_3Sn/Ti	Nb_3Sn/Ta
Twist [mm]	12±3 mm	30 mm	30 mm	12±3 mm
I_c [A] (min) at 4.2 K	110 at 14.6 T	> 1100 at 10 T	> 690 at 10 T	> 400 at 12 T
non-Cu j_c [A/mm^2] at 4.2 K	510 at 14.6 T	> 2000 at 10 T	> 2000 at 10 T	> 1600 at 12 T
Cu/SC ratio	1.0±0.1/1	1.3±0.1/1	1.3±0.1/1	1.0±0.1/1

Table 4.2 Conductor specifications for the wires used in the cables for the $I_c(s)$ tests. The table lists the parameters for the D19H wire, MSUT wires (for comparison) and the EM wire.

[7] Data obtained from literature [4.8], [4.9].
[8] Data obtained from literature [4.10].
[9] Data obtained from [4.11].

4.4 FEA models of composite wires

To investigate the effect of different internal structures on the critical current degradation under applied transverse pressure, FEA models are made of the internal structure of several wires. The models are based on both a generic hexagonal-stacked wire, and a real deformed and reacted wire.

Special attention is paid to the accurate representation of the Kirkendall voids in the wire, since these are a suspected cause of damage to the filaments. When a comparison is made between the I_c degradation in a cable under transverse compressive load in an experiment, and in a real magnet, special attention has to be paid to the reproduction of the actual conditions in the real magnet. In particular, the epoxy-impregnation of the cable is important, since a bare cable will yield a much higher degradation compared to an impregnated one [4.12].

When comparing the models of the wires to a cable, the exact distribution of the transverse load over the cable has to be considered. Even in an impregnated cable, the strands will be subjected to a higher than average load on the crossover points of the wires. The FEA models are created to represent micro-photographs of the cross-sections of reacted wire and cable samples, like the picture shown in figure 4.7.

It is important to construct an accurate representation of the actual geometry in the modeling of composite wire. The Young's modulus of the Nb_3Sn is varied from 26 GPa to 100 GPa to investigate the influence of the material property on the stress distribution within the filament bundles. The average value of $E = 80 \pm 30$ GPa is used (polycrystalline Nb_3Sn [4.13]) for further analysis, but lower [4.14] and higher values [4.15] have been reported.

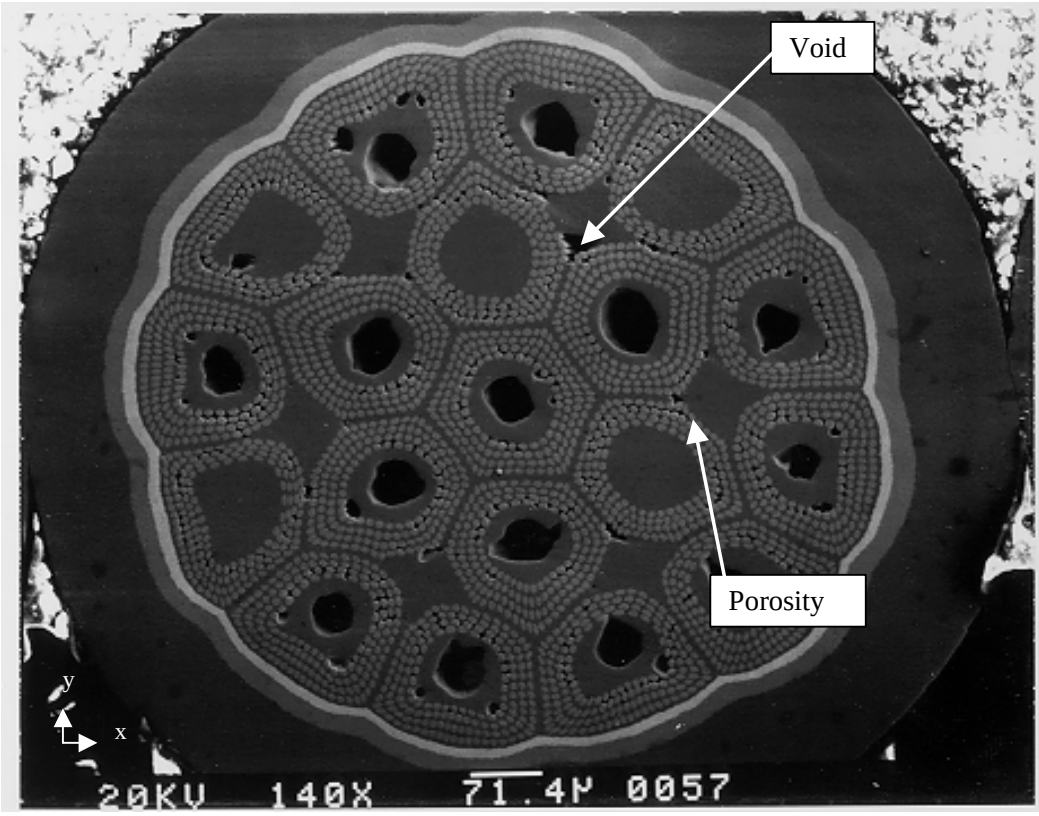

Figure 4.7 Cross-section of an IT wire with both voids and porosity in the filament area.

For the models, only a solution is determined with linear (elastic) material parameters. This solution is also used to determine the error level in the mesh of the model. From the results, the stress concentration

factors for each wire geometry are determined. The applied pressure in each model is 100 MPa; stress concentrations are computed from the FEA solution with respect to the applied pressure.

Since modeling all effects in one large combined model would create computational problems, one is forced to split the models up in successively more detailed representations of the actual wire. Each averaged solution is then applied as a boundary condition to the subsequent more complex case. This method is used for the simulations described in this chapter.

4.2.5 Composite wire model

At first a generic model of a composite wire is created as shown in figure 4.8 and 4.9. All sub-elements are included to assess whether a small section of the wire containing only one or several filament bundles can represent all filament bundles in the wire correctly. The model can be used to represent the MJR, IT and PIT wires by varying the material properties.

It is possible to use the symmetry of the wire to reduce the model size, but for clarity of the picture, the entire wire was modeled. Results from the model are shown in figure 4.10 and listed in table 4.3. The calculation shows that an individual bundle can be used as a good representation for the overall case. Error levels of the models are listed in table 4.4.

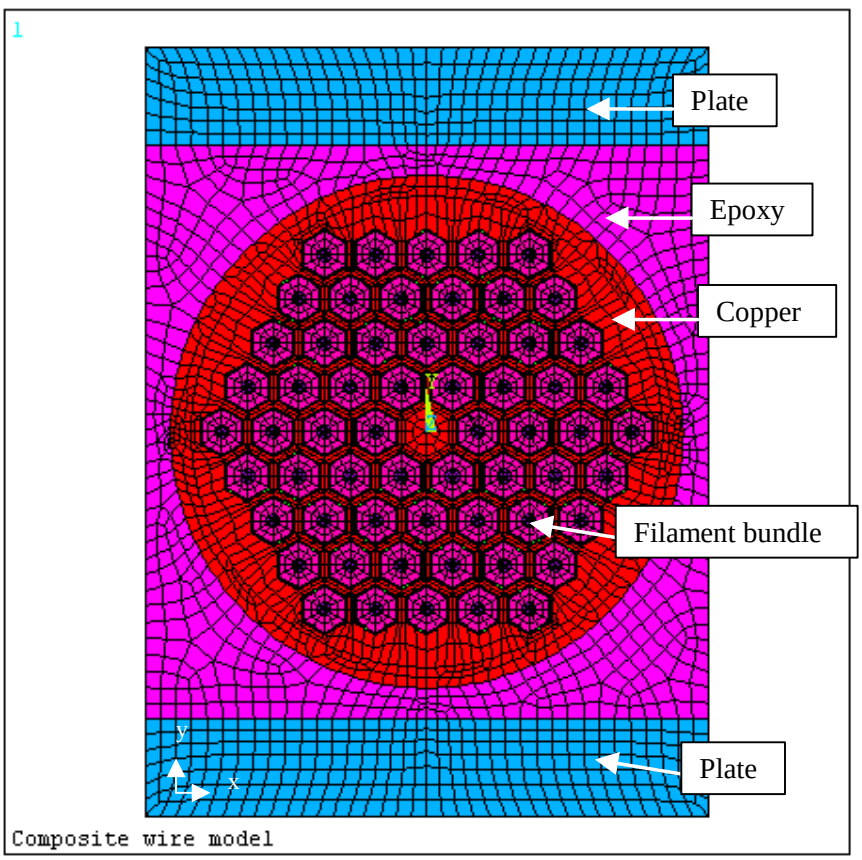

Figure 4.8 *A full model of a generic composite wire. Shown are stainless steel pressure plates, the epoxy filler around the wire, the copper matrix and the filament bundles. The model for the IT wire includes a diffusion barrier around the entire filament area (not shown here). The wire in this model has a diameter of 0.75 mm.*

Table 4.3 lists the minimum, average and maximum equivalent stress S_{eqv} in the Nb_3Sn filament bundles as a function of the Young's modulus of the Nb_3Sn and the barrier material.

The two columns listing the results for tantalum and niobium barriers are representative for a MJR wire. The results for the niobium and tantalum outer ring are representative for an IT wire.

Nb_3Sn Young's modulus [GPa]	tantalum S_{eqv} [MPa]			niobium S_{eqv} [MPa]			niobium and tantalum outer ring S_{eqv} [MPa]		
	min	ave	max	min	ave	max	min	ave	max
26	41	67	98	44	70	102	39	65	97
50	65	84	108	66	87	111	62	83	107
80	84	97	113	86	100	115	82	96	112
100	87	103	113	88	104	116	85	102	113

Table 4.3 Minimum, average and maximum equivalent stresses in the filament bundles as a function of the diffusion barrier material and Nb_3Sn Young's modulus. The applied pressure is 100 MPa.

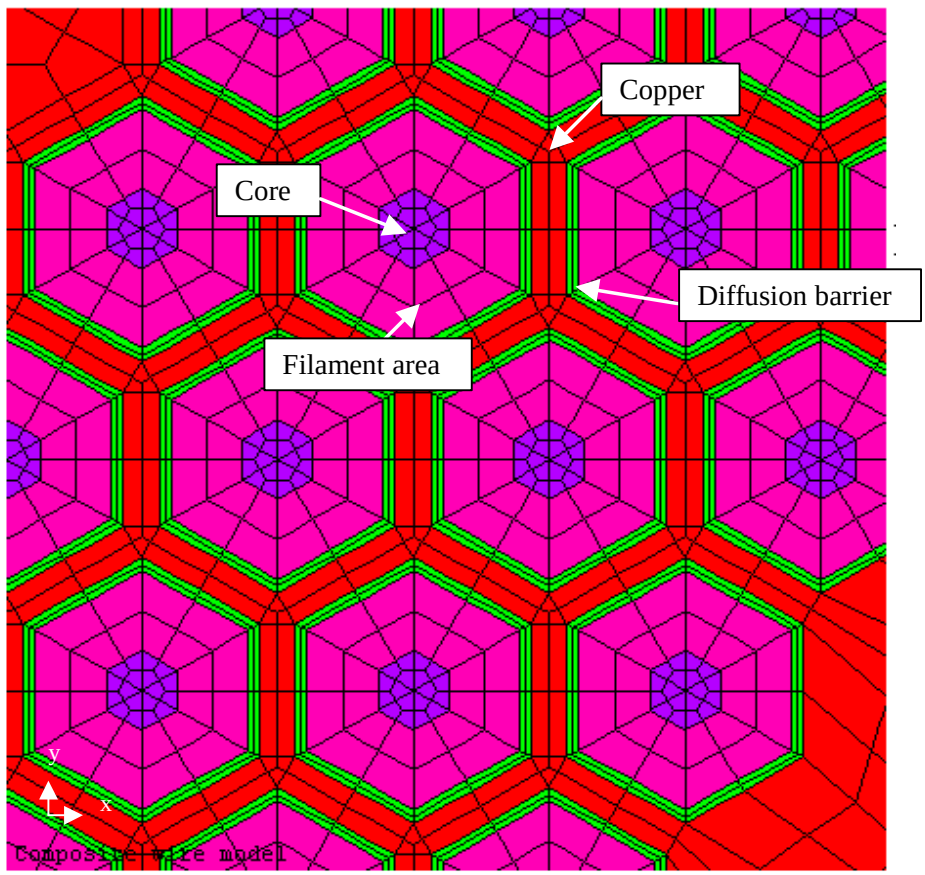

Figure 4.9 Close-up view of the filament bundles in the composite wire model of an MJR wire. For each bundle, from the inside out, the bundle core, filament area, diffusion barrier, and copper matrix are shown. The distance across each filament bundle is approximately 60 mm.

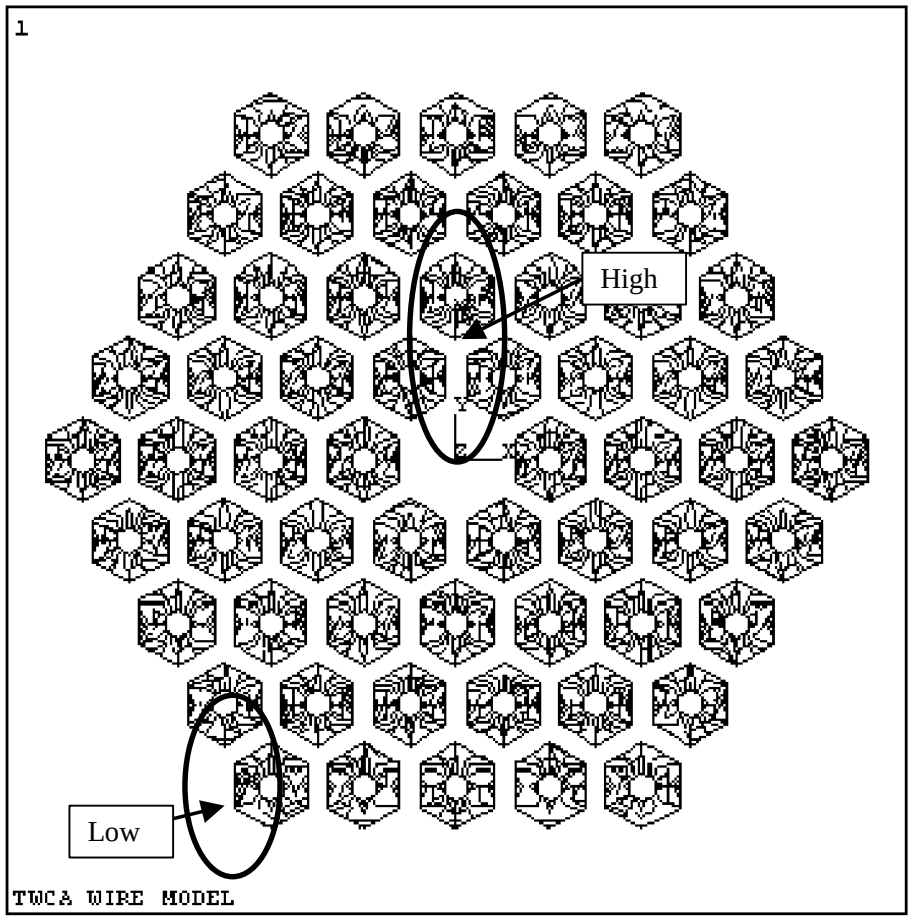

Figure 4.10 Plot of the equivalent stress S_{eqv} (SQEV, in Pa) in the composite wire model. Material parameters are set for an MJR wire. Only the filament bundles are shown. The applied pressure is 100 MPa. The location of the minimum is indicated by the "low" marker (3 MPa), the maximum by the "high" marker (115 MPa). A full-color version of this figure is reproduced in Appendix A.

The maximum stress concentration in the MJR wire is 113-115 % of the applied load of 100 MPa for a Nb_3Sn Young's modulus of 80 GPa. In the IT wire, the maximum stress concentration is 112 %. The slightly lower stress concentration in the Internal Tin wire is due to the extra support provided by the stiff additional diffusion barrier around the entire filament area.

The equivalent stress S_{eqv} is plotted for each filament bundle as a function of the relative distance from the center of the wire r/R_{max} and the circumferential angle in figures 4.11a and 4.11b (for E = 50 GPa) and figures 4.12a and 4.12b (for E = 80 GPa).

The plots show that the average stress reduces by about 10 % with increasing relative distance from the center of the wire. The plots also show that the stress varies plus or minus 8-11 % as a function of the circumferential angle.

The spread of the average stress (listed in table 4.3) in the filament bundles decreases from 58 MPa (Nb_3Sn E = 26 GPa) to 26 MPa (Nb_3Sn E = 100 MPa). For the detailed calculations, an average Young's modulus of 80±30 GPa is assumed [4.15].

Therefore, the variation of the average filament bundle stress across the wire cross-section is neglected with respect to the variation in the material properties of the Nb_3Sn.

Material	Initial coarse model Error [%]	Final refined model Error [%]
filament bundles	14	0.5
epoxy	0.4	1.56
tantalum and/or niobium barrier	30	3.2
copper matrix	11	1.9
stainless steel plates	1.1	1.1

Table 4.4 Error levels in the wire model mesh. Listed are the initial coarse mesh error, and the final refined mesh error.

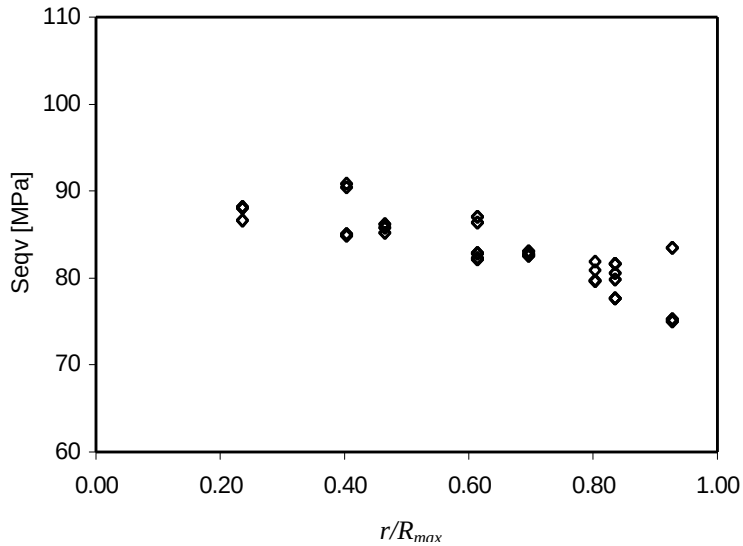

Figure 4.11a Equivalent stress (S_{eqv}) in the filament area for the composite model with tantalum outer barrier, as a function of the relative distance r/R_{max} from the center of the wire. Each marker represents the stress averaged over a filament bundle. The two graphs show the results for a Nb_3Sn Young's modulus of 50 GPa. The applied pressure is 100 MPa.

The subsequent models are of one filament bundle to allow for a more accurate meshing of the internal bundle structure, as shown in figure 4.13 for the MJR wire, and figure 4.16 for the IT wire. The bundle models are then embedded in a square matrix block and loaded with a uniform load. The resulting stress calculated in the bundle then represents the localized concentration of the load due to irregularities like the voids in the center or between the filaments.

Sections 4.4.2 through 4.4.4 describe the detailed FEA models of the individual filamentary areas within the wires. Models are created for the Modified Jelly Roll, Internal Tin and Powder-In-Tube wires. The models are first generated without any voids or porosity in the filament area. Results are analyzed for dependency on the Young's modulus of the Nb_3Sn. Stress concentration factors within the individual filaments are computed.

The Internal Tin and Modified Jelly Roll wire models have mesh error levels less than 2 %. The Powder-In-Tube wire model has a mesh error level of 0.2 %.

Next, voids and porosity are introduced in the models by removing certain elements in the Finite Element mesh. Stress concentration factors as a result of the voids and porosity are computed.

In section 4.5 the results from the FEA models are compared. Characteristics of the void formation in each wire are listed, together with the computed stress concentration factors. In section 4.6 a comparison is

made between the stress concentration factors, computed with the FEA wire models, and an analytical concentration factor derived from round or elliptical holes in plates.

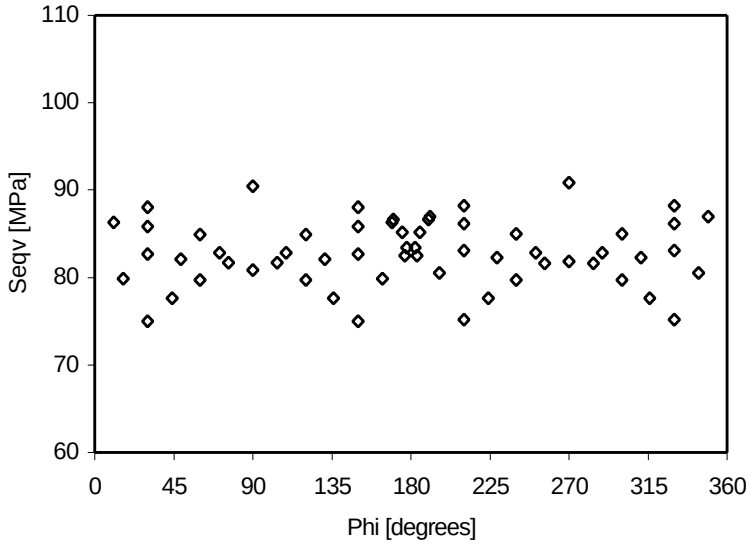

Figure 4.11b Equivalent stress (S_{eqv}) in the filament area for the composite model with tantalum outer barrier, as a function of the circumferential angle. Each marker represents the stress averaged over a filament bundle. The two graphs show the results for a Nb_3Sn Young's modulus of 50 GPa. The applied pressure is 100 MPa.

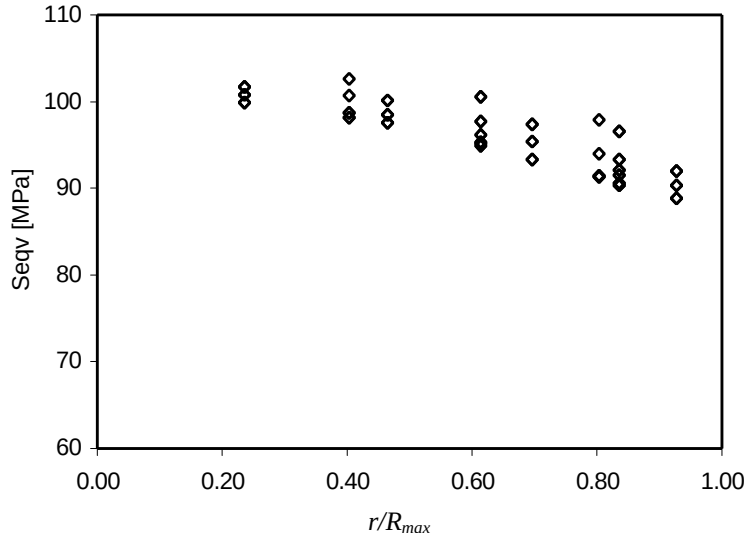

Figure 4.12a Equivalent stress (S_{eqv}) in the filament area for the composite model with tantalum outer barrier, as a function of the relative distance r/R_{max} from the center of the wire. Each marker represents the stress averaged over a filament bundle. The two graphs show the results for a Nb_3Sn Young's modulus of 80 GPa. The applied pressure is 100 MPa.

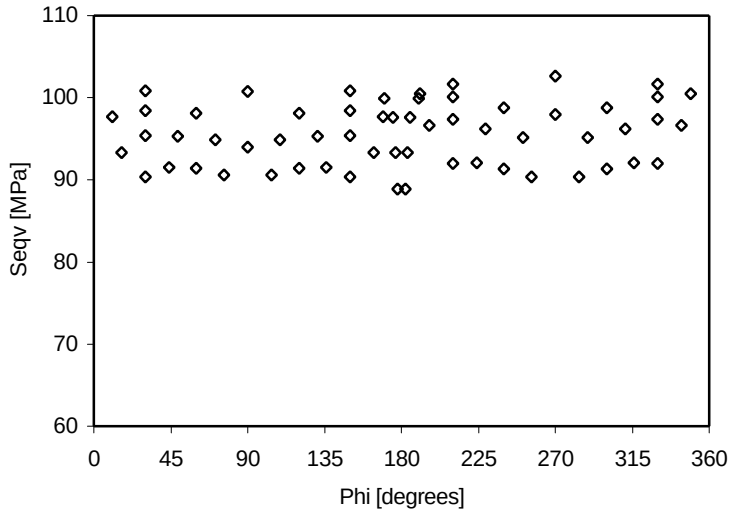

Figure 4.12b Equivalent stress (S_{eqv}) in the filament area for the composite model with tantalum outer barrier, as a function of the circumferential angle. Each marker represents the stress averaged over a filament bundle. The two graphs show the results for a Nb_3Sn Young's modulus of 80 GPa. The applied pressure is 100 MPa.

Section 4.7 shows the correlation between the FEA models of the wires with voids, and a SEM analysis of structural damage to the filaments subjected to applied transverse pressure.

In section 4.8, the influence of the location of the voids on the stress concentration factor is discussed. A recommendation is made for the preferred location and orientation of the voids and porosity, provided they cannot be removed or avoided.

4.4.2 MJR wire model

An FEA model is created of a small section of the filament bundle within an MJR wire. The filament section is modeled after a SEM picture of a moderately deformed strand in the corner of a cable. Figure 4.13 shows the Finite Element mesh without voids. Figure 4.14 shows the same model with voids present. The MJR filament area model is run for four different load cases, each with three values for the Young's modulus of the Nb_3Sn. The Young's modulus is raised from 26 GPa to 50 GPa, and finally to 80 GPa.

The load cases are:

1) load in y-direction, no voids;
2) load in y-direction, voids;
3) load in x-direction, no voids;
4) load in x-direction, voids.

During the cabling operation, the MJR wires are often deformed, resulting in elongated filaments. Since the stress concentration caused by an elliptical void is dependent on the direction of the applied stress, the model is run for loads in both the y- and the x-direction.

Figure 4.15 shows the results from the model calculations. Shown is the average and peak stress (due to the stress concentrations) in the Nb_3Sn. The applied pressure is 100 MPa for all runs.

The figure illustrates the large peak stress caused by stress concentrations around the voids in the filament area. Up to four times the applied stress is found for a load in the y-direction. The directional sensitivity of the stress concentration around the voids is evident from the difference in the maximum stress.

The computed stress concentration factors derived from the FEA models are listed in table 4.5. The factors are computed by dividing the maximum Von Mises stress in the wire by the overall applied pressure. In a strand in a cable, the increase of the filament cross-section is usually in the direction of the width of the cable.

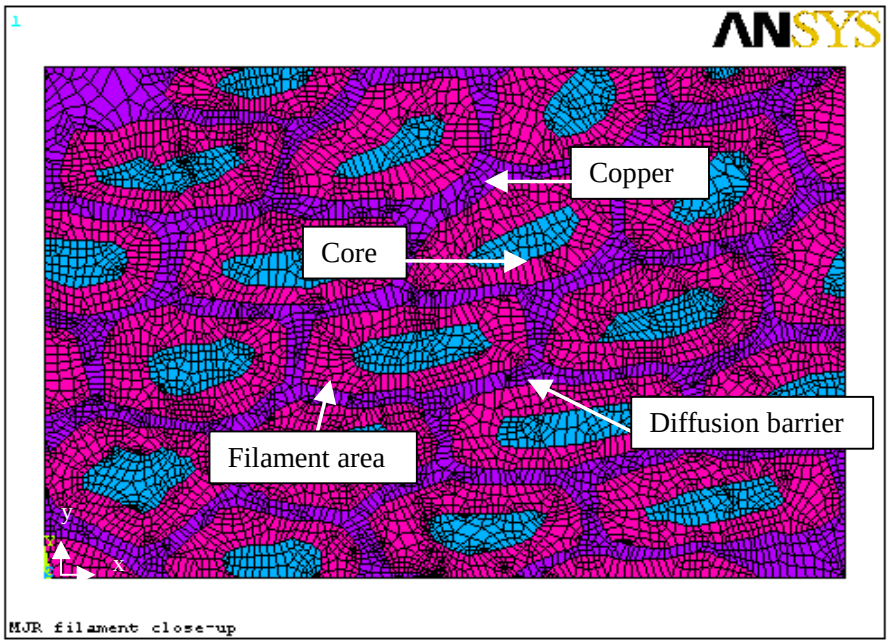

Figure 4.13 MJR filament model. The x-axis is along the horizontal direction, the y-axis along the vertical direction. The loads are applied to the edges of the model.

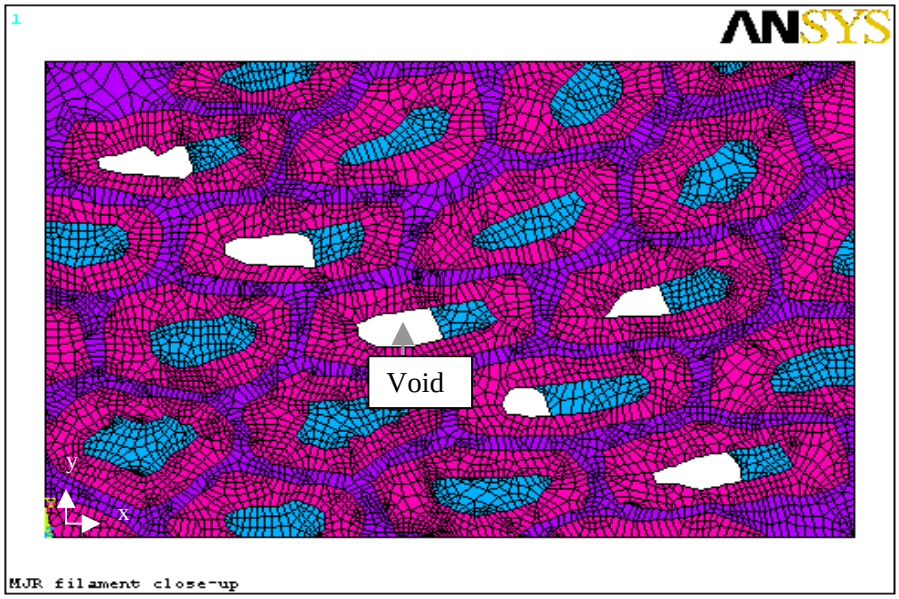

Figure 4.14 MJR filament model with Kirkendall voids. The x-axis is along the horizontal direction, the y-axis along the vertical direction. The loads are applied to the edges of the model.

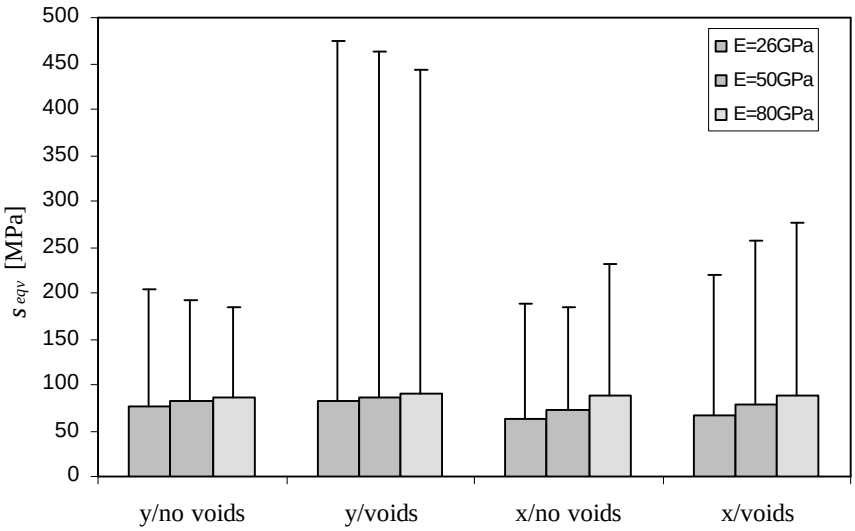

Figure 4.15 Average and peak equivalent stresses in the filaments for three values of the filament Young's modulus. The left two sets show the average stress (bars) and peak stress (lines) for a pressure of 100 MPa in the y-direction. The right two sets show the average stress (bars) and peak stress (lines) for a pressure of 100 MPa in the x-direction.

This means that for cables loaded in the transverse direction, the stress concentrations will be the highest. Based on these results, the preferred direction of the change of shape of the voids is in the direction perpendicular to the wide face of the cable.

Stress concentration [%]	no voids		voids	
Nb_3Sn Young's-modulus [GPa]	y-direction	x-direction	y-direction	x-direction
26	127	125	392	154
50	111	111	375	179
80	98	141	352	189

Table 4.5 Stress concentration factors found in the FEA model shown in figures 4.13 and 4.14 with and without voids present for an applied pressure of 100 MPa.

4.4.3 IT wire model

Figure 4.16 shows a typical filament bundle in an IT wire. The top picture clearly illustrates the void in the center of the filament bundle, and the porosity around the innermost filament ring. The bottom picture shows the resulting Finite Element mesh. The internal area can be removed to create the void. This particular mesh is created to analyze the stress concentration factors around the porosity in the innermost filament ring. The FEA model is first run without any voids to determine the stress concentration factors in the filaments.

In addition, the stress is analyzed as a function of the relative distance from the center of the filament bundle r/R_{max}, and the circumferential angle.

Figure 4.17 shows the equivalent stress S_{eqv} in each element in the filaments as a function of the relative distance from the center of the filament bundle r/R_{max}. No significant correlation is found between

S_{eqv} and r/R_{max}. Also shown is S_{eqv} as a function of the circumferential angle j. Again, no significant correlation is found; the periodical variation is not correlated to the hexagonal structure.

The computed stress concentration factors derived from the FEA models are listed in table 4.6. The factors are computed by dividing the maximum Von Mises (S_{eqv}) stress, and the stress in the x-direction (S_x) and y-direction (S_y) in the wire, by the overall applied pressure of 100 MPa.

The results listed in table 4.6 show that without any voids in the wire cross-section, the maximum stress can be 45 % (E = 50 GPa) to 92 % (E = 80 GPa) higher than the applied transverse stress. The stress concentration becomes higher with increasing Young's modulus of the Nb_3Sn.

Nb_3Sn Young's-modulus [GPa]	Von Mises Stress S_{eqv} concentration [%]			Horizontal Stress S_x concentration [%]			Vertical Stress S_y concentration [%]		
	min	ave	max	min	ave	max	min	ave	max
26	33	52	89	-36	-22	-12	-91	-59	-38
50	55	70	145	-42	-29	-21	-104	-80	-64
80	84	92	192	-12	-3	20	-110	-94	-85

Table 4.6 Results from the FEA model shown in figure 4.16 without voids present. The applied pressure is 100 MPa.

Next, voids are introduced in the FEA model. The increased local stress near the voids is an indication of increased sensitivity to permanent damage under load, since the unsupported filaments in these regions tend to break, as is shown in the SEM picture in figure 4.18.

Table 4.7 lists the stress concentrations computed with the voids present. With voids in the cross-section, stress concentrations of 406 % (Nb_3Sn Young's modulus 50 GPa) up to approximately 430 % (Nb_3Sn Young's modulus 80 GPa) are calculated.

Nb_3Sn Young's-modulus [GPa]	Von Mises stress S_{eqv} concentration [%]			Horizontal stress S_x concentration [%]			Vertical stress S_y concentration [%]		
	min	ave	max	min	ave	max	min	ave	max
26	0	67	411	-131	3	111	-388	-59	41
50	0	88	406	-154	3	130	-416	-79	47
80	0	103	428	-166	2	146	-465	-93	57

Table 4.7 Results from the FEA model shown in figure 4.16 with voids present. The applied pressure is again 100 MPa.

4.4.4 PIT wire model

An FEA model is made of the filament area of a PIT wire. The model is based on the SEM picture shown in figure 4.6. One filament, including the nearest neighbors is modeled. Figure 4.19 shows the mesh without the void (top) and with the void (bottom), in the center of the filament.

The model is run with two values for the Young's modulus of the Nb_3Sn, 50 and 80 GPa respectively. From the center outward, figure 4.19 shows the filament core (this is where the void can form), the Nb_3Sn ring, the remaining un-reacted niobium, and the hexagonal copper matrix. Half of each nearest neighbor filament is also modeled to include the interaction between the filaments.

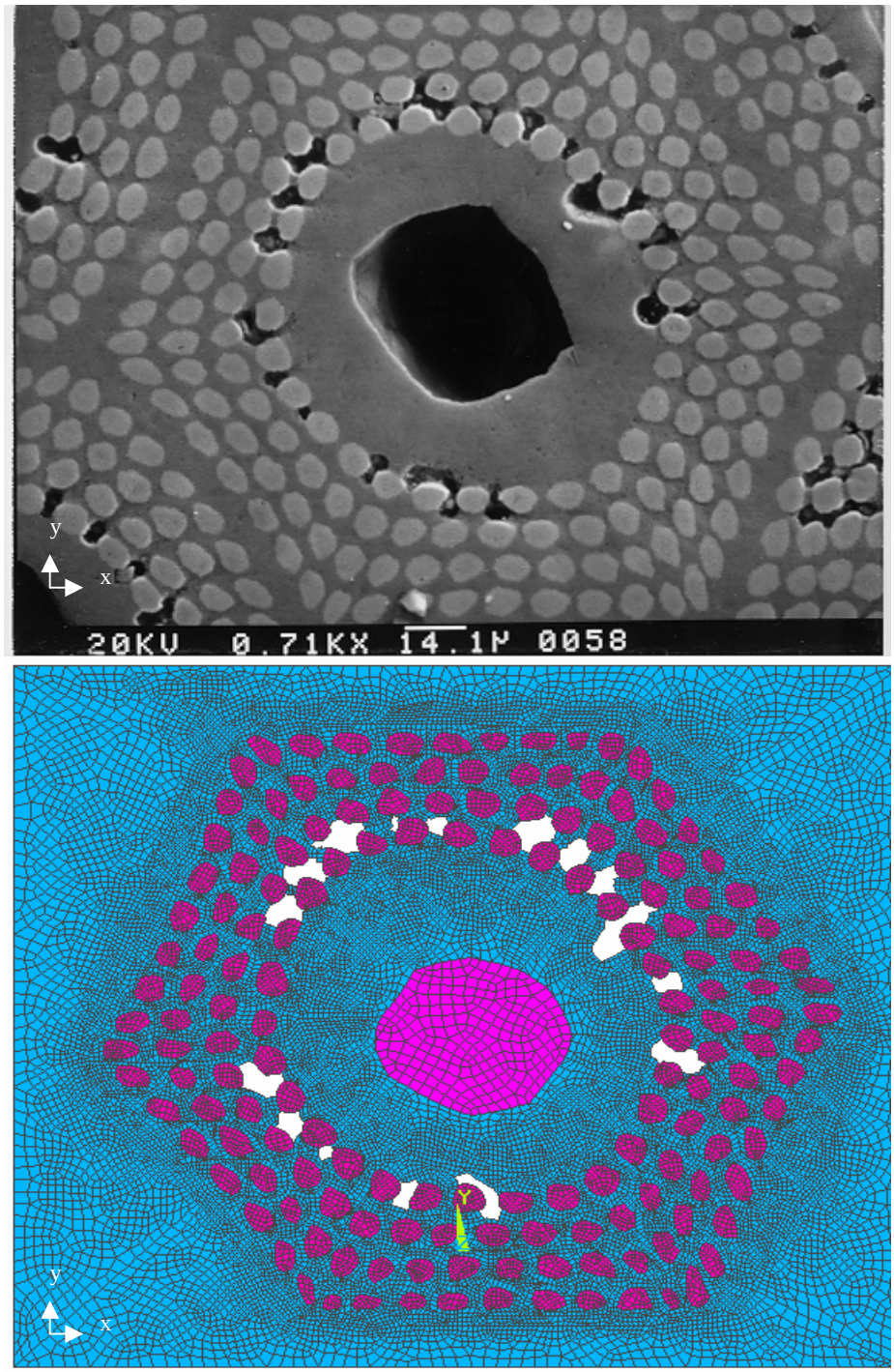

Figure 4.16 A filament bundle model in the IT conductor: the top figure shows a close-up of the voids. The bottom figure shows the resulting Finite Element Model.

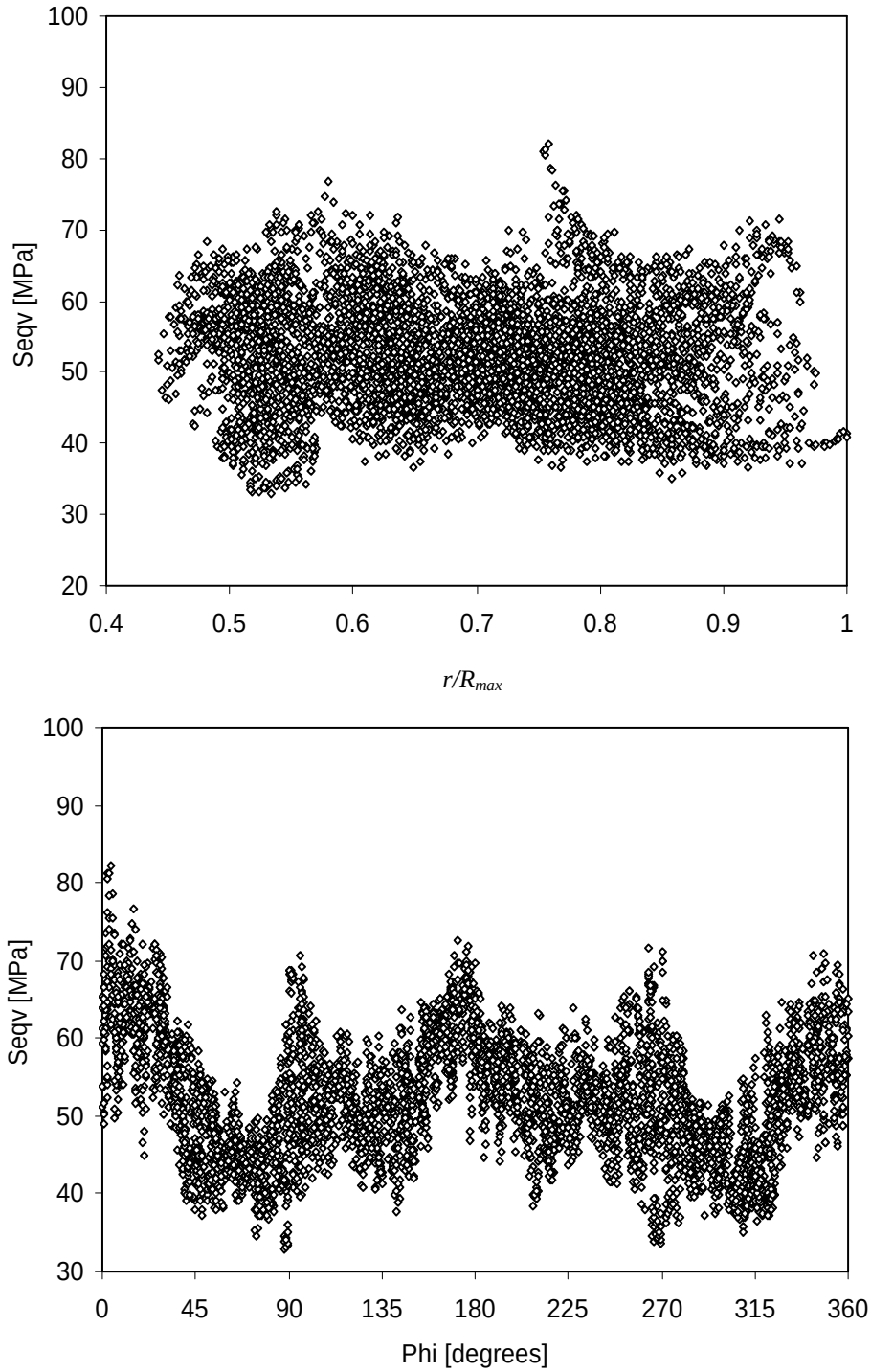

Figure 4.17 Equivalent stress S_{eqv} in the filaments as a function of the distance from the bundle center (top) and as a function of the circumferential angle j (phi)(bottom). The applied pressure is 100 MPa.

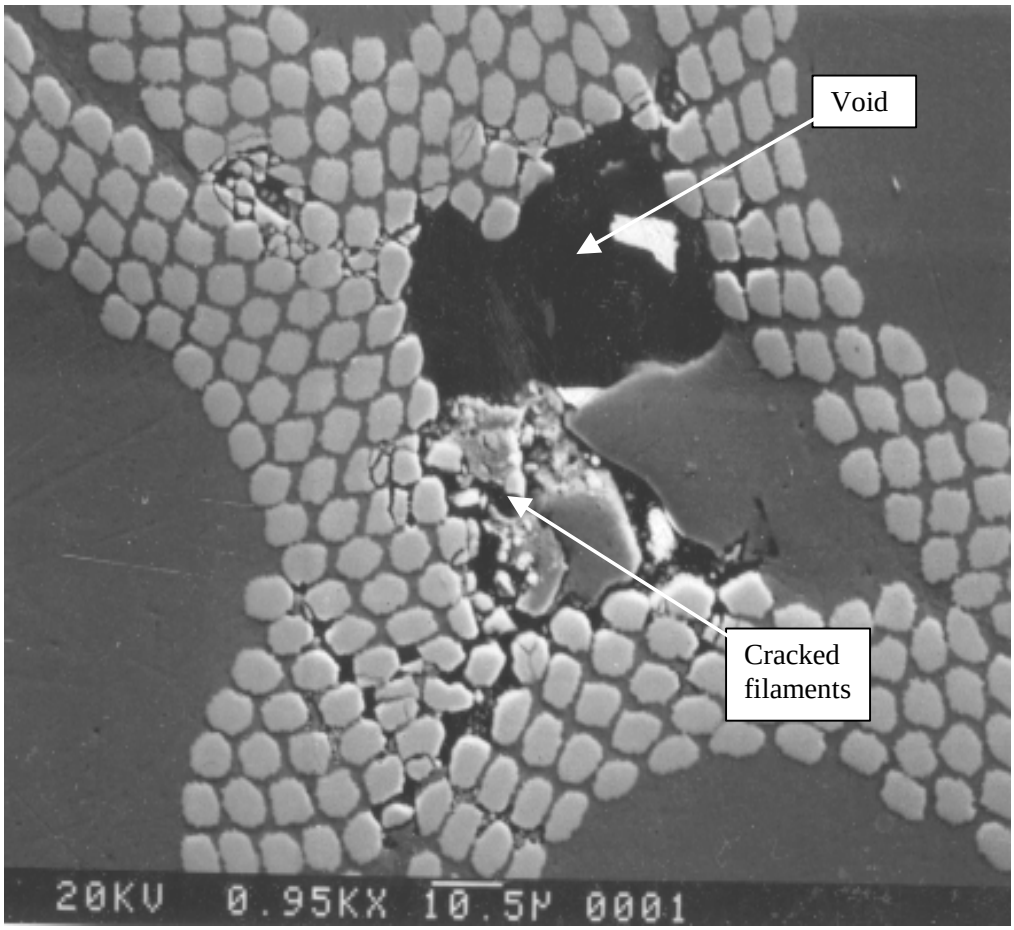

Figure 4.18 SEM photograph of localized damage to the filaments around Kirkendall voids.

The computed stress concentration factors derived from the FEA models are listed in table 4.8. The factors are computed by dividing the maximum Von Mises (S_{eqv}) stress in the wire by the overall applied pressure of 100 MPa. Without the void in the center, the maximum stress in the filament area is only 73-83 % of the applied stress.

With the void present, the maximum stress concentration is 207 %. This value is lower than the theoretical 300 % (see section 4.6) for a round hole in a material. This is because the remaining un-reacted niobium acts as a support arch for the transverse stress.

Nb_3Sn Young's-modulus [GPa]	Stress concentration, no void [%]			Stress concentration, void in center [%]		
	min	ave	max	min	ave	max
50	68	69	73	9	74	160
80	81	82	83	11	93	207

Table 4.8 Results from the FEA models shown in figure 4.19 with and without void present. The applied pressure is 100 MPa.

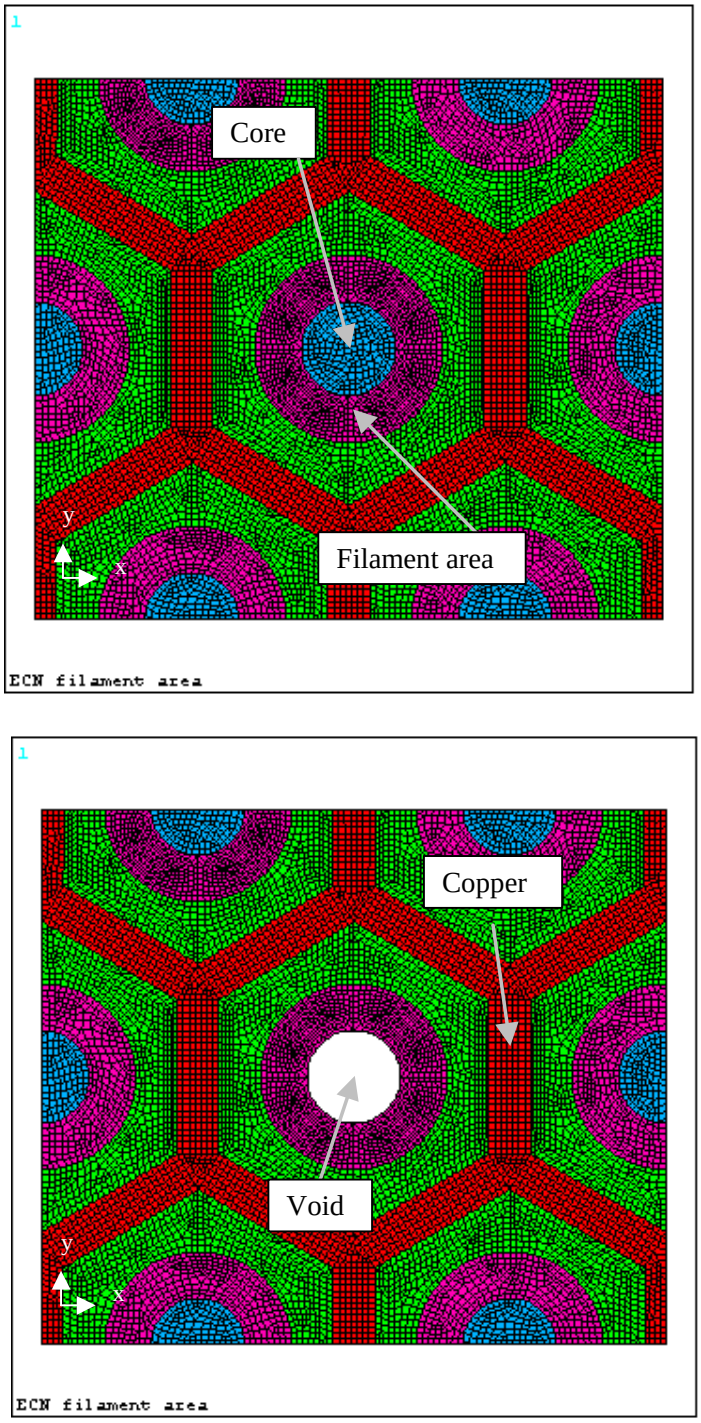

Figure 4.19 *PIT filament area model without void (top), and with void (bottom). Shown from the center outward are the filament core area, the Nb_3Sn region, the remaining niobium, and the copper matrix.*

Consequently, an increase in critical current, through a prolonged reaction time with more Nb_2Sn powder in the core, will enhance the stress concentration with a void present. Therefore, a higher I_c will result in a larger degradation under transverse pressure.

4.5 A comparison of the wire models

When the various wire types are compared, remarkable differences can be noted. First, the results from the models without voids are compared, followed by the models with voids.

For all three, assume an applied transverse pressure of 100 MPa. In the filaments of an Internal Tin wire, the stress ranges from 145 to 192 MPa, in those in a Modified Jelly Roll wire, the stress ranges from 98 to 141 MPa, and in Powder-In-Tube filaments it ranges from 73-83 MPa. Given these values, the sequence in sensitivity to applied stress from low to high for the wires is:

1) Powder-In-Tube (least sensitive);
2) Modified Jelly Roll;
3) Internal Tin(highest sensitivity).

When voids are present in the wire cross-section, the stress concentrations are enhanced. The magnitude of the enhancement depends upon the shape of the voids. Table 4.9 lists the range of the stress concentrations computed with the FEA models with the voids.

Wire type	Characteristics	Local stress multiplication factor
Bronze process	some small voids	not computed
IT	small and large voids	3 (large round void) to 4.3 (small elongated voids)
MJR	small and large voids	3 (large round void) to 4.8 (small elongated voids)
PIT	usually large void in center	2.1 (large round void)

Table 4.9 Computed multiplication factors for the local stress in the filament bundles as a function of the applied transverse stress.

The bronze process wire forms some voids around the filaments since the niobium reacts directly with the bronze embedding the filament. These wires have shown a moderate degradation of the critical current with pressure, without improvement over the years.

Both the IT wires and the MJR wires exhibit the same general behavior. In both wires, a solid tin core is slowly diffused into the surrounding copper matrix material at lower temperatures to form a bronze before the reaction temperature is raised to 650°C to form the Nb_3Sn filaments. Due to this process, the formation of voids somewhere in the matrix is unavoidable. However, it may be possible to influence the location of these voids, as described in detail in chapter 6.

4.6 A comparison with round and elliptical voids

Among the wire internal geometries, the PIT wire is found to have the lowest stress concentration factor. This is because the internal structure generally forms a round void in the center of the filament during reaction, with a ring of Nb_3Sn and niobium around it.

Apart from no hole at all, a perfectly round hole is the most favorable geometry to avoid large stress concentrations, with a stress multiplication factor of three for uni-axial stress. Table 4.10 lists stress concentration factors for a round hole and an elliptical hole for various load conditions.

The table shows that for a round hole, the stress concentration factor ranges from 2 (biaxial stress) to 4 (pure shear). For an elliptical hole, the stress concentration factor is a function of the aspect ratio, and ranges from 2 (biaxial stress, aspect ratio of one) to $2(1+a/b)$, ($a>b$). Here, a is the major axis of the ellipse and b the minor axis.

Round hole		Elliptical hole	
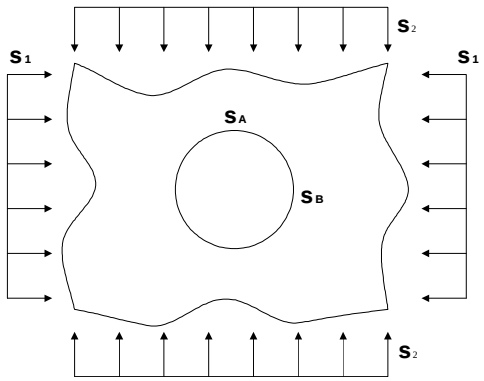		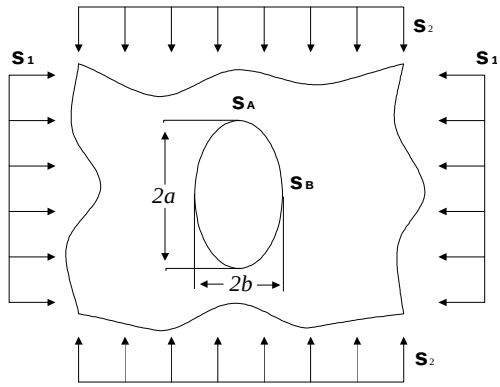	
Uniaxial stress, $\sigma_2 = 0$	$\sigma_A = 3\sigma_1$, $\sigma_B = \sigma_1$	Uniaxial stress, $\sigma_2 = 0$	$\sigma_A = (1+2a/b)\sigma_1$, $\sigma_B = \sigma_1$
Biaxial stress, $\sigma_2 = \sigma_1$	$\sigma_A = \sigma_B = 2\sigma_1$	Biaxial stress, $\sigma_2 = \sigma_1$	$\sigma_A = 2(a/b)\sigma_1$, $\sigma_B = 2(b/a)\sigma_1$
Biaxial stress (shear), $\sigma_2 = -\sigma_1$	$\sigma_A = \sigma_B = 4\sigma_1$	Biaxial stress (shear), $\sigma_2 = -\sigma_1$	$\sigma_A = 2(1+a/b)\sigma_1$, $\sigma_B = 2(1+b/a)\sigma_1$

Table 4.10 Magnitude of stress concentration factors for a round hole and an elliptical hole [4.16].

Often, narrow voids form between filaments, with aspect ratios up to 8, thus creating stress concentrations up to 17 times the transverse load (or 18 times the shear load). In some cases, the voids are even narrower, with higher stress concentrations as a result.

4.7 Enhanced critical current degradation due to stress concentrations

Looking at the locations where the damage seems to occur in the wire cross-sections, the areas with the most damaged filaments coincide with the areas where the highest stress concentrations are found in the FEA models.

In the case of the Internal Tin conductor, the areas in the corners where the three sub-elements come together exhibit enhanced structural damage. The same is true for wires where voids end up within the filament region.

In the Modified Jelly Roll wire, the most obvious damage in the SEM pictures of the filaments is generally found halfway in the filament region. This is also the location where the small voids generally cluster.

For comparison, figure 4.20 shows the equivalent stress in a filament region as a function of the distance from the center of the filament bundle. The Young's modulus of the Nb_3Sn is set to 50 GPa.

Figure 4.21 shows a slanted cross-section of an MJR wire with structural damage to the filaments. Now compare the peak stress in figure 4.20 with the damaged region in figure 4.21.

The region with the highest stress concentrations (up to 400 %), between r/R_{max} of 0.65 to 0.75, coincides with the region in the SEM picture where the filaments are cracked.

This is also the region where voids generally reside in the filament area. This indicates that the combination of high stress concentrations and voids tend to cause structural damage to the filaments.

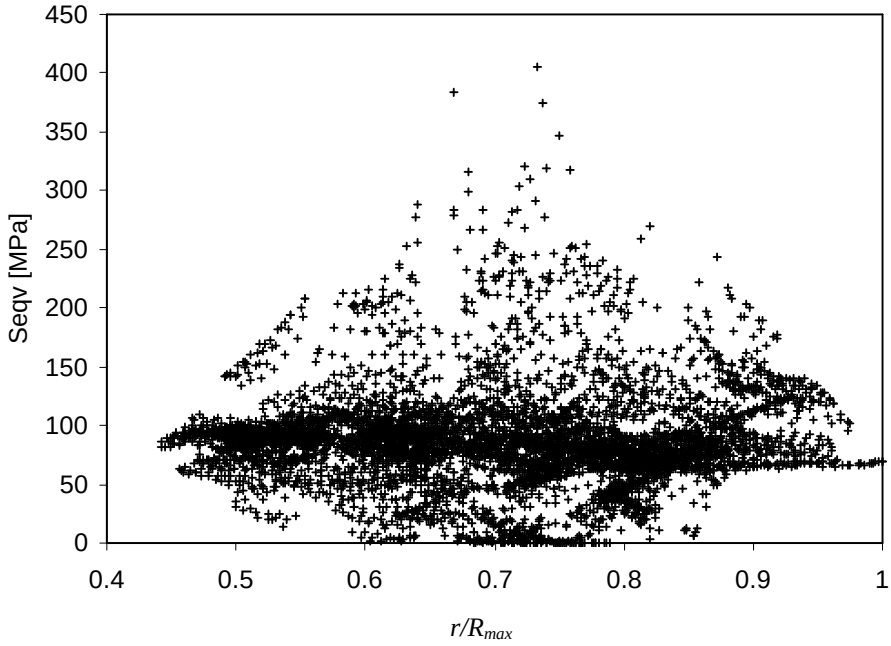

Figure 4.20 Equivalent stress in a filament bundle with a Nb_3Sn Young's modulus of 50 GPa. Plotted is the stress in each element, as a function of the relative distance r/R_{max} from the center of the filament bundle. Note the peak stress about halfway in the filament region. The applied pressure is 100 MPa.

4.8 Preferred void location

If the formation of voids is unavoidable, the question arises what the best location is for the voids in the wire structure. The model calculations show that the increase in the local stress concentrations amounts to a factor 2-3 for the case where a big void is located in the center of the bundle, but increases to 4-5 when the voids are scattered between the filaments.

This is explained by the fact that a large void in the center essentially behaves like a supported arch, while small voids between the brittle filaments lead to collapsing of the voids and breaking of the filaments.

Furthermore, the results shown in figures 4.11 and 4.12 show that the stress is the highest in the inner filament ring. This means that voids located near the inner ring of filaments will cause the highest stress concentrations. Voids near the outer ring will cause stress concentrations about 10 % lower in value.

From these results, the preferred locations for voids are in the center of the filament bundle, or entirely outside the filament area. The former location is generally found in the PIT wires, and under some circumstances in the MJR and IT wires.

The latter location is more difficult to obtain, but can be created by the addition of an external tin source around the filament region. More details are given in chapter 6.

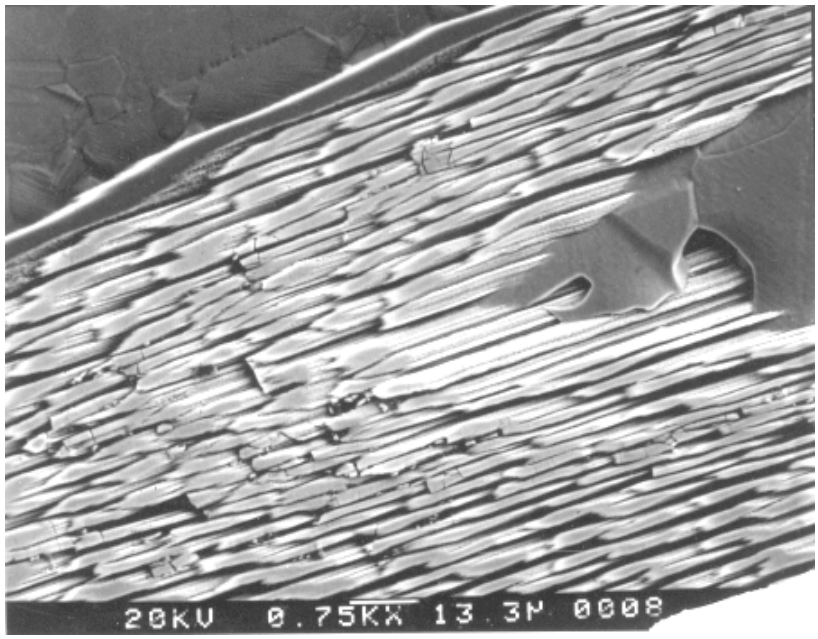

Figure 4.21 Slanted cross-section of an MJR wire. Shown are the filaments in one bundle. Note the fractured filaments halfway from the center of the bundle.

4.9 Conclusions

Finite Element Models of a generic composite wire, and detailed models of the MJR, IT and PIT filament regions have been created. The detailed models have been analyzed with and without Kirkendall voids in the cross-section. In addition, the influence of the Young's modulus of the Nb_3Sn has been investigated.

In an MJR wire, the average stress within the filament bundles can be up to 13-15 % higher than the applied stress. In an IT wire, the average stress can be up to 12 % higher. The stress in the concentration is higher with increasing Young's modulus of the Nb_3Sn.

Within the filament bundles, without voids, the stress concentrations can be up to 140 % for the MJR wire, 190 % for the IT wire, and no stress enhancement in the PIT wire (the internal stress in the Nb_3Sn does not exceed the applied stress).

The peak stress in the filament bundles closest to the center of the wire is an additional 10 % higher (compared to the stress concentration already present) than the stress in the outer filament bundles.

With voids present in the filament bundles, the stress concentrations can be up to 480 % for the MJR wire, 430 % for the IT wire, and 210 % for the PIT wire.

The location of the stress concentrations in the filament bundles coincide with the location where most of the structural damage is found in the SEM pictures of the wire cross-section, as is illustrated in section 4.7.

The preferred location of the voids, if they cannot be avoided, is either in the center of the filament bundle, or entirely on the outside of the filament area. Methods to influence where the voids will form are discussed in chapter 6.

Chapter 5

Critical current degradation in cabled Nb_3Sn superconductor in accelerator magnets

This chapter describes critical current measurements on Nb_3Sn Rutherford cables. First, the cable parameters relevant to the experiments are described.

Next, the experimental setups for extracted strands and full-cables are illustrated. U(I)-curves and $I_c(P)$-curves extracted from the investigations are presented. The correlation between the extracted strand and full-cable experiments is investigated. The dependency of the initial, reversible and permanent cable degradation on the cable parameters is investigated. The correlation between the initial degradation due to cabling and the reversible and permanent cable degradation under pressure loading is discussed.

Due to the limited amount of samples for each conductor type, the conclusions with respect to optimal settings for cable parameters often can not be satisfactory proven. The data is presented here nevertheless, since this is the first time a systematic study of the relation between critical current degradation and the cable parameters has been performed.

An analysis of the optimal values for the cable parameters leads to an optimal cable design. A set of parameters for this design is given.

Finally, the correlation between the shape of the critical current degradation curves and the model predictions from chapter 3 is discussed.

5.1 Introduction

This chapter describes the critical current degradation experiments performed to investigate the reduction in I_c due to initial cable damage and as a function of transverse pressure. Both extracted strand and full-cable experiments are performed on the Internal Tin [5.1] and Modified Jelly Roll conductors [5.2, 5.3]. The results are referenced to the Powder-In-Tube conductor [5.4 - 5.6], and recent cable measurements on a different type of Internal Tin conductor [5.7, 5.8]. In section 5.2, the relevant cable parameters are described. A subset of cable parameters is selected to be more closely investigated. Next, the experimental setup for extracted strands is discussed in section 5.3.1, followed by the setup of the full-cable experiments in section 5.3.2. The results from the extracted strand experiments are summarized in section 5.4. *U(I)*-curves and $I_c(P)$-curves from the cable experiments are discussed in section 5.5. The correlation between the extracted strand and full-cable experiments is investigated in section 5.6. The results for the extracted strand and cable experiments are grouped by conductor type.

The dependency of the initial, reversible and permanent cable degradations on the cable parameters is investigated in detail in sections 5.7 through 5.9. The correlation between the initial cable degradation and the reversible and permanent cable degradation is discussed in section 5.10.

The correlation between the shape of the critical current degradation curves from the experiments and the prediction from the model (3.32) in chapter 3 is evaluated in section 5.12.

5.2 Cable parameters

In order to investigate the influence of the cable parameters on the various components of the critical current degradation, a series of samples of several different cable geometries is made. The cable parameters described in section 3.5.3 are a function of the size parameters set on the cabling machine and the diameter of the wire.

The critical current degradation is investigated as a function of both the dimensional parameters as well as the composition and type of the wire. Table 5.1 lists the adjustable settings on the cabling machine and their relations to the final cable parameters. Figure 5.1 shows a schematic of the cabling process, indicating the adjustable settings and cable parameters.

The following settings are adjustable on the cabling machine:

1) number of strands;
2) mandrel thickness : thickness of the guiding mandrel at the tip;
3) mandrel width : width of the guiding mandrel at the tip;
4) mandrel distance from pinch point : distance from the tip of the mandrel to the pinch point between the rollers in the Turk's head[1];
5) roller width : free space in the x-direction between the rollers in the Turk's head;
6) roller minimum thickness : minimum free space in the y-direction between the rollers in the Turk's head;
7) roller maximum thickness : maximum free space in the y-direction between the rollers in the Turk's head (settings 5-7 define the cable keystone angle);
8) gear ratio between main wheel rotation and cabling speed : this determines the pitch length of the strands in the cable;
9) gear ratio between main wheel rotation and individual strand spool rotation.

Of these parameters, the mandrel size, roller size and gear ratio determining the pitch length are varied. The number of strands is not considered to have a direct influence on the critical current degradation, only indirectly through the resulting compaction factor.

[1] The Turk's head is the component of the cabling machine that compresses the cable into it's final shape with four rollers. The size of the gap between the rollers determines the final cable cross-section. A Turk's head can be either un-powered (rollers are turning by friction only) or powered (rollers are turned by a motor). The LBNL cabling machine uses a powered Turk's head.

The distance from the mandrel to the pinch point is set by the machine operator to produce a "good looking" cable, no specific distance is measured. The gear ratio between main wheel rotation and individual strand spool rotation is adjusted to relieve any residual "spring-back" of the cable.

Each individual strand is twisted in the opposite direction with respect to the main cable twist, effectively canceling the force from the torsion spring created by the cable twist with the summation of the force from the torsion springs of the strands.

<table>
<tr><td></td><td colspan="6">Cabling machine parameters</td></tr>
<tr><td></td><td colspan="2">Mandrel</td><td colspan="3">Rollers</td><td>Gears</td></tr>
<tr><td>Cable parameters</td><td>thickness T_m [mm]</td><td>width W_m [mm]</td><td>width W_r [mm]</td><td>minimum thickness t_1 [mm]</td><td>maximum thickness t_2 [mm]</td><td>pitch length L_p [mm]</td></tr>
<tr><td>Cable average thickness t_{ave} [mm]</td><td>g_{tm}</td><td></td><td></td><td colspan="2">t_{ave}</td><td></td></tr>
<tr><td>Cable keystone angle a [degrees]</td><td></td><td></td><td></td><td colspan="2" rowspan="2">a</td><td></td></tr>
<tr><td>Cable width w [mm]</td><td></td><td>g_{wm}</td><td>g_{wr}</td><td rowspan="3">j</td></tr>
<tr><td>Cable pitch angle j [mm]</td><td></td><td></td><td></td><td colspan="2" rowspan="2">C_p</td></tr>
<tr><td>Cable strand diameter d [mm]</td><td>s_t</td><td colspan="2">s_w</td><td></td></tr>
</table>

Table 5.1 Relation between the cabling machine settings and the final cable parameters. The column headers indicate the settings on the cabling machine that are varied throughout the experiments. The row headers indicate the cable parameters that are a function of the cable machine settings in the columns. The parameters are described in section 5.2.

In figure 5.1, on the top left the entire rotating section of the machine is shown together with the rollers in the Turk's head. The strands run from the individual strand wheels on the main disk through a guide wheel to the mandrel. From the mandrel they are guided through the rollers in the Turk's head to form the cable. On the top right, a close-up of the rollers and the mandrel tip is shown, with a section of finished cable protruding through the rollers. On the bottom left, the mandrel tip is shown. The cable size is determined by the free space between the rollers, as shown on the bottom right.

The following cable parameters (see table 5.1 for inter-relations) are investigated for their influence on the critical current degradation:
the average cable thickness

$$t_{ave} = \frac{(t_1 + t_2)}{2}, \tag{5.1}$$

the cable keystone angle

$$a = \arctan\frac{(t_2 - t_1)}{w}, \tag{5.2}$$

the cable pitch angle

$$j = \arctan\frac{2w}{L_p}, \tag{5.3}$$

the ratio of the average cable thickness to the mandrel thickness

$$g_{tm} = \frac{t_{ave}}{T_m}, \tag{5.4}$$

and the ratio of the width of the cable to the mandrel width

$$g_{wm} = \frac{w}{W_m}. \tag{5.5}$$

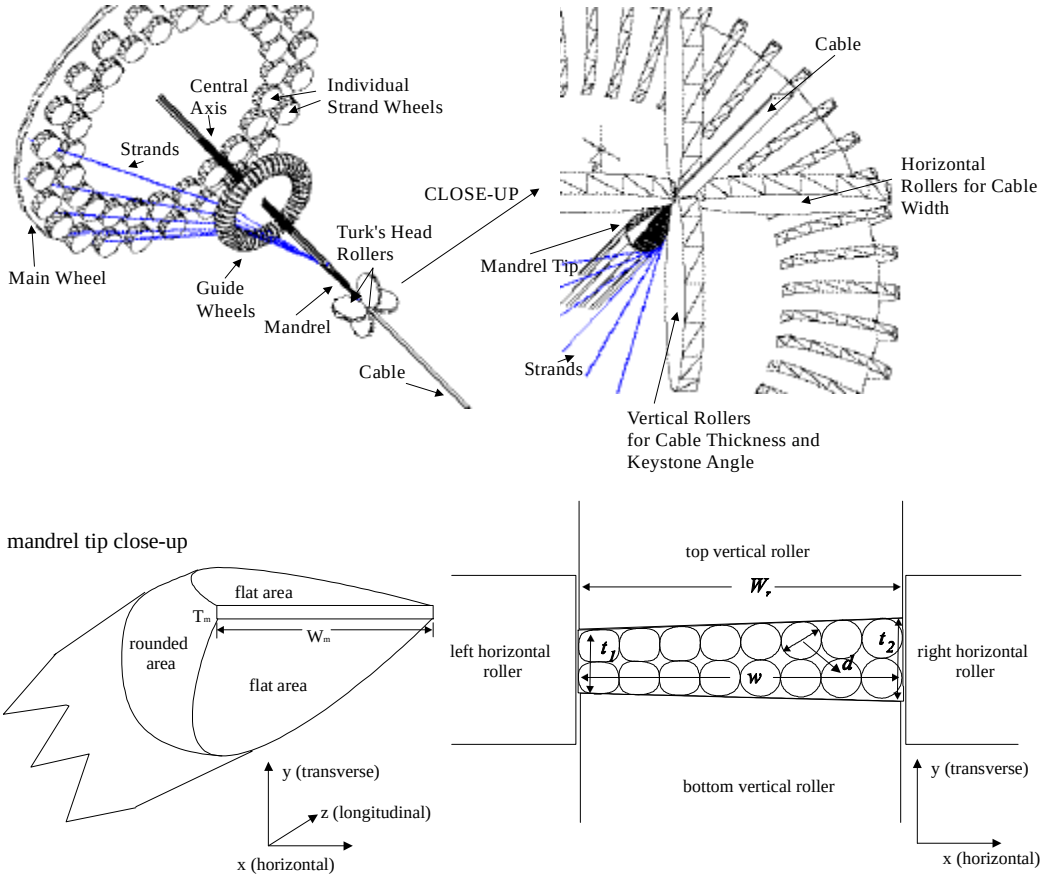

Figure 5.1 Schematic of the cabling process.

Also defined are:
the ratio of the width of the cable to the roller width

$$g_{wr} = w / W_r, \tag{5.6}$$

the cable volume compaction factor

$$C_p = \frac{p}{4} \frac{2w(t_1 + t_2)\cos j}{npd^2}, \tag{5.7}$$

the free space between the mandrel tip and the rollers in the vertical direction (thickness)

$$s_t = (T_{ave} - T_m) / 2d, \tag{5.8}$$

the free space between the mandrel tip and the rollers in the horizontal direction (width)

$$s_w = (W_r - W_m) / 2d, \tag{5.9}$$

the cable strand diameter *d* and finally the cable width *w*.

The listed parameters are chosen because they are directly related to the final dimensions of the cable, or a change in dimension during the cabling process. In addition to the parameters defined in formulas (5.1) through (5.9), four more parameters are defined in equations (5.10)-(5.13), describing the local compaction of the strands in the cable edge areas.

When the cable is compressed in the x-direction between the rollers, the strands at the edge are more severely deformed than the strands in the middle of the cable. This is due to the effect of friction between the strands and the vertical rollers preventing the middle strands from moving towards the center of the cable. The effect is illustrated in figure 5.2.

The localized compaction factor for the edge strands is defined as

$$C_{x,edge} = \frac{p}{4} \frac{\cos j \times d\left(w - \left(\frac{n-4}{2}\right) d\right)}{2p(d/2)^2}, \tag{5.10}$$

with n the number of strands in the cable. Only the four strands at the edge of the cable are used for the calculation. Hence, the width w of the cable is reduced by the width of the interior (n-4) strands. To accomplish this, $d(n\text{-}4)/2$ is subtracted from w in (5.10).

The compaction in the x-direction for the entire cable is defined as

$$C_x = \frac{p}{4} \frac{\cos j \times 2dw}{np(d/2)^2}. \tag{5.11}$$

The compaction factors in the y-direction for the minor edge and major edge are defined as

$$C_{y1} = \frac{p}{4} \frac{\left(t_1 + \frac{2(t_2 - t_1)}{n}\right) \times \left(\frac{2w}{n}\right)}{2p(d/2)^2} \tag{5.12}$$

and

$$C_{y2} = \frac{p}{4} \frac{\left(t_2 - \frac{2(t_2 - t_1)}{n}\right) \times \left(\frac{2w}{n}\right)}{2p(d/2)^2}. \tag{5.13}$$

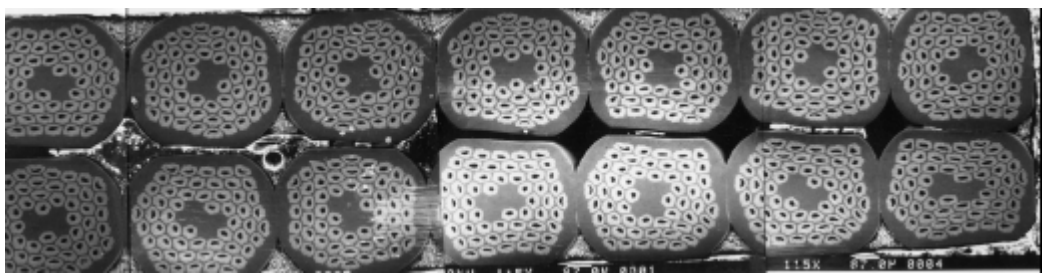

Figure 5.2 A cross-section of a typical cable illustrating the larger deformation of the edge strands. Compare the more deformed strands at the edge to the less deformed strands in the middle of the cable.

The factors defined in (5.12) and (5.13) compute the compaction factor for the four corner strands on either side of the cable as illustrated in figure 5.3. The area to fit the four strands is computed by multiplying the width of two strands ($2d$) times the height at the middle of the trapezoid between the two strands. This height is computed from the edge thickness (t_1 or t_2) by correcting for the slope of the trapezoid $2(t_2\text{-}t_1)/n$ over one strand width d.

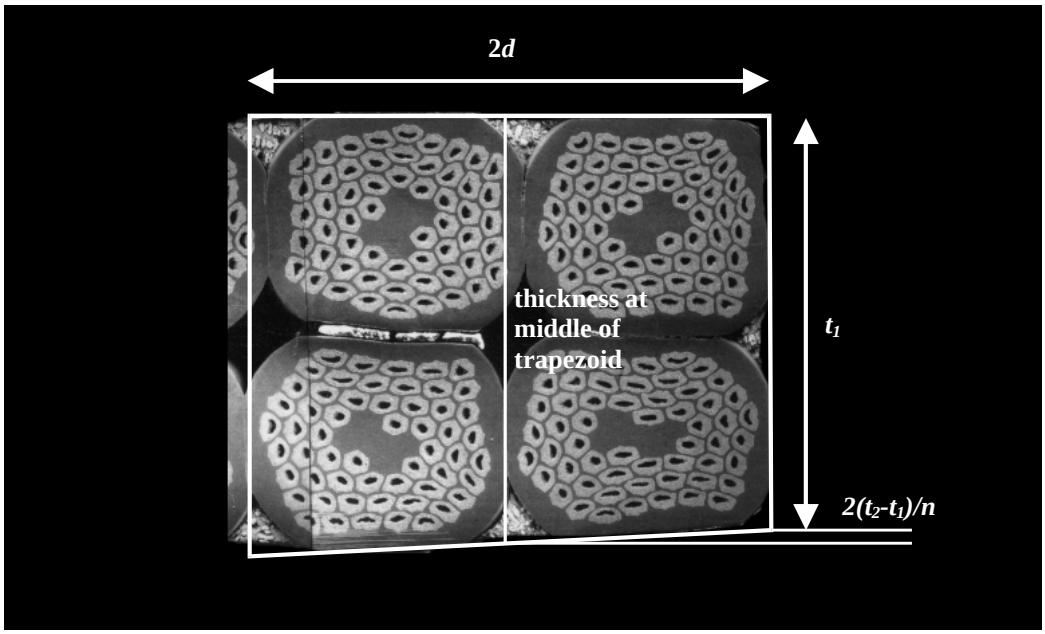

Figure 5.3 Close-up of the narrow edge of the cable illustrating the C_{y1} compaction factor (5.12).

Table 5.2 lists the range of the settings on the cabling machine, and the resulting cable parameters. The formula reference is given between the brackets where applicable. The cabling machine data are only available for cables produced at the LBNL facility, therefore, not all cables tested are represented in the range table.

Cabling machine parameter	Range	Cable parameter (equation)	Range
T_m	0.31-0.71 [mm]	g_{tm} *(5.4)*	2.11-2.82 [-]
W_m	10.28-16.28 [mm]	g_{wm} *(5.5)*	1.03-1.13 [-]
		s_t *(5.8)*	0.41-0.58 [-]
		s_w *(5.9)*	0.34-1.36 [-]
W_r	11.60-18.38 [mm]	w	11.50-21.70 [mm]
t_1	0.80-2.19 [mm]	g_{wr} *(5.5)*	0.95-1.01 [-]
t_2	0.84-2.69 [mm]	t_{ave} *(5.1)*	0.84-2.30 [mm]
		a *(5.2)*	0.0-1.36 [degrees]
		C_p *(5.7)*	82.70-92.49 [%]
		$C_{x,edge}$ *(5.10)*	101.93-145.19 [%]
		C_x *(5.11)*	96.75-101.92 [%]
		C_{y1} *(5.12)*	79.24-96.20 [%]
		C_{y2} *(5.13)*	89.08-103.91 [%]
L_p	73-160 [mm]	j *(5.3)*	12.53-17.67 [degrees]

Table 5.2 Range of the cabling machine parameters and the resulting cable parameters. The ratio's and compaction factors are dimension-less; the compaction factors are given in percent. The smaller the compaction factor, the more the strands are compressed.

In addition to the cable parameters, the correlation of the strand copper content with the critical current degradation is also investigated. For the investigated cables, the copper content of the strands ranges from 30.5 to 56.0 %. Tables 5.3 through 5.5 list the cable parameters for the investigated cable samples. The samples are grouped by conductor type; both literature data and experimental samples are listed.

Test ID	Strand manu-facturer	Strand internal structure or designation	LBNL Cable ID	Number of strands	*d* [mm]	Copper content [%]	*w* [mm]	t_1 [mm]	t_2 [mm]	*a* [deg]	*j* [deg]	C_p [%]
TW1	TWCA	6 elements	T-479	48	0.65	55	15.80	1.01	1.23	0.8	16.2	84.1
TW2	TWCA	36 elements	T-476	26	1.29	55	16.99	2.13	2.47	1.2	15.7	86.4
TW3	TWCA	36 elements	T-476	26	1.29	55	16.99	2.13	2.47	1.2	15.7	86.4
TW4	TWCA	36 elements	T-476	26	1.29	55	16.99	2.13	2.47	1.2	15.7	86.4
TW5	TWCA	120 elements	T-497	37	0.75	50	14.35	1.15	1.37	0.9	17.0	82.7
TW6	TWCA	120 elements	T-501	37	0.75	50	14.47	1.24	1.47	0.9	17.3	89.8
TW7	TWCA	120 elements (two samples)	T-502 T-522	37	0.75	50	14.46	1.35	1.35	0.0	17.3	89.5
TW8	TWCA	56 elements	T-499B	47	0.48	54	11.63	0.80	0.98	0.9	17.7	90.4
TW9	TWCA	56 elements	T-517	47	0.48	54	11.63	0.88	0.88	0.0	16.0	90.3
TW10	TWCA	56 elements	T-527	47	0.48	54	11.63	0.87	0.87	0.0	16.0	89.3
TW11	TWCA	56 elements	T-527	47	0.48	54	11.63	0.87	0.87	0.0	16.0	89.3

Table 5.3 Cabling machine and cable parameters of the MJR conductors.

Test ID	Strand manu-facturer	Strand internal structure or designation	LBNL Cable ID	Number of strands	*d* [mm]	Copper content [%]	*w* [mm]	t_1 [mm]	t_2 [mm]	*a* [deg]	*j* [deg]	C_p [%]
IG1	IGC	D19H (sample)	I-554	30	0.80	32.0	12.33	1.31	1.51	1.0	12.5	88.3
IG2	IGC	D19H (magnet)	I-556	30	0.80	32.0	12.36	1.38	1.50	0.6	15.8	88.8
IG3	IGC	19 elements	I-523	37	0.75	30.5	14.45	1.37	1.37	0.0	17.2	90.0
IG4	IGC	19 elements	I-523	37	0.75	30.5	14.45	1.37	1.37	0.0	17.2	90.0
IG5	IGC	19 elements	I-491	37	0.75	54.5	14.43	1.13	1.39	1.1	17.2	83.7
IG6	IGC	19 elements	I-506	37	0.75	30.5	14.46	1.26	1.49	0.9	17.3	90.3
IG7	IGC	19 elements	I-512	37	0.75	30.5	14.46	1.39	1.39	0.0	17.3	91.2
IG8	IGC	19 elements	I-516	47	0.47	54.5	11.50	0.84	0.84	0.0	17.4	89.7
IG9	IGC	19 elements	I-526	47	0.48	54.5	11.62	0.91	0.91	0.0	16.0	92.5
IG10	IGC	19 elements	I-528	47	0.48	54.5	11.62	0.87	0.87	0.0	16.0	89.2
LM1	LMI	37 elements	none	36	0.825	52.3	14.95	1.46	1.46	0.0	16.0	85.6
LM2	LMI	37 elements	none	36	0.825	52.3	14.95	1.31	1.61	1.2	16.0	85.6

Table 5.4 Cable parameters of the IT conductors. The LMI samples were not cabled at LBNL, hence they have no Cable ID.

Test ID	Strand manu-facturer	Strand internal structure or designation	LBNL Cable ID	Number of strands	d [mm]	Copper content [%]	w [mm]	t_1 [mm]	t_2 [mm]	a [deg]	j [deg]	C_p [%]
EC1	ECN	Sultan (1)	none	36	1.22	55	18.20	1.82	1.82	0.0	12.8	89.7
EC3	ECN	Sultan (3PT)	none	36	1.22	55	18.20	1.82	1.82	0.0	12.8	89.7
EC4	ECN	Sultan (4PT)	none	36	1.22	55	18.20	1.82	1.82	0.0	12.8	89.7
EC5	ECN	Sultan (5PT)	none	36	1.22	55	18.20	1.82	1.82	0.0	12.8	89.7
EC6	ECN	TWEN A	N/A	33	1.22	55	17.38	1.55	1.93	1.3	17.4	87.5
EC7	ECN	MSUT outer	N/A	33	1.27	56	17.41	1.53	1.95	1.4	15.0	88.7
EC8	ECN	MSUT outer	N/A	33	1.27	56	17.38	1.55	1.93	1.3	16.3	87.9
EC9	ECN	MSUT inner	N/A	33	1.27	56	21.70	1.98	2.47	1.3	16.5	88.4
EC10	ECN	LHC-B	none	36	0.90	58	16.60	1.53	1.85	1.1	15.5	91.7

Table 5.5 Cable parameters of the PIT conductors. Samples EC1, EC3-5 and EC10 are not cabled at LBNL, hence they have no Cable ID. Samples EC6-9 were cabled at LBNL, but not assigned an ID.

In section 5.7 the results from the critical current degradation experiments are correlated to the cable parameters listed in these tables. The extracted strands are listed by their cable ID number. The cable samples are referenced by their test ID numbers, as given in the first column of each table. Column two shows the cable manufacturer.

The strand internal structure or designation referenced in column three describes the type of conductor used, or the magnet it is designed for.

In column five, the number of strands is given. For the cables with an uneven number of strands, the volume compaction C_p reflects the true number of strands.

5.3 Critical current degradation experiments

In this section the experimental setup of the critical current degradation measurements is described. The experiments fall in two main categories:

1) extracted strand experiment. For some of the cables, a simple test is done on strands extracted from the cable after the cabling process. The goal is to determine the correlation between the extracted strands and the full-cable experiments. Details of the setup are given in section 5.3.1, and results are presented in section 5.4;
2) full-cable test. A more realistic test is a full-cable test in a transverse magnetic field and under transverse pressure. The tests are performed at the special test facility at the University of Twente, Enschede, The Netherlands, for measuring the critical current versus transverse pressure. Details are given in section 5.3.2, and results are presented in section 5.5.

5.3.1 Extracted strand test setup

For samples TW6-9 and samples IGC5-8, extracted strand experiments are performed. A section of a strand extending several pitch lengths is carefully taken out of an un-reacted cable, then wound on a stainless steel reaction holder, and wrapped with woven S2-glass tape.

The strand is subsequently wrapped with a few more layers of the glass tape to hold it in place during reaction, but without constraining its thermal expansion significantly. The samples are then reacted in a vacuum tube furnace, impregnated with Versamid or Stycast 2850FT, whereafter the critical current is measured. The critical current of the wire is then compared to that of the virgin strand tested in the same configuration. The ratio of the critical current of the cabled and virgin strands expresses the initial cabling degradation.

5.3.2 Cable critical current degradation experiments

The critical current degradation of a full-cable as a function of the transverse pressure is measured at a test facility, specifically designed to perform such tests, at the University of Twente. A detailed description of the system is found in [5.9, 5.10].

A schematic of the sample holder is shown in figure 3.16. A sample of approximately 60 cm length is reacted on a U-shaped form, then transferred to a U-shaped sample holder. The two leads are soldered to the terminals of a superconducting transformer that supplies the sample current. The superconducting transformer can deliver a maximum sample current of approximately 50 kA. The sample current is measured by a superconducting current meter [5.11].

Voltage taps are soldered to select individual strands in the cable to measure the voltage U across the sample as a function of the cable current I. Figure 5.4 shows a typical configuration for the voltage taps. At least four strands are selected, each at a different location within the cable. For most cables, half the pitch length is longer than the length of the pressure block.

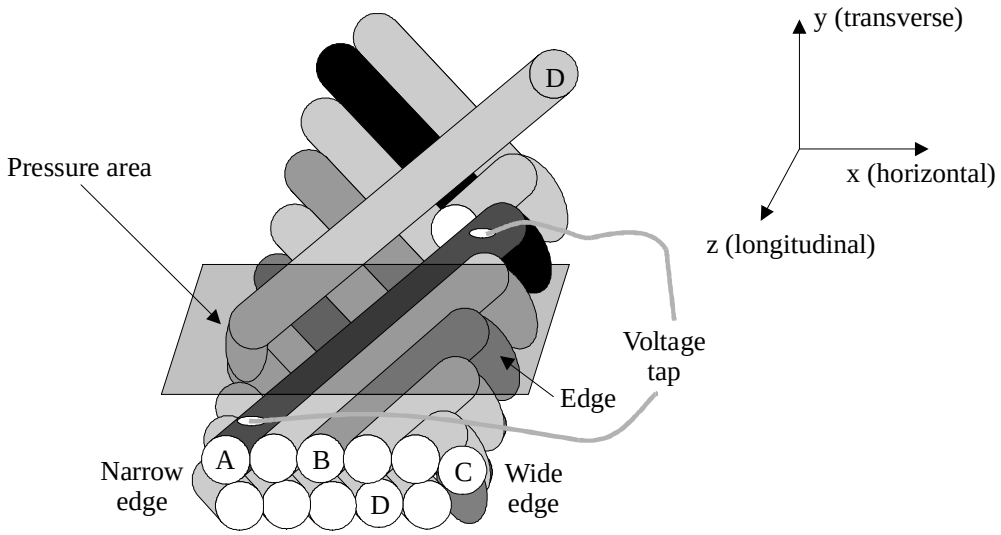

Figure 5.4 Typical voltage tap locations in the cable samples. Straight strands are labeled A (top layer) and C (bottom layer), bent strands B (wide edge) and D (narrow edge). Some strands are omitted for clarity.

This means one can select at least two strands under the pressure block that are not bent around the edge of the cable. Voltage taps are attached to these strands, at least one at the top layer (A) (shown) and one at the bottom layer (C) (not shown). Likewise, one can select at least two strands under the pressure block that are bent around the narrow edge (D) and the wide edge (B). In most cases, two straight strands and four bent strands are selected, for a total of six voltage taps on the individual strands.

Four additional voltage taps are attached to the entire cable sample; one pair is placed across the sample above the joint to the transformer, and another pair is placed across the sample and the joints. In this configuration the resistance of the joint can be determined. The joint resistance typically ranges from 0.3 to 0.5 nΩ, therefore sample heating due to resistive heating at the joints is not considered to be a problem.

After attachment of the voltage taps, the entire sample is tied to the holder with S2 glass tape, and epoxy impregnated with Stycast 2850FT. This is done to ensure that the cable will not move during the experiment due to the Lorentz force, since this might cause damage due to excessive strain.

Next, the sample holder is bolted to a slotted cylinder in which a stainless steel rod can travel. The rod pushes against a pressure block that is shaped to fit the cable dimensions. The effective sample length over which the cable is compressed is 40 mm. To protect the sample from any imperfections in the surface of the stainless steel pressure block, and to create a more uniform pressure on the strands in the cable, a thin sheet of G10 glass-epoxy is inserted between the block and the cable. The sides of the cable are constrained by

stainless steel side support plates in the direction perpendicular to the applied pressure to prevent deformation of the cable in that direction.

The transverse pressure to the rod is supplied by two superconducting solenoids mounted on the bottom of the system. The solenoids are configured to repel each other, thus moving the pressure block up against the cable surface. The press is capable of delivering a force of 250 kN, which for most of the samples results in a maximum transverse pressure in the range of 200-250 MPa.

The sample assembly is placed inside the 80 mm wide bore of an 11.5 T solenoid producing the background field. The field direction is perpendicular to the 40 mm section of cable to be tested (along the y-axis in figure 5.1).

A correction for the self field of the cable is applied. The magnetic field produced by the cable is added to the background field at one side of the cable, and subtracted at the other side, effectively introducing a systematic error in the background field. The average error in a typical cable ranges from 0.06 % (I = 3 kA at 11 T) to 1.1 % (I = 25 kA at 5 T).

The *U(I)*-curves are recorded as a function of B and P for a stepwise increasing pressure P, with a check of the unloaded case after each increase. A typical sequence records the *U(I)*-curves for loads of 5, 25, 5, 50, 5, 75, 5, ….., 250, 5 MPa. For the higher loads, the step-size is increased to 50 MPa intervals.

For each load, the *U(I)*-curve is recorded for field values ranging between 5 and 11 T. The *U(I)*-curves are recorded using stepwise increments in the sample current, usually of the order of 500-1000 A, until the expected I_c is neared.

Then, the current increments are gradually decreased to increase the number of points near I_c. The sample current is increased, and voltages recorded, until the quench current is reached. The sequence is repeated for each field and pressure setting.

Generally, a criterion of 1 μVcm^{-1} is used to determine the critical current I_c from the measured voltage U on the voltage taps, as a function of the sample current I (see also figure 3.5). The accuracy of the system is of the order of 1 % in the current measurement and 2 % in applied pressure.

5.4 Results on extracted strands

This section describes the result of the critical current measurements on the virgin wires and extracted strands. The experimental data is compared to the wire performance as specified by the manufacturer. The results of the wire and extracted strand measurements are given in the following sequence:

1) measured MJR wires (compared to manufacturers data, referenced to the wire ID);
2) MJR extracted strands (with reference to the cable ID);
3) measured IT wires (compared to manufacturers data, referenced to the wire ID);
4) IT extracted strands (with reference to the cable ID).

5.4.1 Modified Jelly Roll Conductor

Figure 5.5 shows the $I_c(B)$ curves of the MJR wires. The upper set of data is taken from measurements of the wires and strands for a 37 strand cable. The wire cable numbers are T501 (TW6) and T502 (TW7). The lower set of data is taken from measurements of the wires and strands for a 47 strand cable.

The cable numbers are T499B (TW8), T517 (TW9) and T527 (TW10/11). Of these, only TW8 was used for extracted strand measurements. The results of the extracted strand measurements are shown in figure 5.6. The top two curves show the critical current for the strands extracted from the 37 strand cable, the bottom curve shows the data for the 47 strand cable.

After the cabling operation to form cable TW8, the strand appeared to be degraded. The degradation amounts to an initial I_c reduction due to cabling of 21 %. Samples TW6 and TW7 show an initial I_c reduction of 16 % and 2 % respectively. Table 5.6 contains a summary of the virgin wire and extracted strand measurements.

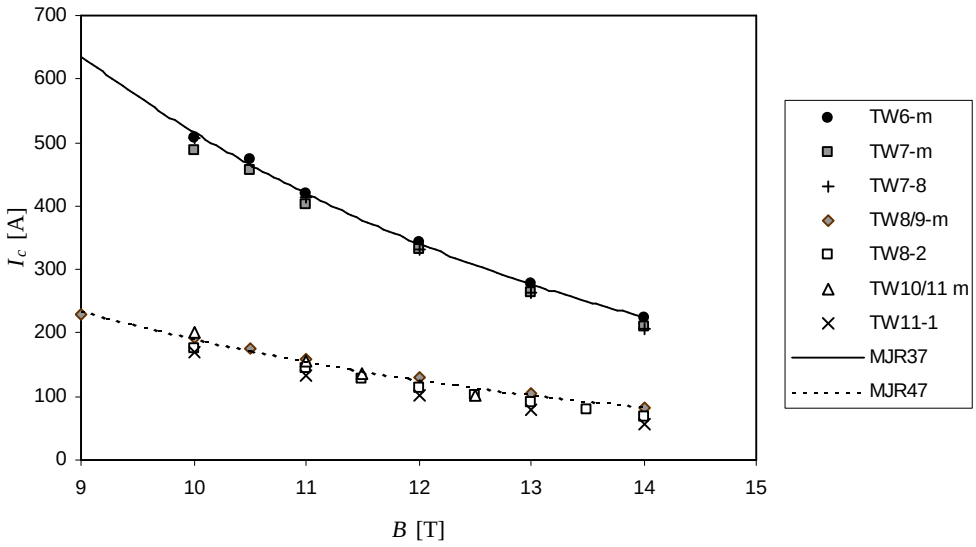

Figure 5.5 *Virgin strand critical current I_c as function of the applied transverse magnetic field B for the MJR wires. The solid lines labeled MJR37 and MJR47 indicate the average of the manufacturers data.*

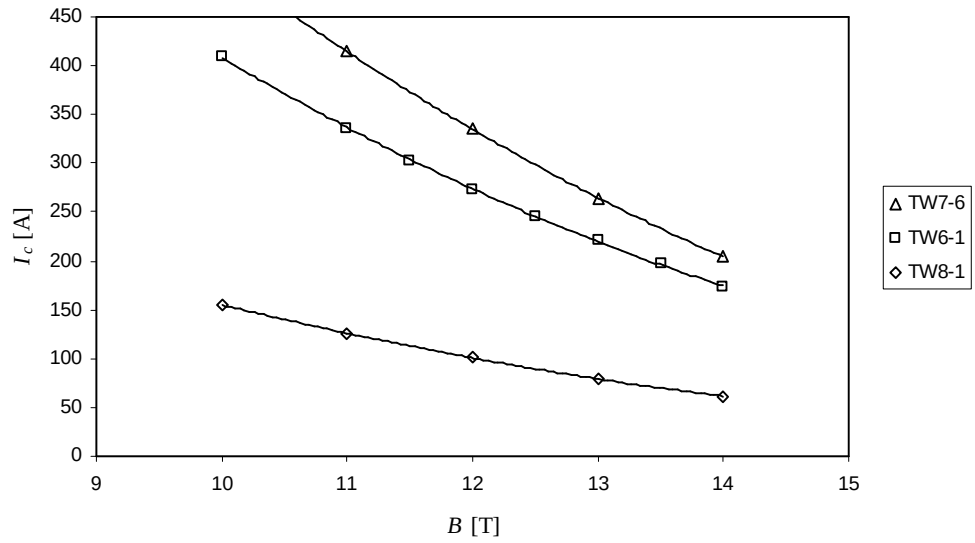

Figure 5.6 *Extracted strand critical current I_c measured as a function of the applied transverse magnetic field B for cables TW7, TW6 and TW8.*

5.4.2 Internal Tin Conductor

Figure 5.7 shows the critical current measurements for the IT virgin strands, while figure 5.8 shows the extracted strand I_c for the IT cable samples. At 11 T, 4.2 K, sample IG8 shows a reduction of 40 %. Sample IG6 shows a drop of 7 % and sample IG7 shows a drop of 2 %. The data are summarized in table 5.6.

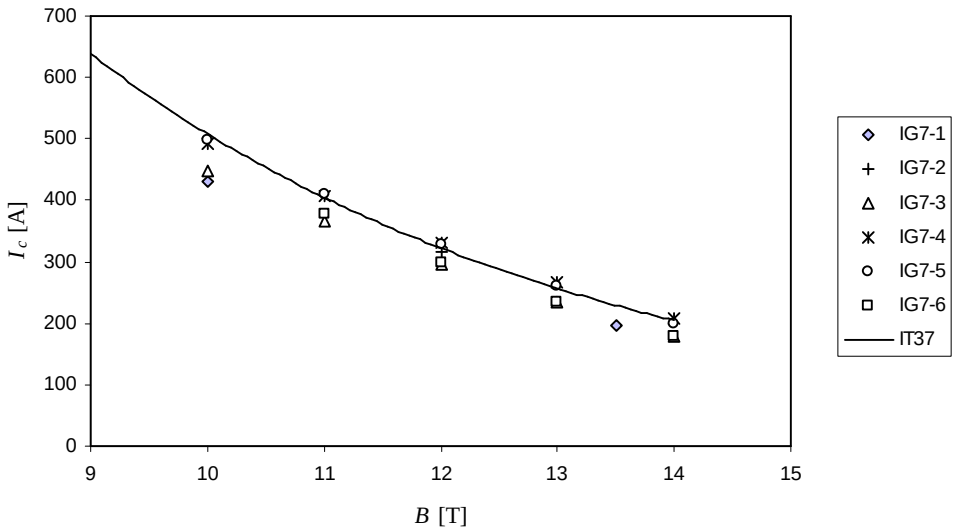

Figure 5.7 Virgin strand critical current I_c as function of the applied transverse magnetic field B for the IT wires. The solid line shows the manufacturers data for the strands for a 37 strand cable as indicated by IT37.

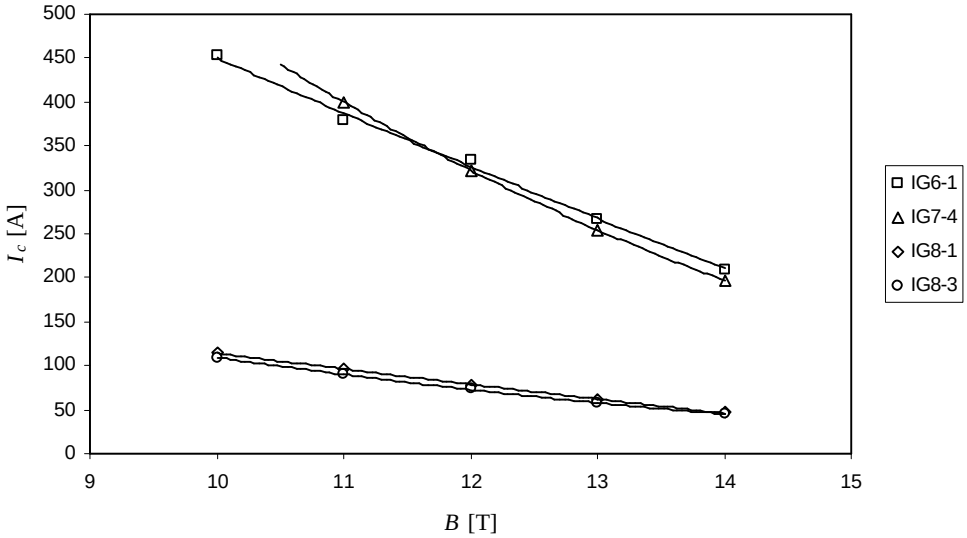

Figure 5.8 Extracted strand critical current I_c as function of the applied transverse magnetic field B for cables IG6, IG7 and IG8.

5.4.3 Summary

The experiments show that for the MJR conductors, the initial critical current reduction is of similar magnitude for both the 0.48 mm diameter and 0.75 mm diameter keystoned cables, of the order of 16-22 %. The sample with a rectangular cross-section shows an initial critical current degradation of 2-4 % only.

Wire and cable type	Manufacturers I_c at 11 T, 4.2 K [A]	Virgin I_c at 11 T, 4.2 K [A]	Extracted I_c at 11 T, 4.2 K [A]	Initial degradation [%]	
				11 T	all fields
MJR, 0.75 mm, 37 strands	402 421	missing 418	336 (TW6) 414 (TW7)	16 2	17 4
MJR, 0.48 mm, 47 strands	158 157	144 133	125 (TW8) missing (TW9)	21 missing	22 missing
IT, 0.75 mm, 37 strands	missing	409	379 (IG6) 400 (IG7)	7 2	2 5
IT, 0.47 mm, 47 strands	missing	161 (scaled)	97 (IG8)	40	40

Table 5.6 Results of critical current measurements of the virgin wires and extracted strands of the MJR and IT conductors. The initial degradation is computed from the manufacturers data when available, or from the virgin strand results otherwise. The current values quoted in the table are all at 11 T, 4.2 K. The initial degradation is listed for the same field, and also computed from all available data (average initial degradation over all field points).

The IT samples show a smaller initial critical current reduction of 2-7 % for the larger diameter wire, regardless of the keystone angle. The 0.47 mm wire has a fairly large initial critical current degradation of 40 %.

This indicates that for the MJR conductors, the keystone angle, and hence the compaction of the strands at the narrow edge, are important parameters for the study of the critical current degradation mechanism. For the IT conductors, the influence of the keystone angle is not clear.

For both conductors, the size of the wire is a factor. The initial critical current degradation tends to increase with decreasing wire size. The influence of the cabling parameters will be investigated in more detail in section 5.6.

5.5 Results on cables under transverse pressure

This section describes the measurements of the critical current I_c as a function of applied transverse pressure P and magnetic field B. The data are gathered over several years of experiments, and is presented here grouped by conductor type.

For both the MJR and IT conductors, selected cables are presented in more detail. The results from all cable tests are summarized in tabular format. The data on the PIT conductors are extracted from literature, and presented here for comparison.

5.5.1 MJR Conductor

A total of 10 cable samples of the MJR conductors are tested: TW1, TW2, TW3, TW4, TW5, TW6, TW7a/b (tested twice), TW10 and TW11. The cable parameters of the samples are listed in table 5.7.

First, two types of cables, based on an older type of MJR wire, are tested with samples TW1, TW2, TW3 and TW4.

Next, a sequence of tests is performed with samples TW5, TW6 and TW7a/b, to investigate the effect of increasing degree of compaction of the cable on the critical current degradation and initial cabling damage.

Samples TW8 through TW11 are taken from cables with a smaller wire diameter (0.48 mm).

ID	g_{tm}	g_{wm}	s_t	s_w	g_{wr}	a	C_p	$C_{x,edge}$	C_x	C_{y1}	C_{y2}
TW1	-	-	-	-	-	0.80	84.1	110.7	97.3	79.7	95.4
TW2	-	-	-	-	-	1.15	86.4	102.6	97.2	84.1	95.3
TW3	-	-	-	-	-	1.15	86.4	102.6	97.2	84.1	95.3
TW4	-	-	-	-	-	1.15	86.4	102.6	97.2	84.1	95.3
TW5	2.80	1.09	0.47	0.72	1.0045	0.86	82.7	124.7	98.8	79.9	93.1
TW6	2.41	1.06	0.45	0.52	1.0049	0.90	89.8	132.0	99.4	87.0	101.0
TW7	2.41	1.06	0.53	0.52	1.0044	0.00	89.5	131.4	99.4	93.7	93.7
TW8	2.61	1.05	0.47	0.58	1.0024	0.92	90.4	126.7	98.0	85.8	103.9
TW9	-	-	-	-	1.0032	0.00	90.3	127.9	98.8	93.9	93.9
TW10	2.82	1.03	0.58	0.37	1.0028	0.00	89.3	125.4	98.6	92.9	92.9
TW11	2.82	1.03	0.58	0.37	1.0028	0.00	89.3	125.4	98.6	92.9	92.9

Table 5.7 Cable parameters for the MJR conductors.

Figure 5.9 shows a typical measurement sequence (up to 100 MPa) of the critical current degradation experiments. First, the critical current is determined at a given field and a slight compressive load (5 MPa), to determine what is called $I_c(0)$. Next, the load is increased with intervals of 25 to 50 MPa, and after each load step, the critical current is determined. After each measurement, the pressure is released to determine the amount of permanent degradation. By successively stepping the load up to 150-200 MPa, the total and permanent critical current degradation curves are determined. The reversible critical current degradation is then given by the difference between $I_c(0)$ and the total degradation curve (see section 3.5.4 for a detailed explanation of this definition). The sequence of the datapoints is numbered.

For this particular example, the slope of the critical current degradation as a function of the pressure increases with increasing pressure. This is a typical behavior for most samples, and also indicative of a well impregnated sample. This sample is fairly sensitive to transverse pressure, and is already degraded to about 45 % of $I_c(0)$ (or 30 % of $I_{c,m}$) at P = 100 MPa.

In figure 5.10, the resulting curves for the critical current degradation as a function of applied pressure are shown. The top curve labeled $I_c(0\text{-}P\text{-}0)/I_c(0)$ shows the irreversible or permanent reduction in critical current after each increase in load. The bottom curve labeled $I_c(P)/I_c(0)$ shows the reversible reduction in critical current. Compare the sequence numbers with figure 5.9 for clarification of the meaning of the two different representation methods.

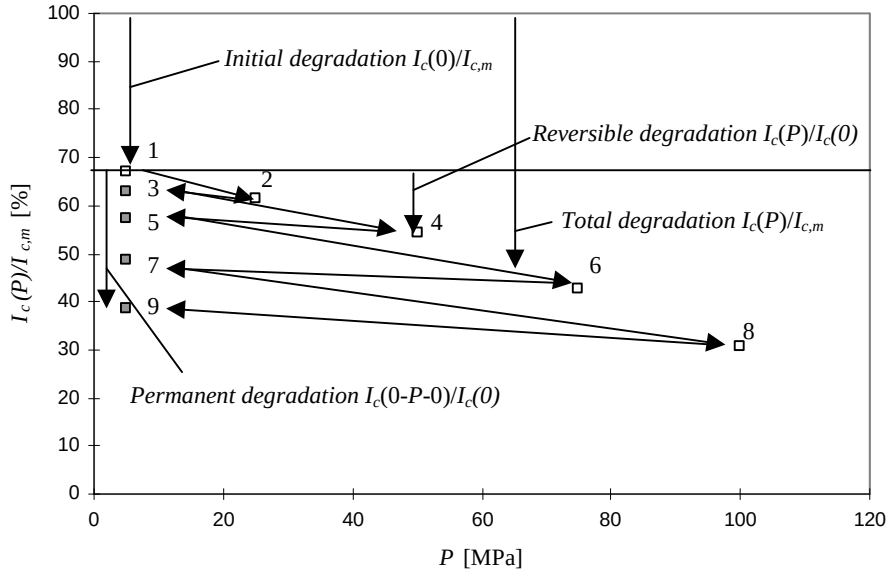

Figure 5.9 *$I_c(P)/I_{c,m}$ data for a typical cable sample. The sequence of the datapoints is numbered for comparison with figure 5.10.*

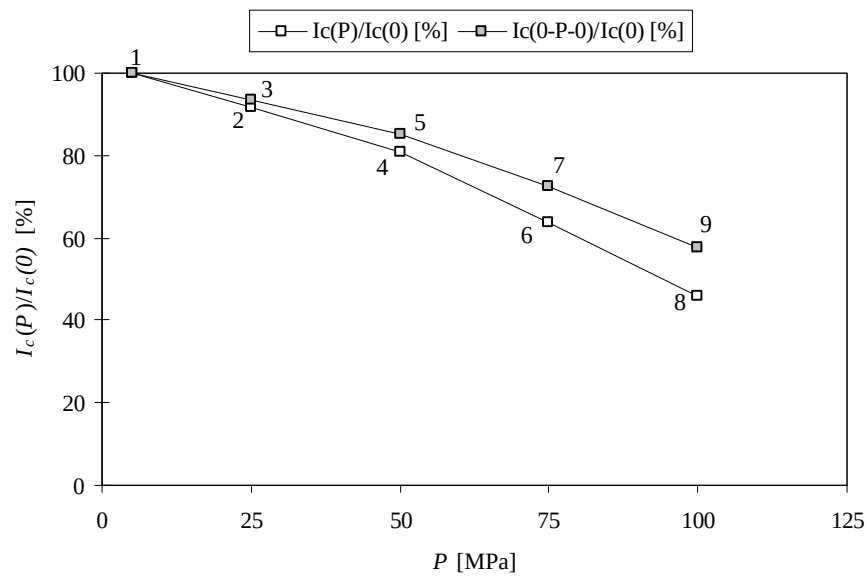

Figure 5.10 *Resulting $I_c(P)/I_c(0)$ curves for a typical cable sample. Compare the sequence of the datapoints with figure 5.9. Total degradation is given by the bottom curve, permanent degradation by the top curve. The difference between the top and bottom curve is the reversible degradation.*

Figures 5.11 and 5.12 show the increased sensitivity of the high compaction sample to critical current degradation under transverse pressure. Since the increased sensitivity to permanent damage is believed to be caused by the increased compaction of the cable, this led to a change in the "D20" design to rectangular cable with a lower volume and minor edge compaction (TW7b). In figure 5.11 the measured *U(I)*-curves are shown for samples TW5, 6 and 7b. In figure 5.12, the resulting critical current degradation curves are illustrated.

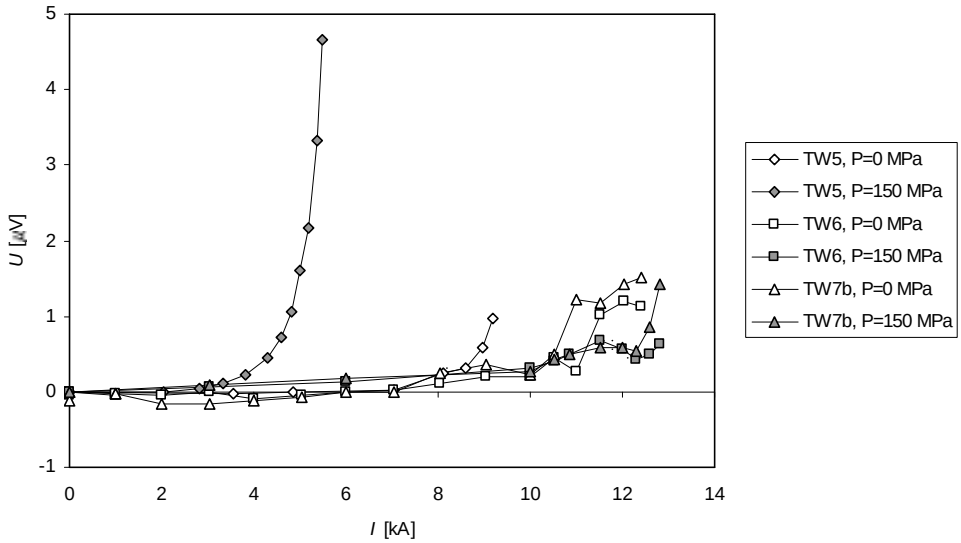

Figure 5.11 U(I)-curves for samples TW5, TW6 and TW7b, at 11 T, 4.2 K.

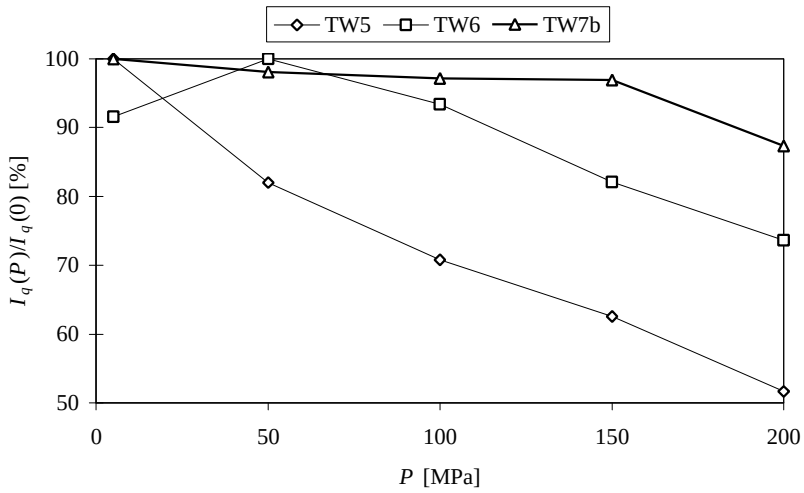

Figure 5.12 $I_q(P)$-curves for the cable samples with varied compaction factor, at 11 T, 4.2 K. Sample TW5 has a volume compaction factor of 82.7 % (high compaction). Samples TW6 and TW7b have a volume compaction factor of 89.8 % and 89.5 % respectively, with TW7b a lower minor edge compaction at 87.0 % (rectangular) compared to TW6 (keystone) at 93.7 %.

Table 5.8 lists the reversible and permanent critical current degradation at 150 MPa for the MJR conductors. A few samples stand out of the list, specifically TW2, TW5, TW7a and TW10. These samples show severe I_c degradation, or increased initial I_c degradation, or both. For sample TW2 this is explained by the fact that this is a fairly old conductor design, known to be sensitive to stress due to a non-optimal design of the filament bundle cross-section. Sample TW5 was over-compacted, and samples TW7a and TW10 were most likely damaged during the installation in the experiment. The average initial critical current degradation is 39 % for the MJR conductors. The average total and permanent I_c degradation are 57 % and 47 % with respect to the manufacturers data ($I_{c,m}$), and 29 % and 13 % with respect to $I_c(0)$.

Sample ID	*extracted strand initial degradation* $I_{c,extr}/I_{c,m}$ [%]	*virgin strand initial degradation* $I_c(0)/I_{c,m}$ [%]	*cable total degradation* $I_c(150)/I_{c,m}$ [%]	*cable permanent degradation* $I_c(0\text{-}150\text{-}0)/I_{c,m}$ [%]
TW1	-	64	38	55
TW2	-	53	20	50
TW3	-	76	60	71
TW4	-	77	62	72
TW5	-	55	34	42
TW6	80	67	55	57
TW7a	77	30	0	6
TW7b	81	87	84	86
TW10	-	43	36	40
TW11	-	60	44	55

Table 5.8 Critical current degradation data for the MJR conductors.

5.5.2 IT Conductor

Three cable samples of the IT conductor are tested. The samples are IGC1, IGC3 and IGC4. The cable parameters of all cable samples are listed in table 5.9.

ID	g_{tm}	g_{wm}	s_t	s_w	g_{wr}	a	C_p	$C_{x,edge}$	C_x	C_{y1}	C_{y2}
IG1	2.43	1.05	0.46	0.36	1.0033	0.95	88.3	116.9	100.2	84.8	96.1
IG2	2.48	1.05	0.50	0.35	1.0056	0.56	88.8	115.7	98.8	88.9	95.6
IG3	2.11	1.07	0.48	0.60	1.0042	0.00	90.0	128.4	99.1	94.2	94.2
IG4	2.11	1.07	0.48	0.60	1.0042	0.00	90.0	128.4	99.1	94.2	94.2
IG5	2.80	1.09	0.45	0.72	1.0099	1.07	83.7	132.1	99.5	79.2	96.0
IG6	2.25	1.04	0.43	0.34	1.0057	0.90	90.2	128.6	99.1	87.5	101.5
IG7	2.57				1.0051	0.00	91.2	128.4	99.0	95.5	95.5
IG8					0.9913	0.00	89.7	145.2	99.6	94.0	94.0
IG9	2.32	1.13	0.53	1.36	1.0024	0.00	92.5	124.1	98.5	96.2	96.2
IG10	2.82	1.03	0.58	0.37	1.0018	0.00	89.2	123.3	98.5	92.8	92.8

Table 5.9 Cable parameters for the IT conductors.

For sample IG1, a 37 strand cable is made of the IT wire using the same low compacting parameters as for the previous MJR-based cable (TW7), and subsequently tested for critical current degradation. Surprisingly, a large initial critical current degradation is found indicating severe cabling damage, and a fairly large reduction as a function of transverse pressure is measured. The subsequent permanent damage

is negligible however, which is an indication that all permanent damage happened before the actual load is applied. This points to bad sample preparation as the cause of the low measured current in the sample.

Figure 5.13 shows the *U(I)*-curves of the IG3 sample, and figure 5.14 shows the $I_c(P)/I_c(0)$- and $I_c(0\text{-}P\text{-}0)/I_c(0)$ curves. This particular sample is typical for a cable with a low sensitivity to applied pressure. The *U(I)*-curves are well defined for all pressures, and the resulting critical current degradation is fairly limited. Hardly any permanent I_c degradation is observed.

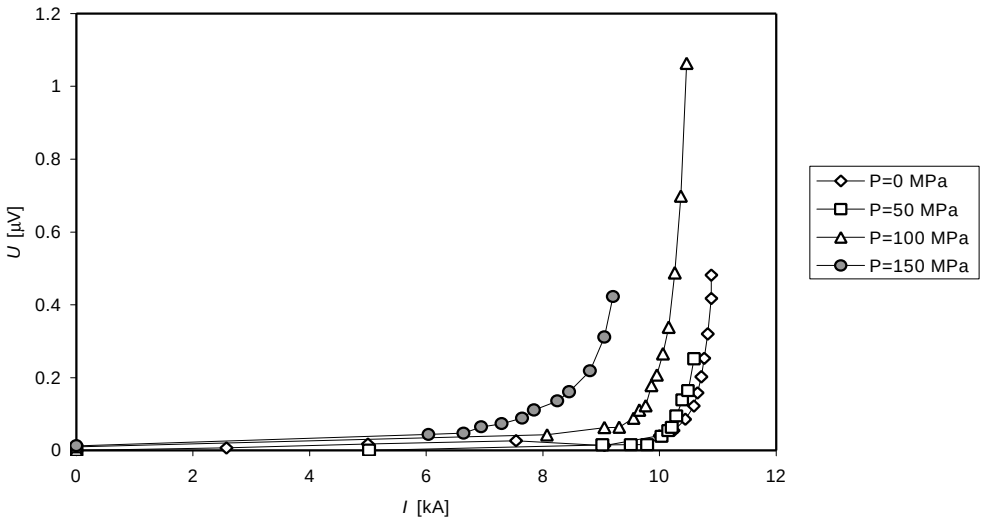

Figure 5.13 U(I)-curves for IG3 at 11 T, 4.2 K, with increasing transverse pressure P.

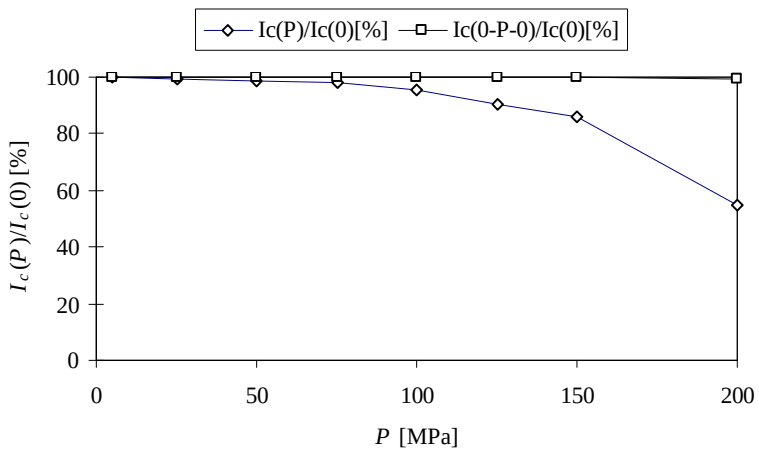

Figure 5.14 The resulting $I_c(P)$-curves for sample IG3 at 11 T, 4.2 K.

As a characteristic example, to illustrate the quality of measurements, in figure 5.15 all measured *U(I)*-curves for sample IG1 are shown with the background field *B* ranging from 8 T to 11 T. The signals from the different voltage tap locations are plotted as individual curves.

The figure illustrates that with respect to the determination of the critical current (at the intersection of the *U(I)*-curve and the line showing the 1 µV/cm criteria), all voltage taps give the same information at low applied transverse pressure. In most cable samples, at low applied transverse pressure, no significant difference was found in the *U(I)*-curve for the individual voltage tap locations.

If pressure is applied, a difference in behavior of the *U(I)*-curves at the voltage taps across the narrow and wide edge strands, and the edge versus straight strands, is visible. In figure 5.16, the narrow edge strand, loaded to 50 MPa, shows the highest voltage trace, followed by the wide edge and the straight strands. Consequently, the narrow edge strand reaches critical current before the straight strands, thereby determining the critical current of the cable.

A further increase in pressure brings the traces closer together. This is most likely due to the more even distribution of the stress in the cable once the strands are compressed past the yield stress of the cable.

Figure 5.16 shows the *U(I)*-curves at a background field $B = 10$ T, for increasing pressure P. Again, the signals from the different voltage tap locations are plotted as individual curves. This particular sample shows a large degradation when the pressure is increased from 5 MPa to 50 MPa, and smaller increments in degradation with further loading up to 150 MPa.

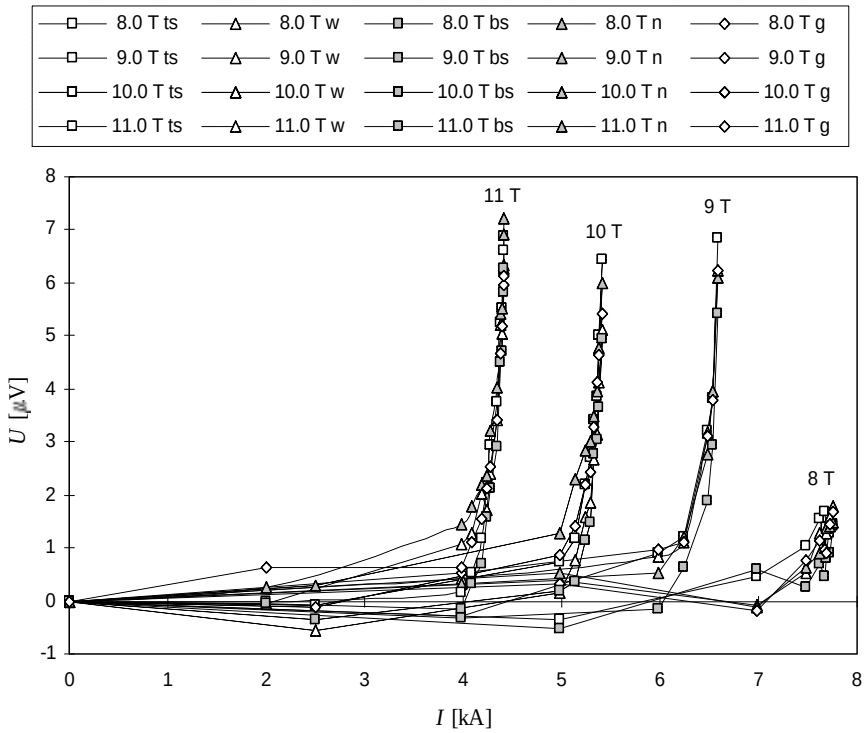

Figure 5.15 U(I)-curves of sample IG1 at 5 MPa, with the background field B ranging from 8 T to 11 T. The voltage tap locations are labeled ts (top straight), w (wide edge), bs (bottom straight), n (narrow edge) and g (global contact).

This behavior is indicative of either a dry (non-impregnated) cable, or an incorrectly mounted cable. Either situation causes large stress concentrations, with a resulting immediate onset of the reversible and permanent degradation.

Note that such condition, local bad impregnation or bad support can also appear in a real magnet. This is a good illustration of the sensitivity of Nb_3Sn. Figure 5.17 shows the sequence of the measured data and figure 5.18 shows the resulting critical current degradation curves.

The reversible critical current degradation immediately jumps to about 25 % at 50 MPa, with a permanent degradation of 12 % with respect to $I_c(0)$. Further increase in the transverse pressure increases the reversible degradation to about 35 % at 150 MPa and the permanent degradation to 18 % at 150 MPa. The slope of the curve decreases with increasing pressure.

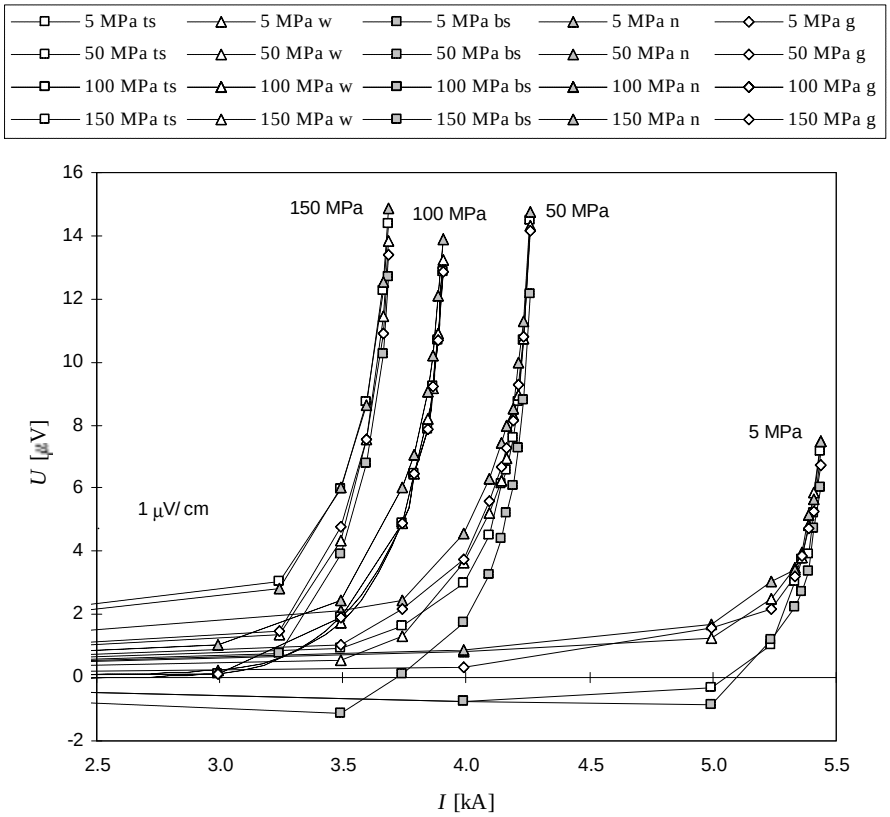

Figure 5.16 U(I)-curves for sample IG1 at 10 T, with increasing transverse pressure P.

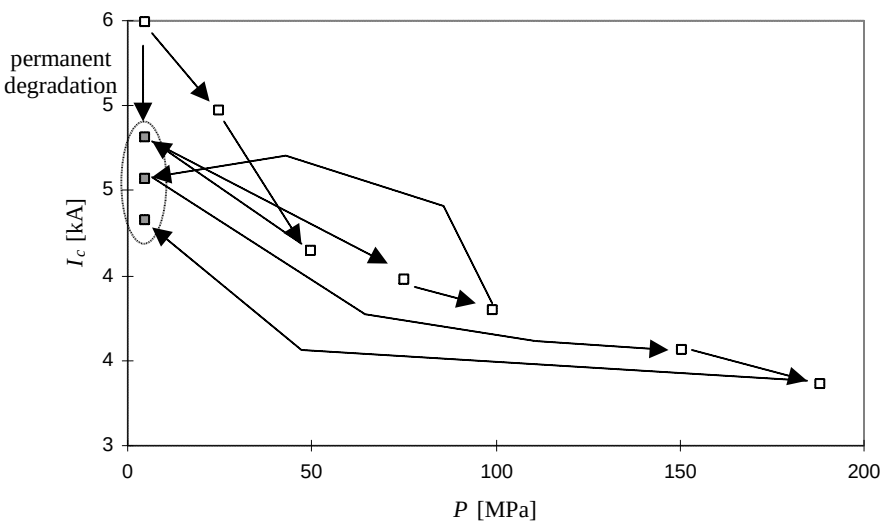

Figure 5.17 Resulting $I_c(P)$ curve for sample IG1, at 11 T, 4.2 K.

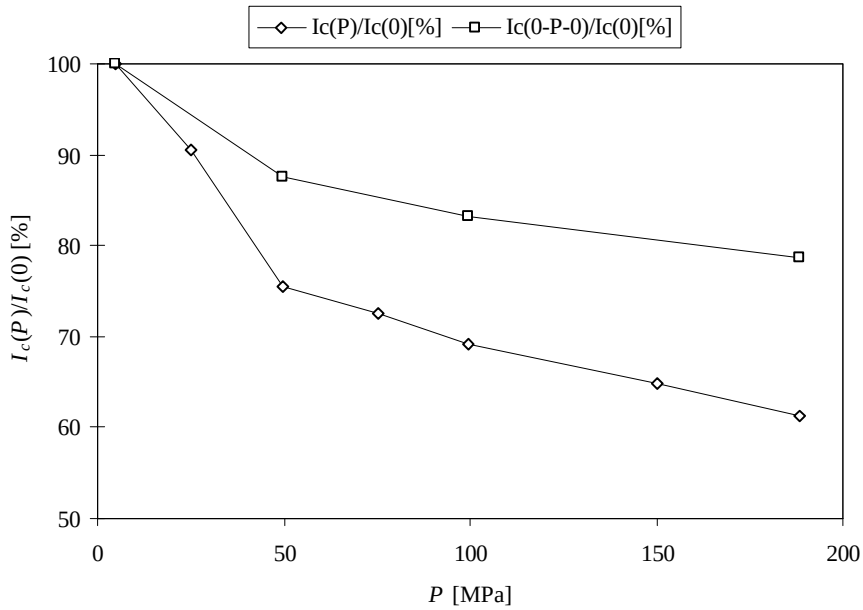

Figure 5.18 Resulting $I_c(P)$ curve for sample IG1, at 11 T, 4.2 K.

The difference in behavior with respect to a well impregnated and correctly mounted sample (see figure 5.14) is incorporated in the critical current degradation model by using two different FEA models for the computation of the plastic deformation as a function of the applied transverse pressure.

The model correlation with the measured data is discussed in section 5.12. Table 5.10 lists the critical current degradation data for the IT conductors. Sample IG10 was most likely damaged during installation.

Sample ID	*extracted strand initial degradation* $I_{c,extr}/I_{c,m}$ [%]	*virgin strand initial degradation* $I_c(0)/I_{c,m}$ [%]	*cable total degradation* $I_c(150)/I_{c,m}$ [%]	*cable permanent degradation* $I_c(0\text{-}150\text{-}0)/I_{c,m}$ [%]
IG1	-	57	37	46
IG3	-	66	5	17
IG4	-	70	59	70
IG6	90	-	-	-
IG7	95	-	-	-
IG8	68	-	-	-
IG10	43	-	-	-

Table 5.10 Critical current degradation data for the IT conductors.

Also, results on cable samples are obtained for two cables made from an LMI Internal Tin conductor. Two samples are tested, the first one is a rectangular cable, the second a keystoned cable with a keystone angle of 1.15°. Both cables perform very well, with only a slight degradation under pressure, and hardly any permanent damage.

The good performance is attributed to the well chosen compaction parameters of the cable. Table 5.11 lists the cable parameters for the LMI samples, and table 5.12 lists the measured critical current degradation.

ID	g_{tm}	g_{wm}	s_t	s_w	g_{wr}	a	C_p	$C_{x,edge}$	C_x	C_{y1}	C_{y2}
LM1						0.00	85.6	101.9	96.8	89.1	89.1
LM2						1.15	85.6	101.9	96.8	80.9	97.2

Table 5.11 Cable parameters for the LMI conductors.

Sample ID	$I_{c,extr}/I_{c,m}$ [%]	$I_c(0)/I_{c,m}$ [%]	$I_c(150)/I_c(0)$ [%]	$I_c(0\text{-}150\text{-}0)/I_c(0)$ [%]
LM1	-	-	96	99
LM2	-	-	91	98

Table 5.12 Critical current degradation data for the LMI conductors.

5.5.3 PIT conductor

Data for the PIT conductors are obtained from literature and internal reports of the UT. Critical current test data as a function of applied pressure are available for samples EC1, EC3, EC4, EC5, EC7, EC9 and EC10. Sample EC8 is too wide for the cable test facility. Samples EC7 and EC8 are cabled at the LBNL facility, therefore cabling data are available. The cable parameters are given in table 5.13.

Critical current degradation data is given in table 5.14. $I_c(P)$ curves and *U(I)*-curves are found in the literature [5.4, 5.5]. Sample EC10 might be damaged, no further explanation is available.

ID	g_{tm}	g_{wm}	s_t	s_w	g_{wr}	a	C_p	$C_{x,edge}$	C_x	C_{y1}	C_{y2}
EC1						0.00	89.7	107.3	98.6	92.0	92.0
EC3						0.00	89.7	107.3	98.6	92.0	92.0
EC4						0.00	89.7	107.3	98.6	92.0	92.0
EC5						0.00	89.7	107.3	98.6	92.0	92.0
EC6						1.25	87.5	137.4	100.5	82.8	100.4
EC7	2.45	1.07	0.41	0.55	1.0016	1.36	88.7	140.6	101.9	82.3	101.4
EC8	2.45	1.07	0.42	1.05	0.9454	1.27	87.9	138.2	101.1	82.7	100.5
EC9						1.29	88.4	130.5	100.1	83.2	101.1
EC10						1.10	92.7	117.8	98.9	88.1	104.3

Table 5.13 Cable parameters for the PIT conductors.

The critical current degradation under transverse pressure was measured on an LHC type cable for loads up to 200 MPa. The reduction in I_c from $I_c(0)$ is of the order of 5-8 % for a pressure of 150 MPa, and shows full reversibility after the cable pressure is released [5.6].

Sample ID	*extracted strand initial degradation* $I_{c,extr}/I_{c,m}$ [%]	*virgin strand initial degradation* $I_c(0)/I_{c,m}$ [%]	*cable total degradation* $I_c(150)/I_{c,m}$ [%]	*cable permanent degradation* $I_c(0\text{-}150\text{-}0)/I_{c,m}$ [%]
EC1	-	94	66	75
EC3	-	79	59	77
EC4	-	72	67	70
EC5	-	60	57	59
EC7	-	65	63	65
EC9	-	84	82	84
EC10	-	39	12	-

Table 5.14 Critical current degradation data for the PIT conductors.

5.6 Correlation between the cable test results and the cable parameters

The goal of this investigation is to determine which cable parameters are of influence on the initial cable degradation and on the sensitivity to transverse pressure. The initial cable degradation, reversible degradation under pressure and permanent degradation after release of the pressure are investigated as a function of the parameters listed in section 5.2. The parameters are grouped by type, as follows:

A) Dimensional and wire parameters:
- d, the cable strand diameter;
- t_{ave}, the average cable thickness;
- w, the cable width;
- a, the cable keystone angle;
- j, the cable pitch angle;
- wire Cu/SC ratio;
- copper matrix and jacket hardness;

B) Cabling machine ratios and constraints:
- g_{tm}, the ratio of the average cable thickness to the mandrel thickness;
- g_{wm}, the ratio of the width of the cable to the mandrel width;
- g_{wr}, the ratio of the width of the cable to the roller width;
- s_t, the free space between the mandrel tip and the rollers (vertical);
- s_w, the free space between the mandrel tip and the rollers (horizontal);

C) Compaction factors:
- C_p, the cable volume compaction factor;
- $C_{x,edge}$, the compaction in the x-direction for the four corner strands on both sides;
- C_x, the compaction in the x-direction for the entire cable;
- C_{y1}, the compaction in the y-direction for the four strands at the minor side edge;
- C_{y2}, the compaction in the y-direction for the four strands at the major side edge.

The following sections describe the influence of each parameter grouped by the three degradation types. The initial cable degradation is described first, followed by total and permanent I_c degradation. Where there is not enough information available to test a correlation, the parameter is omitted.

For the initial cable degradation, also the data for the extracted strands is investigated. The extracted strand data is labeled with "Ex" behind the conductor type. Cable degradation is called excessive if the value is below 0.9 (90 %).

The correlation coefficient r_c for n samples of data-sets x and y is defined as the covariance of x and y divided by the square root of the product of the variances $s^2_{x,y}$ of x and y as in

$$r_c = \frac{\sum_{i=1}^{n} (x_i - \bar{x})(y_i - \bar{y})}{(n-1)\left(s_x^2 s_y^2\right)^{1/2}}, \tag{5.14}$$

with $\bar{x}$ and $\bar{y}$ the means, and s_x and s_y the standard deviations of the data-sets x and y [5.12].

The correlation coefficients between the three types of cable degradation (y) and the cable parameter (x) are given for each investigated parameter. A correlation of 0 means the degradation cannot be described as a linear function of the parameter. The square of the correlation coefficient r_c indicates how many of the datapoints can be described by a linear relation (normalized to the total number of datapoints).

In later sections, the ratio of the random variation to the physical variation, when subtracted from 1.0, is used to describe how well a fitted quadratic or cubic function fits to the data. This ratio is usually expressed as the R^2 value, which is simply the square of the correlation coefficient of the random variation to the physical variation, or fitted function.

The value marked P(invalid) indicates the probability that the data is not correlated, or the so-called *confidence value* of the test [5.13]. This value is generally used to indicate whether one can say with a 95% certainty whether the data is linearly correlated ($P<0.05$). For most tests, the correlation confidence value is greater than 0.05 due to a lack of datapoints. This means, that in most cases, a trend is visible in a plot of the data, but a statistical confirmation of this trend is not possible with sufficient confidence.

In some cases, intelligent sorting of the datapoints greatly improves the confidence of the statistical correlation. Due to duplicate results for similar or identical cable samples, and tests that were repeated for clear reasons of improper experimental procedure, the datapoints are weighed incorrectly. By elimination of duplicate datapoints of which one is clearly low, the fit of the correlation can be improved.

At the end of each section, the expected behavior of the correlation is discussed, then the raw data is sorted, and correlated after sorting for those parameters where a trend is suspected. The data used for the new correlation is the best measured result of all tests. These “best” points are selected from the entire set of data by grouping them along the variable on the x-axis, and then selecting only the samples that show the lowest degradation within that group. The number of divisions is dependent on the number of datapoints available, but generally about 5-6 points are selected. This selection process emphasizes the best samples within the data, thus eliminating bad or dubious datapoints that might not reflect the maximum critical current the particular cable is capable of carrying.

It has to be emphasized here that the limited set of measurements is by no means complete, and in most cases not even conclusive. Also, in most cases, statistical verification of hypotheses can not be satisfactory proven due to a lack of valid datapoints. Nevertheless, the results are published here in full because this is the first time an extensive systematic comparison of the different conductor types is made with respect to the three types of critical current degradation.

5.7 Initial cable degradation

The initial cable degradation $I_c(0)/I_{c,m}$ is investigated as a function of the various cable parameters. $I_c(0)/I_{c,m}$ is calculated from the manufacturers data whenever known, or from the highest measured I_c in the virgin strand at the same temperature and background magnetic field. The highest measured I_c is chosen in order to eliminate the possible effect of bad sample preparation. This in no way guarantees that the measurement represents the best possible I_c, but at least yields the highest I_c for the limited number of samples available. In case no correlation or optimal value is found at all, the parameter is omitted.

5.7.1 Dimensional parameters

The dimensional parameters of the cable are investigated with respect to the initial cable degradation. Intuitively, correlations are expected for the cable strand diameter, which is indirectly related to the cable width and thickness, and the cable keystone angle. In general, the smaller strands degrade worse under pressure, but this might be due to sample mishandling.

The cable keystone angle is generally thought to influence the cable degradation directly. It is in fact incorrect to use the keystone angle for the correlation, as is explained below. The cable minor edge

compaction yields a more accurate representation of the cabling damage due to excessive compaction of the cable minor edge versus the major edge.

Cable strand diameter d

Here the correlation between the initial cable degradation and the strand diameter d is investigated.

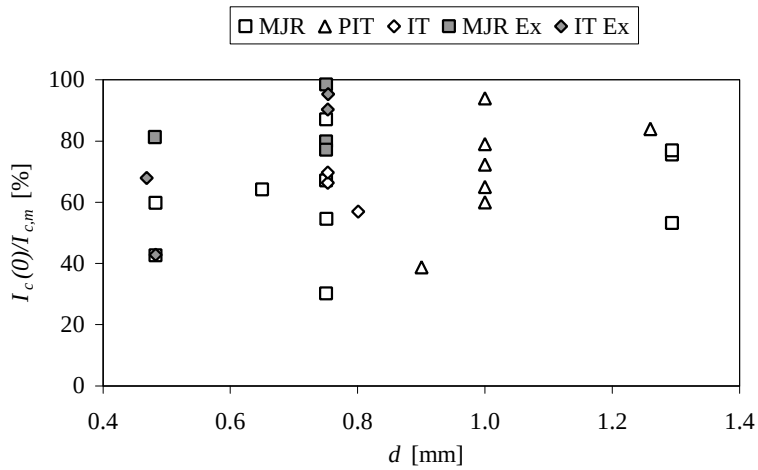

Figure 5.19 Initial cable degradation as a function of the strand diameter for all cable samples (white labels MJR, PIT and IT) and extracted strands (gray labels MJR Ex and IT Ex).

Figure 5.19 shows the initial cable degradation as a function of the strand diameter. Although a linear fit of the data would show an increase in cable damage with decreasing strand diameter, the scatter in the data is too large to conclude that smaller strands are more easily damaged. Table 5.15 lists the correlation coefficient for each wire type.

	All	MJR Cable	IT Cable	PIT Cable	MJR Ex	IT Ex
Correlation coefficient	0.39	0.35	-0.97	0.56	0.20	0.89
P (invalid)	0.09	0.32	0.17	0.19	0.80	0.11

Table 5.15 Correlation between the initial cable degradation and the cable strand diameter.

The correlation coefficient of the initial cable degradation with the strand diameter for all cables is 0.394, with a confidence of 0.086>0.05, hence the hypothesis that the data is correlated can be rejected.

Cable width w

Figure 5.20 shows the correlation between the initial cable degradation and the cable width *w*. The correlation coefficients are listed in table 5.16.

	All	MJR Cable	IT Cable	PIT Cable	MJR Ex	IT Ex
Correlation coefficient	**0.48**	0.39	0.97	0.59	0.20	0.89
P (invalid)	**0.03**	0.27	0.17	0.16	0.80	0.11

Table 5.16 Correlation between the initial cable degradation and the cable width w.

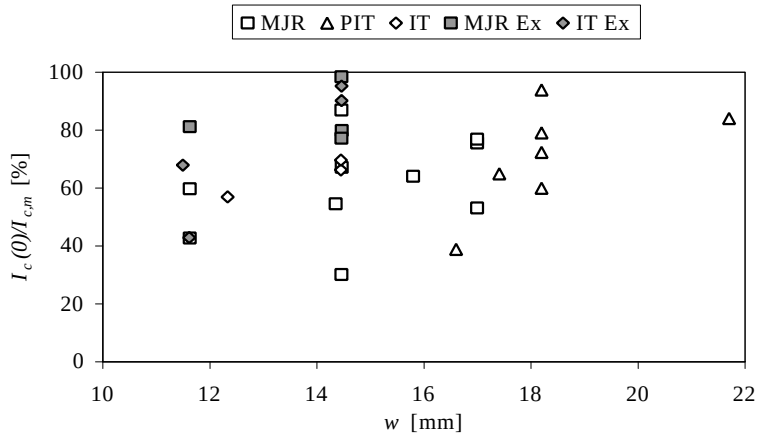

Figure 5.20 Initial cable degradation as a function of the cable width w.

Here, a statistically significant positive correlation between the initial cable degradation and the cable width is found for all cables grouped together, but not for each individual type of cable (not enough samples). The initial cable degradation increases with the cable width according to $I_c(0)/I_{c,m} = 3.1\ w$ [mm] + 16.2 [%]. The correlation is very weak though, a coefficient of 0.48 means that only 23 % of the data is described by this line.

***Cable keystone angle** a*

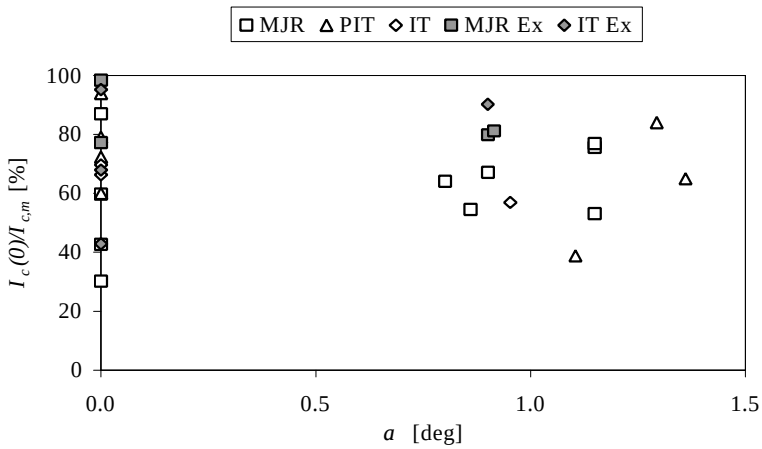

Figure 5.21 Initial cable degradation as a function of the keystone angle a.

The keystone angle is often looked at when discussing cable degradation. However, using the keystone angle solely as a parameter with respect to $I_c/I_c(0)$ is not useful, as shown in figure 5.21. Although a negative trend is visible, no statistically significant correlation is found between the initial cable degradation and keystone angle. While there is a clear increase in critical current with increasing keystone angle, there are even more datapoints at zero degree keystone angle with larger degradation. This is due to the fact that one can design a keystoned cable in which the strands are loosely packed by simply increasing the thin edge thickness to a safe value while increasing the angle. Thus the keystone angle can not be used to predict initial cable degradation.

Copper matrix and jacket hardness

The hardness of the copper in the wire is also investigated for some wires. Only a few data points are available, with Vickers hardness H_v ranging from 87 for wires that went through a 210 °C heat treatment, to 115 for unheated work-hardened material. Two PIT cables however are made of strands that are annealed before cabling. Both cables show a fairly high initial cable degradation of 35 to 40 %. Also, the wire fails a sharp bend test performed before cabling is commenced. This means that a low hardness value of the copper in the wire tends to increase initial cable degradation, though no quantitative numbers are available.

The increased cable damage done in cabling strands with soft copper can be understood when one looks at the final strain state of the composite. With a harder copper matrix and jacket, the strain in the strands due to the cabling operation is partially supported by the copper. When the copper is softened before cabling, the niobium or tantalum diffusion barriers and filaments will be strained more, possibly damaging the internal structure of the filament bundles.

No correlations are found for the following parameters:

1) average cable thickness t_{ave};
2) cable pitch angle j ;
3) wire Cu/SC ratio.

5.7.2 Cabling machine ratios and constraints

This section discusses the correlation between the cabling machine ratios and constraints and the initial cable degradation. For most of the parameters, a linear relation cannot be found, but there seems to be optimal values that can be found by fitting a quadratic or cubic relation to the best datapoints.

Wherever such an optimum is evident, a curve-fit is made to find this optimum.

At LBNL, the selection of the optimal settings of the cabling machine ratios and constraints has always been somewhat of a "black art". The machine operator will initially select a set of parameters to produce the desired cable based on experience. These settings are then fine-tuned over the initial leader length (about 30 m), based on the "look and feel" of the cable.

Based on this experience, optimal settings are expected to be found for the ratios of cable to mandrel thickness and width g_{tm} and g_{wm}, and for the ratio of the cable width to the roller width g_{wr}. The actual values of these optimal settings were not available before the data was sorted and investigated in detail.

The ratio of the average cable thickness to the mandrel thickness g_{tm}

No linear correlation is found. However, an optimum exists at g_{tm} = 2.43, as shown in figure 5.22.

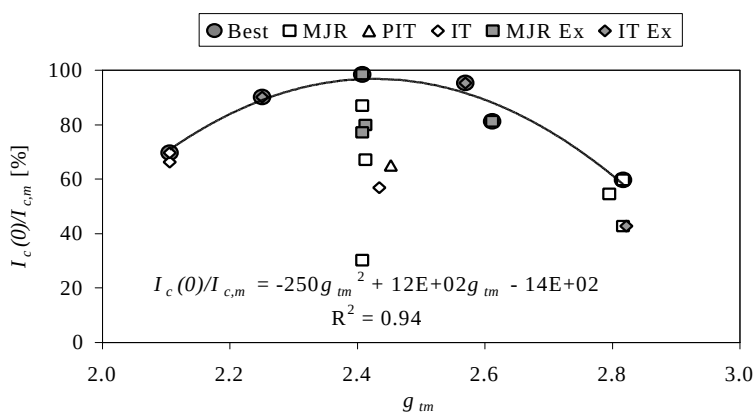

Figure 5.22 The initial cable degradation as a function of the ratio of the average cable thickness to the mandrel thickness g_{tm}.

The curve fitted through the highest datapoints in each group along the horizontal axis is shown in the figure. This fit is made under the assumption that the highest critical current measured is the most representative sample to use.

The ratio of the width of the cable to the mandrel width g_{wm}

In figure 5.23, the initial cable degradation as a function of the ratio of the width of the cable to the mandrel width g_{wm} is shown. An optimum exists for $g_{wm} = 1.06$.

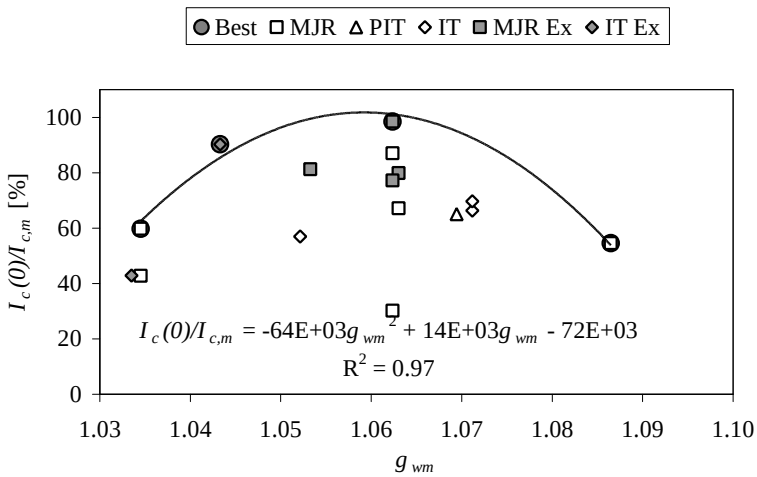

Figure 5.23 The initial cable degradation as a function of the ratio of the width of the cable to the mandrel width g_{wm}.

The ratio of the width of the cable to the roller width g_{wr}

Figure 5.24 shows the relation of g_{wr} to the initial cable degradation.

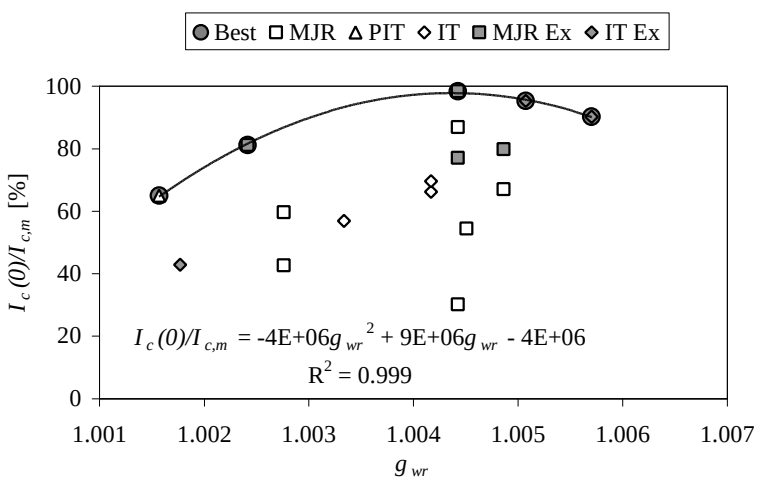

Figure 5.24 The initial cable degradation as a function of the ratio of the width of the cable to the roller width g_{wr}.

The width of the rollers in the powered Turk's head of the cabling machine may be a relevant parameter with regard to the initial cable damage. Generally, the rollers are dimensioned slightly undersize with respect to the desired cable width to accommodate for the elastic spring-back of the strands after they pass through the Turk's head. The initial cable degradation decreases with a decreasing roller width, with the lowest degradation found for a roller undersize of 0.45 %, at g_{wr} = 1.0045. No data points are available for smaller ratios, thus it can not be concluded that this is an optimum value.

The free space between the mandrel tip and the rollers (vertical) s_t

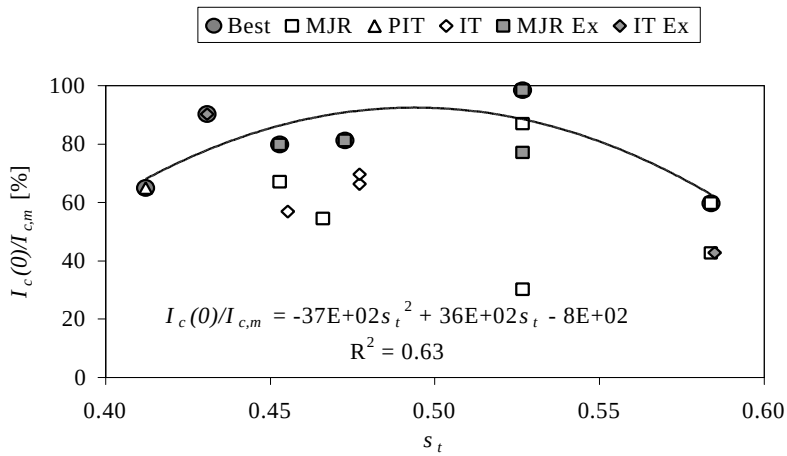

Figure 5.25 The initial cable degradation as a function of free space between the mandrel tip and the rollers (vertical) s_t.

Figure 5.25 shows the relation between the initial cable degradation and the free space between the mandrel tip and the rollers in the vertical direction s_t. An optimum is found at s_t = 0.49, with a low R^2.

The free space between the mandrel tip and the rollers (horizontal) s_w

In figure 5.26, the correlation between the initial cable degradation and the free space between the mandrel tip and the rollers in the horizontal direction s_w is shown.

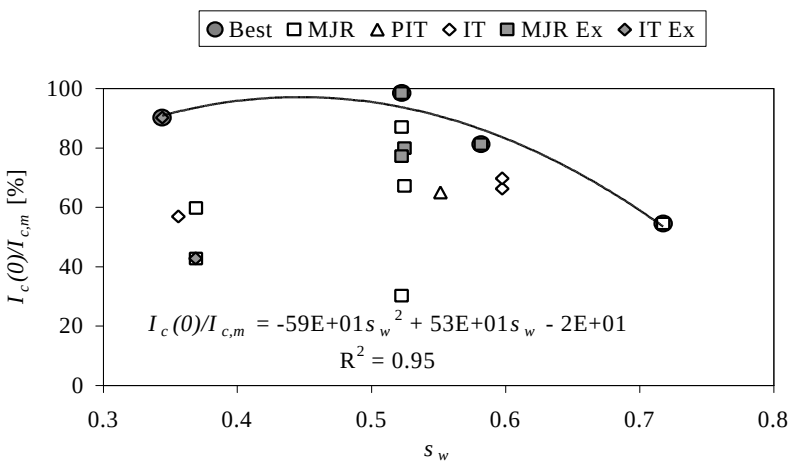

Figure 5.26 The initial cable degradation as a function of the free space between the mandrel tip and the rollers (horizontal) s_w.

An optimum is found for s_w between 0.4 and 0.5. A quadratic fit through the best data shows an optimum at $s_w = 0.45$.

5.7.3 Compaction factors

This section describes the relation between the initial cable degradation and the various compaction factors defined in section 5.2. For each compaction factor, the initial cable degradation is shown in graphs for all three conductor types. The goal of this exercise is to find whether all three conductor types show the same behavior when compacted.

For each of the defined compaction factors, optimum values are expected that minimize the amount of initial critical current degradation. The thought behind this hypothesis is that if a strand in a cable is compressed (and thus deformed) during the cabling operation, this will cause initial I_c degradation due to damage done to the filament structure.

The more severe the deformation, which is the equivalent of more compaction or a lower compaction factor, the more damage is done.

Conversely, if a cable is made in which strands are very loose, the damage to the strands due to the cabling operation itself will be minimal, but when a sample of this cable is then tested, the displacement of the loose strands will be much larger than in a slightly compacted cable, causing excessive strain in the filaments. This in turn will cause the initial I_c degradation to increase with increasing looseness, or larger compaction factor.

The range of the compaction factors only shows this effect for the horizontal compaction factor for the entire cable C_x, since this is the only compaction factor that is typically allowed to be high. In practical cables, allowing the volume compaction factor to be high will cause a cable that is mechanically unstable.

The cable volume compaction factor C_p

The graph of the initial critical current degradation versus the volume compaction factor in figure 5.27 shows how a smaller compaction decreases the $I_c(0)/I_{c,m}$ for the MJR and IT conductors. The decrease starts below about 90 % compaction, and the upper limit decreases almost linearly with a slope of 5-7 % per percent of decreased volume compaction. This means that cable volume compaction should be at least 90 % to minimize initial cable degradation. Table 5.17 lists the correlation coefficients for all conductor types.

	All	MJR Cable	IT Cable	PIT Cable	MJR Ex	IT Ex
Correlation coefficient	0.14	-0.09	0.97	-0.71	-0.32	0.90
P (invalid)	0.51	0.80	0.17	0.07	0.68	0.10
Sorted	**0.99**	**1.00**	0.95	1.00	-	-
P (invalid)	**0.00**	**0.00**	0.21	-	-	-

Table 5.17 Correlation between the initial cable degradation and the cable volume compaction factor C_p for all conductor types. There are only two datapoints available for the PIT conductor, thus the P (invalid) cannot be computed.

Sorting the degradation data by compaction factor C_p, and selecting only the best samples over a limited range, yields a more evident correlation. Linear and quadratic fits through the resulting datapoints are listed in table 5.18.

Table 5.18 shows that for all cable samples, the initial cable degradation increases with decreasing volume compaction (more deformation). The onset of significant initial cable degradation ($I_c / I_c (0) < 90\%$) lies around a volume compaction factor C_p of about 88 % for all conductors, 90 % for the MJR conductors and 89 % for the IT and PIT conductors.

Thus, for all conductors, the initial cable degradation can be limited to about 90 %, when the volume compaction factor is larger than about 90 %.

Figure 5.27 shows the resulting quadratic fit to the best values measured for the initial cable degradation as a function of the volume compaction factor C_p.

	All		MJR Cable		IT Cable		PIT Cable	
$I_c/I_c(0) = a\,C_p^2 + b\,C_p + c$	Linear	Quad	Linear	Quad	Linear	Quad	Linear	Quad
a	0	-0.3	0	-0.2	0	-	0	-
b	5	59	5.6	33	1.4	-	7.6	-
c	$-35\cdot10^1$	$-26\cdot10^2$	$-4\cdot10^2$	$-16\cdot10^2$	-30	-	$-6\cdot10^2$	-
R^2 [%]	97	99	100	100	89	-	100	-
C_p at $I_c/I_c(0)$=90%	90	87	89	91	89	-	89	

Table 5.18 Linear and quadratic fit coefficients for the best results of the initial cable degradation as a function of the cable volume compaction factor C_p. There is insufficient data for a quadratic fit through the IT and PIT data.

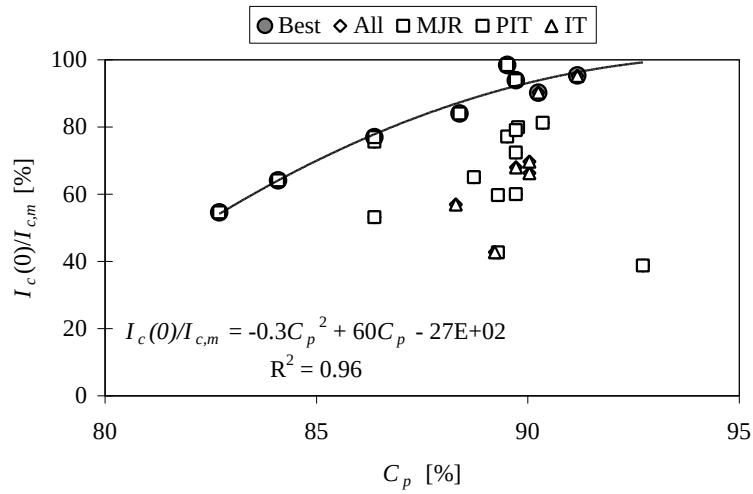

Figure 5.27 Initial cable degradation as a function of the volume compaction factor C_p. Shown is a quadratic fit through the best datapoints for all conductors.

The compaction in the x-direction for the four corner strands on both sides $C_{x,edge}$

The compaction in the edge strands only is calculated by subtracting the width occupied by the inner region strands at zero horizontal compaction from the total cable width, as given in equation (5.10). This parameter is relevant, because the compaction applied in the horizontal direction seems to be applied only to the strands located at the edge of the cable. Figure 5.28 shows a cubic fit through the best data obtained for all samples.

The relevance is evident from cross-section pictures taken from several of the MJR and IT cables, shown in figures 5.29a/b and 5.30, and is explained by the fact that horizontal compaction in the cabling machine is achieved by moving the horizontal rollers (determining the width) inwards. This causes a compressive force in the horizontal direction, which is counteracted by the friction of the vertical rollers and deformation of the strands.

Only part of the applied force in the horizontal direction is transmitted to the next strand inward, limiting the compaction to the outer strands only. Thus increasing the horizontal compaction will quickly result in too much compaction at the outer strands and significant initial cable damage.

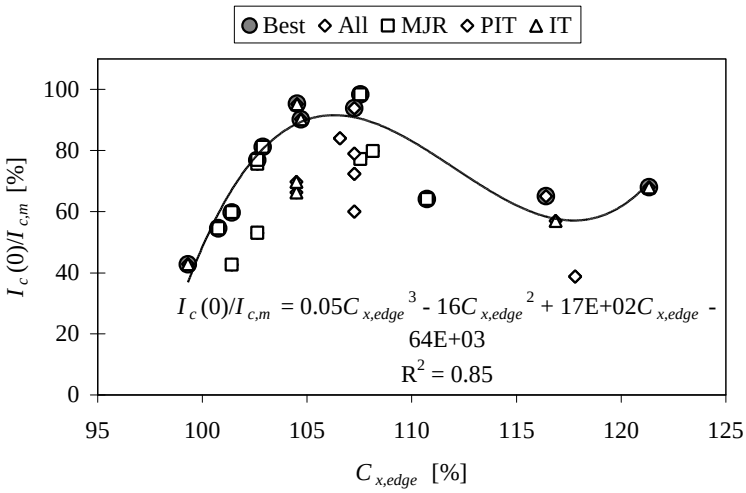

Figure 5.28 Initial cable degradation as a function of the horizontal edge compaction of the cable $C_{x,edge}$. The best fit for the region between 103 and 108 % compaction is the cubic curve shown.

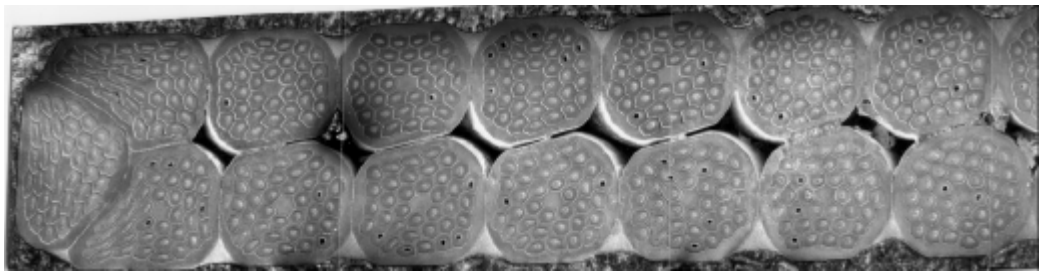

Top : cable T476 narrow edge Bottom : cable T476 wide edge

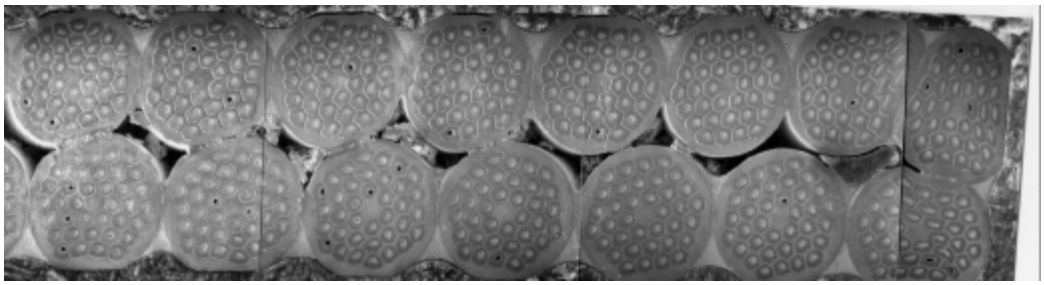

Figure 5.29a Cross-section of a sample of MJR cable (T476) illustrating the deformation at the edge.

The optimum value for compaction in the horizontal direction at the edge strands only is found at 106 %. Lower compaction values seem to increase the initial cable degradation. However, only a few data points are available in this range.

A possible explanation for an increase in cable damage with less compaction is that strands that are not well constrained during the cabling can move and thus are subjected to large strains. This can cause damage to the strands at the edge of the cable where the strain is already large when the strand is folded around the edge.

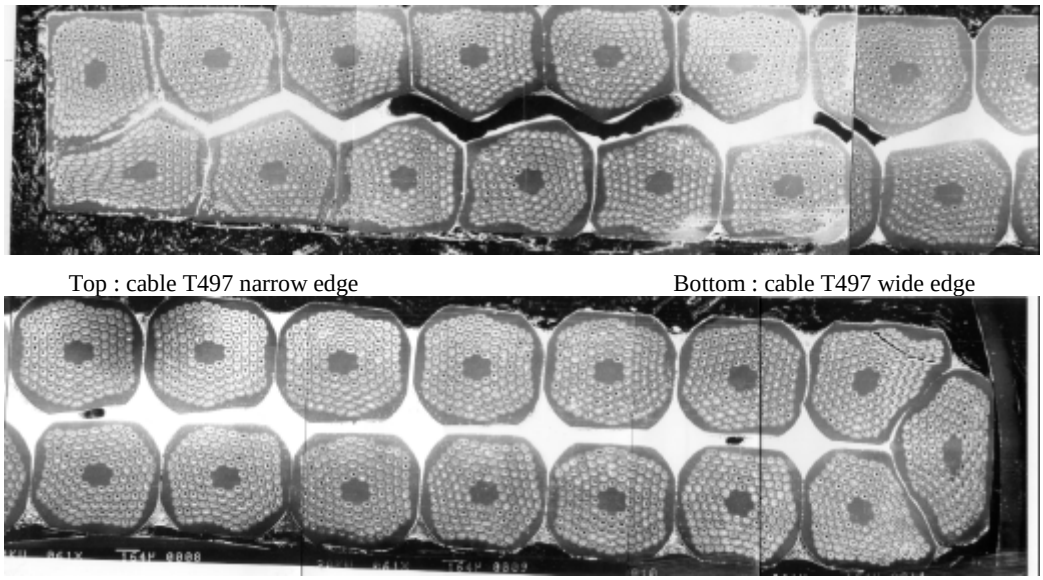

Figure 5.29b Cross-section of a sample of MJR cable(T497) illustrating the deformation at the edge.

Figures 5.29a/b show the cross-section of several MJR cable samples. Note that while the overall horizontal compaction is not significant, the strands near the edge of the cable are heavily deformed in cable T497. When determining cable dimensions, it is thus advisable to minimize the amount of horizontal compaction as much as possible.

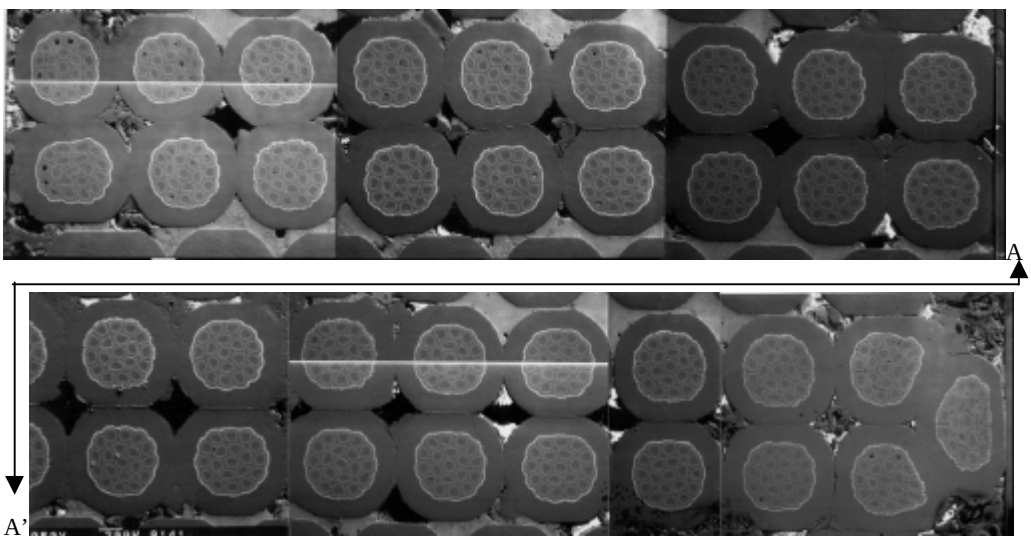

Figure 5.30 Cross-section of an IT cable sample (IG3).

Figure 5.30 shows the cross-section of the 37 strand IT cable I-523 (IG3). The figure contains photographs covering the entire cable from left to right. The figure is cut in two parts, the actual cable is continuous from A to A'; the strands near A' are partially cut off. Note the low distortion of the strands near the edge of the cable (top left and bottom right).

The compaction in the x-direction for the entire cable C_x

Figure 5.31 shows the initial cable degradation as a function of the horizontal cable compaction C_x, for the MJR, IT and PIT conductors. No statistically significant linear correlation is found. A quadratic fit through the best values is shown in the figure.

Only one data-point is available for a loose cable (C_x > 100%) at 102 %. With or without this point, there exists a fairly narrow optimal range for the horizontal compaction factor C_x. This concurs with the experience of the cable machine operator at LBNL; the horizontal compaction factor is always the one that requires the most precise fine-tuning to produce a cable that "feels" right. The quadratic fit through the best values for all conductor types shows an optimum horizontal cable compaction factor of C_x = 99 %, thus, a slight horizontal compaction is preferred.

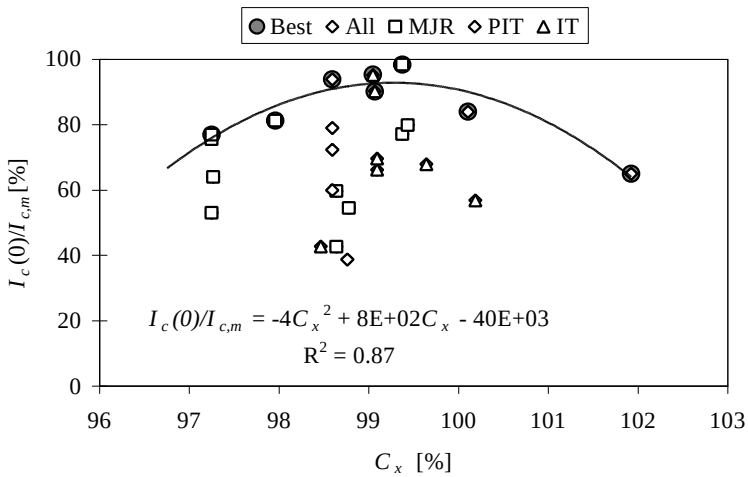

Figure 5.31 Initial cable degradation as a function of the horizontal cable compaction factor C_x.

The compaction in the y-direction for the four strands at the minor side edge $C_{y,1}$

Figure 5.32 shows the relation between the initial cable degradation and the compaction in the y-direction (vertical) for the four strands at the minor edge $C_{y,1}$.

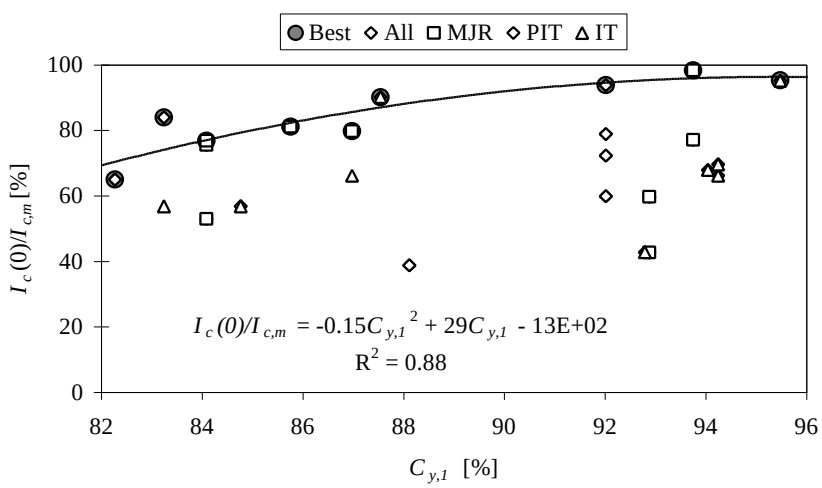

Figure 5.32 The initial cable degradation as a function of the compaction in the y-direction for the four strands at the minor side edge $C_{y,1}$ for all conductors.

Also shown is a quadratic fit through the best values of all conductors. The fit shows an optimum value for $C_{y,1}$ around 95 % compaction.

The compaction in the y-direction for the four strands at the major side edge $C_{y,2}$

Figure 5.33 shows the initial cable degradation as a function of the y-compaction at the major side edge $C_{y,2}$ for all conductors. Also shown is a quadratic fit through the best values for all conductors. An optimum value for the y-compaction is found at $C_{y,2}$ = 94 %.

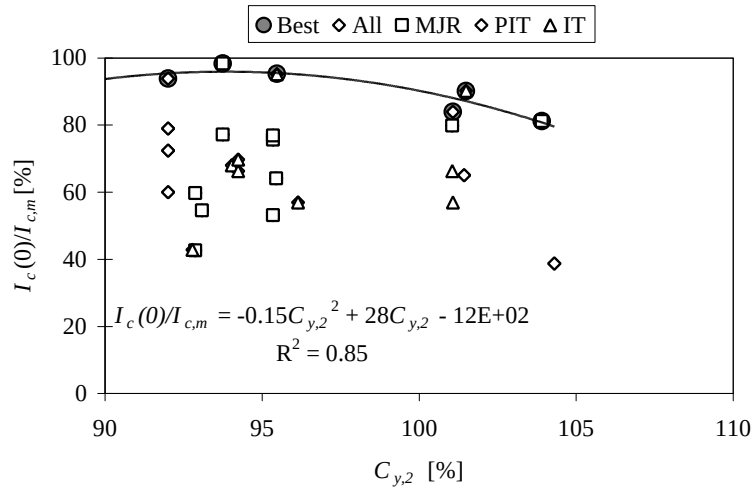

Figure 5.33 The initial cable degradation as a function of the compaction in the y-direction for the four strands at the major side edge $C_{y,2}$ for all conductors.

5.7.4 Summary for the initial cable degradation

Here, a summary of the optimum values found and the type of relation, for the initial critical current or cable degradation and the dimensional, cable and compaction parameters is given. In almost all cases, no linear relation is established, but a quadratic relation is used to describe the best measured values as a function of the parameters investigated. Tables 5.19a/b list whether a linear relation is found, and the optimum value when a curve-fit is used, for each investigated parameter.

Dimensional parameters	Linear correlation found (yes/weak/no) (Corr.coeff./P (invalid))	Optimum value of param. for best $I_c/I_c(0)$ or linear fit
d, the cable strand diameter	weak (0.394/0.086)	-
t_{ave}, the average cable thickness	weak (0.392/0.088)	-
w, the cable width	yes (0.482/0.032)	$I_c/I_c(0)$ = 3.1w + 16.2 [mm]
a, the cable keystone angle	no	-
j, the cable pitch angle	no	-
wire Cu/SC ratio	no	-

Table 5.19a Linear relations or optimum values found for the initial cable degradation as a function of the dimensional parameters.

Cabling ratios	Linear correlation found (yes/weak/no) (Corr.coeff./P (invalid))	Optimum value of param. for best $I_c/I_c(0)$ or linear fit
g_{tm}, the ratio of the average cable thickness to the mandrel thickness	no	2.43
g_{wm}, the ratio of the width of the cable to the mandrel width	no	1.06
g_{wr}, the ratio of the width of the cable to the roller width	no	1.0045
s_t, the free space between the mandrel tip and the rollers (vertical)	weak (-0.597/0.090)	0.49
s_w, the free space between the mandrel tip and the rollers (horizontal)	no	0.45
Compaction factors	Linear correlation found (yes/weak/no) (Corr.coeff./P (invalid))	Optimum value of param. for best $I_c/I_c(0)$ or linear fit
C_p, the cable volume compaction factor	yes (0.986/0.000)	$I_c/I_c(0) = 4.9\ C_p - 350$ [%] $C_p > 90$ % min.
$C_{x,edge}$, the compaction in the x-direction for the four corner strands on both sides	yes (PIT only) (-0.742/0.056)	106 %
C_x, the compaction in the x-direction for the entire cable	no	99 %
C_{y1}, the compaction in the y-direction for the four strands at the minor side edge	no	95 %
C_{y2}, the compaction in the y-direction for the four strands at the major side edge	no	94 %

Table 5.19b Linear relations or optimum values found for the initial cable degradation as a function of the cable and compaction parameters.

5.8 Reversible I_c degradation

This section describes the relation between the reversible I_c degradation and the various dimensional, cabling and compaction parameters. The results are grouped similarly to the previous section.

The reversible I_c degradation is defined here as the ratio of the critical current measured at 150 MPa applied pressure, divided by the initial critical current $I_c(0)$ at zero (or slightly compressive) load, and is indicated by $I_c(150)/I_c(0)$.

Most samples are measured up to at least 150 MPa compressive pressure and released to determine the permanent damage after loading. Whenever the sample degrades more than about 40 % at 100 MPa, the maximum pressure is limited to 100 or 125 MPa.

5.8.1 Dimensional parameters

The reversible critical current degradation is given as a function of the dimensional parameters. Wherever there is a linear correlation, the linear fit is given. If a quadratic relation is more appropriate, the optimum value for the parameter to minimize the reversible critical current degradation is given, together with the goodness of the fit (R^2).

No correlation is expected between any of the dimensional parameters and the reversible critical current degradation. The Cu/SC ratio is expected to be an influence, the higher the copper content, the lower the expected I_c degradation.

No correlation was found between the reversible I_c degradation as a function of the wire diameter d, the average cable thickness t_{ave}, and the keystone angle a. For increasing keystone angle, the spread of the datapoints increases, but the best values do not decrease with increasing keystone angle.

Also, no clear correlation is found for the reversible critical current degradation as a function of the cable pitch angle j.

Figure 5.34 shows the reversible critical current degradation as a function of the strand copper to superconductor ratio. Here, a slight increase in degradation with decreasing Cu/SC ratio is visible for the best values only. This can be due to the decrease in the protection given by the copper matrix and jacket around the filament area, as is shown in the FEA models in chapter 4.

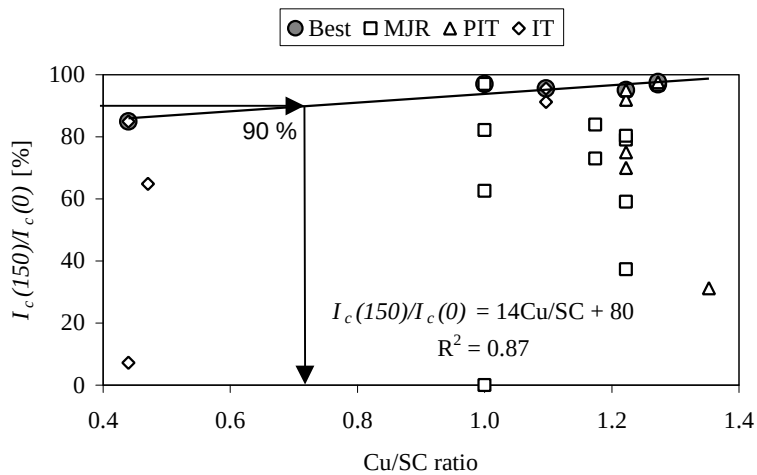

Figure 5.34 Reversible critical current degradation as a function of the cable copper to superconductor ratio Cu/SC.

A linear fit through the best datapoints for all conductors shows an increased degradation with decreasing Cu/SC ratio. An I_c degradation of 90 % ($I_c(150)/I_c(0)$ = 90 %) is reached at a Cu/SC ratio of 0.73. Cu/SC ratios lower than this value cause excessive reversible critical current degradation.

5.8.2 Cabling ratios and constraints

Here, the reversible critical current degradation is given as a function of the cabling ratios and constraints. If a quadratic relation is appropriate, the optimum value for the parameter to minimize the reversible critical current degradation is given, together with the goodness of the fit.

Similar to the initial critical current degradation, optimal values are expected for some of the cable machine ratios, based on the idea that a cable damaged during the cabling operation will be more sensitive to applied transverse pressure.

Figure 5.35 shows the reversible I_c degradation as a function of the cabling ratio g_{tm}. An optimum is found for g_{tm} = 2.45.

Figure 5.36 shows the reversible I_c degradation as a function of the cabling ratio g_{wm}. An optimum is found for g_{wm} = 1.055.

No clear correlation or optimum ratio is obtained for the reversible I_c degradation as a function of the cabling ratio g_{wr} and the cabling constraint s_t.

Figure 5.37 shows the reversible I_c degradation as a function of the cabling constraint s_w. Here, an optimum value is found for s_w = 0.50.

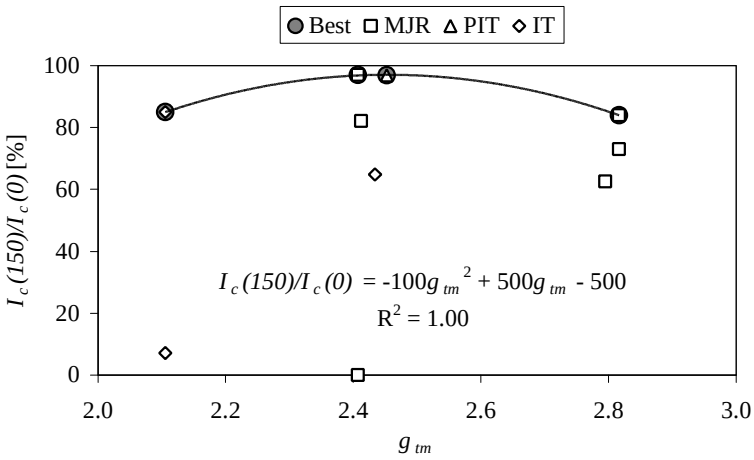

Figure 5.35 Reversible critical current degradation as a function of the cabling ratio g_{tm}.

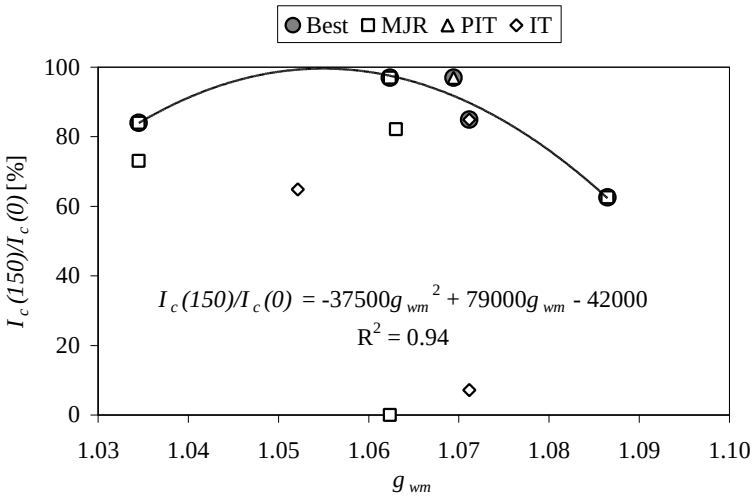

Figure 5.36 Reversible critical current degradation as a function of the cabling ratio g_{wm}.

5.8.3 Compaction factors

The reversible critical current degradation is given as a function of the dimensional parameters. Wherever there is a linear correlation, the linear fit is given. If a quadratic relation is more appropriate, the optimum value for the parameter to minimize the reversible critical current degradation is given, together with the goodness of the fit.

Optimal values are expected for each of the defined compaction factors. The correlation with the measured data will prove which compaction factors are useful in determining the optimal cable design.

Figures 5.38 through 5.40 show the reversible I_c degradation for all conductor types as a function of the volume compaction factor C_p. The degradation at three different applied transverse pressures is given at 50, 100 and 150 MPa.

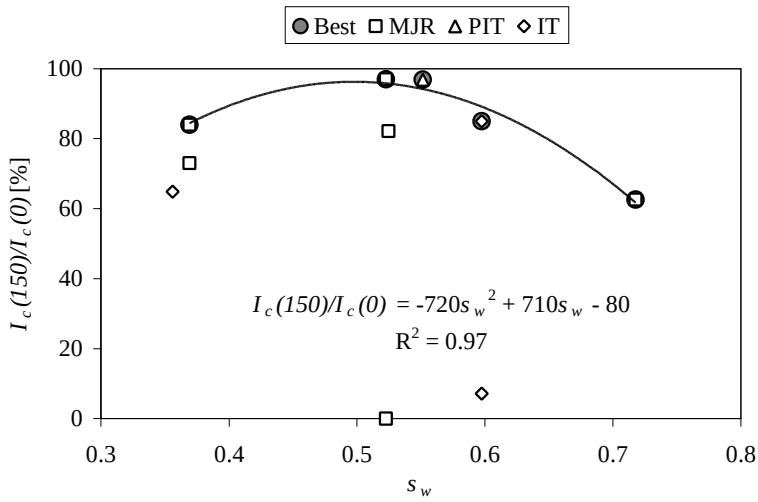

Figure 5.37 Reversible critical current degradation as a function of the cabling constraint s_w.

For all conductors, the spread in the I_c degradation decreases with decreasing compaction factor (more deformation). For the MJR and IT conductors, the onset of the reversible degradation occurs at about 86 % (MJR) and 90 % (IT) compaction.

For the PIT conductors, the sample with the smallest compaction tested is for C_p = 89 %, hence no similar drop is observed for decreasing compaction factor. Increasing the compaction factor for the PIT conductors also shows an increased degradation.

No datapoints with compaction factors larger than 92 % are available for the MJR and IT conductors.

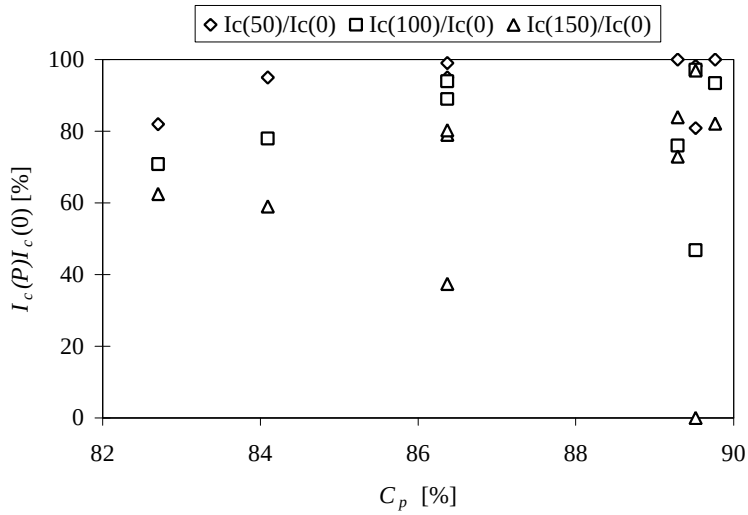

Figure 5.38 Influence of the compaction factor on the reversible degradation for the MJR conductors.

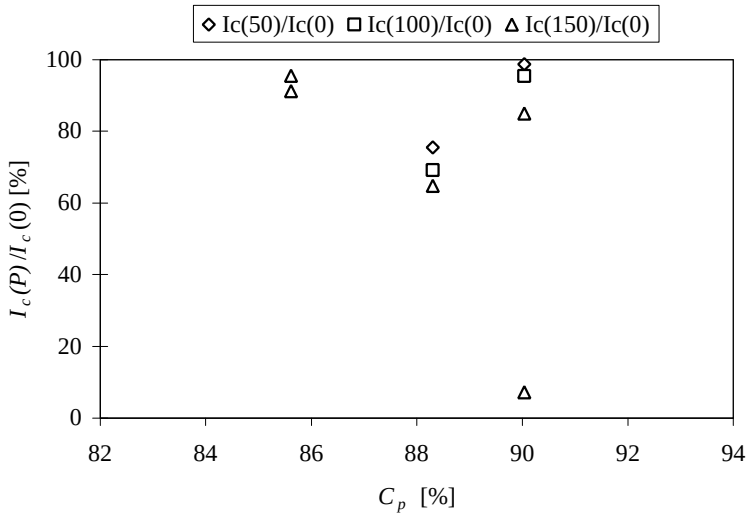

Figure 5.39 Influence of the compaction factor on the reversible degradation for the IT conductors.

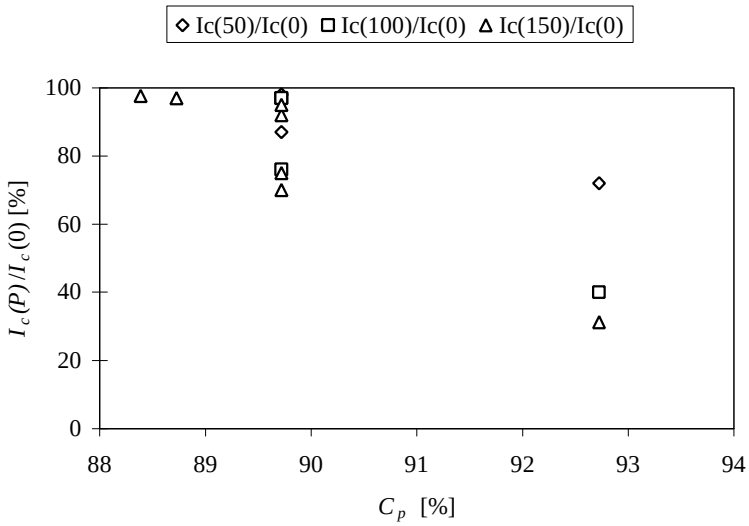

Figure 5.40 Influence of the compaction factor on the reversible degradation for the PIT conductors.

Figure 5.41 shows the reversible I_c degradation for all conductors as a function of the volume compaction factor C_p. There is a maximum in $I_c(150)/I_c(0)$ around 86-90 % volume compaction. The cubic fit through the best datapoints shows an optimum compaction factor around C_p = 88 %, also indicating that a range between 86-90 % is optimal.

The optimum range for the volume compaction is between 86 and 90 %. Increasing the compaction factor seems to result in more susceptibility to pressure, however, only one data point is available at C_p = 93 %. Below about 85 %, the $I_c(150)/I_c(0)$ also falls off rapidly.

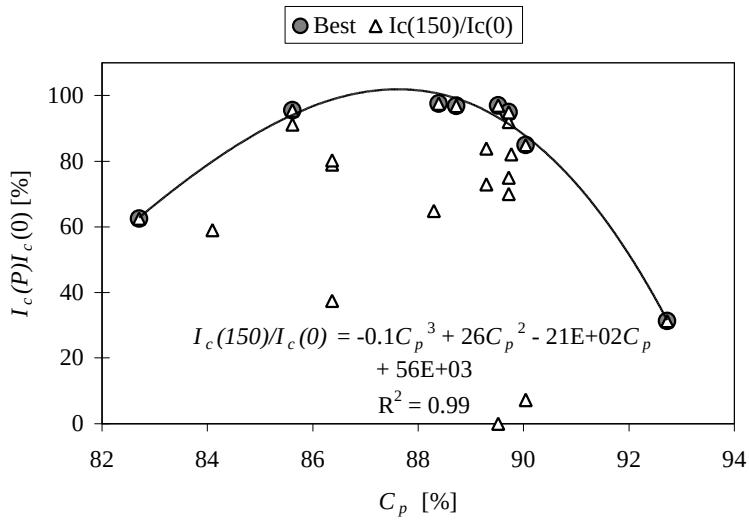

Figure 5.41 Reversible critical current degradation as a function of the volume compaction factor C_p. Shown are the datapoints for all cables at 150 MPa, and a cubic fit through the best results for all cables.

No clear correlation is found for the reversible I_c degradation as a function of the cable horizontal edge compaction $C_{x,edge}$. Also, no correlations are found for C_x, $C_{y,1}$ and $C_{y,2}$.

5.8.4 Summary for the reversible critical current degradation

The influence of the various dimensional, cabling, and compaction parameters on the reversible critical current degradation under transverse load is summarized. Table 5.20 lists the optimum values for the parameters, if any. If no linear correlation is found, and no optimum value either, the parameter is omitted.

Parameter	Linear correlation found (yes/weak/no)	Optimum value of parameter for best I_c (150)/I_c(0)
d, the cable strand diameter	weak	-
w, the cable width	weak	-
wire Cu/SC ratio	$I_c(150)/I_c(0) = 14$ Cu/SC + 80 (low R^2)	(90 % at 0.73)
g_{tm}, the ratio of the average cable thickness to the mandrel thickness	no	2.45
g_{wm}, the ratio of the width of the cable to the mandrel width	no	1.055
s_w, the free space between the mandrel tip and the rollers (horizontal)	no	0.50
C_p, the cable volume compaction factor	no	86-90 % (flat) C_p = 88 % (optimum)

Table 5.20 Optimum values for the various parameters with respect to the reversible critical current degradation.

5.9 Permanent I_c degradation

The relation between the irreversible (or permanent) critical current degradation and the various dimensional, cabling and compaction parameters, is analyzed. The permanent degradation $I_c(0\text{-}P\text{-}0)/I_c(0)$ is measured by increasing the transverse pressure to a given amount, measuring the critical current, then releasing the pressure.

The permanent degradation is given by the difference between I_c before this operation (given by the initial I_c degradation) and after. The values are measured at 50 MPa intervals, for 50, 100 and 150 MPa. The data are labeled $I_c(0\text{-}50\text{-}0)/I_c(0)$, $I_c(0\text{-}100\text{-}0)/I_c(0)$ and $I_c(0\text{-}150\text{-}0)/I_c(0)$. A summary of the influence of the various parameters on the permanent I_c degradation is given in section 5.9.4.

Since the permanent degradation shows almost the same behavior as the reversible degradation, the graphs for the parameters that show no influence on the I_c degradation are omitted.

5.9.1 Dimensional and wire parameters

No relation is found between the permanent critical current degradation and the following dimensional and wire parameters:

1) wire diameter d;
2) cable width w;
3) average cable thickness t_{ave};
4) keystone angle a;
5) cable pitch angle j;
6) wire Cu/SC ratio.

5.9.2 Cabling ratios and constraints

The permanent critical current degradation is given as a function of the cabling ratios and constraints. Similar optimal values for the cabling ratios and constraints are expected as compared to the reversible critical current degradation.

Figure 5.42 shows the permanent I_c degradation as a function of cabling ratio g_{tm}. Unlike the reversible degradation, no optimum is found here. The I_c degradation seems to increase for ratios larger than 2.45-2.5 however.

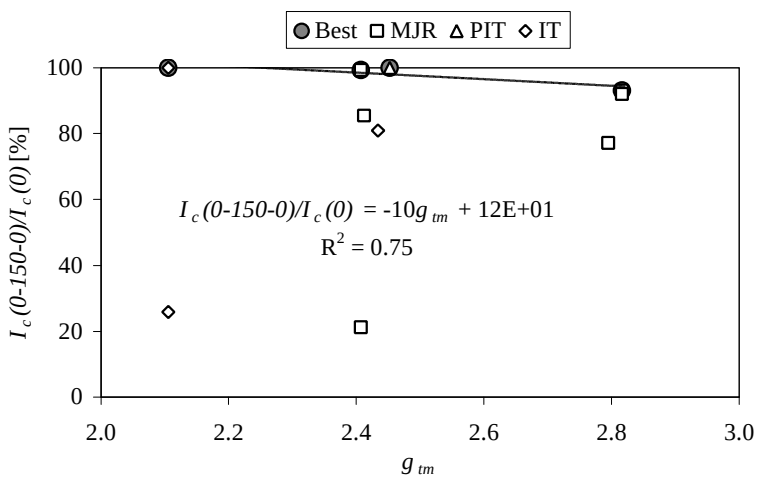

Figure 5.42 Permanent critical current degradation as a function of cabling ratio g_{tm}.

Figure 5.43 shows the permanent I_c degradation as a function of cabling ratio g_{wm}. No significant degradation is observed between about 1.035 and 1.07. An optimum is found at $g_{wm} = 1.055$ for a quadratic fit through the best datapoints.

No correlation is evident for the permanent critical current degradation as a function of the cabling ratio s_t. Figure 5.44 shows the permanent critical current degradation as a function of the cabling ratio s_w. Here, an optimum is found for $s_w = 0.52$.

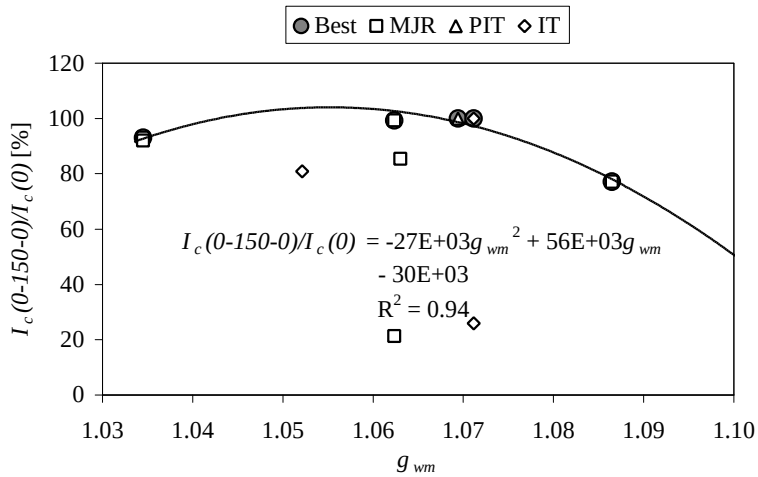

Figure 5.43 Permanent critical current degradation as a function of cabling ratio g_{wm}.

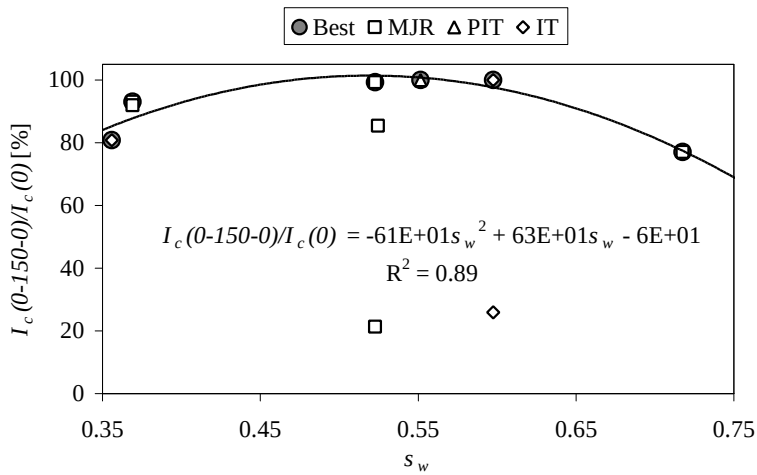

Figure 5.44 Permanent critical current degradation as a function of cabling ratio s_w.

5.9.3 Compaction factors

The permanent critical current degradation is given as a function of the compaction factors. Again, optimal values are expected to exist for the various compaction factors, similar to the relations for reversible critical current degradation. In addition to this, a larger spread is expected due to the influence of the internal filament design and voids on the permanent critical current degradation. This influence is expected to result in a larger spread of the data for a given compaction factor.

Figures 5.45 through 5.47 show the permanent I_c degradation as a function of the volume compaction factor C_p for the MJR, PIT and IT conductors. The graphs show the measured data for applied transverse pressures of 50 MPa, 100 MPa and 150 MPa when available.

For all three conductor types, the spread in the data increases for increasing compaction factor (looser strands within the cable).

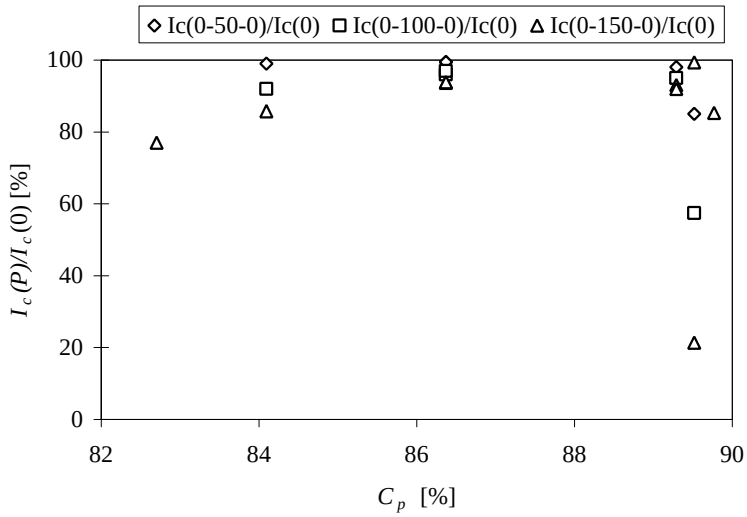

Figure 5.45 Permanent critical current degradation as a function of the compaction factor C_p for the MJR conductors.

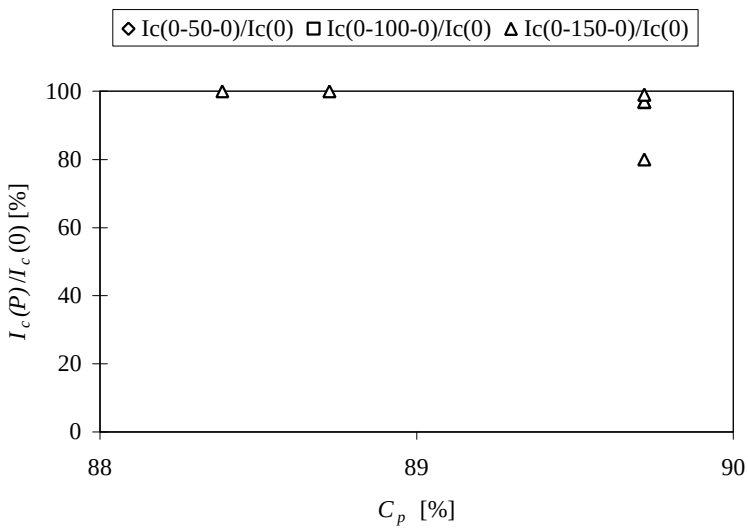

Figure 5.46 Permanent critical current degradation as a function of the compaction factor C_p for the PIT conductors.

In figure 5.45, a shift in the onset of the permanent damage with increasing compaction (decreasing compaction factor) is visible. For an applied pressure of 50 MPa, there is no measurable I_c degradation down to 84 % compaction. For 100 MPa, the I_c degradation is evident for compaction factors below about 86 %, whereas for 150 MPa, permanent damage starts below about 88 %. This value is close to the optimum C_p = 88 % for minimum reversible degradation.

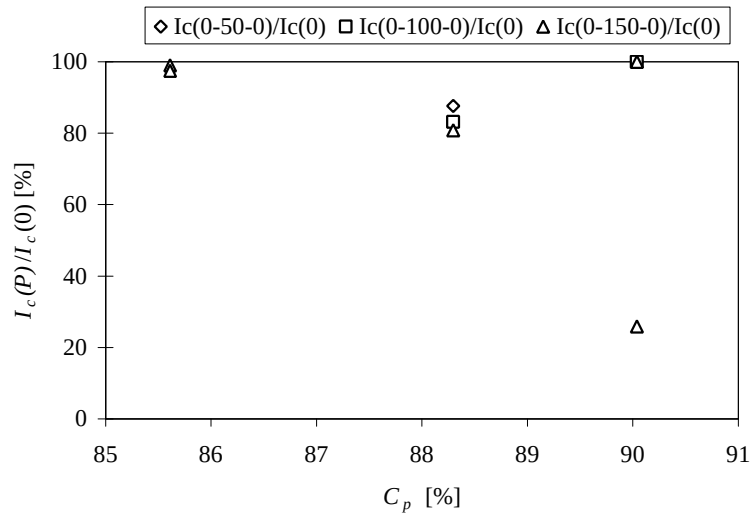

Figure 5.47 Permanent critical current degradation as a function of the compaction factor C_p for the IT conductors.

Figure 5.48 shows the permanent I_c degradation as a function of the volume compaction factor C_p for all conductors.

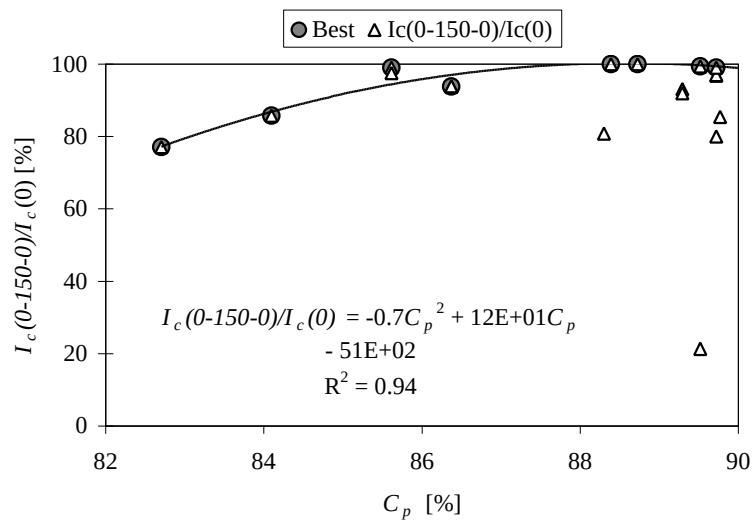

Figure 5.48 Permanent critical current degradation as a function of the compaction factor C_p for all conductors. Also shown is a quadratic fit through the best datapoints for all conductors.

A quadratic fit through the best datapoints yields a C_p of 84.7 % for I_c(0-150-0)/I_c(0) = 90%. No measurable permanent degradation is observed for C_p > 88 %.

5.9.4 Summary for the permanent critical current degradation

Here, a summary of the influence of the dimensional, cabling and compaction parameters on the permanent I_c degradation is given. Parameters without a clear influence on I_c(0-150-0)/I_c(0) are omitted. Table 5.21 lists the parameters for which an optimum is found.

Parameter	Optimum value of parameter for best I_c(0-150-0)/I_c(0)
g_{tm}, the ratio of the average cable thickness to the mandrel thickness	> 2.45-2.50
g_{wm}, the ratio of the width of the cable to the mandrel width	1.055
s_t, the free space between the mandrel tip and the rollers (vertical)	> 0.53
C_p, the cable volume compaction factor	C_p = 85 % gives 90 % I_c(0-150-0)/I_c(0) C_p > 88 % gives no degradation

Table 5.21 Optimum values for the various parameters with respect to the permanent critical current degradation.

Cycling tests on some of the samples showed no further degradation of the I_c, thus the assumption is made that the permanent damage is due to filament breakage in the internal structure of the filament bundles due to a mechanical overload condition.

It is speculated, that once all fragile parts of the bundles are destroyed, no significant further permanent reduction in I_c is observed.

5.10 Correlation between the initial I_c degradation and reversible/permanent I_c degradation under pressure

Based on the results described above, it is thought that apart from the initial cable degradation, which is partly due to the deformation of the strands during the cabling process, the further reductions in critical current that are in excess of the critical current reduction expected from single crystal experiments, are due to stress concentrations in the internal filament structure.

This means that the larger the amount of initial damage done to a strand during the cabling process, the more sensitive a cable could be to applied transverse pressure.

Similarly, the more uniform the initial wire structure after cabling, the less critical current reduction under load is expected.

The relation between initial cable degradation and reversible/permanent degradation is described here.

Relations are obtained for the reversible and permanent critical current degradation as a function of the initial cable degradation.

These relations are of the form

$$\begin{cases} I_c(P)/I_c(0) = 100 + A_r\left(100 - \left(I_c(0)/I_{c,m}\right)\right) + B_r\left(100 - \left(I_c(0)/I_{c,m}\right)\right)^2 \\ I_c(0-P-0)/I_c(0) = 100 + A_p\left(100 - \left(I_c(0)/I_{c,m}\right)\right) + B_p\left(100 - \left(I_c(0)/I_{c,m}\right)\right)^2 \end{cases} \quad [\%], \qquad (5.15)$$

with the coefficients A_r, A_p and B_r, B_p determined by a constrained least squares fit to the data-set. The constraints applied are B_r<*0*, B_p<0 and ($I_c(P)/I_c$(0), I_c(0-*P*-0)/I_c(0)) < 100 % for all points.

This influence of the internal structure of the strands is already described in chapter 4.

5.10.1 Reversible critical current degradation

Figure 5.49 shows an increase of the reversible cable degradation (I_c(P)/I_c(0)) with increasing initial cable degradation (I_c(0)/$I_{c,m}$) for the MJR conductors. Figure 5.50 shows the same for the IT conductors.

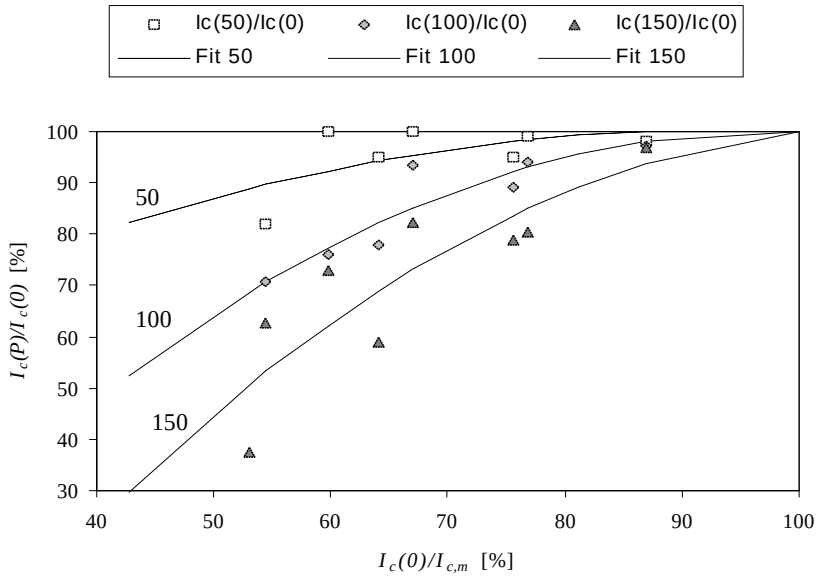

Figure 5.49 Reversible critical current degradation as a function of the initial cable degradation for the MJR conductors.

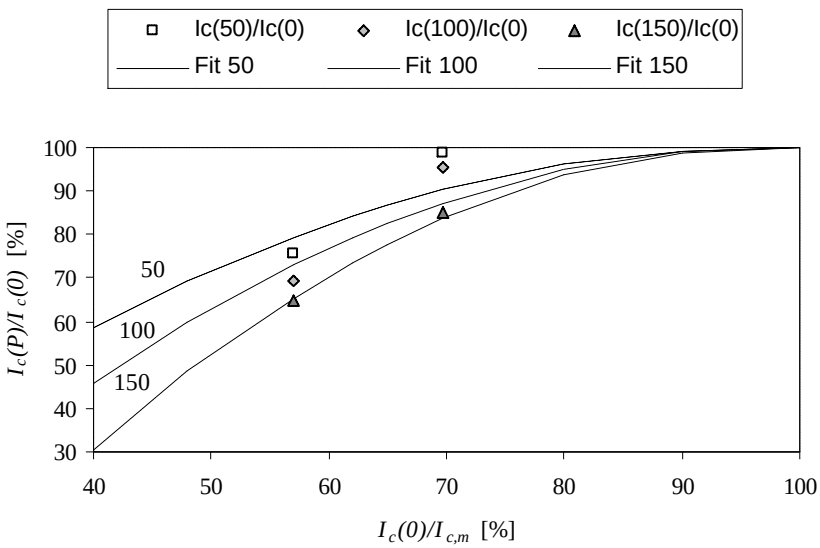

Figure 5.50 Reversible critical current degradation as a function of the initial cable degradation for the IT conductors.

For samples that are degraded to $I_c(0)/I_{c,m}$ = 60-70 % during cabling, the $I_c(150)/I_c(0)$ can still reach 60-80 %. With higher initial damage, $I_c(150)/I_c(0)$ falls off more rapidly.

This means that the more severe the initial cable damage is, the more sensitive the cable becomes to pressure.

There is no data available for $I_c(0)/I_{c,m}$ larger than about 86 % for MJR and IT, and 94 % for PIT. If one assumes the trend to continue to the upper right corner at (100 %, 100 %), the data are described by the fitted quadratic relations in table 5.22, after equation (5.15).

For the IT conductors, a relation similar to the MJR conductors can be fitted, but there are insufficient datapoints to confirm the behavior. A quadratic fit to the data is shown in figure 5.50.

For the PIT conductors, a quadratic relation between the initial I_c degradation and the reversible I_c degradation could not be established easily.

A quadratic fit, shown in figure 5.51, follows the measured data reasonably close, with an drop-off around $I_c(0)/I_{c,m}$ = 60 % for all three transverse loads. The measured data between 60 and 85 % $I_c(0)/I_{c,m}$ actually is higher than the fitted curve. The anomalous data-point at 95 % initial I_c degradation is most likely caused by a dry cable.

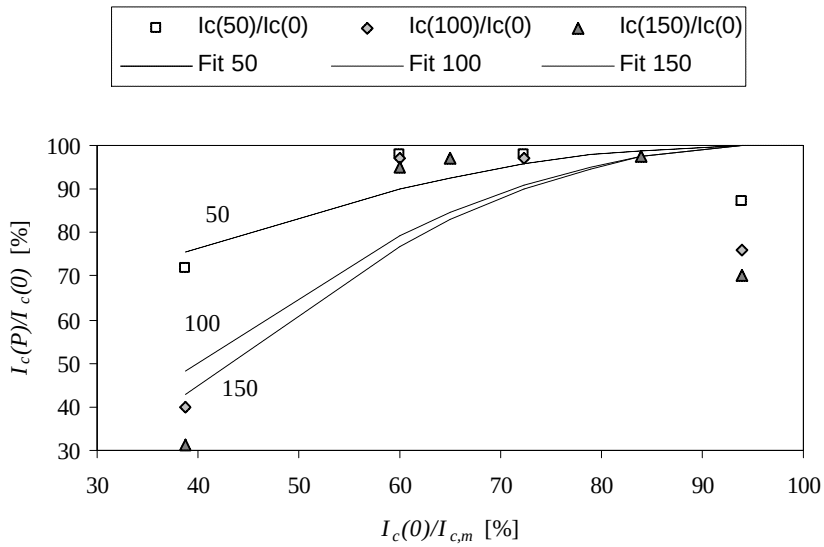

Figure 5.51 Reversible critical current degradation as a function of the initial cable degradation for the PIT conductors.

5.10.2 Permanent critical current degradation

Similar behavior is visible in the permanent damage as a function of the initial cable degradation, illustrated in figures 5.52 through 5.54. However, the amount of permanent damage done after a pressure of 150 MPa is applied, does still fall off with increased cabling damage, but a large amount of scatter is now visible. The magnitude of the scatter increases with increasing pressure. This is explained in part by the influence of the sample quality (impregnation and mounting combined) on the permanent critical current degradation.

The sample point marked “dry” was a badly impregnated cable, explaining the large amount of permanent damage at 150 MPa. The other two low points are a sensitive old design conductor (TW1) and a suspected incorrectly mounted sample (TW6), where the keystone angle of the cable was not matched correctly. The points are included in the presentation nevertheless, to illustrate the importance of good sample preparation.

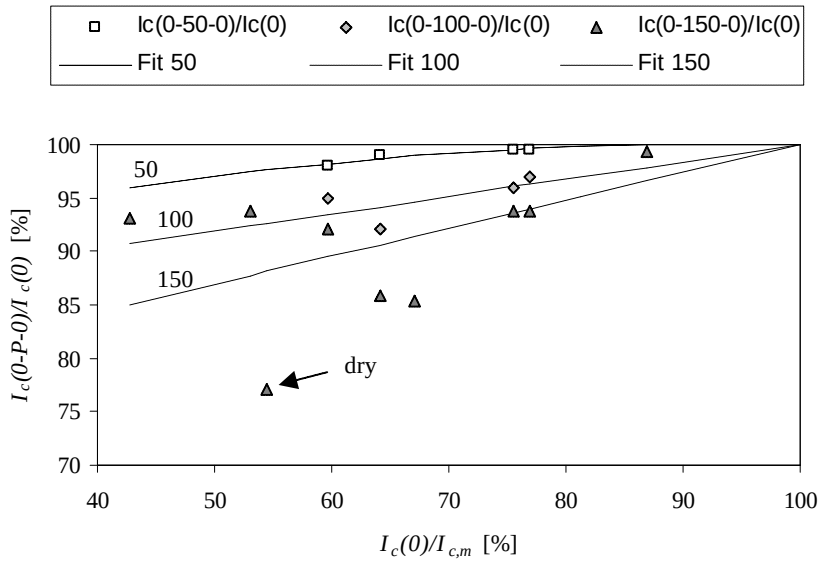

Figure 5.52 Permanent critical current degradation as a function of the initial cable degradation for the MJR conductors.

Figure 5.53 shows the same relation for the IT conductors. Again, only a linear relation should be plotted given the number of datapoints. In figure 5.54, the permanent critical current degradation as a function of the initial critical current degradation for the PIT conductors is shown. Only data for 150 MPa applied transverse pressure is available.

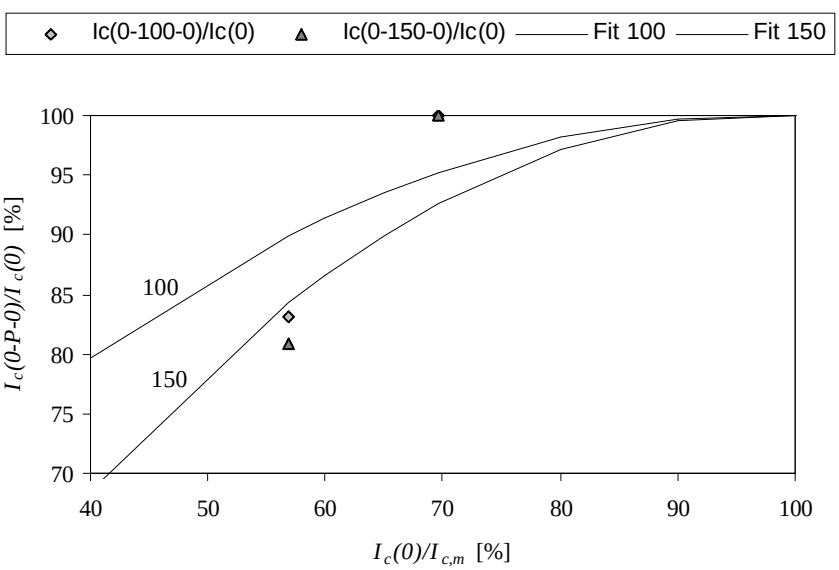

Figure 5.53 Permanent critical current degradation as a function of the initial cable degradation for the IT conductors.

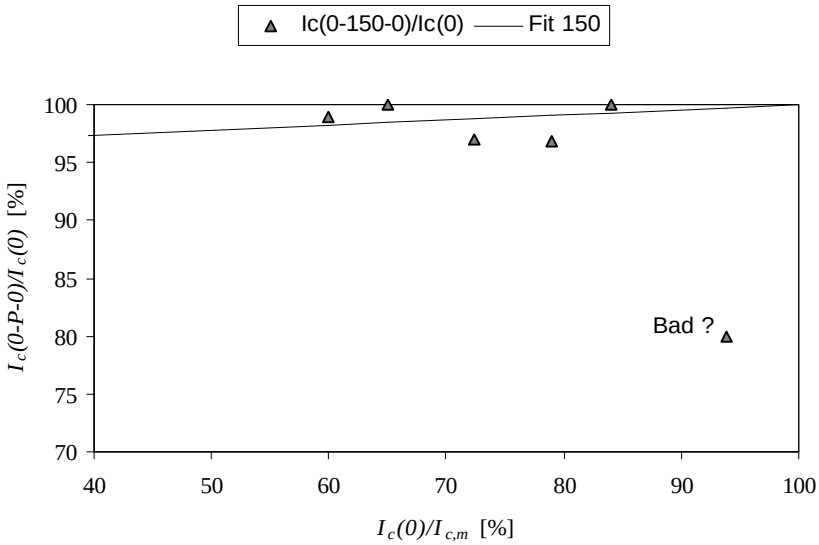

Figure 5.54 Permanent critical current degradation as a function of the initial critical current degradation for the PIT conductors.

No significant increase in permanent critical current degradation with increasing initial cable damage is visible in the PIT conductors. The data-point at $I_c(0)/I_{c,m}$ = 94 % (marked "Bad ?") is questionable since it was only measured only once, and is most likely an incorrectly mounted or impregnated cable.

5.10.3 Summary for all conductors

Table 5.22 lists the coefficients of the quadratic fits for the relation between the reversible and permanent degradation versus the initial cable degradation, using (5.15).

Conductor type	Pressure [MPa]	I_c (P)/I_c(0) [%]		I_c (0-P-0)/I_c(0) [%]	
		A_r	B_r	A_p	B_p
MJR	50	-0.09	-0.01	-0.02	-0.002
	100	-0.06	-0.02	0.16	-
	150	0.26	-0.02	0.26	-
IT	50	-0.06	-0.01	no data	no data
	100	-0.08	-0.02	-0.03	-0.006
	150	-0.10	-0.02	-0.04	-0.010
PIT	50	-0.04	-0.01	no data	no data
	100	-0.09	-0.02	no data	no data
	150	-0.10	-0.02	0.04	-

Table 5.22 Fit coefficients for the quadratic relations between the reversible/permanent critical current degradation and the initial cable degradation using (5.15).

The reversible and permanent I_c degradation seem less sensitive to the initial I_c degradation in the PIT conductors as compared to the MJR and IT conductors. For the reversible degradation, the difference is

small for larger pressure, but for the permanent degradation, the difference is larger for MJR and largest for the IT conductor.

The permanent degradation after 150 MPa, around $I_c(0)/I_{c,m}$ = 50 %, due to the initial cable degradation, is about 5 times larger for the IT conductors, and about 3 times larger for the MJR conductors, when compared to the PIT conductor.

The slope of the permanent degradation as a function of the initial cable degradation is about 4 times smaller for the MJR conductors, and about 2 times smaller for the IT conductors, when compared to the slope of the reversible degradation as a function of the initial degradation. The PIT conductor hardly shows signs of permanent critical current degradation as a function of initial cable degradation.

5.11 Summary of degradation components

The degradation data are again grouped by type, starting with the initial I_c degradation, then followed by the total and permanent I_c degradation. All data are plotted as ratios of the degradation type divided by the manufacturers critical current data (initial cable degradation added to the reversible and permanent degradation and normalized to $I_{c,m}$).

5.11.1 Initial I_c degradation

Figures 5.55 and 5.56 show the initial degradation in critical current for all tested samples. For the PIT samples, extracted strand data are not available. On average, the extracted strand samples show a lower initial I_c degradation (less damage) than the full cable samples. This is probably due to additional degradation introduced by the mounting procedure for the cable tests.

Information on the range of the initial I_c degradation is listed in table 5.23 for the MJR, IT and PIT samples. The suspected bad samples are dropped in the further discussion.

Conductor type	Average $I_c(0)/I_{c,m}$ [%]	Range of $I_c(0)/I_{c,m}$ [%]
MJR cable	67 (61)	(43) 53-87
IT cable	64	57-70
PIT cable	76 (70)	(39) 60-94
MJR extracted	86 (84)	77-98
IT extracted	84 (74)	(43) 68-95
MJR all	72 (68)	(43) 53-98
IT all	74 (70)	(43) 57-95

Table 5.23 Information on the range of the initial critical current degradation for the MJR, IT and PIT samples. The range listed here includes the four suspected bad samples (TW7a, TW10, IG10 and EC10) between brackets.

Overall (cable and extracted strands), all three conductor types have an initial critical current degradation with a mean around 27 % (100-73), with a standard deviation of 15 %.

For the cable experiments (MJR/IT/PIT cable) alone, the MJR samples and IT samples are degraded by 35 % on the average, whereas the PIT samples show the lowest initial I_c degradation with an average of 24 %, The distributions of the two data-sets on cables (MJR/IT cables versus PIT cable) still have a large overlap, but the difference in the means of the two distributions is sufficiently large to make a statistical distinction between the two groups.

This suggests that the PIT conductors might have a slightly lower initial critical current degradation than the MJR or IT conductors. A sound conclusion on such a difference cannot be proven due to the lack of sufficient reliable data. No statistical distinction can be made between the MJR and IT samples due to a large overlap in the distribution of the data, hence both conductors statistically show a similar initial critical current degradation.

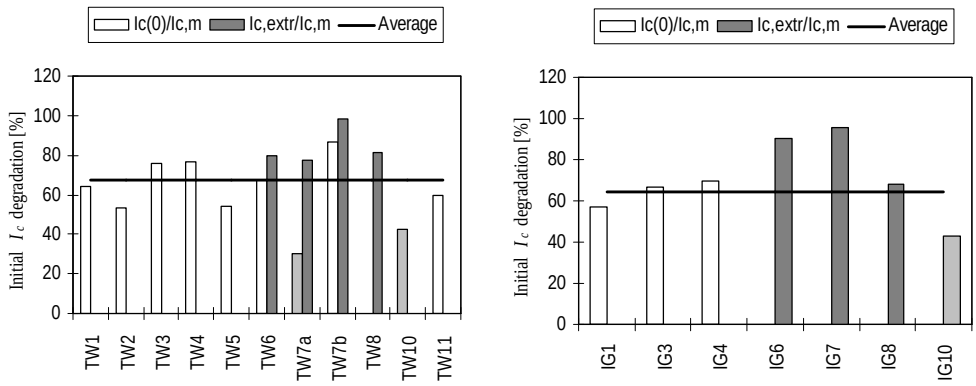

Figure 5.55 Initial critical current degradation for the MJR and IT samples (where data is available, after elimination of the suspected bad samples in light gray). The horizontal line indicates the average.

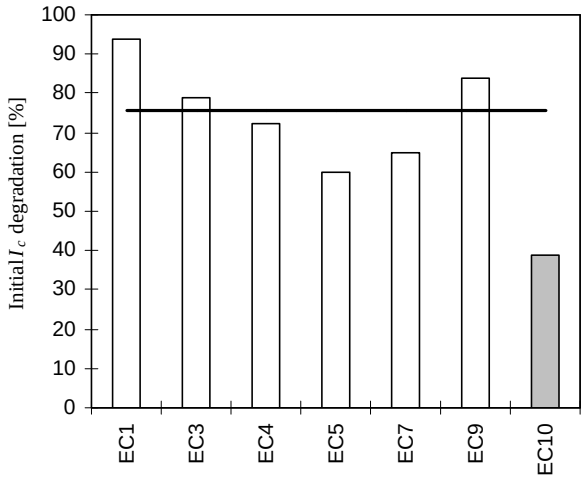

Figure 5.56 Initial critical current degradation for the PIT samples. The horizontal line indicates the average after elimination of the suspected bad sample EC10 (light gray).

The next two sections discuss the correlation between the measured data for reversible and permanent I_c degradation, and the critical current degradation model proposed in chapter 3. Sections 5.11.2 and 5.11.3 show all the measured data.

5.11.2 Total I_c degradation

In this section, the graphs of the total critical current degradation are shown, for use in the comparison with the critical current degradation model in section 5.12.

Figures 5.57 through 5.59 show all measured total critical current degradation data that are available. For most samples, datapoints are available at 50 MPa intervals. Some of the data from literature only list initial data and data at 150 MPa. The data are normalized to $I_{c,m}$ as $I_c(P)/I_{c,m}$ and $I_c(0\text{-}P\text{-}0)/I_{c,m}$ in percent.

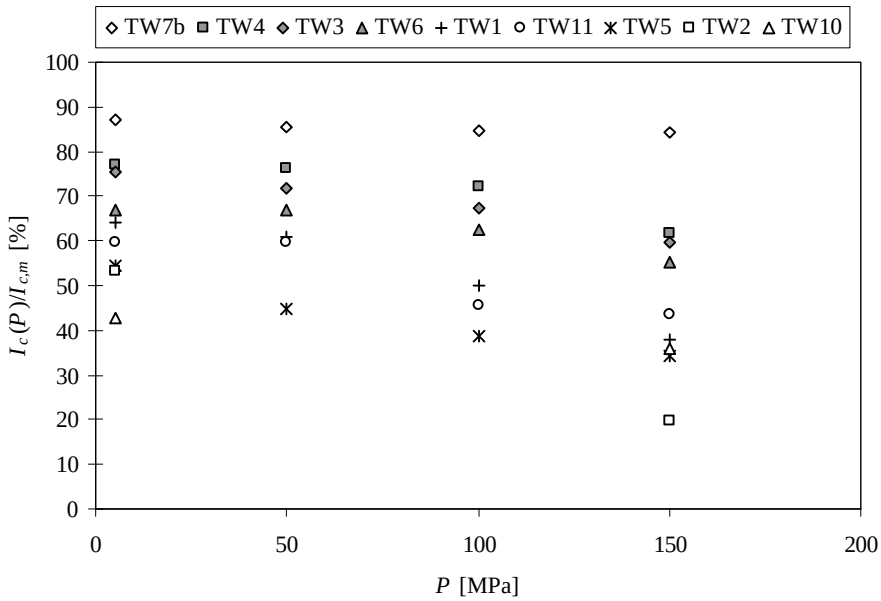

Figure 5.57 $I_c(P)/I_{c,m}$ for the MJR samples.

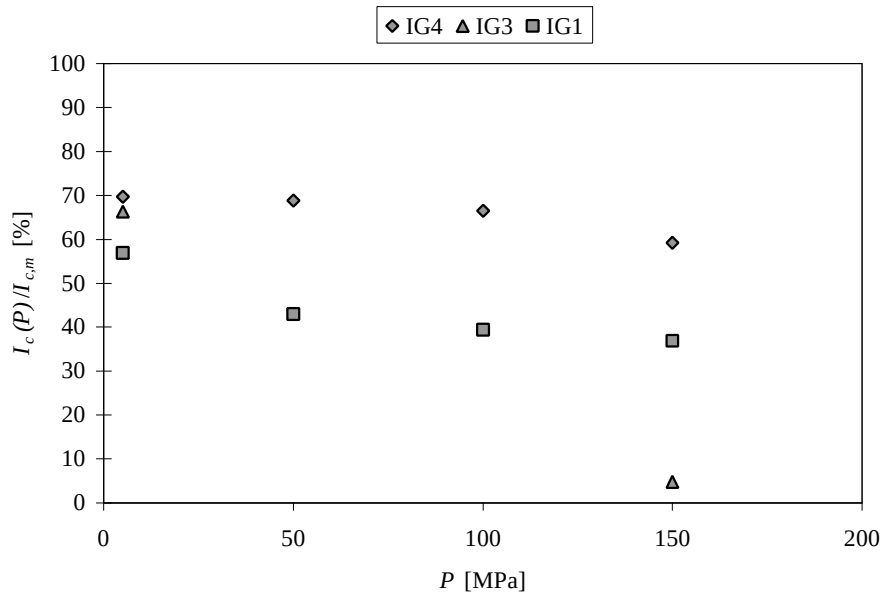

.

Figure 5.58 $I_c(P)/I_{c,m}$ for the IT samples.

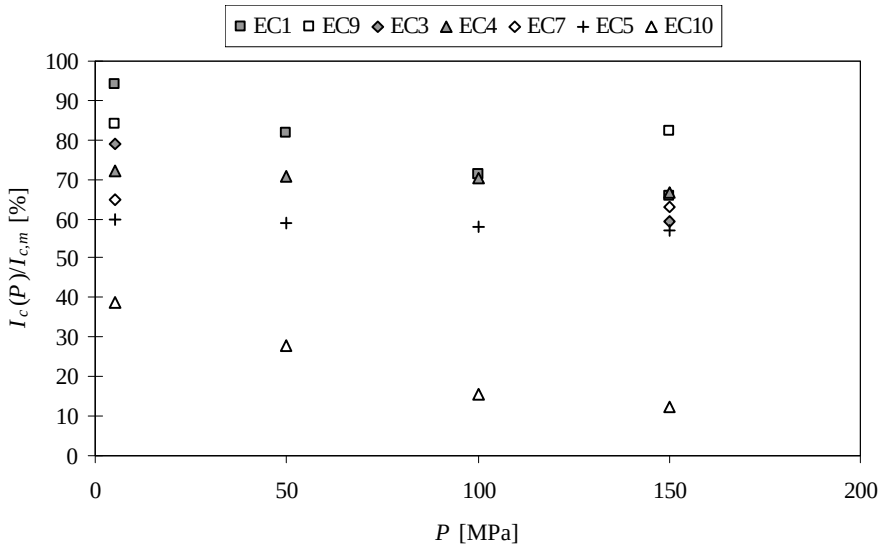

Figure 5.59 $I_c(P)/I_{c,m}$ for the PIT samples.

5.11.3 Permanent I_c degradation

This section contains the graphs of the permanent I_c degradation normalized to the manufacturers $I_{c,m}$ for all samples. The data is used for the correlation with the I_c degradation model in section 5.12. Figures 5.60 through 5.62 show all measured permanent critical current degradation data. Similar to section 5.11.2, the ratio of $I_c(0\text{-}P\text{-}0)/I_{c,m}$ is shown, instead of the more usual $I_c(0\text{-}P\text{-}0)/I_c(0)$.

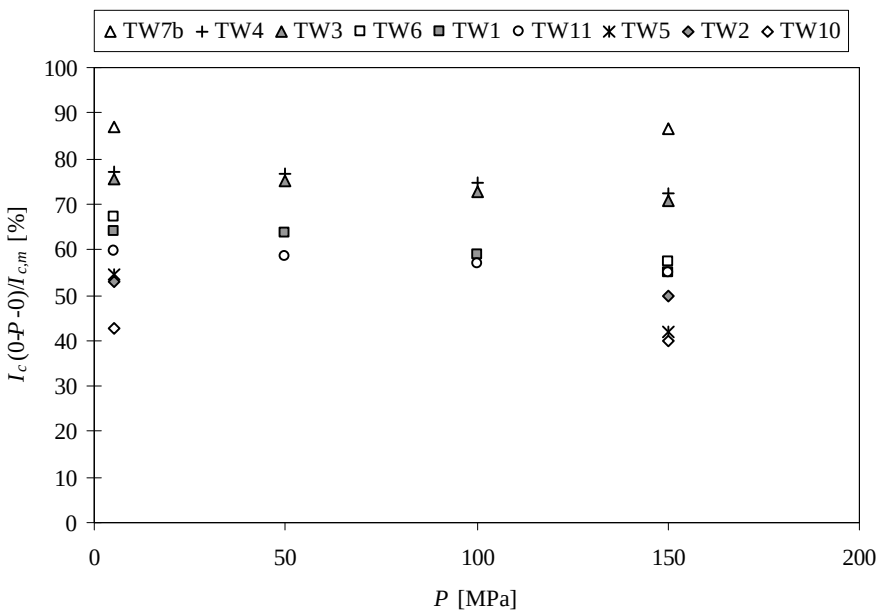

Figure 5.60 $I_c(0\text{-}P\text{-}0)/I_{c,m}$ for the MJR samples.

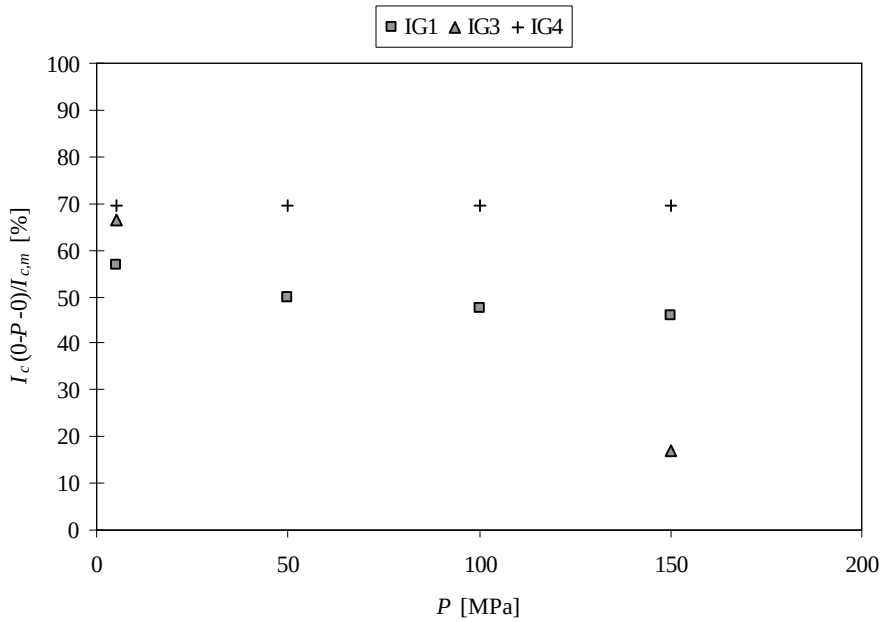

Figure 5.61 $I_c(0\text{-}P\text{-}0)/I_{c,m}$ for the IT samples.

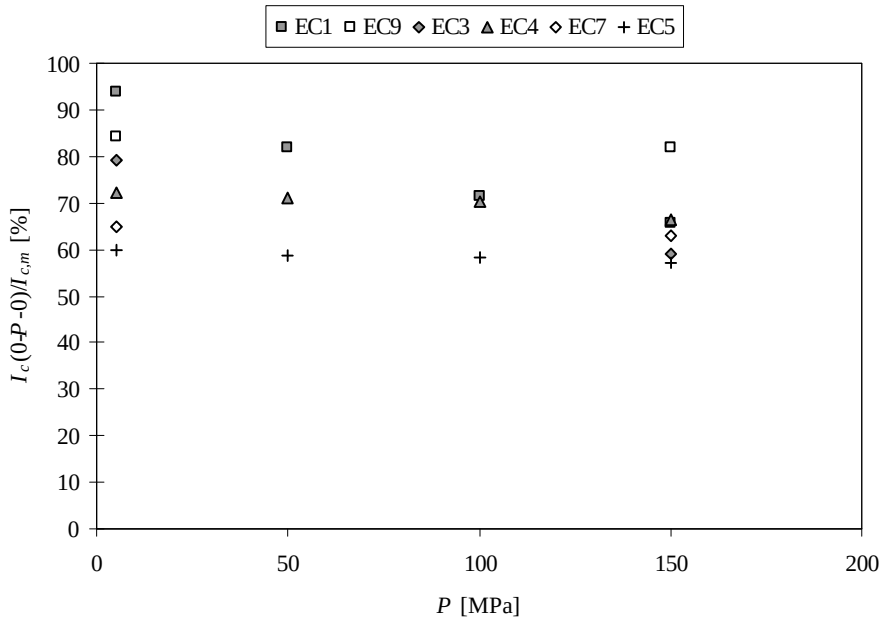

Figure 5.62 $I_c(0\text{-}P\text{-}0)/I_{c,m}$ for the PIT samples.

5.12 Comparison with the combined critical current degradation model

In this section, the correlation between the measured data and the proposed combined empirical/FEA critical current degradation model of section 3.9 is discussed. The measured data are compared to the predicted degradation curves for each conductor sample. The coefficients of the critical current degradation model (3.32) that are computed to match the measured data are presented. The coefficients in the model are fitted using a least squares method based on the four datapoints (when available) at 5, 50, 100 and 150 MPa.

The selection of which FEA model to use to compute the stress on the Nb_3Sn within the filaments as a function of the applied transverse stress on the cable surface is made by determining the quality of the impregnation of the sample.

In essence, the FEA model, which determines the amount of plastic deformation, and the effective Young's modulus of the sample, as a function of the applied transverse pressure, is used as a correction for the influence of the experiment on the critical current degradation measurement.

This correction eliminates the influence of the sample preparation from the comparison of the different conductor types, so that the critical current degradation model of (3.32) can be used to compare the sensitivity of different conductor types directly to eachother. The determination of the correct FEA model to use in the computation is made after the measurement data are known (due to the fact that the determination of the quality of impregnation is only made after a destructive autopsy of the cable sample).

The shape of the curve of the critical degradation as a function of applied transverse pressure is usually a good indication of the quality of the impregnation. For a well impregnated sample, the critical current degradation slowly increases in slope with increasing pressure, the opposite is true for a badly impregnated or dry sample.

The sequence for the determination of the coefficients is as follows:

1) set the initial I_c degradation to match the data-point at $I_c(0)$ and determine the type of FEA model to be used ("impregnated" for a well impregnated sample, "dry" for a non-impregnated sample);
2) determine C_0 to set the slope for $dB_{c2}(P)/dP$;
3) determine C_3 by fitting the permanent degradation to the measured data, leaving C_1 and C_2 zero;
4) determine C_1 and C_2 simultaneously by fitting the reversible degradation to the data.

As an example, the sequence of steps is illustrated here for sample TW3 in more detail, with the graphs showing the result of the model at each step in figures 5.63, 5.64 and 5.65. The end result is in figure 5.65, with the model describing the measured data correctly.

The measured critical current degradation data for sample TW3 is listed in table 5.24. The initial critical current degradation for TW3 is 100% - 75.6% = 24.4 %. This defines the starting point of both the total I_c degradation and permanent I_c degradation curves at $P = 0$ or 5 MPa.

From the data in the table it is evident that the slope of the critical current degradation becomes steeper with increasing pressure. This means that the cable is well impregnated, hence the FEA model for a well impregnated cable is used to compute the plastic deformation and effective Young's modulus as a function of the applied transverse pressure.

Applied transverse pressure [MPa]	Total I_c degradation $I_c(P)/I_c(0)$ [%]	Permanent I_c degradation $I_c(0\text{-}P\text{-}0)/I_c(0)$ [%]
5	76	76
50	72	75
100	67	73
150	60	71

Table 5.24 Measured critical current degradation for sample TW3. Note the increasing slope of critical current degradation with respect to pressure for increasing pressure.

1) The multiplication factor for the initial I_c degradation is 0.756, determined from the first row in the table of total or permanent I_c degradation. Since the slope of the critical current degradation increases with increasing pressure, the FEA model for a well impregnated cable is chosen. The FEA models are pre-

calculated, and a curve of the influence of the plastic deformation as a function of applied transverse pressure is used as the multiplier f_{pl} in equation (3.30).

2) The scaling coefficient C_0 is set to about 700. The resulting model curves after steps 1 and 2 are shown in figure 5.63.

3) The plastic deformation coefficient C_3 is determined by least squares fit to the measured data for the permanent critical current degradation. The resulting value for C_3 is 21.8. The norm of the remaining residuals squared is 1.4 %, and is labeled "Perm. Err." in table 5.25. The resulting model curves after completion of step 3 are shown in figure 5.64.

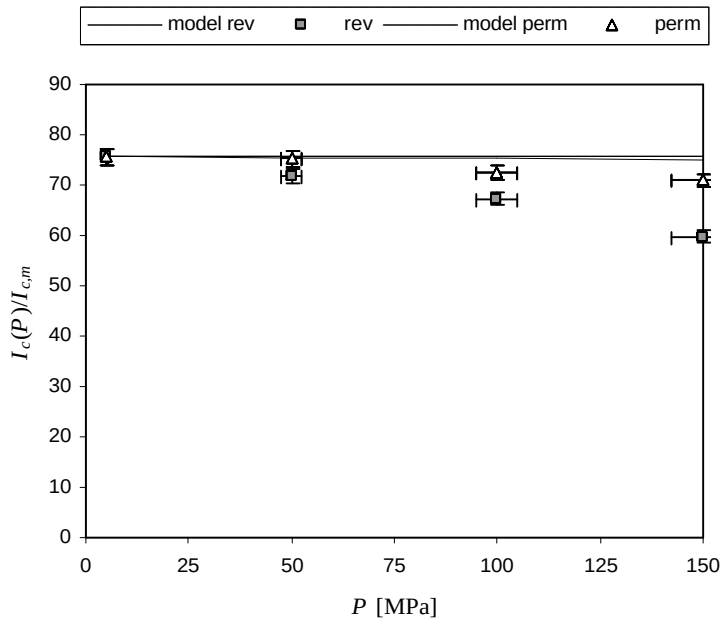

Figure 5.63 Model prediction after steps 1 and 2; initial critical current degradation is matched to the measured data, and C_0 coefficient is applied.

4) Now, the remaining coefficients C_1 (hydrostatic pressure) and C_2 (deviatoric stress) are determined by minimizing the residual of the fitted curve to the measured data for the total critical current degradation. This is again done by the least squares method, with constraints $C_1 < 0$ and $C_2 > 0$. This results in the fitted curves of figure 5.65, and values of $C_1 = -0.35$, $C_2 = 0.69$. The remaining residual (norm of the differences squared) is 0.9 %, and is labeled "Rev. Err." in table 5.25.

Figures 5.65 and 5.66 show an example of a fitted set of curves to the measured data for samples TW3 (MJR) and IG1 (IT). The lower curve shows the combined initial and reversible critical current degradation. This is the curve that is produced by measuring I_c as a function of the applied transverse pressure P.

The upper curve shows the I_c resulting from loading a sample to the corresponding pressure P on the axis in figure 5.65, then releasing the pressure to measure the remaining I_c.

The resulting I_c, while actually measured at P = 0-5 MPa, is plotted here as a function of the pressure before release, to indicate what the permanent effect of subjecting the sample to such a pressure has on I_c.

The measured datapoints are plotted with error bars indicating the approximate measurement error in the experiment. The error in the pressure determination is about 5 %, due to uncertainty in the sample contact surface and alignment with the pressure block.

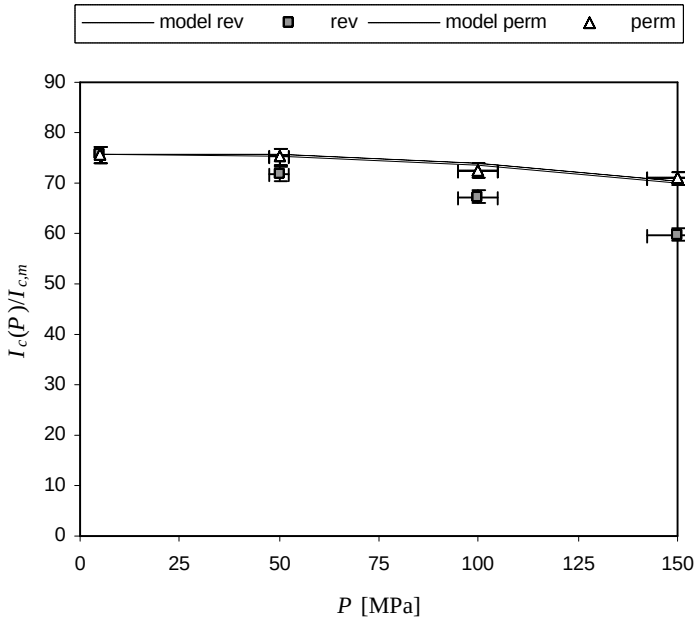

Figure 5.64 Model prediction after step 3); plastic deformation effect is computed.

The error in the critical current measurement is on the average about 2 %, depending on the stability of the current while determining the *U(I)*-characteristics, and the I_c-criteria used to determine the critical current.

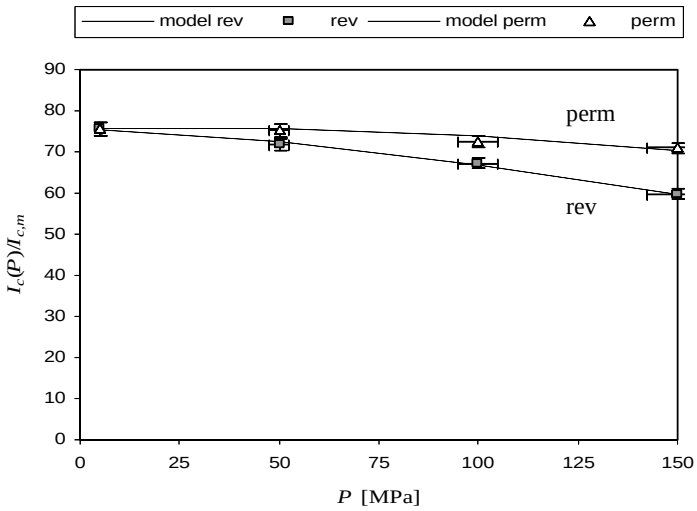

Figure 5.65 Correlation between the measured $I_c(P)$ data for sample TW3 and the computed curves from the critical current degradation model. The FEA model simulating a normal (impregnated) cable is used.

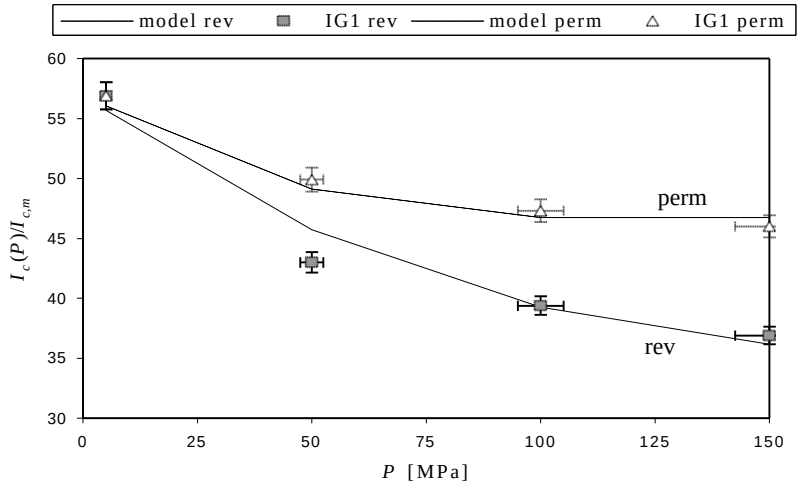

Figure 5.66 Correlation between the measured $I_c(P)$ data for sample IG1 and the computed curves from the critical current degradation model. The FEA model simulating a dry (non-impregnated) cable is used.

Tables 5.25 through 5.27 list the fitted coefficients and an indication of the average error for the fit for the different conductor types. This error determination is computed from the root of the sum of the squares of the residual of the fit, to yield an average error in units of the critical current degradation [%]. The fit error is first determined for the permanent I_c degradation, then for the reversible I_c degradation.

Sample ID	FEA model used	C1 (hydrostatic) (STEP 4)	C2 (deviatoric) (STEP 4)	Rev. Err. [%] (STEP 4)	C3 (plastic) (STEP 3)	Perm. Err. [%] (STEP 3)
TW1	impregnated	-0.8	2.8	2	49	1
TW2	impregnated	-2.3	2.3	0	21	0
TW3	impregnated	-0.3	1.9	1	21	1
TW4	impregnated	-1.1	0.0	1	21	2
TW5	dry	-1.6	0.0	1	16	2
TW6	impregnated	-0.3	0.0	0	47	1
TW7a	impregnated	-6.7	3.5	23	47	10
TW7b	impregnated	0.0	0.5	0	2	1
TW10	impregnated	-0.6	0.6	0	23	0
TW11	impregnated	0.0	3.6	2	28	6
Average		-1.4	1.5	3	27	2
St.dev.		2.0	1.5	7	14	3

Table 5.25 Fitted coefficients from the critical current degradation model for the reversible and permanent degradation of the MJR samples.

Sample ID	FEA model used	C1 (hydrostatic) (STEP 4)	C2 (deviatoric) (STEP 4)	Rev. Err. [%] (STEP 4)	C3 (plastic) (STEP 3)	Perm. Err. [%] (STEP 3)
IG1	dry	0.0	3.6	2	13	4
IG3	dry	-2.6	2.6	4	53	5
IG4	impregnated	-1.2	0.0	0	0	2
LM1	impregnated	-0.3	0.3	0	3	1
LM2	impregnated	-0.4	0.4	0	8	0
Average		-0.9	1.4	1	15	2
St.dev.		1.1	1.6	2	21	2

Table 5.26 Fitted coefficients from the critical current degradation model for the reversible and permanent degradation of the IT samples.

Sample ID	FEA model used	C1 (hydrostatic) (STEP 4)	C2 (deviatoric) (STEP 4)	Rev. Err. [%] (STEP 4)	C3 (plastic) (STEP 3)	Perm. Err. [%] (STEP 3)
EC1	dry	-1.1	0.0	2	14	4
EC3	impregnated	-1.2	1.2	0	10	0
EC4	impregnated	-0.4	0.0	0	10	1
EC5	impregnated	0.0	0.7	0	3	1
EC7	impregnated	-0.2	0.2	0	0	0
EC9	impregnated	-0.1	0.1	0	0	0
EC10	dry	-2.0	2.0	2	30	5
Average		-0.7	0.6	1	16	2
St.dev.		0.7	0.8	1	18	2

Table 5.27 Fitted coefficients from the critical current degradation model for the reversible and permanent degradation of the PIT samples.

The average fit coefficients for the three different conductor types are summarized in table 5.28. The question is now whether there is a statistically significant difference between the coefficients for the different conductor types.

In order to make this determination, a series of two-sample t-tests [5.13] is performed to distinguish between the coefficients for the different conductor types. Table 5.29 lists the tests performed, and the results and corresponding confidence value.

Conductor type	C1 (hydrostatic)	C2 (deviatoric)	Rev. Err. [%]	C3 (plastic)	Perm. Err. [%]
MJR	-1.4	1.5	3	27	2
IT	-0.9	1.4	1	15	2
PIT	-0.7	0.6	1	16	2

Table 5.28 Average fit coefficients from the critical current degradation model for the reversible and permanent degradation of each conductor type.

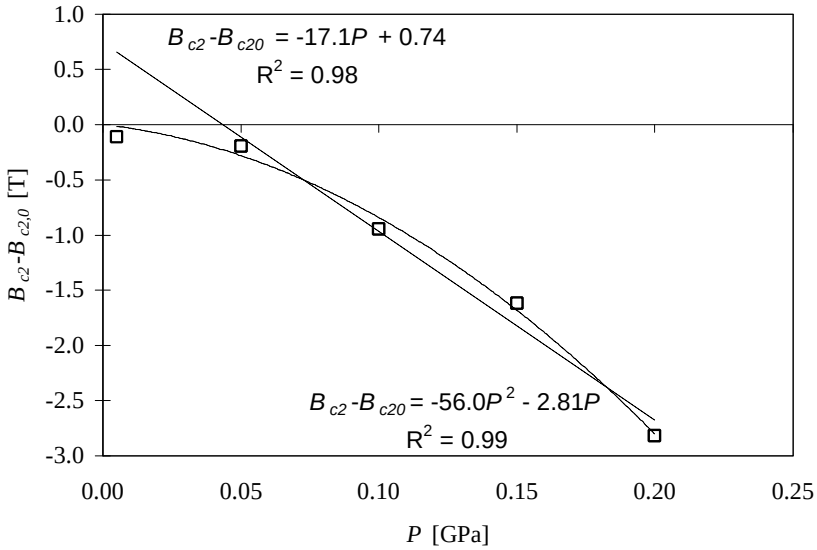

Figure 5.67 Change in B_{c2} as a function of applied pressure P for sample TW2 for comparison with the model by Ten Haken.

Comparing the measurement on sample TW2 to measurements by Ten Haken on Nb_3Sn tapes show a more similar behavior, with reductions in the upper critical field B_{c2} of the order of 1.5 T at 200 MPa. This compares fairly well to a reduction in B_{c2} of 1.7 T at 200 MPa for the model in section 3.6.2. Slopes of the order of –10±2 T/GPa are measured when linear fits are made to the points for $P \geq 50$ MPa.

Given the mismatch between the fit and the prediction using hydrostatic pressure only, it is concluded that the hydrostatic pressure alone cannot account for the observed reduction in B_{c2}, and hence the critical current degradation under pressure.

This confirms the results obtained by Ten Haken, who proposes that the reduction in B_{c2} should be described as a function of both the hydrostatic pressure as well as the deviatoric strain (see (3.4) in section 3.2).

A comparison with the slope of the linear fit on the reduction of B_{c2} in sample TW2 with the slopes predicted by the model by Ten Haken shows a factor of about 1.7 difference. This is in good agreement with the fit factor found for the deviatoric component of 1.8 for this particular sample (see TW2 in table 5.23) from the elastic-plastic stress model prediction in (3.32) (see chapter 3).

5.14 Conclusions

The critical current degradation experiments for all conductors yield some linear correlations and quadratic relations with the cabling parameters. The relations are summarized; where available, the optimum value for the parameter to minimize I_c degradation is given in table 5.30. The right column lists the optimum value for the cable parameter or compaction factor that will most probably produce an optimal cable design. These values may be applicable to all three conductor types.

Additionally, with respect to the critical current degradation, the following relations are found:

1) the initial I_c degradation decreases with increasing cable width w as $I_c / I_c(0) = 3.1w + 16.2$;
2) the initial I_c degradation decreases with increasing compaction factor as $I_c / I_c(0) = 4.87\ C_p - 346$. To minimize the I_c degradation to less than 10 %, $C_p > 90$ % is recommended;
3) the reversible I_c degradation decreases with increasing Cu/SC ratio as $I_c(150)/I_c(0) = 14$ Cu/SC + 80;
4) the slope of the permanent degradation as a function of the initial degradation is about 4 times smaller for the MJR conductors, and about 2 times smaller for the IT conductors, when compared to the slope of the reversible degradation as a function of the initial degradation. The PIT conductor does not show enhanced permanent critical current degradation with increasing initial critical current degradation.

Parameter or factor	Initial cable degradation minimized	Reversible I_c degradation minimized	Permanent I_c degradation minimized	**Optimal cable design**
g_{tm}	2.4	2.5	> 2.4	**2.5**
g_{wm}	1.06	1.06	1.06	**1.06**
g_{wr}	1.005	-	-	**1.005**
s_t	0.49	-	> 0.53	**0.5**
s_w	0.45	0.50	-	**0.5**
$C_{x,edge}$	106 %	-	-	**106 %**
C_x	99 %	-	-	**99 %**
C_{y1}	95 %	-	-	**95 %**
C_{y2}	94 %	-	-	**94 %**
C_p	> 90 %	88 %	> 88 %	**89 %**

Table 5.30 Optimum values found for the cable parameters and compaction factors to minimize the initial cable degradation, reversible and permanent I_c degradation. The right column lists the chosen values for an optimal cable design.

The correlation between the measured data and the critical current degradation model from (3.32) warrants the following conclusions:

5) the hydrostatic coefficient contributing to the I_c degradation is −1.0 and statistically equal for all conductors;
6) the deviatoric coefficient contributing to the I_c degradation is 1.4-1.5 for the MJR and IT conductors and 0.6 for the PIT conductor;

This means that both the MJR and IT conductors should behave similarly under applied pressure with respect to reversible critical current degradation. The PIT conductor is less sensitive with respect to reversible I_c degradation.

In chapter 4, stress enhancement factors (without voids) of 1.4-1.9 (MJR and IT) were found, compared to no enhancement for PIT. The combined enhancement of C_2 is found to be 1.4-1.5 for MJR and IT, versus 0.6 for PIT. This compares well to the results from the FEA models, where the same sequence of sensitivity to applied transverse pressure is found (see chapter 4).

7) only the MJR conductors have a large plastic coefficient of 27;
8) the PIT and IT conductors have a smaller and statistically equal plastic coefficient of 10-15.

This means that the MJR conductor is the most sensitive with respect to permanent critical current degradation, whereas PIT and IT should be comparable. Comparing this result to the FEA models (with voids) in chapter 4, the MJR conductor again ranks as the most sensitive, with an enhancement factor of up to 5, and PIT lowest at 2. For IT, the models with voids predict an enhancement of about 4, but only for a small area of the filaments as compared to the MJR conductor. With voids present, the IT conductor is thus very sensitive with respect to permanent I_c degradation, but without voids it is comparable to the PIT conductor.

In summary, ranking the three conductor types for minimal total critical current degradation, the PIT conductor shows a slightly lower sensitivity, primarily due to the lower initial critical current degradation (by about 10%), with IT showing similar behavior without voids, and MJR the most sensitive. This conclusion is only valid provided the measurements are statistically sound, and sufficient data are available. Due to the limited amount of samples, and the possible influence of several “bad” samples on the resulting relations, these final conclusions are difficult to defend. Nevertheless, the data are presented here in full, since this is the first time a systematic comparison of such a large data-set is performed. Also, trends are sufficiently visible in the data to at least make a qualitative argument about the states differences in sensitivity.

The reduction in B_{c2} with applied transverse pressure for sample TW2 is in good agreement with data and model predictions by Ten Haken [5.15], when the scaling factors found with the elastic-plastic critical current degradation model are applied.

The fact that wire structures like the PIT conductor degrade far less with applied pressure than the MJR or IT conductors points to the internal structure being of importance in the reacted material.

Statistically, the MJR conductor shows the largest sensitivity to plastic deformation. In chapter 4, the MJR conductor also showed the largest increase in stress concentrations due to void formation, but about the same increase in sensitivity without voids as the IT conductor. This again points to Kirkendall voids as a possible cause for the enhanced critical current degradation in MJR conductors with respect to PIT and IT conductors. This phenomenon is further investigated in chapter 6 with the use of SEM techniques.

Chapter 6

Permanent filament damage on a microscopic scale

A series of photographic studies are described aimed at determining the cause of the permanent critical current degradation on a microscopic scale. First, an analysis of cross-sections of compressed Nb_3Sn cables based on Scanning Electron Microscope (SEM) pictures is presented. A differentiation is made between damage introduced by sample preparation, cabling artifacts and that caused by excessive strain and/or stress.

Next, a correlation is made between the damage observed around the Kirkendall voids in the SEM photographs and the locations most prone to damage in the FEA models as presented in chapter 4. This is followed by a discussion of methods that influence the final location of the Kirkendall voids, in order to have them at locations where damage due to transverse stress is minimal.

Finally, the use of a Hot Isostatic Press (HIP) to eliminate the voids altogether is discussed.

6.1 Introduction

The results from the FEA models presented in chapter 4, and the experiments described in chapter 5, indicate that an important factor, that determines the stress sensitivity of the cables, is the internal layout of the Nb_3Sn in the wire. Also, void formation within the filamentary area is indicated as a possible cause of enhanced permanent critical current degradation.

In this chapter a microscopic study of the mechanisms involved in the permanent damage caused by transverse pressure is described. The study is focussed on the effect of Kirkendall voids in the cross-section. In section 6.2, micro-photographs showing the suspected damage, a correlation between the location of the observed damage, and the highest stress location in the FEA models, are discussed. Possible remedies for the damage are discussed in section 6.3.

In section 6.4, a study is presented of methods to influence the final location of the voids within the cross-section by influencing the reaction process. In the wire geometry, the initial composition of the filament bundles can be varied. The effect of the initial tin content in the core of the filament bundles of an IT wire on the void location is investigated.

In the reaction process, several parameters can be varied, including the reaction temperature and duration. An attempt is made to determine the migration speed of the voids through the filamentary area as a function of these parameters. Preliminary results of a dedicated diffusion experiment are discussed in section 6.5.

Finally, the use of a Hot Isostatic Press (HIP) during or after the reaction process is discussed in section 6.6. At the time the experiments for this thesis were terminated, no critical current data was available on the "HIP"-ed samples. Only several years later, a systematic study was concluded on the effect of a HIP treatment on the critical current density in MJR type Nb_3Sn conductors [6.1]. Results from this study are included in the discussion.

6.2 SEM analysis of compressed Nb_3Sn cables

A systematic study is performed on a series of samples subjected to stepwise increasing transverse loads to investigate the mechanisms behind the permanent critical current degradation in Nb_3Sn composite materials. The permanent damage to the strands is analyzed using Scanning Electron Microscopy (SEM).

6.2.1 Types of damage observed

Several pictures of typical damaged areas are shown here, illustrating the different types of damage typically found in the filamentary areas in the uncompressed and compressed samples. Four types of damage related to the transverse pressure experiments are distinguished here:

1) damage due to defects introduced during the cabling operation,
   - *examples are sheared filament bundles and broken diffusion barriers;*
2) damage due to excessive strain on the filament structure (not caused by defects),
   - *broken filaments due to plastic deformation exceeding the strain limit of Nb_3Sn*;
3) damage due to excessive transverse stress on the filament structure (not caused by defects),
   - *broken filaments due to plastic deformation exceeding the stress limit of Nb_3Sn;*
4) damage due to intrinsic defects in the material,
   - *for example stress concentrations around voids in the filamentary area.*

Also, combinations of the damage types are found, such as transverse pressure sensitivity caused by defects introduced during the cabling operation.

The samples require a careful preparation in order not to introduce additional defects. The filamentary area around Kirkendall voids tends to deform easily, usually by pressure exerted on the sample surface during the polishing process. When a coarse polishing compound is used, the walls of these voids sometimes collapse and appear as larger damaged areas in the pictures, as illustrated in figure 6.1.

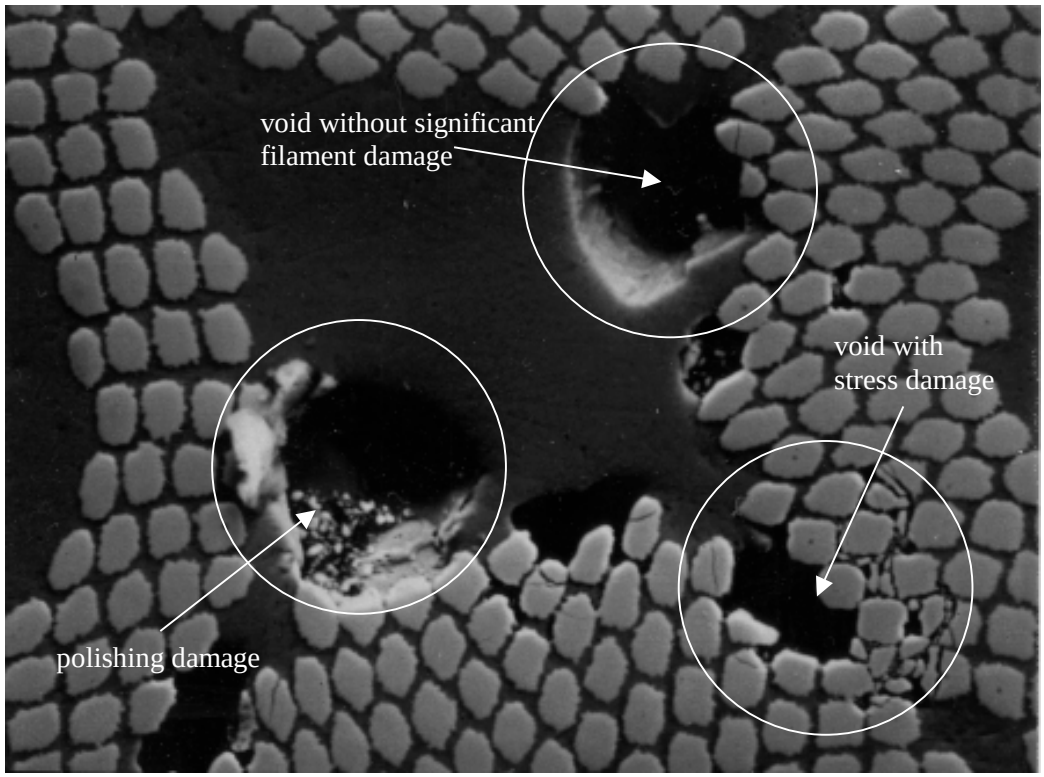

Figure 6.1 Cross-section of an IT wire sample showing both polishing damage and structural damage to the filaments due to excessive transverse pressure.

The solution is to look at these voids in a slanted cross-section of the sample, or the use of more gentle polishing paste over a longer polishing period. When preparation damage is suspected, additional polishing steps can also be made a small distance (usually several tenths of a mm) into the sample to ensure that the observed effect is not a preparation artifact but really present in the sample.

6.2.2 Damage due to defects introduced during the cabling operation

Two examples of damage observed in the photographs of strand cross-sections after the cabling operation are discussed here. First, shear planes and broken diffusion barriers introduced during the cabling operation are shown, followed by an example of a broken diffusion barrier unrelated to shear.

Figure 6.2 shows a problem mostly occurring in the MJR conductor, in cases where the strands are heavily distorted during the cabling operation. The picture shows a strand in the corner area of a cable. If the strand is severely deformed, the filament bundles can shear, opening the diffusion barrier around the bundle, and interrupting the current flow through the filaments.

Figure 6.3 shows a close-up of one of the filament bundles that has been sheared by the cabling operation. The sample has been selectively etched to reveal the structure of the filament bundle. The picture clearly illustrates how the bundle has been split in two parts, and how one part is displaced over about half the bundle diameter. The diffusion barrier surrounding the filament bundle has been split, allowing tin to diffuse out of the core of the filament bundle into the surrounding matrix of copper, thus creating undesired bronze.

If transverse pressure is applied to a strand, in which a shear plane was generated during the cabling operation, the affected areas tend to collapse. The shear planes generally cut through the entire strand, thus interrupting the current flow of all filaments, since these are twisted around the center in the longitudinal direction.

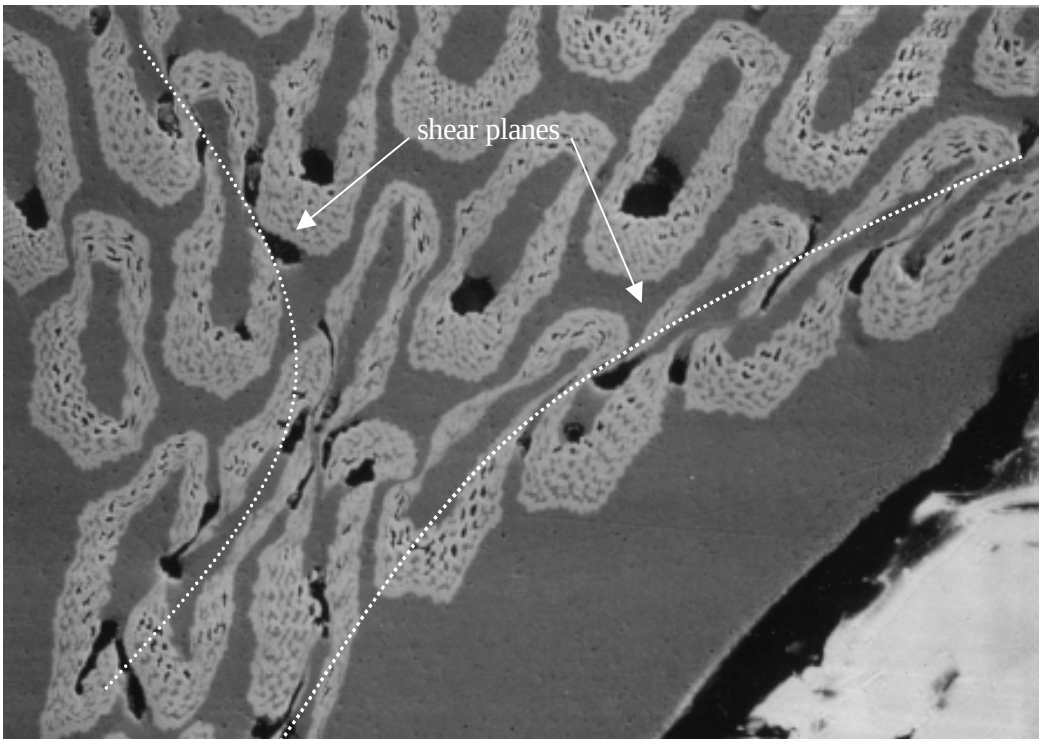

Figure 6.2 Close-up of the corner of an MJR strand after cabling, and reaction. Two shear planes are visible, one from the top left of the picture to the bottom left, the other from the top right to the bottom left.

The copper matrix around the sheared elements is polluted by tin leaking out of the individual bundles, thus decreasing the RRR[1] of the copper, further diminishing the current sharing capability of the strand locally. This has a two-fold effect on the critical current I_c of the cable. The local critical current density j_c of the sheared bundle will be far lower than that of the surrounding elements, causing the super-current to transfer to the surrounding filament bundles. Normally this would not cause a significant I_c degradation, since the resistivity of the matrix material should be low. However, with a contaminated matrix, the resistance of this normal bridge is orders of magnitude larger. This will effectively lower the overall critical current of the cable, but which is not directly affected by the application of external pressure. The presence of tin in the copper matrix was confirmed with X-ray diffraction techniques. Checking the RRR value of a deformed wire sample is a good indication whether this type of damage is present. Normal values of RRR are 40-60 at 10 T, and 2-10 for tin contaminated wires. The measurement is done on several of the extracted strand experiments, and also on a reacted coil segment, but not further discussed here.

Figure 6.4 shows a strand with a shear plane that is reacted and then subjected to transverse compressive stress. The entire area around the shear plane has collapsed under pressure. The shear planes tend to cause large areas of structural damage under compression, but are only found in strands of cables that are severely deformed during the cabling operation.

[1] RRR or Residual Resistivity Ratio is defined as the ratio of the resistivity at room temperature and the resistivity at the operating temperature (in this case 4.2 K). Since the composite wire (copper and superconductor) is superconducting at 4.2 K, the resistivity of the copper cannot be measured at that temperature. The RRR of the wire is generally quoted as the ratio of the resistivity at room temperature and the resistivity just above the critical temperature (usually around 20 K).

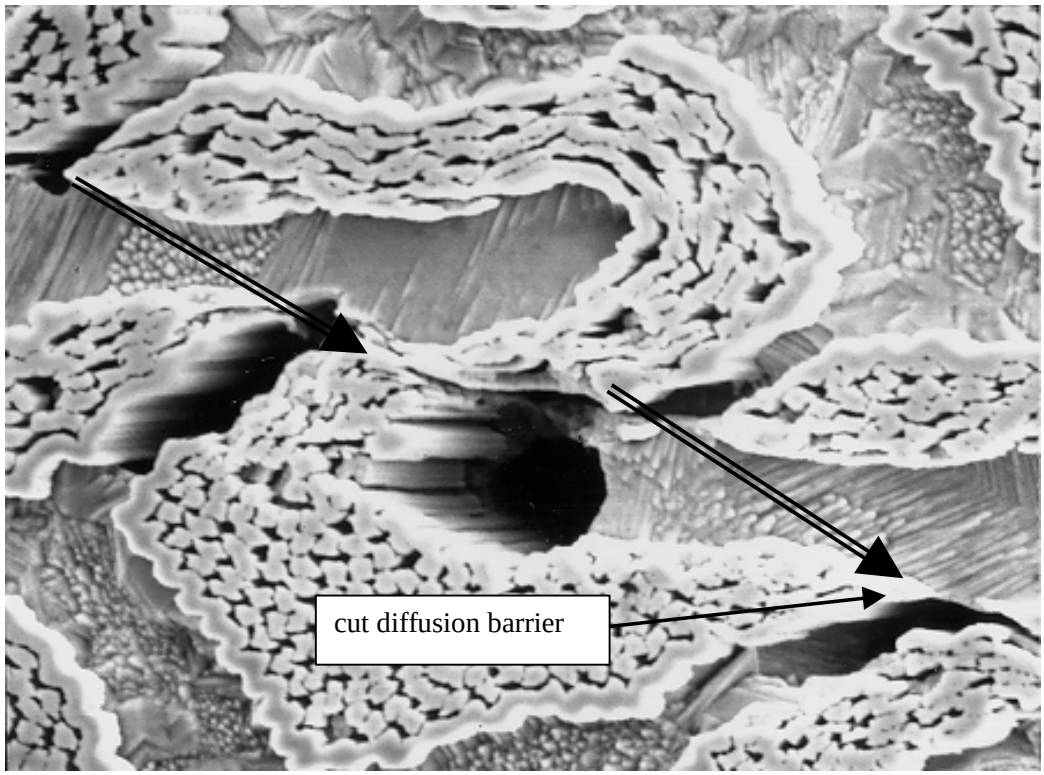

Figure 6.3 Close-up of an MJR filament bundle that was sheared during the cabling operation. The picture taken is of a reacted and etched sample to show the filament structure more clearly. Note the cut diffusion barrier.

Broken diffusion barriers were also found in the IT conductor on one occasion. In this particular case, it is unclear whether the cut in the barrier was caused by the cabling operation, or whether a thinned out region was already present in the strand before cabling. It is reported here, because the resulting leakage of tin is similar to that in the MJR conductor. Figure 6.5 shows the broken barrier found in the IT strand. Some cracked filaments are visible in the corner of the lower filament bundle near the cut in the barrier. These cracks are most likely due to the voids between the filaments.

6.2.3 Damage due to excessive strain on the filament structure

Figures 6.6 and 6.7 show transverse cracks in filaments that are most probably introduced by excessive axial strain on the strands. The cracks can be caused by a mismatch in the thermal contraction coefficients of the cable and other structural support components in a magnet, or in the case of a sample test, between the cable and the reaction or test holder.

The sample shown in figure 6.6 is taken from the side of a U-shaped cable sample of a critical current test, that was not subjected to transverse pressure. The damage is most likely caused by mishandling of the sample, such as excessive bending during installation or transportation.

The sample shown in figure 6.7 is taken from the flat section of a U-shaped cable sample that has been subjected to transverse pressure. Apart from some stress damage, similar cracks are found here, indicating the sample was also stretched past the irreversible limit. This could be due to the applied transverse pressure (the sample is compressed in the transverse direction, which causes an elongation in the longitudinal direction), but could also be due to mishandling of the sample.

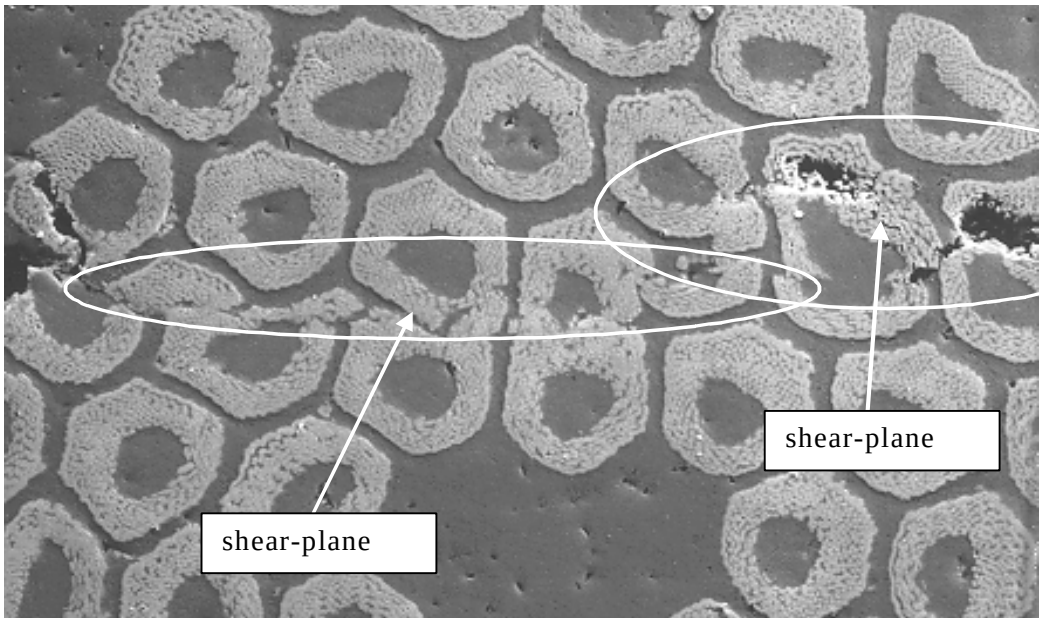

Figure 6.4 *Collapsed shear-plane in an MJR wire. This wire is damaged during the cabling operation. After reaction, the area where the wire was sheared and collapsed under pressure, as is illustrated by the absence of the voids in the shear plane that were present before the pressure application (see figures 6.2 and 6.3).*

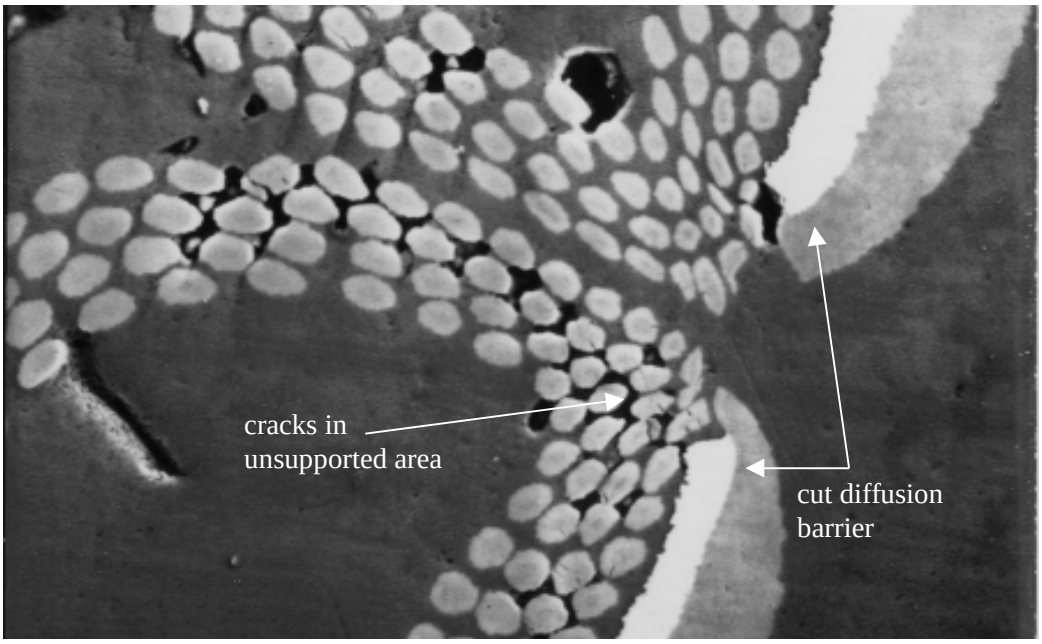

Figure 6.5 *Damaged diffusion barrier in an IT conductor. Note the cracks in the filaments near the cut in the barrier.*

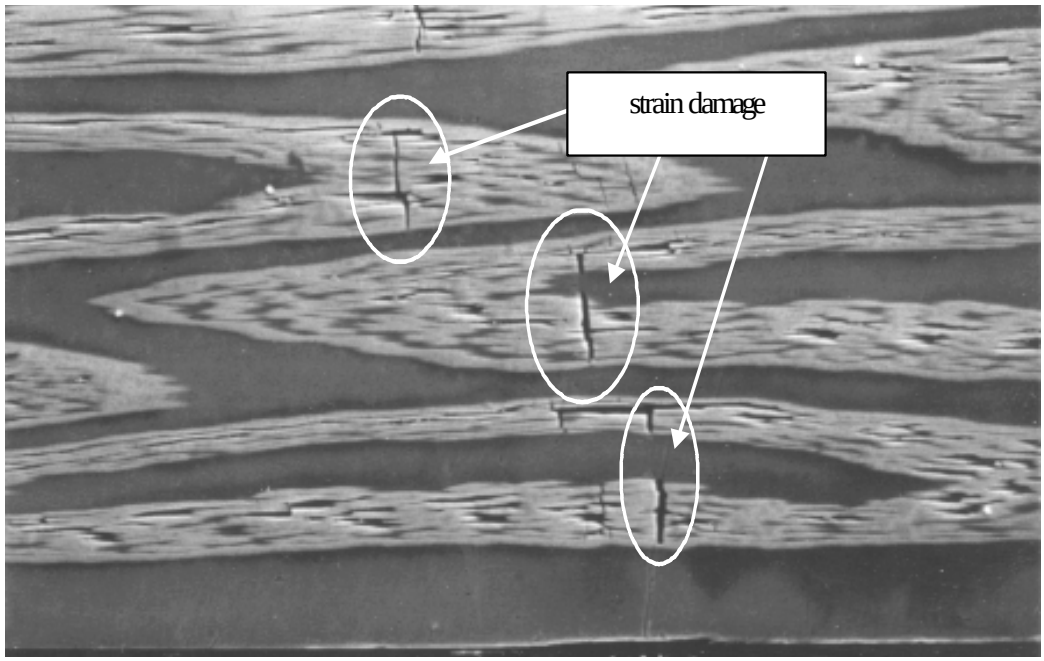

Figure 6.6 Slanted view of damage by excessive strain in the filaments. This type of damage is found in filaments that have been strained past a maximum value relative to the neutral state of the Nb_3Sn (about 0.2 % from the neutral state), usually by excessive tension or bending of the sample.

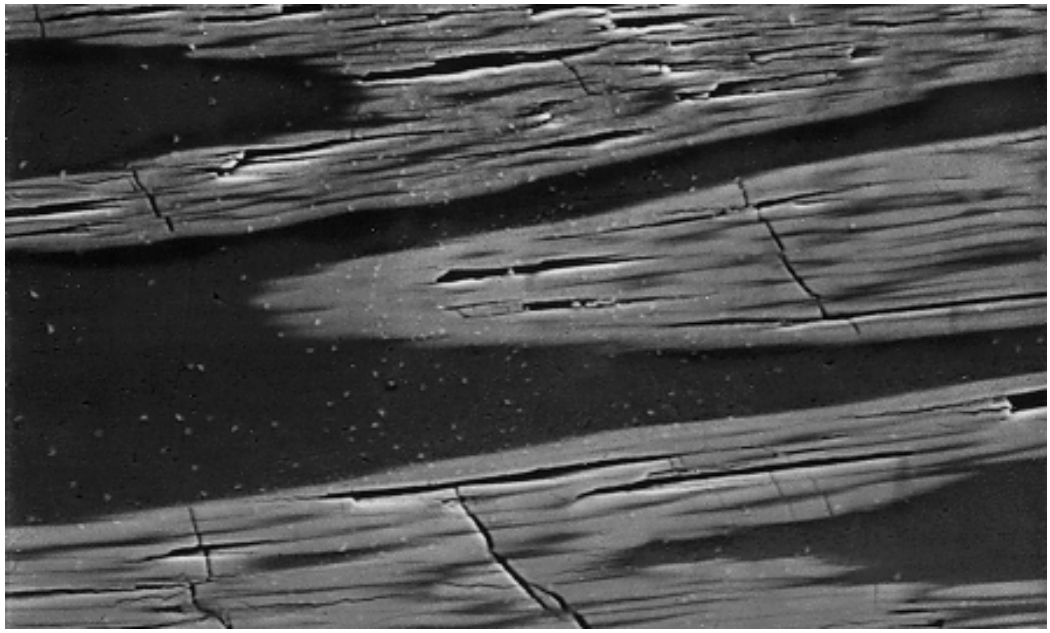

Figure 6.7 Second example of filament damage due to excessive strain. This sample is taken from the compressed section of cable.

In the MJR conductor, the cracks tend to interrupt the current flow inside the individual bundles, but are not propagating through the niobium diffusion barrier. The current can thus still be redistributed through the copper matrix between the filaments.

Crack damage can only be recognized by measuring a slightly lower n-value of the superconducting to normal transition in the *UI*-curve, and is difficult to detect without micro-photography.

6.2.4 Damage due to excessive transverse stress on the filament structure

When transverse pressure is applied to a wire, or a strand in a cable, both the longitudinal strain and transverse stress are increased. Increasing the transverse pressure on the conductor above a certain level tends to produce damage to the filaments.

Particularly in the IT samples, a significant number of cracked filaments are found for loads above 100-125 MPa. This damage is due to the localized plastic deformation of the matrix material, which in turn deforms the filaments past their breaking strain. In general, the damaged areas are concentrated around structural defects already present in the structure before compression, as is already discussed in chapter 4 (see discussion of figures 4.21 and 4.22).

Figure 6.8 shows the un-compressed area of a MJR conductor sample. Only after applying very large compressive loads up to 250 MPa, damage to all filaments is obvious, as shown in figure 6.9 for a same sample of MJR conductor. Damage due to very high loads is visible in both the IT and MJR type conductors. A problem most evident in the MJR conductor is the further damage done to the structure if a sheared area is already present. This type of damage is a combination of structural damage due to the cabling operation and subsequent excessive transverse pressure.

During the reaction process, voids are formed in the sheared region due to tin migration to other areas and into the copper matrix. This yields a structurally weak region that tends to degrade further when transverse pressure is applied. Since such sheared areas can affect large sections of a strand, it can severely limit its current carrying capability.

It essentially means that the MJR conductor is sensitive to applied transverse pressure if it is damaged during the cabling operation. In the case of a cable with low compaction, the MJR conductor shows less sensitivity, only degrading slightly under transverse load. It can be concluded that the MJR material will perform fine if it is treated carefully, as is proven by the samples showing no critical current degradation.

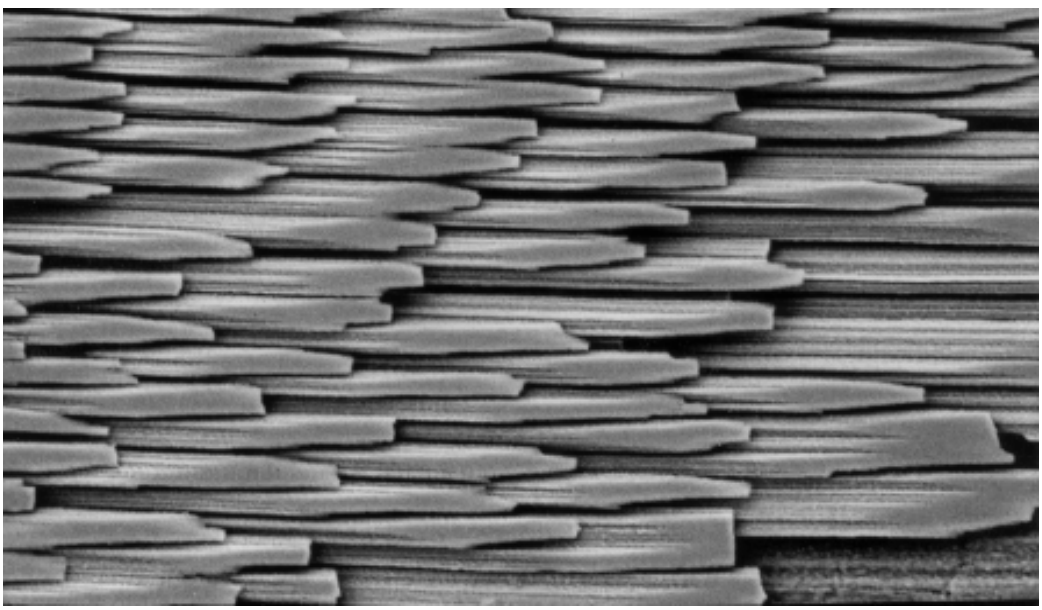

Figure 6.8 Slanted view of the filaments of an MJR conductor: the filaments in this picture were not subjected to transverse strain.

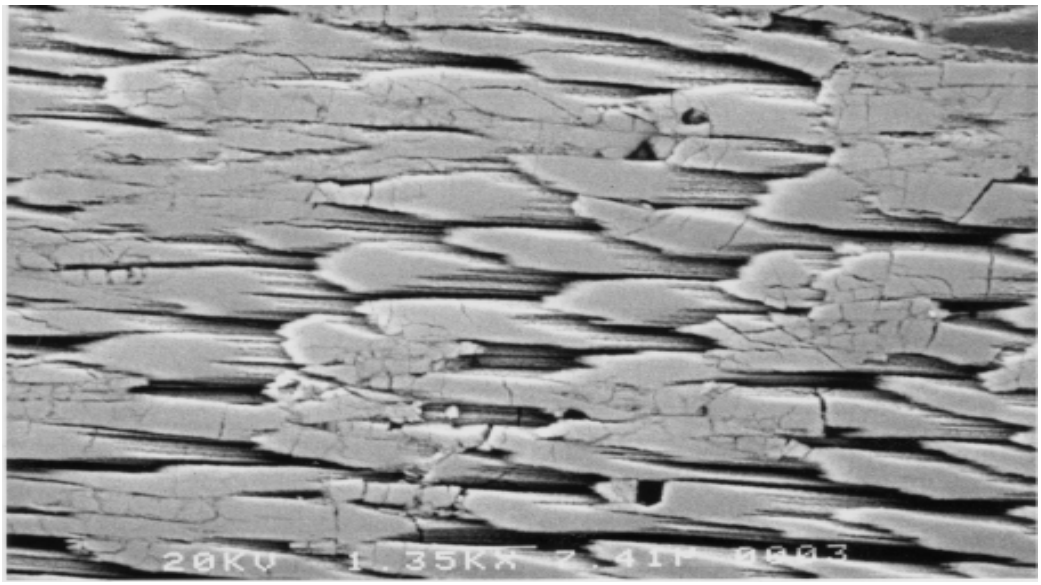

Figure 6.9 Slanted view of stress damage in the filaments of an MJR conductor: the filaments in this picture were subjected to a transverse compressive load of 250 MPa. This pressure exceeds the yield strength of the matrix material, and causes the filaments to crumble.

Figures 6.10 and 6.11 show a similar pair of pictures, taken from another cable sample. Again, structural damage is visible in the sample when it is subjected to large transverse compressive stress.

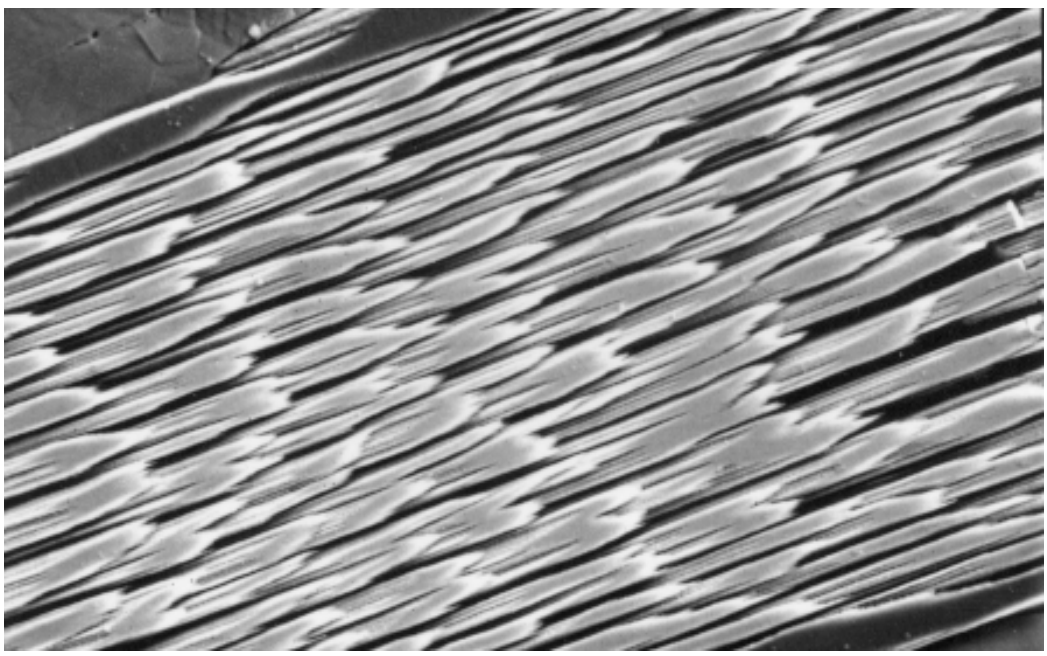

Figure 6.10 Slanted view of un-damaged filaments.

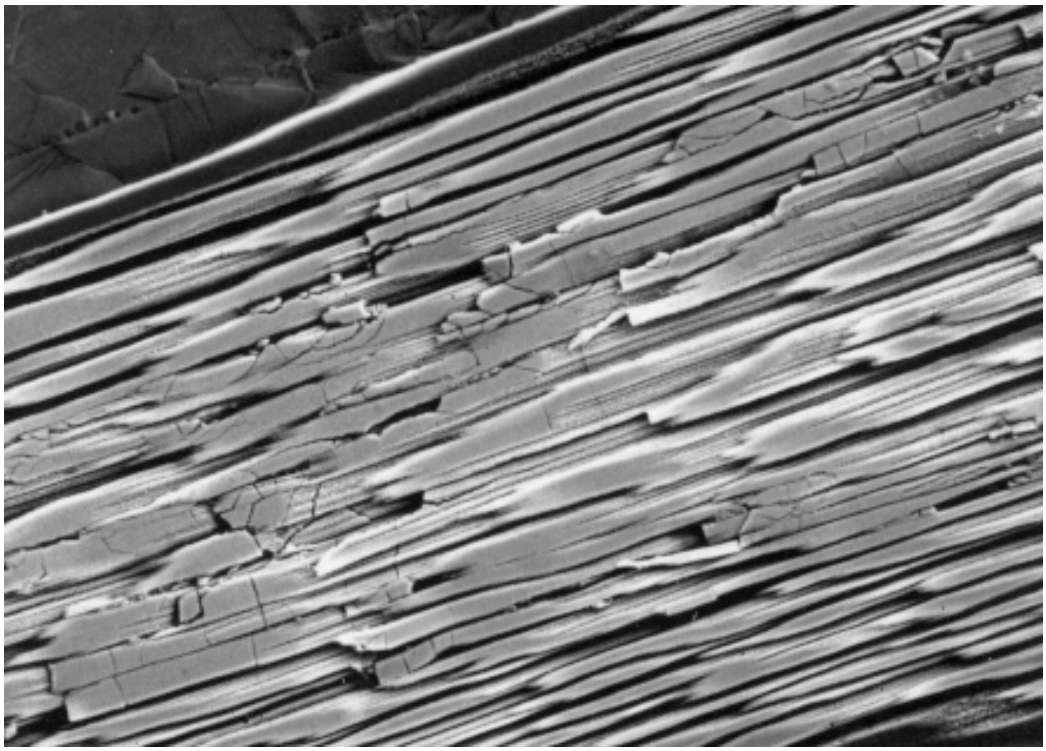

Figure 6.11 Slanted view of stress damage in the filaments.

6.2.5 Damage due to intrinsic defects in the material

In chapter 4, it is suggested that voids formed in the filamentary area, or in the center of a filament bundle, can enhance structural damage due to transverse pressure. In this section, the correlation between the location of the voids and structural damage caused by transverse pressure is investigated through the use of SEM photographs.

The goal is to show clear examples of structural damage concentrated around the voids when a sample is stressed, and to compare these to the same type of voids without damage if no stress is applied. First, the voids most commonly found in IT conductors are discussed, followed by the voids in the MJR conductors.

Figure 6.12 shows the most common damage found in the samples. In this sample, voids were present in the filamentary area. When the sample is deformed due to transverse stress, the areas near the voids tend to crack or collapse, causing damage to the filaments. This effect is most pronounced in the IT conductor, especially in the corners between the three filament bundles, and in the inside edges of heavily deformed filament bundles where large voids are present.

Figure 6.13 shows a similar large void in the corner between the filament bundles. In this particular picture, the damage shown in the lower circle might be due to sample preparation. Figure 6.14 shows a large void with small hairline fractures visible in the filaments. Note there is no suspected polishing damage in this sample.

In the MJR conductors, void formation is restricted to the interior of each individual filament bundle. Any voids migrating through the filamentary area accumulate just at the inside of the diffusion barrier surrounding each bundle.

This means that, unlike in the IT conductors, there is no large void formation in the corners between the filament bundles. Large voids are only found in the center of the filament bundles. Smaller voids are found spread around the filamentary area.

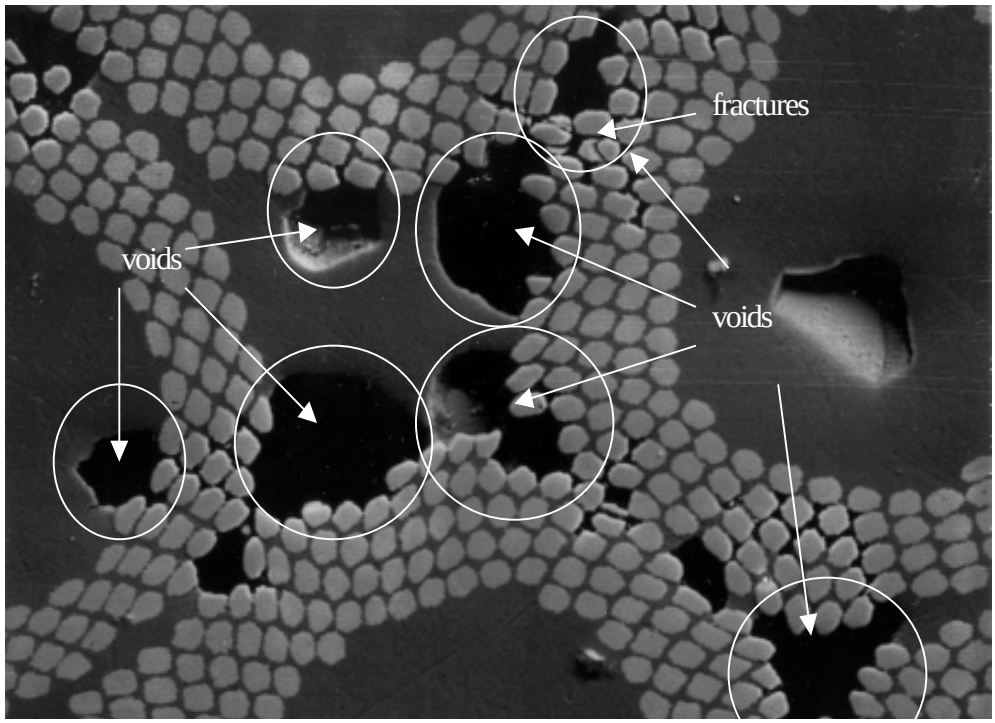

Figure 6.12 IT conductor with large voids, not subjected to transverse pressure. A few fractured filaments are visible.

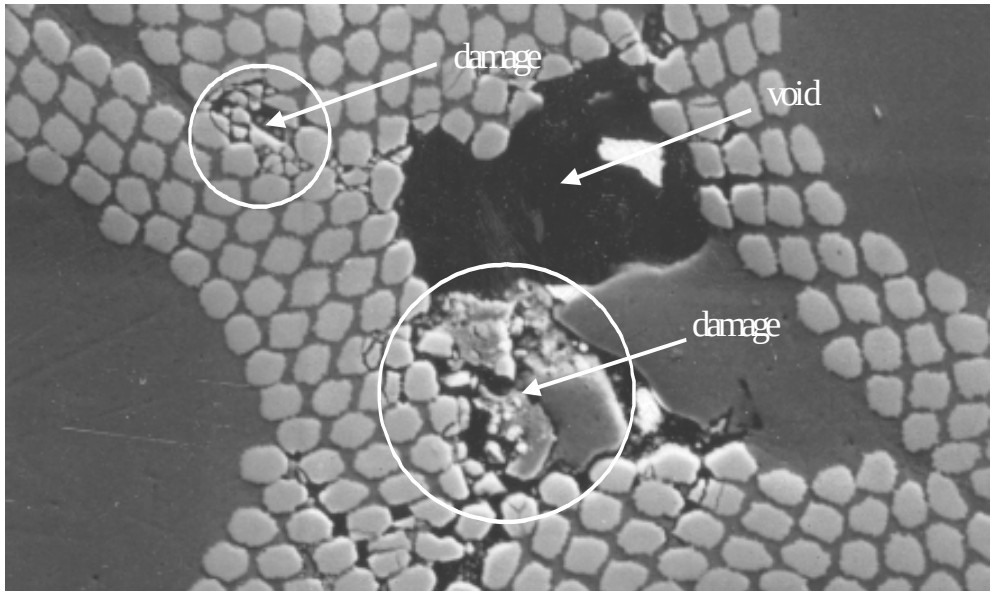

Figure 6.13 This sample has some large voids at the corners between adjacent filament bundles. One large void is shown in the picture. Damage to the filaments due to transverse stress is visible. Some of the damage marked in the lower circle might be due to sample preparation.

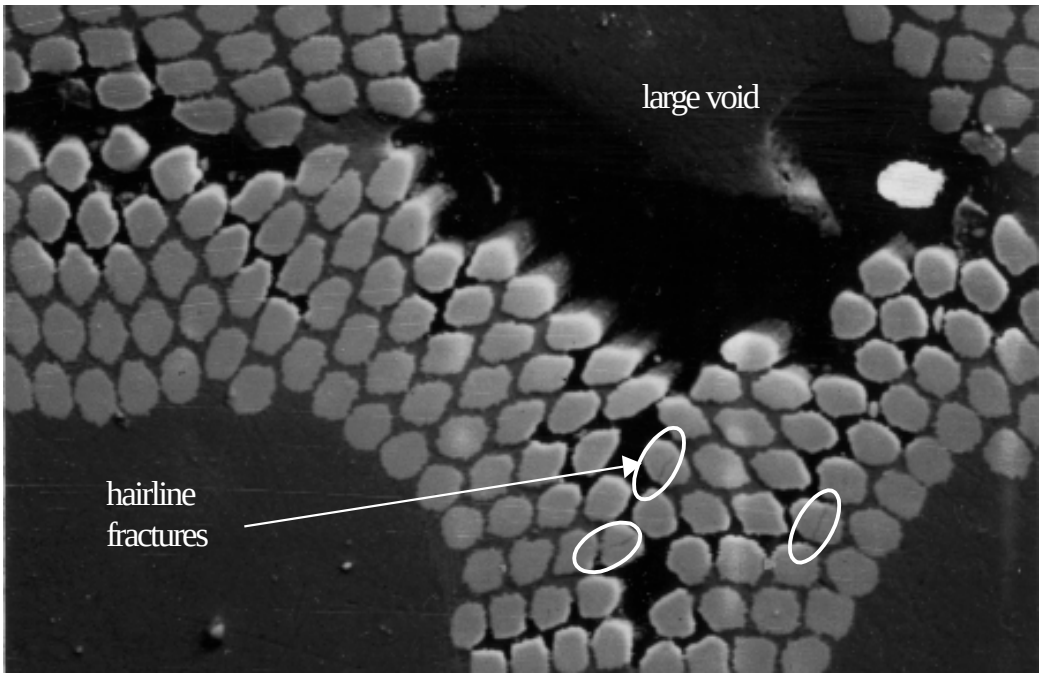

Figure 6.14 Close-up of a large void between the filament bundles in an IT strand. The strand has not been subjected to transverse pressure. Note a few hairline fractures in the filaments.

Figure 6.15 shows a close-up of the filamentary area of an MJR strand. Note the larger voids in the center of some of the filament bundles, and the small voids spread in between the filaments in all bundles. This particular sample was not subjected to transverse stress; no structural damage to the filaments is observed.

In figure 6.16 the cross-section of an MJR strand that has been subjected to transverse pressure is shown. This picture illustrates how the filament bundles developed stress fractures in the areas with small voids in the filamentary area.

No large fractures are observed near the larger voids in the center of the filament bundles. The stress fractures are consistent with the deformation of the strand in the horizontal direction, due to compressive stress in the vertical direction.

The damage observed in the picture confirms the results from the generic FEA models in chapter 4, where the highest stress areas are found in the filament bundles just above and below the center of the strand. Also, the damage is more severe in bundles with small voids throughout the filamentary area, as compared to bundles with large voids in the center.

Finally, figure 6.17 shows a close-up of a filament bundle of an MJR strand that has been subjected to transverse stress. The stress was applied in the horizontal direction. Note the stress fractures in the filamentary area.

As a continuation of this investigation, a series of MJR reacted cables with a uniform cross-section, *without voids*, loaded up to 200 MPa in steps of 50 MPa, did not show significant damage in the cross-section.

The results from that study suggest that the internal structure of the filamentary area is an important factor, and the location of the voids in the cross-section plays an important role in the formation of permanent degradation.

This conclusion is the same as the one found in chapter 4 from the FEA model studies of the effect of voids in the cross-section. This led to a further investigation of the effect of the Kirkendall voids in the critical current degradation, and a study on how to influence the location of the voids, or eliminate them altogether. The work is further described in sections 6.4 through 6.6.

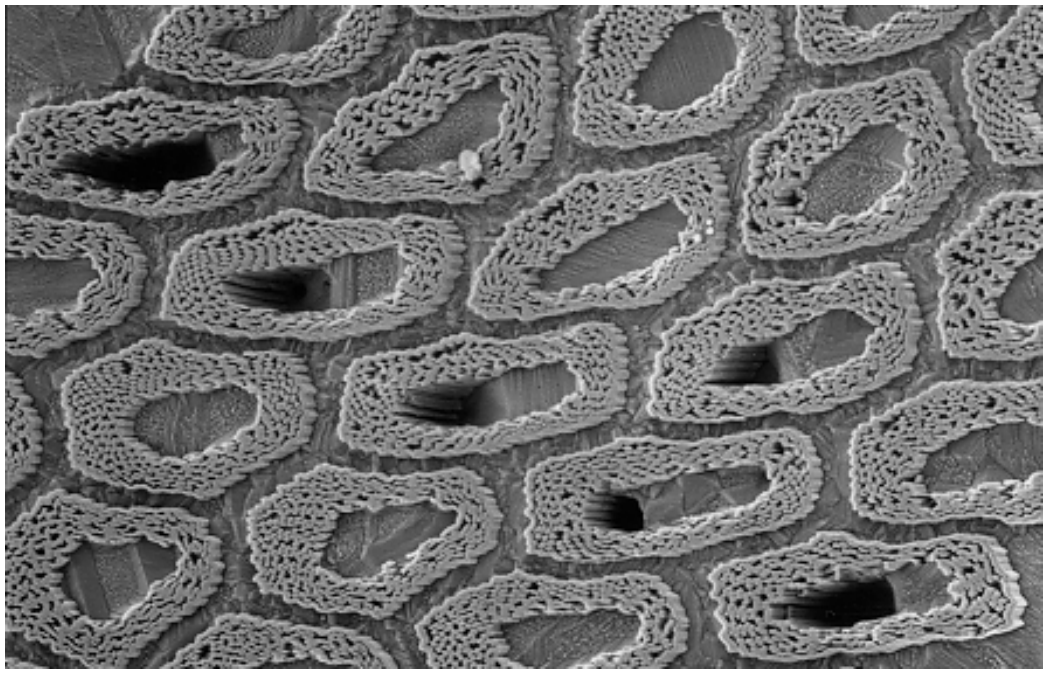

Figure 6.15 Close-up of the filamentary area of an MJR strand that was reacted, and then etched. The strand was not subjected to transverse stress. No damage to the filaments is observed in the picture.

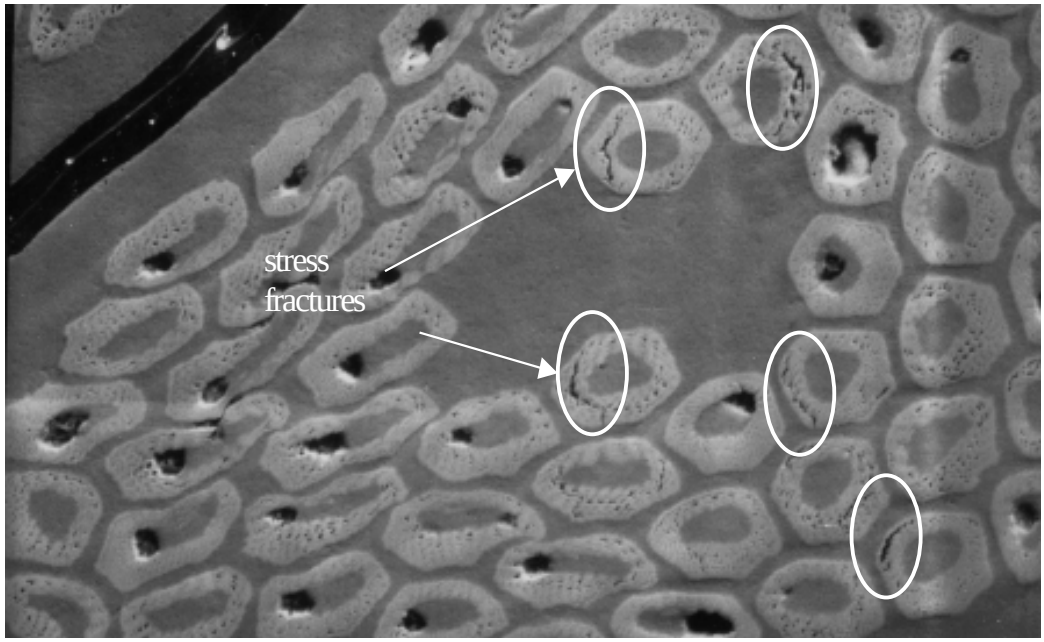

Figure 6.16 Cross-section of an MJR strand that was subjected to transverse stress in the vertical direction. Note the vertical stress fractures in the filament bundles near the center of the strand.

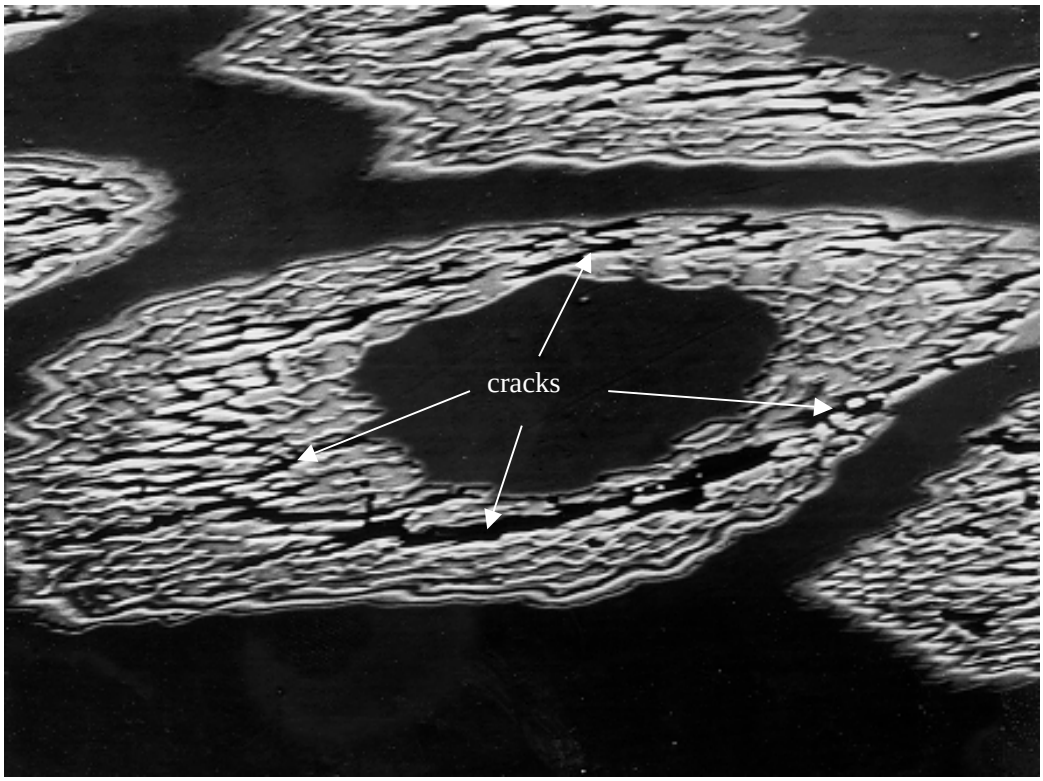

Figure 6.17 Slanted cross-section of a filament bundle of an MJR strand that was subjected to transverse stress in the horizontal direction. Note the cracks throughout the filamentary area.

6.2.6 Voids as a cause of permanent critical current degradation

The SEM analysis of the loaded sections and the unloaded sections of the tested cables suggest the permanent critical current degradation to be caused by irreversible damage to the filaments. Photographs further indicate that most of the structural damage is concentrated around the voids in the filamentary areas. The effect is evident in pictures taken of the MJR conductor as well as the IT conductor. Evidence of increased damage in the IT conductors due to void formation is described next in more detail.

For the IT conductor, the voids seem to be the major cause of the permanent critical current degradation. Unlike the MJR conductor, the strands have one double diffusion barrier around the entire filamentary zone. The structure is inherently stronger due to the higher Young's modulus of the tantalum barrier material (E = 186 GPa for Ta versus E = 103 GPa for Nb). The filament bundles are thus less prone to cabling damage. However, during the reaction process, a large amount of voids is formed in between the filaments.

Depending on the reaction parameters and the initial amount of tin present in the cores, the voids either end up in the center of each bundle, or are scattered throughout the filamentary areas. Usually, a mix of both cases is present, essentially forming a very fragile internal structure.

When the structure is subjected to an applied external load, the voids tend to deform heavily, and filaments tend to shear and shatter close to the boundaries between the individual bundles. This effect causes considerable permanent damage to the filament structure, causing a drop in the critical current of the strand.

6.3 Avoiding cabling damage and excessive strain and stress

The first three types of damage listed in section 6.2 can be avoided by an optimized cable design, and proper treatment of the cable before, during and after reaction. The serious damage caused by an improper set of cabling parameters, such as shear planes and broken barriers, is fairly rare. This type of damage is avoided by keeping the cabling parameters within safe ranges, such as are described in chapter 5.

Likewise, type 2 and 3 damage (excessive strain and stress) can be avoided by keeping the strain and stress within safe limits. Tensile strain limits are not treated specifically in this thesis, but in general a limit of 0.2 % tensile strain is used as an ultimate limit before filament breakage occurs (the limit is taken from the neutral state of the Nb_3Sn).

Excessive stress is a function of the wire and cable geometry, as discussed in chapter 5. Again, safe limits can be established for each conductor type. Keeping the transverse stress below these levels minimizes structural damage caused by excessive stress on the filaments.

6.4 The role of Kirkendall voids in critical current degradation

The correlation between the stress concentrations computed with the FEA models in chapter 4, and the Scanning Electron Microscope (SEM) photographs of the damaged filament bundles and strands were analyzed in section 6.2. The comparison between the predictions and the actual damage photographs points to the voids in the structure as one of the causes of the permanent critical current degradation.

Here, the locations where the voids are most likely to occur in the strands are investigated. To study the void formation process, a diffusion couple study (a diffusion experiment with a well defined interface between two dissimilar metals) is performed. Furthermore, a possible solution is proposed to reduce the sensitivity of the material by relocating the voids to areas where they will be less harmful.

Finally, a reduction of the void spaces is investigated by performing a Hot Isostatic Pressure (HIP) treatment on the conductor during the reaction process after the phase where the voids are formed.

6.4.1 Influencing the location of the Kirkendall void formation

By controlling the location of the voids during the tin diffusion and reaction steps, the sensitivity of a cable to compressive load may be influenced. It was found that moving the voids to the center of the bundles reduced the permanent degradation under transverse pressure. Figures 6.5 through 6.7 show that it is indeed possible to obtain a cross-section with the voids concentrated in a specific area.

The effect is similar for both MJR and IT conductor types, but cross-sections of IT conductors are used here for the illustration of the effect, since the lower magnification needed for the pictures shows the localization of the voids more clearly.

Figure 6.18 shows the cross-section of a typical IT wire. Voids are scattered across the filament bundles, and are concentrated in different radial rings in each filament bundle.

The location of the voids is not very well defined, and there is no obvious correlation between the location of the voids within the bundles, and the location of the bundles within the wire. Since this wire was subjected to a uniform temperature across the cross-section during reaction, a different reaction temperature or ramp rate cannot be the cause of the different distribution of the voids.

This points to an internal variation in the initial tin content, such as a variation in thickness along the length of the wire of the tin core, the so-called *sausaging*, as a possible cause of the variation in the void locations. This possibility is further investigated here.

In figure 6.19, a close-up of the central filament bundle is shown. In this particular bundle, there is a large void present in the center of the filament, and a series of smaller voids in the inner filament ring of the bundle. Figure 6.20 shows a cross-section of a wire with the voids primarily located in the outer rings of the filament bundles.

The correlation between the void location and the size of the tin core within the filament bundle is investigated here. Figure 6.21 shows the same IT wire as in figure 6.18, with ellipses inscribed within the outer boundary of the tin core of each bundle. The average area of the ellipses within the bundles with the voids located near the inner rings is compared to that of the bundles with voids in the outer rings.

Table 6.1 lists the average areas found. Also, the average area of each bundle ring from the inside to the outside of the wire is given.

Area [μm^2]	Void in inner rings	Voids in outer rings	Center bundle	Middle bundle ring	Outer bundle ring
Average	4570	5500	4970	4880	4770
St. dev.	400	400	-	700	600

Table 6.1 Average areas of the ellipses inscribed within the outer boundary of the tin-core of the bundles.

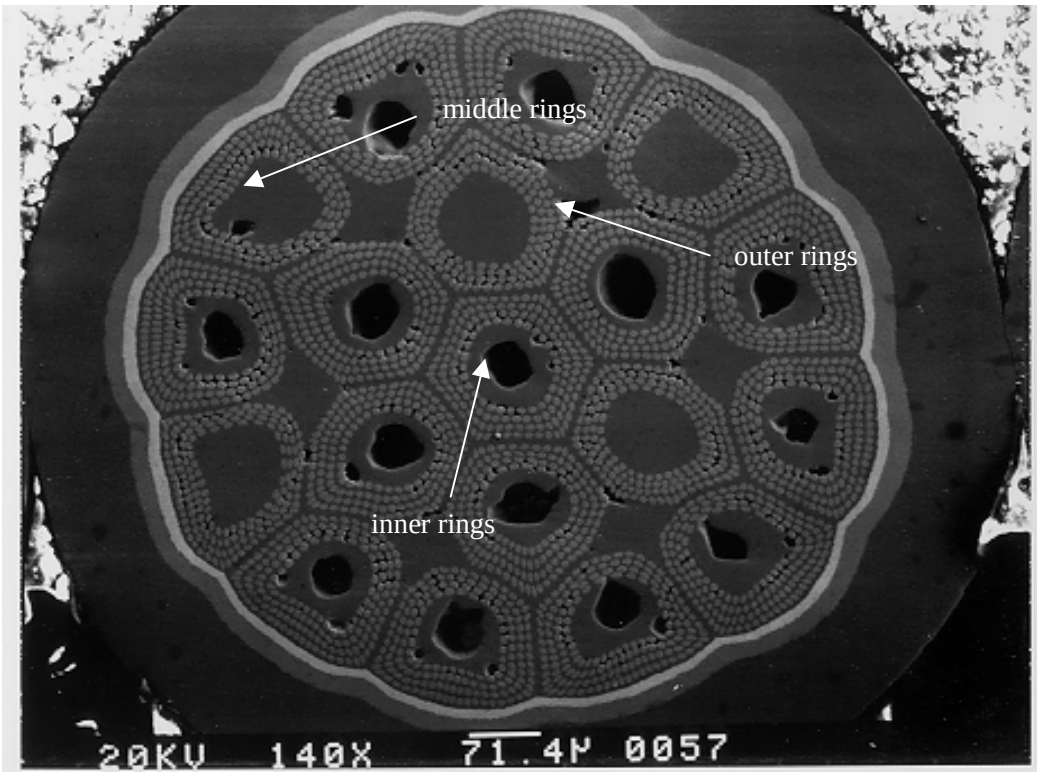

Figure 6.18 Cross-section of an IT wire showing the different locations of the Kirkendall voids in the filament bundles. The wire is built up of two concentric rings of filament bundles around one central bundle. Each filament bundle in this wire consists of four concentric rings of filaments. The arrows indicate regions where the voids are concentrated near the inner filament rings, the middle rings, and the outer rings.

A two-sample t-test [6.2] proves that the average area of the bundles with voids in the inner rings is smaller than that of bundles with voids in the outer rings. The corresponding P-value is 0.0012. Hence, it is concluded that a reduction in tin in the core causes the voids to be located near the center of the bundle, and conversely, an increase in tin in the core causes the voids to be located near the outer rings within the filamentary area. The decrease in average area of the tin-core from the center bundle to the outer bundles, although visible, cannot be proven statistically.

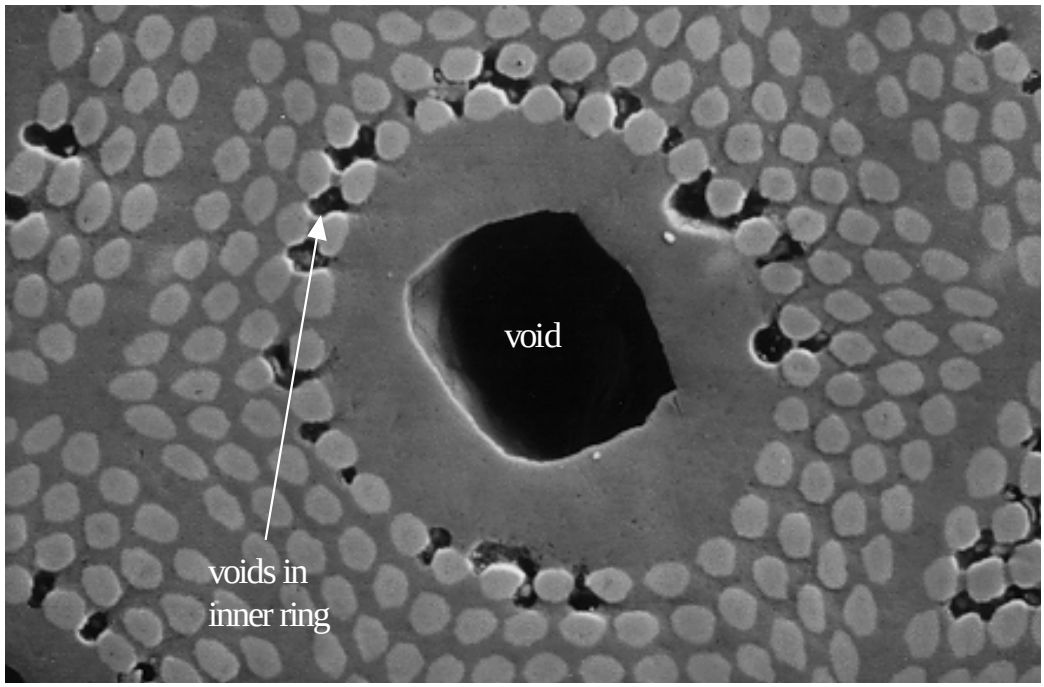

Figure 6.19 Close-up of the central filament bundle from figure 6.18, with the voids primarily concentrated in the inner rings of the filamentary area. Also, a large void is present in the center of the bundle.

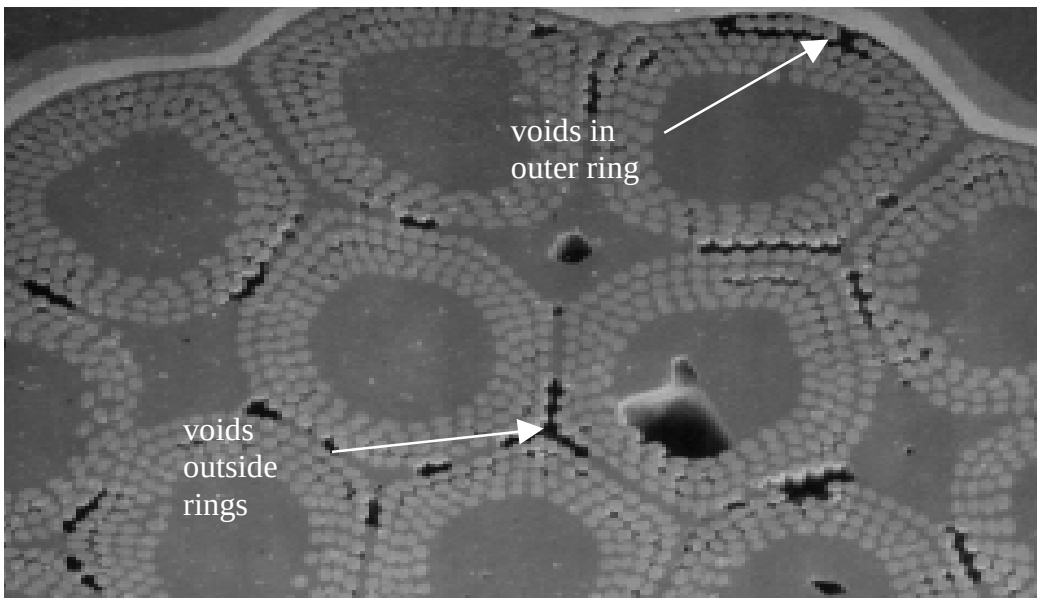

Figure 6.20 Close-up of several filament bundles with the voids primarily located in the outer filament rings and between the individual filament bundles.

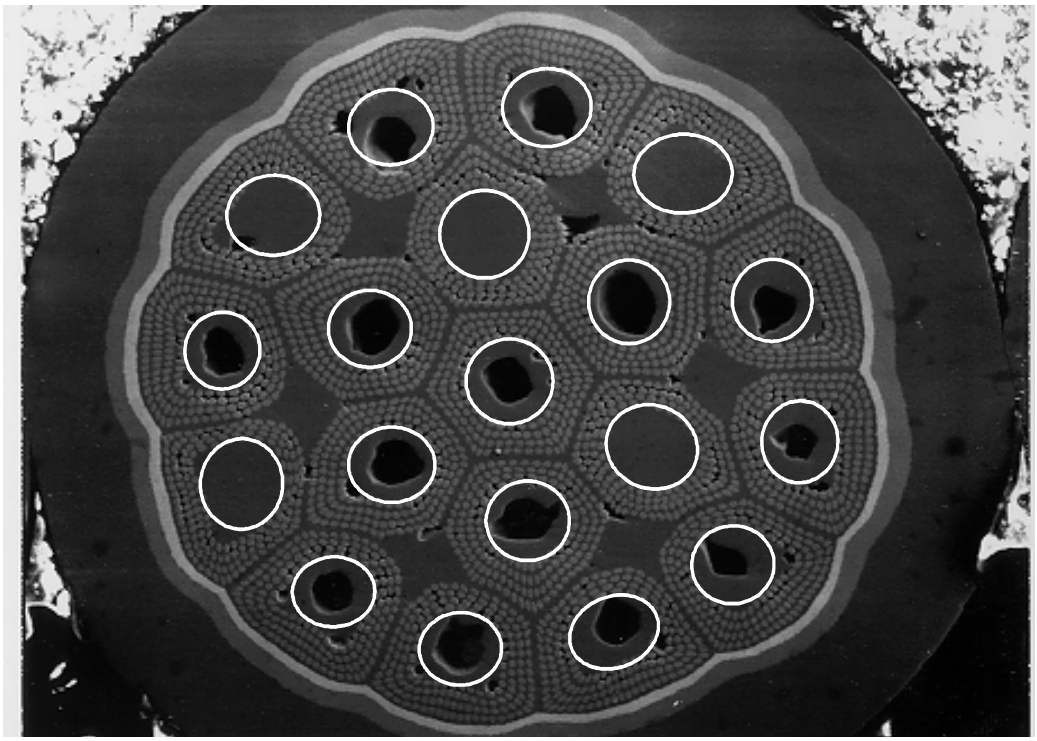

Figure 6.21 Cross-section of a typical IT-wire, with the largest ellipse inscribed within the outer diameter of the tin-core in each filament bundle. The area enclosed by the ellipses is correlated to the location of the voids within the filamentary areas.

A study of the tin diffusion in the copper-tin system is needed in order to understand the void formation. The following sections describe an experiment to analyze the tin-diffusion, and to relate the location of the void formation to the reaction parameters. A brief overview of the diffusion process in the reaction heat treatment is given first.

6.4.2 Tin diffusion in the Cu-Sn system

The heat treatment of the IT or MJR Nb_3Sn is performed in three distinct stages. The duration and the temperature of each phase stage depend on the precise optimization for a specified critical current, and the internal geometry of the wire. A typical heat treatment schedule [6.3] is shown in figure 6.22; this particular schedule is also used for the coils in the D20 magnet.

The first step in the heat treatment is the tin diffusion step at 210 °C, in which the solid tin core is slowly diffused through the surrounding copper matrix to form CuSn bronze. When the temperature is raised to 210 °C, diffusion across the boundary between pure copper and pure tin in both directions causes a change in the composition. The phase boundary migration process is illustrated in figure 6.23. The bronze is formed in order to provide the Nb filaments with a Sn source for reaction at the higher temperature. At the same time copper is also diffusing into the tin core. At the end of the diffusion step, at 210 °C, the bronze will eventually be composed of α-type solid solution (96.4 % Cu-3.6 % Sn), ε-phase (62 % Cu-38 % Sn or Cu_3Sn) and η-phase (39 % Cu-61 % Sn or Cu_6Sn_5).

The ratios of the phases depend on the initial amount of tin present, compared to the copper. The diffusion step is illustrated in the phase diagram in figure 6.24 by the bottom set of arrows [6.4]. The diagram shows the composition of the bronze formed at the interface as a function of the temperature, provided the diffusion process is allowed sufficient time.

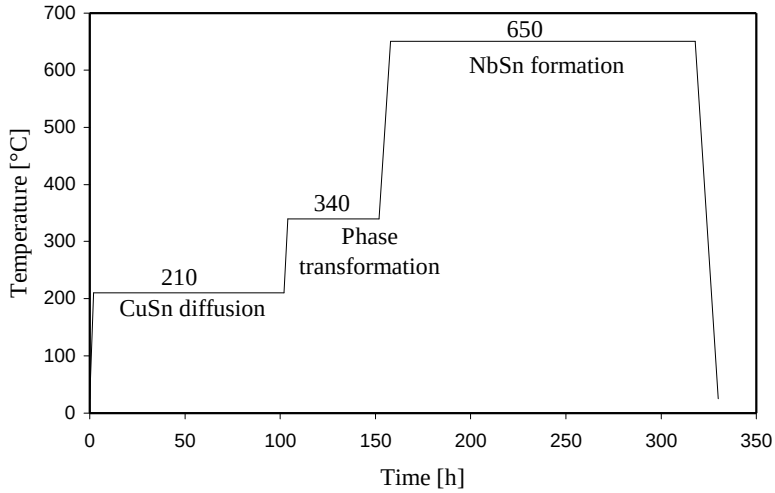

Figure 6.22 Typical heat treatment schedule for Nb_3Sn. Illustrated are the temperature and duration for the three stages in the diffusion and reaction process.

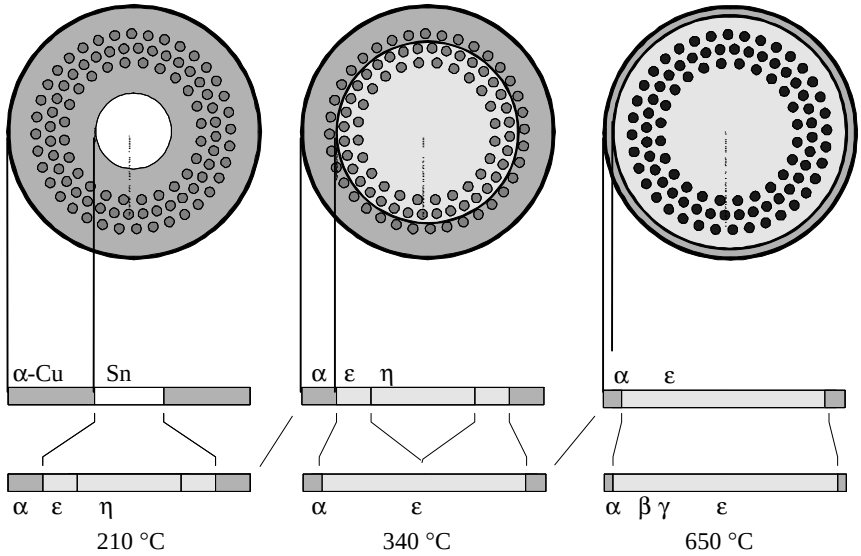

Figure 6.23 Schematic illustration of the phase boundary migration process for the three discrete temperature steps in the diffusion and reaction process.

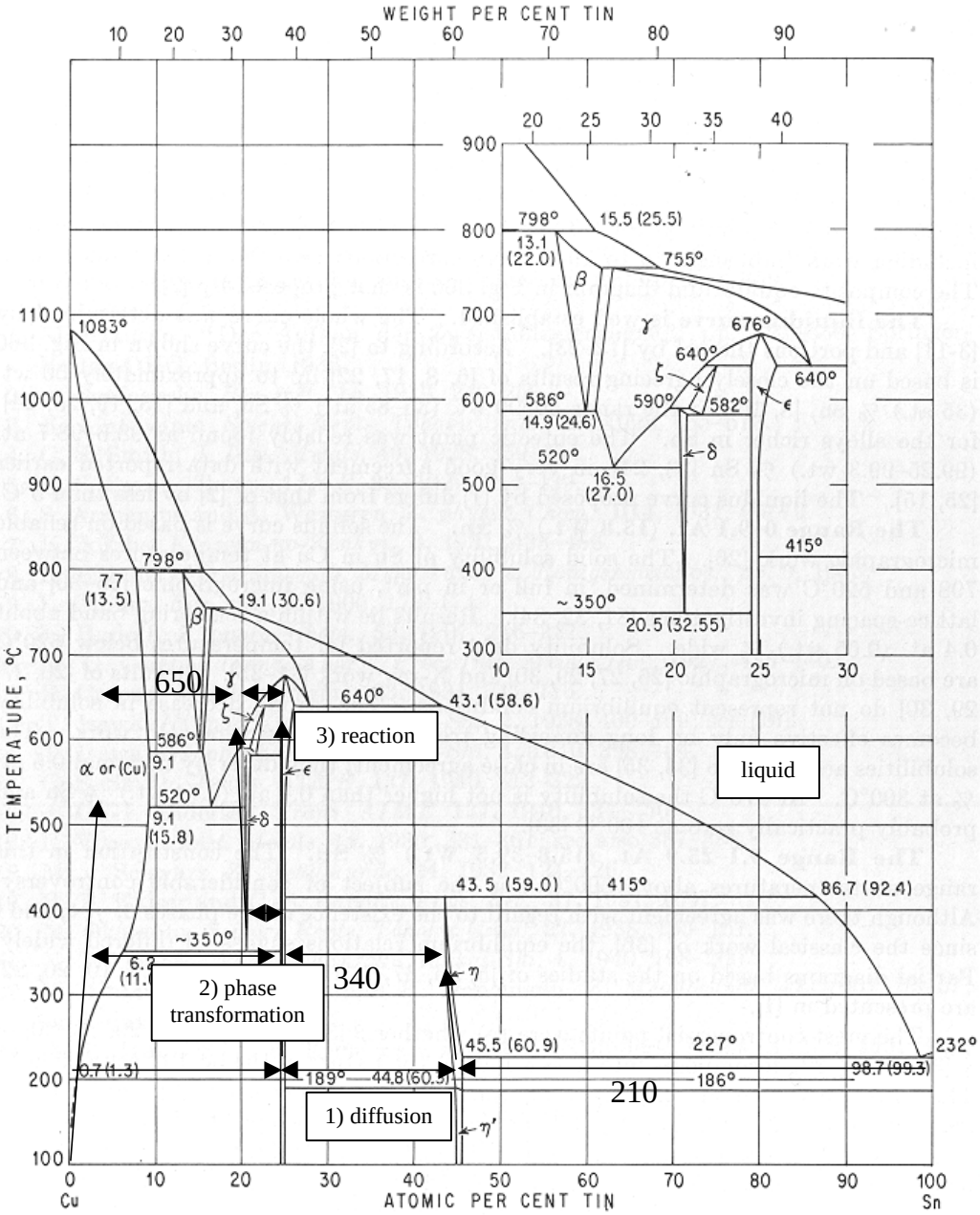

Figure 6.24 The Cu-Sn phase diagram and the reaction process temperatures. The arrows indicate the diffusion process at the three temperatures shown in figure 6.22.

As is shown in the Cu-Sn phase-diagram, the temperature in the first diffusion step has to remain below 232 °C to prevent the tin from melting before it is completely diffused into the surrounding copper. If the temperature exceeds 232 °C, the wire could deform due to loss of structural strength, or the tin could rupture the diffusion barrier contaminating the pure copper outer area.

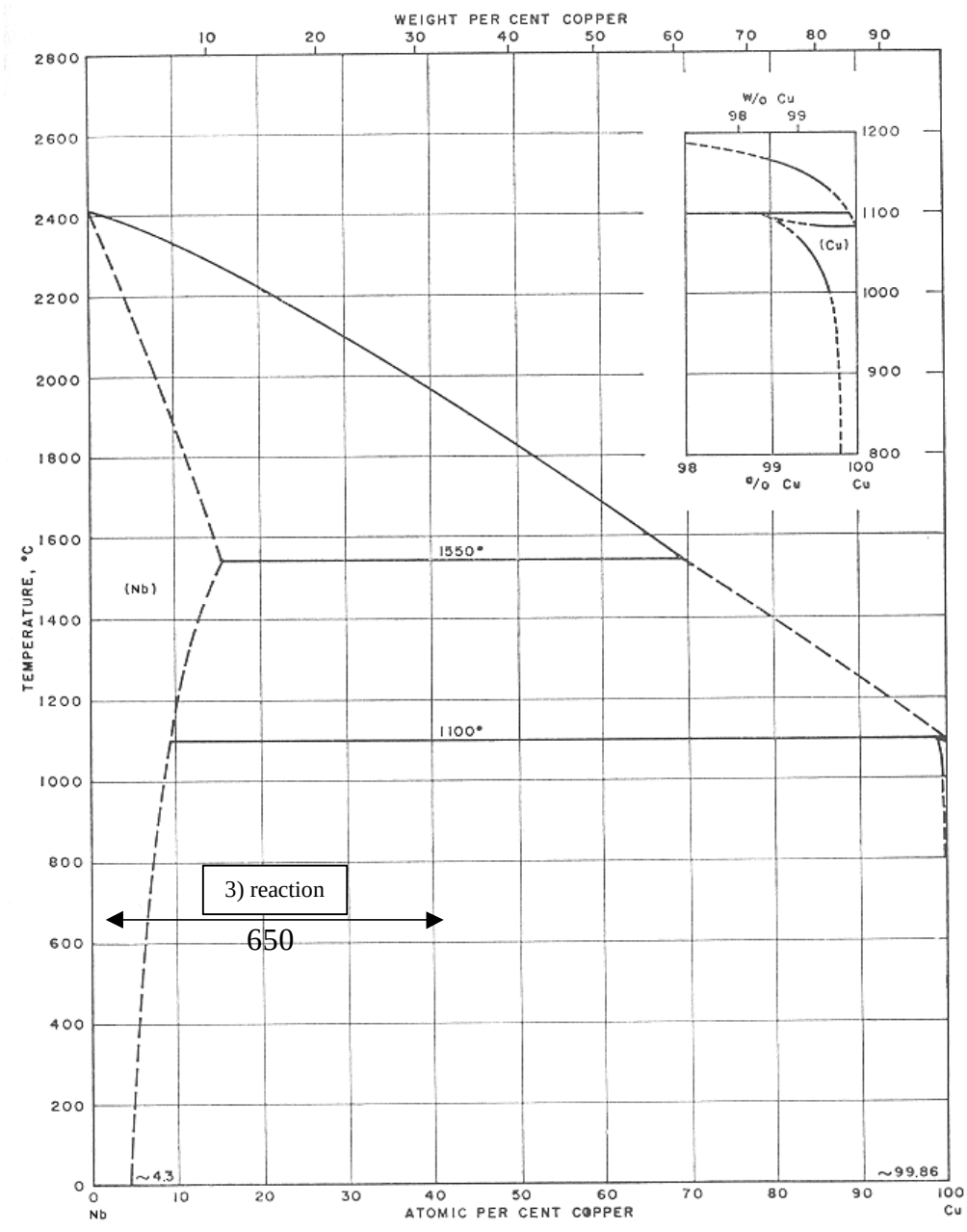

Figure 6.25 The Nb-Cu phase diagram.

At the same time, copper will diffuse into the tin in the core of the bundle at a different diffusion rate. The diffusion rate of the individual elements will prove to be an important factor in the void formation as discussed below.

The second step at 340 °C is a phase transformation of the remaining bronze η-phase into the ε-phase. This step is indicated by the middle set of arrows in figure 6.24. This step is included to ensure the proper amount of tin around the Nb for the Nb_3Sn formation.

The final step raises the temperature to 650 °C for the MJR conductor (up to 680 °C for the IT conductor). At these temperatures, the tin in the bronze reacts with the niobium filaments forming Nb_3Sn. This further reduces the tin-content of the CuSn bronze, thereby reducing the amount of ε-phase and γ-phase, and reducing the Sn content in the α-type solid solution (the ε–α phase boundary still moves further outward).

Figure 6.25 shows the phase diagram for Nb-Cu [6.5]. As is evident from the figure, diffusion of Nb into the copper is only a few percent at 650 °C. Figure 6.26 is a schematic representation of the resulting ternary phase diagram for Cu-Nb-Sn [6.6]. The figure is a best guess at the phase diagram, as literature data for a temperature of 650 °C is not available.

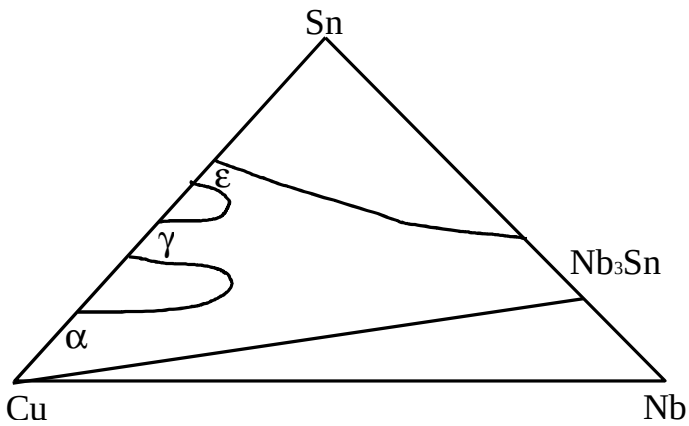

Figure 6.26 Schematic representation of the Cu-Nb-Sn ternary phase diagram at 650 °C.

The schematic of the ternary phase diagram shows the possible reaction paths from the different phases in the CuSn present at the initial stage of the 650 °C reaction step to form Nb_3Sn, as a function of the Cu concentration in the Nb. Nb_3Sn can form from all three phases of CuSn, but the Cu_3Sn ε-phase forms Nb_3Sn with the optimal amount of Sn present to maximize B_{c2}.

6.4.3 Enhanced stress sensitivity

During the diffusion and reaction phases, several processes take place that may influence the initial susceptibility to damage of the filament due to strain or stress. With the tin diffusing out faster into the matrix than the copper diffusion into the tin core, small voids form in the tin core. The voids will later migrate outwards towards the filament regions. These voids, however, are not the cause of the critical current degradation when the material is strained, since they are too small in size to cause any significant structural instability in the filament bundles.

Far more important are the voids formed at the initial stage of the high temperature step at 650 °C. These voids form due to the change in volume of the alloy when the different intermetallic phases form in the Cu-Sn. Table 6.2 shows the lattice constants of several Cu-Sn phases, illustrating the large difference in atomic volume.

The volume change from the larger copper and tin components to the smaller Cu_3Sn and Cu_6Sn_5 causes the formation of large voids (channels of about 50 μm diameter and several mm in length) at the boundary between the ε-phase and α-phase. The phase boundary migrates outward, into the filament region during the reaction phase. The voids migrate outward, following the phase boundary.

The final location of the voids is determined by the initial amount of tin available in the core of the bundle, by the concentration profile of the elements and the duration of the reaction step, determining the eventual location of the phase boundary. Furthermore, the reaction of the niobium filaments with the tin in the bronze also depletes the tin, creating local areas with the suitable concentration of copper and tin prone to form voids. Pictures of the actual void formation process are shown in figures 6.27 and 6.28.

Pure Cu to α-phase	d (nm)	ε-phase	d (nm)	η-phase	d (nm)	Pure Sn	d (nm)
Cu (111)	0.609	Cu_3Sn (100)	0.638	Cu_6Sn_5 (101)	0.696	Sn (200)	0.692
Cu (200)	0.181	Cu_3Sn (002)	0.616	Cu_6Sn_5 (110)	0.609	Sn (101)	0.679
Cu (220)	0.143	Cu_3Sn (101)	0.609	Cu_6Sn_5 (112)	0.162	Sn (220)	0.606
		Cu_3Sn (102)	0.160	Cu_6Sn_5 (103)	0.154	Sn (211)	0.602
				Cu_6Sn_5 (201)	0.171	Sn (112)	0.149
				Cu_6Sn_5 (202)	0.149	Sn (400)	0.143
				Cu_6Sn_5 (004)	0.128	Sn (321)	0.143
				Cu_6Sn_5 (300)	0.121	Sn (312)	0.121

Table 6.2 Lattice constants of the Cu-Sn phases [6.7] (as illustrated in the phase diagram in figure 6.23). The lattice constants are given in nm.

In figure 6.27, a sequence is shown illustrating the formation of voids in the core of the filaments. The pictures are of samples that have been reacted up to the temperature given under the picture, following the regular reaction schedule of figure 6.22. Upon reaching the listed temperature, the samples are then cooled down, and prepared for electron microscopy.

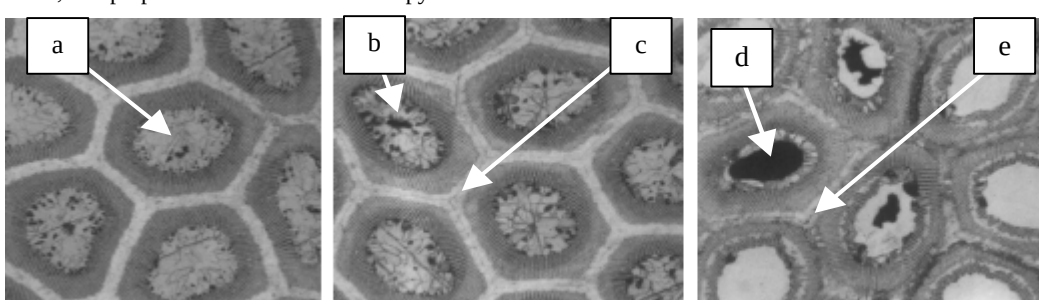

Figure 6.27 Photographs of the phases of the void formation in an IT conductor with increasing temperature. Note the increasing size of voids in the center of the bundles (a to b to d), and the formation of small voids between the bundles (c to e). The temperatures are chosen to represent the intermediate phase between the three reaction step temperatures.

From left to right, the first picture shows the onset of the void formation at the temperature ramp between the 210 °C and 340 °C step. The small voids (Kirkendall voids) are marked by the pointer labeled a. In the middle picture, taken just past the second diffusion stage, the small voids in the center of the bundles have grown slightly (marked b), and more small voids are forming at the outside of the bundles (marked c). The right picture, taken just before the final reaction stage, shows how the large voids form in

the center of the filament bundle (marked d), and the small voids still present at the outside of the bundles (marked e).

Figure 6.28 contains a clear illustration of the phase boundary migration from the core of the filamentary region to the outside. This sample has been reacted at 375 °C for 144 hours. The picture shows the ε–α phase boundary within the filamentary area (in the center filamentary area marked by the arrow).

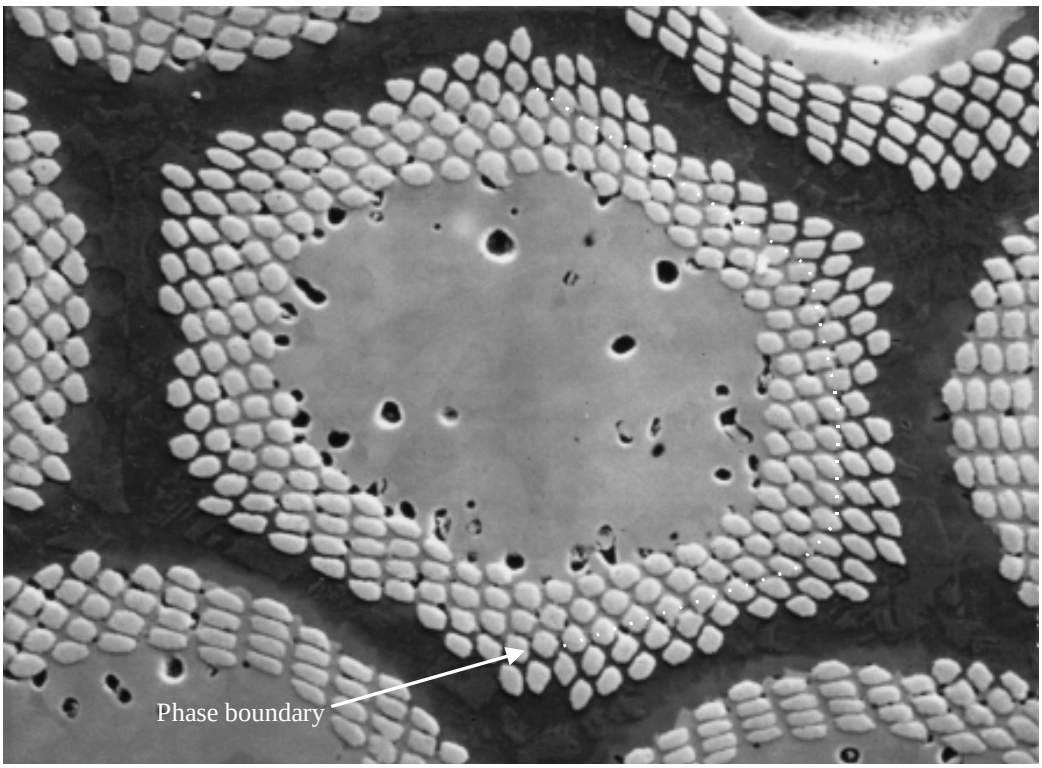

Figure 6.28 Close-up of one filament bundle after reaction at 375 °C for 144 hours. Note the progression of the ε- α phase boundary within the filamentary area, and the formation of small voids in the center of the bundle, and at the phase boundary.

6.4.4 Changing the void location

Given the void formation process, the question arises whether it is possible to influence the final location of the voids. Figures 6.29 and 6.30 show the least- and most vulnerable regions of the bundles in both the MJR and IT conductor. The locations marked here are derived from the FEA models in chapter 4, and the photographs in section 6.2.

If the formation of the voids cannot be prevented, one should at least try to form them in a region where they will not cause mechanical problems when the conductor is strained or subjected to a large compressive load. The sensitive area of the strand is obviously the filamentary area, where the brittle Nb_3Sn filaments are embedded in stiff bronze.

As is shown in the FE analyses in section 4.4, a large void in the core region of the bundle does not cause a significant stress concentration in the filament region. The critical current degradation measured in the experiments on the MJR and PIT conductors indicates this is the least damaging location for the voids to reside.

A second favorable location for the voids would be outside the filamentary area between the outer filament ring and the niobium and/or tantalum diffusion barrier in the case of the MJR conductor. A structure like this, when subjected to a large compressive load, would deform first, reducing the size of the voids, before exerting large loads on the filament region. For the IT conductor, this area corresponds to the bronze between bundles.

In order to get the voids to migrate through the filamentary area the thickness of the outer copper area between the filaments and the diffusion barrier (MJR) or between the bundles (IT) has to be increased.

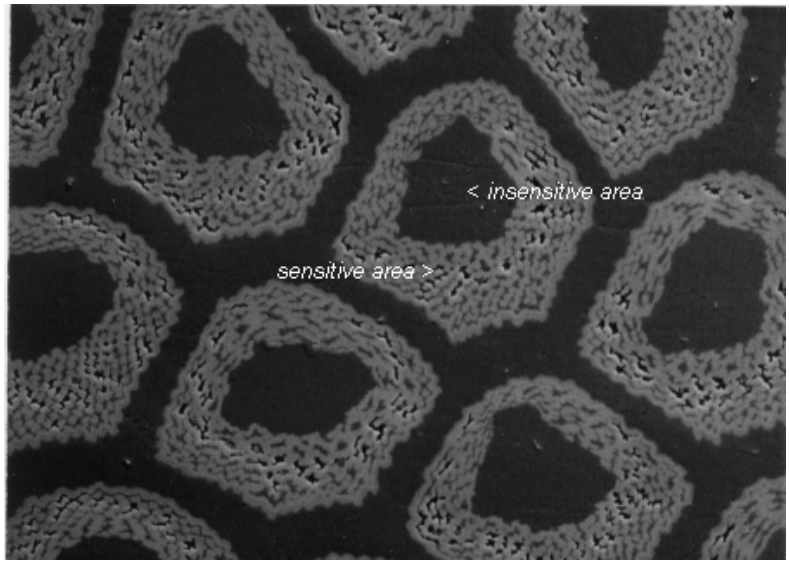

Figure 6.29 Insensitive and sensitive areas of the filament bundle for the MJR conductor.

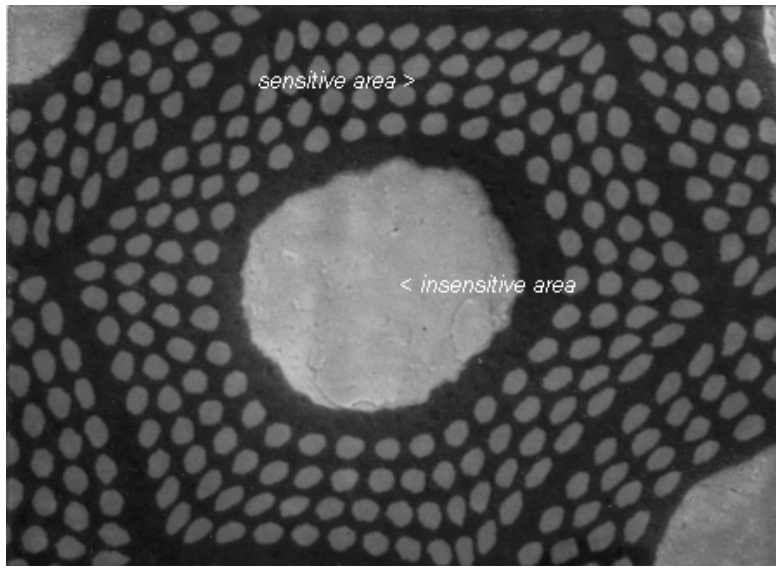

Figure 6.30 Insensitive and sensitive areas of the filament bundle for the IT conductor.

This would reduce the critical current directly since the amount of copper in the cross-section increases. However, it results in a more robust cross-section of the bundles. An optimum has to be found between the amount of critical current degradation under load and the direct I_c reduction.

6.5 A Cu-Sn diffusion couple experiment

In order to investigate the void formation process during the diffusion steps of the wires, a diffusion couple based on a simpler geometry is investigated (pictures courtesy of Dan Dietderich, LBNL [6.8]). To simplify the parameters involved in the diffusion and reaction, the niobium filaments are not incorporated, essentially building an IT wire without the niobium filaments present in the copper. Tantalum markers are incorporated in the copper layers to facilitate the tracking of the phase boundary migration.

It is thought that the void accumulation takes place at the interface between the α-phase and the ε-phase in the Cu-Sn alloy, therefore the couple was set up with a homogeneous Cu_3Sn ε-phase in the core instead of pure tin.

First, a thin walled copper tube is swaged around a stainless steel rod. The copper wall thickness is then etched down to about 200 μm. Next, a sandwich of 75 μm copper foil and 100 μm tantalum mesh is wrapped around the copper clad stainless steel rod. The tantalum mesh is a 70 % open mesh, which acts as a source of diffusion markers (similar to the MJR process) after the rod is drawn down to a wire. Several wraps are wound onto the rod to create a total diffusion length (in the radial direction) after wire drawing (in the longitudinal direction) of the order of 500 μm.

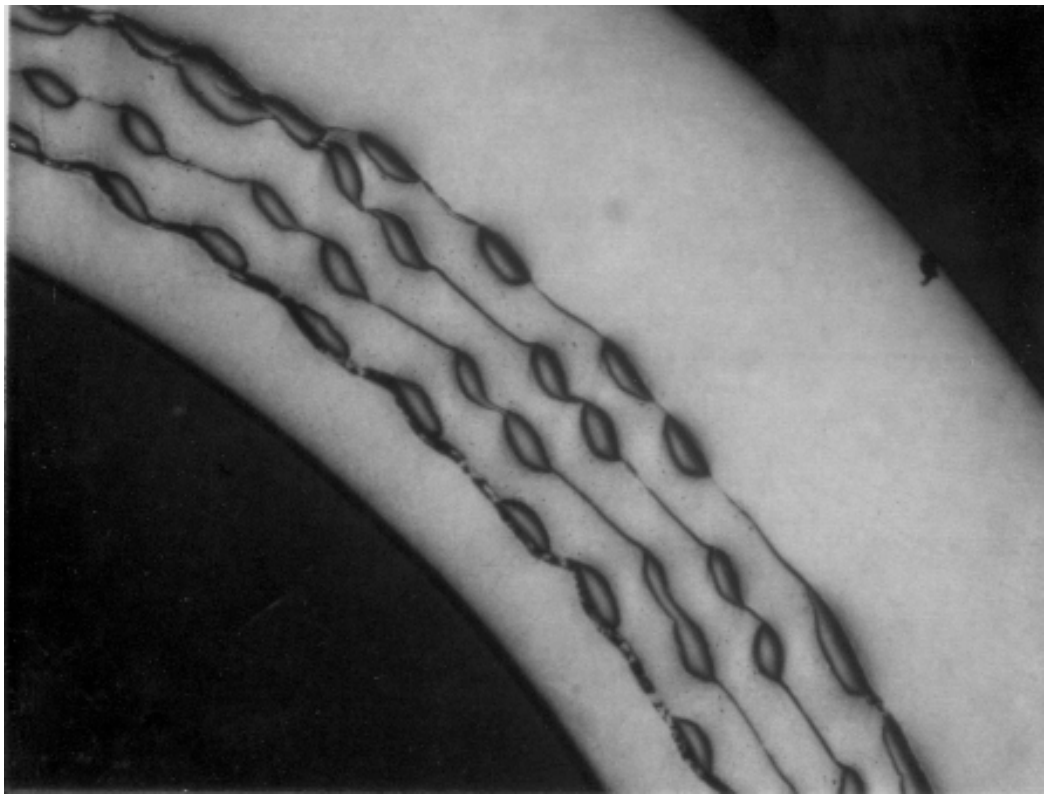

Figure 6.31 The copper-tin diffusion couple with tantalum markers in the copper. The figure shows the copper foil and tantalum mesh roll-up with the copper tube around it. The Cu_3Sn powder is not inserted yet.

The assembly is then inserted in a copper tube and swaged onto the assembly. Next, the stainless steel rod is pushed out of the inner copper tube, leaving an open core for the Cu_3Sn powder. After insertion of the Cu_3Sn powder, and compression of the powder to assure a low initial void fraction, the total assembly is drawn to a wire diameter of 0.48 mm.

The result is a wire with a Cu_3Sn core and a ring of equally spaced tantalum filaments. The tantalum filaments are embedded in a copper matrix, with a thin layer of copper between the Cu_3Sn core and the first tantalum filament row, and a thicker layer of copper on the outside of the filamentary area. The structure is a simulation of an IT wire in which the reactive niobium filaments are replaced with inert tantalum filaments. It simplifies the diffusion study, since no additional tin will react with the niobium to form Nb_3Sn filaments.

Figure 6.31 shows the wire with the tantalum diffusion markers, before the Cu_3Sn powder is inserted. The sample is then sealed and reacted at different reaction temperatures to study the phase boundary migration and void formation. After reaction, the samples are polished, and the resulting cross-sections are investigated using SEM and X-ray back-scatter techniques. The information about the various phases present in the cross-section is obtained using the X-ray back-scatter method. The phases are identified by integration of the surface under the peaks of certain spectral lines. The relative content of the components can then be determined, yielding information related to the phase present.

In figure 6.32 the η-phase has been transformed entirely into ε-phase and some δ-phase at a temperature of 500 °C. The formation of the δ-phase is very slow, thus only a small amount is formed during the short heat treatment period. The black ring in the picture is a void space, partially caused by Kirkendall void formation, and partially by the core shrinking away from the remaining section. The separation of the core from the rest of the diffusion couple inhibits further diffusion of tin into the copper, therefore, a complete diffusion is not possible in this experiment. The separation is not meant to happen, but no further experiment was performed in time for inclusion in this thesis.

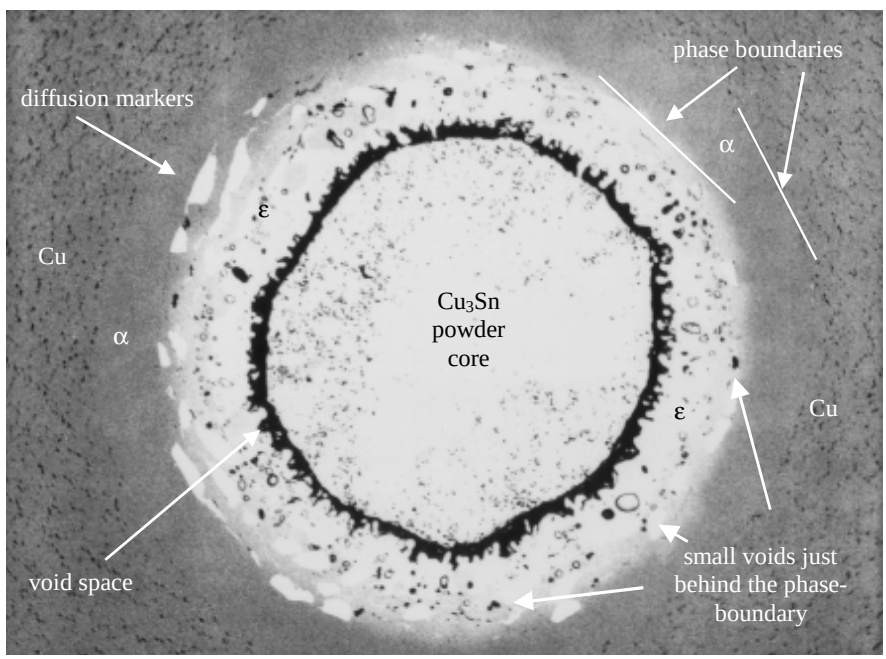

Figure 6.32 Final results from the second diffusion couple heat treatments. The tantalum markers are the white shapes around the lighter region. The large void space is clearly visible as the black ring around the core. Small voids are visible just behind the α-ε phase boundary. The outermost (dark gray) area is pure Cu; just inside (slightly lighter gray) is α-type solid solution; inside that ring (light gray) is ε-phase Cu-Sn.

When the temperature is raised to 550 °C the first significant voids start to form and migrate outward through the copper tube. The γ-phase is formed, but not the ζ-phase or β-phase. The sample reacted at 615 °C showed no δ-phase, only the α-type solid solution, β-phase, γ-phase, ζ-phase and ε-phase. This is the most complex mixture of phases that will be present during the reaction process (see the phase diagram in figure 6.24). The voids redistribute along the ε-α boundary. The presence of the different phases is determined with X-ray back-scatter detection in the SEM. When the temperature is further raised to 658 °C, the voids move further outward into the copper tube. At 658 °C , the ζ-phase is absent, leaving the α-type solid solution, β-phase, γ-phase and ε-phase. Figure 6.33 shows a close-up of the void space area.

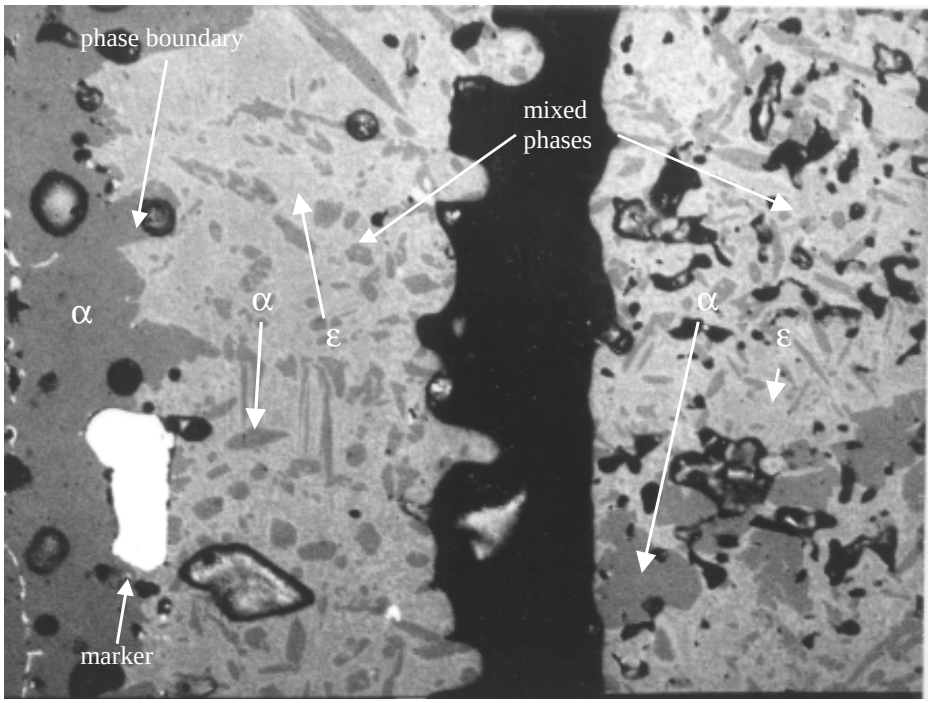

Figure 6.33 A close-up of the phase boundary. Shown is the large void space (black region in the middle) with the e-a interface visible at the left at the marker. The darker region to the left of the boundary is the Cu-rich a-phase. The area to the right of the boundary is still in a mixed state with both e-phase (lighter gray) and a-type solid solution (dark gray) present.

The tantalum markers serve two purposes, the first as a local coordinate system to reference the movement of the interface between the α-type solid solution and the ε-phase in the Cu-Sn alloy, the second as indication of the mass transport due to the difference in diffusion speeds of the individual components.

Although the diffusion couple study provides clear visual evidence of the formation of the voids and the migration of the phase boundary, no useful information with respect to the speed of the migration of the voids was obtained.

6.6 Elimination of the voids by Hot Isostatic Pressing

Another approach to solve the problems associated with void formation in the Nb_3Sn is to eliminate the voids during or after they are formed. One method to accomplish this is to introduce a Hot Isostatic Pressure (HIP) step in the reaction schedule.

Since most of the large voids are formed in the first few hours of the high temperature reaction step at 650 to 680 °C, the HIP-step could take place at that moment.

For a small sample this treatment can be easily realized in situ by constructing a small reaction furnace that can be pressurized during the reaction step. However, in the case of the large coils, it is far more difficult to realize due to the large pressure-vessel requirements.

The method of "HIPping" a Nb_3Sn coil has been tried before on some small solenoids with good results [6.9]. The critical current actually increased (in the order of 18 to 30 %), and the voids were eliminated from the wire cross-section [6.10]. A study was also performed on the elimination of voids in multi-filamentary external tin conductors. It was found that the critical pressure above which the voids started to disappear or move is in the order of 2 to 3.5 MPa for a 0.25 mm wire [6.11].

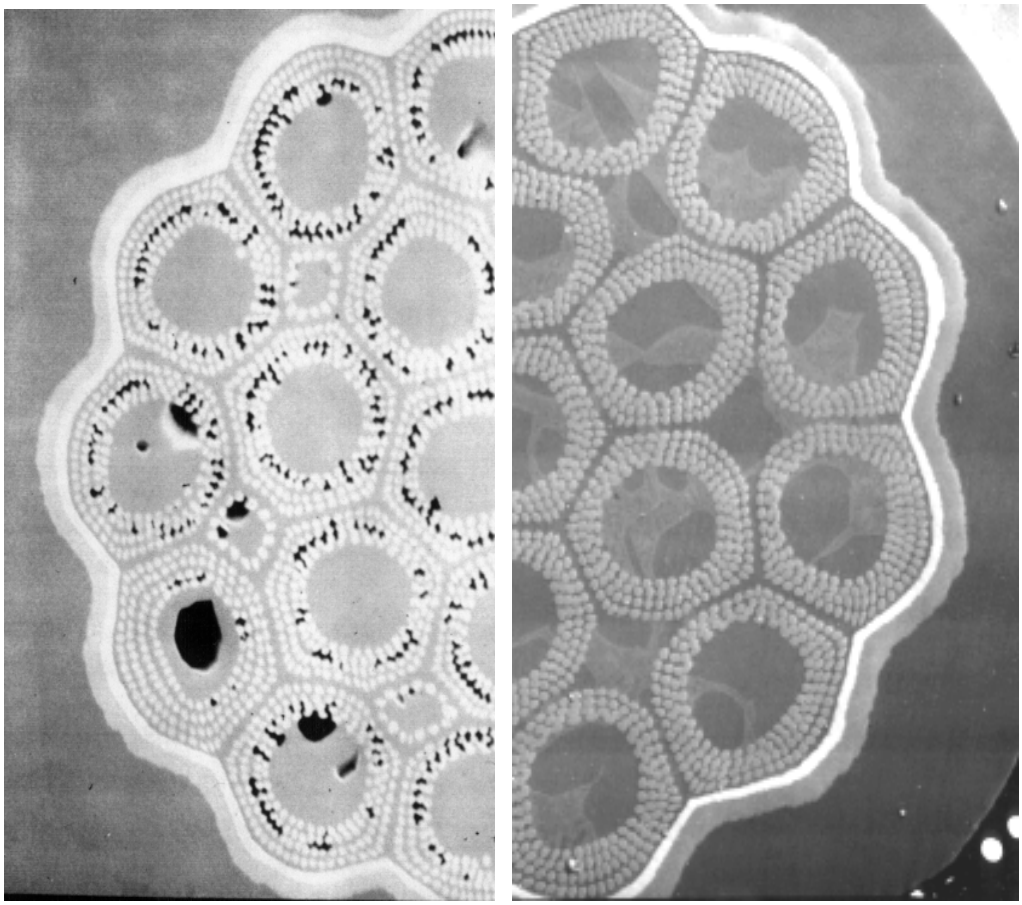

Figure 6.34 Cross-sections of an IT wire reacted without pressure (left) and with pressure (right). The left side shows both small voids in the filament region as well as large voids in the center of the bundles. The right side shows that all voids are eliminated. A side-effect of the HIP treatment is the clustering of the filaments in the areas where the voids would have been present.

The critical pressure is a function of the wire diameter and the internal composition of the matrix. In the case of external tin wires, a relatively soft material resides outside the harder core, thus a low pressure is sufficient to deform the outer area of the wire. In the case of the IT and MJR wires the pressure needed is high due to the higher modulus of the composite material.

Figure 6.34 shows the cross-sections of a wire reacted without pressure (left) and one reacted with pressure (right). The reacted wire sample in figure 6.34 (left) shows numerous voids in the core or the

bundles as well as in the filamentary areas. Note that at a few locations the small voids are combined into a single large void.

The sample wire in figure 6.34 (right) has no voids present in the entire cross-section. For a cable sample reacted in the HIP furnace, out of 20 strands investigated, only two strands showed a few voids present in the core of the bundles, compared to strands with many voids for the sample with the standard reaction.

Voids can even be eliminated from an already partially reacted wire. Figure 6.35 shows an IT strand that is partially reacted (up to the 210 °C step), and then given a HIP treatment during the final reaction steps. During the HIP treatment, the voids are eliminated, bringing the filament bundles closer together, and in some cases joining them at the edges.

The main difference in the results from the first method and this method is the location of the clustering of filaments. If the wire is reacted entirely under pressure, the clustering occurs further inside of the location where the voids would have been present without pressure, usually within the filamentary area. This is due to the fact that the voids never form in the first place, as the pressure from the HIP treatment deforms the wire to close the space.

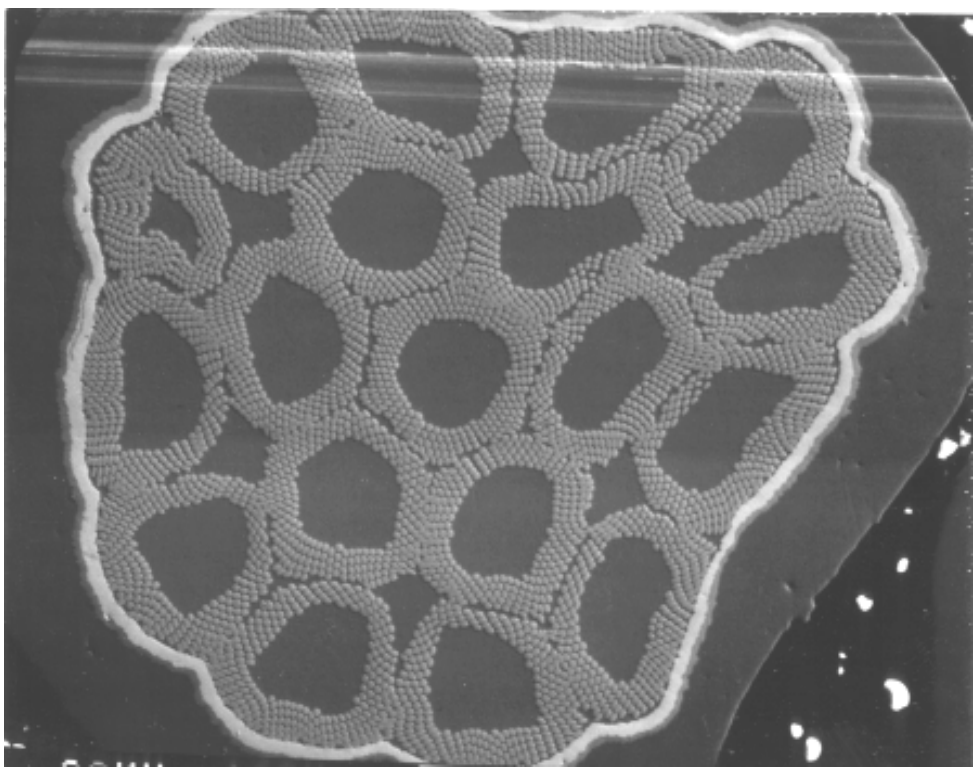

Figure 6.35 Cross-section of a partially reacted (210 ℃) IT wire that was then heat treated in a HIP furnace for the final two steps of the process (340 ℃ and 650 ℃).

If the wire is partially reacted without pressure, and then fully reacted under pressure, the voids first form, both within the filamentary region, and outside in the more deformed filaments. Upon applying the pressure, the voids collapse and further filament growth causes clustering at the previous void locations.

During the HIP treatment after reaction, additional damage is expected due to the breaking of the filaments subjected to large displacements. On the other hand, additional growth during heat treatment might heal damage inflicted in the HIP operation. In order to assess the HIP steps it is recommended to check the effect with cable measurements.

At the time this thesis was written, the critical current measurements on the samples after HIP treatment were still in the planning stage. Meanwhile, a similar investigation is reported by Keys, Cheggour and Hampshire [6.1]. The authors have made a systematic comparison of the strain sensitivity of a HIP treated MJR wire versus a regular heat treatment. The samples investigated were given a standard heat treatment, followed by an elevated temperature treatment at 750 °C under argon at 2000 atm. pressure. This treatment is similar to the one given to the wire shown in figure 6.35, except for the elevated temperature.

The strain tolerance of the HIP treated wires is reported to be greater than that of the normally reacted wires by about a factor 2. The ultimate tensile strain is reported to be unchanged. The critical current density and upper critical field were reduced by a factor of about 9 by the HIP treatment.

These results are encouraging with respect to the reduced strain sensitivity, but the large reduction in critical current due to HIP after the filaments are formed is not practical for high current application in high field magnets.

The critical current degradation as a function of strain, and the expected reduction in critical current due to a HIP treatment in the final stage of the reaction process remains to be measured.

6.7 Conclusions

The results from the microscopic studies point to the void formation as an important cause of permanent critical current degradation in MJR and IT wires. The location of the damaged filaments corresponds to the enhanced stress concentrations found in the FE analyses of wires with voids in chapter 4. These two facts combined suggest that by controlling the location of the void formation, or by total elimination, the stress sensitivity of the Nb_3Sn strands can be greatly reduced.

An investigation of the location of the voids in the cross-section of an IT wire as a function of the initial core area of the filament bundles shows that the larger the area, the further the voids migrate outward between the surrounding filament rings. The area of the core is directly related to the amount of tin present in the core before reaction.

Hence, a lower amount of tin should result in the voids located primarily in the center of the bundles (preferred location). Conversely, a larger amount of tin should result in voids located outside the filamentary area. The latter is also a preferred location, provided the copper area between the bundles is increased in size to prevent filament clustering.

A diffusion couple study was performed to attempt to determine the migration speed of the voids within the filamentary area as a function of the reaction temperature and gradients. Though void formation and migration could be demonstrated, no useful detailed information was obtained from the experiments so far.

Results from an experimental HIP treatment show that for both the IT and MJR wire, the HIP treatment can eliminate the voids formed in the reaction process. This proves the HIP treatment works for both conductor types in eliminating the voids from the cross-section. The void elimination is equally effective for a HIP treatment during, and after the main reaction.

Experiments performed by Keys et.al. indicate a two-fold reduced strain sensitivity for MJR wires that are given a HIP treatment after the regular reaction schedule. The reduced strain sensitivity is however at the expense of a large degradation in the critical current of the wire.

Experiments are planned to investigate the effect of a HIP treatment that is given during and just after the temperature increase to the final reaction step in the schedule. Critical current degradation, and the resulting strain sensitivity still remains to be measured.

Chapter 7

Fiber-optic stress and strain measurement at low temperature

This chapter contains a description of a novel strain measurement technique using fiber-optic sensors at low temperature. This is the first time the use of fiber-optic strain gauges for a direct stress and strain measurement within the coil winding of an accelerator dipole magnet at 4.2 K is reported.

First, a brief introduction to guided light transmission in fibers is given. Next, several methods of strain measurement using fiber-optics are discussed, including sensors that measure intensity and polarization angle, or act as spectral filters. Interferometric techniques with fiber-optics are also shown.

Next, a justification of the choice of the Fabry-Perot sensor for use in the magnet is given, followed by a detailed description of two different readout techniques, the first using monochromatic light, the second using white light.

The accuracy of the fiber-optic strain and stress measuring system is discussed, and an error analysis for the white light readout method is presented.

Finally, the temperature sensitivity and a temperature compensation method is described, and a method to improve the transfer function of the sensor cell is shown.

7.1 Introduction

Thus far, no method of strain measurement has been incorporated in accelerator magnets to measure the local strain distribution and transverse stress in the horizontal symmetry plane of a magnet. Since this is the area where the stress due to Lorentz forces will be the highest, it is important to know what the actual load on the conductor will be. A second important issue is the study of stress gradients and spatial uniformity in order to make the comparison with ANSYS finite element analysis of the magnet mechanics in detail.

Currently, forces and stresses arising from the various operating conditions in accelerator magnets are calculated using Finite Element Analysis (FEA) and checked at room temperature and 77 K by building small sections of the magnets, the so-called "*cookies*". The models are limited to a small slice, and can only be used to test for pre-stress and thermal shrinkage in the transverse direction. A global measurement of the stress on the surface of the pole pieces of the coil winding is usually obtained with bending-bridge type stress transducers positioned in the pole piece. Since the gradients of the forces are very large, and a conventional strain-gauge bridge can only measure a large area outside the windings, there is a need for a miniature stress sensor capable of measuring the gradient across the surface.

Conventional resistive strain gauges consist of a film resistor that is stretched under strain, thereby changing resistance. The resistance as a function of the strain is either measured directly or in a Wheatstone-bridge configuration as described below.

Three disadvantages are associated with resistive strain gauges:

1) the electromagnetic interference from the magnet with the measurement system. The resistive strain gauges are affected by the magnetic field (magneto-resistive effect of the resistor material, induced voltages over the leads);
2) the use of electrical wires in the winding package. Since the voltage between the poles can rise to about 1 kV in the case of a quench of the magnet, the electrical integrity of the system has to be guaranteed. The use of fiber-optical leads is therefore a significant advantage over electrical wires;
3) the influence of temperature changes on the resistive strain gauges. Temperature changes can be compensated for up to a certain range, but a gauge that will produce a reliable signal over a temperature range from 293 K to 4.2 K is difficult to obtain.

To avoid the problems associated with the use of resistive strain gauges, a novel fiber-optic strain gauge system is designed. The gauge elements selected for the system are Fabry-Perot (FP) cavities built with silica-glass fibers and sleeves. The system is capable of measuring strain with a high spatial resolution at 4.2 K. The strain can be monitored during cooling from 293 K to 4.2 K by compensation with a second gauge element.

The FP-based fiber-optical measuring systems are well known and widely used at room temperature. The unique feature here is the specific implementation at 2 and 4 K in a superconducting magnet system, leading to a drastic increase of measuring resolution enabling detailed studies of local strain and feedback to FEA model calculations.

A magnetic field will only influence the readout when the polarization angle of the electromagnetic wave in the fiber is used as a measuring device (Michelson and Mach-Zehnder interferometer). In an FP-cavity, the readout is only dependent on the gap between the two mirrors in the cavity, and is not influenced by any disturbance outside the leads.

When looking at the intensity of the signal (single wavelength readout), additional loss in the fiber leads will still be measured. However, when using multiple wavelength readout (white-light interferometry), the strain is encoded in the spectral information of the signal reflected back from the cell, and will not be influenced by any disturbance on the fiber lead.

An essential advantage of the new fiber-optic sensors is the high spatial resolution. The stress gradient across the cable surface can be resolved over areas of a few square millimeters, as compared to square centimeters with resistive strain gauges.

7.2 Guided light transmission in fibers

This section gives a brief introduction to the theory of guided light transmission in fibers. Only the two types of fibers used here, the single-mode and the multi-mode step-index fiber, are discussed. Section 7.2.1 contains general definitions used; a brief explanation of external and internal reflection is given in section 7.2.2, followed by a description of the fiber types used in section 7.2.3. In section 7.2.4, useful relations for the step-index fibers are given, based on wave equations in the fiber. For a more complete description of wave propagation in dielectric wave-guides, and derivations of the relations given here, the reader is referred to the literature [7.1], [7.2].

7.2.1 General definitions

The *refractive index n* of an optical material is defined as the speed of light in free space $c = 3\times10^8$ m/s divided by the speed of light in the dielectric or insulating material *v*, and is given by

$$n = \frac{c}{v}. \tag{7.1}$$

Typical values of *n* are 1.00 for air and 1.50 for glass.

The speed of light *n* in a medium is related to the *frequency f* and the *wavelength* l by

$$v = f\,l. \tag{7.2}$$

A plane wave traveling in a direction $\vec{k}$ can be represented as

$$\vec{A}(\vec{x},t) = \vec{e}_i A_0 e^{i\left(wt-\vec{k}\cdot\vec{x}\right)}, \tag{7.3}$$

with $\vec{x} = x\vec{e}_x + y\vec{e}_y + z\vec{e}_z$ the position vector and $\vec{k} = k_x\vec{e}_x + k_y\vec{e}_y + k_z\vec{e}_z$ the wave propagation vector. The vector $\vec{A}$ can be used to represent the electric field $\vec{E}$, or the magnetic field $\vec{H}$. In (7.3), A_0 is the amplitude of the wave, and $w = 2pn$. The magnitude of the wave vector $\vec{k}$, also known as the *plane wave propagation constant*, is $k = 2p/l$.

The symbols defined here are used further in the following sections.

7.2.2 Refraction and reflection

When a light ray encounters a boundary separating two different media, part of the ray is reflected back into the first medium and the remainder is refracted as it enters the second medium as shown in figure 7.1. This effect is the result of the difference in the speed of light in the two materials. The relationship between the incident, reflected and refracted angles at the interface is given by Snell's law

$$\begin{cases} n_1 \sin j_1 = n_2 \sin j_2 \\ n_1 \cos q_1 = n_2 \cos q_2 \end{cases}, \tag{7.4}$$

with the angles j and q defined in figure 7.1, and n_1 and n_2 the refractive indices of the two materials.

The reflection off an optically denser material (larger *n*) is called *external reflection*, the reflection off an optically less dense material is called *internal reflection*. As the angle of incidence q_1 in a material with larger *n* becomes smaller, the refracted angle q_2 becomes zero. Beyond that angle the light is totally internally reflected, which means there is no light escaping from the material, like in a optical fiber (tunneling phenomena are neglected).

7.2.3 Different types of optical fibers

An optical fiber is a dielectric waveguide that operates at optical frequencies, and confines electromagnetic energy in the form of light to within its surfaces, and guides this light in a direction parallel to its axis.

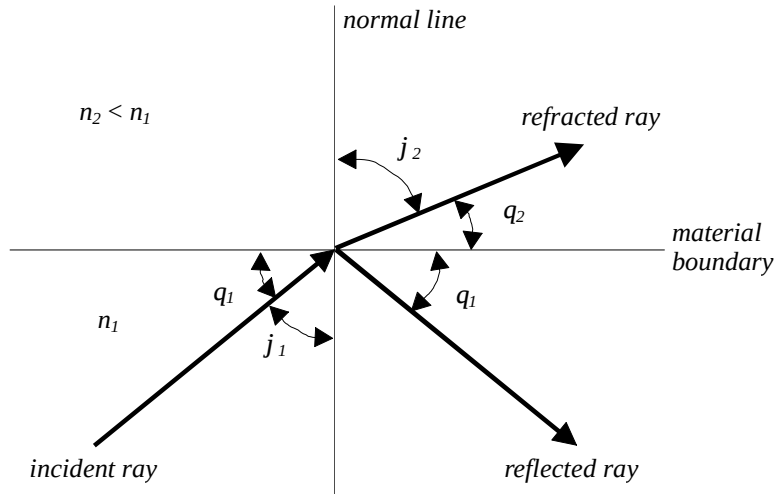

Figure 7.1 Reflection and refraction at a material boundary with $n_2 < n_1$.

The propagation of light along a waveguide can be described in terms of a set of guided electromagnetic waves called the *modes* of the waveguide. Each guided mode is a pattern that is repeated along the fiber at intervals equal to the wavelength. Each type of fiber only guides a certain number of modes.

An optical fiber is generally a circular guide with a *core*, *cladding* and *coating* respectively, as is shown in figure 7.2. A circular solid core of refractive index n_1 is embedded in a cladding with refractive index $n_2 < n_1$. A plastic coating is applied around the glass cladding for protection and reduction of scattering loss due to imperfections at the cladding surface.

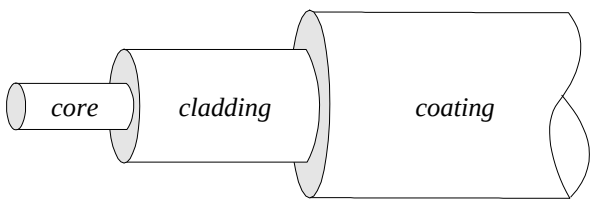

Figure 7.2 Structure of a generic optical fiber, illustrating the buildup of the core, cladding and coating from the inside out.

Two commonly used types of fibers can be distinguished based on the refractive index profile of the core-to-cladding interface, the *step-index* fiber and the *graded-index* fiber. Both types can be divided further in *single-mode* and *multi-mode* fibers. The two types of fiber used in the experiments are of the step-index type, illustrated in figure 7.3. The core radius *a* is typically between 3-6 μm in single mode fibers, and 25 to 100 μm in multi-mode fibers. A discussion of the graded-index fiber is outside the scope of this thesis.

A single-mode fiber is designed to carry only one mode, whereas a multi-mode fiber can typically carry several hundreds of modes. The disadvantage of a single-mode fiber is its small acceptance angle, generally requiring a laser to launch light into the fiber. The advantage is the non-existence of *inter-modal dispersion* - the mixing of several modes traveling at slightly different velocities - since only one mode is guided.

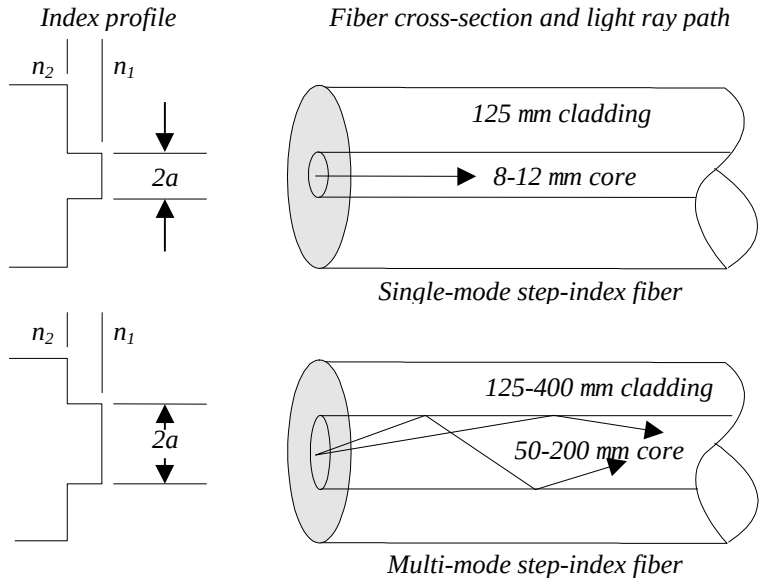

Figure 7.3 Schematic layout of the two types of step-index fibers.

Multi-mode fibers have the disadvantage of inter-modal dispersion, but have a larger acceptance angle as an advantage, allowing the light to be launched with other sources, such as LED's.

If light is focussed on the end of an optical fiber, only rays within a cone described by an angle q to the fiber longitudinal axis, will couple into the core. The sine of this angle is conventionally defined as the *numerical aperture* of the fiber, as

$$NA = \sin q \,. \tag{7.5}$$

The numerical aperture *NA* of the fiber is related to the refractive indices of the core n_1 and cladding material n_2, as

$$NA = \left(n_1^2 - n_2^2\right)^{1/2}. \tag{7.6}$$

7.2.4 Step-index fibers

The electromagnetic field that is guided along an optical fiber can be represented by a superposition of *modes*. Guided modes traveling in the longitudinal direction of a fiber (along the *z*-axis), have a time and *z* dependency given by $e^{i(wt-bz)}$.

The factor b is the *z*-component of the wave propagation constant *k*. The factor b can only assume discrete values, since the field must satisfy the wave equations, and certain boundary conditions at the core-to-cladding interface. The discretization of the guided modes is further explained here.

The wave propagation in a step-index fiber is described by using the solution to Maxwell's equations

$$\left[\frac{\partial^2}{\partial r^2} + \frac{1}{r}\frac{\partial}{\partial r} + \frac{1}{r^2}\frac{\partial^2}{\partial j^2} + \left(k^2 n_j^2 - b^2\right)\right]\begin{bmatrix} E_z \\ H_z \end{bmatrix} = 0\,, \tag{7.7}$$

in cylindrical coordinates (r, j, z) with *z* along the fiber longitudinal axis. The refractive index n_j is equal to n_1 or n_2, depending on whether the core or cladding is considered. The solutions are given by

$$\vec{E} = \vec{E}_0(r, j)e^{i(wt-bz))}, \tag{7.8}$$

and

$$\vec{H} = \vec{H}_0(r, j)e^{i(wt-bz))}. \tag{7.9}$$

When $E_z = 0$, the modes are called *transverse electric* or TE_n modes; when $H_z = 0$ *transverse magnetic* or TM_m modes. In general, the boundary conditions at the core-to-cladding interface lead to coupling of the modes, resulting in *hybrid* modes. These modes are designated as HE_{nm} or EH_{nm} modes. The *order* (n or m) of a mode is equal to the number of times the field is zero across the guide, as in TE_0, TE_1, TM_2, HE_{11}, etc.

Solutions that satisfy the boundary conditions are Bessel functions of the first kind $J_k(ur)$ inside the core, and modified Bessel functions of the second kind $K_k(wr)$ outside the core [7.1]. The expressions for E_z and H_z inside the core are thus

$$\begin{aligned} E_z &= AJ_k(ur)e^{ikj}\, e^{i(wt-bz)} \\ H_z &= BJ_k(ur)e^{ikj}\, e^{i(wt-bz)} \end{aligned} \quad (r < a), \tag{7.10}$$

with A and B arbitrary constants, and $u^2 = k_1^2 - b^2$ with $k_1 = 2pn_1/l$.

Outside the core the expressions for E_z and H_z become

$$\begin{aligned} E_z &= CK_k(wr)e^{ikj}\, e^{i(wt-bz)} \\ H_z &= DK_k(wr)e^{ikj}\, e^{i(wt-bz)} \end{aligned} \quad (r > a), \tag{7.11}$$

with C and D arbitrary constants, and $w^2 = b^2 - k_2^2$ with $k_2 = 2pn_2/l$.

For $wr \to \infty$, $K_k(wr) \to e^{-wr}$; since $K_k(wr)$ must go to zero for $r \to \infty$, w must be positive. This implies that $b \geq k_2$. Inside the core, u must be real, hence $k_1 \geq b$. From these constraints, the permissible range of b is given by $2pn_2/l = k_2 \leq b \leq k_1 = 2pn_1/l$.

An important parameter determining the cutoff conditions in the single-mode fiber is the *normalized frequency V* defined by

$$V^2 = (u^2 + w^2)a^2 = \left(\frac{2p\,a}{l}\right)^2 \left(n_1^2 - n_2^2\right), \tag{7.12}$$

which is a dimensionless number. Together with the *normalized propagation constant*

$$b = \frac{a^2 w^2}{V^2} = \frac{(b/k)^2 - n_2^2}{n_1^2 - n_2^2}\ , \tag{7.13}$$

it defines the number of modes that will be guided by a fiber of a given core diameter. When $b/k = n_2$, a mode is cut off (propagation constant $b = 0$). The HE_{11} mode has no cut-off, and ceases to exist only when $a = 0$. By appropriately choosing a, n_1, and n_2 so that $V \leq 2.405$ (the first zero in the lowest order Bessel function J_0), all modes except the HE_{11} mode are cut off, thus yielding a single-mode fiber.

The parameter V is closely related to the numerical aperture NA by the relation

$$NA = V\frac{l}{2p\,a} = \left(n_1^2 - n_2^2\right)^{1/2} = \sin q\ , \tag{7.14}$$

which is also related to the acceptance angle q of the light rays entering the optical fiber, the wavelength l, and the core radius a.

For the single mode fibers used in the sensors, the core diameter a is about 3.5 μm. At a typical core-cladding index difference (n_1 - n_2) of about 0.2 % this yields a cut-off wavelength of 812 nm and an acceptance angle of 5 degrees.

Waves with a wavelength larger than the cut-off are guided as a single-mode in the fiber. The typical spread in the cut-off wavelength is of the order of 30 nm, and is determined by the accuracy of the fiber production process with respect to the core diameter and the glass composition.

7.3 Fiber-optic sensors

Over the past few decades optical fiber waveguides have been developed primarily for applications in high speed digital communications. However, they can also be employed as analog waveguides or to construct a variety of sensors to measure environmental conditions, such as strain, temperature, electric and magnetic fields, acoustic waves or chemical concentrations.

The sensing method can be based on detecting changes in intensity, phase, wavelength, polarization, time domain properties or modal content of a signal.

The devices can be split up in two distinct classes:

1) the *extrinsic* devices in which the light exits the waveguide, interacts with the environment, and re-enters the fiber;
2) the *intrinsic* devices in which the light is influenced inside the fiber by the external environmental condition [7.3].

7.3.1 Intensity based sensors and bending loss

The intensity based sensors are the simplest. They can be equipped with an external sensing element like a gap-reflector combination, or by simply using the fiber itself as the sensing medium. The light source can be a simple LED in the wavelength range of the fiber used.

When an optical fiber is bent, radiation loss occurs when the radius of curvature exceeds a certain value. Two types of bends can be distinguished, macroscopic bends with radii that are large compared to the fiber diameter (*macro-bends*) and microscopic bends of the fiber axis that can arise when the fibers are cabled or deformed on a scale proportional to the fiber diameter (*micro-bends)*.

The macro-bending loss can occur when the optical fiber is bent around a corner, like the bends in the fiber feed-through from room temperature to a cryostat. When the bending radius is large compared to the fiber radius, the loss is negligible. As the radius decreases, the loss increases exponentially until at a certain critical radius the loss suddenly becomes very large. The loss effects can be explained by looking at the field distribution as shown in figure 7.4.

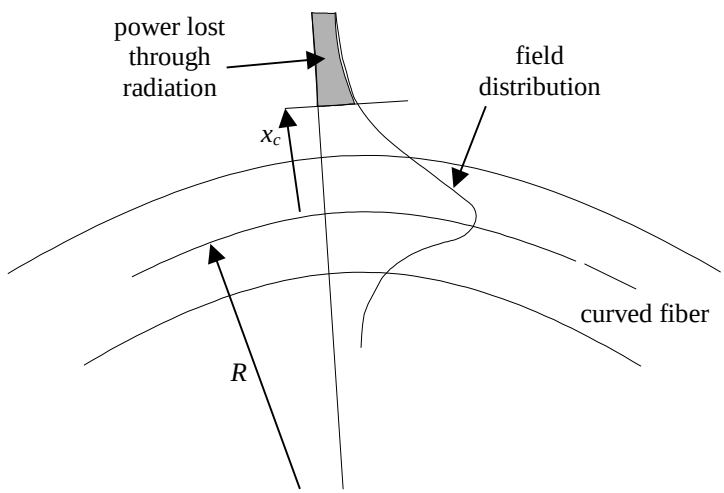

Figure 7.4 Field distribution in a curved fiber.

Any mode traveling in the core has an evanescent field tail in the cladding, that decays exponentially as a function of distance from the core; thus part of the energy is traveling in the cladding. When the fiber is bent, the field tail on the outside of the curve must travel faster to keep up with the field in the core. At a certain critical distance x_c from the center of the fiber the field tail would have to move faster than the speed of light, which means that the optical energy in the tail outside x_c is radiated away. The amount of radiated energy depends on the field strength at x_c and on the radius of curvature R.

An example of a sensor using the fiber itself is the so-called *micro-bend* sensor. Micro-bends are repetitive small-scale fluctuations in the radius of curvature of the fiber axis, as shown in figure 7.5.

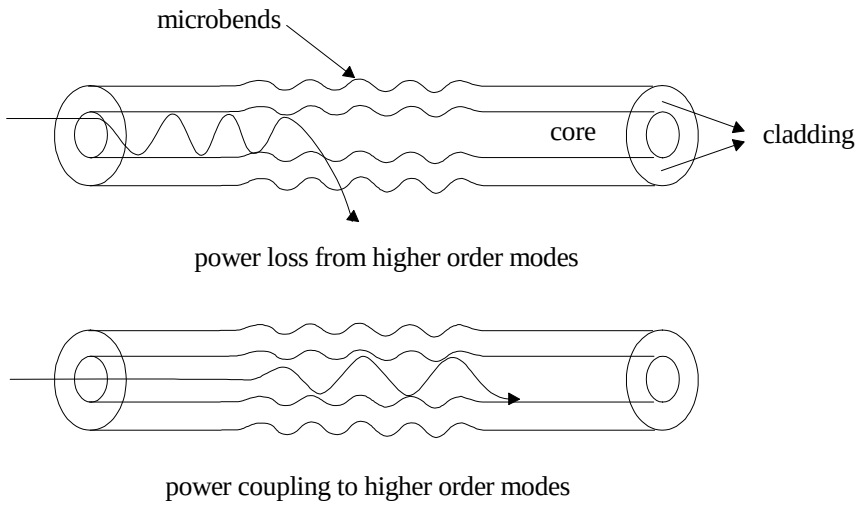

Figure 7.5 Micro-bend losses.

The fluctuations may be caused by non-uniform lateral stresses on the outside of the fiber in a saw-tooth clamping structure, or between two Rutherford cables. An increase in attenuation of the signal results from micro-bending because the fiber curvature causes repetitive coupling of energy between the guided modes and the non-guided modes in the fiber. The energy transferred to the non-guided modes will be radiated away as described above.

An experiment was performed with a micro-bending sensor by embedding an optical fiber between two Rutherford cables with the dimensions of the cable for the dipole magnet. The fiber is shimmed on the side with a thin glass-epoxy sheet with the same thickness as the polyamide coating diameter. Upon loading, the change in signal intensity at the exit of the fiber is compared to the unloaded case. A signal decrease of up to 30 % is measured for a stress of 100 MPa.

The method works well in a small-scale experiment, but complications arise when it is to be used in a magnet sensor. The first complication is the calibration of the intensity change with stress. Since the optical fiber has to be continuous all the way through the magnet and back, it will also be subjected to outside influence along the entire length of the lead and return fiber. Furthermore, the fiber will have to travel from room temperature to 4.2 K and back. This will also influence the transmission of light, and the effect will be indistinguishable from the actual stress applied to the fiber within the magnet. For this reason, this method was not chosen to measure stress in the magnet windings.

7.3.2 Polarization based sensors

The use of the polarization of a traveling wave through an optical medium is a very powerful method of extracting information about the external influences on the medium. Most fiber-optic temperature, strain and magnetic field sensors use this principle. For a strain-sensor in a superconducting magnet the polarization-based sensing scheme has some inherent disadvantages.

The first, and most important, is the influence of the magnetic field itself on the guided wave, the so-called Faraday or magneto-optic effect. When a magnetic field parallel to the fiber is applied (in the propagation direction of the electromagnetic wave), the plane of vibration will be rotated over an angle b as in

$$b = x\,Bd\,, \tag{7.15}$$

with B the static magnetic flux density in tesla, d the traveled length in m and x the Verdet number, which is of the order of 3×10^5 arc-min$\times$T^{-1}m^{-1} [7.4]. This coefficient is a function of both temperature and frequency. Since the fiber leads will reside in a time variable high magnetic field with some parallel component, and pass through an area with a temperature gradient from 4.2 K to a time varying room temperature, the application of a polarization based sensing scheme is not advisable.

Furthermore, the polarization angle is also influenced by the intrinsic strain in the guiding fiber, which makes the entire fiber lead sensitive to external influences. The sensing scheme could be adapted to measure an integrated strain over the entire magnet length, but is not suitable for a localized measurement.

7.3.3 Intrinsic wavelength dependent device

An application of an intrinsic wavelength dependent device is presented here. The influence of applied strain on a coupler element can be used directly to measure strain by embedding the sensor in a material which strain state is to be investigated. It can also be used indirectly to measure stress, by use of a deforming element that translates stress into strain along the sensor, such as a bending bridge.

In a fused bi-conical tapered 2x2 coupler [7.5], shown in figure 7.6, the transmitted output power P_t (light travels into input 1 and out of output 1) and the coupled power P_c (light travels into input leg 1 and out of output leg 2), are given by

$$\begin{aligned} P_t &= P_0 \cos^2 C_0 L_c, \\ P_c &= P_0 \sin^2 C_0 L_c. \end{aligned} \tag{7.16}$$

L_c represents the effective interaction length (defined as the length over which the cores are close enough for coupling), and P_0 is the input power. C_0 is the coupling strength dependent on the minimum fiber core spacing h_0 as in

$$C_0 = \frac{l}{2pn_1} \frac{u^2}{a^2 V^2} \frac{K_0(wh_0/a)}{K_1^2(w)}, \tag{7.17}$$

where u, w and V are the guide parameters as defined in section 7.2.4, l is the wavelength, a is the core radius, h_0 is the core distance and n_1 is the core refractive index. K_0 and K_1 are modified 0^{th} and 1^{st} order Bessel functions. The resulting dependency of P_t and P_c as a function of the wavelength l is shown in figure 7.7.

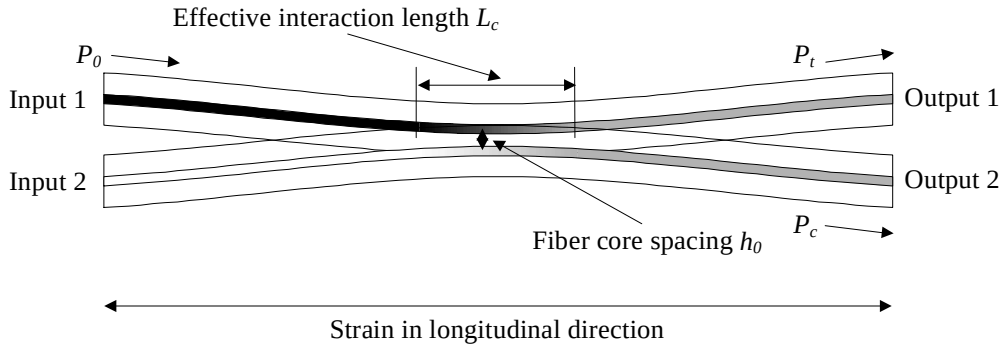

Figure 7.6 Cross-section view of a fused bi-conical tapered 2x2 coupler. Shown is an untwisted coupler; in reality the fibers are twisted and fused together, resulting in multiple points with small core spacing.

When the fiber core spacing h_0 (see figure 7.6) is changed by straining the coupler in the longitudinal direction or by applying transverse stress, the coupling strength C_0 will vary. Also, the effective interaction length L_c is directly affected by longitudinal strain and indirectly by transverse pressure. As an example, the relation of $P_t(e)$ is derived below.

Assume the coupler is tensioned in the longitudinal direction. This results in a change of the effective interaction length L_c of ΔL_c, hence $L_c' = (L_c + \Delta L_c) = L_c(1+e)$, with e the longitudinal strain.

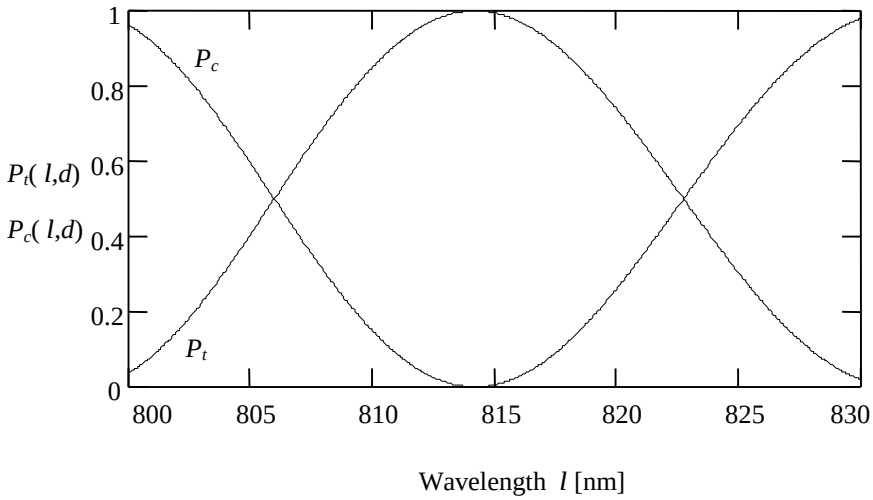

Figure 7.7 The computed wavelength dependence of a typical 2x2 fused bi-conical tapered coupler.

The coupling strength is affected through changes in the core distance h_0, the core radius a and the normalized cut-off frequency V, since V is again a function of a, see (7.12). Both h_0 and a become smaller by a factor (1-ne) when the coupler is subjected to a longitudinal strain e; n is the Poisson's ratio of the silica glass (n=0.16 [7.6]).

Substituting $L_c' = L_c(1+e)$ for L_c in (7.16), $a' = (1-ne)a$, $h_0' = (1-ne)\,h_0'$, and rewriting V' as $V'^2 = \left(2pa'/l\right)^2\left(n_1^2 - n_2^2\right)$, yields the following relation for $P_t(e)$:

$$P_t(e) = P_0 \cos^2\left(\frac{l^3}{8p^3 n_1}\left(\frac{u^2}{(1-ne)^4 a^4\left(n_1^2 - n_2^2\right)}\right)\left(\frac{K_0(wh_o/a)}{K_1^2(w)}\right)\right)L_c(1+e). \qquad (7.18)$$

$P_c(e)$ can be derived in a similar fashion. Figure 7.8 shows the theoretical change in P_t and P_c with strain.

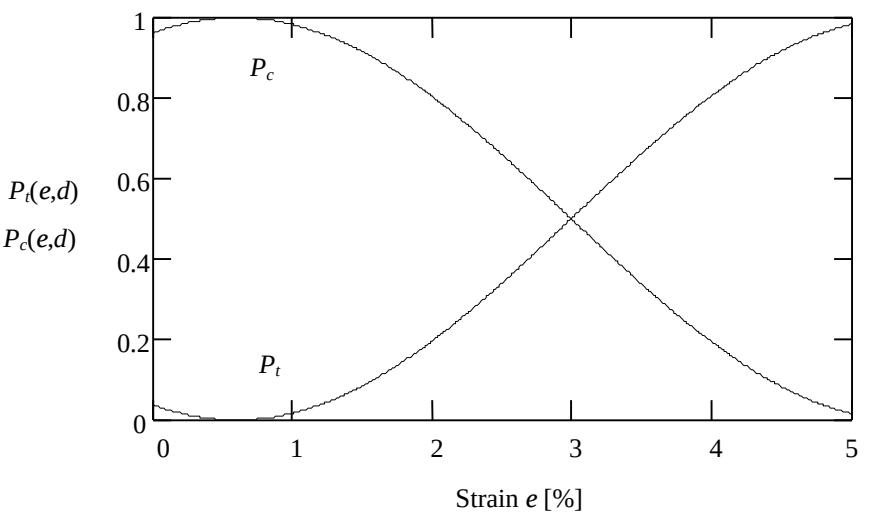

Figure 7.8 Theoretical response of a coupler based strain sensor as a function of longitudinal strain (see figure 7.6) for a fixed wavelength.

By comparing the two output signals with the sum of the signals, an absolute reading of the stress or strain is obtained. The intensity of the signal at the two output legs can be used to measure strain by dividing either one of the signals by the sum of the square of the signals. The signal can be normalized by dividing through $(P_t^2 + P_c^2)^{1/2}$ (since $\cos^2 + \sin^2 \equiv 1$), eliminating the intensity loss in the output leads.

An experiment was performed to investigate this sensing scheme for use in the strain gauge system for the magnet. It was found that despite the ease of the readout scheme and a nice fit of the experimental data to the theoretical curves, the method can not be applied when large compressive stresses are present on the coupler. Since the couplers are manufactured by fusing two glass fibers together while elongating them in the heated stage, the resulting fused area is very thin and fragile. It is found that the couplers could not reliably be loaded under transverse stress without causing permanent damage to the device. A further disadvantage is that the coupler has four leads, of which three have to be used for the readout method.

7.3.4 Interferometric device: the extrinsic Fabry-Perot sensor

An extrinsic Fabry-Perot (FP) optical fiber sensor consists of two spliced fibers that are inserted in an aligning fixture to form a low-finesse cavity. The aligning fixture can be a hollow core glass fiber or a stainless steel tube. The glass-air and air-glass interfaces act as reflectors to generate an interference of the incoming light. The interference of the reflection from the glass-air interface and the reflection from the air-glass interface is dependent on the gap distance in terms of a plane-wave approximation [7.7]. The sensor is depicted in figure 7.9; the readout system is discussed in more detail in section 7.4.

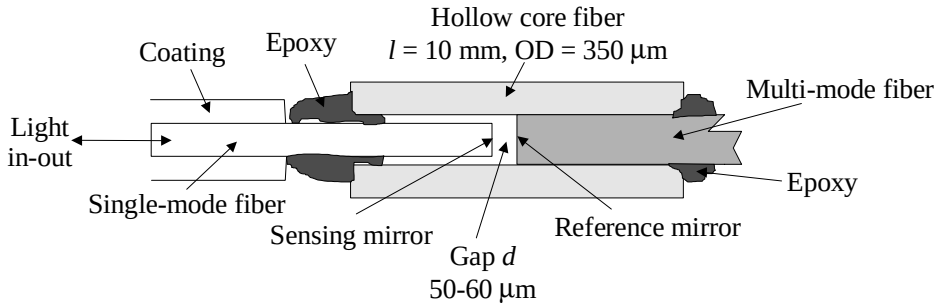

Figure 7.9 Schematic layout of the extrinsic FP sensor. Shown is a cross-section of the sensor, with the single-mode fiber on the left, and the section of multi-mode fiber functioning as a mirror, on the right.

The extrinsic FP sensor is constructed by inserting a cleaved 125 μm multi-mode fiber section (right) into a hollow core glass fiber (middle) with an inner diameter of approximately 130 μm. The multi-mode fiber is used for cost reduction. This fiber is then fixed with a drop of Stycast 2850FT [7.8]. Next, a 100-125 μm OD single-mode fiber is inserted in the other side (left in figure 7.9) of the glass tube, the gap distance d is set to the desired range, and the fiber is fixed. The single-mode fiber length is set at about 3 meters to allow for the leads to exit the cryostat. The length of the glass tube is determined by the desired resolution in the strain measurement, the longer the tube, the higher the resolution but less localization for axial strain. Typically, the tube is about 10 mm in length.

A plane wave can be described as

$$\begin{cases} U_s(x,z,t) = A_s e^{(ij_s)} \\ U_r(x,z,t) = A_r e^{(ij_r)} \end{cases}, \tag{7.19}$$

with U_s the reflection from the sensing mirror and U_r the reflection from the reference mirror, and A_s and A_r the reflection coefficients of the sensing and reflecting mirrors, j_s and j_r the phase of the light at these mirrors. The sensing reflection coefficient A_s can be approximated by the following relation

$$A_s = A_r\left(\frac{ta}{a+2d\,\tan(\sin^{-1}(NA))}\right), \tag{7.20}$$

where a is the fiber core radius, t is the transmission coefficient of the glass-air interface, d is the gap distance and NA is the numerical aperture of the single-mode fiber [7.9]. The measured intensity I/I_{in} at the detector will be the sum of the two amplitudes and is given by:

$$\frac{I}{I_{in}} = |U_s + U_r|^2 = A_s^2 + A_r^2 + 2A_sA_r\cos(j_s - j_r), \tag{7.21}$$

with I_{in} the intensity of the incoming light. When combined with (7.20), it yields:

$$\frac{I}{I_{in}} = A_r^2\{1+\frac{2ta}{a+2d\,\tan(\sin^{-1}(NA))}\times\cos\left(\frac{4pd}{l}\right)+\left(\frac{ta}{a+2d\,\tan(\sin^{-1}(NA))}\right)^2\}, \tag{7.22}$$

where it is assumed that $j_r = 0$ and $j_s = 2d(2\pi/l)$ with l the wavelength of the laser-light in free space. Equation 7.22 shows the drop in average signal intensity with increasing distance d between the mirrors. The theoretical response of an FP-sensor is shown in figure 7.10.

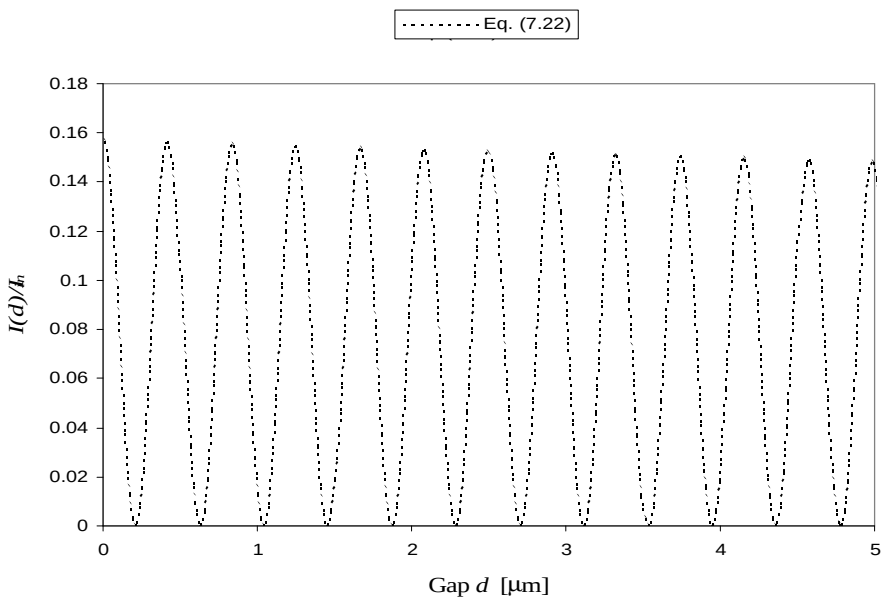

Figure 7.10 Theoretical response of the FP sensor: normalized intensity as a function of the gap distance d at l = 830 nm, for 0 < d < 5 mm.

The relation of normalized intensity I/I_{in} at the detector does not take into account the effect of multiple reflections within the cell cavity. For cells made without a coating on the glass-air interface, this simplification is valid, since only a small fraction of the incoming signal is reflected at the interface. When a coating is applied to the mirror surfaces, the effect on the transfer function is described in section 7.4.6.

Figure 7.10 shows the transfer function of a cell as a function of the gap distance d for $0 < d < 5$ μm. The average intensity of the response drops with increasing gap distance. The response has alternating maxima and minima, with the distance between subsequent maxima equal to half the wavelength l of the incoming light. The distance between the peaks, or fringes, is 415 nm at l = 830 nm. Counting these fringes as a function of applied strain gives an accurate measure of the change in length of the cell, with a resolution of the order of the wavelength of the laser light used. Figure 7.11 shows the transfer function for the typical cell length of 60 μm used in the experiments.

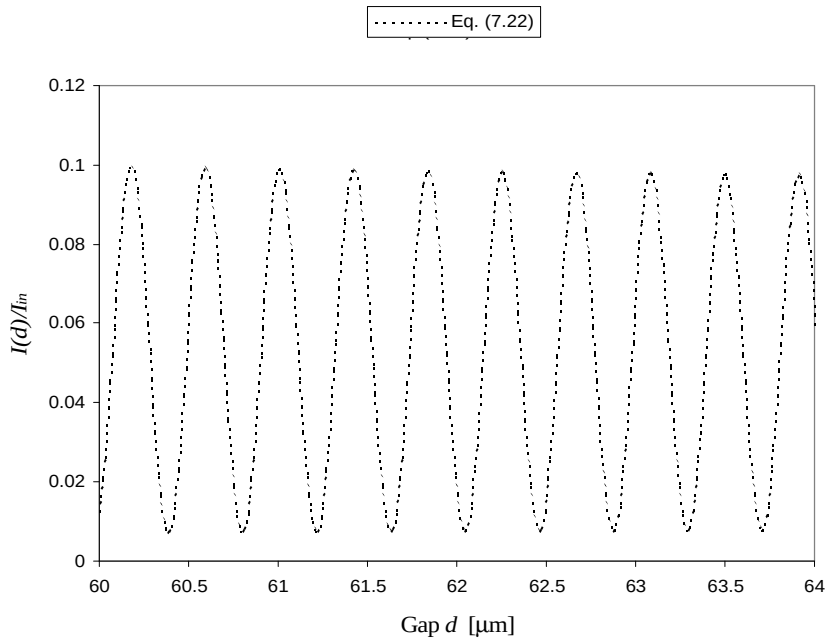

Figure 7.11 Theoretical response of the FP sensor: normalized intensity as a function of the gap distance d at l = 830 nm for 60 < d < 64 mm.

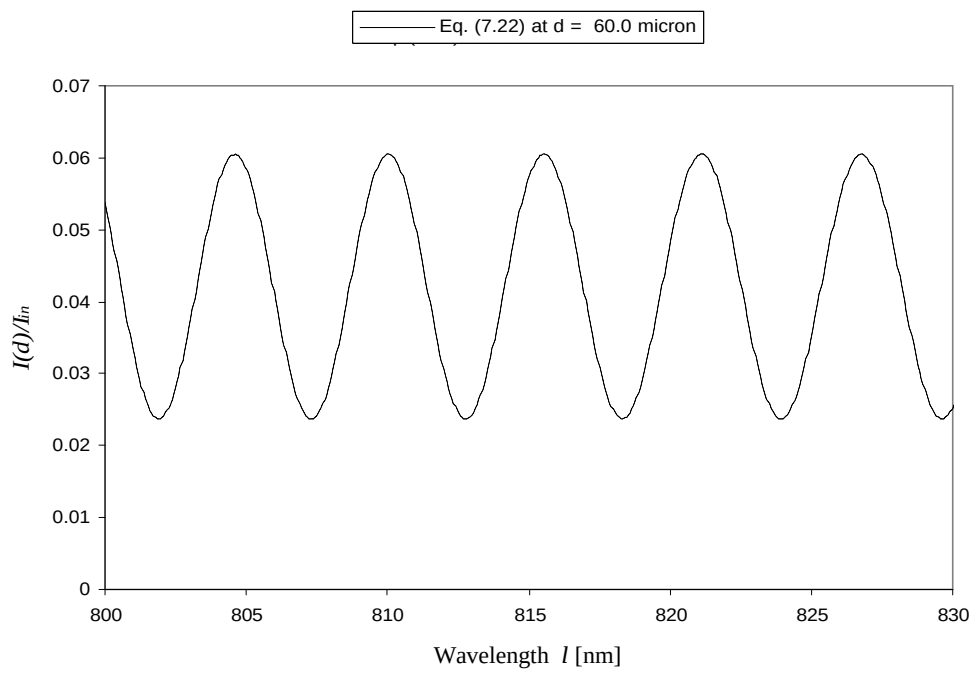

Figure 7.12 Theoretical response of the FP sensor: normalized intensity as a function of the wavelength at gap d = 60 mm for 800 < l < 830 nm.

The gap distance *d* is set to optimize the fringe contrast, while keeping the sensing and reference mirrors from touching each other due to the thermal contraction of the tube (of the order of 40 μm when embedded in the coil windings of a magnet) when it is cooled from room temperature to 4.2 K. Figure 7.12 shows the transfer function of a 60 μm cell as a function of the wavelength.

7.4 Sensor selection for strain and stress measurements in an accelerator magnet

In order to select the best candidate as a sensor for strain and stress measurements in an accelerator magnet, several considerations have to be taken into account. In table 7.1, the advantages and disadvantages of the different sensors types discussed in the previous sections are summarized. Also included are some other sensing methods not discussed here, but considered as possible candidates.

Method	Sensor type	Advantages	Disadvantages	Tested
intensity	Reflection (not discussed)	simple easy to calibrate diameter 1-2 mm one fiber	external stimuli	yes
	micro-bend (section 7.3.1)	simple diameter 0.25 mm two fibers	external stimuli difficult to calibrate	yes
polarization	Birefringence (section 7.3.2)	simple diameter 0.25 mm two fibers very sensitive	external stimuli magnetic field sensitive	yes
spectral	filtered Fabry-Perot (not discussed)	diameter 0.35 mm one fiber	difficult to build difficult to calibrate	no
	Coupler (section 7.3.3)	simple easy to calibrate	four fibers diameter 4-5 mm very fragile device	yes
interferometry	Mach-Zehnder (not discussed)	diameter 0.25 mm very sensitive	external stimuli needs reference leg magnetic field sensitive integrating sensor four fibers	yes
	intrinsic Fabry-Perot (not discussed)	diameter 0.25 mm one fiber	fragile device difficult to build	no
	extrinsic Fabry-Perot fixed wavelength (section 7.3.4, 7.4.1)	*diameter 0.35 mm one fiber easy readout*	*relative measurement*	*yes*
	extrinsic Fabry-Perot variable wavelength (section 7.3.4, 7.4.2)	*diameter 0.35 mm one fiber easy calibration*	*complex readout scheme*	*yes*

Table 7.1 Matrix of the different sensor types and their advantages and disadvantages.

The main selection criteria for the application of a sensor in an accelerator magnet are:

1) small size (width at least smaller than half the minimum Rutherford cable width, or about 5 mm, length not as important);
2) rugged sensor (needs to survive compressive loads up to 200 MPa);
3) insensitivity to external stimuli along the fiber leads from the sensor to the detector;
4) minimum number of fiber leads to each sensor.

Out of the list of table 7.1, the coupler sensor is eliminated for size; all other sensors are comparable in size. The intrinsic Fabry-Perot sensor is not chosen for its fragility (it is similar in principle to the extrinsic FP-sensor, but made without the hollow core. Instead it is made with more fragile fused glass fibers). Sensitivity to external stimuli eliminates all intensity- and polarization-based devices, and the Mach-Zehnder interferometer. The latter is often used for strain measurements, but needs a reference leg that is not influenced during the measurements. In experiments in a cryogenic environment, this is difficult to implement; therefore this sensor is also eliminated from the list of candidates.

The best candidate remaining is the extrinsic Fabry-Perot (FP) interferometer, with three possible readout schemes. The first one, not discussed further here, is based on wavelength filters, but is difficult to calibrate. The two remaining schemes, relative readout using monochromatic light, and absolute readout using white light, can be alternated while using the same sensor type. This fact, combined with the small size, single fiber lead, and easy calibration, led to the selection of the FP-interferometer as the best candidate.

The application of the extrinsic FP-interferometer is described next. Two readout methods are described, the first based on a monochromatic light source, the second on a broadband light source. The discussion of the readout methods is followed by a brief analysis of error sources, temperature compensation, and methods to improve the response function of the sensor.

7.4.1 FP-sensor: laser interferometry

A schematic layout of a readout system using laser light is shown in figure 7.13. Coherent light from the source (typically a laser diode) enters the sensor cell through the single-mode fiber, after passing through a 2x2 coupler and a connector, and is partially reflected at the glass-air interface (sensing mirror, see figure 7.9). The transmitted part is partially reflected at the air-glass interface (reference mirror), and passes back through the air-glass interface (sensing mirror). The terminated right side of the sensor is made of multi-mode fiber for cost reduction. The two resulting waves traveling back through the single-mode fiber interfere, forming the signal described in (7.19)-(7.22).

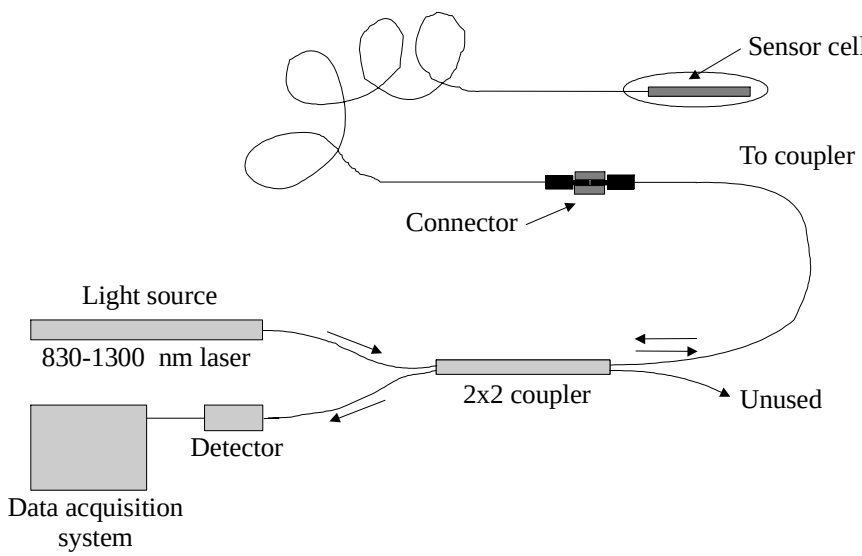

Figure 7.13 Schematic layout of the extrinsic FP sensor readout using a monochromatic light from a laser system.

Higher order reflections are neglected in this analysis, since the reflection coefficient of the air-glass interfaces is only 0.04. The resulting wave passes back through the connector and 2x2 coupler to the detector.

Test performed	Answers	P-value all samples	P-value impregnated samples only	Conclusion
C_1 MJR < C_1 IT	no/no	0.28	0.19	C_1 MJR < C_1 IT is not proven
C_1 MJR < C_1 PIT	no/no	0.18	0.11	C_1 MJR < C_1 PIT is not proven
C_1 IT ≠ C_1 PIT	yes/yes	0.75	0.52	C_1 IT is equal to C_1 PIT
C_2 MJR > C_2 IT	no/yes	0.44	0.01	C_2 MJR > C_2 IT for impregnated samples only
C_2 MJR > C_2 PIT	no/yes	0.06	0.02	C_2 MJR > C_2 PIT for impregnated samples only
C_2 IT > C_2 PIT	no/no	0.18	0.77	C_2 IT > C_2 PIT is not proven
C_3 MJR > C_3 IT	no/yes	0.15	0.001	C_3 MJR > C_3 IT for impregnated samples only
C_3 MJR > C_3 PIT	yes/yes	0.006	0.001	C_3 MJR > C_3 PIT is proven
C_3 IT > C_3 PIT	no/no	0.30	0.61	C_3 IT > C_3 PIT is not proven

Table 5.29 Two-sample t-tests performed to determine whether the coefficients for the different conductor types are statistically distinguishable. The answers in the second column are for tests with all samples/ impregnated samples only.

The two-sample t-test results listed in table 5.29 show that the following conclusions can be made:

1) the hydrostatic coefficient contributing to the I_c degradation is statistically equal for all conductors;
2) the deviatoric coefficient contributing to the I_c degradation is statistically equal for all conductor types when all samples are compared, however, when the impregnated samples are compared separately, the deviatoric coefficient is larger for MJR than for IT or PIT. This means that the MJR conductor is more sensitive to applied pressure for the reversible degradation in impregnated samples;
3) the plastic coefficient for the MJR conductors is larger than that for the PIT conductors (and IT conductors for impregnated samples only). This means that the MJR conductors exhibit more permanent damage due to applied transverse pressure than the IT or PIT conductors;
4) the PIT and IT conductors have a smaller and statistically equal plastic coefficient (the permanent critical current degradation in PIT and IT conductors is similar in magnitude).

In summary, the MJR conductor is the most sensitive of the three, exhibiting larger sensitivity to applied pressure for both reversible and permanent critical current degradation. The IT and PIT conductor are statistically indistinguishable.

5.13 $B_{c2}(P)$ relation

For sample TW2, enough data is available to make a reliable extrapolation for B_{c2} as a function of the applied pressure P. This allows a comparison with data measured by Ten Haken on Nb_3Sn tapes under transverse pressure [5.14]. Figure 5.67 shows a plot of $B_{c2} - B_{c2,0}$ as a function of applied pressure P, with P up to 200 MPa.

Two fits are made to the measured data, one a linear fit to the points for $P \geq 50$ MPa, the second a quadratic fit through all points and the origin. The linear fit shows a slope of –17.1 T/GPa. This is about an order of magnitude larger that the predicted value for a single crystal subjected to hydrostatic compression only. Measurements by Ten Haken show a slope of -1.2 ± 0.2 T/GPa for polycrystalline Nb_3Sn under hydrostatic pressure, whereas a value of –1.7 T/GPa is found in literature ([3.32], see section 3.6.1).

If the gap displacement is large (at least 10 times the wavelength of the light source), the readout of the cell can be performed by counting fringes during the change in length. Alternatively, if the displacement is of the order of the laser wavelength, the change in length is computed from the change in signal intensity using (7.22). The readout method is limited to *relative displacement* only. The instant the laser is turned off, the gap length reference is lost.

A second limitation is the fact that the detection of the displacement is only possible in one direction. When the sensor sees varying tension and compression along the longitudinal axis, the direction of the signal change (increasing or decreasing strain) may not be detected when it coincides with a maximum or minimum of the reflected signal.

The problem of the sign change of the displacement can be solved by using two sensors, each detecting the same displacement but with their transfer functions out of phase by 90° [7.10]. With two cells, the direction change is detected, since one cell will be in the steep section of the transfer function at the time when the other cell might pass through a maximum or minimum.

Accuracy of the sensor for direct strain measurement is limited by the accuracy of the measurement of the cell length in the initial state. This length measurement is limited to about 1 % for a cell length of 10 mm, thus resulting in a maximum strain accuracy of 1 %.

7.4.2 FP-sensor: white light interferometry

The simplified form of the transfer function in (7.22) is of the form

$$I = I_0 \cos(\frac{4p}{l} d + j_0) + C_0 , \tag{7.23}$$

with I_0 the maximum amplitude of the signal, l the wavelength of the laser light, d the gap distance, j_0 the phase offset, and C_0 the initial offset in the signal. This simplification neglects the decrease of the average intensity with increasing cell length, since deviations from the initial cell length of 20-60 µm typically are of the order of 1 µm. When a broad-band light source, such as a super luminescent diode (SLED) or a halogen source is used, as illustrated in figure 7.14, multiple wavelengths are interfering at the detector. An expression for the cell length is obtained by rewriting (7.23), assuming the cell length d being constant (steady state), and looking at different wavelengths with a phase difference of p in the transfer function,

$$\left\{ \begin{array}{c} \frac{4p}{l_1} d = 2pn \\ \frac{4p}{l_2} d = 2p\left(n + \frac{1}{2}\right) \end{array} \right\} \rightarrow \frac{4p}{l_2} d - \frac{4p}{l_1} d = \pm p \rightarrow$$

$$4d(\frac{1}{l_2} - \frac{1}{l_1}) = \pm 1 \rightarrow \frac{l_1}{l_1 l_2} - \frac{l_2}{l_1 l_2} = \frac{\pm 1}{4d} \rightarrow |d| = \frac{\pm 1}{4} \frac{l_1 l_2}{l_1 - l_2} , \tag{7.24}$$

in which l_1 and l_2 are the wavelengths corresponding to a subsequent maximum and minimum as illustrated in figure 7.15. A typical experimental setup is shown in figure 7.15.

By capturing a spectrum of the reflected light that includes multiple maxima and minima of the transfer function, with a spectroscope, an accurate determination of the cell length is made possible. An example of a theoretical spectrum is shown in figure 7.15 for a gap length d of 60 µm and 75 µm respectively.

Using figure 7.15, the gap distance d can be computed from each pair of subsequent maxima and minima in the transfer function. As an example, the theoretical transfer function of the 60 µm cell is used to compute the cell length back from the wavelengths of the maxima and minima. Table 7.2 lists the phase angles for the computation, and their corresponding wavelengths. In the right column, the computed gap distance d from (7.24) is listed for each pair of wavelengths.

In figure 7.16, the measured response of a cell with a gap of approximately 15 µm is compared with the theoretical approximation of (7.22). The amplitude and average of the measured signal is scaled to the theoretical response.

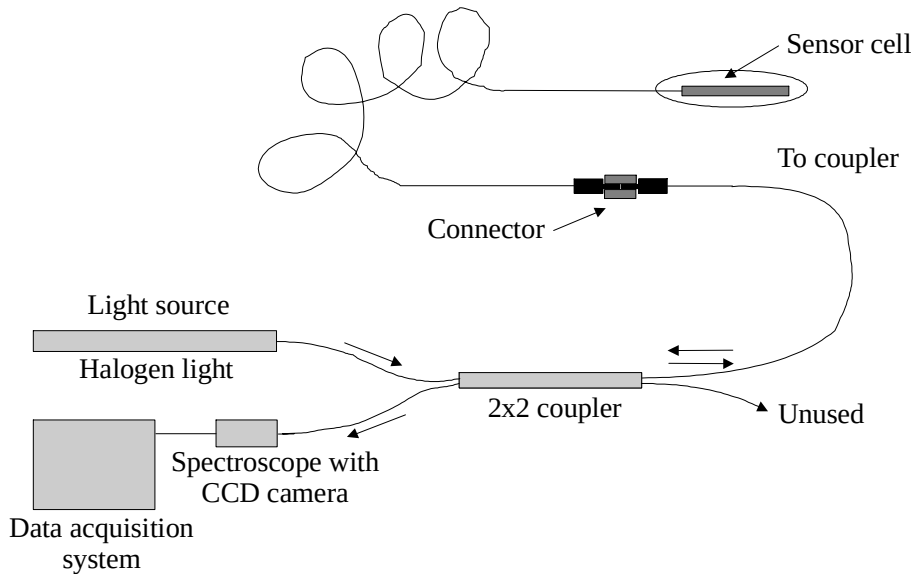

Figure 7.14 Schematic layout of the extrinsic FP sensor readout using a white light system.

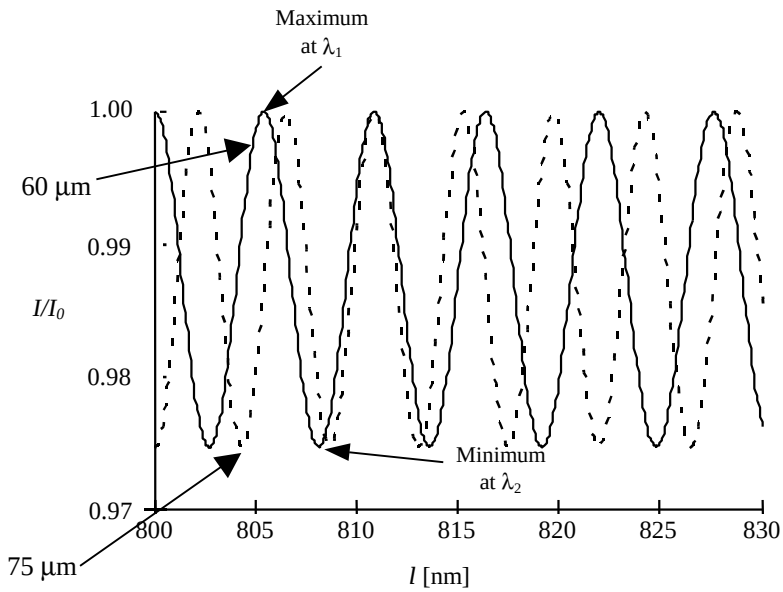

Figure 7.15 Theoretical response of the FP sensor as a function of the wavelength for gap lengths of 60 mm (solid line) and 75 mm (dotted line).

The mismatch in the minimum is caused by a slight error in the calibration of the wavelength versus pixel number in the spectroscope. The gap of the cell is determined to be 15.0±0.5 μm by fitting the two maxima in the theoretical response to the maxima in the measured response (this yields 15.4 μm), or by fitting the first maximum and minimum to the theoretical ones (this yields 14.5 μm). The actual fit is performed by minimizing the square of the difference of the two curves as a function of the gap distance *d*.

Phase angle	Maximum/minimum	Wavelength [nm]	Gap *d* from (7.24)
0	max (l_1 in fig.7.14)	805.35	59.16
π	min (l_2 in fig.7.14)	808.10	60.67
2π	Max	810.80	59.97
3π	Min	813.55	59.30
4π	Max	816.35	60.79
5π	Min	819.10	60.11
6π	Max	821.90	59.46
7π	Min	824.75	59.87
8π	Max	827.60	60.29
9π	Min	830.45	
		Average cell length [μm]	60.0
		Standard deviation [μm]	0.6

Table 7.2 Example computation of the cell length for a theoretical transfer function with d = 60 mm. Note how the rounding of the wavelength to the 0.05 nm resolution affects the determination of the gap d.

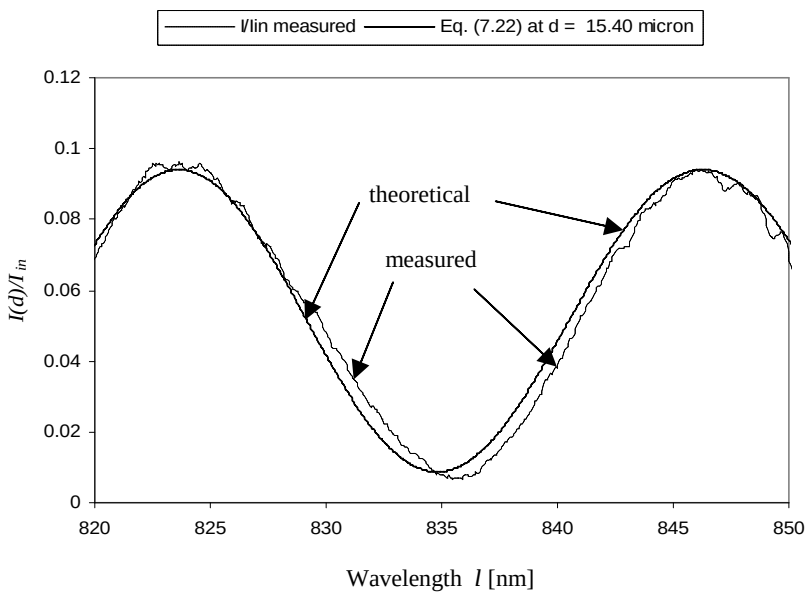

Figure 7.16 Theoretical response function versus measured data on a cell with d @ 15 micron. The maxima of the transfer function are matched at 823 and 846 nm. Note how the minimum near 836 nm is not accurately matched.

It is clear from both table 7.2, and figure 7.16, that errors are introduced in the computation of the gap distance *d* from the spectrum. Both numerical rounding errors, as well as noise and other disturbances in the measurement of the spectrum cause errors in the determination of the gap distance. The error sources for both readout schemes are further discussed in the next section.

7.4.3 Error sources in the white-light sensing schemes

As briefly noted in section 7.4.2, both computation methods for the determination of the gap distance *d*, and hence the strain or stress on the cell, introduce errors. The error in the final result is a combination of the following factors (following the light from source to detector in figure 7.14):

1) non-uniform intensity as a function of wavelength of the light source;
2) transfer function of the 2x2 coupler changes the intensity as a function of the wavelength;
3) influence of the connector (or multiple connectors);
4) excessive strain or stress on the fiber lead (although this will not influence the determination of the gap distance d, it might affect the signal to noise ratio due to excessive signal loss);
5) influence of the connector (second pass);
6) transfer function of the 2x2 coupler (second pass, this time the other leg is used);
7) sensitivity of the detector/spectroscope as a function of the wavelength;
8) resolution of the spectroscope diffraction grating;
9) digital quantization of the spectrum (pixels/nm digitization);
10) calibration accuracy of the detector/spectroscope.

Each of the discrete elements in the measurement system has its own transfer function, which results in a typical measured spectrum as illustrated in figures 7.17 and 7.18. The scans are typical examples of the signal measured at the detector end. Figure 7.17 shows a cell without any error signal from the light source, coupler or connector, whereas figure 7.18 shows an offset in the carrier signal, due to the combined effect of the transfer function of the coupler and light source. The qualitative effect of all the error sources is discussed below. A transfer function of the sensor system, for the measured intensity I at the detector, normalized to its maximum I_0, is given by

$$F_{system}(l,d) \equiv \frac{I}{I_0} = A_{source}(l) \cdot P_t(l) \cdot B_{conn}^2 \cdot D_{cell}(l,d) \cdot P_c(l), \tag{7.25}$$

with $A_{source}(l)$ a function describing the intensity of the light source as a function of the wavelength, $P_t(l)$ the transmitted power through the 2x2 coupler from (7.16), B_{conn}, the transfer function of the connector, $D_{cell}(l,d) = I/I_{in}$ the transfer function of the sensor cell from (7.22) and $P_c(l)$ the coupled power through the 2x2 coupler from (7.16).

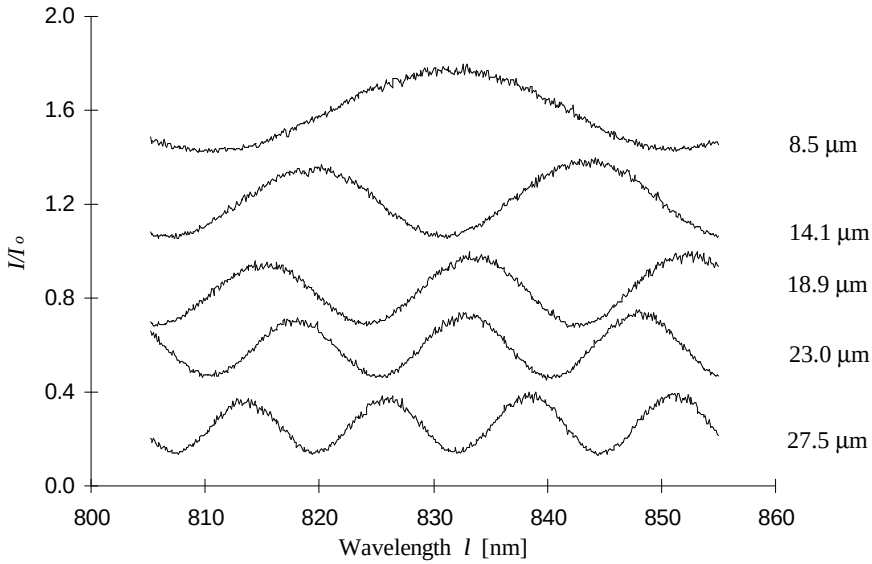

Figure 7.17 Typical transfer function of the sensor element in a laboratory setup. Plotted is the intensity of the signal at the detector for five gap distances, normalized to the maximum signal in the spectrum. The scans are offset on the y-axis to separate the traces. This particular scan shows no effect of offsets in the carrier signal.

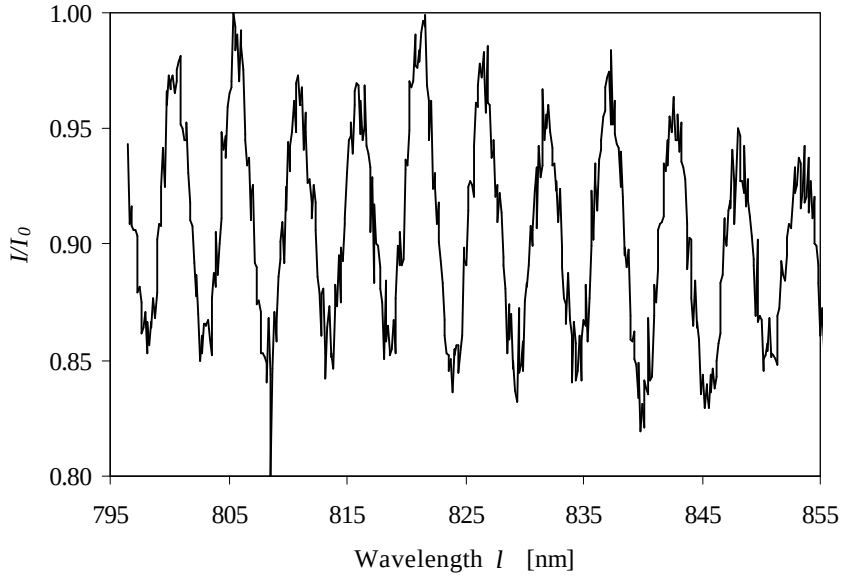

Figure 7.18 Typical transfer function of the sensor element for longer gap lengths. Plotted is the intensity of the signal at the detector, normalized to the maximum signal in the spectrum. This particular scan from 795 to 855 nm illustrates the offset in the carrier signal.

In section 7.4.3.1 the influence from the light source is discussed, followed by the influence of the coupler element in section 7.4.3.2. In section 7.4.3.3, the connector is discussed briefly, followed by a description of the errors introduced by the spectroscope and digitization in section 7.4.3.4. The description of the error terms is followed by an example computation of the gap distance d for the measured response function shown in figure 7.18.

7.4.3.1 Light source

The light source used for all the measurements is a halogen-type light-bulb, which radiates a flat spectrum in the visible light range, and reduces rapidly towards either ultraviolet or near infrared. Since the cut-off wavelength of the single-mode fibers is 750 nm, the spectral range covering the readings from the interferometer will be in the near infrared. This means that the spectrum is a modulation on a carrier signal that is not uniform in intensity over the scanned wavelength range, but decreasing in intensity with increasing wavelength. The signal can be corrected by fitting a straight line or second order curve through the average of the encoded signal, then subtracting the carrier signal, as illustrated in figures 7.19 and 7.20 for the signal from 7.18.

7.4.3.2 Coupler element

The second element in the transfer function is the 2x2 coupler. The coupler divides light into two wavelength ranges, each being transmitted into a different leg, as illustrated in figure 7.6. In essence, the element behaves as a spectral filter, and thus it has a strong influence on the spectral information that is encoded in the interferometer. The transfer function of the coupler is given by equation (7.16). The couplers used in the experiments are selected to have a small variation in transmitted intensity $P_t(l)$ and coupled intensity $P_c(l)$ over the scanned wavelength, typically 795-855 nm. The correction applied for the slope in the carrier signal from the coupler is similar to the one for the light source. It is typically applied as one simultaneous correction of the carrier as discussed in section 7.4.4.

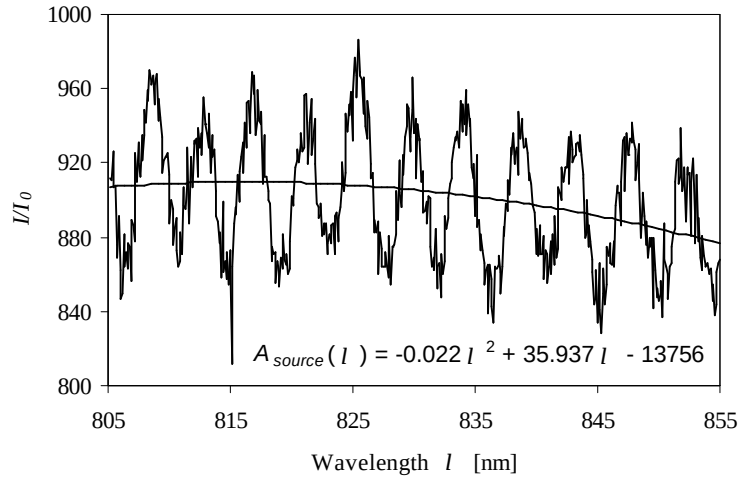

Figure 7.19 Typical measured response from a sensor cell, with a second order fit describing the carrier signal of the light source.

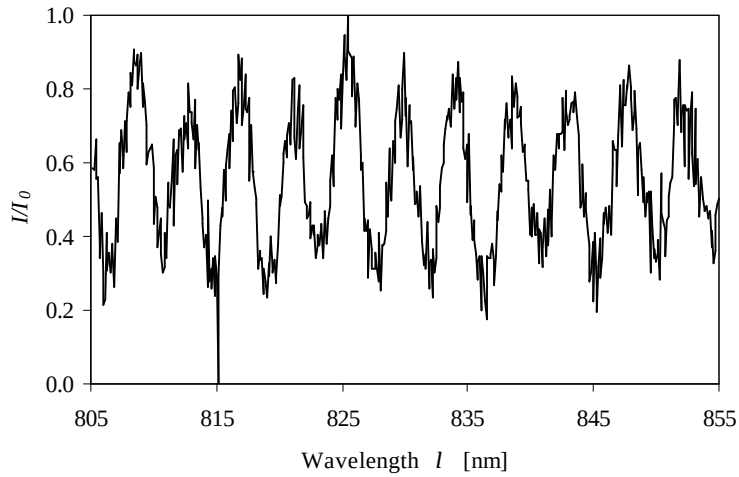

Figure 7.20 Response from the same sensor cell as in figure 7.19, after correction for the non-uniform carrier signal.

7.4.3.3 Connector

The connectors used in the experiments are so-called ST-connectors [7.11]. They function by positioning the two fiber ends so that their cores are aligned. The ends are pressed against each other, and a small amount of index-matching gel is present in the gap between the fiber ends to eliminate reflections within the connector. Typically, the connector does not cause any change in the spectral content of the signal, only a slight attenuation of the signal is present, caused by a small amount of remaining misalignment of the fiber cores. Therefore, the transfer function of the connector B_{conn} can be eliminated from (7.25) by combining the attenuation factor in the normalization to I_0.

7.4.3.4 Spectroscope calibration and digitization of the spectrum

The CCD-camera, which is coupled to a spectroscope, has to be calibrated with a reference spectrum. Figure 7.21 shows such a reference spectrum for a neon light source.

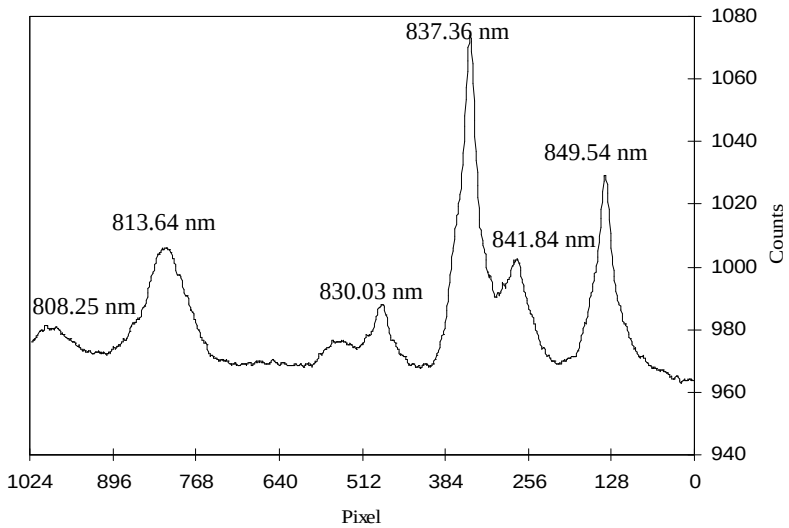

Figure 7.21 Recorded calibration spectrum for a neon light. The spectral lines used for the calibration computation are labeled. The vertical axis shows photon counts on the CCD-detector.

Since the surface of the CCD-detector is flat, and the exit light from the spectroscope is focused on a spherical surface, a minor correction is needed for the small shift in wavelength versus pixel location. The correction factor becomes larger when closer to the edge of the chip. It is typically implemented in the sampling software, with a transfer function for the wavelength as a function of the pixel number on the CCD-chip. The light source used for the calibration is typically a neon light. As an example, the transfer function of the wavelength as function of the pixel number p for the 600 grooves/mm grating, calibrated with the spectrum shown in figure 7.22, is

$$l(p) = 856.76 - 4.936 \cdot 10^{-2}\, p - 2.521 \cdot 10^{-5}\, p^2 + 2.567 \cdot 10^{-8}\, p^3 \qquad (7.26)$$

for a central frequency around 830 nm. The deviation of the calibration curve from the actual spectral lines ranges from 0.02 nm around 800 nm to 0.003 nm at 850 nm for the transfer function of (7.27). The resulting error in the gap d is listed in table 7.3 for various phase differences.

Wavelength pair [nm]	Phase difference	Calibration shift [nm]	Computed gap d [μm]	Error [%]
805.35 – 808.06	π	0.02	60.003	0.005
805.35 – 810.79	2π	0.02	60.003	0.005
805.35 – 816.31	4π	0.02	60.003	0.005
827.60 – 830.46	π	0.003	60.0004	0.0007
824.75 – 830.46	2π	0.003	60.0004	0.0007
819.10 – 830.44	4π	0.003	60.0004	0.0007

Table 7.3 Computation errors in the gap distance d due to calibration error of the spectroscope for various phase differences between the two selected wavelengths, for a cell with a gap of 60 mm.

As is evident from table 7.3, the error introduced by the calibration of the spectroscope is independent of the selection of the phase difference, and negligible in magnitude. This is due to the fact that the error is systematic in nature, hence both wavelengths are offset by a similar amount, which only creates a small error term in the computation of the gap distance.

All spectra are digitized with either 512 or 1024 pixels per scan. Due to the digitization, the smallest wavelength difference that can be resolved is equal to the difference between two adjacent pixels. This truncation of the wavelength is the ultimate resolving power of the spectroscope for a given grating, and is listed in table 7.4, with the resulting error in the computed gap *d*.

The largest error occurs for the 512 pixel scan, where the lower wavelength is rounded up by 0.11/2 = 0.055 nm, and the higher wavelength rounded down the same amount. Around 830 nm this results in an error of 4 % for a phase difference of π, and 1 % for a phase difference of 4π.

Range [pixels]	Delta λ [nm]	Phase difference	Truncated wavelength pair [nm]	Pixel pair	Computed gap *d* [μm]	Error [%]
512	0.11	π	827.61 – 830.47	526 – 474	60.07	0.1
		2π	824.73 – 830.47	580 – 474	59.6	-1
		4π	819.14 – 830.47	692 – 474	60.04	0.1
1024	0.055	π	827.60 – 830.47	526 – 474	60.07	0.1
		2π	824.78 – 830.47	579 – 474	60.19	0.3
		4π	819.10 – 830.47	693 – 474	59.79	-0.3

Table 7.4 Typical computation errors in the gap distance d due to truncation error of the CCD-camera for various phase differences between two selected wavelengths around 830 nm, with a gap of 60 mm.

The worst case error of 4 % for 512 pixels corresponds to 2 % at 1024 pixels. In reality, these worst case truncations only occur for some pixels out of the set, thus the total error will be smaller. For example, using the same 60 μm gap, the gap distance is computed using nine subsequent maxima and minima in the transfer function between 808 and 830 nm. In table 7.5, the computed gap distance *d*, and the resulting standard deviation σ and error (3σ) are listed for the phase difference ranging from π to 6π.

Pixel	Wavelength [nm]	π	2π	3π	4π	5π	6π
999	808.09	60.38	60.13	59.97	60.14	60.07	60.08
900	810.80	59.87	59.77	60.06	59.99	60.02	59.88
822	813.56	59.67	60.16	60.03	60.05	59.88	59.91
754	816.34	60.65	60.20	60.18	59.93	59.96	
693	819.10	59.77	59.95	59.70	59.79		
635	821.91	60.13	59.66	59.80			
580	824.73	59.21	59.64				
526	827.61	60.07					
474	830.47						
	Mean	60.0	60.0	60.0	59.98	59.98	59.96
	σ	0.4	0.24	0.18	0.13	0.08	0.1
	Error at 3σ [%]	2	1	0.9	0.7	0.4	0.5

Table 7.5 Computed gap distance for a 60 mm gap as a function of the phase difference, illustrating the effect on the error in the computation.

Table 7.5 shows that an increase in the phase difference between the chosen peaks initially will reduce the truncation error, but at the expense of data. The smaller the amount of data, the larger the statistical error will become. For the experiments, usually a phase difference of π or 2π is used, resulting in a truncation error of the order of 1-2 % in the gap distance.

In order to increase the apparent resolution of the spectroscope, interpolation of the transfer function of the cell can be used to determine the wavelength of the maxima and minima more accurately. For a one-time computation of the gap distance, this interpolation is not needed, since a length measurement at 1-2 % is accurate enough. However, for strain measurements, where small changes in the cell length of the order of 1-2 μm need to be resolved, better accuracy is needed. This method is discussed in more detail in the example computation in the next section.

7.4.4 Example computation

After subtraction of the carrier signal of the light source and coupler, a "clean" spectrum is obtained, which can be used to determine the original cell length. There are two methods of determination of the gap *d*:

1) use (7.22) to fit a spectrum that is the closest match to the experimental data; *d* follows directly;
2) use (7.24) and a table similar to table 7.5 to fit the wavelength to the known phase angle for the maxima and minima of the spectrum. The gap *d* is computed from a fit of wavelength versus phase.

Both methods are illustrated below, using the corrected spectrum of figure 7.20 as an example. This particular cell has a gap distance of approximately 79.3 μm. Both methods will be used to compute the gap; for the second method pixel interpolation will be discussed.

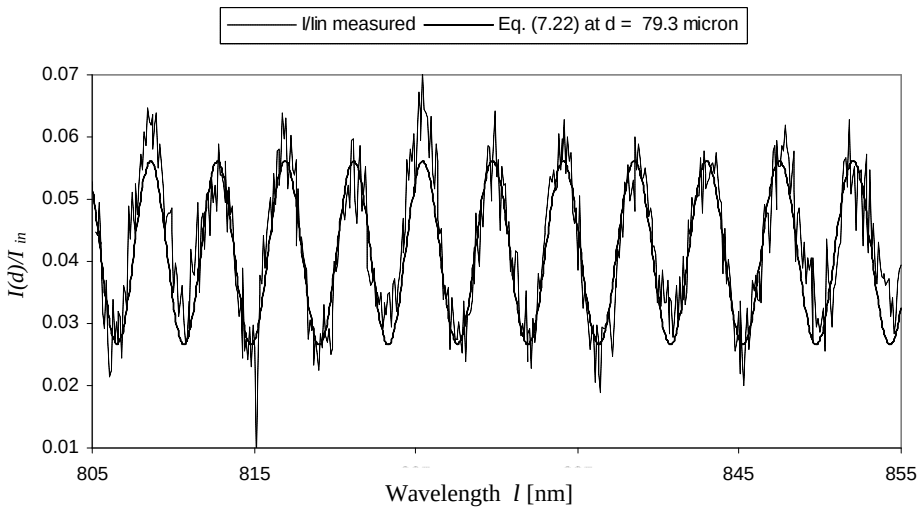

Figure 7.22 Corrected spectrum from figure 7.21 compared to the theoretical spectrum for d = 79.3 mm.

In figure 7.22 the measured signal is shown, with the theoretical spectrum of a cell with $d = 79.3$ μm overlapping the data according to method one. The fit is done by scaling the measured data, which is already scaled by an arbitrary factor I_0, to the theoretical amplitude I/I_{in}, then changing the gap d to match the two functions. Once the gap is determined, the phase angle in (7.22) is shifted to create the overlap. Fitting is done by hand in this method, the approximate error in the gap distance is of the order of 1 %.

Figure 7.23 shows the relation of the wavelength versus the phase angle, used in the determination of the gap distance using method two.

Method two uses the wavelengths corresponding to the extrema of the spectrum. The corresponding wavelengths of all extrema of the transfer function are plotted versus the phase angle.

The gap distance *d* is listed as a function of the pixel, approximate wavelength and the corresponding phase angle in table 7.6, together with the mean, standard deviation and error for each column. The columns differentiate between different steps in the phase angle, from π to 6π. The gap distance is determined to be 79.3 ± 0.6 μm from column 6π, which has the lowest error at 2 %.

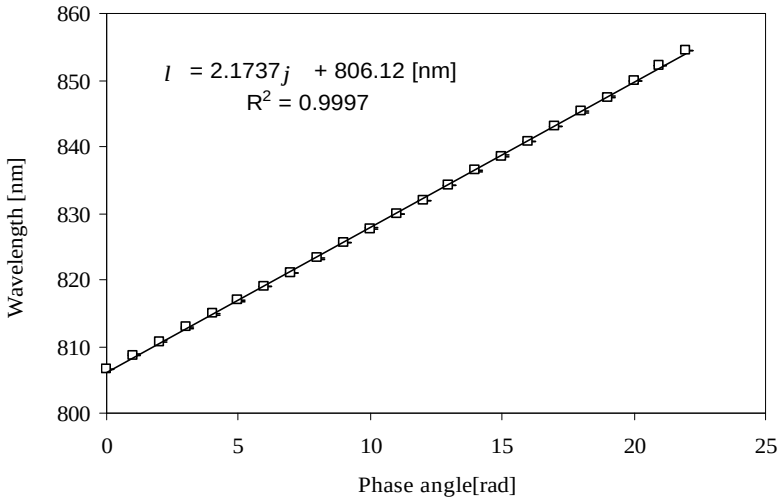

Figure 7.23 Plot of the wavelength as a function of the phase angle. The truncation error in the wavelength is approximately 0.05 nm.

A derivative of method two takes the list of wavelengths of table 7.6, and plots the wavelength as a function of the phase angle, as shown in figure 7.23. This yields a linear relation, with the slope determining the cell length *d* by using the two endpoints on the line, and computing *d* with (7.24). In this way, the phase difference is maximized for the computation, which produces a slightly higher accuracy. The gap distance is 79.2±0.2 μm (0.4 % error).

To summarize, the best method to determine the gap distance *d* from the measured spectrum is the fit of a line through the wavelengths as a function of the phase angle. The typical error is of the order of 0.4 % (worst case) in the gap measurement for a single scan.

Figure 7.24 shows the error in the strain measurement as a function of the strain for various cell lengths and number of captured spectra, followed by an example for a 10 mm cell around 0.1 % strain, with one scan.

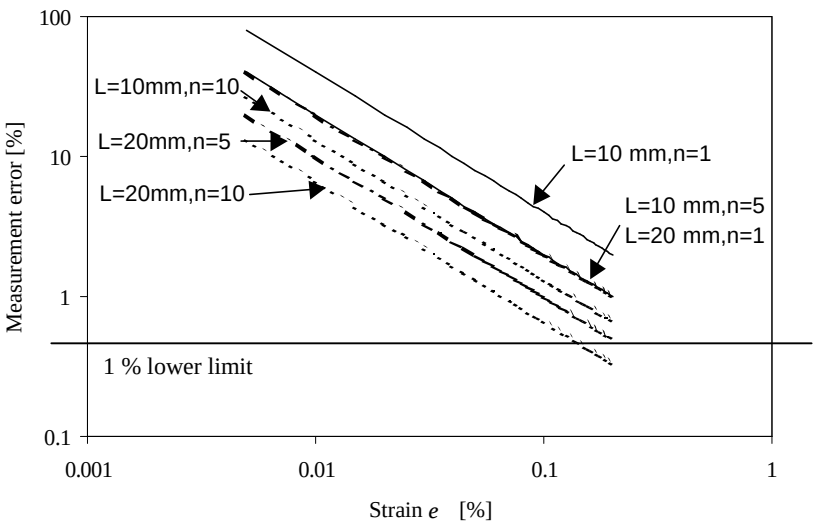

Figure 7.24 Accuracy of the strain measurement as a function of the strain for various cell lengths and number of captured spectra.

Statistical averaging, or an increase in cell length, can be used to increase the resolution. Assuming a normal distribution for the gap measurement, with the worst case error at $\pm 3\sigma$, the error can be improved by running multiple spectra of the same gap distance. Averaging the data results in a decrease of the error with $1/\sqrt{(n-1)}$, with n the number of acquired spectra.

In order to determine the strain in a cell, the gap distance measurement is made before and after the application of the load. The typical gap distance for the cells is between 20 and 60 μm, with a cell length of 10-20 mm. If a 10 mm cell is strained by 0.1 %, this results in a change in gap distance of $0.001 \cdot 10^4$ μm = 10 μm. With an accuracy of about 0.2 μm per measurement, the error in the strain measurement is 4 % at the worst case for a strain of 0.1 %. The error in the strain measurement scales linearly with the error in the gap measurement. The lower bound of the error in the strain measurement is still 1 % due to inaccuracy of the cell length itself, as discussed in section 7.4.1.

Pixel	Wavelength [nm]	π	2 π	3 π	4 π	5 π	6 π
994	806.55	76.11	78.08	78.89	79.39	79.78	79.49
950	808.70	80.15	80.35	80.55	80.76	80.20	80.53
908	810.74	80.55	80.76	80.96	80.22	80.61	80.31
866	812.79	80.96	81.16	80.11	80.62	80.26	78.89
824	814.83	81.37	79.68	80.51	80.09	78.49	78.70
782	816.88	78.07	80.08	79.67	77.81	78.18	78.50
738	819.02	82.21	80.50	77.72	78.21	78.59	78.91
696	821.06	78.87	75.65	76.97	77.74	78.29	78.72
652	823.21	72.69	76.05	77.37	78.14	78.69	78.55
604	825.54	79.73	79.94	80.14	80.35	79.84	79.58
560	827.69	80.15	80.35	80.56	79.87	79.55	79.99
516	829.83	80.56	80.77	79.78	79.40	79.96	79.81
472	831.97	80.98	79.39	79.02	79.81	79.66	79.64
428	834.11	77.86	78.07	79.42	79.34	79.38	79.47
382	836.35	78.28	80.23	79.85	79.77	79.80	78.77
336	838.59	82.27	80.66	80.27	80.19	78.86	78.63
292	840.73	79.10	79.31	79.52	78.06	77.94	79.03
246	842.97	79.52	79.74	77.71	77.65	79.01	
200	845.21	79.95	76.84	77.05	78.88		
154	847.45	73.96	75.68	78.54			
104	849.89	77.47	81.05				
56	852.23	84.96					
12	854.37						
	Mean	79	79	79	79	79.3	79.3
	σ	3	1.8	1.3	1.0	0.8	0.6
	Error at 3σ [%]	10	7	5	4	3	2

Table 7.6 Computed gap distance for a 79.3 mm gap as a function of the phase difference, illustrating the effect on the error in the computation.

7.4.5 Temperature compensation

Since the measurement principle of the extrinsic Fabry-Perot sensor is based on a displacement of the two mirrors, the thermal contraction of the sensor has to be taken into account in the analysis. It is inherent to the design of the sensor head that the mechanical strain acting on the sensor can not be separated from the thermal strain due to shrinkage or elongation of the tube during a temperature change. This means that the temperature change has to be compensated for in the analysis of the results.

The easiest way to implement temperature compensation on the sensor is to embed an identical second FP-sensor next to the strained sensor. This sensor is not subjected to the mechanical strain of the main sensor. This way, the thermal shrinkage can be measured independently of the main strain sensor, thereby canceling the influence of a temperature change in the data processing phase. In the experiments in the magnet, there was no need for a measurement of the strain as a function of the temperature and time during cool-down or warm-up, hence the compensation method was not implemented on the sensors. Instead, intermediate strain and stress measurements are taken in liquid nitrogen at 77 K in steady state.

7.4.6 Further optimization of the sensor cell transfer function

To further improve the sensitivity of the cells, the application of a thin gold coating to the surfaces of both fiber ends is investigated. Its purpose is to increase the reflection coefficient r of the glass-air interface, thereby increasing the effect of the higher order reflections in the cell cavity. The response function given in (7.22) essentially neglects any higher order reflections between the mirrors. The approximation of the transfer function works well for the glass-air interface, but a gold coated cell requires a more precise analysis.

Assuming a phase difference of $j = (4\pi/l)nd\cos a$, with $a = 0$ the angle of incidence of the light, $n = 1$ the refractive index of the medium between the mirrors, d the distance between the mirrors and r the reflection coefficient, the normalized intensity I_d / I_{in} at the detector is [7.12]:

$$\frac{I_d}{I_{in}} = 1 - \frac{F \sin^2(\frac{2pd}{l})}{1 + F \sin^2(\frac{2pd}{l})}, \quad F = \frac{4r}{(1-r)^2}. \tag{7.27}$$

Figures 7.25 shows the theoretical response of a cavity as a function of the wavelength for a reflection coefficient $r = 0.1$, which yields $A_r = \sqrt{(1\text{-}r)^2} = \sqrt{(1\text{-}0.9)^2} = 0.44$ in (7.19). Absorption at the metal layer is neglected.

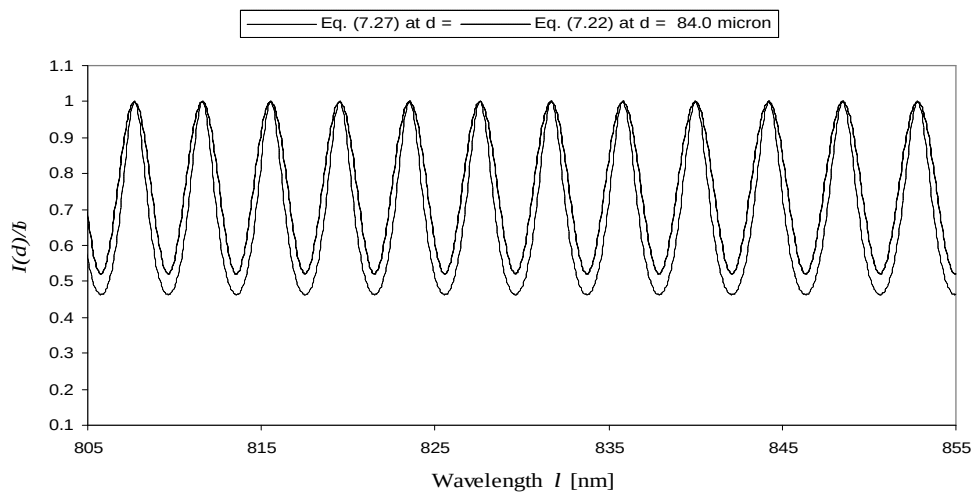

Figure 7.25 Normalized intensity as a function of the wavelength for $A_r = 0.44$ for equations (7.22) and (7.27).

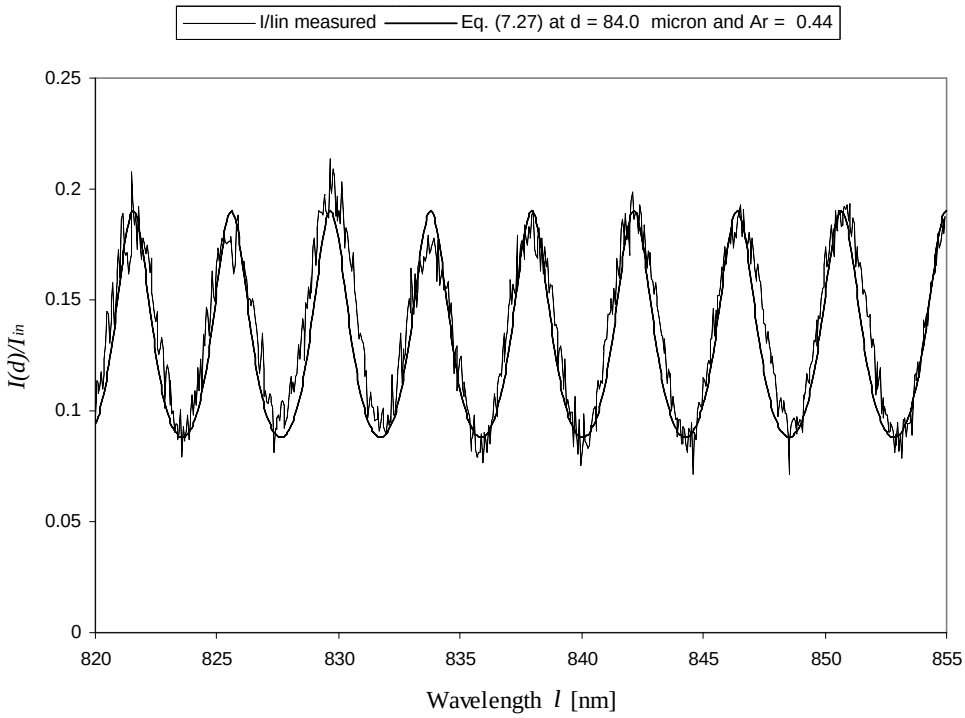

Figure 7.26 Measured response of a sensor cell with a gold mirror compared to a theoretical spectrum from (7.27), with d = 84.0 mm and A_r = 0.44.

Figure 7.26 illustrates how the sensitivity of the cells can be improved by increasing the gold mirror reflection coefficient A_r. An actual spectrum of a cell with a cold coating is shown. The amplitude of the signal is increased by 12%, and the peaks are narrower, which makes it easier to determine the corresponding wavelength. However, the curve in figure 7.25 for equation (7.27) only shows the signal at a zero incidence angle. In reality, a cone of light is emitted from the fiber end, up to an angle of about 20 degrees, which causes a small reduction in the signal to noise ratio. Still, the net effect of the application of a gold mirror is beneficial to increase the sensitivity of the cell. Increasing the amount of gold further enhances the effect. For the experiment, no special effort is made to ensure an optimal transfer function during the cell manufacturing process. Due to the complexity of the application of the gold mirror, the method is not applied for the sensors used in the magnet test.

7.5 Summary

The extrinsic fiber-optic Fabry-Perot sensor is selected as the best candidate to measure stress, strain or temperature in an environment with large electromagnetic fields. The sensor has some major advantages over conventional electrical measurement techniques:

1) small in size (fiber coating outer diameter (OD) is 250 μm, sensor OD is 350 μm);
2) not influenced by electromagnetic (EM)-fields;
3) non-conductive material (no possibility of short circuits between the cables).

These characteristics allow for direct stress and strain measurements within coil windings, as for example in the 13 T Nb_3Sn dipole magnet.

The accuracy of the sensors in absolute strain readout mode, using white light, is a function of the cell length and the number of captured spectra. For the relevant range of 0.01-0.15 % strain, and a typical cell length of 10 mm, the measurement error ranges from 10 % down to 1 %. Typically, samples of five spectra are measured in the experiments.

The following sections illustrate the use of these sensors in an experimental setup to measure strain and stress within the coil windings of an accelerator dipole magnet.

Chapter 8

Stress and strain measurements in the accelerator dipole model magnet

A detailed analysis of the stress and strain measurements in the 13T Nb_3Sn model accelerator dipole magnet "D20" is presented. Design details of the magnet, relevant to the stress and strain measurements, are discussed in more detail in this chapter. A prediction of the critical field of the magnet is given, based on the measured cable performance described in chapter 5, and the stress predictions from FEA models of the magnet design.

A description of the application of fiber-optic sensors in an accelerator magnet coil winding for stress and strain measurements is given. The design of a complete readout system, and the results from tests in a model of a section of the magnet are presented.

The strain and stress measurements performed during the construction of the model sections of the magnet (cookies) and during coil construction and assembly are discussed. Both the results from the resistive strain gauges as well as those from the fiber-optic sensors are analyzed.

First, the designs of stress transducers for both the model test and the coils are shown. Next, the test results from the demonstration transducers are discussed, followed by the results from the mechanical model test.

Thereafter, the changes in stress and strain in the winding package during construction, cooling-down and warming-up are shown; these result in an updated prediction of the critical field.

Finally, the training behavior of the magnet is analyzed. Results from both the electrical and fiber-optic gauges are discussed to demonstrate the feasibility of the use of fiber-optic sensors in accelerator dipole magnets.

8.1 Introduction

In chapter 1, the need for accurate stress and strain measurements within the coil winding of accelerator dipole magnets was discussed. Here, the design, construction, and test results of stress and strain sensors, specifically made for this purpose, are analyzed.

In section 8.2, the mechanical structure of the magnet is discussed in more detail. The method of control of pre-stress during assembly, cooling-down and operation is analyzed. In section 8.3, the resulting stress on the individual cables and strands is computed, followed by a prediction of the magnet performance in section 8.4. This prediction is based on the critical current degradation measurements, and FEA models of the magnet. The fiber-optic strain and stress measurement system is discussed in section 8.5. The design of a stress transducer for the pole-piece of the magnet is illustrated. This transducer is used for both the resistive strain gauge system, as well as a fiber-optic system. Also, a thin sensor matrix for incorporation in the mid-plane of the magnet is shown. Test results of the sensor matrix at 293 K and 77 K are analyzed.

In section 8.6, the calibration and reproducibility of the conventional resistive stress transducers for both the model "cookie" test and the magnet test is discussed. This is followed by the test results of the model test. Stress measurements during assembly and cooling-down are analyzed. The analysis of the test results is followed by a summary of the stress measurements in the model test, and an updated prediction of the critical field of the magnet, in section 8.8.

In section 8.9, the measurement plan and experimental setup of the stress and strain gauges for the magnet test are discussed. The experimental setup is different from the original one discussed in section 8.5, resulting in the elimination of the mid-plane stress transducers in the y-direction, and a reduction of the amount of simultaneous channels available.

In sections 8.10 through 8.13, the magnet performance, and detailed stress and strain measurements are analyzed. The magnet has reached 12.78 T at 4.4.K, after a significant number of 34 *training*[1] quenches. The training behavior is analyzed, and changes in stress, strain and end-force of the magnet are discussed. Significant mechanical imbalance is found in the end-plate loads in the longitudinal direction. Finally, in section 8.14, the implications of rapid warming-up of the magnet is discussed.

8.2 Details of the magnet mechanical structure

In this section, the mechanical structure of the model dipole magnet is discussed in more detail. The design details are selected to provide a more thorough understanding of the behavior of the structure of the magnet during cooling-down, operation and warming-up. The expected design pre-stress at various locations in the coil winding is shown, for the three distinct stages of magnet assembly, cooling-down to 4.3 K, and operation at full field of 13 T. The design stress is used in section 8.4 to predict the ultimate performance of the magnet. The constraining method chosen for the magnet is the support of the Lorentz forces through the iron yoke, which is method B in figure 2.4, chapter 2. This choice is based on the required large magnetic field and consequently large Lorentz force. In order to generate a 13 T field with the minimum amount of superconductor, the iron has to be placed as close as possible to the coils to fully utilize the mirror currents for added field strength. This necessitates the use of a thin collar, making method B the most suitable option. A schematic layout of the cross-section of the coils and collar (upper half) is shown in figure 8.1.

The upper half of the coils is assembled out of two coil segments, each containing two layers impregnated as one component using CTD-101 epoxy [8.1]. Both components have a different pole angle, thus two pole-pieces with a flat surface along two layers are used. The entire assembly is contained in a thin aluminum-bronze collar, and surrounded by the iron yoke, shown in figure 8.2.

---

[1] Training of a magnet is the repeated ramping of the current until a quench occurs. Usually, each subsequent quench occurs at a higher field, until no further improvement is evident. The field at which this happens is called the *plateau* field. This phenomenon is due to mechanical disturbances in the magnet, for example causing stick-slip motion of the conductor towards the ideal location. Training quenches are undesirable, a well designed and constructed magnet could ramp to design field without any training.

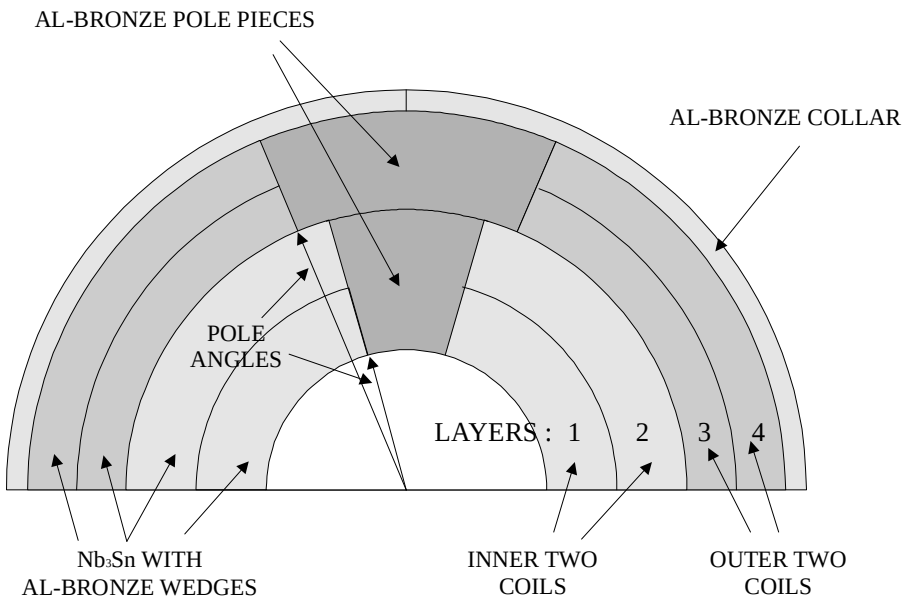

Figure 8.1 Schematic layout of the cross-section of the upper half of the coils.

Due to the fact that the magnet system is designed to be a test-bed for coils made of new superconductors, the system has to be designed so it can be easily disassembled. For this reason, a novel method is used to apply the pre-stress [8.2].

After the placement of the iron yokes around the collared coil, a 3 mm wide stainless steel band is wrapped around the yokes with a tension of 863 N, hence the name "wire wrap". Each successive wrap presses the yokes further onto the coils, adding approximately 4 MPa of pre-stress to the coils. The process can be continued until the required pre-stress is reached, it can also be easily reversed to disassemble the magnet.

The accumulation of the stress is not completely linear due to the fact that each additional layer compresses the structure, thus reducing a small fraction of the tension on the previous layers. This effect is small, and did not prove to be a problem in the construction of the magnet.

The longitudinal cross-section in figure 8.3 illustrates the method of constraining the ends of the coil. Due to the large Lorentz forces acting radially, and the radial constraint of the collar and yoke, the coils will elongate in the longitudinal direction through the Poisson effect.

To restrict the coil from elongating beyond the maximum strain of 0.2 %, the ends are held in place by torque bolts that react the force against a stainless steel shell. The thickness of the plate is designed to carry the entire end load, and thus limit the strain on the coils for a worst case load.

In reality, a large fraction of the longitudinal load is transmitted through friction between coil and collar, and collar and yoke plates, to the bolts constraining the yoke plates. The exact balance between the fraction of the load carried on the end-plates, and on the yoke bolts, is difficult to predict. This is due to the fact that the friction at the various interfaces is a function of the applied transverse load at that interface and the history of the loads. The transverse load in turn is determined by the mechanical tolerances on the components. The tolerances are generally sufficiently large to make an accurate prediction of the end load difficult.

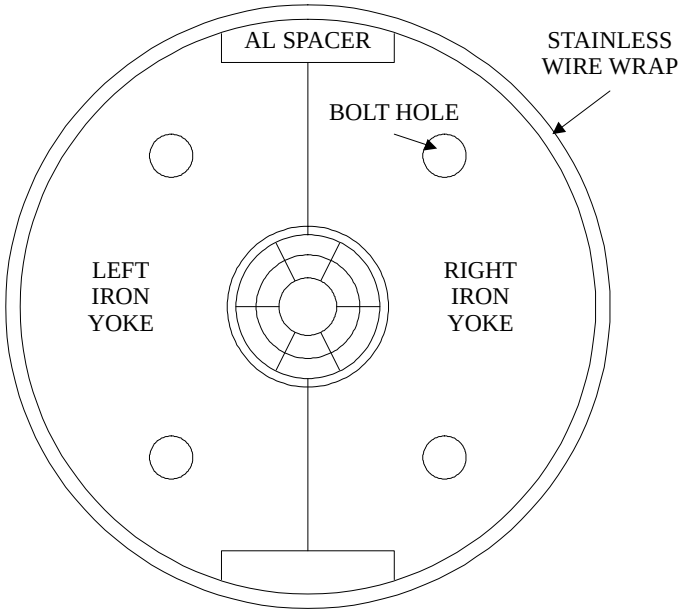

Figure 8.2 Schematic cross-section of the mechanical assembly.

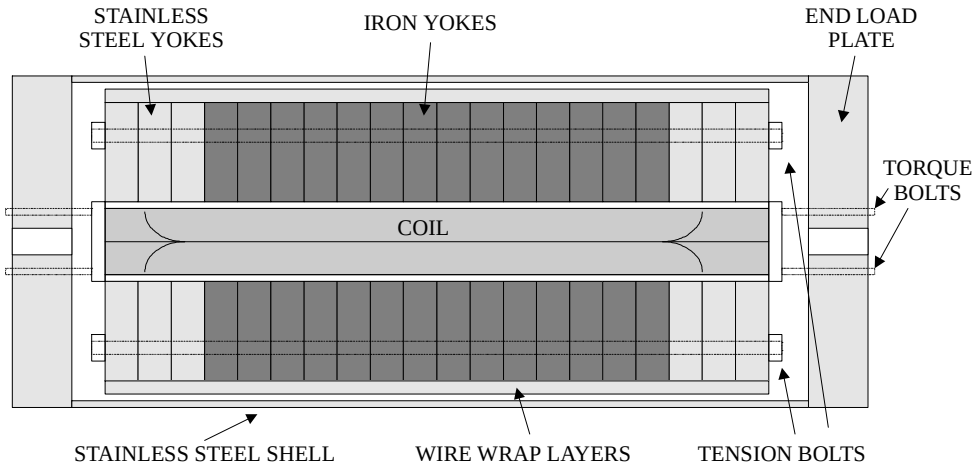

Figure 8.3 Schematic longitudinal cross-section of the coil structure.

8.2.1 Control of the pre-stress

A feature is added to the mechanical structure of the magnet, designed to control the maximum pre-stress applied to the coil during assembly and cooling to 4.3 K. Due to the large Lorentz forces generated by the 13 T field, and the decision to maintain positive stress at the pole face, the pre-stress has to be high. If no special features are incorporated in the design, the required pre-stress on the winding would be in excess of 180 MPa. Since the Nb_3Sn coils are easily damaged by excessive compressive stress, it is essential to limit the maximum pre-stress on the coil. Also, since critical current is reduced by applied stress, the stress on the winding at full field needs to be limited as much as possible.

To ensure that the remaining pre-stress on the coil is sufficient at 4.3 K and full field, but not excessive at room temperature, an aluminum spacer bar is added to the structure, as shown in figure 8.4. The width of the spacer bar is calculated to be less than the space in the iron yokes (gap partially open). The gap between the iron yokes is open at room temperature and tapered with the smaller gap near the coils.

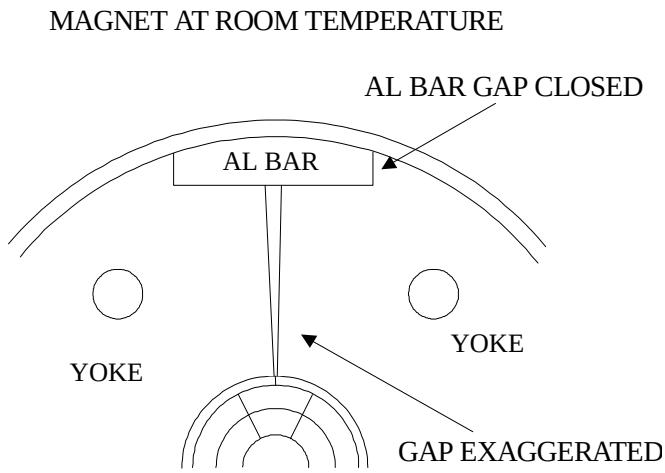

Figure 8.4 Illustration of the use of an aluminum spacer bar to control the maximum stress during assembly and cooling down (room temperature configuration).

When the pre-stress is applied through the wire wind method, the gap gradually closes, compressing the coils primarily in the horizontal plane. At about 80 MPa the iron yokes will close onto the aluminum bar, with a gap of about 50 μm left between the yokes. Further application of pre-stress will partially compress the aluminum bar, thus reducing the further accumulation of compression on the coils. Table 8.1 lists the averaged design stress at the different locations at room temperature, 4.3 K and at 13 T [8.3].

Area	Coil layer	Pre-stress applied at 300 K [MPa]		Cooled to 4.3 K [MPa]		Energized at 13 T [MPa]	
		average	range	average	range	average	range
Mid-plane	1-2	79	85-74	65	30-84	77	108-63
	3-4	85	84-89	75	68-78	131	133-130
Pole-piece interface	1-2	83	134-60	76	152-29	18	9-20
	3-4	86	100-76	75	85-65	15	14-16

Table 8.1 Averaged design stress and range for various locations and phases of construction and operation.

The numbers listed in table 8.1 show that the averaged stress in the coils is fairly uniform across the different locations, but large gradients still exist across the coil surfaces. The small fiber-optic sensors are designed to measure these gradients. The gradients are present at both the mid-plane location and at the interface between the coils and the pole-piece, and exist when the pre-stress is applied, and after cooling-down, as discussed in the next section.

8.2.2 Cooling-down

When the magnet is cooling down to 4.3 K or 1.8 K, part of the pre-stress is lost due to the difference in thermal contraction of the coils and the containment structure. The different components of the magnet cross-section have different thermal expansion coefficients, which will cause a change in the stress distribution of the coil package. The total shrinkage of each component is determined by the integral of the thermal expansion coefficient $\alpha(T)$ from room temperature to liquid helium temperature, as in

$$\frac{\Delta l}{l} = \int_{T=293}^{T=4.3} a\,(T)dT\,. \tag{8.1}$$

Table 8.2 lists the integrated thermal expansion coefficients of the materials used in the magnet. In this magnet, the epoxy impregnated coil package will shrink more than the surrounding iron yokes, effectively lowering the pre-stress that is applied at room temperature. This means that the required pre-stress at room temperature has to be increased by this amount of reduction due to the shrinkage to assure a positive stress at the pole-piece interface when the magnet is energized. The excess pre-stress is partially taken up by the compressed aluminum bar, and partially by additional compression of the coils at the pole-piece interface.

Material/component	Integrated thermal expansion coefficient	Reference
Coil structure/Nb_3Sn cables (impregnated)	-2.8×10^{-3} to -3.5×10^{-3}	[8.4]
Aluminum (5%) bronze (collar)	-3.8×10^{-3}	[8.5]
Iron yoke	-2.0×10^{-3}	[8.5]
Stainless steel (yoke)	-2.97×10^{-3}	[8.5]
Stainless steel (wire wrap)	-2.97×10^{-3}	[8.5]
CTD-101 epoxy	-12×10^{-3}	[8.1]

Table 8.2 Integrated thermal expansion coefficients of the materials used in the magnet.

In figure 8.5, the events in the cooling-down process are illustrated graphically. As is evident from table 8.2, the coil and stainless steel wire wrap will shrink more than the iron yoke. While the structure is shrinking, the iron will initially follow the shrinking aluminum bar (it is pressed against it by the tensioned wire wrap), until the gap in the inner section of the iron yoke is closed.

After the aluminum bar loses contact at about 100 K, the remaining yoke gap continues to close. At about 40 K, the gap will close completely [8.3]. Further lowering of the temperature results in reduction of pre-stress on the coils.

The size of the aluminum bar[2] determines the temperature at which the gap between the iron yokes closes, and hence the final pre-stress on the coils[3]. Increasing this closure temperature decreases the final pre-stress on the coils. Figure 8.6 shows the final state of the gap at the aluminum bar.

In the longitudinal direction, the same difference in shrinkage changes the stress on the ends of the coil, as illustrated in figure 8.7. The yoke plates are held together by tension bolts. These bolts shrink by about the same amount as the coils and the stainless steel outer shell. The iron yoke plates shrink less, thus straining the coil and the bolts.

[2] In both the mechanical model assembly and the magnet assembly, the actual size of this aluminum bar is fixed, but the remaining gap between the slots in the yoke plates and the aluminum bar is fine-tuned with stainless steel shims of varying thickness.

[3] The final pre-stress is also determined by additional shim sheets placed on the outer radius of the coils, between the coils and the collar. Also not shown in figure 8.5 are quench heater foils at this location.

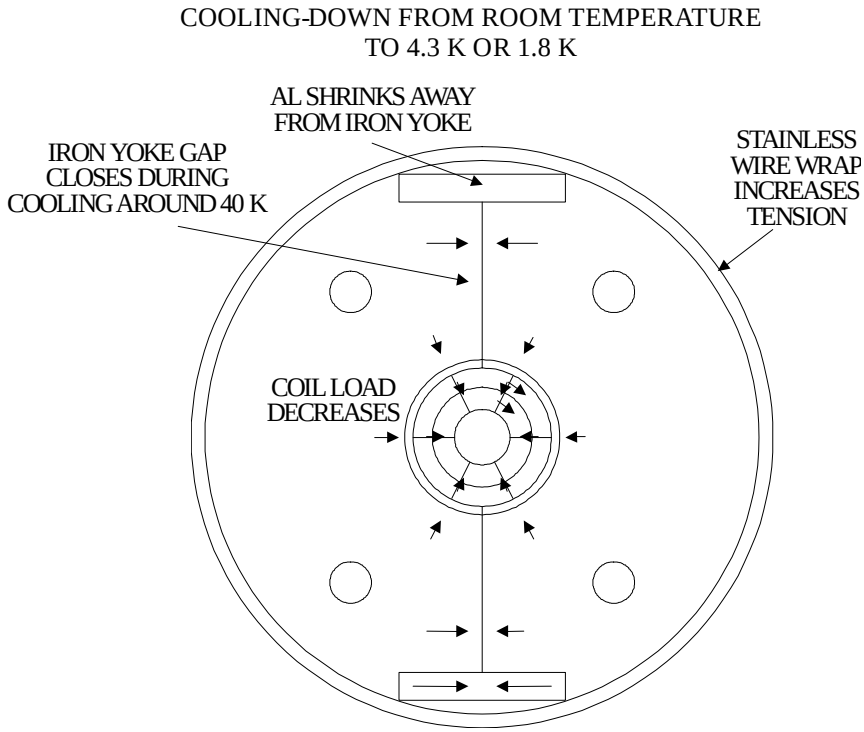

Figure 8.5 Schematic cross-section of the coil structure during cooling-down from room temperature to 4.3 K or 1.8 K.

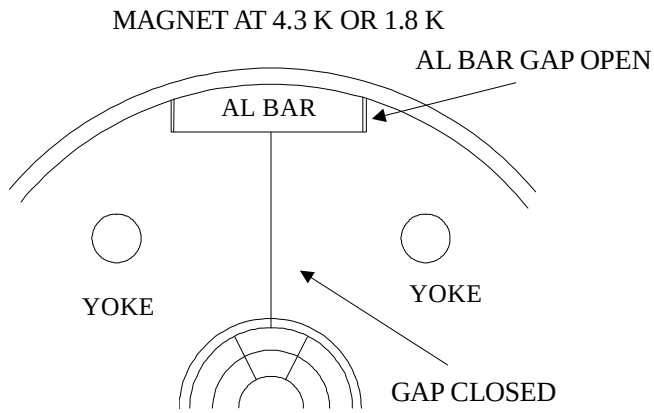

Figure 8.6 Illustration of the use of an aluminum spacer bar to control the maximum stress during assembly and cooling-down (cold configuration).

Because the smaller shrinkage of the iron yokes counteracts the larger shrinkage of the coils and stainless steel shell, the final pre-stress on the coil ends is difficult to determine. Assuming that the friction coefficient is high enough to prevent the coil from slipping inside the iron yokes, the pre-stress will increase on the end-plates during the cooling-down of the magnet.

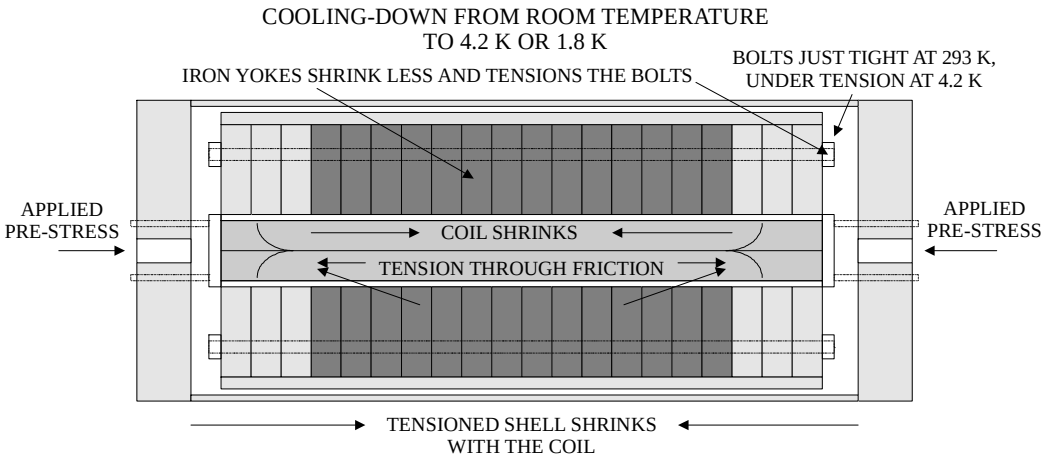

Figure 8.7 Longitudinal cross-section of the coil structure.

8.2.3 Lorentz force at the operating current

When the magnet is in operation at low temperature and full current, the stress on the pole-piece interface is low, but still compressive. When the magnet is energized, the coils will move towards each other in the median plane, and outward radially, thereby increasing the stress on the horizontal symmetry plane. The collar expands 63 μm in the horizontal direction and contracts 58 μm in the vertical direction as a result of the forces. Figure 8.8 illustrates the direction of the forces.

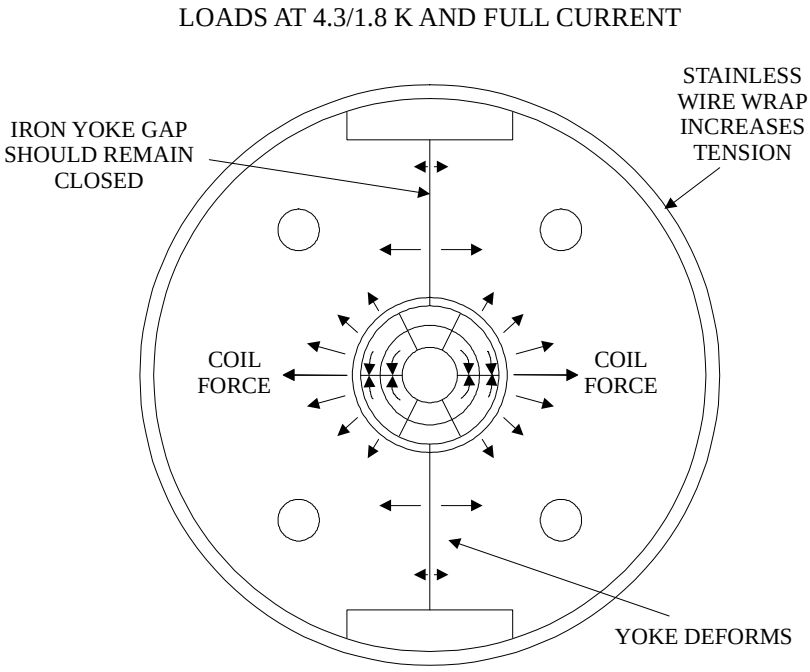

Figure 8.8 Simplified illustration of the direction of the forces during operation of the magnet.

A balance has to be found in the design to assure contact at all times in the pole areas to avoid the epoxy bond at the pole-piece interface from breaking, while minimizing the stress on the horizontal median plane to avoid damaging the conductor. It has to be mentioned here that this particular design, in which the coils and pole-pieces are impregnated as an integral unit, relies on this interface to be in full contact.

As shown in figure 8.8, the Lorentz force on the coils tries to bend the yoke plates outward, decreasing the compression on the yoke gap. Since this gap has to remain closed during operation to ensure structural integrity of the support structure, the applied pre-stress has to be large enough to counteract the bending moment on the yoke plates.

The amount of stored compression in the yoke plates is again determined by the initial gap width and the size of the aluminum spacer bar. Measurement of the exact temperature at which the gap closes and at which the aluminum bar is released in the mechanical model test is thus essential to determine the correct bar and gap size.

Figure 8.9 illustrates the direction of the forces on the coils in the longitudinal direction.

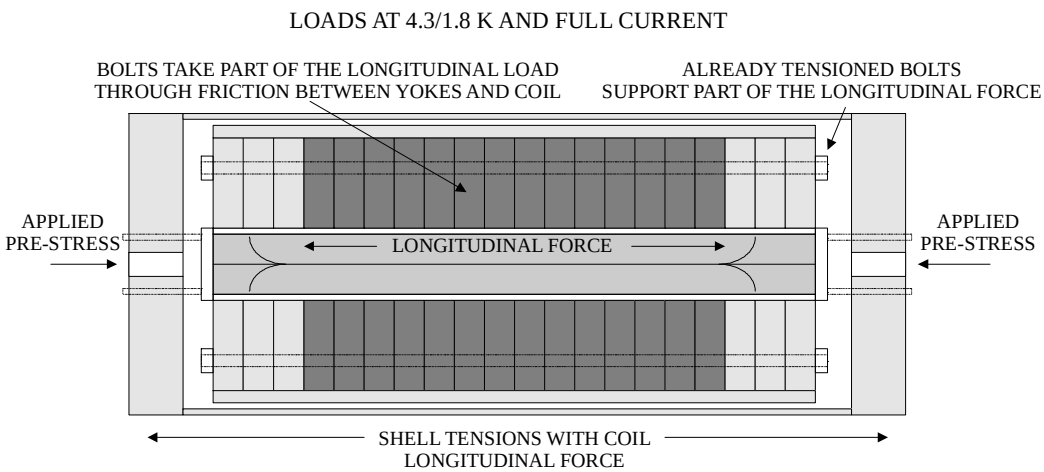

Figure 8.9 Simplified illustration of the direction of the longitudinal forces during operation of the magnet.

The Lorentz force elongates the coils due to the radial constraint and the Poisson effect. The magnitude of the force acting in the longitudinal direction is 820 kN per side. This longitudinal force is partially reacted directly against the end-plates by bolts pushing against the coil ends.

The rest of the force is transmitted through the yoke plates onto the tension bolts holding the yoke plates together. The actual ratio of the two forces is determined by the friction coefficient between the coil, collar and yoke.

8.2.4 Stress concentrations in the coil cross-section

The local stresses in the coil winding can be higher than the overall stress due to the difference in material properties and shape of the coil, amounting to stress concentrations of up to 120 MPa in the inner layers and 140 MPa in the outer layers under full operating current.

FEA models of the coil cross-section [8.6] show stress concentrations around the aluminum-bronze wedges, and at the outside surfaces of layers 2 and 4. The highest concentration is found at the outer surface of layer 4, at 142 MPa. This effect has to be taken into account in the design of the magnet by adding a safety margin of up to about 20 % of the maximum pre-stress in the coils. Also, stress concentrations up to 20 % are present near the wedges and the outer surface of the coils [8.2].

8.3 Stress on the individual cables and strands

The stress on the coils as described in the previous section can now be applied directly to the cables for a correlation with actual cable measurements. From the FEA models of the coil structure the actual stress and stress gradient across the cable surface was determined in table 8.1.

Given this information, an estimate can be made of the actual stresses on the cables, and of the stresses on the individual strands within the cables. In chapter 3 the FEA models of cables are described. Using the stress concentration factors computed in that chapter, and in the FEA models of the coil structure, table 8.3 lists the estimated peak stress in the cables and strands of the coil winding at full operating load at 13 T.

Location and conductor type	Computed stress s from the magnet FEA model (range in-out) [MPa]	Estimated peak stress on the cables [MPa]	Estimated peak stress on the strands [MPa]
Layer 1 MJR	108-73	120	133
Layer 1 IT			147
Layer 2 MJR	73-63	88	98
Layer 2 IT			128
Layer 3 MJR	133-130	133	148
Layer 4 MJR	130-132	142	155

Table 8.3 Estimated stress in the cables and strands of the coil winding at 13 T, 4.3 K. Accuracy data is not available for the computed stress values.

In table 8.3 it is evident that the estimated peak stress on the cables is the highest in the mid-plane of the outer two layers (3 and 4) of the coil winding. The second highest stress is found at the inner edge of the cable in layer 1. Of these two locations, the inner cable is the most critical location, since the magnetic field is also high at the inner cable.

8.4 Prediction of the magnet critical field

Knowing the degradation with applied stress of the critical current in the Nb_3Sn cables that are used, as described in chapter 5, and the predicted pressure on each layer from table 8.3, a prediction of the magnet quench current is made.

The *load line* of a magnet is defined as the peak magnetic field B as a function of the current I at a certain position in the magnet, at constant temperature. To predict the quench current due to stress, the maximum load on a cable in terms of B, T and stress s has to be known. For B, the peak field in the coils is taken. The temperature T for the prediction is 4.2 K.

A correction is made in the end for the slightly elevated operation temperature of 4.4 K of the magnet. The stress s is derived from an ANSYS model (see table 8.3) for certain critical locations. Table 8.4 lists the peak magnetic field B and the estimated peak stress s at the cable for the four layers at the most critical locations. The intersection of the load line with the curve of the critical current I_c as a function of the peak magnetic field B and stress s of the cable determines the critical field of the magnet.

Figure 8.10 shows the most critical locations from table 8.4 in the coil winding. Layers 1 and 2 are wound with the inner cable. Layers 3 and 4 are wound with the outer cable. Of the critical locations, the limiting locations are layer 1 at 108 MPa, 12.8 T for the inner cable, and layer 3 at 133 MPa, 6.3 T. Using the results from the cable critical current measurements as a function of stress described in chapter 5, and the computed stress on the cables at the most critical locations, as reported in table 8.4, a prediction of the magnet performance can be made.

	Mid-plane	Field B [T]	Stress *s* [MPa]		Other areas	Field B [T]	Stress *s* [MPa]
A	Layer 1	12.8	108	E	Pole 1	13.3	18
B	Layer 2	9.5	73	F	Pole 3	10.4	15
C	Layer 3	6.3	133	G	Wedge in 2	9.8	115
D	Layer 4	2.5	133	H	Outside 4	3.6	142

Table 8.4 Magnetic field B and estimated peak stress on the cable for the locations in figure 8.10.

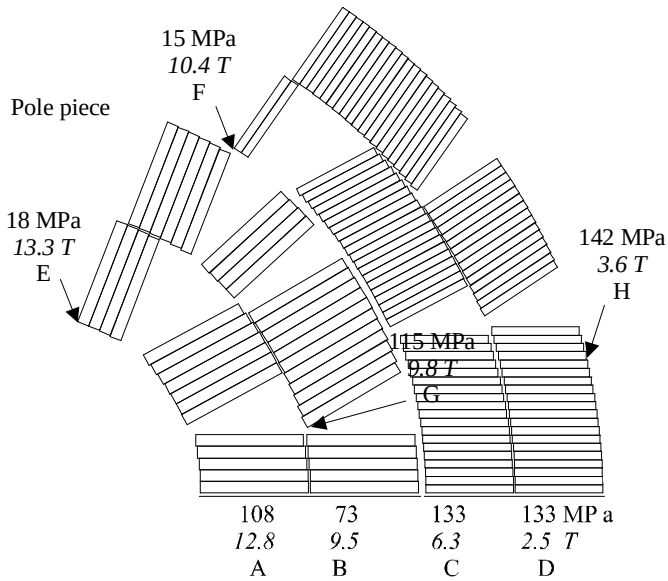

Figure 8.10 The most critical locations in each layer of the coil winding with respect to critical current, as a function of magnetic field B and stress s at 4.2 K.

Figure 8.11 shows the intersection of the magnet load lines for the critical locations with the measured critical current of the cables for the computed stress. The critical current degradation at the relevant pressures, and the peak magnet current and resulting field in the bore are listed in table 8.5. Limiting current values that exceed the mechanical design limit of the structure are between brackets.

	Stress [MPa]	Degradation [%] MJR 1-2 TW7b	Degradation [%] IT 1-2 IG4	Degradation [%] MJR 3-4 TW11	Current [A]	Field [T]
A	108	3	6	-	6280	12.8
B	73	2	2	-	(7870)	(16.0)
C	133	-	-	27	6960	14.1
D	133	-	-	27	(10600)	(21.5)
E	18	1	1	-	6140	12.6
F	15	-	-	0	5960	12.3
G	115	3	7	-	(7590)	(15.4)
H	142	-	-	27	(9000)	(18.3)

Table 8.5 Critical current degradation (in %) at the marked locations in the cross-section for the different cables, and the resulting magnet critical current and peak bore field for each location at 4.2 K.

Three different cables are used in the magnet. The inner two layers (1-2) of one coil half are made of conductor TW7b (MJR), the other half is made of IG4 (IT). Both halves of the outer two layers (3-4) are made of TW11 (MJR).

The limiting point in the magnet is location F in the outer layers. The maximum current at F is 5960 A, which results in a central bore field of 12.25 T at 4.2 K.

The next limiting location is point E in the inner layers for the IT conductor. The maximum current at E is 6140 A, which results in a central bore field of 12.55 T at 4.2 K.

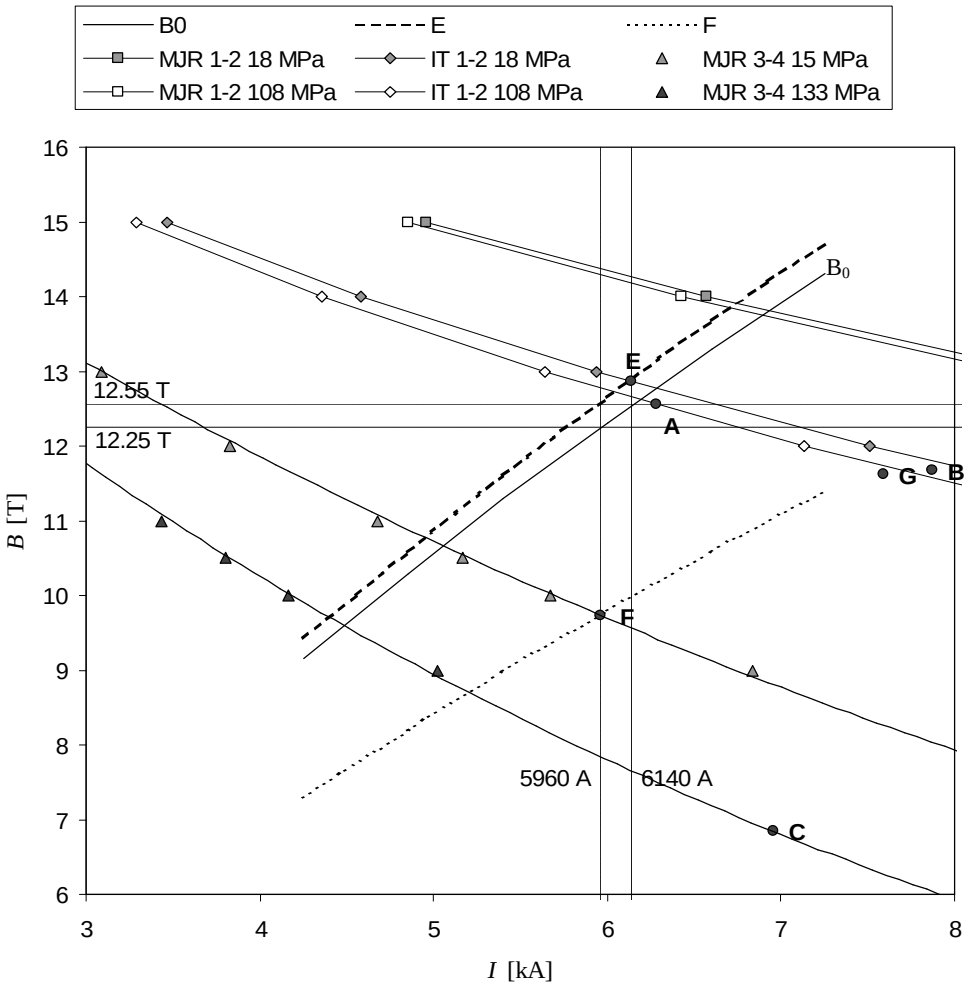

Figure 8.11 Critical field of the cables versus current at 4.2 K. The load line of the magnet is labeled B0.

The intersection of the load line for the inner cable top corner (labeled E) and the corresponding cable critical current curve (labeled IT 1-2 18 MPa in the figure legend) defines the maximum magnet operating current at 6140 A and field at 12.55 T if the inner cable is the limiting factor. Similarly, the outer cable would limit the magnet at 5960 A and 12.25 T at position F.

Correcting both numbers to 4.4 K results in central bore fields of 12.19 T and 12.49 T respectively. The same point E in the inner layers has a margin of 8 % for the coil made of the MJR conductor. This would limit the current at 6597 A, resulting in a central bore field of 13.26 T at 4.4 K.

In summary, the magnet is predicted to reach 12.19 T as 4.4 K, limited by the outer cable.

8.5 The fiber-optic strain and stress measurement system

To monitor the strain in the 13 T dipole magnet D20, three independent stress and strain measurement systems are incorporated in the design, as illustrated in figures 8.12 and 8.13:

1) pole-piece combined fiber-optic and resistive stress transducers;
2) mid-plane fiber-optic stress and strain matrix;
3) end load resistive stress gauges.

The purpose of each system is briefly described here, and in detail in the following sections.

1) Pole-piece transducers

The first system utilizes conventional stress transducers mounted in the pole-pieces. It is designed to measure the stress on the outer turns of the four layers during assembly, pre-stress application, and operation of the magnet. It is also used to correlate the readout of a set of electrical strain gauges, mounted on the same transducers, to the set of fiber-optic strain gauges in it.

The stress transducers in the pole are instrumented with fiber-optic and resistive strain gauges for layers 1 and 2. The stress transducer in the pole for layers 3 and 4 is instrumented with resistive gauges only.

2) Mid-plane matrix

The second system is developed to measure the stress gradient and strain in the radial and longitudinal directions. It is located in the horizontal symmetry plane of the windings, where the stress will be maximal during operation.

Allowing for measurements of the transverse stress in the median plane, a gap of 0.8 mm has been left between the two poles of the magnet.

The mid-plane is instrumented with a matrix with transverse (y), longitudinal (z) and radial (x) fiber-optic strain gauges. The system consists of a sensor matrix that is put in between the upper and lower coils. It incorporates sensors measuring the strain in the longitudinal and radial direction, and a thin stress transducer measuring the gradient of the transverse stress across the coils.

The leads are fed out vertically through the collar and yoke, as shown in figure 8.13, and then led to the return end (right side in figure) of the magnet.

The design specifications of both systems are listed in table 8.6.

Specification	Pole transducers	Mid-plane transducers
Expected stress at 13 T	152 MPa	133 MPa
Maximum design stress	250 MPa	200 MPa
Bridge deflection at design stress	20 μm	10 μm
Estimated design error	5 %	5 %
Measurement method	fiber-optic and resistive	fiber-optic

Table 8.6 Design specifications for the fiber-optic and combined stress transducers.

3) End load gauges

A third system is incorporated into the end-plate structure of the magnet, and is designed to directly measure the load exerted by the coil winding onto the end-plate. It consists of bolts that transmit the load between the coil winding and the end-plate.

The ends of the magnet have four bolts with resistive gauges on each side. The gauges measure the stress exerted by the coils on the end-plate.

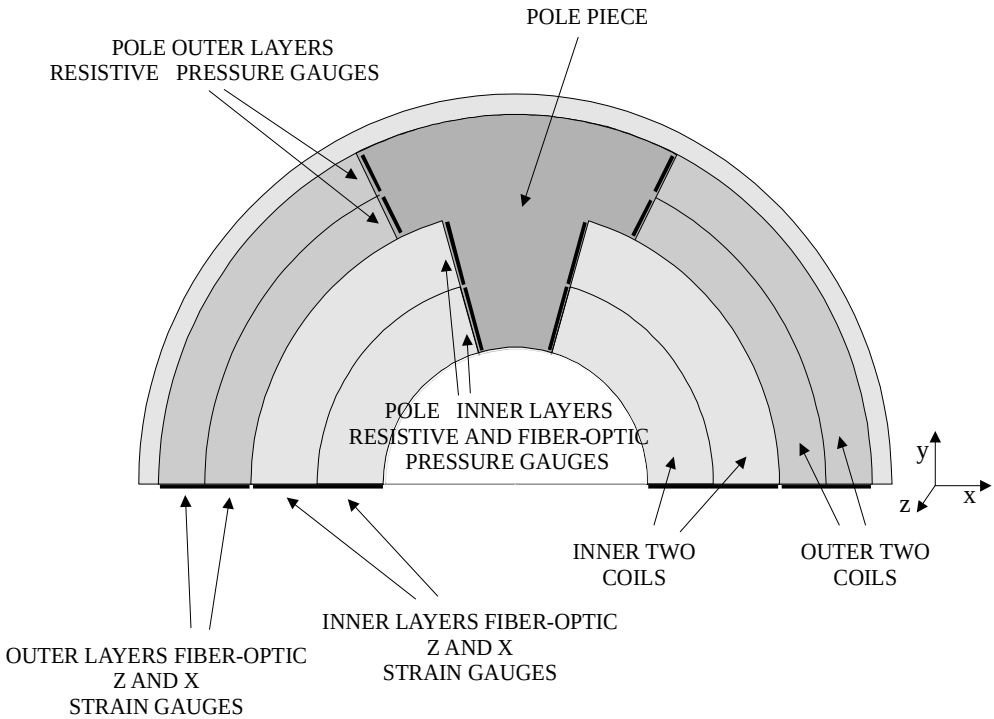

Figure 8.12 Radial view of the position of the sensors in the magnet.

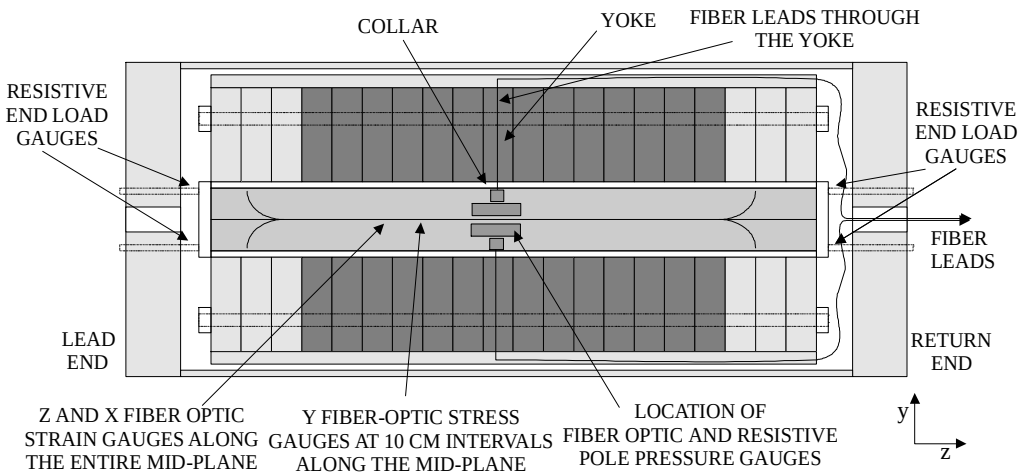

Figure 8.13 Longitudinal view of the position of the sensors in the magnet, and route of the fiber leads.

8.5.1 Stress transducer for the pole gauges

The stress transducer for the pole gauges in the pole-pieces is designed to measure stress up to 200 MPa with an absolute measurement error in the order of 5 %. The combined optical and electrical stress gauges built into the pole-pieces are shown in figure 8.14.

The stress transducer is made of Inconel 718 (E = 214 GPa). The deflection is designed for a maximum of 20 μm that limits the strain on the cable to 0.10 %. The bridge has two sensing channels per block, de-coupled by a narrow slit in the sensor block.

The assembly is mounted in a cavity machined in the pole-piece of layers 1 and 2. The sensor block is approximately 28 mm high (y) by 70 mm long (z). Layers 3 and 4 have a shorter transducer of 40 mm length, without the fiber-optic sensors.

Each channel has a resistive strain gauge bridge mounted on it, with the fiber-optic sensors mounted on the top surface of the electrical gauge. An additional fiber-optic sensor is mounted to compensate for an offset in the temperature of the system, together with a Cernox [8.7] resistive temperature sensor.

Additional slits are made in the interior of the block to provide internal channels to loop the fiber-optic leads back to the feed-through.

8.5.2 Fiber-optic stress transducer for the median plane

The stress transducer for the fiber sensors in the median plane sensor matrix is designed to measure stress up to 150 MPa with an absolute measurement error in the order of 5 %. The optical strain gauges embedded in the matrix read the strain variations during magnet operation. The layout of the sensor matrix is shown in figure 8.15.

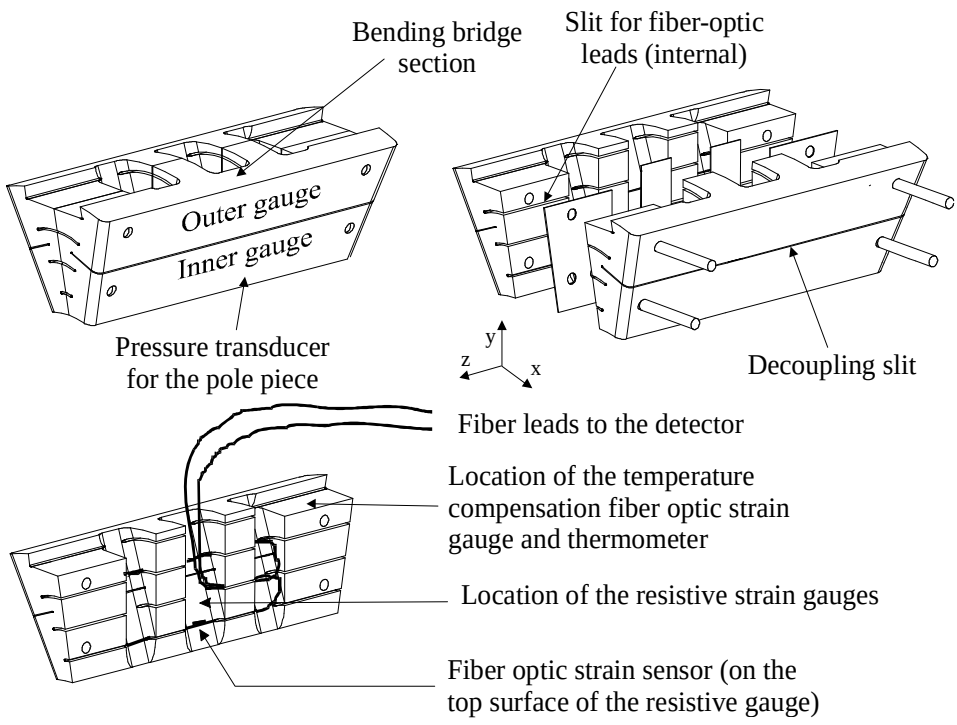

Figure 8.14 The combined optical and electrical strain gauge stress transducer. The top left picture shows the assembled unit, top right shows the exploded view of the components. On bottom left the mounting locations of the resistive and fiber-optic sensors are illustrated.

Each sensor matrix has two transverse stress transducers embedded to measure the stress gradient over the coil winding in the x-direction. The axial (z) positions of the sensor elements are irrelevant, since the coil section is constant in size in the axial direction. The transducers are made of stainless steel by spark erosion. The fiber sensors are glued in small grooves.

The transducer has to be made of a stiffer material than the rest of the matrix to ensure a small deflection of the beam, and to withstand the high compressive load on the beam surface. Stainless steel is chosen over inconel or titanium alloys for cost reasons.

At the top of figure 8.15 the overall layout of the end section of the sensor matrix (a) is shown. Each matrix covers two coils (either layers 1-2, or 3-4) over its entire length. At the end, several strain sensors are embedded in the x-direction. Along the length at 10 cm intervals, arrays of stainless steel stress transducers (b) are embedded with 6 channels (for layers 3-4) or 7 channels (for layers 1-2) of individual sensors.

The 6 or 7 channels per coil measure the stress gradient across the coil in the x-direction. On the bottom, a side-view (c) of a transverse stress transducer is shown, illustrating the principle of operation. Stress is measured by elongation of a fiber cell mounted under a stainless steel bending bridge, similar to the measurement principle used in the pole transducer.

For the model-test described in section 8.7, a special short section of the transducer matrix is designed to check the operation of the three different types of sensors, i.e. the transverse stress transducer, the longitudinal strain sensor and the radial strain sensor. The strain in the horizontal (x) direction is measured by positioning a set of sensors with a 45° angle with the longitudinal axis, and compensating for the longitudinal (z) component with a sensor in the z-direction.

A part of the model-matrices is shown in figure 8.16. The reason for this scheme is the limited radius over which the fibers may be bent due to bending losses in the signal. This layout also allows for the placement of multiple sensors in the horizontal direction for better spatial resolution in the x-direction.

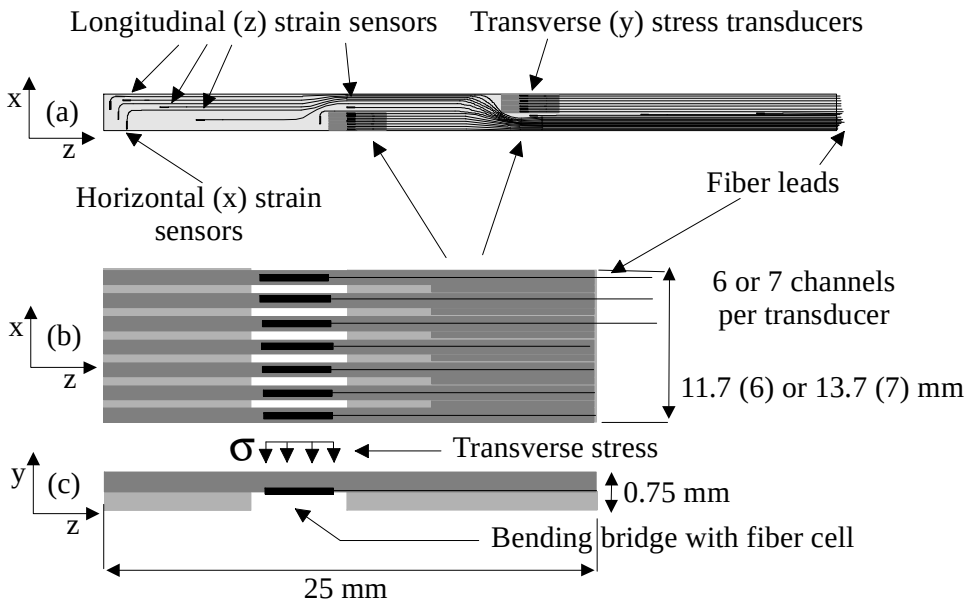

Figure 8.15 A schematic layout of the sensor matrix and transverse stress transducer.

Two different matrices are manufactured, dedicated to either the inner layer or the outer layer of the coils. To avoid epoxy cracking during thermal cycling the construction process of the matrices is changed from a wet lay-up to a milled G10 base plate.

A G10 plate of the same width as the coil segment and 0.6 mm thickness is used as a carrier material. In this plate, slots are milled with a diamond cutter to provide safe guides for the fiber leads. At the positions allocated for the transverse stress transducers, slots are milled to fit the stainless steel parts.

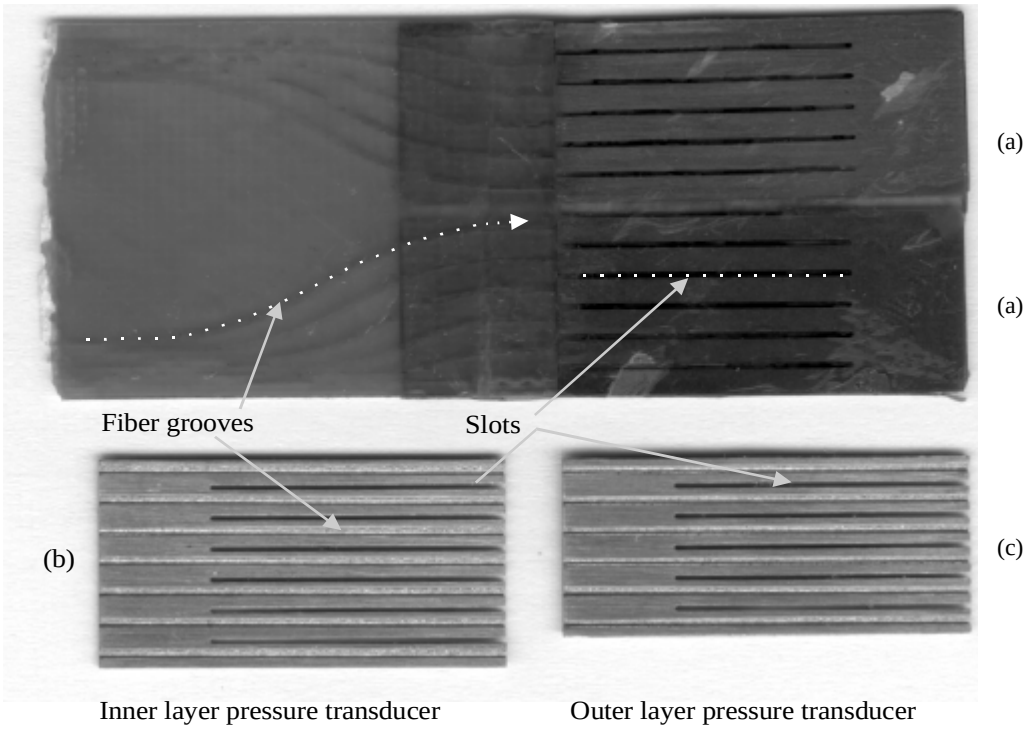

Figure 8.16 The second iteration milled strain sensor matrices for the model-test.

Shown are two outer layer stress transducers (a) embedded in a section of the sensor matrix with the fiber leads going towards the slots. Shown below are the wire-cut stainless steel bending beams for the inner (b) and outer layer (c) with the etched grooves for the fiber sensors (bottom view). The groove dimensions are approximately 300 by 300 μm, the spacing between the grooves is 2 mm. This allows for 7 sensor positions in the radial direction in the inner layer cables and 6 in the outer layer cables. Refer to figure 8.15 for a side-view (c) and illustration of the bending direction.

Several matrices of this type are manufactured and instrumented for the model-test. To ensure a smooth surface and electrical integrity between the two coil halves the matrices are coated with a thin layer of Stycast 2850FT [8.8] and sandwiched between two layers of Kapton foil. The finished matrix has a total thickness of only 0.8 mm. The same design is also used for the sensor matrices in the magnet test.

8.5.3 Readout system

A schematic of the readout system is shown in figure 8.17. From the sensors, the optical fibers are connected within the cryostat to a multi-channel fiber feed-through with plastic ST-connectors [8.9], suitable for operation at 4.2 K.

The feed-through runs from the cryostat through a protected tube that is terminated in a series of ST-connectors at room temperature. Active sensor selection is performed at this location by connecting the leads from the sensors in the magnet to the leads feeding to the 2x2 couplers.

From the couplers, the light travels back to either the detector (laser light) or the spectroscope (white light). The CCD camera reads up to three signals in parallel, with a maximum scan speed of about 1 Hz.

The data acquisition and analysis for matrix readout using laser light (relative strain or stress readout) is done directly by the magnet test station data acquisition system. In this way, strain and stress can be determined as a function of the magnetic field. During the current ramp, the sensors are read out at a scan frequency of 1 Hz; after quench initiation, the scan frequency is increased to 2-5 kHz. The start of the readout of the sensors at higher speed can be triggered by the electrical quench detection circuitry.

The detection and data analysis system for the matrix readout using white light (absolute strain or stress readout) is built around a liquid nitrogen cooled CCD-camera system mounted on a 0.5 m spectroscope with gratings from 600 grooves/mm to 2400 grooves/mm. The CCD-camera is controlled by a computer, which functions as the data acquisition and stress/strain computation system.

8.5.4 Test results of the multi-channel matrix

To test the viability of the sensor matrix in the magnet, a dummy gauge is made with ten fiber sensors embedded in a 0.6 mm glass fiber reinforced epoxy strip. The test matrix has a length of 30 cm, covers two cable widths of the outer layer cables, and uses one partially instrumented stress transducer. The matrix is manufactured by a wet lay-up process using CTD-101 epoxy, and a subsequent heat treatment to cure the epoxy.

The bending bridge deflection is computed using a closed form analytical solution [8.10]. The computation assumes linear material properties and no yield. The resulting deflection of the bridge yields the expected elongation of the fiber sensor, which is glued directly to the bottom of the bending bridge.

The resulting curve of elongation as a function of load is plotted in figure 8.18 along with experimental data for one run up to 55 MPa, and the expected results are listed in table 8.7.

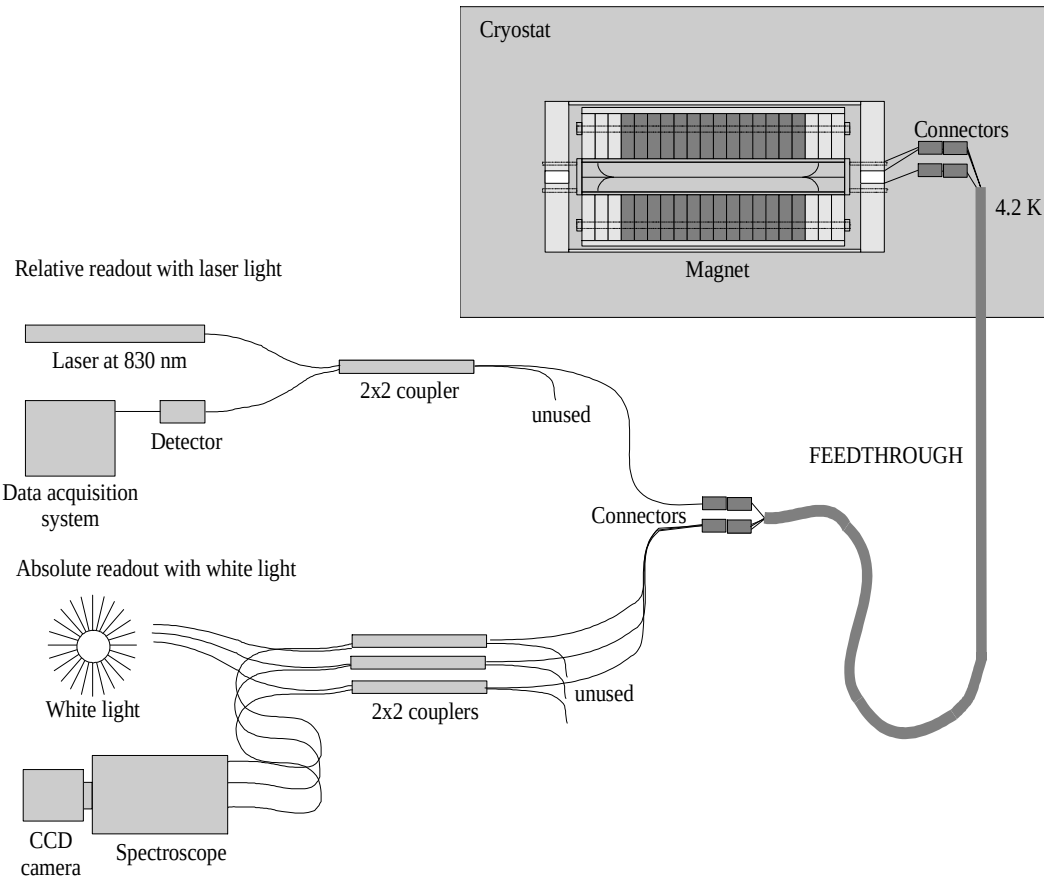

Figure 8.17 The set-up for absolute and relative readout of the fiber sensors.

Stress [MPa]	Computed deflection [μm]	Computed elongation *dl* [μm]
20	0.8	0.2
40	1.6	1.0
100	3.9	6.0
200	24.0	7.8

Table 8.7 Theoretical computation of the elongation of a fiber cell mounted to the bending bridge.

The matrix is tested at room temperature and at 77 K in liquid nitrogen, and is cycled in temperature several times to assure it is not damaged by rapid cooling-down. The matrix is first cycled several times from 0 to 55 MPa with a G10 pressure block and a Kapton sheet between the gauge and the pressure block. Figure 8.18 shows the computed and measured elongation (absolute measurement method with white light) of the cell as a function of the applied pressure on the sensor for the experiment at room temperature with the G10/kapton pressure block.

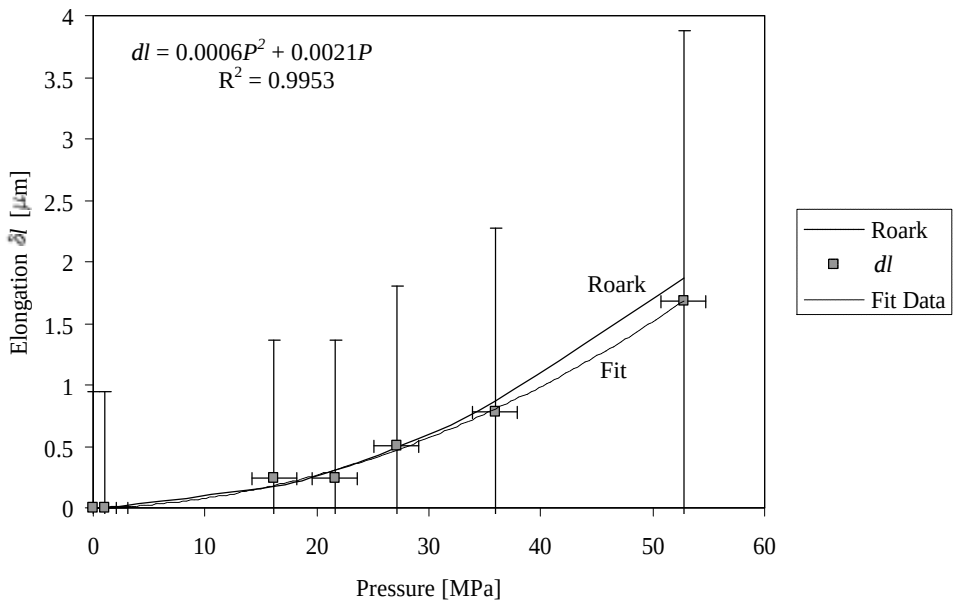

Figure 8.18 Elongation of the sensors using absolute measurement with a G10/kapton pressure block. The curve marked "Roark" is computed [8.10]; dl and Fit Data mark the measured data.

The computed curve matches the data-points of the measured data well, up to the yield strength of the epoxy at about 35-40 MPa, with only a slightly lower elongation as a function of the applied pressure. In table 8.8 the coefficients of the second order fits used to describe the computed and measured response are listed. Also, the resulting maximum error in the stress measurement is given.

Subsequently, the matrix is loaded several times up to 200 MPa, well past the yield strength of the epoxy holding the sensors, this time using a stack of ten epoxy-impregnated cables as the pressure block to simulate the actual loading conditions in the magnet. The test results are shown in figure 8.19 for three separate runs, and compared to curves computed with an ANSYS model, and a third order fit to the data. Each curve contains data for the stress increasing from 0 MPa to 175 MPa, then decreasing back to 100 MPa. The model uses non-linear material parameters to simulate the non-linear behavior of the epoxy holding the sensor to the bridge [8.11].

Coefficient (dl [μm] = $C_1P+C_2P^2$) (P in MPa)	Computed [8.10]	Measured
C_1	0.4	2.0
C_2	0.00060	0.00056
Error [MPa]	NA	±4 (up to 53 MPa)

Table 8.8 Computed and measured response for a mid-plane sensor loaded with a G10 pressure block and a Kapton sheet as cushion between the block and the sensor.

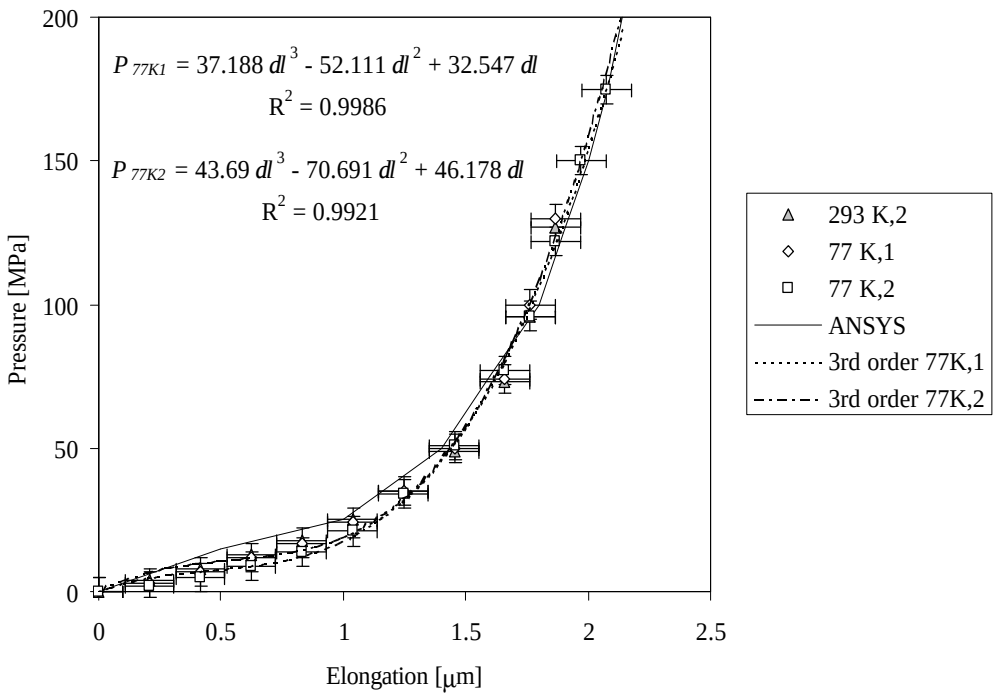

Figure 8.19 Computed and measured response curves for a test bending bridge at room temperature and in liquid nitrogen at 77 K.

The first curve is measured at 293 K, followed by two curves from different sensors at 77 K, measured simultaneously. Table 8.9 lists the resulting error and reproducibility of the measurements. As is evident from a comparison of figures 8.18 and 8.19, the bridge deflection behaves quite different when loaded with a stiffer pressure block like the cable stack. The slope of the deflection reduces with increasing load, which is due to the non-linear deformation in both the epoxy holding the sensor, as well as the bridge itself.

The curve computed with the ANSYS model matches the measured data for the higher stress well, but is off for stress up to about 50 MPa. For this reason, an experimental calibration of the sensors is done for the sensors used in the magnet experiment [8.12].

As shown in table 8.9, the maximum error in the stress measurement is of the order of 10 MPa for the two tested sensors. Reproducibility for each sensor between runs is of the order of 4 MPa. Reproducibility between the two sensors is about 8 MPa. The overall stress measurement accuracy is therefore about 10 MPa, or 7-10 % in the range of 100-150 MPa to be measured in the magnet.

Curve	Measurement versus fit error (max and average) [MPa]	Reproducibility (max and average) [MPa]
77 K,1	±9 (3)	±4 (2)
77 K,2	±7 (3)	±4 (2)
77 K,1 to 77 K,2	± 8 (3)	±8 (3)

Table 8.9 Reproducibility of the elongation measurements at 77 K, with a sensor mounted on a bending bridge. Listed are errors between the fits and measured data, reproducibility for subsequent runs at the same sensor, and a comparison between the two sensors at the same stress.

8.6 Conventional resistive strain gauges

In order to provide a redundant system for the measurements of stress and strain in both the magnet and the model test, conventional resistive strain gauges are also incorporated. In the magnet, the pole sensors are instrumented with the resistive strain gauges as illustrated in figure 8.14.

In the model test, the same pole stress transducers are used, and additional strain gauges are placed in the horizontal symmetry plane of the coil section. These gauges are borrowed from a previous magnet, and occupy about 5 mm of space in the y-direction.

To make space for the larger stress transducers, the first two cables of the conductor block closest to the median plane have milled slots (material is actually removed from two of the superconducting cables, since this model is only meant for mechanical evaluation).

The median plane stress transducers are made by bonding Micro-Measurements [8.13] resistive strain gauges to an Inconel 718 stress transducer in a fully temperature compensated bridge configuration [8.14]. The gauges have a resistance at room temperature of 1000 Ω. Each transducer has two full bridges bonded to the surface.

The two bridges are wired in series with the current source. The bridges are powered by a constant current source of 1 mA; the voltage across each bridge is read as a function of the applied stress. The design of the transducers is similar to the pole transducers shown in figure 8.14, but in a rectangular configuration.

The transducers are calibrated against a known transverse stress in a vertical test setup [8.15] and subsequently glued in place in the slots. Next, a second check of the calibration is done to ensure a repeatable reading of the transducers [8.16].

8.6.1 Calibration of the stress transducers

All median plane stress transducers are calibrated against a known stress in a vertical hydraulic material test system [8.17]. The recorded voltage as a function of the applied stress is then used to compute a fitting curve for the stress as a function of the voltage.

It was found that the response of the stress transducer is highly sensitive to the material properties of the block applying the stress. Also, the alignment is critical in obtaining reliable readings from the gauges. Since the total deflection in the vertical direction of the transducer bridge is in the order of 30-40 μm, any mismatch in the surfaces of the pressure block and the beam will cause erroneous readings.

The stress on the gauges in the calibration setup is applied through a stack of ten impregnated cables, emulating a coil package. The measured Young's modulus of the package is about 38 GPa [8.18]. Assuming the gauge surface will bend, and the pressure block will follow the bending beam completely, the vertical strain at the surface of the beams is 0.21 % at 84 MPa. This corresponds to a deflection of about 80 μm in the inner layer of the coils at the gauge surface. To limit the strain exerted on the Nb_3Sn cable this deflection is actually limited even further to prevent damage to the cable, thus reducing the deflection of the sensing bridge.

The pole sensor elements are designed to deflect 20 μm at a stress of 150 MPa (expected maximum stress), which means that the surface accuracy has to be in the order of 1 μm to ensure a reliable reading. This problem is far more pronounced in the strain measurements in epoxy impregnated Nb_3Sn coils, since the Young's modulus of the coil package is 5-10 times higher compared to NbTi coil packages.

Attaining a good fit between the cable surface and the bending bridge can only be achieved by either polishing both surfaces perfectly flat and aligning them in parallel, or by gluing the bending bridge in place. Since the first option is not suitable for the brittle reacted coils, the median plane transducers are glued in place in the model test. The pole gauges can not be glued yet, since they have to be removed later to mount them in the main magnet assembly. Hence, the surfaces of the transducers are covered with a 75 μm Teflon tape that will yield and deform to match the two surfaces.

The detailed calibration result for both the median plane and pole sensors is found in [8.17].

8.6.2 Reproducibility of the stress transducers

A significant influence of the material properties of the winding on the deflections of the stress transducers is found during the calibration runs. For each calibration, the stress is checked with a sheet of stress sensitive Fuji paper[4] [8.19] on the gauge surface. From these sheets it is found that the gauge reading strongly depends on the stiffness of the material used to apply the stress to the bending beam.

For a pressure block made of a stiff material like stainless steel, the recorded signal is fairly small. For softer materials like G10 epoxy with 0.1 mm Kapton the signal is about four times larger. This is obvious, since the stiffer the material, the more the pressure block will act like a beam itself, applying more stress to the support legs next to the bending beam, thus reducing the total stress recorded on the transducer.

Calibration tests and cross-checks with an ANSYS model [8.20] showed that for materials with an Young's modulus of about 90 GPa or lower, the recorded stress corresponds well with the readings on the Fuji-paper (within about 10 %), all stiffer materials yield a signal that is lower in proportion to the actual applied stress on the transducer.

This effect is very important for the calibration of the sensors, since a factor of four in difference of the calibration curve due to the material properties of the pressure block creates a significant error in the reading. For the calibration a pressure block is used that approximates the coil material properties closely. A cable stack with all shims and Kapton foils between the bending beam surface and the pressure block is ideal. This is confirmed for the stress transducers used in the median plane of the model test. Fairly reliable readings are obtained even if the gauges are glued in place with a thin layer of epoxy between cable surface and bending beam. The readings approximate the applied stress, for stresses exceeding the yield strength of the epoxy by about 10 MPa (stress exceeding 35 MPa), within about 10 % [8.17].

For the pole gauges in both the model test and the magnet test, the material applying the stress onto the bending beam is a 1 mm thin sheet of aluminum bronze to protect the cable from dents due to the difference in thermal contraction between the bronze pole island and the Inconel gauge block. During the application of the ceramic insulation layer, these bronze sheets warp slightly, creating a bad match between the plate applying the stress and the bending beam.

As a result of this mismatch, the readings of the pole gauges have a large uncertainty between tests. Errors up to 40 % in stress are found between calibration checks when the gauge block is removed and placed back in the cavity. This means that the readings from the pole-piece stress transducers for both the model test as well as the main magnet test are only reliable when a good fit between gauge surface and the cavity is ensured by careful assembly techniques or epoxy impregnation.

[4] The Fuji-paper contains small spheres filled with a color developing layer and a micro-capsule layer that combine under pressure. The color intensity is a measure of the amount of pressure applied to the paper. Because the coloration is permanent, only the highest pressure applied to the paper is read. The pressure is read out with a calibrated light source and diode, or by digitally scanning the paper and comparing the intensity to a reference chart.

8.7 The mechanical model

In order to check the mechanical behavior of the magnet cross-section, and the viability of the wire-winding pre-stress technique, a dummy section of the magnet is built, a so-called "*cookie*". The main purpose of the model is to test the viability of the wire-winding scheme, and to verify the validity of the ANSYS models that predict the pre-stress of the magnet as a function of the number of wire wraps. The test is also used to determine the desired thickness of the mechanical shims between the two coil halves and the effective Young's modulus of the coil segments.

This same setup is used to test the installation and operation of the multi-channel fiber-optic strain gauges and the computerized readout-system. For the initial tests the fiber-optic mid-plane matrix gauges are not tested to simplify the mechanical behavior and the assembly of the winding package. Therefore, only the results from the resistive gauges are shown for the tests with the mechanical model during the wire wrapping.

8.7.1 Experimental setup

A schematic layout of the model and magnet wire wrapping layout is shown in figure 8.20. All fiber leads coming out of the magnet are guided through a stainless steel protection tube to prevent fiber breakage during the wire winding process (not shown in the figure).

Since the magnet is turning during the wire wrapping process to apply pre-stress, it is not practical to continue the readout of the optical strain gauges. Consequently, the resistive and optical strain gauges are scanned during each stop in the winding process to check the predicted compression of the coil package against the measurements. This limits fiber-optic readout to absolute measurement using white light only.

In figure 8.20, the following components are shown (from the outside in): stainless steel wire wrap (up to 25 layers), thin wrapping cylinder, aluminum shrink-bar, iron yoke plates, bronze collar, coils and the pole-pieces (the embedded sensors are not shown; neither are thin Teflon layers inserted at the horizontal symmetry plane between the coils). Figure 8.21 shows the location of the various transducers in the model. Table 8.10 lists the transducer location, name label for the plots, method of measurement, and function in the measurement scheme.

During wire wrapping, the model is rotated in the counter-clockwise direction to spool the tensioned wire on the wrapping cylinder. Winding is stopped when each layer is complete, and the wire is locked at the edge using a wedge. Stress measurements are taken at every completed layer, and compared to the predicted stress on the coils. The results from the measurements are discussed next in sections 8.7.2 to 8.7.4.

Location		Names	Method	Function
Mid-plane	Layer 1 (L1)	M1T, M1B	Resistive bridge	Stress
	Layer 2 (L2)	M2T, M2B	Resistive bridge	Stress
	Layer 3 (L3)	M3T, M3B	Resistive bridge	Stress
	Layer 4 (L4)	M4T, M4B	Resistive bridge	Stress
	Layers 1-4	NA	FP matrix	Stress + Strain
Pole-piece	Layer 1	P1	Resistive + FP bridge	Stress
	Layer 2	P2	Resistive + FP bridge	Stress
	Layer 3	P3	Resistive + FP bridge	Stress
	Layer 4	P4	Resistive + FP bridge	Stress

Table 8.10 Summary of the location and purpose of the sensors in the mechanical model test.

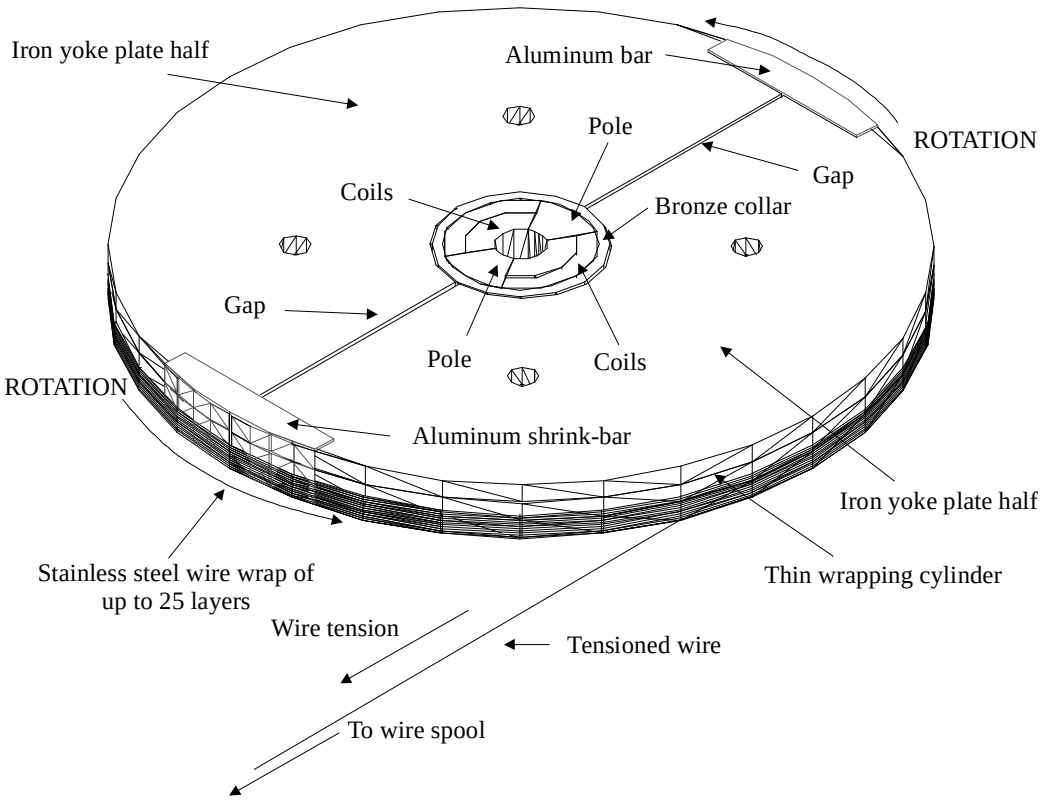

Figure 8.20 Close-up of the layout of the model in the wire wrapping system. Shown is the model section with a thickness of three iron yoke plates.

8.7.2 Results at room temperature

The stress transducers are calibrated, and stress sensitive Fuji-paper is placed at all relevant surfaces to verify the measured stress on the gauges with the average maximum stress recorded by the paper. Next, a first wire wrap of the model is performed. After unwrapping, the Fuji-paper is inspected to verify the applied stress. Figure 8.22 shows the Fuji-paper imprints with the corresponding stress readings. Average stress recorded on the paper is 64 MPa (L1), 62 MPa (L2), 61 MPa (L3) and 62 MPa (L4).

This additional verification of the calibration is needed to ensure that the pole-piece transducers are seated correctly in the slots in the pole-piece. Based on the results from the Fuji-paper, the appropriate calibration curves from the high stress runs in the test setup are then chosen for the pole sensors in the main model test run. halve half

Figure 8.23 shows the stress increase on the median plane. The increase in stress with each consecutive wrap layer stays fairly linear, but the final pre-stress is lower than the 84 MPa required for the magnet. Sensor M4B is inactive.

To increase the pre-stress, a test is performed, with no changes to the shims between the coils, and a 0.05 mm increase in the outer radial shim to compensate for a reduction in size of the coil package after the first model wrap. Correction factors are applied to the readings from the median plane sensors to match them to the stress recorded on the Fuji-paper. These correction factors adjust for errors in the reading due to misalignment and fitting errors of the gauge surfaces.

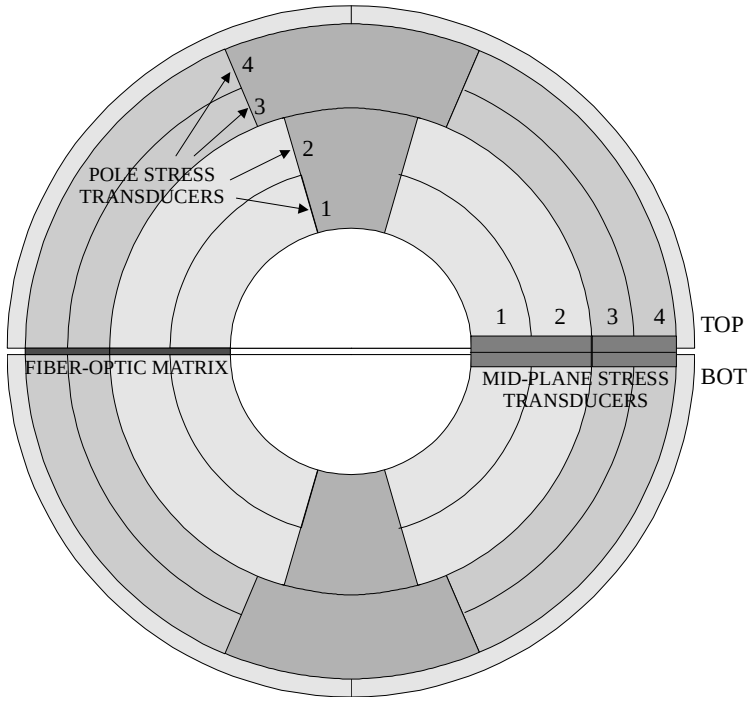

Figure 8.21 Position of the sensors in the mechanical model test.

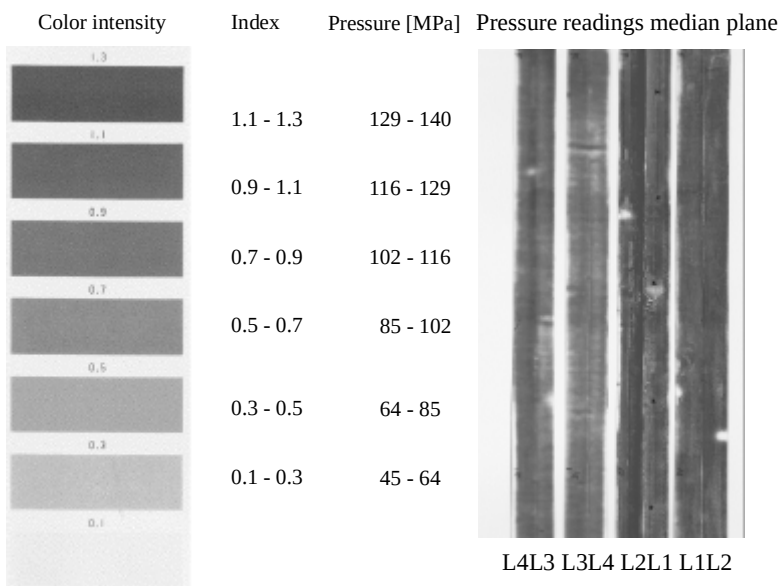

Figure 8.22 Stress sensitive Fuji-paper readings from the first wire wrapping test. On the left is the calibration scale used for the readout. On the right is a section of paper from the median plane of the coil.

The recorded stresses on the Fuji-paper and gauges are about 25 % lower than the required pre-stress of 84 MPa to keep the coil from separating from the pole-piece during operation at full current. The lower pre-stress is partly due to the fact that the model is free to expand in the axial direction, thus the Poisson effect has to be taken into account.

The second cause for the lower pre-stress is the presence of soft materials like Teflon in the cross-section. This is evident from the protrusion of Teflon out of the model during the test. Cycling the stress once eliminates part of the slack, effectively increasing the overall Young's-modulus of the coil package.

The elimination of the slack has to be performed on the magnet coils as well to make sure the coils will follow a reversible stress-strain curve on subsequent cycling. Without this step, the pre-stress applied in the wire winding does not reach the full predicted value, since too much of the wire tension is lost due to the large displacements in the first layers.

Figure 8.24 shows the measured stress on the pole sensors. Layers 1, 3 and 4 show a consistent behavior compared to the median plane gauges, with readings of 67, 65 and 61 MPa respectively, but the sensor at pole layer 2 shows a much higher stress of 95 MPa.

The stress measured at the second layer was also too high in the first test run as confirmed by the Fuji-paper shown in figure 8.22, but the absolute value can not be verified at the sensor surface. A possible explanation is a bad fitting surface between the bronze pole and the gauge surface, causing the gauge to read high. The predicted and measured stress are listed in table 8.11.

The conclusions from the tests in the model are :

1) the resistive stress sensors at the mid-plane correlate well with the recorded stress on the Fuji-paper;
2) a good surface fit at the gauge is necessary to ensure correct stress readings;
3) the wire wrap is a viable technique for the application of pre-stress.

In the next section, the model is cooled down to 77 K. Stress measurements are reported during the cooling-down and compared to the predicted final stress from the ANSYS model, as reported in table 8.1.

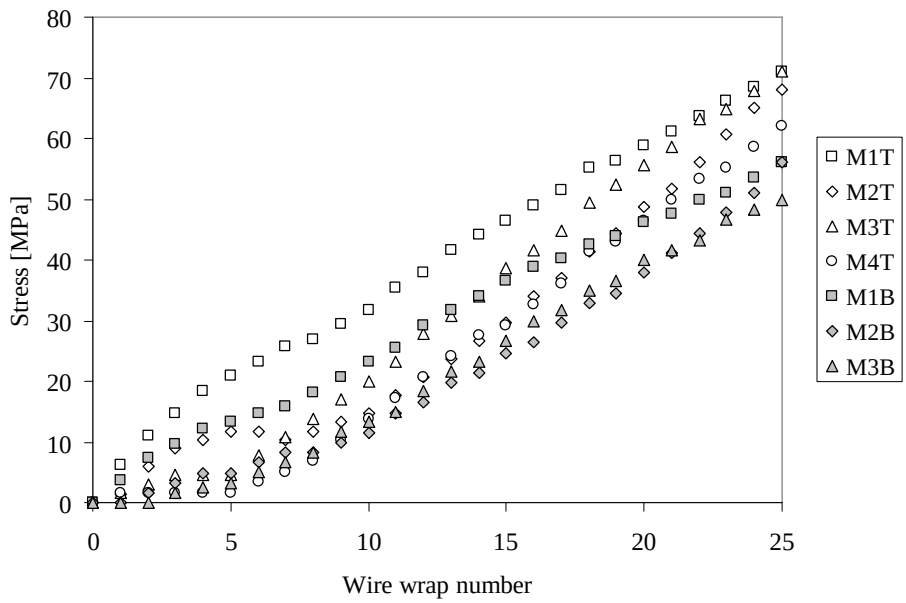

Figure 8.23 Increase in pre-stress on the coils as a function of the wire wrap number measured at the horizontal symmetry plane of the coils.

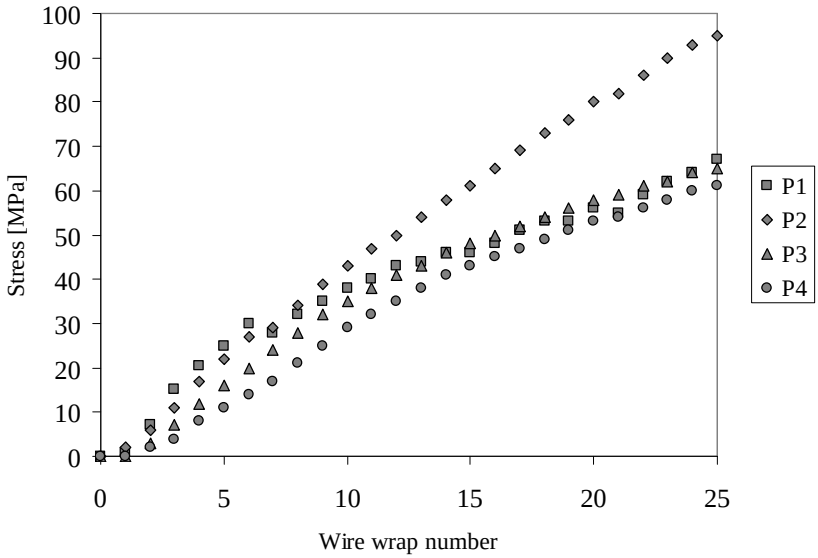

Figure 8.24 Increase in pre-stress on the layers as a function of the wire wrap number measured at the pole of the model.

Area	Coil layer	Predicted pre-stress at 300 K [MPa]		Measured stress at 300 K [MPa]	
		average	range	Fuji-paper	Gauges
Mid-plane	1	79	85-74	64±5	64±8
	2			62±5	62±6
	3	85	84-89	61±5	61±11
	4			62±5	62±9
Pole-piece interface	1	83	134-60	NA	67±7
	2				*(95±9)*
	3	86	100-76		65±7
	4				61±6

Table 8.11 Averaged design stress and measured stress at the mid-plane and pole-piece locations in the model test at 300 K. The range of pressure is given for the radius from the inside to the outside of the layer.

8.7.3 Results of the model during cooling-down to 77 K

After completion of the room temperature measurements of the stress, the model is cooled down to a temperature of 77 K using liquid nitrogen. Table 8.12 lists the predicted and measured stress at the gauges at 77 K. The stress as a function of time on all strain gauges is shown in figure 8.25. The gauges first show a rapid change in the signal due to the fast cooling of the exposed coils themselves, then a gradual increase in stress due to the delayed shrinking of the yoke assembly. The coil package shrinks more than the stainless steel yoke blocks, thus a net reduction in stress is expected due to the temperature change. All final stress readings are taken after about 3 hours to ensure thermal equilibrium in the model, and listed in table 8.12. Sensor P1 broke during cooling-down.

Area	Coil layer	Predicted pre-stress at 77 K [MPa]		New predicted stress at 77 K [MPa]	Measured stress at 77 K[MPa]
		average (normalized [%])	range	average (normalized [%])	gauges
Mid-plane	1	65 (82)	30-84	53 (67)	47
	2			51 (65)	46
	3	75 (88)	68-78	54 (63)	42
	4			55 (64)	34
Pole-piece interface	1	76 (92)	152-29	61 (74)	-
	2			87 (105)	*47*
	3	75 (87)	85-65	57 (66)	44
	4			53 (62)	37

Table 8.12 Averaged design stress and measured stress at the mid-plane and pole-piece locations in the model test at 77 K. The range of pressure is given for the radius from the inside to the outside of the layer.

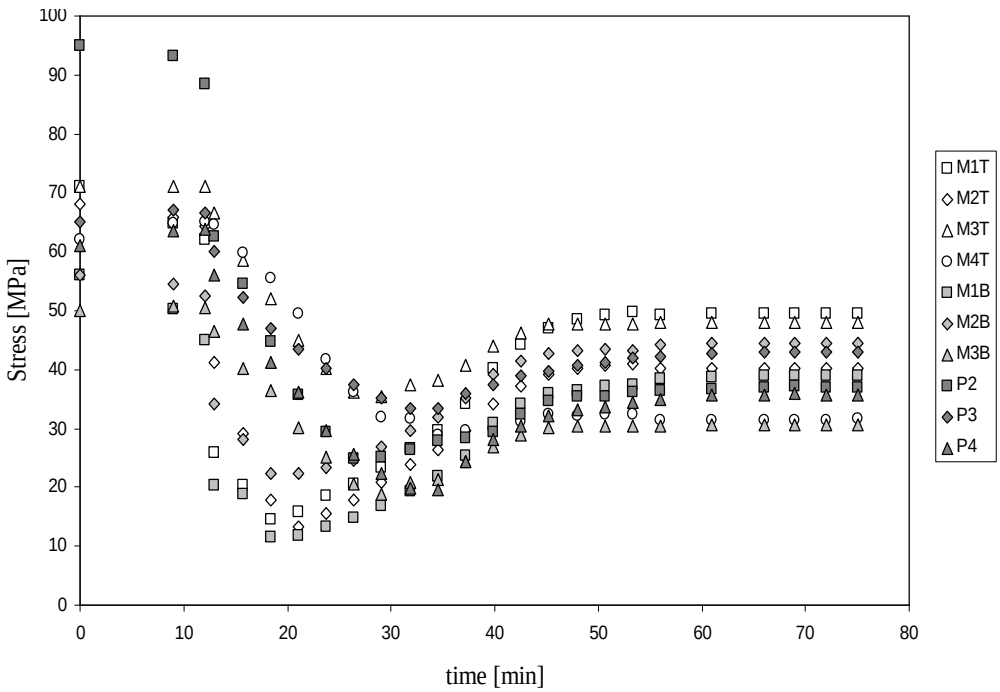

Figure 8.25 Stress as a function of time during the cooling-down of the model. Note the large decrease in pre-stress between 15-25 minutes, and a gradual recovery up to about 60 minutes.

The stress reduces from an average of 62 MPa on the horizontal symmetry plane to 42 MPa (32 % reduction), and from 72 MPa on the pole gauges to 42 MPa (41 % reduction). For the readings below about 150 K, the zero reference values measured in the cold calibration tests at 77 K are used.

The measured stress at 77 K is on average 20% lower than the new predicted stress for the mid-plane, and 33 % lower for the pole area. The lower than expected pre-stress after cooling-down is explained by the gap between the yoke and aluminum bar closing too soon, causing the coils to be unloaded more than the calculated amount. The aluminum bar length was adjusted.

8.7.4 Model warming-up

Figure 8.26 shows the stress on the sensors as a function of the model temperature during the subsequent warming up to room temperature. The temperature is measured directly inside the coil segment. The stress on the pole gauges approximately recovers to the measured stress before the cooling-down, while the mid-plane stress is about 20 % higher, as shown in table 8.13.

Note how the anomalous high reading of the sensor on pole-piece 2 seems normal after the temperature cycle, and mid-plane 1 is now high. This suggests a possible rotation of the inner two layers of the coil section.

The actual stress on all channels is slightly above the measured value after the creep test discussed in the next section, indicating that the observed creep is not irreversible. Upon reaching the higher stress the readings will start to creep again from the new maximum value, which lies between the initial high stress before the creep test and the equilibrium value after a few days of relaxation.

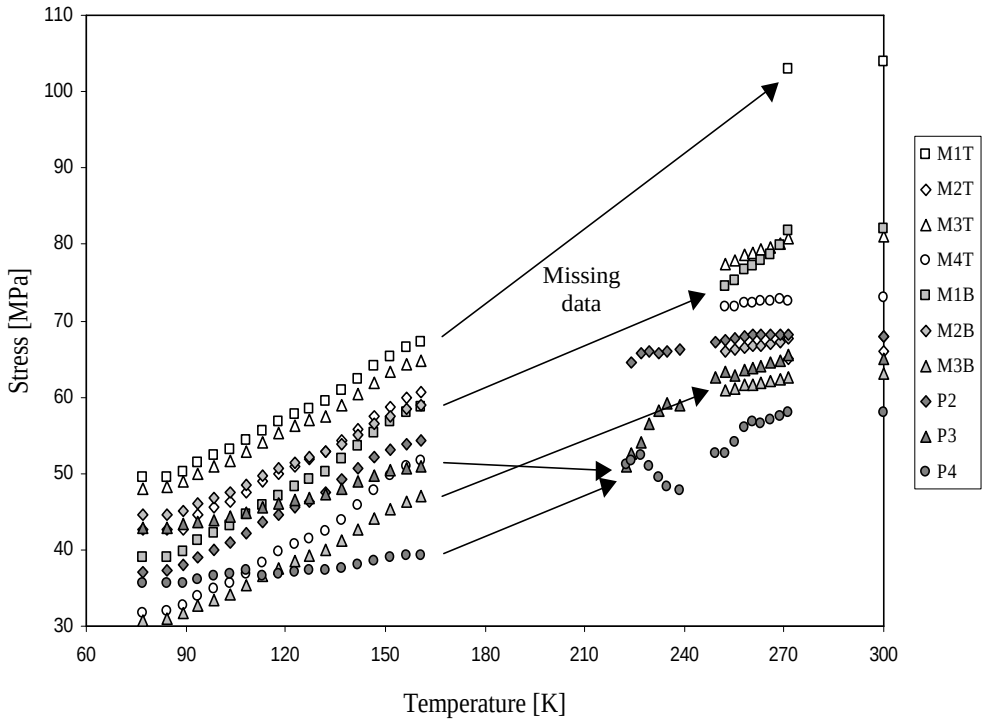

Figure 8.26 Stress on the sensors as a function of the model temperature. The gaps in the temperature range from 165 K to 230 K are due to missing data.

Area	Coil layer	Stress at 300 K before cycle [MPa]	Stress at 77 K [MPa]	Stress at 300 K after cycle [MPa]
Mid-plane	1	64±8	39±4	92±8
	2	62±6	45±5	66±7
	3	61±11	39±4	72±7
	4	62±9	32±3	73±7
Pole-piece interface	1	67±7	Broken sensor	62±6
	2	(95±9)	*37±4*	68±7
	3	65±7	43±4	65±7
	4	61±6	36±4	58±6

Table 8.13 Measured stress at the mid-plane and pole-piece locations in the model test at 300 K before the cooling-down cycle, at 77 K and at 300 K after the warming-up cycle.

8.7.5 Observed creep in the model coil windings after pre-stress application

After the application of the pre-stress with the wire wind method, the stress as measured by the sensors is recorded to observe the relaxation over time. Since the pre-stress applied exceeds the yield strength of several of the materials (epoxy, copper), some relaxation and redistribution of the applied load within the coil package is expected. The reduction of the stress on the pole surfaces is particularly interesting, since this value has to be larger than the load decrease generated by the Lorentz forces during excitation of the magnet to prevent the pole surface from separating from the first layer of the coil winding. The stress change over time on all sensors is shown in figure 8.27; table 8.14 lists the change in stress (creep) normalized to the initial value, averaged per layer.

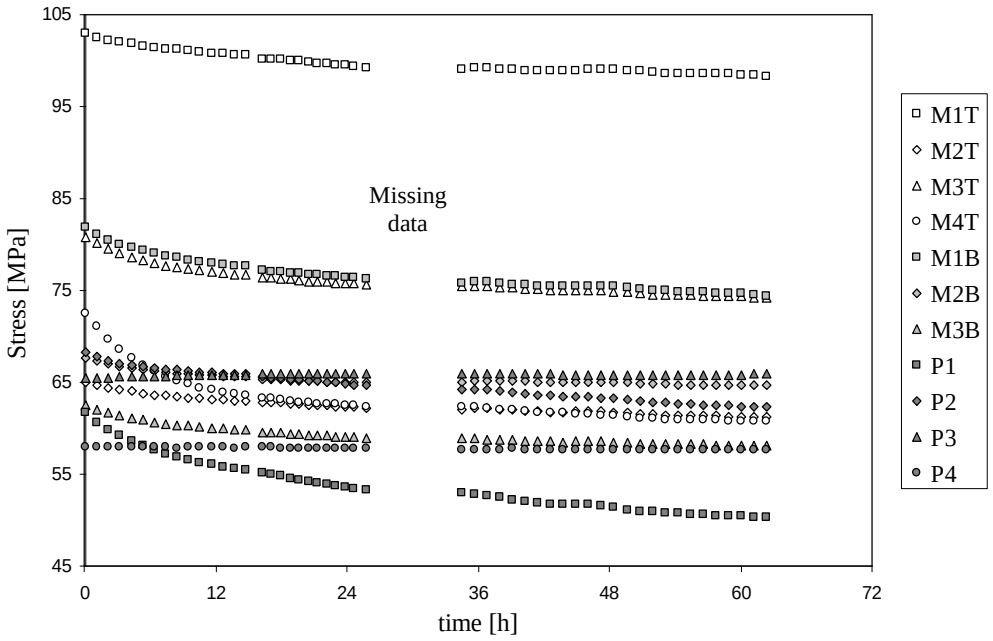

Figure 8.27 Observed relaxation of the pre-stress on the stress transducers in the model test.

Area	Coil layer	Normalized stress reduction [%]	Area	Coil layer	Normalized stress reduction [%]
Mid-plane	1	7	Pole	1	18
	2	5		2	9
	3	8		3	-1
	4	16		4	1

Table 8.14 Stress creep at the mid-plane and pole-piece transducers.

The stress in the mid-plane area shows the highest creep in the outer layers, while at the pole-piece the opposite is true. The differences in creep rates suggest a non-uniform load pattern initially, with the load on the inner layers at the pole higher than on the horizontal plane. It is followed by a redistribution of the load due to creep in the coil package.

The creep results obtained from the model test cannot easily be transformed for use in the main magnet, since end effects will be dominant in such a short structure. One explanation for the apparently larger creep in layer 1 compared to layer 2 is the larger ratio of soft copper spacers to conductor in the inner layer.

The copper spacers used in the model are annealed due to the reaction bake, given them a yield strength in the order of 42 MPa. This means these will creep as well, in contrast to the magnet coils, where aluminum bronze is used with a yield strength of about 144 MPa. The creep in the copper spacers is evident at the ends of the model, where the spacers protruded out of the surface of the coil package. This effect will account for some of the reduction of the pre-stress as observed on the stress sensors.

8.8 Summary of the transducer performance and the mechanical model test

Two novel fiber-optic stress measurement methods based on FP sensors, for use between 293 K to 4.2 K in superconducting magnet coil windings, are described in section 8.5.1 and 8.5.2. A sensor system using these two methods has several major advantages over conventional electrical strain sensors, the most important being the miniature size and the ease of use in a cryogenic environment. The sensors are capable of measuring absolute and relative stress and strain with a maximum resolution of about 10 % within the range of 100 to 150 MPa. The use of the mid-plane fiber-optic sensor matrix was successfully demonstrated up to a transverse stress of 175 MPa.

The calibration of the stress transducers proved to be difficult, due to the large influence of the stiffness of the material used to apply the pressure to the gauge on the transfer function of the bridge. Also, large errors up to 40 % in the stress measurement can be introduced in the pole-piece transducers due to surface mismatches between the gauge block and the cavity holding the gauge. It is found that an epoxy impregnation gives the best repeatability of the stress readings, therefore the pole-piece transducers are glued in place in the magnet test described in the next sections. The calibration problems affect both the fiber-optic and resistive stress measurements.

The wire wrapping method for the application of pre-stress (described in section 8.7.1) on the coil windings has proven to be a successful substitute for other methods like shrink cylinders or press and welded shells. The actual applied total pre-stress is slightly lower than predicted, but follows the calculated increase per layer nicely. Benefits of the wire winding technique are the possibility of corrections in the pre-stress if the designed value is not obtained at first, and the ease of disassembly of the structure. For a welded shell or shrink cylinder pre-stress application, disassembly becomes difficult and costly; with the wire wind technique the wire can be unwound, and rewound as desired.

The prediction of the critical field of the magnet made in section 8.4 remains unchanged, since the critical locations E & F (see figure 8.10) did not see significant changes in stress.

8.9 Experimental setup for the magnet test

In this section, the measurement plan and experimental setup of the stress and strain measurement system for the main magnet test is described in detail. The configuration of the fiber-optic sensor matrix at the mid-plane, described in this section, is different from the one described in section 8.7 for the following reasons :

1) several longitudinal and all radial strain sensors were damaged during a machining operation performed after the initial tests of the sensor matrices. The machining operation (shaving the sensor matrices from a thickness of 0.8 mm to 0.6 mm) was imposed due to a redesign of the electrical insulation layers between the coil halves;
2) the transverse stress transducers are eliminated from the mid-plane due to concerns raised about possible damage to the superconductor by stress concentrations. These stress concentrations are due to the reduction in thickness from 0.8 mm to 0.6 mm, which necessitated the reduction in thickness of two protective Kapton layers;
3) only two scanner channels were made available on the data acquisition system for the fiber-optic sensors, instead of the 32 channels originally requested.

As a consequence, only the transducers in the poles are available for a reading of the winding stress. Figures 8.28 and 8.29 show the location and purpose of the reduced set of available sensors in the magnet.

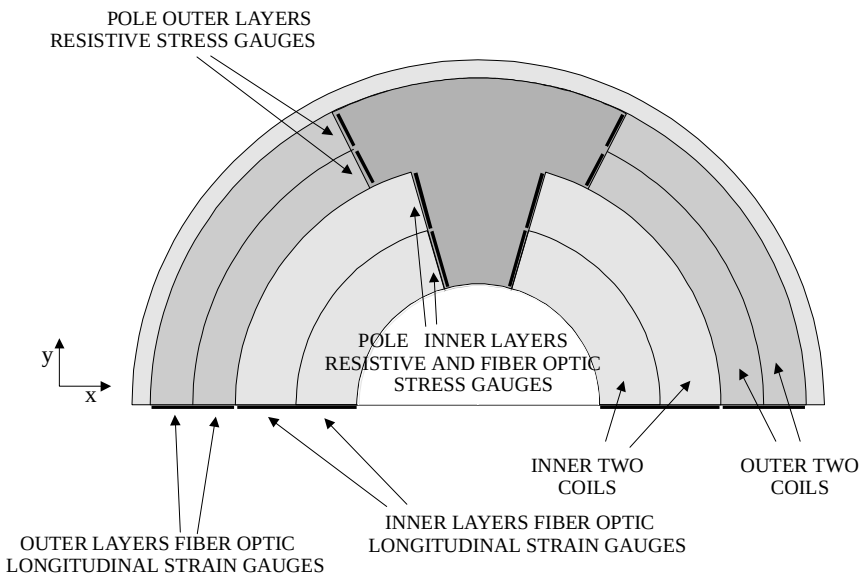

Figure 8.28 Locations of the available sensors in the magnet. The stress transducers in the pole are instrumented with fiber-optic and resistive gauges for layers 1 and 2. The stress transducers in the pole for layers 3 and 4 are instrumented with resistive gauges only. The mid-plane is instrumented with 5 longitudinal fiber-optic strain gauges.

Two scanners are available for the readout, the first scanning at 1 Hz for monitoring purposes (without time-limit), the second at 2 or 5 kHz during a quench (1024 data-points, referred to as the high-speed scanner). The measurement scheme is as follows:

1) before a quench, one fiber-optic sensor in the mid-plane and one in the pole stress transducer is connected to the high-speed scanner. The selection of the two different sensors is alternated between quenches to scan all available sensor positions;
2) during cooling-down, ramping of the magnet, and warming-up, all resistive strain gauges and two fiber-optic strain sensors are connected to the 1 Hz scanner. The sensor selection is alternated between scans.

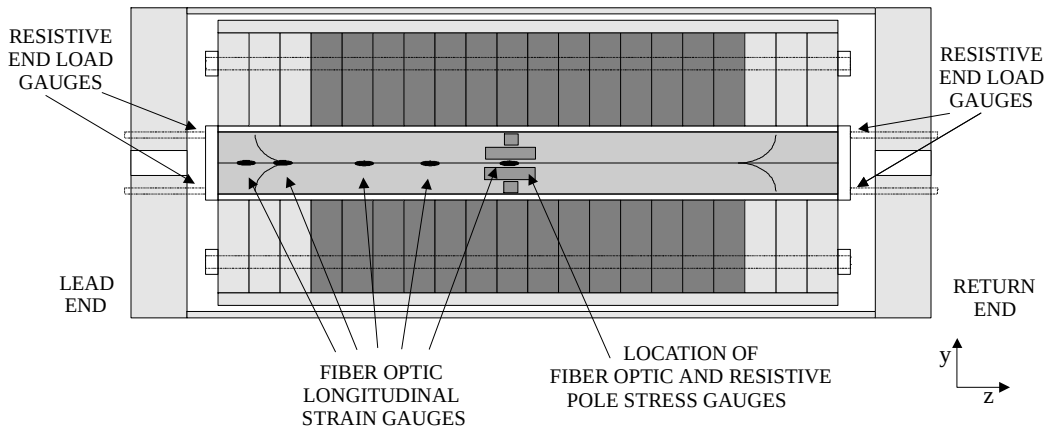

Figure 8.29 Locations of the available sensors in the magnet. The ends of the magnet have four bolts with resistive strain gauges on each side. The bolts read the stress exerted by the coils on the end-plate (or strain in the coils).

8.10 Final magnet assembly

This section describes the stress measurements taken during the final assembly of the magnet. The assembly sequence consists of the following steps:

1) the four coil halves are assembled with the sensor matrices and shims in the collar halves;
2) the partially assembled system is wrapped with ten layers of wire wrap for pre-compression;
3) the partial assembly is allowed to creep and relax for several days;
4) the wire wrap is removed, and clamps are placed on the collar to keep the partial assembly under slight compression of the order of 3-5 MPa;
5) the clamps on the collar are removed one by one and replaced with the yoke plates;
6) the yoke plates are tightened around the collar with chain-clamps;
7) the wire wrap is applied around the yokes (the wire is wound on a thin stainless steel sheet that provides a smooth surface for the wire wrap; it is not shown in figure 8.29).

This sequence is then followed by the application of the final pre-stress by the wire wrapping process. The stress on the coils is again monitored after each fully wrapped layer. The wrapping sequence is continued until the required pre-stress is achieved. The following sections detail steps 2, 3, 4 and 7 of the process.

8.10.1 Pre-compression and creep in the coil assembly

This section describes the pre-compression (step 2) and creep (step 3) in the final coil assembly. To eliminate the effect of the initial shape change of the assembly during the pre-stress application, the coils are partially loaded by wrapping 10 layers of tension wire directly on the collar. The assembly remains compressed for a few days to allow the coils to creep. Next, the wire wraps are removed, and the coils are kept under a slight compressive force (of the order of 3-5 MPa). Figure 8.30 shows the average measured stress on the pole-pieces in the four layers as a function of the number of wire wraps. It is unevenly distributed, as is evident from the large increase in stress on layer 2 compared to the other three layers. The average increase in stress is 1.9 MPa per wire wrap, with the second layer gaining 4 MPa per wire wrap.

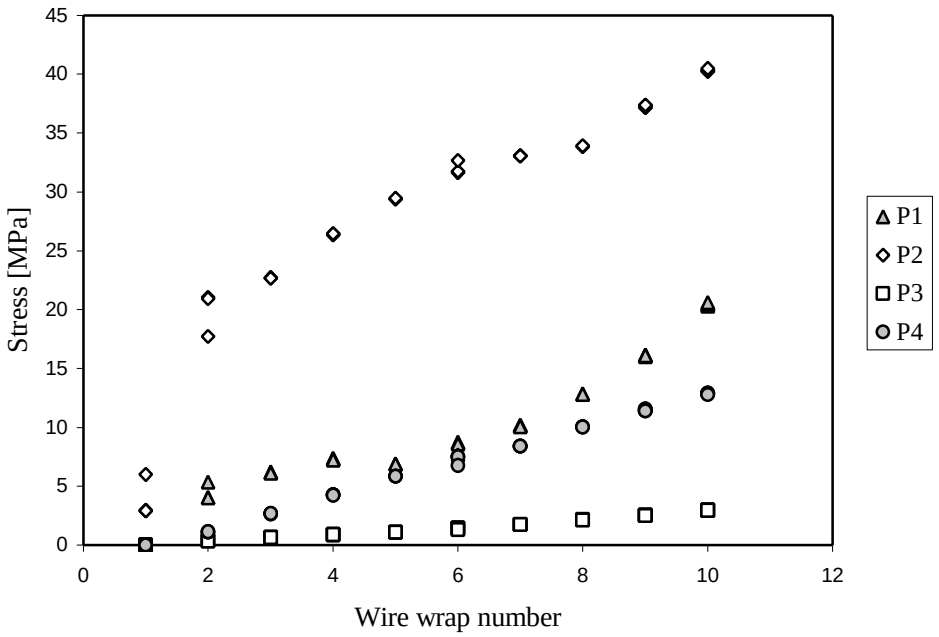

Figure 8.30 Average stress on the pole sensors for each layer as a function of the number of wire wraps. Note the large increase in stress in layer 2 compared to the other three layers.

The stress at each layer after wrapping is complete, and after the creep period, is listed in table 8.15. On average, about 7 % of the applied pre-stress is lost due to creep in the assembly.

The reason for the different behavior of the two inner layers as compared to the two outer layers is an initial tilt in the mid-plane surface of the inner coil assembly (layers 1 and 2). The coil is slightly too large at layer 2, and slightly too small at layer 1.

When compressed, the coil slowly straightens itself, causing the stress on layer 2 to increase more rapidly. This is also the likely reason that the observed creep in layer 1 is larger than in the other layers.

The wire wraps are removed after approximately 4 days. After unwrapping, the coils are kept under stress with clamps on the collar until final assembly.

Pole-piece transducer	Stress after 10 layers [MPa]	Stress after creep period [MPa]	Normalized change in pre-stress [%]
P1	21	17	-19
P2	40	41	3
P3	3	3	0
P4	13	11	-15
		Average	-7

Table 8.15 Average stress at the pole-piece transducer for the four layers at winding complete and after the creep period, and the change in pre-stress normalized to the initial value (in percent).

8.10.2 Final pre-stress application

After completion of step 6, the stainless steel wrapping wire is wound onto the wrapping cylinder layer by layer. Stress measurements are taken at each completed layer using the resistive stress sensors. The completed layers are referred to as number of wire wraps in the graphs. Figure 8.31 shows the increase in stress in the four layers of the coils with an increasing number of wraps. The lines are linear extrapolations towards the design goal of 25 wraps. Wrapping is continued to 18 layers to increase the outer layer pre-stress to about 60 MPa. At this point, wrapping is stopped to not further increase the pre-stress on the inner layers for fear of coil damage due to the tilted surface of the inner two coils. Table 8.16 lists the predicted pre-stress from the ANSYS model (see table 8.1) compared to the final pre-stress after wrap 18, and the extrapolated values at 25 wraps.

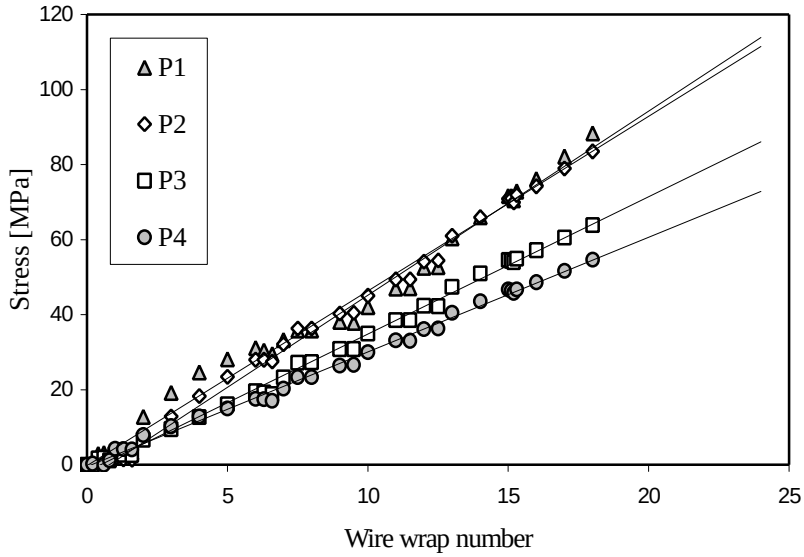

Figure 8.31 Average of the measured stress in the four layers of the coils as a function of the number of wire wraps. The stress in the inner layers increases more rapidly than in the outer layers, with an average increase of about 4 MPa per wire wrap.

Pole-piece gauge	Predicted average pre-stress at 18 wraps [MPa]	Final measured pre-stress at 18 wraps [MPa]	Predicted average pre-stress at 25 wraps [MPa]	Extrapolated pre-stress at 25 wraps [MPa]
P1	84	88±9	116	122
P2	*57*	*83±8*	*79*	*115*
P3	68	64±6	94	89
P4	59	55±6	82	76

Table 8.16 Predicted pre-stress compared to the final pre-stress after wrap 18.

It is evident from table 8.16, that further wrapping up to layer 25 would have over-compressed the second layer. At wrap 18, the average pre-stress on coils 1, 3 and 4 is still about 29 % too low, but coil 2 is already exceeding the design pre-stress. This matches the prediction very well, with 18 out of 25 wraps complete, the predicted pre-stress is 28 % too low.

Figure 8.32 shows the average stress increase per wire wrap for the cookie, wire-on-collar, and final assembly. For the final assembly the stress increase is approximately 4 MPa per wire wrap. This is a larger increase than the 2-2.5 MPa/wrap in the cookie and wire-on-collar test by about 60 %.

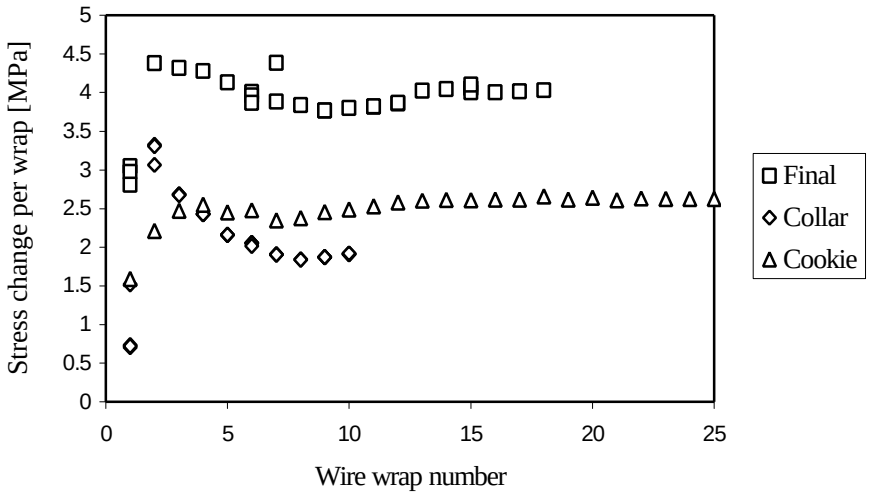

Figure 8.32 Average stress change per wire wrap number for the cookie, wire-on-collar test, and the final assembly. The stress increase per wrap in the cookie and wire-on-collar test average about 2-2.5 MPa/wrap, compared to 4 MPa/wrap in the final assembly.

This effect is attributed to the larger stiffness of the final coil package due to the pre-compression step of the wire-on-collar test. *This proves conclusively that the pre-compression method works in elimination the "slack" from the coil assembly.*

Figure 8.33 shows the last set of stress readings before the magnet is inserted into the cryostat. After completion of the wire wrapping, stress readings are taken over a period of 18 days. The first 9½ days (up to 230 hours) the magnet was not moved. During this period creep measurements are taken to monitor the change in pre-stress. A small decrease in pre-stress is recorded, with an average drop of 4.5 MPa (6.2 %).

Next, the magnet is removed from the wire wrapping station and rotated to a horizontal position for transport and insertion into the cryostat. An average stress increase of 4.5 MPa is recorded. The magnet is left in the horizontal position for a period of 5 days, during which the stress is recorded continuously. Note the small periodical change in pre-stress due to the daily day-night temperature cycle.

The last two data-points are recorded after the magnet is transported from the assembly area to the cryogenic test facility. An average stress increase of 2.8 MPa is recorded, which might be attributed to movement during transport. Table 8.17 lists a summary of the design pre-stress, and the measured stress at the various steps in the assembly, creep and transportation stages. Note how layer 1 gained some of the pre-stress, and is now only 16 % below the predicted full design pre-stress. The pre-stress in layers 3 and 4 is still not at the required level, and did not change much over time. The final column lists the stress recorded before magnet cooling-down is commenced. Cooling-down is discussed next in section 8.11.

Pole-piece gauge	Design (ANSYS) [MPa]	Predicted at 18 wraps [MPa]	After 18th wrap [MPa]	After creep [MPa]	Magnet horizontal [MPa]	After transport [MPa]
P1	116	84	88±9	82±8	93±9	98±10
P2	79	57	83±8	80±8	84±8	86±9
P3	94	68	64±6	58±6	61±6	64±6
P4	82	59	55±6	48±5	52±5	57±6

Table 8.17 Summary of the design pre-stress, and the measured pre-stress at the various stages in the assembly process.

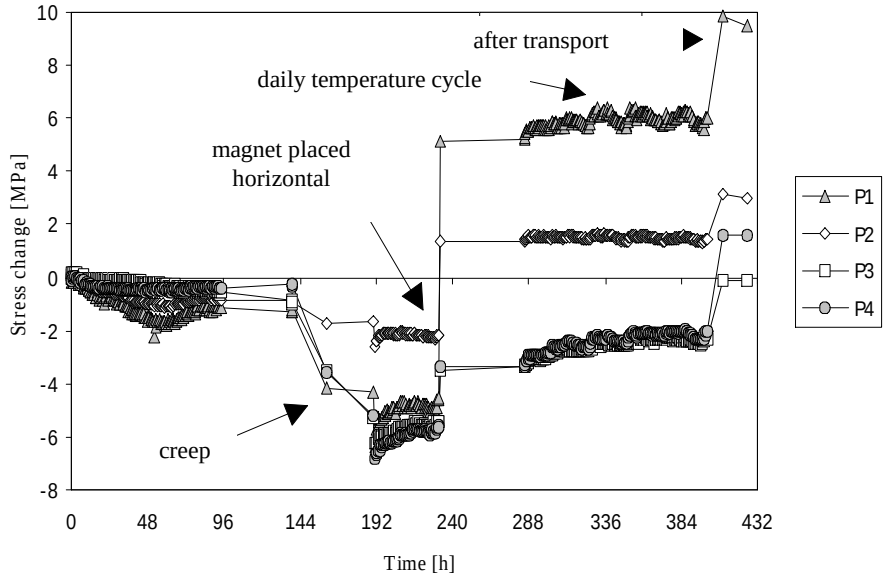

Figure 8.33 Average change of the measured stress in the four layers of the coils after winding. Distinct events are marked in the graph.

8.11 Cooling-down

The magnet is now cooled down from room temperature at 293 K to 4.3 K. Stress is measured at the pole-piece transducers in layers 1 to 4. The measured stress is compared to the predicted stress from the ANSYS model of the cooling-down [8.21]. The end load is measured at both ends of the magnet. The fiber-optic sensors were not used during the cooling-down.

Table 8.18 lists the stress before the start of the cooling-down period, the predicted stress at 4.3 K from ANSYS, and predicted stress corrected for the actual stress at 300 K. Also listed are the maximum stress during cooling-down and measured stress at 4.3 K. The locations of the active gauges are shown in figures 8.28 and 8.29. In figure 8.34 the average stress at the pole-piece gauges is shown.

Pole-piece gauge	Measured stress before cooling-down [MPa]	Predicted stress at 4.3 K (ANSYS) [MPa]	Predicted stress (corrected) at 4.3 K [MPa]	Maximum stress during cooling-down [MPa]	Measured stress at 4.3 K [MPa]
P1	98±10	121	103±10	103±10	68±7
P2	86±9	80	67±7	104±10	62±6
P3	64±6	60	50±5	92±9	52±5
P4	57±6	70	45±5	82±8	63±6

Table 8.18 Stress before cooling-down, predicted, maximum and measured stress at 4.3 K.

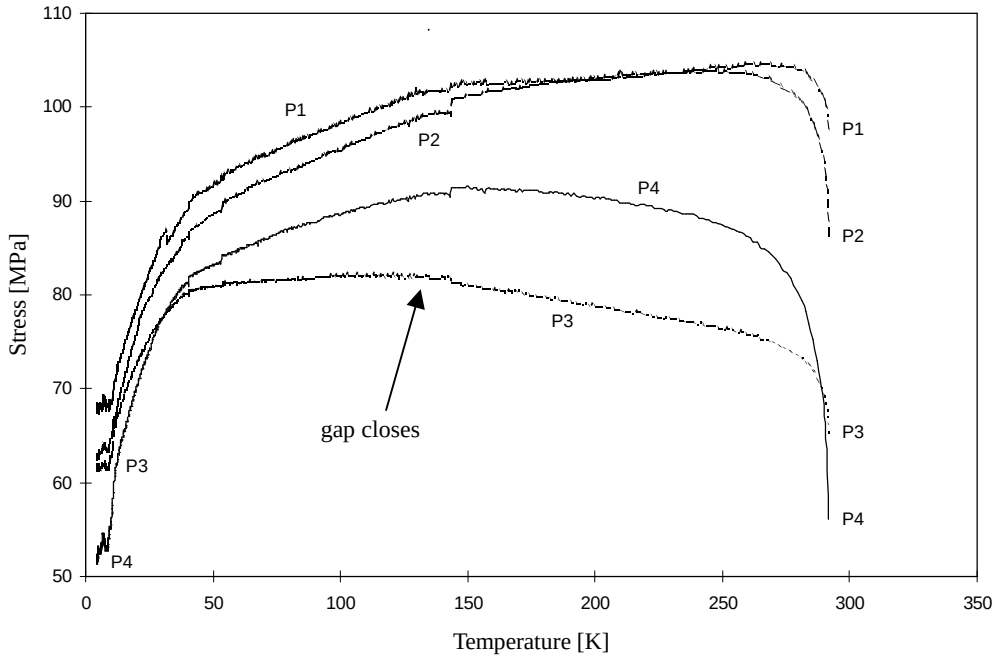

Figure 8.34 Average of the stress measured by the four pole-piece gauges on each layer during the cooling-down from 293 K to 4.3 K. Note the slope change at the closure of the gap around 145 K.

The stress is plotted as a function of the temperature, which is recorded at the gauge block of the top pole-piece in layers 1 and 2. The temperature sensor itself cools down faster than the coils, collar and iron yoke, therefore, a significant reduction in stress is still measured at temperatures below 50 K, where the integrated thermal contraction of the materials would normally not amount to such a large change.

Figure 8.35 shows the force on the lead-end and return-end gauges as a function of the temperature. The figure shows an increase in force due to the yokes shrinking around the coils, which compresses the coil and elongates them towards the end-plates on either side.

The large difference in measured force on the lead end and return end gauges indicates that there is a difference in the friction between the yokes, collar and coils at each end. This follows from the fact that the two ends initially see roughly the same increase in force, but after closure of the gap the return end force reduces, while the lead end force increases. Constraining the coils near the return end, while leaving them free to slide towards the lead end could cause such a difference, but would not explain the reduction in load at the return end. The average end force is 167 kN at 4.3 K, with the return end at 121 kN and the lead end at 213 kN.

Both the pole-piece gauge readings shown in figure 8.34, and the end gauge readings shown in figure 8.35 show that the gap closes at about 145 K. It is indicated by the “bump” in the recorded data, and the subsequent change in slope of the measured stress with decreasing temperature on the pole-piece gauges.

The gap closure occurred at a higher temperature than the 100 K predicted by the ANSYS model [8.21], just as in the mechanical model, resulting in an additional loss of pre-stress of about 23 MPa (average of the four layers) at 4.3 K. The pre-stress on the inner layers is about 33 % low, while the pre-stress on the outer layers is about 12 % high. The total compressive load on the mid-plane is low by 27 %. This factor matches the reduction in pre-stress due to the reduced number of layers. Using 18 layers instead of 25 results in a pre-stress reduction of 28 %.

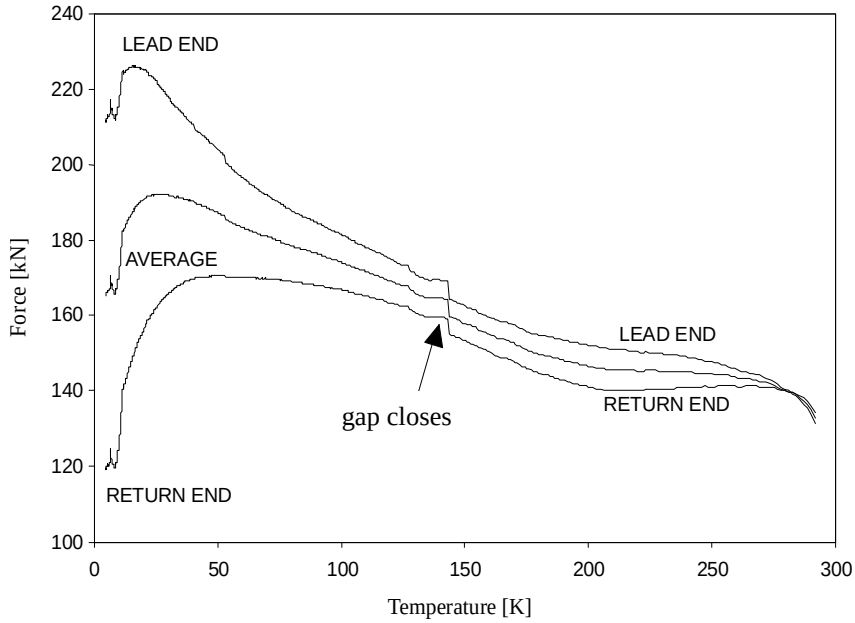

Figure 8.35 Sum of the forces measured by the end gauges on the lead and return end of the magnet.

8.12 Magnet performance

This section describes the test results of the magnet, with emphasis on the stress and strain measurements. The magnet is initially tested at 4.4 K[5], then *trained* to obtain the maximum field (defined as the *plateau* field, where subsequent quenches do not significantly increase the field). The stress and strain sensor readings are recorded for all quenches. First the resistive gauge measurements are discussed, followed by the fiber-optic stress and strain measurements.

The measured pre-stress on the pole-piece gauges after cooling-down to 4.3 K is lower than the required pre-stress to maintain compression on the interface between the coils and the pole-piece. As a result of the lower pre-stress, significant training is expected below the design field due to mechanical motion at the coil to pole-piece interface.

Table 8.19 lists the required pre-stress, measured pre-stress, and estimated magnetic field at which separation of the coil to pole-piece interface could occur. The field is estimated by computing the required stress reduction to bring the pre-stress on the coil to pole-piece interface to zero. This stress then yields the magnetic field in the bore, since the stress scales with the square of the field. Training is expected to be significant above these estimated field values.

From table 8.19 it follows that the first significant training quenches can be expected in the field range of 9.8-10.8 T. Separation at layer 2 could occur between 12.3-13.5 T. Separation at layers 3-4 is less likely to occur, since the magnet should not reach such a high central field at 4.4 K. In the following section, the training history is discussed in more detail, and an extrapolation is made of the critical field of the magnet at 4.4 K.

[5] The pressure in the test cryostat was slightly elevated during the tests as compared to the initial cooling-down. The temperature increase from 4.3 K to 4.4 K does not have a significant effect on the mechanical behavior, but causes a slight decrease of about 0.5 % in the predicted values for critical current and field.

Coil layer	Required pre-stress [MPa]	Expected stress reduction at 13 T [MPa]	Measured pre-stress [MPa]	Estimated magnetic field for separation [T]
1	121	109	68±7	10.3±0.5
2	80	63	62±6	12.9±0.6
3	60	45	52±5	14.0±0.7
4	70	55	63±6	13.9±0.7

Table 8.19 Required pre-stress, expected stress reduction at 13 T, measured pre-stress, and estimated magnetic field at which the coil could separate from the pole-piece.

8.12.1 Training quenches

In general, accelerator dipole magnets exhibit training behavior, usually about 5-10 quenches [8.22, 8.23] are needed to reach the plateau. Some magnets need more quenches, such as the CERN LHC model dipole [8.24]; some need none at all, such as the MSUT 11.5 T dipole [8.25].

Figure 8.36 shows the maximum magnetic field in the bore for all recorded quenches. The first quench, located in the inner turns of the first layer near the pole, reached 10.19 T; training increased the maximum field to 11.34 T at quench 12. The magnetic field of the first training quench matches the predicted field of 10.3 T well, and the location confirms a possible separation of coil layers and its pole-piece interface. Next, the temperature is cycled between 4.4 K and 1.8 K, and the magnet is further trained up to a field of 13.32 T at training quench 27 at 1.8 K.

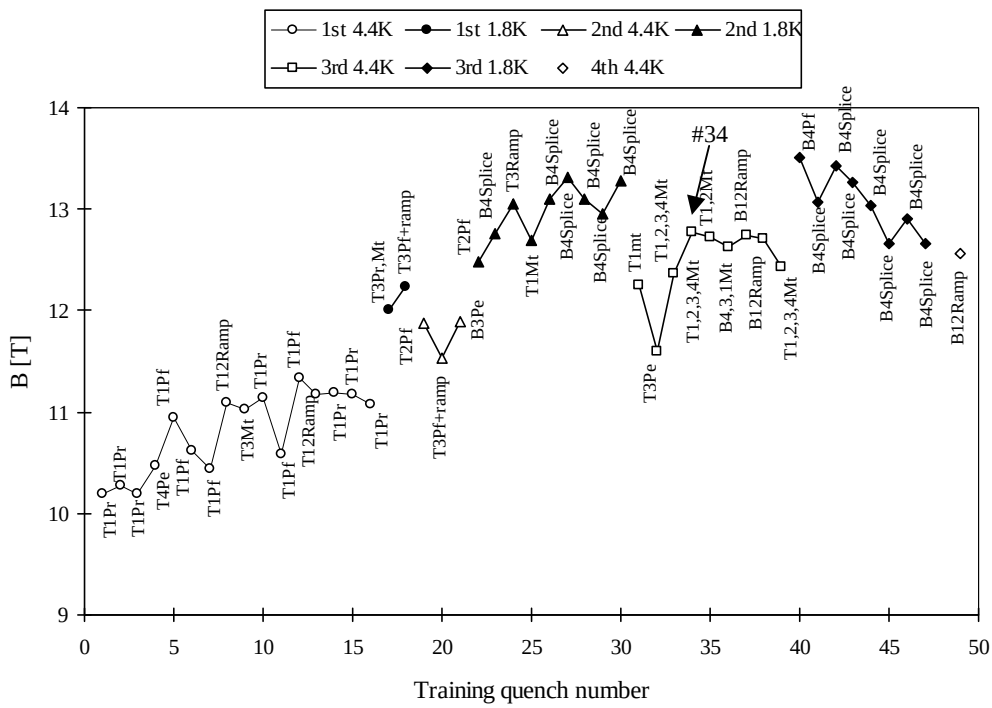

Figure 8.36 Magnet training curve: maximum magnetic field for recorded quenches (up to 49) at 4.4 K and 1.8 K as a function of the quench number.

After increasing the temperature back to 4.4 K, the magnet reached 12.78 T at quench 34. Further training increased the maximum field to 13.51 T at 1.8 K [8.26], with a gradual decrease in the subsequent training due to quenching at the splice between the two coil halves. The sequence is terminated at quench 49. Table 8.20 lists a sequence of selected training quenches.

Quench number	Label	Location	Temp. [K]	Field [T]
1	T1Pr	Top coil, layer 1, pole turn, return end	4.4	10.19
12	T12Ramp	Top coil, ramp from layer 1 to layer 2	4.4	11.34
16	T1Pr	Top coil, layer 1, pole turn, return side	4.4	11.08
17	T1Pr	Top coil, layer 1, pole turn, return side	2.1	12.01
18	T2Pf	Top coil, layer 2, pole turn, lead end	1.72	12.23
19	T3Pr,Mt	Top coil, layer 3, pole turn + mid-plane	4.3	11.88
22	T2Pf	Top coil, layer 2, pole turn, lead end	1.74	12.49
27	B4Splice	Bottom coil, layer 4, splice	1.73	13.32
30	B4Splice	Bottom coil, layer 4, splice	1.88	13.28
31	T1Mt	Top coil, layer 1, mid-plane	4.4	12.25
34	B12Ramp	Bottom coil, transition layer 1 to layer 2	4.4	12.78
40	B4Pf	Bottom coil, layer 4, pole turn, lead end	1.79	13.51
49	B12Ramp	Bottom coil, transition layer 1 to layer 2	4.5	12.56

Table 8.20 Location, temperature and field of selected training quenches.

The maximum field reached at 4.4 K is 12.8 T (I = 6303 A), which corresponds to approximately 12.9 T at 4.2 K (I = 6352 A). In order to determine whether 12.8 T is the true maximum field at 4.4 K, or if a little margin still exists, a so-called fast-ramp experiment is performed.

The magnet current is held steady below the expected quench current until the temperature is stable. Then a fast ramp is started, which heats the coil, until a quench is initiated. The difference between the quench current I_q and start current I_{start} is directly proportional to the margin of the superconductor [8.27]. Repeating the experiment for increasing start current (and field) as illustrated in figure 8.37, yields the limit of the margin for $I_q - I_{start} \rightarrow 0$. A second order fit is used to determine the limit of the margin.

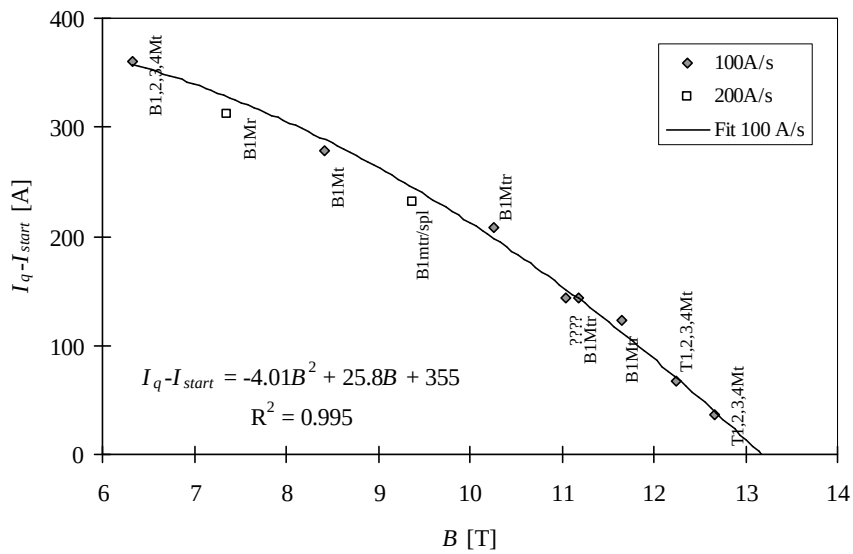

Figure 8.37 Fast ramp margin study at 4.4 K to determine the critical field of the magnet.

The extrapolated critical field in the fast ramp margin experiment is 13.1±0.2 T. These values correspond well with the predicted critical field of 13 T (I = 6400 A) at 4.2 K. The required current to reach 13 T is 6433 A, or 0.5 % higher than predicted.

Based on the good match between the predicted and measured critical field, the critical current degradation in the magnet corresponds well with the measured degradation in the cable experiments.

The quench location and type can also be used to determine whether the cables still have some margin. Most early quenches in the training sequence occur in the end regions in the inner layer near the pole-piece. The quenches are also preceded by a large amount of mechanical movements (recorded as fast motions or imbalances on the voltage taps), and sometimes even by measurable mechanical jolts [8.28].

Later in the sequence, after quench 28 at 12.5 T, 1.8 K, the quenches originate in the straight section, and sometimes start in multiple layers simultaneously. No significant mechanical movement is recorded preceding the latter quenches, indicating that the quenches now occur due to a cable section reaching the critical current somewhere in the magnet.

8.12.2 Summary

The final pre-stress on the coils did not reach the design pre-stress; the pre-stress is on average 27 % below the design value. This value matches the reduced application of pre-compression, since only 18 of the 25 wire wrap layers were used.

Anomalous behavior of the force distribution in the longitudinal direction is observed. The force on the lead end of the magnet is almost two times higher than the force on the return end of the magnet. A possible explanation for this imbalance is a difference in the friction between the coil assembly and the yoke plates from one end to the other. This difference is most likely due to slight mechanical size differences in the components.

The magnet almost reached the design field of 13 T at 4.3 K (I = 6400 A), but only after 34 training quenches. The highest measured field at 4.4 K is 12.78 T, at a current of 6303 A.

The prediction of the field of the first training quench at 10.3±0.5 T matches the measured field at 10.19 T well. It can be concluded that the stress measurements at the pole-piece stress transducers are accurate.

8.13 Detailed resistive and fiber-optic stress and strain measurements

In this section selected results of low speed fiber-optic and resistive stress and strain measurements are analyzed in more detail. The first series of training quenches is preceded by a series of artificially triggered quenches at low field, to test the quench protection and energy extraction circuitry. At the beginning of the first training quench, the stress measured at the pole-piece transducers was changed significantly as compared to the last measurement after cooling-down was complete. Table 8.21 lists the predicted stress, measured stress just after cooling-down, and the measured stress just before the first training quench.

Pole-piece gauge	Predicted stress at 4.3 K (ANSYS) [MPa]	Predicted stress at 4.3 K [MPa]	Measured stress at 4.4 K [MPa]	Measured stress before quench 1 [MPa]
P1	121	103±10	68±7	93±9
P2	80	67±7	62±6	57±6
P3	60	50±5	52±5	60±6
P4	70	45±5	63±6	38±4

Table 8.21 Predicted (at 4.3 K) and measured stress (at 4.4 K), compared to the measured stress just before the first training quench.

The stress on the inner layer is increased by about 37 %, while the stress on the outer layer is reduced by 40 %. The total force on the four coil surfaces at the pole-piece has increased by 2 %. These changes are attributed to a redistribution of the forces within the coil assembly.

The total force on the end gauges is plotted as the sum of the measurements of four force transducers. In total, there are ten such bolts per side, of which four are instrumented. Hence, the total force on the end-plates is 2.5 times larger than the measured number.

8.13.1 Average stress as a function of the quench number

Figures 8.38 and 8.39 show the recorded average stress on the pole-pieces of the four layers, and the total force on the four end gauges, for the 1st and 43rd quench (last quench with processed stress data on file at the time of this chapter's completion). Table 8.22 lists the predicted and measured stress and end forces.

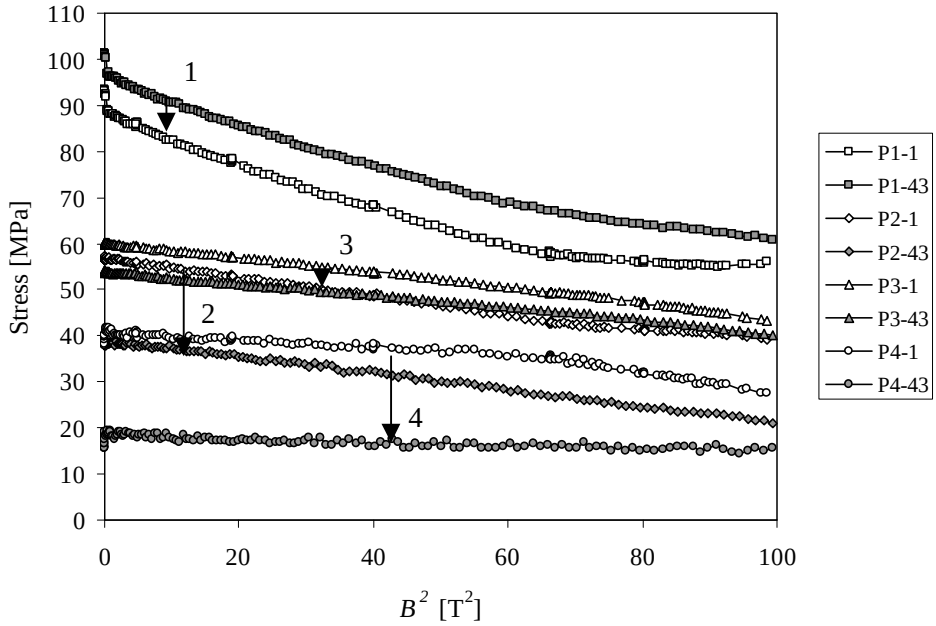

Figure 8.38 Quench 1 and 43 resistive pole-piece stress transducer readings. Traces for quench 1 are in white; traces for quench 43 in gray. Note the pressure drop, especially in layers 2 and 4.

Quench 1					Quench 43				
Gauge	0 T		9.9 T		Gauge	0 T		9.9 T	
	Pred. [MPa]	Meas. [MPa]	Pred. [MPa]	Meas. [MPa]		Pred. [MPa]	Meas. [MPa]	Pred. [MPa]	Meas. [MPa]
P1	121	93±9	30±9	56±6	P1	121	101±10	38±9	61±6
P2	80	57±6	20±6	39±4	P2	80	39±6	2±6	22±2
P3	60	60±6	34±6	43±4	P3	60	54±6	28±6	40±4
P4	70	38±4	6±4	27±3	P4	70	17±4	loose	15±2
P1-4	85	63±7	23±7	42±6	P1-4	85	55±8	17±7	36±5
End	Pred. [kN]	Meas. [kN]	Pred. [kN]	Meas. [kN]	End	Pred. [kN]	Meas. [kN]	Pred. [kN]	Meas. [kN]
Lead	NA	213	232	228	Lead	NA	221	240	235
Return	NA	121	140	128	Return	NA	130	149	137
Average	NA	167	186	178	Average	NA	176	195	186

Table 8.22 Predicted and measured stress at the pole-piece, and force on the four end gauges for quench numbers 1 and 43. Accuracy data on the end gauges is unavailable.

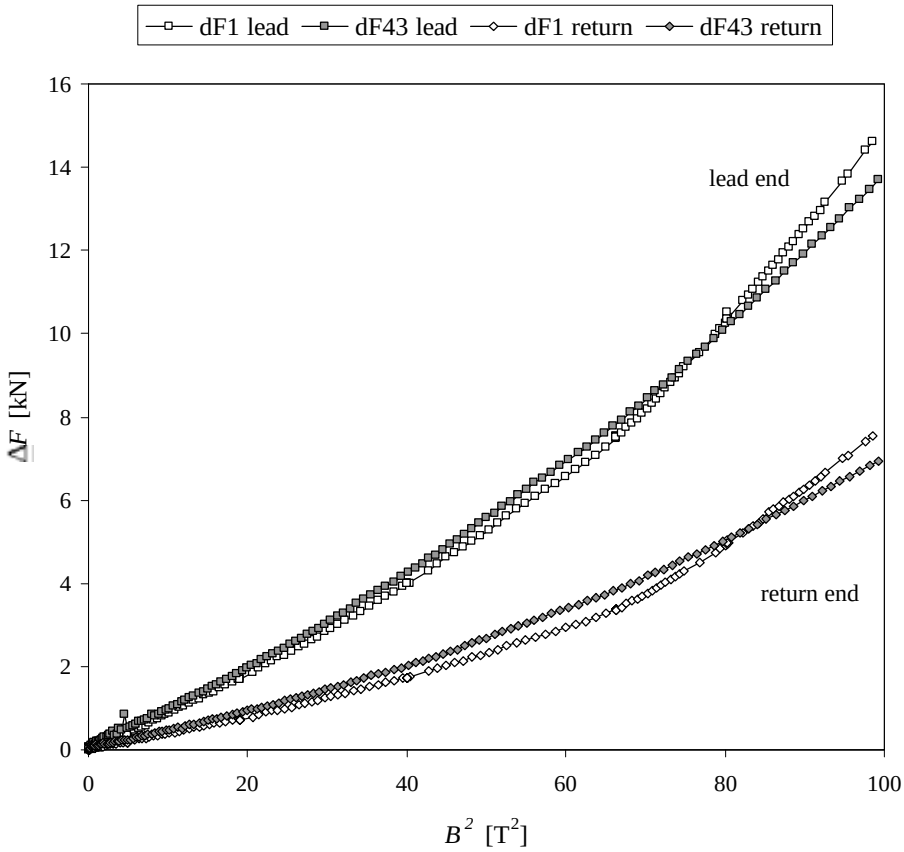

Figure 8.39 Quench 1 and 43 resistive end force transducer readings. The top two traces show the force change dF on the end force transducers (sum of the four gauges) as a function of the square of the field B.

The stress predictions at 9.9 T are based on the measured stress at 4.4 K. The end force prediction is based on the ANSYS model of the Lorentz force at 13 T [8.3]. One-tenth of the load on the coils is assumed to be transferred directly to the end-plates. The rest is transmitted through the structure to the bolts holding the yoke plates [8.29].

From the table and figures, it is clear that the average stress on all four pole gauges at zero field is decreasing over time, just like in the creep experiments. Also, the total force at the end gauges increases over time, while the change in force measured at the end gauges at a fixed field decreases over time.

For example at 9.9 T (last data-point for the first quench), the increase of force at the lead end is 14.6 kN (start at 213.2 kN) at quench 1, while it is 13.5 kN (start at 221.2 kN) at quench 43. The average force change dropped from 11 kN to 10 kN.

According to the ANSYS prediction, the change in force on the four gauges should amount to 19 kN at 9.9 T. The average measured force is only 11 kN at quench 1, and 10.5 kN at quench 43. This is low by about 43-45 %, which suggests that only about 4.5 % of the force is actually transmitted to the end-plates, with the rest supported by the bolts in the yoke plates.

The combination of decreasing stress in the pole area and increasing residual force on the end gauges indicates a plastic deformation (elongation) of the coils. The reduced total pole stress at the later quenches results in less force transmitted through the Poisson effect to the end gauges, thus resulting in a lower change in force. Essentially, the pre-stress on the coils is slowly extruding the coil assembly towards the ends of the magnet.

8.13.2 Maximum stress change as a function of the quench number

A slow reduction in pre-stress at the pole-piece of the inner layers is evident when the amplitude of the stress change in the layers is plotted as a function of the quench number. The amplitude of the stress change is scaled by $B_{\max}^2 / B_i^2$ for each quench, with B_{max} the highest field reached in all quenches, and B_i the maximum field at each quench i, to compare quenches around both 4.4 K and 1.8 K. Figure 8.40 shows the scaled maximum change in stress per layer for the first 43 quenches from zero field to quench.

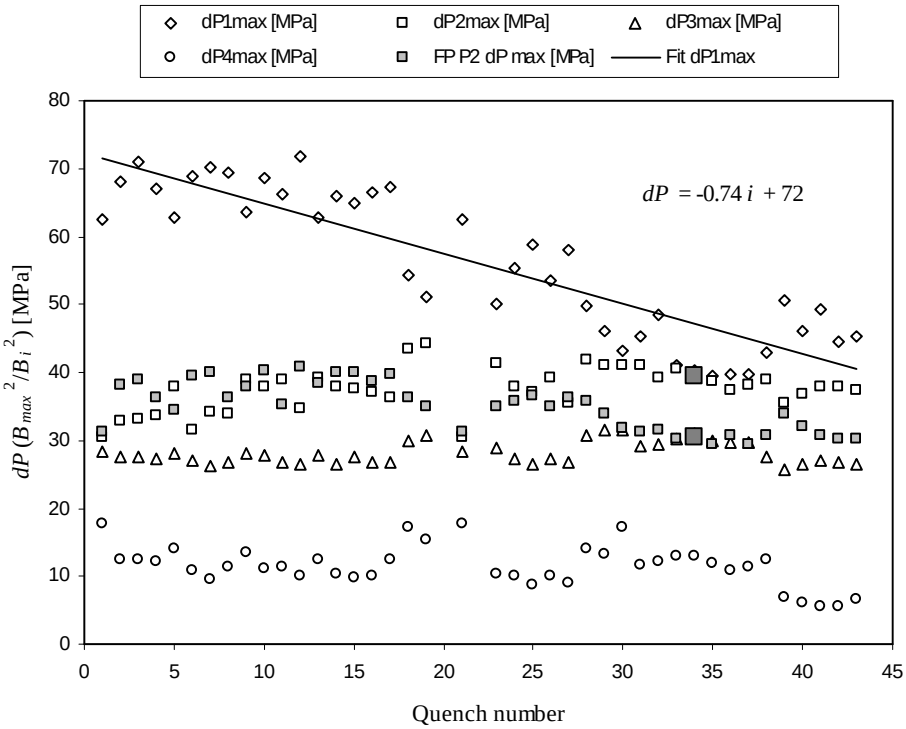

Figure 8.40 Stress decrease on the resistive and fiber-optic pole gauges scaled to the maximum quench stress. The reading on FP gauge P2 is included for comparison. The highlights on traces "dP1max" and "FP P2 dP max" mark the highest field reached at 4.4 K in quench 34.

Figure 8.40 clearly shows the gradual decrease in the scaled pressure change on layer 1. The maximum pressure change is reduced by 0.74 MPa per quench on the average. This decrease is due to the plastic deformation of the coil, especially the inner layer, where the stress is the highest. It is less pronounced in layer 2, 3 and 4. The decrease is expected to level out when the coils are no longer loaded significantly above the yield stress of the material.

An interesting note is that the highest field at 4.4 K is reached about where the stress change on layer 1 and the FP-gauge is at a minimum. The point is marked in dark gray in the graph.

Figure 8.41 shows the gradual increase in the scaled force measured by the end gauges with increasing quench number. Again, the explanation for the gradual increase in scaled force is plastic deformation of the coil package.

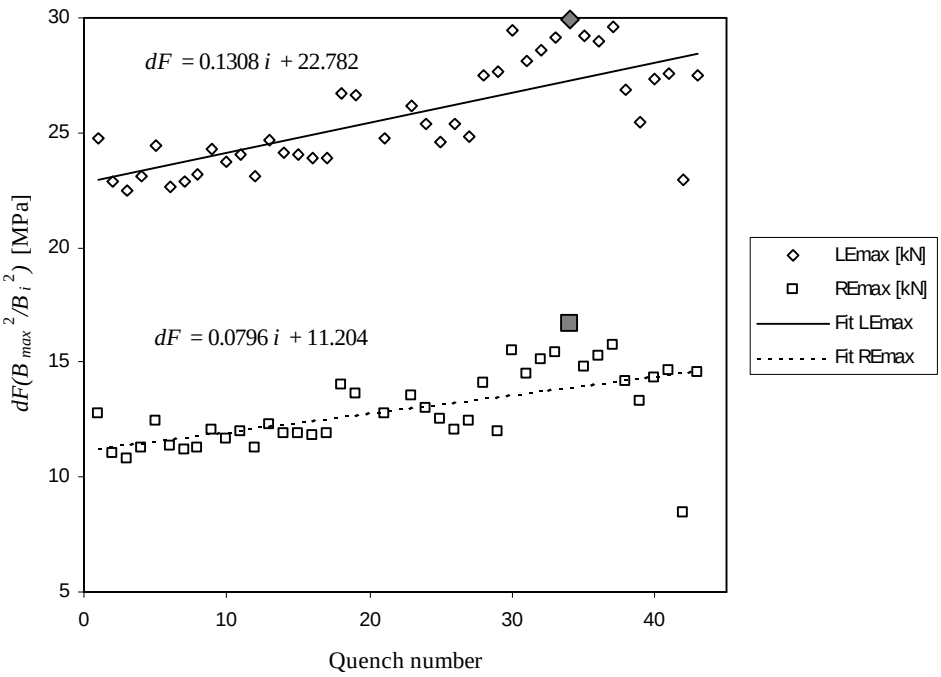

Figure 8.41 Change in force readings at the end gauges for quenches up to number 43. Shown is the gradual increase in force exerted on the end gauges by the coils at maximum field. The highlights on the traces (dark gray) mark the highest field reached at 4.4 K in quench 34.

In the longitudinal direction, the scaled force is a measure of how far the coils are stretched before a significant motion causes a quench. In most of the quenches, a larger force is followed by a fall-back to a smaller force, indicating that a small permanent displacement occurred in the coil package. The coils are essentially elongating in small irregular steps.

The scaled change in force increases by 0.13 kN per quench on the lead end, and 0.08 kN per quench on the return end. This increase amounts to about 0.6 % of the average pressure change per quench. The increase on the return end is higher by 30 % when corrected for the force imbalance between the two ends. The reason for the difference in behavior is not investigated further.

The highest field reached at 4.4 K coincides with the largest scaled force change on the end gauges.

In summary, the scaled stress change on the pole-piece gauges, and the scaled force change on the end gauges, both indicate an ongoing plastic deformation of the coil package. No asymptotic behavior of the plastic deformation is observed up to this point in the training sequence. The highest field reached at 4.4 K coincides with a small change in scaled pressure at the pole-piece gauge at layer 1, indicating no significant displacement at the pole, and the largest scaled change in force at both end gauges, indicating a large deformation in the longitudinal direction. This corresponds with the observed location of quench 43, which occurred in the mid-plane of all four layers almost simultaneously, unlike most preceding quenches in the poles.

8.13.3 Strain as a function of the quench number

In this section, readings from the fiber-optic longitudinal strain gauges in the mid-plane are analyzed. Figure 8.42 shows the measured longitudinal strain in the mid-plane of the coils as a function of the quench number. Information about the highlighted quenches is listed in table 8.23.

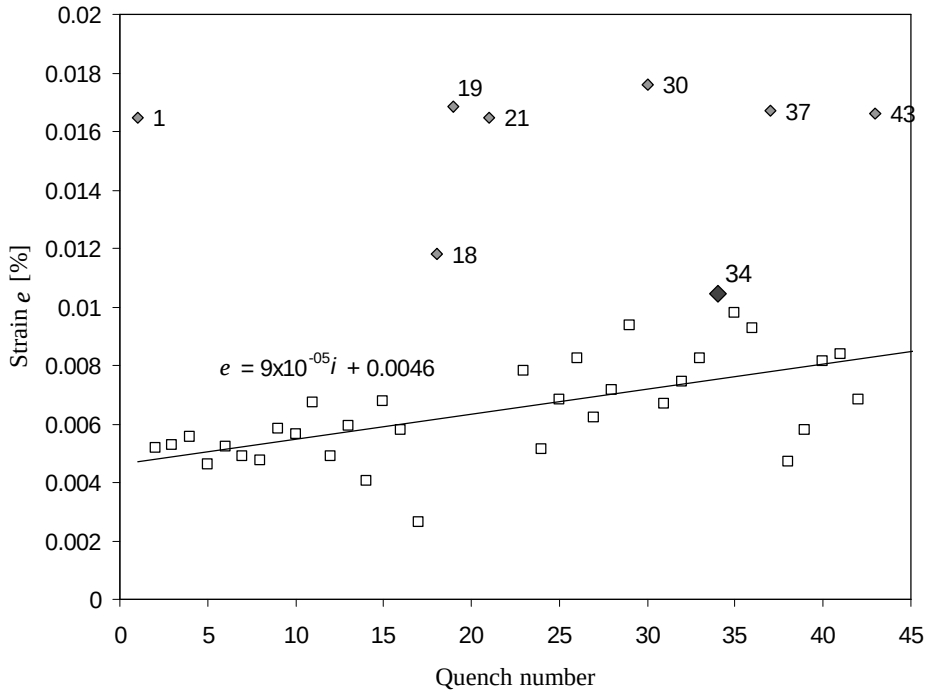

Figure 8.42 Longitudinal strain at the mid-plane as a function of the quench number. Highlighted are selected quenches (see table 8.23) where the strain change is particularly large, indicating an abrupt motion within the coil assembly. The black marker highlights the highest field at 4.4 K in quench 34.

Quench number	Strain [%]	Comments or preceding events	Temperature [K]	Field [T]
1	0.016	First full training quench	4.4	10.19
18	0.012	First cooling-down to 1.8 K (2nd quench)	1.72	12.23
19	0.017	Warming-up to 4.4 K	4.3	11.88
21	0.016	-	4.3	11.80
30	0.018	Last in series at 1.8 K, all at splice	1.88	13.28
34	0.010	Highest in series at 4.4 K	4.4	12.78
37	0.017	First quench at B1-2ramp splice	1.79	13.51
43	0.017	-	1.82	13.26

Table 8.23 Strain, comments or preceding events, temperature and field of the highlighted training quenches of figure 8.42.

Most of the quenches with a significant strain occurred after a temperature change of the magnet, with the exception of number 37, which is the first quench at the transition between layers 1 and 2. A gradual increase of the measured strain in the mid-plane of the coils with increasing quench number is visible. This is due to the rise in maximum field towards the end of the training sequence. The strain increase is of the order of $9 \cdot 10^{-5}$ % per quench, or about 1.5 % of the average strain per quench. The data-points showing large strain coincide with a subsequent large change in maximum field, and most follow a temperature change of the magnet. This indicates a mechanical event (stick-slip motion or glass-epoxy de-lamination at the poles) resulting in a better settling of the coils.

From the measured strain, and the corresponding force on both end-plates, the Young's modulus E of the coil package can be determined as in

$$E \equiv \frac{s_z}{e} = \frac{F_{lead-end} + F_{return-end}}{A_{coils} e}, \qquad [8.1]$$

with s_Z the stress in the longitudinal direction, and e the longitudinal strain. The stress is computed from the measured end forces $F_{lead\text{-}end}$ and $F_{return\text{-}end}$, and the cross-sectional area A_{coils} of the coil package. Figure 8.43 shows the resulting plot of the Young's modulus as a function of the quench number.

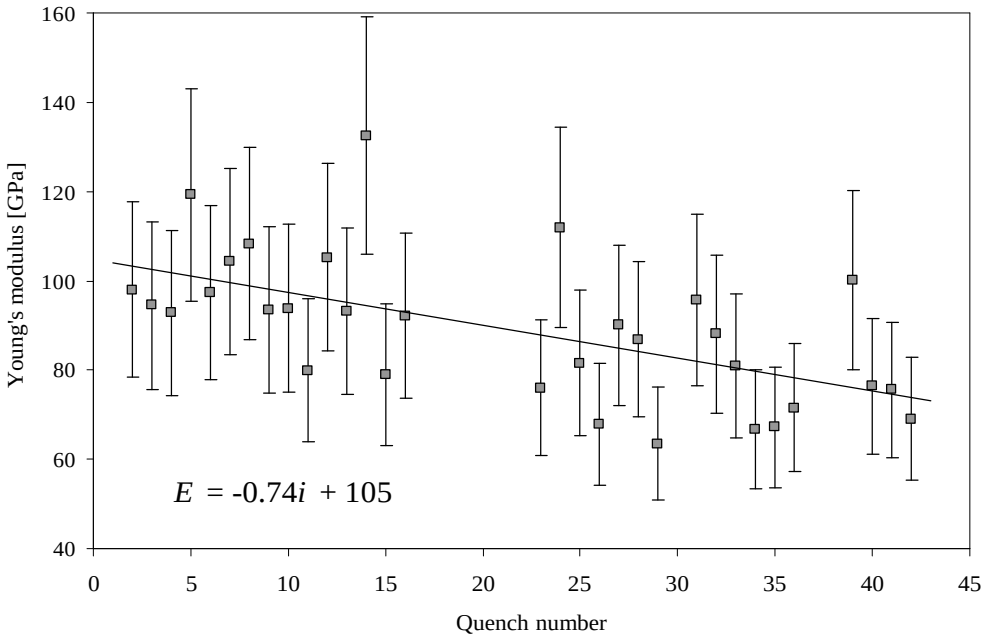

Figure 8.43 Computed Young's modulus of the entire coil assembly as a function of the quench number.

From the figure it is evident that the entire coil package is getting softer with increasing quench number. This is due to plastic deformation of the package, and the gradual increase in the strain with increasing quench number at a larger rate (1.5 % per quench) than the gradual increase in the end load (0.6 % per quench). The Young's modulus decreases with about 0.74 GPa per quench; it starts at 105 GPa at the beginning of the training sequence, and ends at 73 GPa at quench number 43. With a copper (E = 117 GPa) to epoxy (E = 40 GPa) fraction of 95 % in the coil assembly, the expected Young's modulus is 107 GPa, which matches the initial measured number well.

8.14 Warming-up

In this section, the stress on the pole-piece gauges in the final phase of the first training series of the magnet is discussed. Stress measurements during the first part of the warming-up are analyzed, and the implications of the measured high stress on the poles is discussed.

If the magnet is slowly warmed up from 4.4 K to room temperature, while keeping all components of the magnet at the same temperature during the warming-up, the expected magnitude of the stress change is the same as computed for the cooling-down from room temperature to 4.4 K.

Table 8.24 lists the expected stress during warming-up, and the measured maximum values during cooling-down and warming-up for comparison. Figure 8.44 shows the stress measured at the pole-piece gauges in the four layers of the magnet as a function of time.

Pole-piece gauge	Predicted stress at 4.3 K (ANSYS) [MPa]	Predicted stress at 4.3 K [MPa]	Maximum stress during cooling-down [MPa]	Measured stress during warming-up [MPa]
P1	121	103±10	103±10	177±7
P2	80	67±7	104±10	109±6
P3	60	50±5	92±9	79±5
P4	70	45±5	82±8	81±6

Table 8.24 Expected stress during warming-up, and measured maximum values during cooling-down and warming-up.

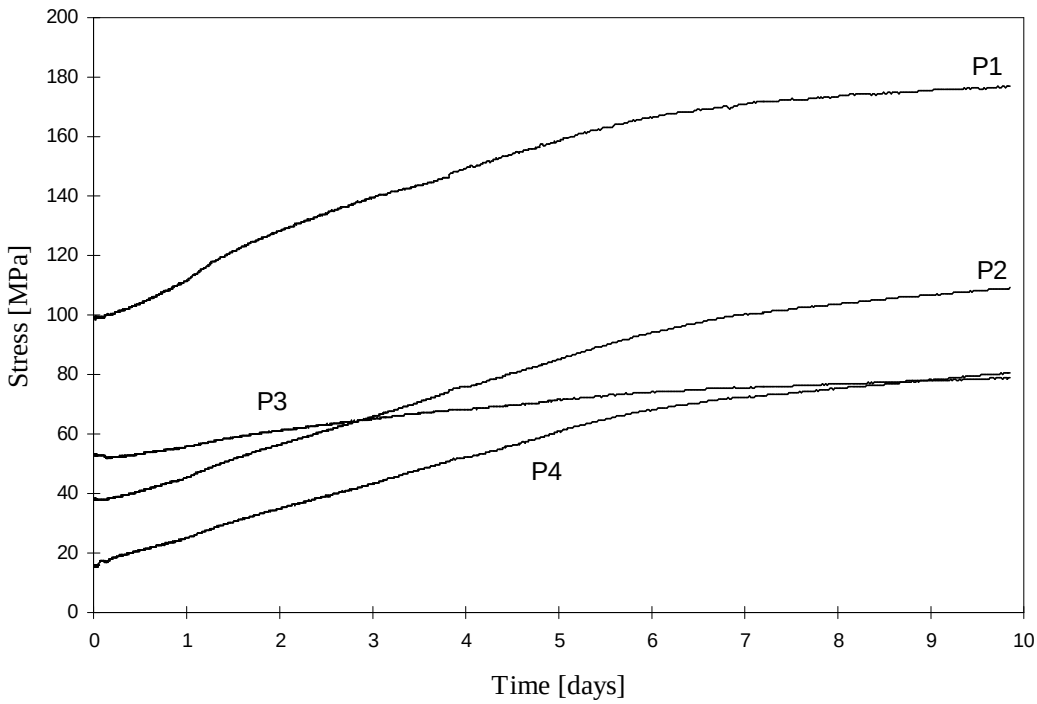

Figure 8.44 Recorded stress on the pole-piece gauges for the four layers of the magnet.

If however the warming-up is performed at a higher rate in certain locations of the magnet, temperature differences can cause larger localized stress to occur during the warming-up. The effect is similar to the measured drop in stress during cooling-down, but reversed in sign.

In the case of the warming-up illustrated in figure 8.44, the maximum stress recorded at the pole layer 1 gauges reached about 180 MPa.

The data-set for the warming-up is incomplete, with the final part of the curves for temperatures above approximately 240 K missing. The data are collected over a ten days period, with varying warming-up rates. Temperature was not recorded during this period; therefore all data are plotted as a function of time (in days) instead of temperature.

The increase in stress to a much greater value than the initial pre-stress is due to the same temperature lag of the iron yoke with respect to the coils, visible during cooling-down. In this case, the iron yoke warms up more slowly than the coils, resulting in a temporary increase in stress during warming-up. The faster the warming-up is performed, the larger the temperature difference between coils and yokes, since the large heat capacity of the yokes prevents them from warming up quickly.

This effect is thus very important for proper treatment of the fragile Nb_3Sn coils. When the magnet is cooled down rapidly, the coils are not harmed by excessive stress, but during rapid warming-up the stress could exceed the threshold where significant permanent damage is done to the cables.

For the cables used in the magnet, this threshold (with permanent critical current degradation exceeding 10 %) is about 175 MPa for the MJR outer cable, and larger than 200 MPa for both the MJR and IT inner cables. The maximum stress on the outer layers never approached the threshold, whereas the inner layer reached about 180 MPa. No permanent damage is expected on the inner layer due to this applied stress; both the MJR and IT inner cable did not show permanent critical current degradation exceeding 1 % up to 200 MPa.

Subsequent testing of the magnet at a later date provided no conclusive evidence of increased cable damage, as the magnet reached 13.5 T at 1.8 K without significant problems. [8.30].

8.15 Conclusions

Conclusions are presented on five separate topics; first the magnet design and performance is summarized, followed by conclusions on the accuracy of the critical current degradation experiments. Finally, the performance of the resistive stress transducers, and the fiber-optic stress and strain sensors is summarized.

Magnet mechanical design

The control of the pre-stress during assembly and cooling-down using an aluminum bar between the yoke plates works in theory. The effect of a reduction in ultimate pre-stress is demonstrated in figure 8.34 with the slope change in the stress as a function of temperature after the gap is closed. The temperature of 145 K at which the gap closed did not match the predicted temperature of 100 K, causing loss of pre-stress on the coils.

The wire winding technique of pre-stress application is proven to be successful in both a mechanical model test and in the magnet. Benefits of the method include the possibility to unwind the wire and repeat the operation several times. This is beneficial for two reasons:

1) the possibility to cycle the coils several times before applying the full pre-stress to pre-compress the coils to their desired stiffness. The effectiveness of this pre-compression is demonstrated in sections 8.10.1 and 8.10.2. The gain in stress per wire wrap (which is linearly proportional to the coil stiffness) increased from 2.5 MPa/wrap to 4 MPa/wrap;
2) the gradual increase in pre-stress using the wire wrapping technique allows for a carefully controlled pre-stress application. In conventional locking collar methods, the pre-stress is determined by the dimensions of collar and coil, and can only be adjusted by mechanical shims.

Magnet performance

The magnet reached a central bore field of 12.8 T at a current of 6303 A at 4.4 K. This corresponds to 12.9 T at 4.2 K (I = 6352 A). At 1.8 K, the maximum central bore field is 13.51 T.

The extrapolated critical field in the fast ramp margin experiment is 13.1±0.2 T. These values correspond well with the predicted critical field of 13 T (I = 6400 A) at 4.2 K. The required current to reach 13 T is 6433 A, or 0.5 % higher than predicted.

The first quench reached 10.19 T; which matches the predicted field of the first quench at 10.3 T well. The location of this quench confirms a possible separation of the coil and the pole-piece interface.

Based on the measured peak stress of 180 MPa during operation and warming-up, and subsequent successful operation of the magnet [8.30], it is concluded that the Nb_3Sn cables are not significantly degraded during the magnet operation and warming-up.

The applied magnet pre-stress is low by 29 %, which corresponds to the reduced number of wire wraps on the structure (18 instead of 25). The reduced pre-stress is the most probable cause. The magnet exhibits significant training to reach 12.8 T, close to the design field of 13 T at 6400 A at 4.3 K. A total number of 34 quenches is needed to reach this point. This behavior is disappointing; even though the design field was

reached eventually, the total number of training quenches needed to reach it makes this magnet unusable for application in an accelerator.

Critical current degradation experiments

The predicted central bore fields are 12.19 T, limited by the outer coils, and 12.49 T, limited by the inner coil of the IT conductor, at 4.4 K. The magnet reached a central bore field of 12.8 T at 4.4 K.

The first limiting point in the coil is the inner top corner of the outer coil (position F in figure 8.10). Since the magnet is not limited at this point, and no quenches are recorded at this location, it is concluded that the results from the critical current measurements for cable TW11 are too low. All cable measurements for the outer cables resulted in large initial I_c degradation, which points to excessive damage during the sample mounting procedure.

The next limiting point is the inner top corner of the inner coil (position E in figure 8.10) for the IT conductor. Again, the prediction of the critical current is low, this time by 2 %. This prediction can be considered correct, since the error margin on the critical current measurements is of the order of 1-2 % for the inner cables. The MJR conductor still has about 8 % margin at this point.

Resistive stress transducers

Stress transducers for the pole-piece of the magnet are designed, tested, and successfully used in the magnet. The transducers were initially designed for 5 % accuracy in stress. The final accuracy is determined to be approximately 10 % in stress for the range of 100-150 MPa, provided the surface of the transducer is in perfect contact with the part applying the stress. Surface mismatches are found to cause up to 40 % error in the stress measurements.

Fiber-optic stress and strain sensors

The use of fiber-optic sensors embedded in the horizontal mid-plane of the magnet is the first published direct measurement of strain in the coil windings. A transverse stress and longitudinal strain measurement matrix is designed and successfully tested at 293 K and 77 K in an experimental setup.

The same matrix, without the transverse stress measurement function, is successfully used in the magnet at 4.4 K and at full operating load. The fiber-optic strain sensors are used, in combination with conventional resistive end-load gauges, to analyze the change in Young's modulus in the longitudinal direction of the coil package during training. The Young's modulus decreases with about 0.74 GPa/quench from 105 GPa to 73 GPa at quench number 43.

On the pole-piece transducers, the fiber-optic sensors are not used to provide any information in addition to the resistive stress sensors. The sensors are solely tested as a demonstration of the viability of the technology.

Based on the good correlation between the resistive gauges and the fiber-optic gauges on the pole-piece stress transducers, it is concluded that the fiber-optic sensors are reliable at low temperature.

Chapter 9

Summary of conclusions and recommendations

The main topic of this thesis is the critical current reduction in cables made with Nb_3Sn superconductor. When this research was started as a follow-up of several recent dissertations at the UT on the sensitivity of Nb_3Sn to stress and strain, and the use of Nb_3Sn in accelerator magnets, the goal was formulated to try to optimize the behavior of the Nb_3Sn material in a cable as best as possible, reducing the sensitivity of the cabled conductor to transverse pressure in such a way that the manufacturing of very high field dipole magnets (B_y larger than 15-16 T) would become feasible. The research was not to be limited to a formulation of the problem, but to produce a viable solution to the critical current degradation problem.

Next, specific conclusions are presented at the end of each chapter. The general conclusions presented here, sorted by chapter, are a summary of the most important conclusions, intended to point to possible promising future research directions. The sections on the critical current degradation in chapters 3 to 6 are followed by recommendations to reduce the I_c degradation.

Finally, a summary of the conclusions of chapters 7 and 8 is presented. In addition, several recommendations for alternate optimization methods and alternate methods of dipole magnet design, specifically designed to reduce the compressive stress on the superconductor, are discussed.

9.1 Critical current versus transverse stress relation

A linear elastic displacement model can estimate the effective Young's modulus of a cable dominated by the strand material (dry or impregnated with a low strength epoxy). For a typical strand with E = 117 GPa, the effective Young's modulus E_{eff} can be as low as 20 GPa initially, then increase to about 26-30 GPa at 150 MPa applied transverse pressure.
This means that in magnet assembly, a pre-compression step of the coils might be needed to assure sufficient pre-stress.

A matrix material with a higher Young's modulus (stiffer) is preferred over a softer material (copper) with a lower yield point to reduce the total strain on the filaments. The effective Young's modulus of the cable is also increased. A cable with an epoxy with higher Young's modulus will degrade less under applied pressure.
A stiffer material results in higher stress, but less deformation, which is preferred to limit the amount of permanent damage to the Nb_3Sn at high loads.

The local stress on the top layer of strands in the critical current degradation experiments, described in chapter 5, can be as much as 34 % higher than the average applied pressure.
This means that the critical current measurements are not necessarily representative of the actual load condition of a cable in a magnet. The critical current measurements might have a locally higher load than the overall load condition, however, a non-uniform load condition can also exist in a magnet.

The reversible and permanent critical current degradation can be predicted with a model based on independent relations for the plastic deformation and elastic stress. The permanent degradation is determined by the amount of plastic deformation of the strands in the cable.
Separation of the two variables allows for the use of FEA models to eliminate the influence of the cable geometry and experimental procedure on the critical current degradation model (3.32). Selection of an appropriate FEA model is based on the quality of the impregnation of the cable.

9.2 Influence of the internal structure of the wire on the $I_c(P)$ relation

In an MJR wire, the average stress within the filament bundles can be up to 13-15 % higher than the applied stress. In an IT wire, the average stress can be up to 12 % higher. The stress in the concentration regions is higher with increasing Young's modulus of the Nb_3Sn. Within the filament bundles, without voids, the stress concentrations can be up to 140 % for the MJR wire, 190 % for the IT wire, and no stress enhancement in the PIT wire (the internal stress in the Nb_3Sn does not exceed the applied stress).
Ranking the three conductor types with respect to increased sensitivity to applied transverse pressure due to stress concentrations, the sequence from most sensitive to least sensitive is IT, MJR and PIT.

The peak stress on the filament bundles closest to the center of the wire is an additional 10 % higher (compared to the stress concentration already present) than the stress on the outer filament bundles. With voids present in the filament bundles, the stress concentrations can be up to 480 % for the MJR wire, 430 % for the IT wire, and 210 % for the PIT wire. The location of the stress concentrations in the filament bundles coincide with the location where most of the structural damage is found in the SEM pictures of the wire cross-section.
The combination of these two conclusions leads to a recommendation to avoid formation of voids in the area of the filament bundles closest to the center of the wire, since this would result in additional stress concentrations.

The preferred location of the voids, if they cannot be avoided, is either in the center of the filament bundle, or entirely on the outside of the filament area. A large void in the center of the filament bundle is the best case, since the local threefold stress concentration falls of rapidly with increasing radius, and thus does not affect the filament area too much. *This void location would be preferable for the IT conductor.*

The second best case would have the voids formed in the outer copper region outside the filament area, close to the niobium or niobium-tantalum diffusion barrier. This is not possible for the Internal Tin method, since the individual elements do not have a diffusion barrier around them. *For the MJR conductor however, this would be a possible remedy against excessive reversible and irreversible I_c degradation.*

In both the IT and MJR conductors, these void locations can be optimized by variation of the initial tin content of the filament bundle.

9.3 I_c degradation in Nb_3Sn Rutherford cables

Both the MJR and IT conductors behave similarly under applied pressure with respect to reversible critical current degradation. Statistically, the PIT conductor should also behave similarly, but when the sensitivity is compared (see table 5.23), the PIT conductor is less sensitive with respect to reversible I_c degradation.

In chapter 4, stress enhancement factors (without voids) of 1.4-1.9 (MJR and IT) were found, compared to no enhancement for PIT. The combined enhancement of C1 and C2 (-C1+C2) is found to be 1.4-1.5 for MJR and IT, versus 1.2 for PIT.

Ranking the three conductor types for minimal total critical current degradation, the PIT conductor shows a slightly lower sensitivity, primarily due to the lower initial critical current degradation (by about 10%), with IT showing similar behavior without voids, and MJR the most sensitive. This conclusion is only valid provided the measurements are statistically sound, and sufficient data are available.

Due to the limited amount of samples, and the possible influence of several "bad" samples on the resulting relations, these final conclusions are difficult to defend. Nevertheless, the data are presented here in full, since this is the first time a systematic comparison of such a large data-set is performed. Also, trends are sufficiently visible in the data to at least make a qualitative argument about the stated differences in sensitivity.

The indication that wire structures like the PIT conductor degrade less with applied pressure than the MJR or IT conductors confirms the importance of the optimization of the internal structure of the wire.

9.4 Permanent filament damage on a microscopic scale

The results from the microscopic studies point to the void formation as an important cause of permanent critical current degradation in MJR and IT wires. The location of the damaged filaments corresponds to the enhanced stress concentrations found in the FE analyses of wires with voids in chapter 4.

These two facts combined suggest that by controlling the location of the void formation, or by total elimination, the stress sensitivity of the Nb_3Sn strands might be significantly reduced.

The formation of shear planes is found in the MJR conductor, that have the potential of causing extensive structural damage under compressive load.

This means that the deformation of the strands during the cabling operation has to be limited to avoid this type of structural damage. This will restrict the maximum keystone angle of the cable.

In some samples strain cracks were found that seem to be caused by excessive longitudinal strain in the sample. This can only be caused by a mismatch of thermal contraction coefficients between the sample and the sample holder, or in case of a magnet between coil and pole-piece.

From the pictures is it clear that great care has to be taken to assure a good match between the different materials in the magnet, especially if the relatively short 1 m model magnets are to be scaled up to full length dipole magnets.

9.5 Fiber-optic stress and strain measurement at low temperature

With the increased loads inherent to high field accelerator dipole magnets, and the high sensitivity of the Nb_3Sn superconductor to damage due to excessive stress and strain, the accurate determination of the stress and strain states of the coils in the magnet becomes an important issue. Up until recently, no accurate sensors existed that can measure the stress, stress gradients and strain within the coils.

The Fabry-Perot fiber-optic sensor is a good candidate for stress and strain measurements within the impregnated coils of accelerator dipole magnets. The small size and insensitivity to the changes in the magnetic field make this sensor the best candidate for use in this environment, compared to other interferometric or polarization based techniques.

9.6 Stress and strain measurements in the accelerator dipole model magnet

The wire winding technique of pre-stress application is proven to be successful in both a mechanical model test and in the magnet. Benefits of the method include the possibility to unwind the wire and repeat the operation several times in a research and development phase of a project.

The wire winding technique is useful in applying pre-compression to the coils to eliminate the reduction in pre-stress due to the initially lower Young's modulus of the cables.

The magnet reached a central bore field of 12.8 T at a current of 6300 A at 4.4 K. This corresponds to 12.9 T at 4.2 K (I = 6350 A). At 1.8 K, the maximum central bore field is 13.5 T. The predicted central bore fields are 12.2 T, limited by the outer coils, and 12.5 T, limited by the inner coil of the IT conductor, at 4.4 K. Based on the measured peak stress of 180 MPa during operation and warm-up, and subsequent successful operation of the magnet, it is concluded that the Nb_3Sn cables are not significantly degraded during the magnet operation and warm-up.

The fact that the magnet reached a maximum field that exceeds the prediction from the critical current degradation experiments suggests that the cable-under-pressure tests yield a too pessimistic value of the critical current.

The applied magnet pre-stress is low by 29 %, which corresponds to the reduced number of wire-wraps on the structure (18 instead of 25). Due to the reduced pre-stress, the magnet exhibits significant training to reach 12.8 T, close to the design field of 13 T at 6400 A at 4.4 K. A total number of 34 quenches is needed to reach this point.

This behavior is disappointing; even though the design field was reached eventually, the total number of training quenches needed to reach it makes this magnet unusable for application in an accelerator.

The use of fiber optic sensors embedded in the horizontal mid-plane of the magnet is the first published direct measurement of local strain in the coil windings. A transverse stress and longitudinal strain measurement matrix is designed and successfully tested at 293 K and 77 K in an experimental setup. The same matrix, without the transverse stress measurement function, is successfully used in the magnet at 4.4 K and at full operating load.

Based on the good correlation between the resistive gauges and the fiber optic gauges on the pole-piece stress transducers, it is concluded that the fiber optic sensors are reliable at low temperature.

9.7 Recommendations for an alternate optimization method

The widely applied conductor design used for accelerator dipole magnets based on the cosine-q layout places a restriction on the magnet design. In general, all optimization codes used by the magnet designers to produce these layouts are programmed to find the optimum solution by minimizing the harmonic field distortions and simultaneously maximizing the dipole field, using an optimization function $I_c = I_c(B)$, only based on the critical current density as a function of the local magnetic field. This produces a highly compact and optimized design, which by default will be small in volume. The compact design results in large stresses in the conductor when the high currents are combined with the small conductor area.

This design philosophy is applicable to NbTi magnets, but creates problems when used in the design of Nb_3Sn dipoles. Due to the critical current degradation of the Nb_3Sn cables at high stress, the stress has to be taken into account in the optimization function. Using a function $I_c = I_c(B, s)$ will provide a more realistic solution (and possibly a higher field), but at the cost of a significant increase in optimization effort.

9.8 Alternative low stress magnet designs: block versus cosine-q

With all the inherent problems related to the use of the cosine-q layout, a study of the use of alternative magnet designs for high field dipoles (B_y in excess of 13 T) is warranted. The methods of magnet design carried over from the NbTi era can not be directly applied to the design of high field Nb_3Sn dipoles. Since the stress sensitivity plays a crucial role in the success or failure of a Nb_3Sn magnet, great care has to be taken in the minimization of stress concentrations and mismatches in material properties in the magnet assembly. Also, increasing the field above 13 T greatly limits the use of conventional design techniques and optimization routines to find the optimum coil cross-section.

With the forces increasing with the square of the field, the optimized cosine-q layout quickly reaches the maximum practical stress of the Nb_3Sn superconductor. Especially when wedges and spacers are used to shape the field harmonics, these spacers will create local stress concentrations in the coil cross-section. Also, angle mismatches in the cables can cause stress gradients in the mid-plane, as was evident in the stress measurements on the model magnet experiment. A block design reduces these stress concentrations and gradients.

From the standpoint of cable optimization to reduce the I_c degradation, a constant optimal compaction factor across the entire cable is preferred over a key-stoned cable. The block design magnets are naturally more suited for rectangular cable as compared to the cosine-q layout.

References

Chapter 1 Introduction

[1.1] Supercolliders and superdetectors, Proceedings of the 19th and 25th workshops of the INFN Eloisatron project, Eds. W. Barletta and H. Leutz, Erice, Italy, World Scientific, New Jersey, 1993.

[1.2] R. M. Scanlan, W.A. Barletta, D. Dell'Orco, A. McInturff and others, "Superconducting magnet technology for future hadron colliders", Proceedings of the Joint US-CERN-Japan International School: Frontiers of Accelerator Technology, Maui, HI, USA, 3-9 Nov. 1994). Edited by: S.I. Kurokawa, M. Month, and S. Turner, Singapore, World Scientific, 1996. p. 359-78.

[1.3] J.W. Ekin, "Mechanical properties and strain effects", Superconductor Materials Science: metallurgy, fabrication and application, S. Foner and B.B. Schwartz, eds., Plenum Press, New York, (1981), pp.455-505.

Chapter 2 The origin of stress and strain in superconducting accelerator dipole magnets

[2.1] D. ter Avest, "Properties of the superconductor in accelerator dipole magnets", Ph.D. Thesis, University of Twente, Universiteits Drukkerij, Enschede, The Netherlands, 1991.

[2.2] D. Dell'Orco, S. Caspi, J. O'Neill, A. Lietzke and others, "A 50 mm bore superconducting dipole with a unique iron yoke structure", (1992 Applied Superconductivity Conference, Chicago, IL, USA, 23-28 Aug. 1992), *IEEE Transactions on Applied Superconductivity*, vol.3, (no.1, pt.2), March 1993, p.637-41.

[2.3] D. Leroy, J. Krzywinski, L. Oberli, R. Perin, F. Rodriguez-Mateos, A. Verweij and L. Walckiers, "Test results on 10 T LHC superconducting one metre long dipole models", (1992 Applied Superconductivity Conference, Chicago, IL, USA, 23-28 Aug. 1992), *IEEE Transactions on Applied Superconductivity*, vol.3, (no.1, pt.2), March 1993, p. 614-21.

[2.4] S. Caspi, K. Chow, D. Dell'Orco, R. Hannaford, H. Higley, A. Lietzke, A. McInturff, M. Morrison, L. Morrison, R. Scanlan and J. van Oort, "Design and construction of a hybrid – Nb_3Sn, NbTi – dipole magnet", *IEEE Transactions on Applied Superconductivity*, V7 (N2-Pt.1) , June 1997, p. 547-50.

[2.5] A. den Ouden, S. Wessel, E. Krooshoop, R. Dubbeldam and H.H.J. ten Kate, "An experimental 11.5 T Nb_3Sn LHC type of dipole magnet," *IEEE Transactions on Magnetics*, vol. 30, no. 4, July 1994.

[2.6] D. Dell'Orco, R.M. Scanlan and C.E. Taylor, "Design of the Nb_3Sn dipole D20," *IEEE Transactions on Applied Superconductivity*, vol. 3, March 1993, pp. 82-86.

[2.7] Craig Peters, "Construction and assembly of a four layer Nb_3Sn dipole magnet", SC-MAG Note 17, July 25, 1984, E.O. Lawrence Berkeley National Laboratory.

[2.8] J.M. van Oort and R.M. Scanlan, "Design of a 16 T Nb_3Sn twin bore accelerator dipole with a window-frame conductor layout", (1994 Applied Superconductivity Conference, Boston, MA, USA, 16-21 Oct. 1994*), IEEE Transactions on Applied Superconductivity*, vol.5, (no.2, pt.1), June 1995, p. 1008-11.

[2.9] K.Watanabe, S. Awaji, J. Sakuraba, K. Jikihara, and others, "Cryogen-free split-pair superconducting magnet with a phi 50 mm*10 mm room temperature gap", Advances in Cryogenic Engineering (Vol.41*). Proceedings of the 1995 Cryogenic Engineering Conference*

ICMC/CEC 1995, Columbus, OH, USA, 17-21 July 1995), Ed. P. Kittel, New York, NY, USA: Plenum Press, vol.1, 1996, p. 319-24.

[2.10] P.D. Vobly, S.F. Mikhailov, and L.G. Morgunov, "The choice of the superconducting magnet for the SuperLEAR magnetic system", *Proceedings of the SuperLEAR Workshop*, Zurich, Switzerland, 9-12 Oct. 1991). Ed. C. Amsler, D. Urner. Bristol, UK: IOP, 1992. p. 35-41.

[2.11] E. Badea, P.M. McIntyre and S. Pissanetzky, "The Pipe Magnet - Compact 13 Tesla Dual Dipole for Future Hadron Colliders," presented at the Annual High Field Accelerator Magnet Workshop, Lawrence Berkeley Laboratory, March 9-11, 1993; P.M. McIntyre, W. Shen and R.M. Scanlan, "Ultra-high-field magnets for future hadron colliders", (1994 Applied Superconductivity Conference, Boston, MA, USA, 16-21 Oct. 1994), *IEEE Transactions on Applied Superconductivity*, vol.5, (no.2, pt.1), June 1995, p. 1099-102.

[2.12] J.M. van Oort, "Integral thermal expansion coefficient from 77 K to 293 K for a block of CTD-101 epoxy", LBNL internal laboratory note.

[2.13] J.M. van Oort, "Experimental determination of the cookie section integrated thermal contraction in the longitudinal direction from 293 K to 77 K", SC-MAG 567, E.O. Lawrence Berkeley National Laboratory.

[2.14] D.B. Chelton and D.B. Mann, "Cryogenic data book", NBS Cryogenic Engineering Laboratory, Boulder CO, May 15, 1956 (or UCRL-3421).

[2.15] D. Dell'Orco, "D20 mechanical analysis notes", private communication, LBNL, and also [2.6].

Chapter 3 Critical current versus transverse strain relation

[3.1] D.O. Welch, "Alteration of the superconducting properties of A15 compounds and elementary composite superconductors by non-hydrostatic elastic strain", *Advances in Cryogenic Engineering*, 26, 1980, p. 48.

[3.2] B. ten Haken, A. Godeke, and H.H.J. ten Kate, "Investigation of microscopic strain by X-ray diffraction in Nb_3Sn tape conductors subjected to compressive and tensile strains", *Advances in Cryogenic Engineering*. Materials (Vol.42), Columbus, OH, USA, 17-21 July 1995). Ed. L.T. Summers, New York, NY, USA: Plenum Press, 1997, p. 1463-70 vol.2.

[3.3] B. ten Haken and H.H.J. ten Kate, "The degradation of the critical current density in a Nb_3Sn tape conductor due to parallel and transversal strain. (Third International Toki Conference on Plasma Physics and Controlled Nuclear Fusion: Applied Superconductivity for Nuclear Fusion Research, Toki, Japan, 3-5 Dec. 1991), *Fusion Engineering and Design*, vol.20, Jan. 1993, p. 265-70.

[3.4] W. Specking, W. Goldacker and R. Flükiger, "Effect of transverse compression on I_c of Nb_3Sn multi-filamentary wire", *Advances in Cryogenic Engineering*, 34, 1987, p. 569.

[3.5] H. Boschman, "On the resistive transition of composite superconductors", Ph.D. Thesis, University of Twente, Universiteits Drukkerij, Enschede, The Netherlands, 1991.

[3.6] S.L. Bray and J.W. Ekin, "Critical current degradation in Nb_3Sn composite wires due to locally concentrated transverse stress", *Advances in Cryogenic Engineering*, 38, 1992, p. 579.

[3.7] J.W. Ekin, "Strain dependence of the critical current and critical field in multi-filamentary Nb_3Sn composites. (1978 Applied Superconductivity Conference, Pittsburgh, PA, USA, 25-28 Sept. 1978), *IEEE Transactions on Magnetics*, vol.MAG-15, Jan. 1979, (no.1), p. 197-200.

[3.8] B. ten Haken, T.N. Zaitseva, and H.H.J. ten Kate, "Modeling of strain in multi-filamentary wires deformed by thermal contraction and transverse forces. (Fifteenth International Cryogenic Engineering Conference, Genova, Italy, 7-10 June 1994), *Cryogenics*, vol.34, 1994, suppl.issue, p. 513-16.

[3.9] L.T. Summers, M.W. Guinan, J.R. Miller and P.A. Hahn, "A model for the prediction of Nb_3Sn critical current as a function of field, temperature, strain, and radiation damage. (1990 Applied Superconductivity Conference, Snowmass, CO, USA, 24-28 Sept. 1990), *IEEE Transactions on Magnetics*, vol.27, March 1991, (no.2, pt.3), p. 2041-4.

[3.10] ANSYS ® Theory Manual, Swanson Analysis Systems, 1995, http://www.ansys.com.

[3.11] B. ten Haken, "Strain effects on the critical properties of high-field superconductors", Ph.D. Thesis, University of Twente, Universiteits Drukkerij, Enschede, The Netherlands, 1994, Chapter 5.

[3.12] D.B. Chelton and D.B. Mann, "Cryogenic data book", NBS Cryogenic Engineering Laboratory, Boulder CO, May 15, 1956 (or UCRL-3421).

[3.13] C. Kittel, "Introduction to solid state physics", 6th ed. New York, Wiley, c1986.

[3.14] W.A. Fietz and W.W. Webb**, "**Hysteresis in superconducting alloys-temperature and field dependence of dislocation pinning in niobium alloys", *Physical Review*, vol.178, (no.2), Feb. 1969. p.657-67.

[3.15] J.W. Ekin, "Mechanical properties and strain effects", Superconductor Materials Science: metallurgy, fabrication and application, S. Foner and B.B. Schwartz, eds., Plenum Press, New York, (1981), p.455-505.

[3.16] B. ten Haken, "Strain effects on the critical properties of high-field superconductors", Ph.D. Thesis, University of Twente, Universiteits Drukkerij, Enschede, The Netherlands, 1994.

[3.17] S.L. Bray, J.W. Ekin, T. Kuroda, "Critical-current degradation in multi-filamentary Nb_3Al wires from transverse compressive and axial tensile stress", (1992 Applied Superconductivity Conference, Chicago, IL, USA, 23-28 Aug. 1992), *IEEE Transactions on Applied Superconductivity*, vol.3, March 1993, (no.1, pt.3), p. 1338-41.

[3.18] Teledyne Way Chang Albany, advertising brochure of the Nb_3Sn multi-filamentary wires, and J.C. McKinnell, D.B. Smathers, M.B. Siddall and P.M. O'Larey, "Improved superconducting critical current density in modified jelly roll Nb_3Sn by the application of niobium (Nb) diffusion barriers", (1994 Applied Superconductivity Conference, Boston, MA, USA, 16-21 Oct. 1994), *IEEE Transactions on Applied Superconductivity*, vol. 5, June 1995, (no.2, pt.2), p. 1768-72.

[3.19] E. Gregory, E. Gulko, T. Pyon and L.F. Goodrich, "Properties of internal-tin Nb_3Sn strand for the International Thermonuclear Experimental Reactor*"*, *Advances in Cryogenic Engineering*, Materials (Vol.42), Columbus, OH, USA, 17-21 July 1995). Ed. L.T. Summers, New York, NY, USA: Plenum Press, vol.2, 1997, p. 1319-28.

[3.20] J.W. Ekin and A.F. Clark, "Effect of strain on critical current of Nb_3Sn and NbTi multi-filamentary composite wires", (Magnetism and Magnetic Materials - 1976 1st Joint MMM-INTERMAG Conference, Pittsburgh, PA, USA, 15-17 June 1976), *AIP Conference Proceedings*, (no.34), 1976, p. 81-3.

[3.21] B. ten Haken, A. Godeke, H.H.J. ten Kate, and W. Specking, "The critical current of Nb_3Sn wires for ITER as a function of the axial tension and compression", (Proceedings 14th International Conference on Magnet Technology, Tampere, Finland, 11-16 June 1995), *IEEE Transactions on Magnetics*, vol.32, July 1996, (no.4, pt.1), p. 2739-42.

[3.22] J.W. Ekin, "Strain scaling law for flux pinning in practical superconductors. Part 1: Basic relationship and application to Nb_3Sn conductors", *Cryogenics*, 20, 1980, p.611.

[3.23] J.W. Ekin and S.L. Bray, "High compressive axial strain effect on the critical current and field of Nb_3Sn superconductor wire", *Advances in Cryogenic Engineering*, Materials (Vol.42), Columbus, OH, USA, 17-21 July 1995). Ed. L.T. Summers, New York, NY, USA: Plenum Press, vol.2, 1997. p. 1407-14.

[3.24] R. Flukiger, R. Isernhagen, W. Goldacker, W. Specking, "Long-range atomic order, crystallographical changes and strain sensitivity of j_c in wires based on Nb_3Sn and other A15 type compounds", *Advances in Cryogenic Engineering Materials*, Vol.30, Proceedings of the Fifth International Cryogenic Materials Conference, Colorado Springs, CO, USA, 15-17 Aug. 1983), Ed. Clark, A.F.; Reed, R.P. New York, NY, USA: Plenum, 1984. p. 851-8.

[3.25] C. King, C.; M. Benz, M, D. Grey, D, A. Mantone and others, "Strain studies on superconducting Nb_3Sn tape using differential thermal contraction and other methods", *Advances in Cryogenic Engineering*, Materials (Vol.42), Columbus, OH, USA, 17-21 July 1995). Ed L.T. Summers, New York, NY, USA: Plenum Press, vol.2, 1997. p. 1455-62.

[3.26] M. Poirier et al., "Elastic behaviour of polycrystaline Nb_3Sn at low temperatures", *Applied Physics Letters*, 47, 1985, p.92.

[3.27] B. ten Haken, A. Godeke, H.H.J. ten Kate, "The influence of compressive and tensile axial strain on the critical properties of Nb_3Sn conductors", (1994 Applied Superconductivity Conference, Boston, MA, USA, 16-21 Oct. 1994), *IEEE Transactions on Applied Superconductivity*, June 1995, vol.5, (no.2, pt.2), p. 1909-12.

[3.28] K. Katagiri, T. Kuroda, H. Wada, H.S. Shin and others, "Tensile strain/transverse compressive stress effects in bronze processed Nb-matrix Nb_3Sn wires", (1994 Applied Superconductivity Conference, Boston, MA, USA, 16-21 Oct. 1994*), IEEE Transactions on Applied Superconductivity*, June 1995, vol.5, (no.2, pt.2), p. 1900-4.

[3.29] K. Katagiri, K. Watanabe, H.S. Shin, Y. Shoji and others, "Tensile strain/transverse compressive stress effects in Nb_3Sn multi-filamentary wires with CuNB reinforcing stabilizer", *Advances in Cryogenic Engineering*. Materials (Vol.42), Columbus, OH, USA, 17-21 July 1995). Ed. L.T. Summers, New York, NY, USA: Plenum Press, vol.2, 1997, p. 1423-32.

[3.30] R. Flukiger, W. Schauer, W. Specking, B. Schmidt and others, "Low temperature phase transformation in Nb_3Sn multi-filamentary wires and the strain dependence of their critical current density. (Seventh International Conference on Magnet Technology MT-7 1981, Karlsruhe, West Germany, 30 March-3 April 1981), *IEEE Transactions on Magnetics*, vol. MAG-17, (no.5), Sept. 1981, p. 2285-8.

[3.31] C.W. Chu and L.J. Vieland, "The superconducting transition temperature and its high pressure behavior of tetragonal Nb_3Sn", *Journal of Low Temperature Physics*, 17, 1974, p.25.

[3.32] R.J. Wijngaarden and R. Griessen, "Superconducting materials under pressure", 1992, p. 583 out of J. Evetts, "Concise encyclopedia of magnetic & superconducting materials", Pergamon Press, Oxford, UK, 1992.

[3.33] B. ten Haken, "Strain effects on the critical properties of high-field superconductors", Ph.D. Thesis, University of Twente, Universiteits Drukkerij, Enschede, The Netherlands, 1994, p. 99.

[3.34] M.S. Lubell, "Empirical scaling formulas for critical current and critical field for commercial NbTi", *IEEE Transactions on Magnetics*, MAG-19, 1983, p. 754-757.

[3.35] N. Cheggour and D.P. Hampshire, "Unifying the strain and temperature scaling laws for the pinning force density in superconducting niobium-tin multifilamentary wires", *Journal of Applied Physics*, Vol. 86, No. 1, July 1999, p. 552-5.

[3.36] B. ten Haken, A. Godeke and H.H.J. ten Kate, "The strain dependence of the critical properties of Nb_3Sn conductors", *Journal of Applied Physics*, Vol. 85, No. 6, March 1999, p. 3247-53.

[3.37] ANSYS 5.4 theory manual , chapter 19, paragraph 7.1, error approximation technique for displacement based problems.

[3.38] Roark's formulas for stress and strain, W.C. Young, 6^{th} Ed., McGraw-Hill, Inc. New York, 1989, p.651.

[3.39] H. Boschman, A.P. Verweij, S. Wessel, H.H.J. ten Kate and L.J.M. van de Klundert, "The effect of transverse loads up to 300 MPa on the critical currents in Nb_3Sn cables", *IEEE Transactions on Magnetics*, V27 (N2), March 1991, p. 1831-34.

[3.40] S. Ochiai, S. Nishino, M. Hojo and K. Watanabe, "Relation of the strength distribution of Nb_3Sn to the critical current of a pre-stressed multi-filamentary composite super-conductor", *Superconductor Science & Technology*, vol.8, (no.12), Dec. 1995, p. 863-9.

[3.41] S. Hong and D. Dell'Orco, LBNL internal laboratory notes.

[3.42] A. den Ouden, private communication.

[3.43] Mark's Standard Handbook for Mechanical Engineers, E.A. Avallone and T. Baumeister III, Eds., 9^{th} Edition, McGraw-Hill, NY, 1987.

[3.44] B. ten Haken, "Strain effects on the critical properties of high-field superconductors", Ph.D. Thesis, University of Twente, Universiteits Drukkerij, Enschede, The Netherlands, 1994, p. 102.

Chapter 4 Influence of the internal structure of the wire on the $I_c(P)$ relation

[4.1] Physical Metallurgy, 4th Ed., R.W. Cahn and P. Haasen, Eds., North-Holland, Amsterdam, 1996, p. 608.

[4.2] Picture of bronze Airco conductor, from "Filamentary A15 Superconductors", Ed. M. Suenaga and A.F. Clark, Plenum, NY, pg.56, reproduced with permission.

[4.3] Teledyne Way Chang Albany, "Modified Jelly Roll (Nb_3Sn) wire", TWCA, Albany, OR, October, 1994 and J.C. McKinnell, D.B. Smathers, M.B. Siddall and P.M. O'Larey, "Improved superconducting critical current density in modified jelly roll Nb_3Sn by the application of niobium (Nb) diffusion barriers", (1994 Applied Superconductivity Conference, Boston, MA, USA, 16-21 Oct. 1994), *IEEE Transactions on Applied Superconductivity*, vol. 5, June 1995, (no.2, pt.2), p. 1768-72.

[4.4] Teledyne Way Chang Albany, "Modified Jelly Roll Update" , TWCA, Albany, OR, USA, November 1992.

[4.5] E. Gregory, "Conventional wire and cable technology", (Superconductors), AIP Conference Proceedings, AIP Conf. Proc., USA, no.249, pt.2, 1992, p.1198-299.

[4.6] H.H.J. ten Kate, private communication.

[4.7] H.H.J. ten Kate, "Critical Currents in Powder in Tube Nb_3Sn wires", Report UT-SMI 94-1, Applied Superconductivity Centre, University of Twente, Enschede, The Netherlands, September 1994.

[4.8] A. den Ouden, private communication.

[4.9] A. den Ouden, S. Wessel, E. Krooshoop, R. Dubbeldam and H.H.J. ten Kate, "An experimental 11.5 T Nb_3Sn LHC type of dipole magnet," *IEEE Transactions on Magnetics*, vol. 30, no. 4, July 1994.

[4.10] A. den Ouden, S. Wessel, E. Krooshoop, R. Dubbeldam and H.H.J. ten Kate, "An experimental 11.5 T Nb_3Sn LHC type of dipole magnet," *IEEE Transactions on Magnetics*, vol. 30, no. 4, July 1994.

[4.11] H.H.J. ten Kate, private communication, and Europa Metalli, spa., "Internal Tin Nb_3Sn Superconducting Wire", EM Superconductors Division, Florence, Italy.

[4.12] Johannes M. van Oort, "Critical current degradation in Nb_3Sn cables for D20", LBNL internal laboratory notes, LBNL, Berkeley, CA, USA, 1994.

[4.13] B. ten Haken, "Strain effects on the critical properties of high-field superconductors", Ph.D. Thesis, University of Twente, Universiteits Drukkerij, Enschede, The Netherlands, 1994, p. 62.

[4.14] M. Poirier et al., "Elastic constants of polycrystaline Nb_3Sn between 4.2 and 300 K", Journal of Applied Physics, Vol. 55, 1984, p. 3327.

[4.15] J.F. Bussiere, H. LeHuy and B. Faucher, "Elastic behavior of polycrystaline Nb_3Sn, V_3Ga and Nb_3Ge", Advances in Cryogenic Engineering, Vol. 30, 1983, p. 859.

[4.16] Roark's formulas for stress and strain, W.C. Young, 6th Ed., McGraw-Hill, Inc. New York, 1989, p.732.

Chapter 5 Critical current degradation in cabled Nb_3Sn superconductors in accelerator magnets

[5.1] D.R. Dietderich, R.M. Scanlan, R.P. Walsh and J.R. Miller, "Critical current of superconducting Rutherford cable in high magnetic fields with transverse pressure", *IEEE Transactions on Applied Superconductivity*, vol.9, no.2, pt.1, (1998 Applied Superconductivity Conference, Palm Desert, CA, USA, 13-18 Sept. 1998.), June 1999, p. 122-5.

[5.2] J.M. van Oort, R.M. Scanlan, H.W. Weijers, S. Wessel and others, "The reduction of the critical current in Nb_3Sn cables under transverse loads", *IEEE Transactions on Applied Superconductivity*, March 1993, vol.3, no.1, pt.2, p. 559-62.

[5.3] H.H.J. ten Kate, H.W. Weijers and J.M. van Oort, "Critical current degradation in Nb_3Sn cables under transverse pressure", *IEEE Transactions on Applied Superconductivity*, March 1993, vol.3, no.1, pt.3, p. 1334-7.

[5.4] H. Boschman, P.P.E. Fornerod and L.J.M. van de Klundert, "The influence of transverse, compressive stress on the critical current of multifilamentary Nb_3Sn and NbTi wires", *IEEE Transactions on Magnetics*, vol.25, (no.2), 1988 Applied Superconductivity Conference, San Francisco, CA, USA, 21-25 Aug. 1988, March 1989, p. 1976-9.

[5.5] H. Boschman, A.P. Verweij, S. Wessel, H.H.J. ten Kate and L.J.M. van de Klundert, "The effect of transverse loads up to 300 MPa on the critical current of Nb_3Sn cables", *IEEE Transactions on Magnetics*, V27 (N2), March 1991, p. 1831-34.

[5.6] H. Boschman, A.P. Verweij, S. Wessel, H.H.J. ten Kate and others, "The effect of transverse loads up to 300 MPa on the critical currents of Nb_3Sn cables (for LHC). (1990 Applied Superconductivity Conference, Snowmass, CO, USA, 24-28 Sept. 1990), *IEEE Transactions on Magnetics*, March 1991, vol.27, no.2, pt.3, p. 1831-4.

[5.7] A. den Ouden, private communication.

[5.8] A. den Ouden, private communication.

[5.9] H. Boschman, "On the resistive transition of composite superconductors", Ph.D. thesis, University of Twente, Universiteits Drukkerij, Enschede, The Netherlands, 1990.

[5.10] H. Boschman, "On the resistive transition of composite superconductors", Ph.D. Thesis, University of Twente, Universiteits Drukkerij, Enschede, The Netherlands, 1991, chapter 6.

[5.11] H.H.J. ten Kate, W. Nederpelt, P. Juffermans, F. van Overbeeke and L.J.M. van de Klundert, "A new type of superconducting direct current meter for 25 kA", Advances in Cryogenic Engineering, Vol. 31, 1986, p. 1309-1312.

[5.12] C. Lipson and N.J. Sheth, "Statistical design and analysis of engineering experiments", McGraw-Hill, New York, 1973, p.374.

[5.13] R. Walpole, R. Myers, S. Myers, "Probability and statistics for engineers and scientists, 6th Ed.", Prentice Hall, Upper Saddle River, NJ, 1998.

[5.14] B. ten Haken, "Strain effects on the critical properties of high-field superconductors", Ph.D. Thesis, University of Twente, Universiteits Drukkerij, Enschede, The Netherlands, 1994, p. 64.

[5.15] B. ten Haken, "Strain effects on the critical properties of high-field superconductors", Ph.D. Thesis, University of Twente, Universiteits Drukkerij, Enschede, The Netherlands, 1994, p. 99.

Chapter 6 Permanent filament damage on a microscopic scale

[6.1] S.A. Keys, N. Cheggour and D.P. Hampshire, "The effect of Hot Isostatic Pressing on the strain tolerance of the critical current density found in Modified Jelly Roll Nb_3Sn wires", (1998 Applied Superconductivity Conference, Palm Desert, CA, USA, September 13-18, 1998), *IEEE Transactions on Applied Superconductivity*, June 1999, vol.9, (no.2, pt.2), p. 1447.

[6.2] R. Walpole, R. Myers and S. Myers, "Probability and statistics for engineers and scientists, 6th Ed.", Prentice Hall, New Jersey, 1998.

[6.3] R. Scanlan and D. Dietderich, private communication.

[6.4] M. Hansen, "Constitution of binary alloys", McGraw-Hill, New York, 1958.

[6.5] R.P. Elliott, "Constitution of binary alloys, first supplement", McGraw-Hill, New York, 1965.

[6.6] J.D. Livingston, "Metallurgy of bronze-process A-15 superconducting composites", GE Technical Information Series Note 78CRD140, GE Corporate R&D, 1978.

[6.7] R.C. Weast, Chemical Rubber Company, "CRC Handbook of Chemistry and Physic", Boca Raton, Florida, CRC Press, 65th Edition, 1984-1985.

[6.8] D. Dietderich, private communication.

[6.9] Y.S. Hascicek, M.J. Goringe, "Effects of HIPping on bronze-processed multi-filamentary Nb_3Sn wires and magnets", Cryogenics, 1992, vol. 32 (no.3) 323-6.

[6.10] E. Gregory, private communication.

[6.11] J.D. Klein, G. Warshaw, N. Dudziak, S.F. Cogan and R.M. Rose, "On the suppression of Kirkendall porosity in multi-filamentary superconducting composites", *IEEE Transactions on Magnetics*, Vol.MAG-17, No.1, Jan. 1981, 380-2.

Chapter 7 Fiber-optic stress and strain measurement at low temperature

[7.1] G. Keiser, "Optical fiber communications", McGraw-Hill series in electrical engineering. Communications and information theory, New York, McGraw-Hill, 1983.

[7.2] L. B. Jeunhomme**, "**Single-mode fiber optics : principles and applications", 2nd ed., New York, Marcel Dekker, 1990.

[7.3] R.O. Claus, K.D.Bennet, A.M. Vengsarkar and K.A. Murphy, "Embedded optical fiber sensors for materials evaluation", *Journal of Nondestructive Evaluation*, Vol.8, No.2, 1989.

[7.4] E. Hecht and A. Zajac, "Optics", Reading, Mass., Addison-Wesley Pub. Co., 1974, p.262

[7.5] P. Roychaudhuri, M.R. Shenoy, and B.P. Pal, "Flame-fused optical fiber directional couplers fabrication and automated process control", *IETE Journal of Research*, vol.43, (no.6), Instn. Electron. & Telecommun. Eng, Nov.-Dec. 1997. p.433-8.

[7.6] R.E. Bolz,; G.L. Tuve, , Chemical Rubber Company, "CRC handbook of tables for applied engineering science", Boca Raton, Florida, CRC Press, 1973. 2d ed. 1973, p. 163.

[7.7] T.A. Tran, W.V. Miller III, K.A. Murphy, A.M. Vengsarkar, and R.O. Claus, "Stabilized extrinsic fiber-optic Fizeau sensor for surface acoustic wave detection", *Journal of Lightwave Technology*, vol.10, (no.10), Oct. 1992, p.1499-506.

[7.8] Stycast 2850FT alumina filled epoxy, Emerson and Cuming, Inc., Woburn, MA, USA.

[7.9] B.R. Fogg, A. Wang, M.S. Miller, K.A. Murphy and R.O. Claus, "Optical fiber sensor for absolute measurement", in Fiber Optic Sensor-Based Smart Materials and Structures, Ed. R.O. Claus, Papers Presented at the Fifth Annual Smart Materials and Structures Workshop, Blacksburg, VA, USA, 15-16 April 1992, Bristol, UK, IOP Publishing, 1992. p.51-4.

[7.10] K.A. Murphy, M.F. Gunther, A.M. Vengsarkar and R.O. Claus, "Quadrature phase-shifted, extrinsic Fabry-Perot optical fiber sensors", Optics Letters, vol.16, (no.4), 15 feb. 1991. p.273-5.

[7.11] G. Keiser, "Optical fiber communications", McGraw-Hill series in electrical engineering. Communications and information theory, New York, McGraw-Hill, 1983.

[7.12] M. Born, E. Wolf, "Principles of optics: electromagnetic theory of propagation, interference and diffraction of light", Oxford, New York , Pergamon Press, 1980. 6th ed.

Chapter 8 Stress and strain measurements in the accelerator dipole model magnet

[8.1] CTD-101 thermal expansion internal note, from Composite Technologies Development, Lafayette, Colorado, USA, http://www.ctd-materials.com.

[8.2] D. Dell'Orco, R.M. Scanlan and C.E. Taylor, "Design of the Nb_3Sn dipole D20," *IEEE Transactions on Applied Superconductivity*, vol. 3, March 1993, pp. 82-86.

[8.3] D. Dell'Orco, R.M. Scanlan, C.E. Taylor, A. Lietzke, S. Caspi, J.M. van Oort and A.D. McInturff, "Fabrication and component testing results for a Nb_3Sn dipole magnet", *IEEE Transactions on*

Applied Superconductivity, vol.5, (no.2, pt.1), (1994 Applied Superconductivity Conference, Boston, MA, USA, 16-21), Oct. 1994.

[8.4] J.M. van Oort, "Experimental determination of the cookie section integrated thermal contraction in the longitudinal direction from 293 K to 77 K", SC-MAG 567 (LBNL Internal Note).

[8.5] D.B. Chelton and D.B. Mann, "Cryogenic data book", NBS Cryogenic Engineering Laboratory, Boulder CO, May 15, 1956 (or UCRL-3421).

[8.6] D. Dell'Orco, FEA models showing stress concentrations, private communication and analysis notes, LBNL, Berkeley, CA, USA.

[8.7] Lakeshore Cernox temperature sensors, from Lake Shore Cryotronics, Westerville, OH, USA, www.lakeshore.com.

[8.8] Stycast 2850FT alumina filled epoxy, Emerson and Cuming, Inc., Edison, NJ, USA, http://www.emersoncuming.com.

[8.9] Plastic sleeve single-mode fiber-optic ST-connectors, Data Path Inc., Hauppauge, NY, USA., http://www.connectworld.net/datapath/dat4.html.

[8.10] Roark's formulas for stress and strain, W.C. Young, 6th Ed., McGraw-Hill, Inc. New York, 1989, p.104.

[8.11] D.B. Chelton and D.B. Mann, "Cryogenic data book", NBS Cryogenic Engineering Laboratory, Boulder CO, May 15, 1956 (or UCRL-3421).

[8.12] J.M. van Oort, internal laboratory notes, LBNL, Berkeley, CA, USA.

[8.13] Micro-Measurements resistive strain gauges, Measurements Group Inc., Raleigh, NC, USA, http://www.measurementsgroup.com.

[8.14] Micro-Measurements tech note TN-507, Measurements Group Inc., Raleigh, NC, USA, http://www.measurementsgroup.com.

[8.15] Materials testing System, from MTS Systems Corporation, Eden Prairie, MN, USA, http://www.mts.com.

[8.16] J.M. van Oort, internal laboratory notes, LBNL, Berkeley, CA, USA.

[8.17] J.M. van Oort, internal laboratory notes, LBNL, Berkeley, CA, USA.

[8.18] H. Tsui, internal laboratory notes, LBNL, Berkeley, CA, USA.

[8.19] Fuji pressure measuring film, "Fuji Prescale Film", Fuji Photo Film Co., Ltd., from Sensor Products, New Jersey, USA, http://www.sensorprod.com.

[8.20] J.M. van Oort, internal laboratory notes on ANSYS models and calibration check of the mid-plane sensors and beam stiffness, LBNL, Berkeley, CA, USA.

[8.21] D. Dell'Orco, private communication.

[8.22] A.F. Lietzke, R. Benjegerdes, S. Caspi, D. Dell'Orco, W. Harnden, A.D. McInturff, M. Morrison, R.M. Scanlan, C.E. Taylor and J.M. van Oort, " Test results for a Nb_3Sn dipole magnet", *IEEE Transactions on Applied Superconductivity*, vol.7, (no.2, pt.1), (1996 Applied Superconductivity Conference, Pittsburgh, PA, USA, 25-30 Aug. 1996.) IEEE, June 1997. p.739-42.

[8.23] W. Nah, A. Akhmetov, M. Anarella, R Bossert, T. Bush and others, "Quench characteristics of 5-cm-aperture, 15-m-long SSC dipole magnet prototypes", (1992 Applied Superconductivity Conference, Chicago, IL, USA, 23-28 Aug. 1992), *IEEE Transactions on Applied Superconductivity*, March 1993, vol.3, (no.1, pt.2), p. 658-61.

[8.24] D. Leroy, J. Krzywinski, L. Oberli, R. Perin, F. Rodriguez-Mateos, A. Verweij and L. Walckiers, "Test results on 10 T LHC superconducting one metre long dipole models", (1992 Applied Superconductivity Conference, Chicago, IL, USA, 23-28 Aug. 1992), *IEEE Transactions on Applied Superconductivity*, March 1993, vol.3, (no.1, pt.2), p. 614-21.

[8.25] A. den Ouden, S. Wessel, E. Krooshoop and H. ten Kate, "Application of Nb_3Sn superconductors in high-field accelerator magnets", *IEEE Transactions on Applied Superconductivity*, vol.7, no.2, pt.1, (1996 Applied Superconductivity Conference, Pittsburgh, PA, USA, 25-30 Aug. 1996.), June 1997, p. 733-8.

[8.26] A.D. McInturff, R. Benjegerdes, P. Bish, S. Caspi, K. Chow, D. Dell'Orco, D. Dietderich, R. Hannaford, W. Harnden, H. Higley, A. Lietzke, L. Morrison, M. Morrison, R. Scanlan, J. Smithwick, C. Taylor, and J.M. van Oort, "Test results for a high field (13 T) Nb_3Sn dipole", Ed. M. Comyn, M.K. Craddock, M. Reiser, J. Thomson, (vol.3), (Proceedings of the 1997 Particle Accelerator Conference, Vancouver, BC, Canada, 12-16 May 1997.) Piscataway, NJ, USA, IEEE, 1998, vol.3, p. 3212-14.

[8.27] A.P. Verweij, "Electrodynamics of superconducting cables in accelerator magnets", Ph.D. Thesis, University of Twente, Universiteit Twente, Enschede, The Netherlands, 1995.

[8.28] J.M. van Oort, "Measurement traces from the high-speed fiber-optic scans showing quench initiators", internal laboratory notes, LBNL, Berkeley, CA, USA.

[8.29] D. Dell'Orco, R.M. Scanlan and C.E. Taylor, "Design of the Nb_3Sn dipole D20," *IEEE Transactions on Applied Superconductivity*, vol. 3, March 1993, pp. 82-86, and D. Dell'Orco, private communication.

[8.30] A.D. McInturff, private communication on further quench testing of the D20 magnet.

Nomenclature

Symbol	Description	Units
A	Area	m^2
A	Constant	-
A_{total}	Total area of all elements	m^2
a	Fiber core radius	m
a	Contact point width (wire to wire)	m
$\vec{A}$	Wave propagation vector	(Varied)
A_0	Wave amplitude	-
A_r	Reflector mirror reflection coefficient	-
A_s	Sensor mirror reflection coefficient	-
B	Constant	-
B	Magnetic induction (magnitude)	T
$\vec{B}$	Magnetic induction (vector)	T
B_x, B_y	Magnetic induction (x and y direction)	T
B_t	Magnetic induction (tangential direction)	T
b	Ratio of B/B_{c2}	-
b	Normalized propagation constant	-
b	Contact point width (wire to plate)	m
B_{c2}	Upper critical field	T
B_{c20}	Upper critical field at zero intrinsic strain	T
c	Speed of light in vacuum	ms^{-1}
C, C_0, C_1, C_2, C_3	Constants	(Varied)
C_p	Volume compaction factor	-
C_x	Cable x-compaction	-
$C_{x,edge}$	Corner strand x-compaction	-
C_{y1}	Minor edge y-compaction	-
C_{y2}	Major edge y-compaction	-
D, d	Strand diameter	m
d	Lattice constant	nm
d	Traveled length	m
D	Constant (3.20)	T
$[D]$	Stress-strain matrix	-
DMX	Maximum displacement (ANSYS)	m
e_i	Energy error (FEA)	
E	Electric field	Vm^{-1}
E	Elasticity or Young's modulus (isotropic)	Pa
E_x, E_y, E_z	Elasticity or Young's modulus (anisotropic, x, y and z)	Pa
E_{eff}	Effective Young's modulus	Pa
Epel, EPel	Elastic strain component	-
Eppl, EPpl	Plastic strain component	-
EPELEQV	Maximum equivalent elastic strain (ANSYS)	-
EPPLEQV	Maximum equivalent plastic strain (ANSYS)	-
F	Force (magnitude)	N
F_x, F_y	Force (x and y direction)	N
$\vec{F}$	Force (vector)	N
f	Frequency	Hz
f_{pl}	Multiplier function for I_c degradation	-
g_{tm}	Cable to mandrel thickness ratio	-

g_{wm}	Cable to mandrel width ratio	-
g_{wr}	Cable to roller width ratio	-
h	Height	m
H	Magnetic field	Am^{-1}
h_0	Minimum fiber core spacing	m
i	Integer counter	-
I, I_{in}, I_{out}	Current	A
$\vec{I}$	Current (vector)	A
I_c	Critical current	A
$I_c(0)$	Virgin critical current at zero pressure	A
$I_c(0\text{-}P\text{-}0)$	Permanently reduced critical current	A
$I_c(P)$	Critical current at pressure P	A
$I_{c,extr}$	Extracted strand critical current	A
$I_{c,m}$	Critical current as defined by the manufacturer	A
I_q	Quench current	A
j, j_q, j_0, J	Current density	Am^{-2}
$\vec{J}$	Current density (vector)	Am^{-2}
J_k	Bessel function of the first kind	-
j_c	Critical current density	Am^{-2}
k, k_1, k_2	Plane wave propagation constants	m^{-1}
$\vec{k}$	Wave propagation vector	m^{-1}
K_k	Modified Bessel function of the second kind	-
L, l	Length	m
L_c	Effective interaction length	m
L_p	Cable pitch length	m
m	Mass	kg
n	n-value, number of strands, parameter	-
n, n_1, n_2	Refractive index	-
N	Constant	-
NA	Optical fiber numerical aperture	-
NLSEPL	Plastic component of equivalent stress (ANSYS)	Pa
p	Momentum	$kgms^{-1}$
p	Parameter	-
p	Load per unit length	Pam^{-1}
P	Pressure	Pa
P_0	Coupler input power	W
P_c	2x2 Coupler coupled power	W
P_{hyd}	Hydrostatic pressure	Pa
P_{max}	Maximum pressure over time	Pa
P_t	2x2 Coupler transmitted power	W
q	Charge	C
q	Parameter	-
$\vec{r}$	Position (vector)	m
R, r, r_1, r_2	Radius	m
R	Radius of curvature	m
r_c	Radius (cylinder)	m
r_c	Correlation coefficient	-
R_{max}	Maximum radius of filamentary area in a strand	m
s	Distance (between center of two cylinders)	m
s_t	Free vertical cabling space ratio	-
s_w	Free horizontal cabling space ratio	-
S_x, S_y	Horizontal and transverse stress (in FEA print-out)	Pa
Sel	Elastic stress component	Pa
SEQV, Seqv	Equivalent or Von Mises stress (ANSYS)	Pa

SMN, SMNB	Minimum stress (element, nodal minimum) (ANSYS)	Pa
SMX, SMXB	Maximum stress (element, nodal maximum) (ANSYS)	Pa
Spl	Plastic stress component	Pa
T	Temperature	K
t	Ratio of T/T_c	-
t	Glass-air interface transmission coefficient	-
t_1	Minor edge thickness	m
t_2	Major edge thickness	m
t_{ave}	Average cable thickness	m
T_c	Critical temperature	K
T_m	Mandrel thickness	m
u	Displacement (magnitude)	m
u_x, u_y, u_z	Displacement (x, y and z direction)	m
$\vec{u}$	Displacement (vector)	m
u	Relativistic velocity	ms^{-1}
U	Voltage	V
U_c	Critical voltage	V
U_{en}	Strain energy (FEA)	J
U_r	Reflector mirror reflection amplitude	-
U_s	Sensor mirror reflection amplitude	-
v	Velocity	ms^{-1}
n	Speed of light in a medium	ms^{-1}
V	Volume	m^3
V	Normalized frequency	-
w	Width, cable width	m
W_m	Mandrel width	m
W_r	Roller width	m
$\vec{x}$	Position vector	m
x, y, z	Carthesian coordinates	-
x_c	Distance from center of optical fiber	m
y	Displacement	m
$\vec{z}$	Complex vector $x + iy$	m

Greek symbol	**Description**	**Units**
a	Thermal expansion coefficient	K^{-1}
b	Wave propagation constant (z-component)	m^{-1}
b	Rotation angle	deg
e	Strain	-
e_0	Intrinsic strain (wire)	-
e_1, e_2, e_3	Principal strain components	-
e_{dev}	Deviatoric strain	-
e_{diag}	Product of principal strain components	-
$e_{el,eqv}$	Elastic equivalent strain	-
e_{eqv}	Von Mises or equivalent strain	-
e_{hyd}	Hydrostatic strain	-
e_{max}	Maximum strain	-
$e_{pl,eqv}$	Plastic equivalent strain	-
j	Keystone angle	deg
j_1, j_2	Angle to normal (incident/refracted)	deg
j_r	Reflector mirror phase	deg
j_s	Sensor mirror phase	deg
g	Parameter	-

q_1, q_2	Angle to boundary (reflected/refracted)	deg
q, q_1, q_2	Angle	deg
k	Ginzburg-Landau parameter	-
l	Wavelength	m
m_0	Permeability of vacuum	Hm^{-1}
n, n_{xy}	Poisson's ratio	-
n	Parameter	-
r	Resistivity	Ωm
s	Stress	Pa
$\vec{s}$	Stress (vector)	Pa
s_1, s_2, s_3	Principal stress components	Pa
s_c	Maximum (contact) stress	Pa
s_{elast}	Elastic stress component	Pa
s_{dev}	Deviatoric stress component	Pa
s_{eqv}	Equivalent or Von Mises stress	Pa
s_{hyd}	Hydrostatic stress component	Pa
s_c	Contact stress, stress in y-direction	Pa
$\vec{s}_n^{\,i}$	Stress vector at node *n* of element *i*	Pa
$\vec{s}_n^{\,a}$	Averaged stress vector at node *n*	Pa
x	Verdet number	$degT^{-1}m^{-1}$
w	Angular velocity	$degs^{-1}$

Samenvatting – Summary in Dutch

Teneinde steeds kleinere afstanden te kunnen bestuderen hebben hoge-energie fysici behoefte aan versnellers met steeds hogere botsingsenergie. Hierdoor wordt de behoefte aan magneten met een veld hoger dan 10 T steeds groter.

Om magnetische velden boven de 10 T te bereiken is het gebruik van Nb_3Sn, in plaats van NbTi, een noodzaak. Nb_3Sn is net als andere supergeleiders in de A15 klasse materialen bros.

Dit proefschrift behandelt verschillende aspecten van de ontwikkeling van een 13 T Nb_3Sn model versneller dipool-magneet. De succesvolle werking van dergelijke magneten vereist een grondige kennis van de gevoeligheid van de Nb_3Sn supergeleider voor spanning en druk, en een gedetailleerde meting van de spanning en druk in de windingen van de magneet.

Volgende generatie versnellers: naar hoog veld dipool-magneten

De verhoging van de versneller energie van toekomstige hadron versnellers naar 100 TeV geeft een sterke impuls aan onderzoek naar de eigenschappen van supergeleidende materiaalen in velden hoger dan 10 T. Het werkpaard van de supergeleidende magneetindustrie is momenteel het goed vervormbare NbTi. Dit materiaal heeft een kritiek veld van ongeveer 10.8 T bij 4.2 K en 11.5 T bij 1.8 K. Het gebruik van NbTi in hoog-veld magneten is in de praktijk gelimiteerd tot een veld van ongeveer 9 T. De meerderheid van versneller dipool-magneten zijn gemaakt van NbTi en opereren in velden tot 8.4 T.

Tenzij zeer grote versneller ringen worden ontworpen, zoals de Eloisatron met een lengte van 355 km [1.1] zijn dipool-magneten met een veld tussen 10-12 T vereist. Magneten van dergelijke veldsterkte zijn ook potentiele kandidaten voor energie-verdubbelaars in de LHC (momenteel onder constructie, met een dipool-sterkte van 8.4 T en een lengte van 27 km), en andere voorgestelde versnellers zoals muon versnellers en 100 TeV versnellers (VLHC).

De nadruk op de vereiste maximale velden ligt ruimschoots onder 10 T in de grootschalige projecten die momenteel uitgevoerd worden (LHC, Tevatron modernisering). Hierdoor raakte het onderzoek naar Nb_3Sn op de achtergrond. Dit materiaal is namelijk interessanter voor velden hoger dan 10-11 T, waar NbTi ontoereikend is. Desalniettemin is er veel vooruitgang geboekt in onderzoek naar zowel NbTi and Nb_3Sn, met als resultaat een toename van de kritieke stroom-dichtheid in technische NbTi geleiders met een factor twee gedurende de periode 1985-1990 [1.2]. Het merendeel van het onderzoek naar Nb_3Sn is gericht op een toename van de kritieke stroom door middel van verbeteringen in het fabricage-proces, en de toevoeging van kunstmatige pinning-centra. De kritieke stroom als functie van druk en spanning in bulk materiaal en draden is bestudeerd over de afgelopen 20 jaar.

De grootste hindernis om 11-15 T te bereiken met Nb_3Sn wordt veroorzaakt doordat Nb_3Sn een bros materiaal is. De combinatie van zeer hoge druk (120-180 MPa), lage temperaturen (1.8-4.2 K) en hoog veld (11-15 T) maakt het ontwerp van Nb_3Sn dipool-magneten moeilijker.

Verscheidene onderzoeksgroepen over de wereld werken aan technische oplossingen voor Nb_3Sn versnellermagneten, die economisch verantwoord zijn voor gebruik in hoge energie deeltjesversnellers.
Onder deze groepen bevinden zich meerdere met grootschalige onderzoeksprogramma's, zoals CERN (Zwitserland), Fermi National Laboratory (VS), E.O. Lawrence Berkeley National Laboratory (VS) en de Universiteit Twente (Nederland).

Het werk beschreven in dit proefschrift is grotendeels uitgevoerd aan het E.O. Lawrence Berkeley National Laboratory en de Universiteit Twente, als een gezamenlijk onderzoeksprogramma.

Doel van het onderzoek

Het in dit proefschrift beschreven onderzoek volgt het ontwerp, de realisatie en de tests van de 13 T Nb_3Sn 1 meter model versneller dipool-magneet "D20" aan het E.O. Lawrence Berkeley National Laboratory (LBNL).

Tijdens de constructie en het bekrachtigen van supergeleidende dipool-magneten treden grote krachten en dientegevolge grote spanningen op in de spoelwikkelingen. Omdat de kritieke stroomdichtheid van Nb_3Sn afneemt met toenemende druk en spanning, is een grondige kennis van de gevoeligheid van Nb_3Sn voor druk en spanning essentieel voor een succesvolle werking van de magneet.

Grote verschillen in de gevoeligheid van het materiaal en de geleiders voor druk en spanning zijn beschreven in de literatuur. Deze verschillen worden toegeschreven aan de samenstelling van het materiaal, geometrie van de draad, warmtebehandeling, etc.

Dit proefschrift is geschreven met als doel om the kritieke stroomdichtheid van Nb_3Sn Rutherford kabels in versneller dipool-magneten te verbeteren, en om de verkregen kennis te gebruiken om het magneet- en kabel-ontwerp te optimalizeren voor minimale degradatie van de kritieke stroomdichtheid.

Wat is vereist

Voor een goed begrip van de eigenschappen van de kritieke stroomdichtheid in kabels in een magneet, is het onderzoek toegespitst op de volgende drie aspekten.

1) *De kritieke stroomdichtheid als functie van de dwarsdruk op de kabel.*
   Grote verschillen zijn gevonden in de gevoeligheid, zelfs voor proefstukken van identiek materiaal en draadgeometrie. Om dit gedrag nader te onderzoeken is een systematische studie van de kritieke stroomdichtheid als functie van de druk in Nb_3Sn kabels vereist.
2) *De microstructuur van de draad in een kabel.*
   Om de oorzaak van de verschillen in gedrag van kabelproefstukken, die geometrisch identiek zijn, maar gemaakt van verschillende draden, te bepalen, is een nauwkeurige analyse van de microstructuur voor en na drukken nodig.
3) *De druk en spanningsverdeling in de spoelwikkeling.*
   De volgende stap is het bepalen van de werkelijke druk en spanning waaraan de kabels zijn blootgesteld in de spoelwikkeling in de magneet. Nauwkeurige metingen van de lokale druk en spanning in de magneet zijn noodzakelijk, inclusief een meting van de drukgradienten op de poolvlakken en horizontale vlakken van de magneet.

Experimentele aanpak

Om de hierboven genoemde gebieden nader te onderzoeken zijn de volgende experimenten uitgevoerd:

1) *Meting van de kritieke stroomdichtheid*
   De methodes gebruikt in dit proefschift zijn kritieke stroom metingen aan draden, draadstukken genomen uit een kabel, en korte proefstukken van kabels. De experimenten aan draden zijn uitgevoerd aan LBNL (VS); de kabelmetingen zijn gedaan aan de Universiteit Twente.
2) *Analyse van de microstructuur*
   Deze analyse is uitgevoerd door middel van foto's genomen met een electronen-microscoop (SEM), in combinatie met eindige elementen modellen van de microstructuur. De SEM foto's zijn gemaakt voor en na de kabelexperimenten; ter vergelijking zijn stukken genomen uit belaste en onbelaste delen van de kabel.
   Eindige elementen modellen zijn gemaakt in ANSYS van de magneet, de kabelgeometrie in het experiment, de structuur van de kabel, de structuur van de draad, en als laatste de microstructuur in het deel van de draad waar de filamenten zich bevinden.

3) Druk en spanningsmetingen in de wikkelingen

Een gedetailleerd onderzoek naar de verdeling van druk en spanning is nodig voor een nauwkeurige voorspelling van de prestatie van een magneet, waarin de druk in de wikkelingen dermate groot is dat degradatie van de kritieke stroom optreedt.

Tot op heden worden deze druk en spanningsverdelingen alleen berekend met eindige elementen modellen. In enkele gevallen werden metingen gedaan met grote sensoren (over de volle breedte van de kabels, met een lengte van enkele centimeters) in speciale mechanische modellen.

Een nieuwe techniek voor druk en spanningsmetingen, met verbeterde precisie en ruimtelijke resolutie, is ontworpen, getest, en gebruikt in de magneet. De methode maakt gebruik van direct ingelijmde fiber-optische interferometers als sensors. Ter verificatie van hun werking zijn de fiber-optische sensoren in het mechanische model van de magneet geplaatst naast electrische sensoren.

Conclusies van het onderzoek

Een lineair elastisch verplaatsingsmodel kan gebruikt worden om de effectieve elasticiteitsmodulus van een kabel, die gedomineerd wordt door het materiaal van de strand (droge kabel of geimpregneerd met een lage sterkte epoxy), te bepalen. Voor een typische draad met E = 117 GPa, de effective elasticiteitsmodulus E_{eff} kan varieren van 20 GPa zonder druk tot 30 GPa bij 150 MPa dwarsdruk.

Dit betekent dat een pre-compressie stap van de wikkelingen voor de assemblage van de magneet vereist kan zijn om voldoende voorspanning te garanderen.

Om de totale spanning in de filamenten te verminderen verdient een matrix materiaal met een hogere elasticiteitsmodulus (stijver) de voorkeur boven een zachter materiaal (zoals koper) met een lagere reksterkte. De effectieve elasticiteitsmodulus wordt hierdoor eveneens verhoogd. Een kabel met een epoxy met een hogere elasticiteitsmodulus vertoont een lagere degradatie onder dwarsdruk.

Een stijver materiaal veroorzaakt een hogere druk, maar minder deformatie, hetgeen de hoeveelheid permanente schade aan het Nb_3Sn onder hoge druk beperkt.

De lokale druk in de bovenste laag van draden in de kritieke stroomdichtheids degradatie experimenten kan tot 34 % hoger zijn dan de gemiddelde dwarsdruk, aangezien druk-concentraties aanwezig zijn op de hoeken van het drukblok van de meetopstelling.

Dit betekent dat de metingen van de degradatie van de kritieke stroomdichtheid niet noodzakelijk representatief zijn voor de werkelijke druk op de kabel in een magneet. Metingen van de kritieke stroomdichtheid hebben mogelijk een lokale hogere druk dan de gemiddelde druk.

De reversibele en permanente degradatie van de stroomdichtheid kunnen voorspeld worden met een model gebaseerd op onafhankelijke relaties voor de plastische deformatie en de elastische druk. De permanente degradatie wordt bepaald door de mate van plastische deformatie van de draden in de kabel.

Separatie van de twee variabelen maakt het gebruik van eindige elementen modellen mogelijk om de invloed van de kabelgeometrie en experimentele procedure te elimineren. Deze modellen worden gebruikt om de kritieke stroomdichtheid als functie van de dwarsdruk te voorspellen. De selectie van het correcte eindige elementen model is gebaseerd op de kwaliteit van de impregnatie van de kabel.

In de MJR geleider kan de gemiddelde druk in de filament-bundels tot 13-15 % hoger zijn dan de dwarsdruk. Voor de IT geleider bedraagt dit 1 %. De lokale druk in de concentraties neemt toe met toenemende elasticiteitsmodulus van het Nb_3Sn. In de filament-bundels zonder holtes kunnen druk-concentraties tot 140 % optreden voor de MJR geleider en 190 % voor de IT geleider. Voor de PIT geleider is de interne druk niet hoger dan de aangebrachte dwarsdruk.

De rangorde van de drie geleidertypes met betrekking tot toenemende gevoeligheid voor dwarsdruk door druk-concentraties is PIT, MJR en IT.

De maximale druk in the filament-bundels het dichtst bij het centrum van de draad is 10 % hoger (vergeleken met de al aanwezige druk-concentraties) dan de druk in the filament-bundels gelegen in de buitenste regio van de draad. Als er holtes aanwezig zijn in de filament-bundels, kunnen er druk-concentraties optreden tot 480 % voor de MJR-geleider, 430 % voor de IT geleider, en 210 % voor de PIT geleider. De locatie van de druk-concentraties in de filament-bundels valt samen met de locatie waar de meeste structurele schade is gevonden in electronen-microscoop foto’s van de doorsnede van de draad.

De combinatie van deze twee conclusies leidt tot een aanbeveling om de vorming van holtes in de filament-bundels dichtbij het centrum van de draad te vermijden, aangezien dit kan resulteren in verhoogde druk-concentraties.

De preferentiële locatie van de holtes, als ze niet kunnen worden vermeden, is ofwel in het centrum van de filament-bundel, of geheel buiten de regio van de filamenten. Een grote ronde holte in het centrum van de filament-bundel is het ideale geval, aangezien de locale drievoudige druk-concentratie snel afvalt met toenemende straal, waardoor de regio van de filamenten niet erg sterk wordt beinvloed. *Deze locatie van de holtes is te prefereren voor de IT geleider.*

Het andere preferentiële geval zijn holtes die ontstaan in de buitenste koperen regio om de filamenten, dicht bij de niobium of niobium-tantaal diffusie-barrière. Dit is niet mogelijk voor de IT methode, aangezien de individuele elementen geen diffusie-barrière hebben. *Voor de MJR geleider is dit een mogelijkheid om hoge reversibele en irreversibele I_c degradatie te voorkomen.*

In zowel de IT als de MJR geleider kan de locatie van de holtes geoptimaliseerd worden door variatie van het initiele tin-gehalte in de filament-bundel.

De MJR en de IT geleider vertonen een vergelijkbare reversibele degradatie van de kritieke stroom onder druk. De PIT geleider is minder gevoelig wat betreft reversibele I_c degradatie.

De rangorde van de drie geleider-types voor minimale totale degradatie van de kritieke stroom is PIT, met een lagere gevoeligheid, voornamelijk veroorzaakt door een lagere initiele degradatie van de kritieke stroom (ongeveer 10 %), dan IT met identiek gedrag zonder holtes, gevolgd door MJR. Deze conclusie is alleen geldig voor het geval dat de metingen statistisch gezien correct zijn, en voldoende datapunten zijn gemeten.

Door een beperkt aantal proefstukken en de mogelijke invloed van verscheidene onbetrouwbare proefstukken op de resulterende vergelijkingen, zijn deze uiteindelijke quantitatief en statistich onvoldoende onderbouwd. Desalniettemin zijn alle metingen hier in z'n geheel gepresenteerd, aangezien dit de eerste keer is dat een systematische vergelijking is uitgevoerd met een dergelijke uitgebreide data-set. Tevens zijn trends in de metingen voldoende zichtbaar om op z'n minst een kwalitatieve uitspraak te kunnen maken over de verschillen in gevoeligheid.

De mogelijkheid dat draadstructuren zoals in de PIT geleider minder degradatie vertonen onder druk dan de MJR en IT geleiders bevestigt het belang van de optimalisatie van de interne structuur van de draad.

De resultaten van de microscopische studies wijzen naar de formatie van holtes als een mogelijke belangrijke oorzaak van de permanente degradatie van de kritieke stroom in de MJR en IT geleiders. De locatie van de beschadigde filamenten komt overeen met de verhoogde concentratie van de druk die gevonden is in de eindige elementen modellen van draden met holtes (zie hoofdstuk 4).

De combinatie van deze twee feiten suggereert dat door controle van de locatie van de holtes, of door totale eliminatie ervan, de gevoeligheid van Nb_3Sn draden voor druk verminderd kan worden.

De formatie van schuifvlakken, die potentieel aanzienlijke schade kunnen veroorzaken onder druk, is gevonden in de MJR geleider.

Dit betekent dat de deformatie van de draad tijdens de verkabeling beperkt moet worden om dit type beschadiging te voorkomen, hetgeen een bovengrens stelt aan de maximale keystone hoek van de kabel.

In verscheidene proefstukken zijn breukvlakken gevonden die veroorzaakt lijken te zijn door overmatige spanning in de longitudinale richting van het proefstuk van de kabel. Dit kan alleen worden veroorzaakt door een verschil in de thermische expansie coefficiënten van het proefstuk van de kabel en de houder, of in het geval van een magneet, tussen de wikkeling en de pool.

In de micro-foto's is duidelijk te zien dat grote zorg besteed moet worden aan een goede aansluiting van de verschillende materiaalen in de magneet, en in het bijzonder bij het opschalen van een relatief korte model magneet naar dipool-magneten met een grotere lengte.

Door de verhoogde druk die altijd geassocieerd is met hoog-veld dipool-magneten en de grote gevoeligheid van de Nb_3Sn supergeleider voor schade door overmatige druk en spanning, is een nauwkeurige bepaling van de druk en spanning in de spoelen van een magneet zeer belangrijk.

Door zijn geringe afmetingen en ongevoeligheid voor veranderingen in het magnetische veld is de Fabry-Perot fiber-optische sensor een geschikte kandidaat voor gebruik in een dergelijke omgeving vergeleken met andere interferometrische en op polarisatie gebaseerde meet-technieken.

De draad-wikkel techniek voor het aanbrengen van voorspanning is succesvol gebruikt in zowel een mechanisch model als in de magneet. De voordelen van de methode zijn de mogelijkheid om de draad af te wikkelen en de operatie verscheidene keren te herhalen in een ontwikkelingsfase van een project.

De draad-wikkel techniek is goed bruikbaar voor het aanbrengen van een extra voorspanning op de wikkeling om de reductie in voorspanning door de initiële lagere elasticiteits-modulus van de kabel te voorkomen.

De magneet heeft een centraal veld van 12.8 T bereikt bij een stroom van 6300 A bij 4.4 K. Dit correspondeert met 12.9 T bij 4.2 K (I = 6350 A). Bij 1.8 K, het maximale centrale veld is 13.5 T. Het voorspelde centrale veld is 12.2 T, gelimiteerd door de I_c van de buitenste wikkeling, en 12.5 T, gelimiteerd door de binnenste wikkeling gemaakt van IT geleider, bij 4.4 K.

Gebaseerd op de gemeten maximale druk van 180 MPa tijdens bedrijf en opwarming en de daarop volgende succesvolle operatie van de magneet, kan geconcludeerd worden dat de Nb_3Sn kabels in deze kritieke stadia niet gedegradeerd zijn.

Het feit dat de magneet een maximaal veld bereikt heeft dat hoger is dan de voorspelde waarde, gebaseerd op de experimenten voor kritieke stroomdichtheid als functie van druk, suggereert dat de kabel-onder-druk tests een te pessimistische waarde van de kritieke stroom opleveren.

De aangebrachtte voorspanning op de magneet is 29 % te laag, wat overeenkomt met het gereduceerde aantal draadwikkelingen op de structuur (18 in plaats van 25). Door de gereduceerde voorspanning vertoont de magneet een vrij significant trainingsgedrag tot 12.8 T. Een totaal aantal van 34 quenches was nodig om dit punt te bereiken.

Hoewel het ontwerp-veld uiteindelijk is bereikt, is het totaal aantal trainings-quenches te hoog om de magneet bruikbaar te maken voor toepassing in een versneller.

Het gebruik van fiber-optische sensoren in het horizontale middenvlak van de magneet is de eerste gepubliceerde toepassing van lokale spanningsmeting in de wikkeling. Een matrix voor meting van de dwarsdruk en longitudinale spanning is ontworpen en succesvol getest bij 293 K en 77 K in een experimentele opstelling. Een soortgelijke matrix, zonder de dwarsdruk sensoren, is succesvol gebruikt in de uiteindelijke spoelen.

Gebaseerd op de goede correlatie tussen de resistieve sensoren en de fiber-optische sensoren gemonteerd in de pool, is geconcludeerd dat de fiber-optische sensoren betrouwbaar zijn bij lage temperaturen.

De algemeen toegepaste ontwerpmethode voor versneller dipool-magneten, gewoonlijk gebaseerd op een cosinus-q doorsnede, beperkt de magneet-ontwerper. In het algemeen zijn alle optimalisatie-programmas, in gebruik door magneet-ontwerpers, geprogrammeerd om de optimale oplossing te vinden door minimalisatie van harmonische veld-verstoringen, terwijl ze tegelijk het dipool-veld maximalizeren. De optimalisatie functie is gebaseerd op $I_c = I_c(B)$, ofwel alleen gebaseerd op de kritieke stroom als functie van het lokale magnetische veld. Dit resulteert in een uitermate compact ontwerp. De combinatie van hoge stroom met een klein geleider-oppervlak produceert echter hoge druk in de geleider.

Een dergelijke ontwerp-filosofie is geschikt bij NbTi magneten, maar veroorzaakt problemen bij het ontwerp van Nb_3Sn dipool-magneten. Door de degradatie van de kritieke stroom in Nb_3Sn kabels onder hoge druk moet er rekening gehouden worden met de druk in de optimalisatie-functie. Het gebruik van een functie als $I_c = I_c(B,\sigma)$ produceert een meer realistische oplossing en mogelijk een hoger veld.

Door alle inherente problemen gerelateerd aan het gebruik van een cosinus-q ontwerp, is een onderzoek naar alternatieve magneet-ontwerpen voor hoog-veld dipool-magneten (B_y groter dan 13 T) verantwoord. Aangezien de gevoeligheid voor druk een cruciale rol speelt in het slagen of falen van een Nb_3Sn magneet, moet er bijzonder veel aandacht worden besteed aan de minimalisatie van de druk-concentraties en verschillen in materiaal-eigenschappen in de magneet.

Aangezien de krachten toenemen met het kwadraat van het veld, bereikt een optimaal cosinus-q ontwerp snel de maximale practische bovengrens van druk op de Nb_3Sn supergeleider. In het bijzonder, als hoekstukjes en wiggen van een verschillend materiaal gebruikt worden voor de optimalisatie van het veld, worden lokale druk-concentraties veroorzaakt door deze componenten. Ook kunnen druk-gradienten worden veroorzaakt door een kleine hoek in het middenvlak, zoals gevonden is in de drukmetingen in het mechanische model van de magneet. Een ontwerp opgebouwd uit blokvormige spoeldelen reduceert dergelijke druk-concentraties en gradienten.

Vanuit het standpunt van kabel-optimalisatie om de degradatie van de kritieke stroom te verminderen, verdient een constante optimale compactie-factor over de gehele kabel de voorkeur over een kabel met een schuine kant. Een blok-ontwerp magneet is hierdoor van nature meer geschikt voor een rechthoekige kabel vergeleken met een cosinus-*q* ontwerp.

Appendix A

Color figures

In this Appendix certain figures from the main text are reproduced in full color print. The selection of the figures, mainly depicting FEA models and results from chapters 3 and 4, is based on the loss of clarity of the figure in the main text, which is due to the gray-scale print. The figure numbers and captions correspond directly to the figures in the main text.

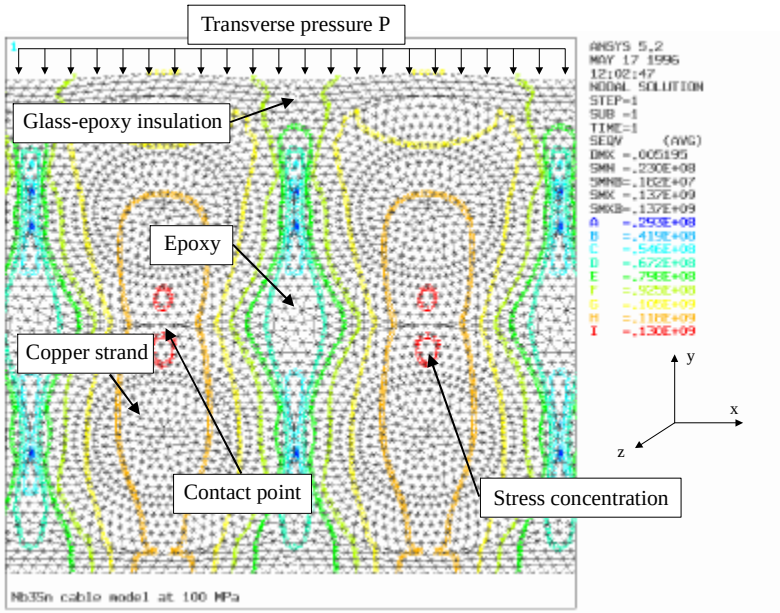

Figure 3.13 *Part of the cable cross-section model to calculate the stress distribution in the individual strands at 100 MPa transverse pressure in the y-direction on the top surface. The y-axis is along the transverse direction, the x-axis along the radial direction, the z-axis is along the length of the cable. Shown is the initial coarse mesh before refinement to reduce the model error level.*

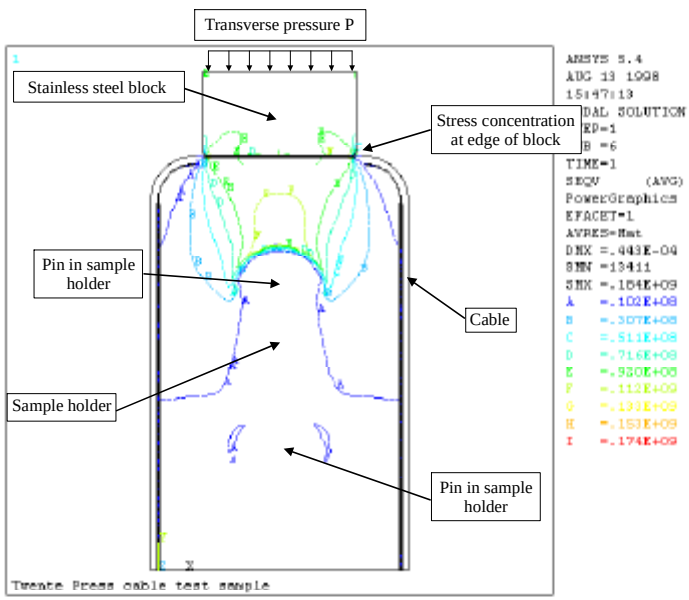

Figure 3.17 *The linear test sample model for the U-shape configuration in the critical current versus applied transverse pressure experiments. Shown is the Von Mises stress in the cable and sample holder for an applied stress of 100 MPa on the top surface of the pressure block.*

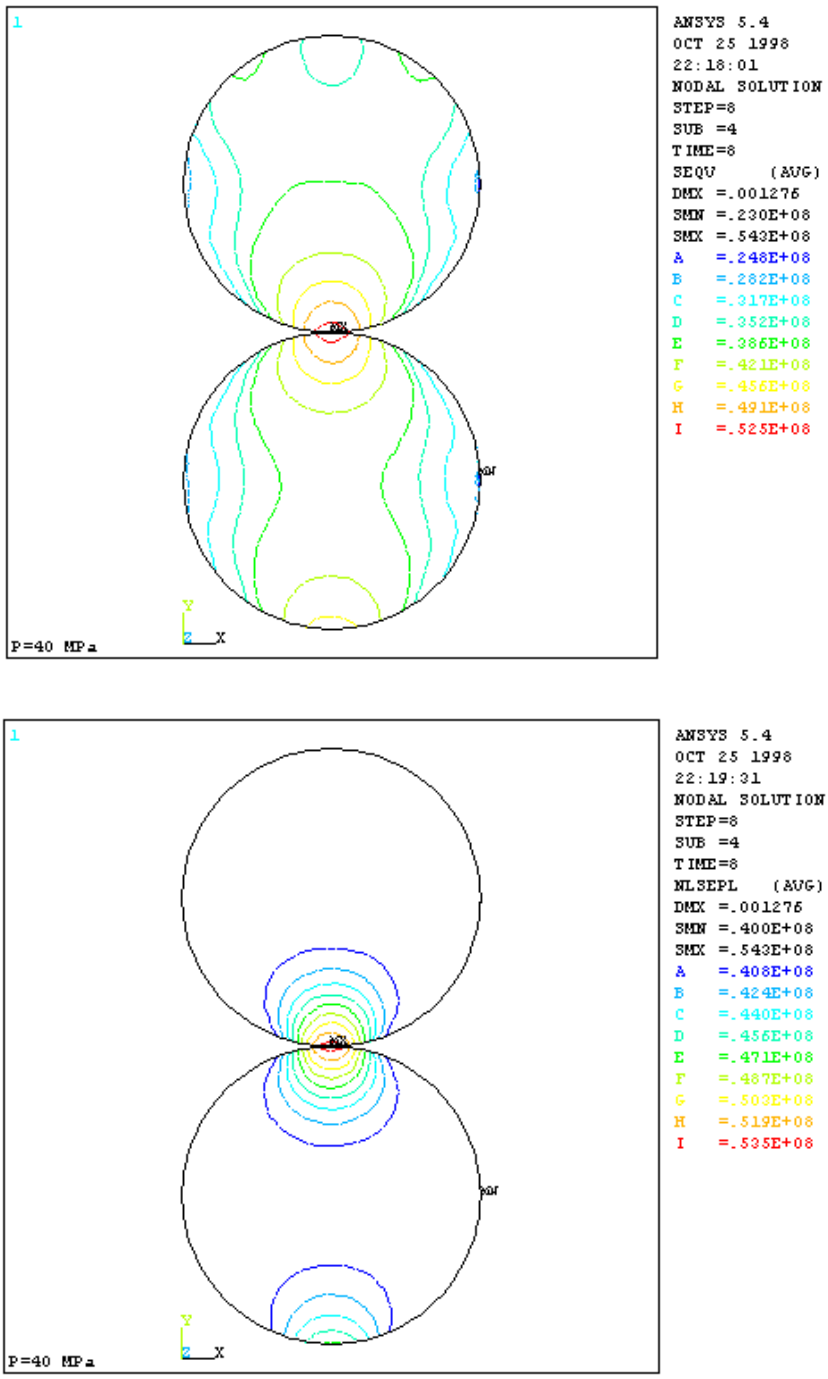

Figure 3.21 A plot of the elastic (top) and plastic (bottom) component of the Von Mises or equivalent stress in the strands for an applied transverse pressure of 40 MPa. The stress is the highest near the contact point of the strands. Note the onset of plastic deformation near the contact point for an applied transverse pressure equal to the yield stress of the strand material.

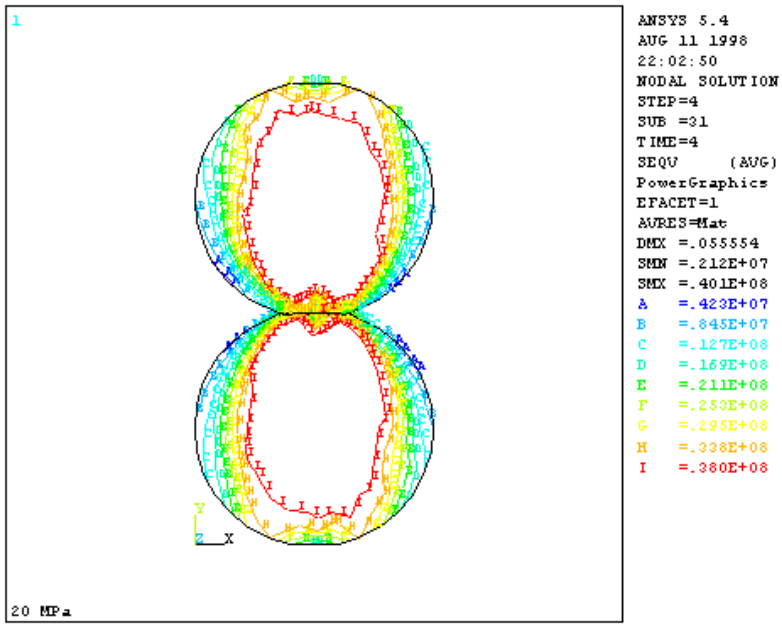

Figure 3.24 *The non-linear dry cable cross-section model to calculate the stress distribution in the individual strands for increasing transverse pressure on the top plate. The y-axis is along the transverse direction, the x-axis along the wide side of a cable. The applied pressure is 20 MPa.*

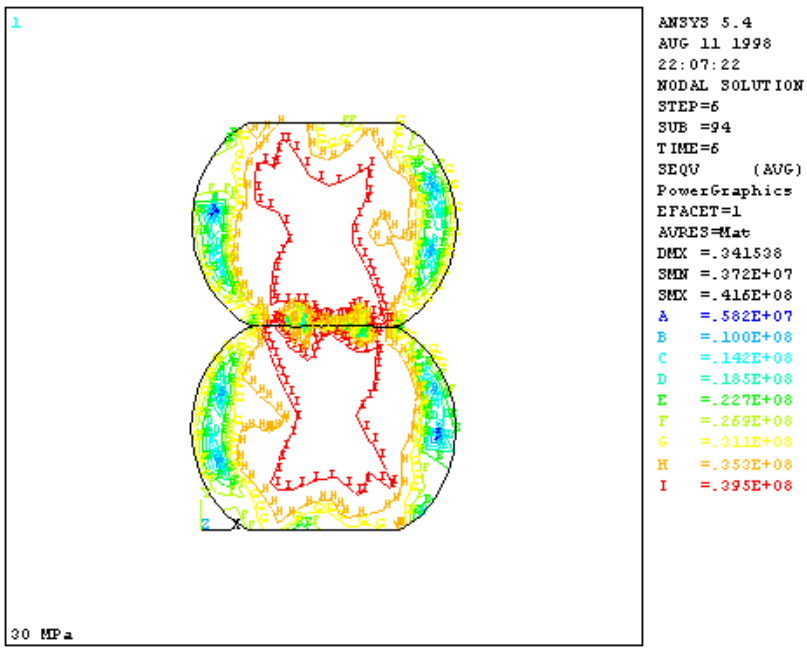

Figure 3.25 *The non-linear dry cable cross-section model at an applied pressure of 30 MPa.*

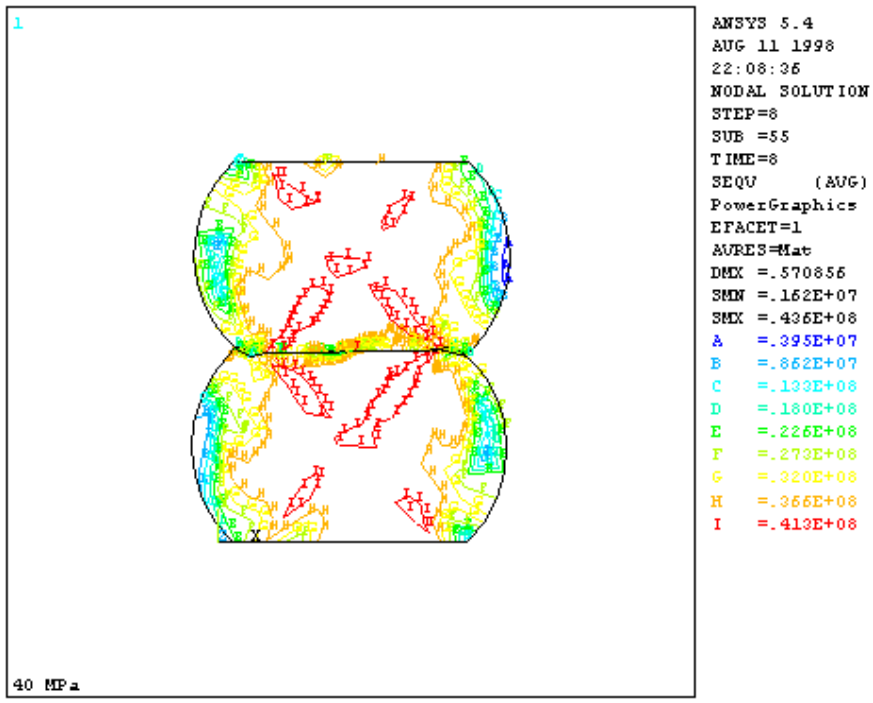

Figure 3.26 The non-linear dry cable cross-section model at an applied pressure of 40 MPa.

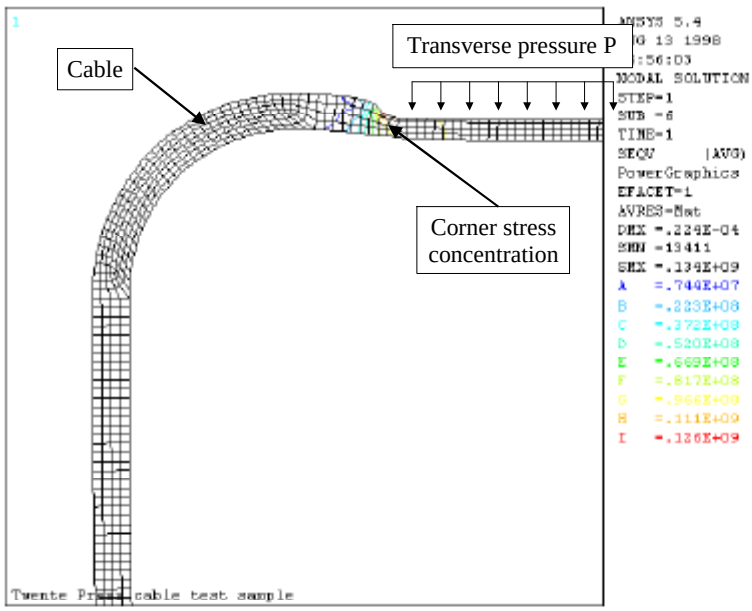

Figure 3.29 The corner area where the pressure block imprints on the cable enlarged. Shown is the Von Mises stress in the cable elements. The cable deformation is enlarged tenfold.

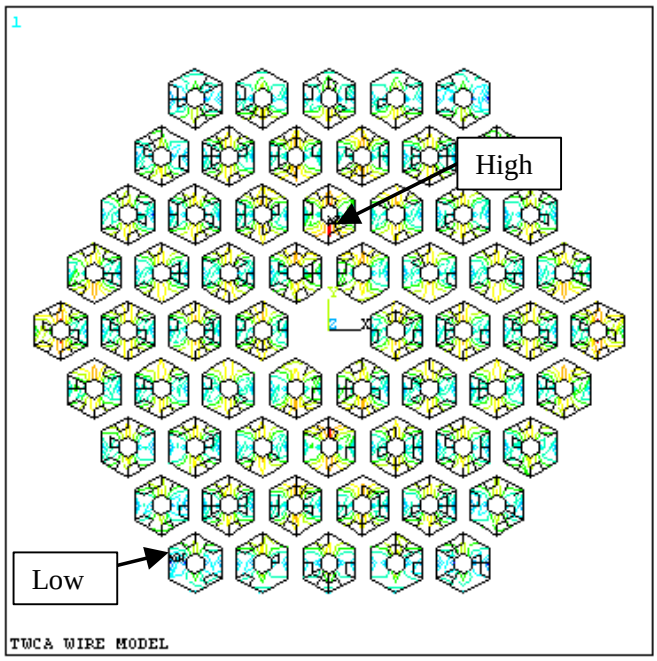

Figure 4.10 *Plot of the equivalent stress S_{eqv} (SQEV, in Pa) in the composite wire model. Material parameters are set for an MJR wire. Only the filament bundles are shown. The applied pressure is 100 MPa. The location of the minimum is indicated by the "low" marker (3 MPa), the maximum by the "high" marker (115 MPa).*

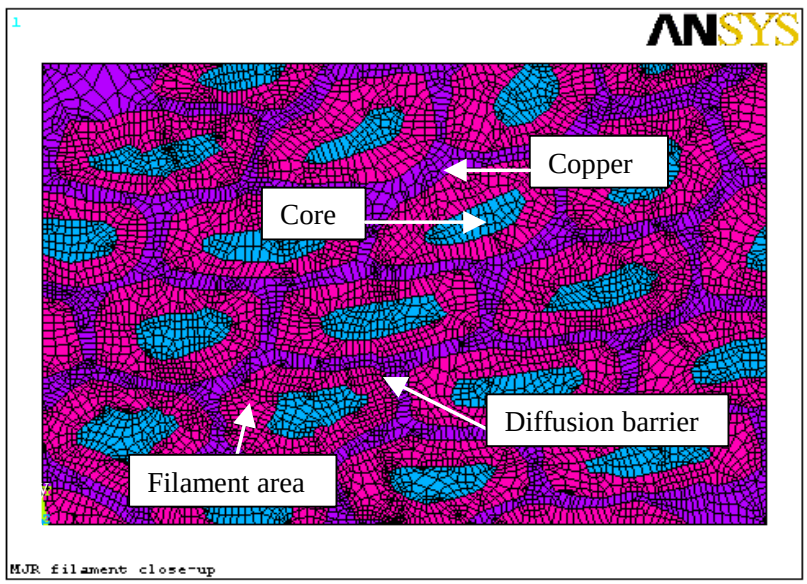

Figure 4.13 *MJR filament model. The x-axis is along the horizontal direction, the y-axis along the vertical direction. The loads are applied to the edges of the model.*

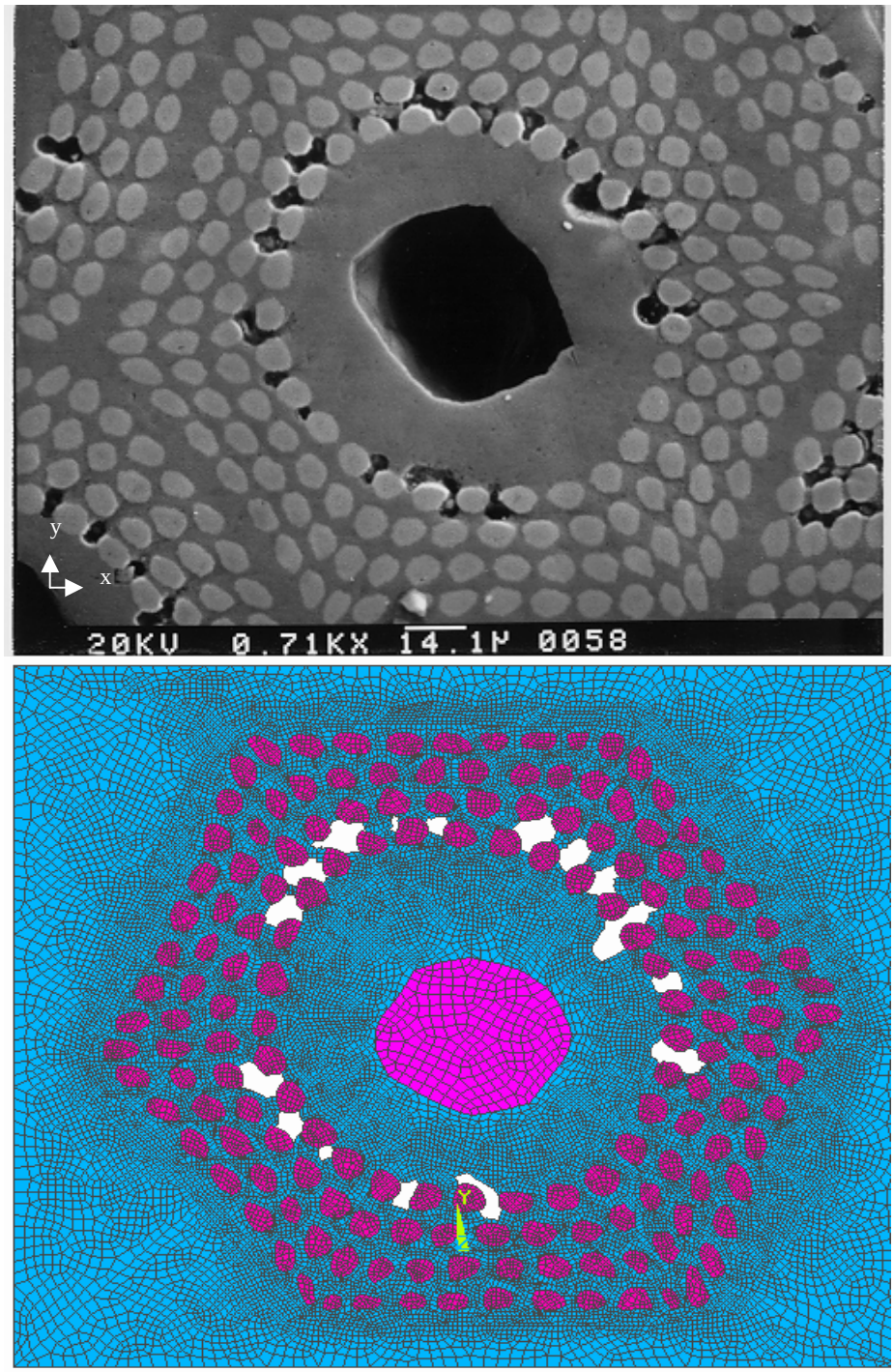

Figure 4.16 A filament bundle model in the Internal Tin conductor: the top figure shows a close-up of the voids. The bottom figure shows the resulting Finite Element Model.

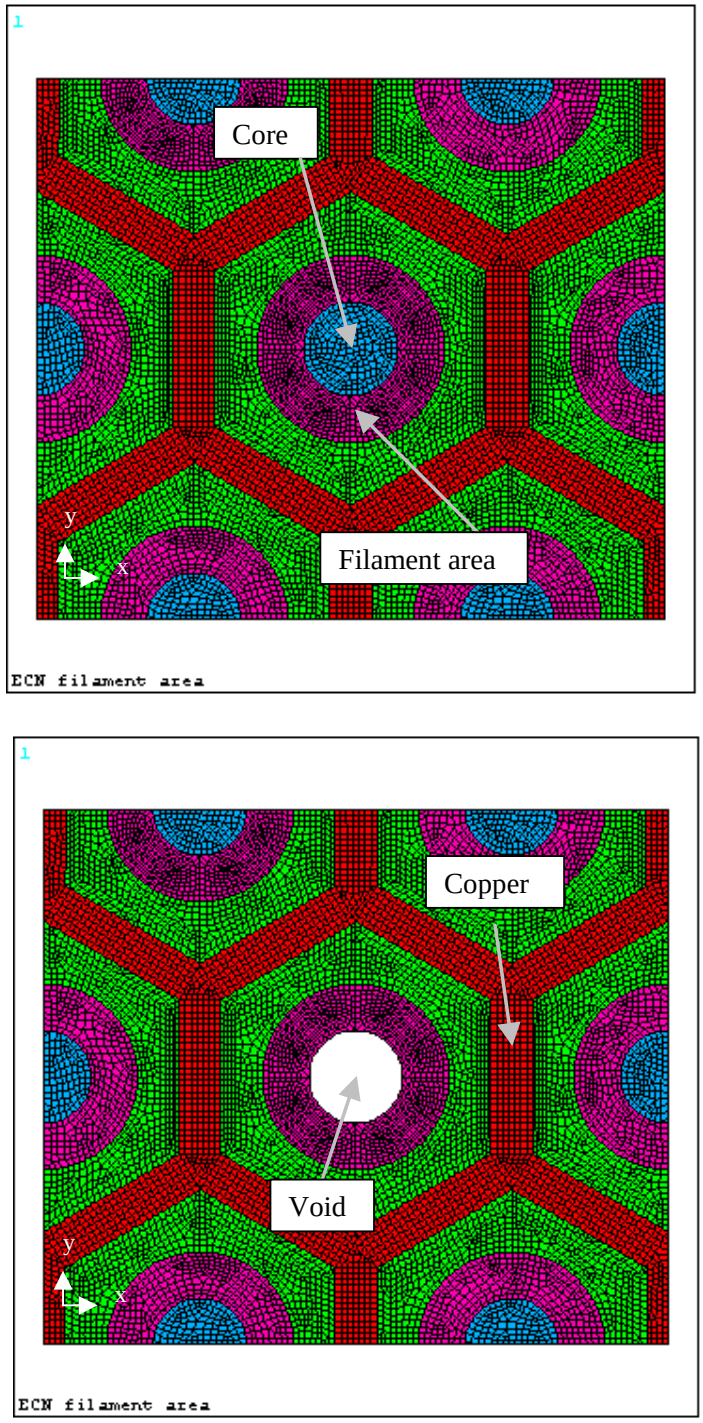

Figure 4.19 *PIT filament area model without void (top), and with void (bottom). Shown from the center outward are the filament core area, the Nb_3Sn region, the remaining niobium, and the copper matrix.*